INCOHERENT SCATTER

Theory, Practice and Science

Collection of lectures given in Cargese, Corsica, 1995.

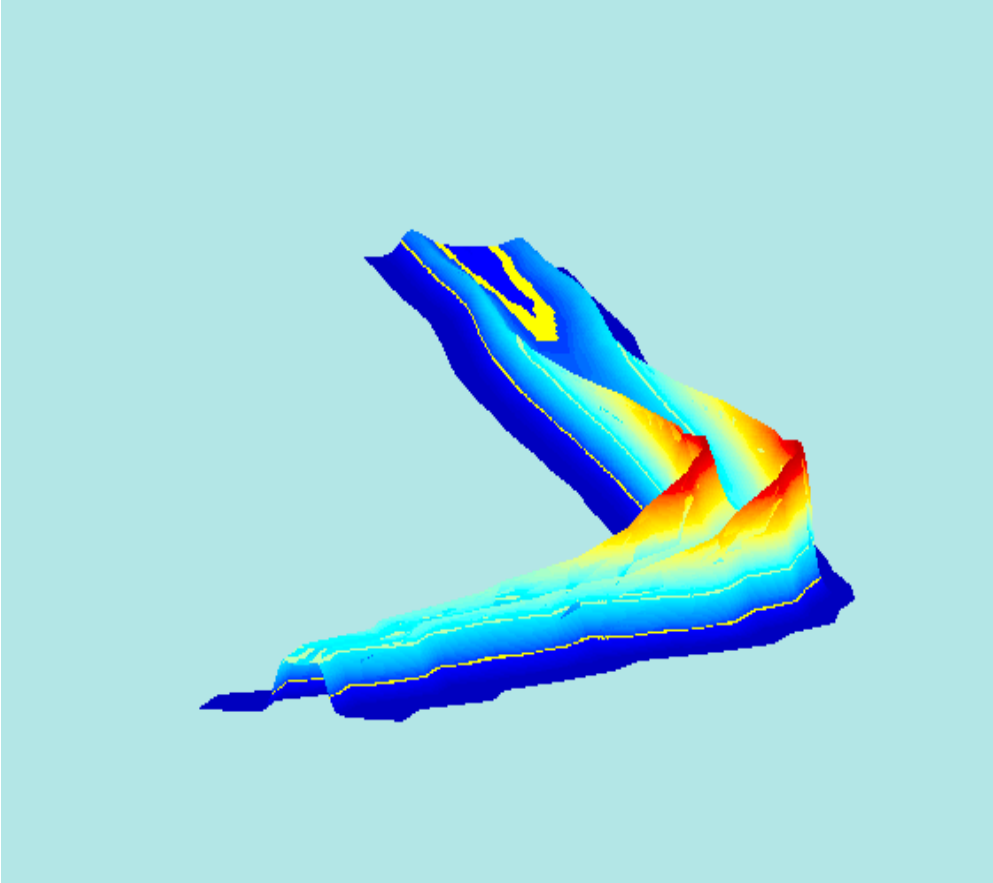

Incoherent Scatter spectra computed with a typical EISCAT observation of the ionosphere in the ~ 120 - 500 km altitude range. The spectra shape varies with the altitude as function of the observed electron temperature and of the ion temperature and composition. The spectral power is scaled to the electron density and the spectra are plotted along a line shape representing the altitude profile of the electron density.

Denis Alcaydé - Editor

Technical Report 97/53 - EISCAT Scientific Association
Printed version - November 1997
Electronic version – December 2001

Table of Contents

Vademecum:

Denis Alcaydé, Dr. (Editor) Denis.Alcayde@cesr.fr
Centre d'Etude Spatiale des Rayonnements
F-31028 Toulouse Cedex 4 - France

Tor Hagfors, Prof.: Hagfors@linmpi.mpg.de
Max Planck Institut für Aeronomie - Postfach 20
D-37189 Katlenburg-Lindau - Germany

Asko Huuskonen, Dr.: Asko.Huuskonen@fmi.fi
Finnish Meteorological Institute
Helsinki - Finland

Yoshuke Kamide, Dr.: Kamide@stelab.nagoya-u.ac.jp
Solar Terrestrial Environment Laboratory
Nagoya University - Toyogawa-Aichi 442 - Japan

Wlodek Kofman, Dr.: Wlodek.Kofman@Obs.ujf-grenoble.fr
Laboratoire de Planétologie de Grenoble
122 rue de la Houille Blanche - F-38041 - Grenoble - France

Markku Lehtinen, Dr.: Markku.Lehtinen@sgo.fi
Sodankylä Geophysical Observatory
University of Oulu - Sodankylä - Finland

Mike Lockwood, Prof.: M.Lockwood@rl.ac.uk
Rutherford Appleton Laboratory
Chilton-Didcot - OX11 0QX - UK

Arthur D. Richmond, Dr.: Richmond@ucar.edu
High Altitude Observatory - NCAR
Boulder - Colorado - 80307-3000 - USA

Jürgen Röttger, Dr.: Roettger@linmpi.mpg.de
Max Planck Institut für Aeronomie - Postfach 20
D-37189 Katlenburg-Lindau - Germany

Kristian Schlegel, Prof.: Schlegel@linmpi.mpg.de
Max Planck Institut für Aeronomie - Postfach 20
D-37189 Katlenburg-Lindau - Germany

Editor's Foreword

The idea of this book came with the necessity of organising an introductory series of lectures for welcoming the Japanese Scientists to the European Incoherent Scatter Association. Indeed, after nearly 15 years of EISCAT operations, incoherent scatter theory, technique, practice and science have significantly changed, new radars have been constructed (EISCAT-ESR) and are planned for the future (the Polar Cap Radar project). Thus, in conjunction with the VIIth EISCAT Workshop organised in Cargese (Corsica-France) in fall 1995, a series of lectures were invited and given before the Workshop holding: this book reflects most of these given lectures.

This book is intended for use by graduate students for entering the field of Incoherent Scatter Research; it is felt however (and also hoped) that the various chapters of this book can be of some interest for more senior scientists. The book organisation is such that one can find at the beginning the main theoretical aspects of the Incoherent Scattering, followed by practical considerations on signal modulation, echoes and data analysis, and then scientific application aspects:

- **the first two chapters deal with the theoretical descriptions of scattering of plasma waves by the ionospheric plasma; Chapter one (Tor Hagfors) describes the "classical" Incoherent Scattering, while Chapter two (Wlodek Kofman) introduces the non thermal and instabilities effects.**
- **in Chapter three (Asko Huuskonen and Markku Lehtinen) are introduced the basics of the modulation of the radio waves for pulsed radars. Once ionospheric echoes are received, some analysis can be made which lies upon some basic physics described in Chapter four (Kristian Schlegel).**
- **the Solar Wind Magnetosphere interaction, Auroras and their ionospheric effects, Thermospheric Physics and the contributions made (or foreseen) by the Incoherent Scatter Observations are described in the following three Chapters (Chapter five, Mike Lockwood; Chapter six, Yoshuke Kamide and Chapter seven, Arthur Richmond, respectively).**
- **the final Chapter (Chapter eight, Jürgen Röttger) deals with the theory, technique and science achieved with atmospheric backscatter and reflection processes of radio waves.**

The Editor has tried to keep as much uniformity as possible trough the various styles of the Authors. Notes in the text and references are printed in italics. The scalar symbols are in italic, the vectors are in boldface and the tensors (or matrices) are underlined and bold.

Acknowledgements:

The Editor is happy to thank all the Authors who very hardly worked for producing a written version of their Cargese lecture; all Authors have kindly provided the Editor with almost all the necessary materials (texts, equations and figures) close to their final form, thus making the Editor work much simplified.

The Editor would like also to deeply acknowledge the Director of EISCAT, Dr. Jürgen Röttger, who have accepted to use the "EISCAT-Technical Reports" series as the practical printing, publishing and distribution of the book. Thanks are also given to several colleagues who have, in the CESR, "peu ou prou" contributed to the final edition of the book, and finally to Anette Snallfot in EISCAT-HQ who has so kindly helped and served as the intermediate between the Publisher and the Editor.

This Editor's work has been made possible through partial funding of the GdR Plasmae of CNRS.

EISCAT is an international association, supported the research councils of Finland, France, Germany, Japan, Norway, Sweden and the United Kingdom.

Denis Alcaydé - November 1997

Electronic version – December 2001

PLASMA FLUCTUATIONS EXCITED BY CHARGED PARTICLE MOTION AND THEIR DETECTION BY WEAK SCATTERING OF RADIO WAVES

Tor Hagfors

1. Introduction

If spatial fluctuations or variations in refractive index exist in a medium a wave cannot propagate through it unperturbed because energy will be scattered by the refractive index variations into other directions. In most cases the spatial fluctuations are also time dependent, and the time variation of the scattered wave will no longer be the same as that of the unperturbed wave. Such phenomena have been studied in many branches of physics, notably in connection with tropospheric and ionospheric scattering of radio waves by irregularities caused by turbulence. In the latter case the density fluctuations are caused through the action of external macroscopic sources. The fluctuations that we are about to discuss in the present paper are caused by the fact that the plasma is built of discreet charged particles. When these particles are moving through the plasma they will excite electron density fluctuations which can be detected by electromagnetic wave scattering. This is the type of scattering which has become known as "*incoherent scattering*".

There is available a large number of papers dealing with the theory of incoherent scattering of radio waves, particularly with reference to the ionosphere. [*Gordon*, 1958; *Fejer*, 1960; *Dougherty and Farley*, 1960; *Salpeter*, 1960; *Renau* 1960; *Hagfors*, 1961; *Rosenbluth and Rostoker*, 1962]. Later important additional contributions have been made by *Woodman* [1965], *Moorcroft* [1964] and *Perkins et al*. [1965]. Rather complete discussions of the subject matter have been given by *Sitenko* [1967] and by *Sheffield* [1975].

The observations made over the last decades have shown that incoherent scattering has become one of the most fruitful methods of investigating the ionosphere to heights of several thousand kilometres from the ground. [*Bowles*, 1958; *Pineo et al.*, 1960; *Millman et al.*, 1961; *Bowles et al.*, 1962]. Excellent reviews of the experimental work have been given by *Evans* [1968] and *Beynon and Williams* [1978]

The method is particularly useful because in addition to providing data on electron density it is also capable of giving information on parameters such as electron and ion temperatures, the ionic composition, or the orientation of the magnetic field. The extension of routine measurements to include the region above the peak of the ionosphere is of great importance to the understanding of

the behaviour of the ionospheric layers. It is interesting that incoherent scattering has also found application as a diagnostic tool for hot plasmas in thermonuclear research following the development of practical laser sources. [*Rosenbluth and Rostoker*, 1962].

The first suggestion that incoherent scattering might be used to measure electron density in the ionosphere was made by *Gordon* [1958]. Gordon estimated the total scattered power by adding powers scattered by individual electrons and concluded that present day radars had sufficient sensitivity. He also inferred that the waves scattered by the plasma would be subject to Doppler broadening, and predicted the amount of broadening by adding power scattered by individual electrons travelling with velocities corresponding to a Maxwellian velocity distribution. The first observations by *Bowles* [1958] showed that the predicted spectral broadening in particular was seriously in error.

Subsequent theoretical work explained the discrepancy as due to neglect of particle interactions in the original theory. It was shown that the width of the broadened lines should correspond with the thermal speed of the ions rather than that of the electrons. The total power scattered was shown to be less than predicted by Gordon by a factor of 1/2 in most cases of interest provided ions and electrons are at the same temperature. For hot electrons and cold ions - a situation which often prevails in the ionosphere - the power is often less than this [*Buneman*, 1962].

When an external magnetic field is included in the considerations additional complications arise. *Bowles* [1961] suggested that spectral distributions might contain lines corresponding to ionic gyro resonances. This suggestion has been confirmed theoretically, and the conditions have been given under which ion lines might be observed, [*Salpeter*, 1961; *Hagfors*, 1961; *Farley et al.*, 1961; *Fejer*, 1961].

It appears that the theoretical analysis - i.e. the first order analysis - is more or less complete in that several workers have arrived at identical or nearly identical conclusions based on widely different approaches. In all results, however, with the exception of that of *Farleyet al.* [1961], the excitation of hydromagnetic waves by the microscopic motions is missing. Discussions of the interaction with transverse modes have also been given by *Sitenko* [1967] and by *Sheffield* [1975]. In most calculations of fluctuations only Coulomb interactions are accounted for and this seems to be adequate for ionospheric purposes.

In the present paper an attempt is made to rederive the expressions for the scattering from first principles and fairly readily understandable pictures. This becomes particularly simple when we make full use of the concept of "*dressed particles*" first introduced into plasma physics by *Rosenbluth and Rostoker*

[1962]. The gain in physical insight using the dressed particle concept is purchased at the cost of some rigor.

Section 2 deals with the problem of evaluating the total scattered power and the spectral distribution of this power in terms of the properties of the plasma. A general discussion is then given in Section 3 of the various factors determining these properties of the plasma, beginning with a plasma of noninteracting particles, with or without an external magnetic field, proceeding with the effect of paricle interaction in the form of collective electrostatic interaction, and ending up with power spectra of the fluctuations under various physical conditions.

2. The Relationship of Scattering to Electron Density Fluctuations

We first compute the power reradiated by a certain volume V of a plasma which is irradiated by a plane monochromatic wave with wave vector κ at a frequency ω much higher than the plasma frequency for electrons ω_{pe} defined by:

$$\omega_{pe} = \left\{ \frac{n_0 \, q_e^2}{m \, \varepsilon_0} \right\}^{1/2} \tag{1}$$

where:

n_0 = electron density
q_e = electron charge
m = mass of an electron
ε_0 = dielectric constant of free space.

Rationalized MKSA units will be adhered to throughout.

The field scattered by a single electron within the volume V, see Figure 1, will then be:

$$E_p = E_{in} \exp\{ i \, (\omega_0 \, t - \kappa . \mathbf{r}_p(t)\} \, \frac{1}{R_0} \exp\{-i \, \frac{\omega_0}{c} \, R_0 \, \} \, \sigma_0 \exp\{ i \, \mathbf{K}.\mathbf{r}_p \, (t) \, \} \tag{2}$$

Here $\mathbf{r}(t)$ is the position of the particle at time t and σ_0 is the effective scattering "*radius*" of the electron defined by:

$$\sigma_0 = r_0 \sin\chi = \left(\frac{q_e^2}{4\pi \, \varepsilon_0} \right) \frac{1}{m \, c^2} \, \sin\chi \tag{3}$$

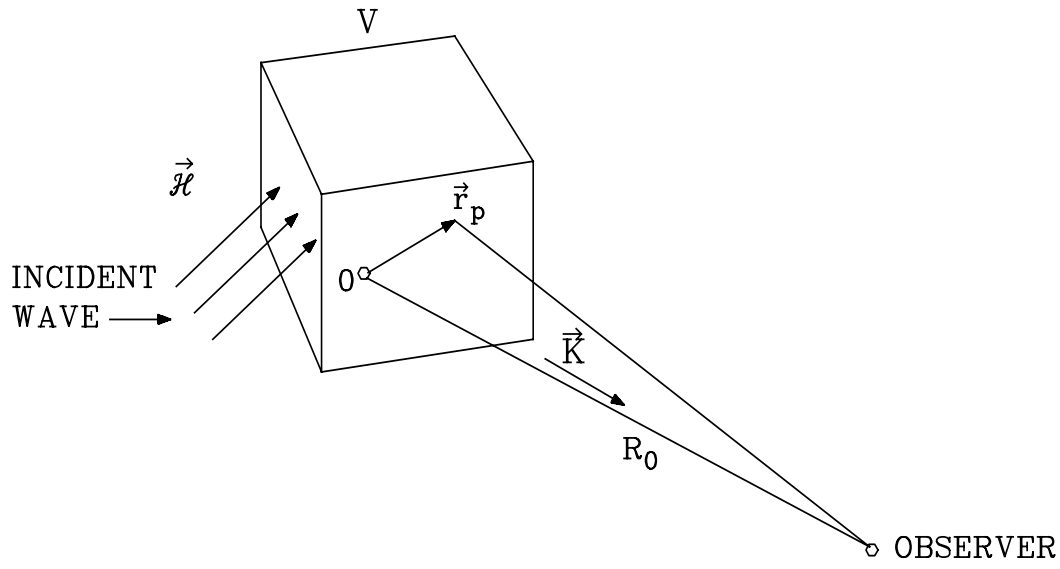

Figure 1. Scattering from electron at position $r_p(t)$.

where χ is the angle between the electric field vector of the incident wave and **K**, i.e. the direction toward the observer. Certain complications might arise through the presence of an external magnetic field, but these will not be considered here.

We see that the scattering is determined by the difference of the wave vectors of the incident and the scattered waves, $\mathbf{k} = \kappa - \mathbf{K}$. On the assumptions of weak scattering the total field at the observer becomes:

$$E_{obs} = \frac{E_{in}\,\sigma_0}{R_0} \exp\left\{ i\,(\omega_0\,t - \frac{\omega_0}{c})\,R_0 \right\} \sum_p \exp\{-i\,\mathbf{k}.\mathbf{r}_p\,(t)\} \qquad (4)$$

where the summation is extended over all the electrons within the volume *V*.

It will prove convenient to express the scattered field in terms of electron density $n(\mathbf{r},t)$. Because electrons are here considered as point particles the number density is most easily expressed as a sum of δ-functions in space:

$$n(\mathbf{r},t) = \sum_p \delta\{\mathbf{r} - \mathbf{r}_p\,(t)\} \qquad (5)$$

We now expand in spatial Fourier series within a periodicity cube of volume *V*:

$$n(\mathbf{r},t) = \sum_{k} n\,(\mathbf{k},\mathrm{t})\ .\ \mathrm{e}^{\,i\,\mathbf{k}.\mathbf{r}} \qquad (6_a)$$

with:

$$n\,(\mathbf{k},\mathrm{t}) = \frac{1}{V}\int d(\mathbf{r})\ n(\mathbf{r},t)\ \mathrm{e}^{\,i\,\mathbf{k}.\mathbf{r}} \qquad (6_b)$$

The observed field E_{obs} can therefore be expressed as:

$$E_{obs} = \frac{\sigma_0}{R_0} E_{in}\ .\ V\ .\ n(\mathbf{k},\mathrm{t})\ \exp\{\ -i\ (\ \omega_0\ t - \frac{\omega_0}{c} R_0\ )\} \qquad (7)$$

It follows from this result that the signal observed at the receiver with a plane monochromatic wave incident on the volume V has the character of a modulated signal centred on the carrier frequency ω_0 [*approximately !*] and with complex amplitude proportional to $n(\mathbf{k},t)$, $\mathbf{k}$ being the wave vector difference as introduced above. The complex amplitude hence becomes:

$$A_{obs}\,(t) = \frac{\sigma_0}{R_0}\ E_{in}\ v\ .\ n(k,t) \qquad (8)$$

The statistical properties of the complex amplitude at the receiver are therefore the same as those of $n(\mathbf{k},t)$. The received signal is conveniently described statistically by the autocovariance:

$$\langle\ A^*(t)\ A(t+\ \tau)\ \rangle_{av} \qquad (9)$$

and the power spectrum is found by Wiener - Khinchine's theorem as the Fourier transform of this:

$$P_{obs}\,(\omega) = \frac{\sigma_0^2}{R_0^2}\ E_{in}^2\ .\ N\ .\ \phi\,(\mathbf{k},\omega) = N\ .\ P_T\ .\phi\,(\mathbf{k},\omega) \qquad (10)$$

where P_T is the total power scattered by a single electron under the same geometrical conditions, N is the total number of electrons in the volume V and $\phi\,(\mathbf{k},\omega)$ is the Fourier transform of the autocorrelation function of electron density fluctuations:

$$\rho(\mathbf{k},\tau) = \frac{V^2}{N}\ \langle\ n^*(\mathbf{k},t)\ n(\mathbf{k},t+\ \tau)\ \rangle_{av} \qquad (11)$$

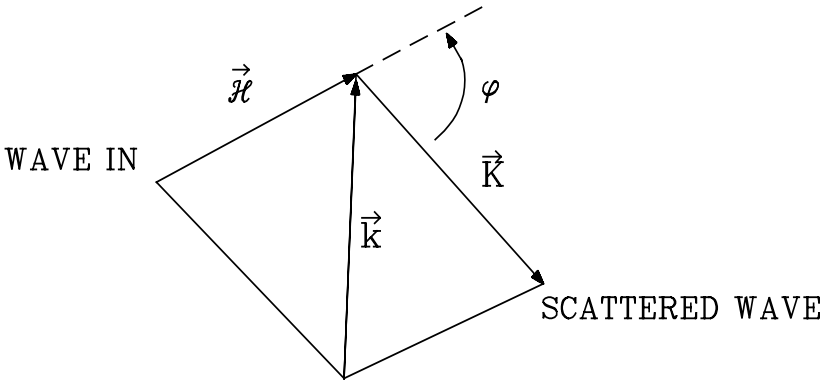

Figure 2. Geometry of incident and scattered waves.

Note that the omission of the exponential time variation $\exp\{i\ \omega_0\ t\}$ has shifted the power spectrum of the received signal $P_{obs}(\omega)$ down to zero frequency. The frequency ω from now on only corresponds to the amount of Doppler displacement from the transmitted frequency ω_0.

Physically we may visualize the scattering to occur as follows: at any given time there is present in the scattering volume electron density waves travelling in all different directions with all different wavelengths. The transmitter-receiver geometry represented by the wave vectors κ and **k** picks out one particular of these "*waves*" as responsible for the scattering. With a scattering angle φ, see Figure 2, the wavelength of these density waves is:

$$\Lambda_{dens} = \frac{\lambda}{2 \sin(\varphi / 2)} \qquad (12)$$

where λ is the radio wavelength. The strong resemblance of this formula with the condition for reflection in a crystal lattice given by Bragg should be observed [Figure 2].

Doppler shift ω now corresponds to motion of our particular density variation. For each velocity there is a corresponding Doppler frequency ω. The velocity *v*, positive along positive **k**, is related to the Doppler shift frequency ω through:

$$v = \frac{\lambda_{dens} \cdot \omega}{2\pi} = - \frac{\omega \cdot \lambda}{4\pi \sin(\varphi / 2)} = - \frac{\omega}{|\mathbf{k}|} \qquad (13)$$

With this discussion the whole problem of the scattering process has been tied to properties of the plasma and density fluctuations therein. Such fluctuations are studied in detail in the following sections.

3. Electron Density Fluctuations

In the discussions to follow we neglect the effect of binary collisions on the density fluctuations. This is a good approximation in a sufficiently dilute plasma such as the upper part of the ionosphere, where collective interactions tend to dominate. In the first of the subsections to follow we also neglect long range interactions, and consequently begin our considerations with a gas of non-interacting particles. Such a gas will lack many of the familiar properties of gases - for instance it will be unable to support ordinary sound waves. A discussion of such a peculiar plasma is nevertheless useful; because, as will be shown later on, a plasma with particles interacting through electromagnetic fields will in first order behave as if the particles move independently, but with a cloud of charge surrounding them - as if "*dressed*".

The random thermal motion of individual particles will represent charge and current fluctuations due simply to the discreetness of the particles. This is a sort of "*intrinsic fluctuation*" associated with the atomicity of the gas. When in the second subsection we go on to consider electromagnetic field interactions it will be shown that the interaction fields can be regarded as excited by the charge and current fluctuations caused by the thermal motion of individual particles. These fields in turn will induce fluctuations in the plasma, and these "*induced fluctuations*" are superimposed on the intrinsic fluctuations caused directly by the discreet nature of the particles. The discussion will allow non-equilibrium situations to prevail, although the distributions must be stationary in the Vlasov sense. Most formulae actually given explicitly will apply to a quasiequilibrium situation where electrons and ions are separately in equilibrium but not necessarily at the same temperature. Whenever explicit calculations are carried out the velocity distributions will be taken as Maxwellian.

3.1. Fluctuations in a Gas of Non-Interacting Particles

We consider the motion of charged particles in rotating coordinates defined as follows:

$$\begin{pmatrix} \text{Cartesian:} & \text{Rotating:} \\ \mathbf{r} = \{x,y,z\} & r_1 = \frac{1}{\sqrt{2}}(x + i\,y) \\ & r_{-1} = \frac{1}{\sqrt{2}}(x - i\,y) \\ & r_0 = z \end{pmatrix} \tag{14}$$

Here the z-axis which is the axis of symmetry coincides with the direction of the external magnetic field $\mathbf{B}_0$. From Eq. 14 it is obvious that there is a unitary transformation between Cartesian and rotating coordinate systems. For the equation of motion of a single particle we obtain:

$$\dot{v}_\alpha = - i \frac{q B_0}{m} \alpha v_a = - i \alpha \Omega v_a \quad (\alpha = 1, -1, 0) \tag{15}$$

For the time being we allow the gyrofrequency Ω to be negative for electrons and positive for ions. This brings out the real advantage in using rotating coordinates: the equations of motion are diagonalized.

If at the present time t the velocity and position of the particle are $\mathbf{v}(t) = \{v_{+1}; v_{-1}; v_0\}$ and $\mathbf{r}(t) = \{r_{+1}; r_{-1}; r_0\}$ then the particle velocity and position at an earlier time t' must have been:

$$v_\alpha(t') = v_\alpha(t - \tau) = v_\alpha(t) \cdot e^{i \alpha \Omega t} \tag{16$_a$}$$

Or in vector form:

$$\mathbf{v}(t - \tau) = \dot{\Gamma}(\tau)\, \mathbf{v}(t) \tag{16$_b$}$$

where $\dot{\Gamma}(\tau)$ is a matrix transforming from present to past velocities. In polarised coordinates the matrix is on diagonal form. Similarly past and present particle positions are related through:

$$r_\alpha(t - \tau) = r_\alpha(t) - \frac{e^{i \alpha \Omega t} - 1}{i \alpha \Omega} v_\alpha(t) \tag{17$_a$}$$

or again in vector form:

$$\mathbf{r}(t - \tau) = \mathbf{r}(t) - \Gamma(\tau)\, \mathbf{v}(t) \tag{17$_b$}$$

$\Gamma(\tau)$ transforming from present to past position is also on diagonal form in our coordinate system. The elements of the matrices describing the screw motion of the particles are:

$$\dot{\Gamma}_{\alpha\alpha} = \dot{g}_\alpha = e^{i \alpha \Omega t} \tag{18}$$

and

$$\Gamma_{\alpha\alpha} = g_{\alpha\alpha} = \frac{e^{i \alpha \Omega t} - 1}{i \alpha \Omega} \tag{19}$$

In Section 2 we saw that each particle contributes an amount

$$n_p(\mathbf{k},t) = \frac{1}{V} e^{-i\,\mathbf{k}.\mathbf{r}_p(t)} \tag{20}$$

to the Fourier transform of the particle density giving rise to the scattering. The complex autocorrelation in particle density associated with a single particle becomes:

$$\langle n_p^*(\mathbf{k}, t)\, n_p(\mathbf{k}, t+\tau)\rangle_{av} = \langle n_p^*(\mathbf{k}, t-\tau)\, n_p(\mathbf{k}, t)\rangle_{av} =$$

$$\frac{1}{V^2} \langle e^{(-i\,\mathbf{k}_{-\alpha} g_\alpha v_\alpha)}\rangle_{av} = \tag{21}$$

$$\frac{1}{V^2} \int d(\mathbf{v})\, f_o(\mathbf{v})\, e^{-i\,\mathbf{a}.\mathbf{v}}$$

Here $f_0(\mathbf{v})$ is the velocity distribution of the particles and **a** is a vector defined by:

$$a_{-\alpha} = k_{-\alpha} g_\alpha = k_{-\alpha} \frac{e^{i\,\Omega\,\alpha\,\tau} - 1}{i\,\Omega\,\alpha} \tag{22}$$

The complex autocorrelation function normalized as in Eq. 11 becomes:

$$\rho(\mathbf{k},\tau) = \langle e^{-i\,\mathbf{a}.\mathbf{v}} \rangle_{av} \tag{23}$$

The correlation function for density fluctuations in a gas of non-interacting particles is therefore a function of the vector **a** and of the parameters of the single particle velocity distribution.

The Fourier component of single particle current density similarly becomes:

$$\mathbf{j}_p(t) = \frac{q}{V} \mathbf{v}_p(t)\, e^{-i\,\mathbf{k}.\mathbf{r}_p(t)} \tag{24}$$

A statistical description of this random current is provided by the autocovariance of the rotating components of the current:

$$\langle \mathbf{j}_\mu^*(\mathbf{k}, t)\, \mathbf{j}_\nu^*(\mathbf{k}, t+\tau)\rangle_{av} = \langle \mathbf{j}_\mu^*(\mathbf{k}, t-\tau)\, \mathbf{j}_\nu^*(\mathbf{k}, t)\rangle_{av} =$$

$$\frac{q^2}{V^2} \dot{g}_{-\mu} \left(- \frac{\partial^2}{\partial a_\mu\, \partial a_\nu} \right) \rho(\mathbf{k},\tau) \tag{25}$$

Because of the independency of the particles the expression for the total current is obtained by multiplication by *N*, the total number of particles.

The normalized autocorrelation function $\rho(\mathbf{k},\tau)$ thus enters both in the determination of current and charge density fluctuations. Before giving a specific form for $f_0(\mathbf{v})$ and hence for $\rho(\mathbf{k},\tau)$ it is worthwhile to discuss in a rather qualitative manner some of the properties of this function, or its Fourier transform which is the power spectrum.

As was explained in Section 2 the density fluctuations can be thought of as a superposition of density waves travelling in all different directions with all different velocities and wavelengths. Suppose first the **k** is along the magnetic field. The particle motion in this direction is independent of the field and we expect the density fluctuations to be the same as if no magnetic field were present.

The density waves are carried along **k** by beams of particles with thermal velocities equal to the wave velocities, and with amplitudes proportional to the number of particles in the beams. Because the number of particles in each beam specified by the velocity $v = \omega/k$ is proportional to $f_0(\mathbf{v}_{//})$ the power spectrum in this case is just proportional to the velocity distribution along the magnetic field with $\mathbf{v}_{//}$ replaced by (ω/k). The autocorrelation $\rho(\mathbf{k},\tau)$ is the Fourier transform of this power spectrum.

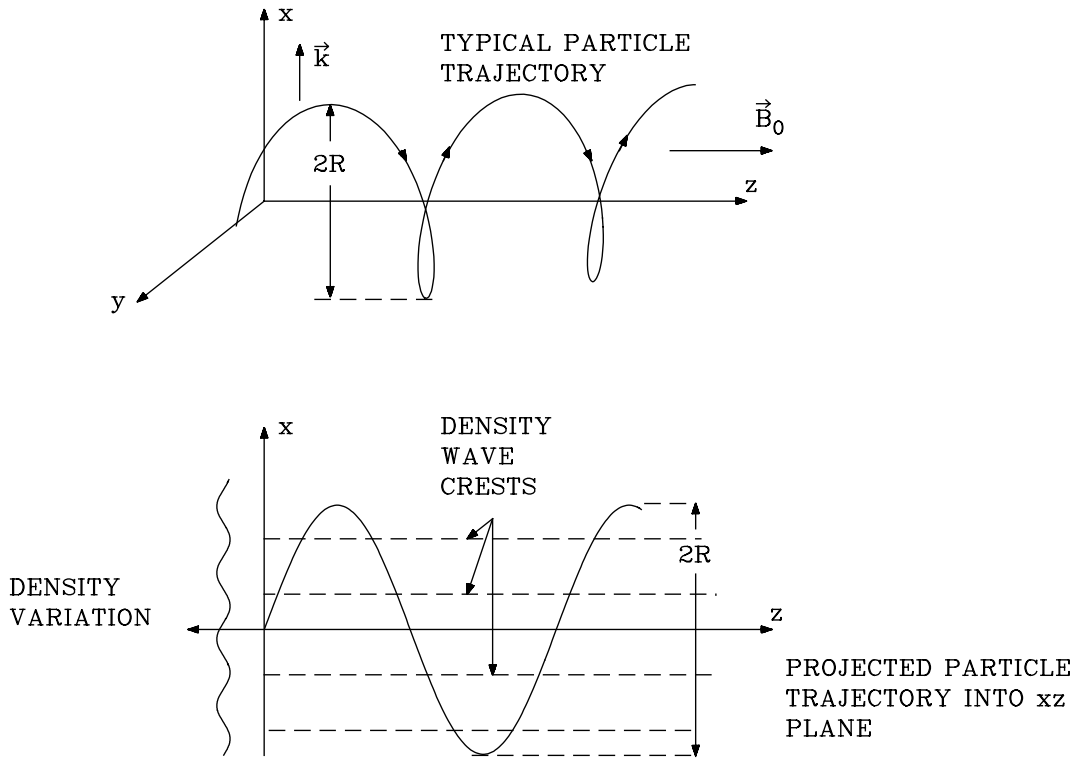

Figure 3. Typical particle trajectory shown in relation to a density wave . Transverse case, $\beta = 90°$*, large Larmor radius.*

At the other extreme, that of **k** perpendicular to $\mathbf{B}_0$ the density waves are travelling at right angles to the field. In Figure 3 the magnetic field is along the z-axis and the waves are travelling in the x-direction. Furthermore the radius of gyration, or the Larmor radius defined by:

$$R = \frac{\sqrt{2}\, v_{th}}{\Omega} \tag{26}$$

[*where v_{th} is the r.m.s. thermal velocity*] is large compared with the density wavelength. Suppose the particle density projected into the x-y plane at $t = 0$ is of the form shown to the extreme left. Redistribution of particles along the x = constant plane will have no influence on the density component under consideration. If we pick out any straight line parallel to the magnetic field characterized by x_0y_0 the particles leaving this line with any velocity in any direction will return to this line after exactly one period of gyration $T = 2\pi/\Omega$. The density will therefore be a repetitive time function with period T, and this periodicity must also appear in the autocorrelation function.

In the example shown in Figure 3 the radius of gyration of a thermal particle is large compared with the wavelength of the density waves and the particles can travel along with the density wave at least for a few wavelengths before being bent away from the direction of the wave. Had we chosen the radius small compared with the wavelength of the density variation, the time variation would lose the character of a wave phenomen because the particles would be so strongly attached to the magnetic field lines that they would no longer be able to transport a spatial variation along **k** by even as little as one wavelength.

The spatial variation would then tend to appear as a nearly stationary pattern, and the power spectrum would be extremely [Figure 3] narrow. In the autocorrelation picture a small Larmor radius, i.e. a strong magnetic field, would give an autocorrelation function close to unity for all time shifts τ. The periodic modulation of $\rho(\mathbf{k},\tau)$ so prominent for large Larmor radii would be rather shallow in this case.In scattering of radio waves from the ionosphere at frequencies less than about 1000 MHz the Larmor radius of electrons will be small and that of the ions large compared with the density scale of interest, i.e. $\Lambda_{dens} = \lambda / 2 \sin(\varphi / 2)$.

As we have just seen there is no effect of a magnetic field in the longitudinal case [$\beta = 0°$] but there is a profound effect for the transverse case [$\beta = 90°$]. Let us now examine what happens in the intermediate range. We start by letting decrease β slightly from 90°.

As long as β is exactly 90° motion of the particles along the magnetic field does not matter because this only corresponds to motion along planes of constant

phase of the density waves. As soon as the perpendicularity condition is relaxed, motion along the field does indeed matter, because when the particle gyrates once round the field line that it left *T* seconds earlier, it might at the same time have slid along the field line to such an extent that it no longer fits into the original phase relationship with the density wave. In the case of large Larmor radius the condition for spectral lines to occur in the power spectrum can be found by considering Figure 4.

The projection is here shown of a typical particle trajectory into a plane containing the magnetic field $\mathbf{B}_0$ and the propagation vector **k**. The typical velocity along the magnetic field is v_{th} where v_{th} is the thermal velocity in the z-direction. The typical distance of motion of this particle along the magnetic field during one period of gyration becomes:

$$1 = v_{th} \,.T = v_{th} \,. \frac{2\pi}{\Omega} = \sqrt{2}\ \mathrm{R} \,. \frac{\sqrt{2} \,. v_{th}}{\Omega} = \sqrt{2}\ \pi \,. R \qquad (27)$$

where *R* is again the Larmor radius as defined in Eq. 26. The motion of the particle along the wave normal **k** during the same time becomes:

$$\Delta s = 1 \,. \cos \beta = \sqrt{2}\ \pi R \cos \beta = \sqrt{2}\ \pi R \sin\ \psi \qquad (28)$$

Now, if the motion of the particle along the field line during one period of gyration has caused the particle to get out of step, or out of phase with the density variation, then the deep periodic modulation of the autocorrelation function will disappear. For large Larmor radii the condition for the magnetic field to have an appreciable influence on the spectrum becomes:

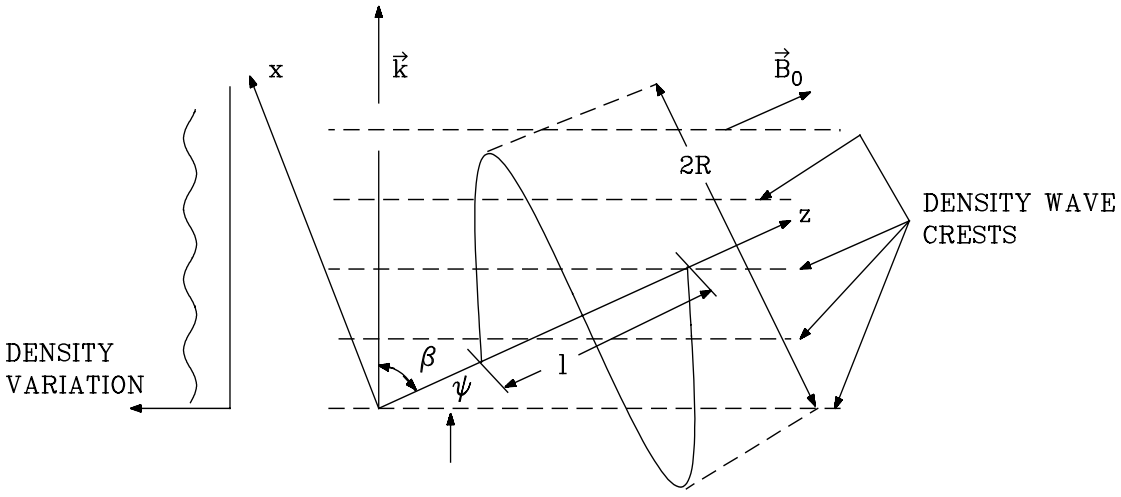

Figure 4. Particle trajectory in relation to a density wave for arbitrary β.

$$k \,.\, \Delta s < \frac{\pi}{2} \qquad \text{or:} \qquad \sin \psi < \frac{1}{2\sqrt{2}\, k\, R} \tag{29}$$

which is the condition for the particle to keep in phase with the density variation for at least one period of gyration.

For small Larmor radii the modulation of the spectrum is never very prominent. In passing from $\beta = 90°$ to $\beta = 0°$ the autocorrelation function will just gradually shrink from being close to unity for all τ at $\beta = 90°$ to the no-magnetic field case at $\beta = 0°$. The spectrum will therefore be narrow when $\beta = 90°$ and identical with the no-magnetic field case at $\beta = 0°$ with a gradual transition between the two cases. This is easily understood by considering the particles as completely constrained to move along the field lines. The *r.m.s.* motion along the direction of **k** - and this is the component of motion giving rise to the spectral broadening - is then simply:

$$v_k = v_{th} \,.\, \sin \psi \tag{30}$$

and the width of the power spectrum is just proportional to $v_{th}^2 \sin^2 \psi = v_{th}^2 \cos 2 \beta$.

In order to check the rather intuitive conclusions regarding the properties of $\rho\,(\mathbf{k},\tau)$ this function was evaluated for a Maxwellian velocity distribution:

$$f_0\,(\mathbf{v}) = \left(\frac{2\pi}{v_{th}^2}\right)^{3/2} e^{-\mathbf{v}^2/2v_{th}^2} \tag{31}$$

where v_{th} is the r.m.s. thermal velocity defined by:

$v_{th}^2 = \theta / m$ θ being the absolute temperature, in energy units.

The result is:

$$\rho\,(\mathbf{k},\tau) = e^{\{-\frac{1}{2} v_{th}^2 |\mathbf{a}|^2\}} = e^{-(kR)^2 \{(\frac{1}{2}\Omega\tau)^2 \cos^2\beta + \sin^2(\frac{1}{2}\Omega\tau_p) \sin^2\beta\}} \tag{32}$$

This result is plotted on a log-linear diagram in Figure 5, correlation against normalized time shift $\Omega\tau/2\pi = \tau/T$ [T = *time of gyration*] with the angle β as parameter. It will be seen from Figure 5 that the autocorrelation function exhibits exactly the properties arrived at by the more qualitative arguments just presented. Modulation is only prominent when β is close to 90° and Larmor radius large, depth of modulation decrease with Larmor radius.

The integral over the spectrum $\Phi\,(\mathbf{k},\omega)$ over all frequencies f, which is proportional to the total scattered power, is equal to $\rho\,(\mathbf{k},\omega)$. This is unity in all cases

considered so far. Independent particles therefore scatter incoherently, i.e. the scattered power is obtained by adding powers scattered by individual particles. The effect of magnetic field is to redistribute the power whilst all the time keeping the total scattered power constant.

The actual spectral function $\Phi(\mathbf{k},\omega)$ becomes:

$$\Phi(\mathbf{k},\omega) = Re\left\{\int_{-\infty}^{\infty} \rho(\mathbf{k},\tau)\, e^{-i\omega\tau}\, d\tau\right\} \tag{33}$$

because $\rho(\mathbf{k},\tau)$ will be assumed to be real and symmetric in τ. When steady drifts are superimposed this is no longer the case and the spectrum must be obtained with some care. For the Maxwellian velocity distribution the spectrum becomes:

$$\Phi(\mathbf{k},\omega) = 2\int_{0}^{\infty} e^{-\frac{1}{2} v_{th}^2 |\mathbf{a}|^2} \cos\omega\tau\, d\tau \tag{34}$$

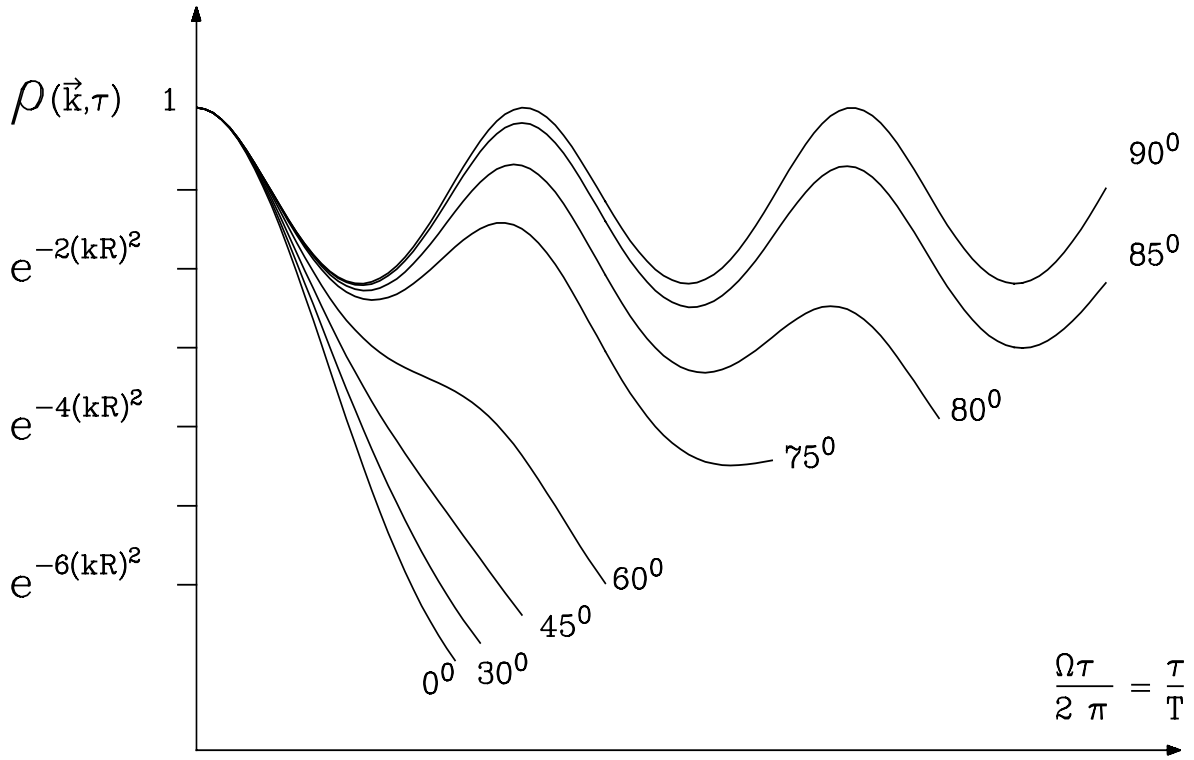

Figure 5. Autocorrelation of independent particle number density [logarithmic scale] versus normalized time shift [$\omega\tau/2\pi$] with angle β as parameter.

For later purposes we define the function

$$G(\mathbf{k},\omega) = \int_0^\infty e^{-\frac{1}{2} v_{th}^2 |\mathbf{a}|^2 - i\omega\tau} \, d\tau \qquad (35)$$

and term it a Gordeyev integral. In terms of this function the spectrum may be expressed as:

$$\Phi(\mathbf{k},\omega) = 2 \, \mathrm{Re} \, \{G(\mathbf{k},\omega)\} \qquad (36)$$

3.2. The Effect of a Random Electric Field

With electromagnetic particle interaction present the motion of individual particles becomes more complicated because each particle moves in the field of all the others. In this subsection we want to determine the density variations induced by the interaction field. Such density variations come in addition to the density fluctuations caused by the discreetness of the particles, i.e. the intrinsic fluctuation dealt with above. The induced fluctuations may be computed as if the particles were smeared out into a continuum. The fields giving rise to these induced fluctuations must, however, be computed from the discreet particle picture of the non-interacting gas. From this we realize that there are two contributions to the density fluctuations, one from the discreetness of the particles, the intrinsic part, and another one due to fluctuations induced by the fields - which in turn are caused by the discreetness of the charged particles. A charged particle moving through the plasma in itself constitutes a fluctuation, but in addition it induces a fluctuation in the surrounding medium due to the fields it sets up. The particle plus the charge cloud surrounding it is often referred to as a "*dressed particle"* [*Rosenbluth and Rostoker*, 1962].

Assume first that the force per unit mass is known throughout the plasma, and let this force be denoted by $\mathbf{F}(\mathbf{r},t)$. The density fluctuation induced by this force in a volume element having velocity $\mathbf{v}$ at position $\mathbf{r}$ at time t is then found from the Vlasov equation to be:

$$\delta n \, (\mathbf{r},\mathbf{v},t) = - n_0 \int_{-\infty}^{t} \mathbf{F}(\mathbf{r}',t') \cdot \frac{\partial f_0 \, (\mathbf{v}')}{\partial \mathbf{v}'} \, dt' \qquad (37)$$

The integration is extended over the orbit of the volume element at all *earlier* times. If the unperturbed velocity distribution $f_0(\mathbf{v})$ is isotropic the force $\mathbf{F}(\mathbf{r},t)$ can be expressed as $q\,\mathbf{E}(\mathbf{r},t)$ where $\mathbf{E}$ is the internal electric field caused by the

discreetness of the particles. The magnetic force vanishes because under the isotropy assumption this force is perpendicular to $[\partial f_0 / \partial \mathbf{v}]$. The presence of externally applied fields can always be accounted for in the computation of individual particle orbits. With a Maxwellian velocity distribution we obtain:

$$\delta n(\mathbf{r},\mathbf{v},t) = \frac{n_0 q}{m v_{th}^2} \int_{\infty}^{t} \mathbf{E}(\mathbf{r}',t') \cdot \mathbf{v}' f_0(\mathbf{v}') \, dt' \qquad (38)$$

Physically this corresponds to the energy acquired by the volume element arriving at **r** at time t with velocity **v** from the electric field divided by the mean energy of a thermal particle. The integration is along actual particle orbits. If the fluctuating field is rather small the perturbation in particle orbits due to the random field will be small, and the integration can be carried along orbits which are unperturbed by the random field. Relations between past and present velocities and positions are therefore the same as in a gas of noninteracting particles as studied in the previous section.

In this study we are interested in spatial fluctuations irrespective of the velocity of arrival **v** and we therefore average over all velocities of arrival making use of the fact that $f_0(\mathbf{v}) = f_0(\mathbf{v}')$ for unperturbed orbits, and obtain:

$$\delta n(\mathbf{r},t) = \frac{n_0 q}{m v_{th}^2} \int d(\mathbf{v}) f_0(\mathbf{v}) \int_{-\infty}^{t} \mathbf{E}(\mathbf{r}',t') \, dt' \qquad (39)$$

We next expand the electric field $\mathbf{E}(\mathbf{r}',t')$ in a spatial Fourier series:

$$\mathbf{E}(\mathbf{r}',t') = \sum_{k} \mathbf{E}(\mathbf{k},t') \, e^{i\mathbf{k}.\mathbf{r}'} \qquad (40)$$

Putting $t' = t - \tau$ and making use of the relations between past and present positions derived in Section 3.1 we obtain:

$$\delta n(\mathbf{r},t) = \frac{n_0 q}{m v_{th}^2} \sum_{k} e^{i\mathbf{k}.\mathbf{r}} \int_{0}^{\infty} d\tau \, \mathbf{E}(\mathbf{k},t-\tau) \int d(\mathbf{v}) f_0(\mathbf{v}) \, \dot{\Gamma}(\tau) \, v \, e^{-ik\Gamma(t)v} \qquad (41)$$

It follows that the spatial Fourier components of the field induced fluctuation become:

$$n^1(\mathbf{k},t) = \frac{n_0\, q}{m v_{th}^2} \int_0^\infty d\tau\, \mathbf{T}(\mathbf{k},\tau) \cdot \mathbf{E}(\mathbf{k},t-\tau) \tag{42}$$

where we have introduced a vector $\mathbf{T}(\mathbf{k},\tau)$ with rotating components:

$$T_a(\mathbf{k},\tau) = \int \mathrm{d}(\mathbf{v})\, f_0(\mathbf{v})\, \dot{g}_a(\tau)\, v_a\, e^{-i\mathbf{a}.\mathbf{v}} = \dot{g}_a(\tau)\left(\mathrm{i}\frac{\partial}{\partial a_{-a}}\right)\rho(\mathbf{k},\tau) \tag{43}$$

where **a** is again the vector defined in Eq. 22, and where $\rho(\mathbf{k},\tau)$ is the autocorrelation function of density fluctuations of non-interacting particles.

Equation 42 should be compared with the equation relating the current density and the electric field in a dispersive medium:

$$\mathbf{j}(\mathbf{k},t) = \int_0^\infty d\tau\ \sigma(\mathbf{k},\tau)\, \mathbf{E}(\mathbf{k},t-\tau) \tag{44}$$

where $\sigma(\mathbf{k},\tau)$ is the conductivity tensor of the medium. We might say that $\sigma(\mathbf{k},\tau)$ describes the way in which the medium responds with a current to an applied electric field. In the same way we might interpret the vector $(n_0\, q)/(mv_{th}^2)\ \mathbf{T}(\mathbf{k},\tau)$ as describing the way in which the medium responds with a density variation to an applied electric field.

The superscript "*1*" will henceforth be used to signify the field-induced fluctuation as distinguished from the intrinsic fluctuation which henceforth will be labelled by superscript "*0*". The total fluctuation in the plasma now becomes:

$$n(\mathbf{k},t) = n^0(\mathbf{k},t) + n^1(\mathbf{k},t) \tag{45}$$

As the field **E** and the response vector **T** appear as a one-sided convolution integral it will be more convenient to work in the frequency domain. In this way we determine power spectra directly without going via the autocorrelation function which proved so convenient in the description of a gas of non-interacting particles. For the induced fluctuation we obtain:

$$n^1(\mathbf{k},\omega) = \mathbf{E}(\mathbf{k},\omega)\ \mathbf{T}(\mathbf{k},\omega)\left(\frac{n_0\, q}{m v_{th}^2}\right) \tag{46}$$

We must be careful in defining $\mathbf{T}(\mathbf{k},\omega)$ - it is a one-sided Fourier transform:

$$\mathbf{T}(\mathbf{k},\omega) = \int_0^\infty \mathbf{T}(\mathbf{k},\tau)\, e^{-i\omega\tau}\, d\tau \qquad (47)$$

This is due to the one-sided convolusion which in turn is caused by the fact that only the past not the future can determine the fluctuation at the present time.

The field $\mathbf{E}(\mathbf{k},\omega)$ is a superposition of the fields from the individual particles of the plasma. If we compute the field from one particular particle we will be able to determine the fluctuation induced by this particle alone. Let this induced one-particle fluctuation be denoted by $n_p^1(\mathbf{k},\omega)$. Suppose we are interested in electron density fluctuations. The contribution to these from a particular electron *p* becomes:

$$n_p\,(\mathbf{k},\omega) = n_p^0\,(\mathbf{k},\omega) + \left(\frac{n_0\, q}{m v_{th}^2}\right)\mathbf{E}_{pe}\,(\mathbf{k},\omega).\mathbf{T}_e\,(\mathbf{k},\omega) \qquad (48)$$

where $n_p^0\,(\mathbf{k},\omega)$ is the intrinsic fluctuation associated with electron *p*. In the second term which represents induced fluctuation, the electric field $\mathbf{E}_{pe}\,(\mathbf{k},\omega)$ is that associated with particle *p* only. The intrinsic term may thus be associated with the "*bare*" particle and the second term with the "*dressing*" surrounding the particle - on the average an electron repels other electrons thus creating an electron deficiency in its neighbourhood. In addition to the "*electron dressing*"the electron will also be accompanied by an "*ion dressing*" due to the average attraction of ions by the electron.

For a Maxwellian velocity distribution the components of $\mathbf{T}(\mathbf{k},\omega)$ can be determined by means of Gordeyev integrals:

$$T_a\,(\mathbf{k},\omega) = -\,v_{th}^2 \,.\, k_a \,\frac{G(\mathbf{k},\omega - \alpha\Omega) - G(\mathbf{k},\omega)}{\alpha\,\Omega} \qquad (49)$$

For $\alpha = 0$ or when $\omega \to 0$ we must take the limit of this which does not exist. For $\alpha = 0$ we have:

$$T_0\,(\mathbf{k},\omega) = v_{th}^2 \,.\, k_0 \,.\, \frac{\partial\, G(\mathbf{k},\omega)}{\partial\, \omega} \qquad (50)$$

We see that, when $\omega \rightarrow 0$ the vector $\mathbf{T}(\mathbf{k},\omega)$ becomes parallel to the vector $\mathbf{k}$. This means that the only component of the electric field which can induce fluctuations is that along $\mathbf{k}$, i.e. $\mathbf{E}_L$ defined by:

$$\mathbf{E}_L = \frac{1}{k^2}\ \mathbf{k}\ (\mathbf{k}\ .\mathbf{E}) \tag{51}$$

As this component of the field is determined by the charge fluctuations alone it means that the Coulomb interaction approximation is no approximation at all but an exact solution of the first order fluctuation problem in this particular case.

An ion can of course only contribute to electron density fluctuations through an induced fluctuation, or, if we like, through its electron "*dressing*". The electron density fluctuation associated with an ion p is therefore:

$$n_p(\mathbf{k},\omega) = \frac{n_0\, q_e}{m v_{th}^2}\, \mathbf{E}_{pi}\ (\mathbf{k},\omega)\ .\ \mathbf{T}_e\ (\mathbf{k},\omega) \tag{52}$$

where $\mathbf{E}_{pi}\ (\mathbf{k},\omega)$ is the field induced by the particular ion p.

Once these elementary contributions have been determined the total electron density fluctuation can be found as a superposition of contributions from all the "*dressed electrons*" plus all the ion "*dressings*":

$\langle |n(k,\omega)|^2 \rangle_{av} =$ contribution from "*dressed electrons*"

$+$ contribution from ion "*dressings*".

Before further progress can be made we must calculate the electric field set up in the plasma as a result of the motion of a charged particle along an unperturbed orbit. As most calculations of this electric field in connection with plasma fluctuations tacitly assume the longitudinal interaction [= *Coulomb interaction*] to be the only form of interaction,we shall devote the next subsection to the calculation of this field.

3.3. The Effective Field of a Charged Particle Moving Through the Plasma

The inducing electric field $\mathbf{E}_p(\mathbf{k},\omega)$ associated with the motion of a charged particle may be calculated by solving Maxwell's equations in vacuo by a Fourier transform in space and time assuming the field to be excited by a current $\mathbf{j}_p(\mathbf{k},\omega)$ which consists of two terms, one is the driving or intrinsic term $\mathbf{j}_p{}^0(\mathbf{k},\omega)$ caused directly by the motion of the discreet particle - this is identical with the current studied in Section 3.1 - and the other term is an induced current caused by the field set up.

We now imagine the field $\mathbf{E}_p(\mathbf{k},\omega)$ to be split in a longitudinal part $\mathbf{E}_L$ [*see Eq. 51*] and a transverse part $\mathbf{E}_T(\mathbf{k},\omega)$ defined as:

$$\mathbf{E}_T(\mathbf{k},\omega) = -\frac{1}{k^2}(\mathbf{k} \times (\mathbf{k} \times \mathbf{E})) \tag{53}$$

Here we shall consider only the longitudinal interaction. This is exactly correct when there is no magnetic field so that the transverse and the longitudinal modes decouple exactly. When there is a magnetic field present there is a coupling, but the transverse field in general only becomes important for such small values of **k** that it is of no interest in scattering from the ionosphere. We obtain:

$$n^1{}_p(\mathbf{k},\omega) = \frac{n_0\, q_e}{m v_{th}^2}\,\mathbf{E}_T \cdot \mathbf{T} = \frac{n_0\, q_e}{k^2 m v_{th}^2}\,[\,\mathbf{k}.\mathbf{E}_p(\mathbf{k},\omega)\,]\,[\,\mathbf{k}.\mathbf{T}_0(\mathbf{k},\omega)] \tag{54}$$

and the scalar product $\mathbf{k}.\mathbf{E}_p(\mathbf{k},\omega)$ can be related directly to the charge density fluctuation associated with the motion of a particle *p*. If this particle is an electron, the charge density fluctuation becomes:

$$\rho_{pe}(\mathbf{k},\omega) = q_e\,\{\,n^0{}_p(\mathbf{k},\omega) + n^1{}_p(\mathbf{k},\omega)\,\} + q_i\, N^1{}_p(\mathbf{k},\omega) \tag{55}$$

The last term $q_i\, N^1{}_p(\mathbf{k},\omega)$ is the fluctuation induced by the electron *p* in the ion density. When several ionic constituents are present it must be summed over similar terms, one for each constituent. For simplicity we only assume one type of positive ions to be present, and that these have mass *M*, thermal velocity V_{th} and average density N_0 sufficient for neutrality of the plasma as a whole. Introducing Debye lengths for electrons and ions we have:

$$\begin{pmatrix} D_e^2 = \varepsilon_0\, m v_{th}^2/n_0\, q_e^2 = (v_{th}/\omega_{pe})^2 & \text{(electrons)} \\ D_i^2 = \varepsilon_0\, M V_{th}^2/N_0\, q_i^2 = (V_{th}/\omega_{pi})^2 & \text{(ions)} \end{pmatrix} \tag{56}$$

where ω_{pe} and ω_{pi} are the plasma frequencies for electrons and ions respectively. The Debye length is therefore the distance travelled by a thermal particle during one period of a plasma oscillation. Combination of these quantities with Eq. 54, 56 and with the equation

$$\mathbf{k}.\mathbf{E}_p(\mathbf{k},\omega) = -\,\rho_{pc}(\mathbf{k},\omega) \tag{57}$$

which follows from Maxwell's equations, gives for the longitudinal field:

$$\mathbf{E}_{Lp}(\mathbf{k},\omega) = \frac{-\,i\,\mathbf{k} \cdot (q_e/\varepsilon_0 k^2)\, n^0{}_{pe}(\mathbf{k},\omega)}{1 + i\,\{(1/kD_e)^2\,\mathbf{k}.\mathbf{T}_e + (1/kD_i)^2\,\mathbf{k}.\mathbf{T}_i\}} \tag{58}$$

When the field-inducing particle is an ion we only have to replace $q_e n^0_{pe}(\mathbf{k},\omega)$ by the similar expression for an ion, viz. $q_i N^0_{pL}(\mathbf{k},\omega)$. Replacing the expression $i\,(1/kD)^2\,\mathbf{k.T}$ by the more commonly used longitudinal susceptibility $\chi = \mathbf{k}\chi_t\,\mathbf{k}/k^2$, we see that the denominator in Eq. 58 enters as a dielectric constant of the plasma, and the field set up is a screened field.

From these considerations we can write down directly the total fluctuation associated with a single electron:

$$n_{pe}(\mathbf{k},\omega) = \frac{(1+\chi_i)\, n^0_{pe}(\mathbf{k},\omega)}{1+\chi_i+\chi_e} \tag{59}$$

and for the electron density fluctuation induced by a single ion [*assuming* $q_e = -\,q_i$ *!*]:

$$n_{pe}(\mathbf{k},\omega) = = \frac{\chi_e\, N^0_{pi}(\mathbf{k},\omega)}{1+\chi_i+\chi_e} \tag{60}$$

The total fluctuation of electron density is obtained as a superposition of fluctuations from all the individual particles - now being regarded as independent. This procedure, which has been termed by *Rosenbluth and Rostoker* [1962] a "*superposition of dressed test particles"* gives the correct first order fluctuation for Coulomb interaction only. By inverting the above expression for electron-density fluctuation from k,ω space into r,t space we could study in detail the electron cloud associated with the motion of an ion. Fast ion motion would give a wake of electron density disturbance travelling away from the inducing ion. The above expression therefore represents the kinetic theory result of the problem of a charged particle passing through a plasma. It should be observed that the above expressions are valid for Coulomb interaction only.

3.4. Spectral Distribution of Fluctuations

From Eq. 59 and 60 we can now construct the spectral distributions by simple superposition of independent dressed particles. For electrons and one kind of positive ions we obtain:

$$\langle |\, n_e(\mathbf{k},\omega)\,|^2 \,\rangle_{av} = \frac{|1+\chi_i|^2\,\langle |n^0_e(\mathbf{k},\omega)|^2\rangle + |\chi_e|^2\,\langle |\mathrm{N}^0_i(\mathbf{k},\omega)|^2\,\rangle}{|\,1+\chi_e+\chi_i\,|^2} \tag{61}$$

where $\langle |n^0_e(\mathbf{k},\omega)|^2\rangle$ and $\langle |N^0_i(\mathbf{k},\omega)|^2\rangle$ are the power spectra of independent electrons and independent ions as studied in Section 3.1.

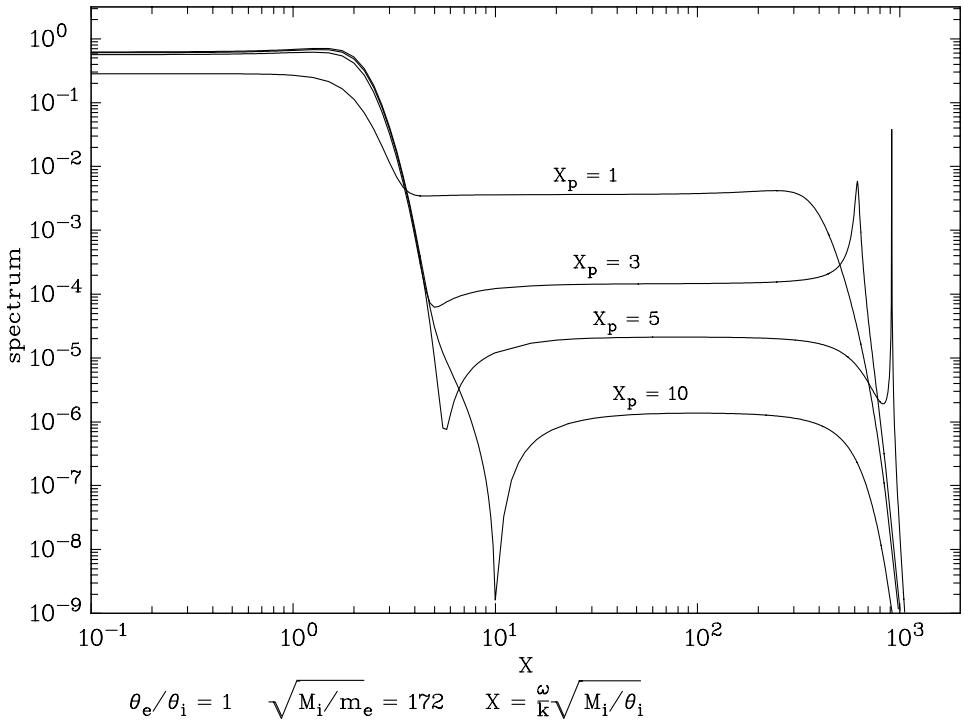

Figure 6. Characteristics of the equilibrium spectra for various Debye lengths, expressed in terms of $X_p = 1/kD$

This result is identical with results derived by other workers. In our derivation of Eq. 61 we did make use of Maxwellian velocity distributions for ions and electrons to define v_{th}. We are, however, perfectly free to prescribe a non-equilibrium situation with electrons and ions at different temperatures. Also, with many different types of ions present we only have to replace the ion terms above by a sum of such ion terms subject only to neutrality of the plasma as a whole. This has been carried out by *Buneman* [1961] in detail. We also observe that by starting with a non-Maxwellian velocity distribution we can work through exactly the same steps as above and end up with distributions for relative drifts of electrons and ions or other non-equilibrium situations we might like to examine. The procedure of superposing dressed particles is therefore a very flexible one. Figure 6 shows power spectra for equilibrium conditions as $kD=1/Z_p$ changes.

Here we shall retain the Maxwellian distributions of velocity - but allow electrons and ions to be at different temperatures. Figure 7 shows the ion line spectra for various values of θ_e/θ_i. For small wavelengths of the density fluctuations, when $kD \to \infty$ we see that the electron density fluctuations become identical with the no-interaction case. - Over distances less than the Debye length the charged particles then move as if completely free. - As the wavelength of the fluctuation increases, the ions are able to induce a fluctuation in the electron density at the scale of the wavelength.

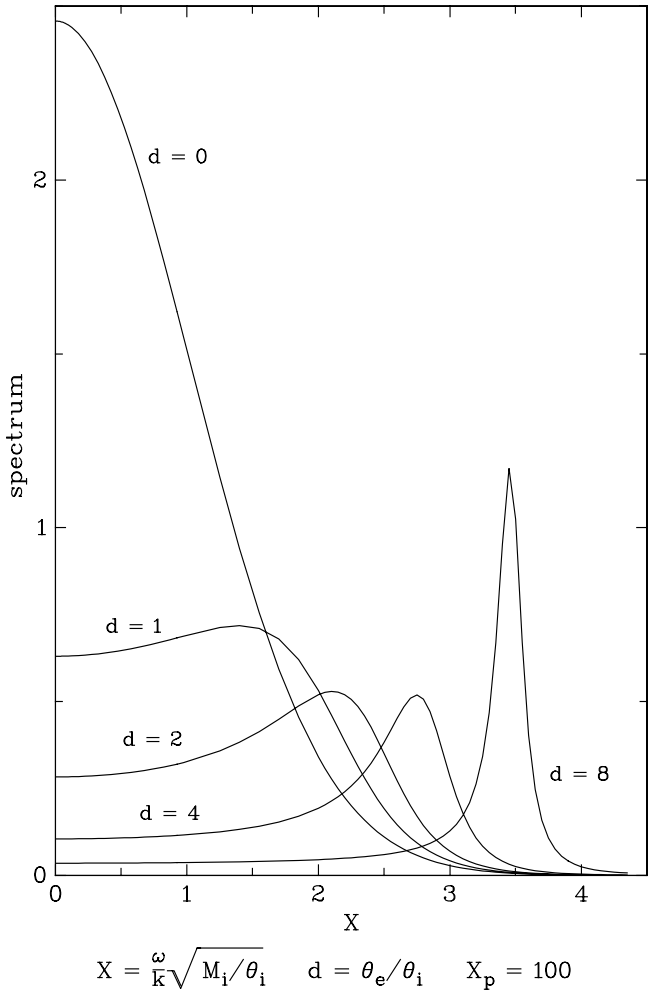

Figure 7. Ion line fluctuation spectra for varying temperature ratios θ_e/θ_i

At frequencies ω less than about kV_{th}, V_{th} being the ionic thermal velocity, the term $\mathbf{kT}_e$ is roughly equal to i, or of order unity. Within the same frequency range the term $\mathbf{kT}_i$ is at most of order unity. At the same time the unperturbed electronic spectral density is of order $1/kv_{th}$ and that for the ions of order $1/kV_{th}$. The order of magnitude of the terms induced by the ions and from dressed electrons in the nominator becomes:

$$\frac{\text{electronic term}}{\text{ionic term}} \quad \frac{(1/\theta_i)^2 \,.\, 1/v_{th}}{(1/\theta_e)^2 \,.\, 1/V_{th}} \sim \left(\frac{\theta_e}{\theta_i}\right)^{3/2} \left(\frac{m}{M}\right)^{1/2} \tag{62}$$

Note that here θ_e and θ_i are electron and ion temperatures respectively. As long as the temperatures are of the same order of magnitude the electronic term is unimportant because $(m/M)^{1/2} \leq 1/43$. At moderate temperature ratios the electron density fluctuations are mainly caused by fluctuations induced by ions, as long as $\omega < kV_{th}$ and $kD < 1$. The main features of the spectrum at low frequencies

must exhibit many of the same characteristics as the ion spectrum. In particular the condition for lines to occur in the electronic spectrum must be determined as in our discussion of Section 3.1 with ion parameters. The shape of the spectrum is however different from the independent particle case because of the modifying influence of the denominator as we will discuss shortly. If the electronic Larmor radius is small and the ionic Larmor large compared with the density wavelength an exception occurs in the rule that the low frequency part of the electronic spectrum is determined by ion induced electron clouds when $\beta \to 90°$. The electrons will then be constrained to move along the field lines and can no longer follow the ion motion across the field lines. This will begin to affect the ion-induced spectrum when:

$$v_{th} \cos\beta \cong V_{th} \qquad \text{or when} \quad \cos\beta = \frac{V_{th}}{v_{th}} = \left(\frac{\theta_i}{\theta_e}\right)^{1/2} \left(\frac{m}{M}\right)^{1/2} \tag{63}$$

The last of the ion-induced spectral lines will have vanished from the spectrum when

$$kv_{th} \cdot \cos\beta \cong \frac{\Omega_i}{4} \qquad \text{or when} \quad \cos\beta \approx \frac{1}{2\sqrt{2}kR_i}\left(\frac{\theta_i}{\theta_e}\right)^{1/2} \left(\frac{m}{M}\right)^{1/2} \tag{64}$$

When $\cos\beta$ is smaller than this limiting value the spectrum is a single large peak round $\omega = 0$. For frequencies in the range $kV_{th} < \omega < kv_{th}$ the spectrum is essentially due to dressed electrons. As we have seen the spectral density is here usually considerably lower than in the ion-induced region.

We now study the properties of the denominator. The most prominent feature is the plasma resonance. This arises as follows: when kD_e is small, $X = \omega/kv_{th}$ must be large for χ to approach unity. This occurs at such a high frequency that the ion term is essentially zero in the denominator. The first term in an asymptotic expansion for χ_e for large ω in the absence of a magnetic field is:

$$\chi \to -\frac{1}{(kD_e)^2}\left(X^{-2} + 3\,X^{-4} + 15\,X^{-6} \ldots\right) \tag{65}$$

The denominator therefore vanishes when:

$$\omega = \omega_{pe}\left(1+1.5(kD_e)^2\right) \tag{66}$$

at this frequency there is a peak in the spectrum corresponding to longitudinal plasma oscillations or Langmuir oscillations. When the scale is decreased or the Debye length increased the plasma resonance effect is washed out because the real part of χ_e becomes non-negligible at this frequency. The area under the

plasma peak will be so small that the scattered energy will not be appreciable. See a discussion of this point by *Salpeter* [1960], and the discussion of photo electron enhancement below.

We must next discuss the modification on the unperturbed spectra introduced by the denominator in the low-frequency part of the frequency spectrum, when $\omega < kV_{th}$. At equilibrium when $\theta_e = \theta_i$ the denominator has a minimum at about $\omega \approx \sqrt{2}\ kV_{th}$. For frequencies $\omega < kV_{th}$. the denominator is decreasing so that the spectrum is approximately. At $\omega \approx \sqrt{2}\ kV_{th}$ there will therefore be a slight maximum in the spectrum. With increasing electron temperatures this maximum becomes more pronounced because the electron term in the denominator becomes increasingly small. The minimum in the ion function χ_i never becomes very pronounced, however, so the ion peak never becomes sharp.

The development so far presented has assumed that the test particles in the plasma travel along unperturbed orbits, only influenced by the presence of a magnetic field. For a more accurate treatment the effect of the microfield on the orbits must also be taken into account. For the physical conditions in the ionosphere this refinement can be ignored. An effect which cannot be ignored, however, is the orbital perturbation caused by the binary collisions in the plasma. In their presence the charged particles will no longer travel along deterministic paths, but will be subject to probabilistic laws of motion. The question of type of collisions comes in, whether it is elastic or not, or in-between, and whether a charge exchange occurs in the collision.

A correct treatment becomes exceedingly complicated and we shall therefore here only crudely study the effect of binary collisions by assuming that the particles collide elastically with a background of neutral particles, and effectively diffuse through space. Such particle diffusion has been studied by *Chandrasekar* [1943] and others. Adopting this formulation we obtain results which are identical to those obtained by using a Fokker-Planck collision term in the Boltzmann equation. Other options are available, for instance the Bhatnagar-Gross-Krook approximation. The spectra predicted by these methods are nearly indistinguishable as far as their shape is concerned, and only show slight variations in the derived apparent collision frequencies. In the Fokker-Planck case, without an external magnetic field all one has to do to derive the power spectra is to replace the correlation function $\rho(\mathbf{k},\tau)$ of Eq. 32 in the expressions for the susceptibilities $\chi(\mathbf{k},\tau)$ and in the independent particle spectra $N°(\mathbf{k},\tau)$ with the expression:

$$\rho(\mathbf{k},\tau) = \exp\left\{ - \left(\frac{k\, v_{th}}{\upsilon_c} \right)^2 \left\{ \upsilon_c\, \tau - 1 + \exp(- \upsilon_c\, \tau) \right\} \right\} \qquad (67)$$

where υ_c is the collision frequency in this model. The distortion in the ion spectra for a thermal equilibrium plasma for various values of the normalised ion-neutral collision frequency $X_i = \upsilon_i / k\, V_{th}$ for a fixed value of $X_p = \omega_{pe} / k\, v_{th}$ is shown in figure 8. As can be seen increasing collision frequencies cause the spectra to narrow and become more Gauss-like.

The case of multiple ion species is also of importance as there is a tendency in the ionosphere for the lighter mass ions to be found at the highest altitudes, and the transition from one to the other is often of considerable interest. The treatment of this case is a relatively trivial extension of what has been presented. One must replace the ion components of the spectral expressions, both in $\chi(\mathbf{k},\tau)$ and $N°(\mathbf{k},\tau)$ with weighted mean values of the expressions for the various ion species, making sure that the plasma remains neutral in the mean. Figure 9 shows the spectra for various mixing fraction of oxygen and hydrogen ions. Note that the normalised frequency is referred to the hydrogen thermal velocity $V_{H,}$ i.e. $X = \omega / k\, V_H$. The fraction f refers to the fraction of hydrogen ions.

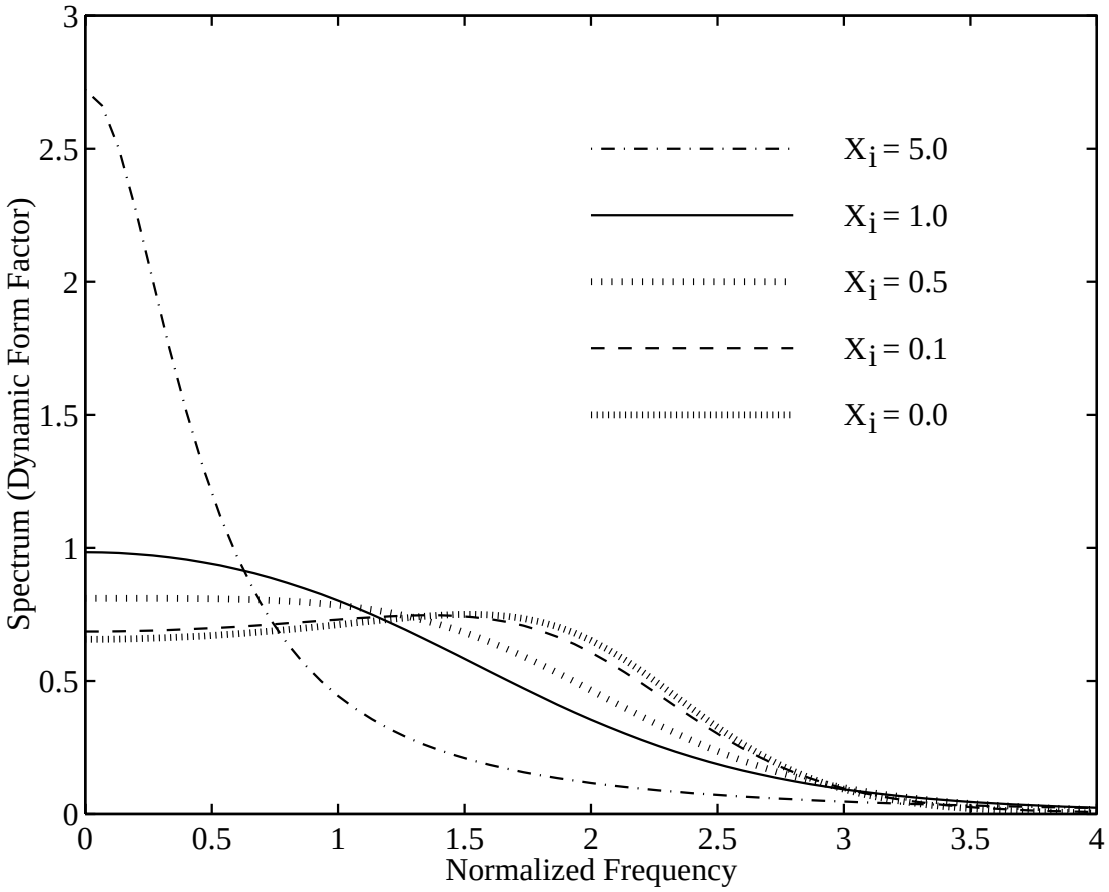

Figure 8. Ion power spectra for thermal equilibrium for various values of ion-neutral collision frequencies expressed as $X_i = \upsilon_i / k\, V_{th}$ *for a fixed value of* $X_p = \omega_{pe} / k\, v_{th}$.

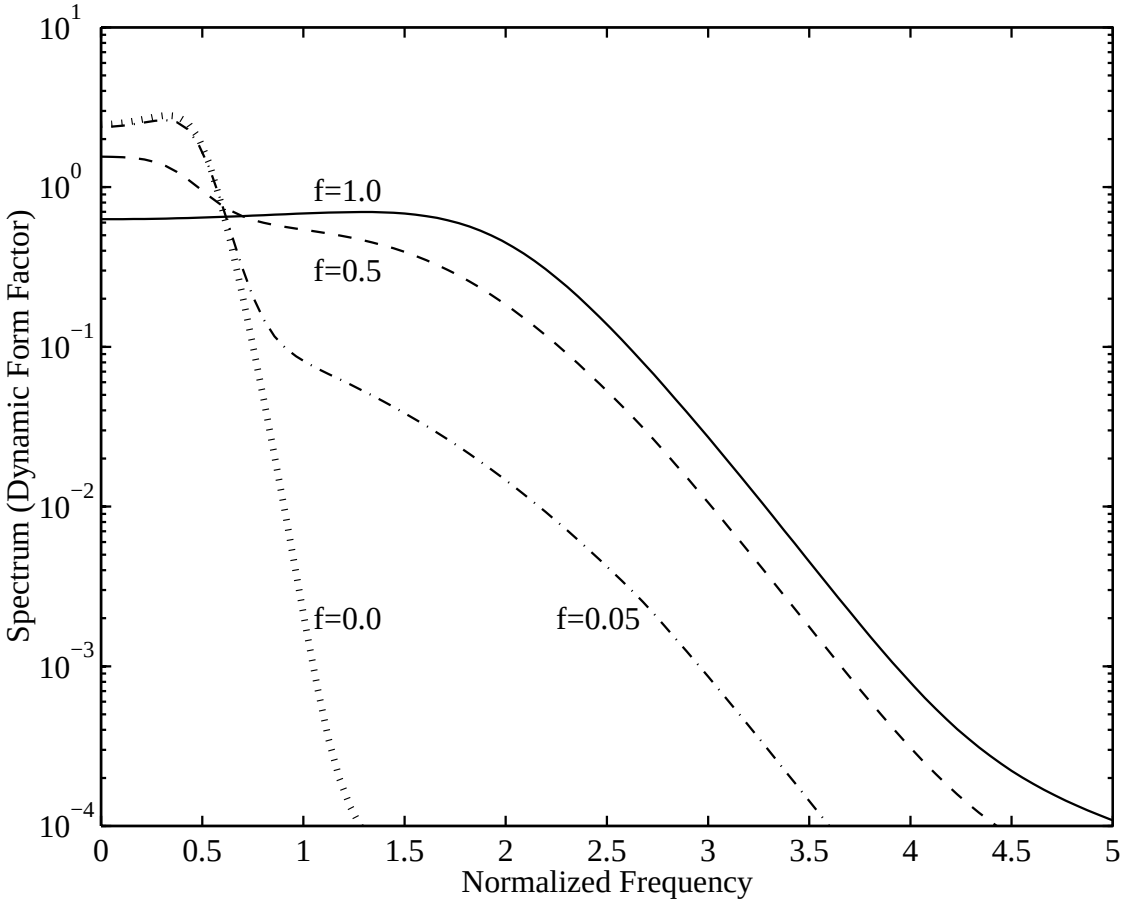

Figure 9. Ion power spectra for a mixture of hydrogen and oxygen ions. The mixing ratio $f = N_H / (N_H + N_O)$*. Note that the normalized frequency X refers to hydrogen, i.e.* $X = \omega / \omega_{pH}$.

Finally let us briefly touch the problem of computing the total scattered power. This has been done by *Buneman* [1962] and we only briefly give the results here for completeness. The total fluctuation caused by dressed electrons and by the ion induction are treated separately. For the electron contribution it is argued that $\mathbf{k}\,\mathbf{T}_i \approx 0$ over the larger portion of the frequency range contributing. Using this simplification integration over ω shows:

$$\frac{1}{2\pi}\int \Phi(\mathbf{k},\omega)\,\mathrm{d}\omega\Big|_{electrons} \approx \frac{(kD_e)^2}{1+(kD_e)^2}) \tag{68}$$

In the low frequency range where ion dynamics are important the integration is carried out by putting $\mathbf{k}\,\mathbf{T}_e = -i$. The result is:

$$\frac{1}{2\pi}\int \Phi(\mathbf{k},\omega)\,\mathrm{d}\omega\Big|_{ions} \approx \frac{1}{[(kD_e)^2+1]\,[(kD_e)^2+1+\theta_e/\theta_i]}) \tag{69}$$

It is not quite clear how accurate these results are in general. However, they do reduce to the correct values for equal temperatures $\theta_e = \theta_i$. In this case the total fluctuation may be derived directly from thermodynamic arguments, see *Fejer* [1960], *Hagfors* [1961].

It is in most cases very difficult to detect a well developed plasma line because the total power is proportional to $(kD_e)^2$, which must be small for Langmuir waves to exist. The exitation of Langmuir waves can, however be strongly enhanced by the presence of a tail of suprathermal electrons caused either by photo electrons created in the production process of the ionospheric plasma through solar ultraviolet radiation, or through the precipitation of energetic charged particles at high latitudes. As a model of the suprathermal electrons we shall assume a Maxwellian distribution at a temperature θ_1 and with a density which is a small fraction f of the total electron density N_e. Using the simple expression for the power spectrum near the plasma line as derived from Eq. 16 we obtain:

$$\Phi(\mathbf{k},\omega) = VN_e \frac{|1 + \chi_i(\mathbf{k},\omega)|^2 \, \Phi^0{}_e(\mathbf{k},\omega)}{|1 + \chi_e(\mathbf{k},\omega) + \chi_i(\mathbf{k},\omega)|^2} \tag{70}$$

Assuming that we are in the parameter regime which corresponds to well defined plasma oscillations at the Langmuir frequency $\omega_L \approx \omega_p \, (1+1.5 \, (kD_e)^2)$ the real part of the ion susceptibility is on the order $kD_e \, (m/M)^{3/2}$ and can be ignored. What remains of the spectrum becomes:

$$\Phi(\mathbf{k},\omega) = VN_e \frac{\Phi^0{}_e(\mathbf{k},\omega)}{|1 + \chi_e(\mathbf{k},\omega)|^2} \tag{71}$$

Expanding the denominator about the resonance frequency ω_R to second order in $\omega - \omega_R$ and making use of the expression for the susceptibility in terms of the $G(\omega)$ we obtain for the total power in each of the two plasma lines:

$$\Phi(\mathbf{k}) = \frac{VN_e}{\omega_p{}^4} \left(\frac{\mathrm{d}^2 G_I(\omega)}{\mathrm{d}\omega^2} \right)^{-1} \left(\frac{\mathrm{d}^2 G_R(\omega)}{\mathrm{d}\omega^2} \right)^{-1} G_R(\omega) \tag{72}$$

In this equation we have put:

$G(\omega) = G_R(\omega) + i \, G_I(\omega)$

For a Maxwellian plasma without magnetic field and collisions we have:

$$G_R(\omega) = \sqrt{\frac{\pi}{2}}\frac{1}{k}\, e^{-\frac{1}{2}X^2} \qquad \text{for all } X$$

$$G_I(\omega) = \frac{1}{k}\left(X^{-1} + X^{-3} + 3\,X^{-5} \ldots\right) \qquad X \gg 1 \qquad (73)$$

$$G_I(\omega) = \frac{1}{k}\left(X - \frac{1}{3}X^3 + \frac{1}{5}X^5 \ldots\right) \qquad X \ll 1$$

and $X=\omega/kv_{th}$. With two overlapping electron Maxwellian velocity distributions at different temperatures and different densities, one for the background at density $(1 - f)\, N_e$ and temperature θ_1, and the other for the photo electrons with density $f\, N_e$ and temperature θ_2, one obtains:

$$G(\omega) = (1 - f)\, G_1(\omega) + f\, G_2(\omega) \qquad (74)$$

where f is the fraction of the electron density carried by the photo electrons, θ_1 the temperature of the thermal electrons and θ_2 the temperature of the photo electrons. The functions G_1 and G_2 are found by substituting the appropriate temperatures into the G-functions defined above.

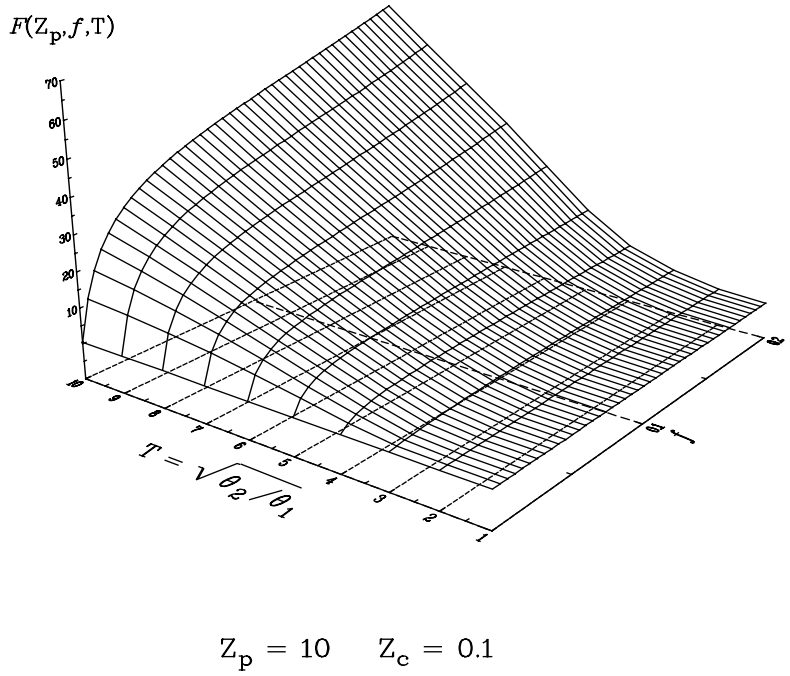

Figure 10. Plasma line enhancement factor plotted against the fraction of photoelectrons f and $T=\sqrt{\theta_2/\theta_1}$ *where* θ_2 *is the temperature of the photoelectrons and* θ_1 *the temperature of the background.*

Figure 10 shows the normallized plasma line radar cross section as a function of the fraction f of photo electrons, and the temperature ratio θ_2/θ_1 for two different values of $kD_e=1/X_p$. As can be seen the plasma line enhancement can be quite substantial when photo electrons, or other suprathermal electrons are present. Because of the limited sensitivity of the ISR installations plasma line observations are nearly always made when there is a substantial enhancement. From such observations the "*temperature"* and the density of suprathermal electrons may be assessed.

4. - Conclusion

In the present report we have rederived and extended certain well known expressions for the scattering of electromagnetic waves by thermal electron density fluctuations in a plasma. The derivation was based on a first order solution of the Vlasov equation in a homogeneous plasma with an external magnetic field present. In the derivation the concept of superposition of dressed particles as introduced into plasma physics by *Rosenbluth and Rostoker* [1962] was exploited fully in order to stress the physical processes determining the properties of the thermal fluctuations. The results can be used in non-equilibrium situations where electrons and ions are at different temperatures but individually in equilibrium. The method can also be used to study non-Maxwellian plasmas provided they are not unstable.

It was also indicated how in the same framework transverse electromagnetic particle interaction can be taken into account. This was not developed in much detail, however, because such interactions are not of much interest in the interpretation of scattering from the ionosphere.

The foregoing discussion is believed to present a fairly complete picture of the present state of development of the theory of density fluctuations in the ionospheric plasma. Further problems that obviously must be studied more closely in future are those relating to instabilities caused by currents passing through the ionosphere, and those connected with the fact that the ionosphere is only partly ionized and that therefore collisions play some part in determining the fluctuations, and must be considered in greater detail.

Acknowledgement:

The author has benefited greatly from cooperation and discussions with Dr. Buneman and Dr. Eshleman of Stanford University during the initial phases of this work, and later through numerous EISCAT colleagues. Dr. Galina Sukhorukova has carried out the numerical calculations for the illustrations.

5. References

Beynon W.J.G., **P.J.S. Williams**, Incoherent scatter of radio waves from the ionosphere, *Rep. Prog. Phys.*, ***41***, 909-956, 1975.

Bowles K.L., Observations of vertical incidence scatter from the ionosphere at 41 Mc/s, *Phys. Rev. Letters*, ***1***, 454, 1958.

Bowles K.L.,Incoherent scattering of free electrons as a technique for studying the ionosphere and exosphere: Some observations and theoretical considerations, *J. Res. N.B.S.*, ***65D***, 1, 1961.

Bowles K.L., **G.R. Ochs**, **J.L. Green**, On the absolute intensity of incoherent scatter echoes from the atmosphere, *J. Res. N.B.S.*, ***66D***, 395, 1962.

Buneman O., Fluctuations in a multicomponent plasma, *J. Geophys. Res.*, ***66***, 1978-1979, 1961.

Buneman O., Scattering of radiation by the fluctuations in a nonequilibrium plasma, *J. Geophys. Res.*, ***67***, 2050-2053, 1962.

Chandrasekhar S., Stochastic problems in Physics and Astronomy, *Rev. Mod. Phys.*, ***15***, 1-89, 1943.

Dougherty J.P., **D.T. Farley**, A theory of incoherent scattering of radio waves by a plasma, *Proc. Roy. Soc.*, ***259A***, 79-99, 1960.

Dougherty J.P., **D.T. Farley**, A theory of incoherent scattering of radio waves by a plasma, 3. Scattering in a partly ionized gas, *J. Geophys. Res.*, ***68***, 5473-5486, 1963.

Evans J.V, Theory and practice of ionosphere study by Thomson scatter radar, *Proc.IEEE*, ***57***, 496-530, 1969.

Farley D.T., **J.P. Dougherty**, **D.W. Barron**, A theory of incoherent scattering of radio waves by a plasma, 2. Scattering in a magnetic field, *Proc. Roy. Soc.*, ***263A***, 238-258, 1961.

Fejer J.A., Scattering of radio waves by an ionized gaz in thermal equilibrium, *Can. J. Phys.*, ***38***, 1115-1125, 1960a.

Fejer J.A., Scattering of radio waves by an ionized gaz in thermal equilibrium in the presence of a uniform magnetic field, *Can. J. Phys.*, ***39***, 716-740, 1961.

Gordon W.E., Incoherent scattering of radio waves by free electrons with applications to space exploration by radar, *Proc. I.R.E.*, ***46***, 1824-1829, 1958.

Hagfors T., Density fluctuations in a plasma in a magnetic field with applications to the ionosphere, *J. Geophys. Res.*, ***66***, 1699-1712, 1961.

Millman G.H., **A.J. Moceyunas**, **A.E. Sanders**, **R.F. Wyrick**, The effect of Faraday rotation on incoherent backscatter observations, *J. Geophys. Res.*, ***66***, 1564-1568, 1961.

Moorcroft D.R., On the determination of temperature and ionic composition by electron backscattering from the ionosphere and magnetosphere, *J.Geophys Res*, ***69***, 955-970, 1964.

Perkins F.W., **E.E. Salpeter**, **K.O. Yngvesson**, Incoherent scatter from plasma oscillations in the ionosphere, *Phys. Rev. Letters*, ***14***, 579, 1965.

Pineo V.C., **L.G. Kraft**, **H.W. Briscoe**, Ionospheric backscatter observations at 440 Mc/s, *J. Geophys. Res.*, ***65***, 1620-1621, 1960.

Renau J., Scattering of electromagnetic waves from a nondegenerate ionized gas, *J. Geophys. Res.*, ***65***, 3631-3640, 1960.

Rosenbluth M.N., **N. Rostoker**, Scattering of electromagnetic waves by a nonequilibrium plasma, *Phys. Fluids*, ***5***, 776-788, 1962.

Salpeter E.E., Electron density fluctuations in a plasma, *Phys. Rev.*, ***120***, 1528-1535, 1960.

Salpeter E.E., Plasma density fluctuations in a magnetic field, *Phys. Rev.*, ***122***, 1663-1674, 1961.

Sheffield J., "*Plasma Scattering of Electromagnetic Radiation*", Academic Press, New York, San Fransisco London, 1975.

Sitenko A.G., "*Electromagnetic Fluctuations in Plasmas*", Academic Press, New York, London, 1967.

Woodman R., Incoherent scattering of electromagnetic waves by a plasma, *Thesis*, Harvard, 1965.

PLASMA INSTABILITIES AND THEIR OBSERVATIONS WITH THE INCOHERENT SCATTER TECHNIQUE

Wlodek Kofman

1. Introduction

This chapter deals with the presentation of non-linear processes in the auroral ionosphere which are observable by the incoherent scatter technique. These non-linear phenomena can be directly seen on the shape of the spectrum or indirectly on the ionospheric parameters. In a first part, one starts with the simplified, classical and linear description of the wave modes in the plasma. The concept of the unstable waves which can grow in space and/or in time is then introduced in the second part. These are the normal modes of plasma which, in the presence of the "*free energy*" source, become unstable. These modes have a well-defined relationship between the κ vector and the angular frequency ω which implies that the plasma fluctuations are weak. The quasi-linear theory is suitable to outline the physics. We use this quasi-linear description of the waves in the plasma in order to derive the instabilities measurable by radars. In the third part, illustrations are given with incoherent scatter measurements and various auroral processes; "*free energy*" sources responsible for these instabilities like electric convection field and precipitations are discussed.

2. Waves in the plasma.

In this chapter, the simplified theory of the plasma waves is developed using two approaches : fluid and kinetic, this in order to introduce the normal modes in the plasma, which are usually observed with the incoherent scatter technique. These modes are unstable in some situations; their description is the goal of this paper.

2.1. Fluid equations

The total charge and the current density in the plasma are described by the following equations :

$$\begin{aligned} \rho &= n_i\, q_i + n_e\, q_e \\ \mathbf{j} &= n_i\, q_i \mathbf{v}_i + n_e\, q_e \mathbf{v}_e \end{aligned} \qquad (1)$$

In this description, we do not use a single particle motion but the fluid velocity **v** which corresponds to the average velocity of particles.

The Maxwell equations describe the relations between the electric and the magnetic fields in the plasma, respectively **E** and **B**.

$$\begin{aligned} &\varepsilon_0 \, \nabla \mathbf{E} = \rho \\ &\nabla \mathbf{B} = 0 \\ &\nabla \times \mathbf{E} = -\frac{\partial \mathbf{B}}{\partial t} \\ &\mu^{-1} \nabla \times \mathbf{B} = \mathbf{j} + \varepsilon_0 \frac{\partial \mathbf{E}}{\partial t} \end{aligned} \qquad (2)$$

where subscripts ε_0 and μ represent the dielectric constant and the permeability, respectively, and **j** is the current density.

To obtain the fluid description, one has to introduce the momentum and continuity equation in addition:

$$\begin{aligned} &m_j \, n_j \left[\frac{\partial \, \mathbf{v}_j}{\partial \, t} + (\mathbf{v}_j \nabla) \, \mathbf{v}_j \right] = q_j \, n_j \, (\, \mathbf{E} + \mathbf{v}_j \times \mathbf{B} \,) - \nabla \, p_j \\ &\frac{\partial \, n_j}{\partial \, t} + \nabla \, (\, n_j \, \mathbf{v}_j \,) = 0 \end{aligned} \qquad (3)$$

where subscript *j* corresponds to ions and electrons; *m*, *n*, **v** and *q* are the particle mass, density, velocity and charge, respectively; $p_j = C_j \, n_j^c$ is the thermodynamic equation of state with *c* being the ratio of specific heats, and C_j is constant. In general, $\underline{\underline{\mathbf{P}}}$ is a stress tensor which, for the Maxwellian plasma, takes the form of a diagonal matrix with the same elements p_j. In this case, one obtains $\nabla . \, \underline{\underline{\mathbf{P}}} = \nabla p_j$.

For the isothermal plasma $c = 1$ and in more general cases $c = \frac{2 + N}{N}$ where *N* is the number of degrees of freedom of the gas, $c = 3$ for one dimensional adiabatic compression.

The solution of these equations gives a self-consistent set of fields and motions in the fluid approximation.

In a plasma, it is usually possible to assume $n_i = n_e$ and $\nabla \cdot \mathbf{E} \neq 0$ at the same time. One calls this approximation a quasi neutrality. As long as motions [*waves*] are slow enough for both ions and electrons to have time to move, it is legitimate to replace Poisson equation by $n_i = n_e$. If it is not the case, one has to find **E** from Maxwell equations.

The traditional development of the linear theory of waves in the plasma is the application of the Fourier/Laplace analysis in space/time, in which one assumes that the fluctuations are in the following form :

$$n = n_1 \exp[\, j\, (\, \kappa \,.\, \mathbf{r} - \omega t\,)] \qquad \mathbf{E} = \mathbf{E}_1 \exp[\, j\, (\, \kappa \,.\, \mathbf{r} - \omega t\,)] \tag{4}$$

where κ is a wave vector, $\mathbf{r}$ is a position and ω an angular frequency. From the momentum and continuity equations, the fluctuating particle densities and current densities are obtained and are then inserted into Maxwell equations to obtain a dispersion equation. This equation relates ω and κ and therefore determines normal modes of plasma. This global and full dispersion equation obtained from the whole set of linearised equations has a complicated form. The various approximations can be derived from this general solution giving modes of the plasma. In this chapter, we adopted a different approach using the suitable assumption in order to start with simplified equations.

The dispersion equation may be solved either as a boundary value problem [ω *real and* κ *complex*] or as an initial value problem [κ *real and* ω *complex*]. In this paper, we will use the latter approach. We will suppose $\omega = \omega_r + j\, \gamma$, where γ is a growth or dumping rate. For $\gamma > 0$, the plasma is unstable. For the Maxwellian particle distribution, the dispersion equation typically yields non growing modes. The "*free energy*" [*anisotropy, inhomogeneity, relative drift between different species*] is necessary to produce instabilities.

The weakness of the fluid approach is that one can include the damping [*growth*] rate depending only on collisions.

From the point of view of the analysis, it is advantageous to separate the fluctuations fields into two types :

- longitudinal: $\kappa \times \mathbf{E} = 0$
- transverse: $\kappa \,.\, \mathbf{E} = 0$

The plasma fluctuations that only have a longitudinal component have no magnetic field [$\mathbf{B} = 0$] and are named "*electrostatic*". Indeed, the complete solution of the general dispersion equation will typically have contributions from two fields : transverse and longitudinal. The transverse component is a purely electromagnetic one. Most fluctuations in space plasmas have both components.

2.1.1. Electron plasma wave.

To analyse the electron plasma waves, let us imagine that the ions form a uniform background. If the electrons are displaced by some perturbation, an electric field will build up in such a direction as to restore the neutrality. Because of their inertia, the electrons will overshoot and oscillate around their equilibrium positions. We are presently interested in the fast oscillations [$\omega > \kappa\ (k\ T / m_e)^{1/2}$]. The massive ions do not have time to respond to the oscillating field and it is why they may be considered as fixed. To simplify, let us assume that the motion only occurs in one direction.

In this chapter, we are interested in the electron plasma waves which are the electrostatic mode. The condition according to which the electric field is parallel to the κ vector leads to the application of only the Poisson equation from the set of Maxwell equations [$\mathbf{B} = 0$, $\kappa \times \mathbf{E} = 0$]. Therefore, we have a set of following equations.

$$
\begin{aligned}
& m_e\, n_e \left[\frac{\partial\, \mathbf{v}_e}{\partial\, t} + (\mathbf{v}_e \nabla)\, \mathbf{v}_e \right] = -\, e\, n_e\, \mathbf{E} - \nabla\, p_e \\
& \frac{\partial\, n_e}{\partial\, t} + \nabla\, (\, n_e\, \mathbf{v}_e\,) = 0 \\
& \varepsilon_0\, \nabla \cdot \mathbf{E} = e\, (\, n_i - n_e)
\end{aligned}
\qquad (5)
$$

where subscripts e and i stand for electrons and for ions, respectively.

As we said before, the replacement of the Poisson equation by $n_i = n_e$ is possible in the case of slow motions. The electron plasma waves are fast and the density fluctuation occurs.

In the small amplitude approximation, one can linearise equations.

$$n_e = n_0 + n_1; \quad v_e = v_0 + v_1; \quad E = E_0 + E_1$$

One supposes that the uniform field and neutral plasma are at rest at the beginning, which leads to the following conditions and equations.

$$
\begin{aligned}
& \nabla\, n_0 = v_0 = E_0 = 0 \text{ and:} \\
& \frac{\partial\, n_0}{\partial\, t} = \frac{\partial\, v_0}{\partial\, t} = \frac{\partial\, E_0}{\partial\, t} = 0 \\
& m_e\, n_0 \left[\frac{\partial\, \mathbf{v}_1}{\partial\, t} + (\mathbf{v}_1 \nabla)\, \mathbf{v}_1 \right] = -\, e\, n_0\, \mathbf{E}_1 - \nabla\, p_e \\
& \frac{\partial\, n_1}{\partial\, t} + n_0\, \nabla\, v_1 + v_1\, \nabla\, n_0 = 0
\end{aligned}
\qquad (6)
$$

The second term in the momentum equation is quadratic in amplitude and we linearise by neglecting it. We did the same for other second order terms [$n_1 E$, $n_1 \partial v_1 / \partial t$].

The third term in the continuity equation is zero due to our assumptions.

Applying the Fourier/Laplace method, one obtains the set of equations:

$$\begin{aligned}
&\varepsilon_0 \nabla.\mathbf{E}_1 = - e n_1 \\
&- j \kappa E_1 \varepsilon_0 = - e n_1 \\
&- j m_e v_1 n_0 \omega = - e n_0 E_1 - \nabla p_e \\
&- j \omega n_1 = - n_0 j \kappa v_1 \\
&\nabla p_e = c k T_e \nabla n_e \\
&c = \frac{N+2}{N}
\end{aligned} \qquad (7)$$

with $c = 3$ for one dimensional problem, and k being the Boltzmann constant.

By eliminating E_1 and n_1 from the previous equations, the dispersion relation for electron plasma waves in the fluid approximation is obtained :

$$\omega^2 = \frac{n_0 e^2}{\varepsilon_0 m_e} + \frac{3 k T_e}{m_e} \kappa^2 \qquad (8)$$

where one terms the plasma angular frequency where n is in m^{-3} units

$$\omega_p^2 = \frac{n_0 e^2}{\varepsilon_0 m_e} \text{ (rad.s}^{-1})^2 \text{ and } f_p \cong 9 \sqrt{n_0} \qquad (9)$$

Defining the thermal velocity as $v_{th}^2 = \frac{2 k T_e}{m_e}$, this dispersion relation is often written:

$$\omega^2 = \omega_p^2 + \frac{3}{2} \kappa^2 v_{th}^2 \qquad (10)$$

This relation is presented in Figure 1 in the ω-κ. coordinates.

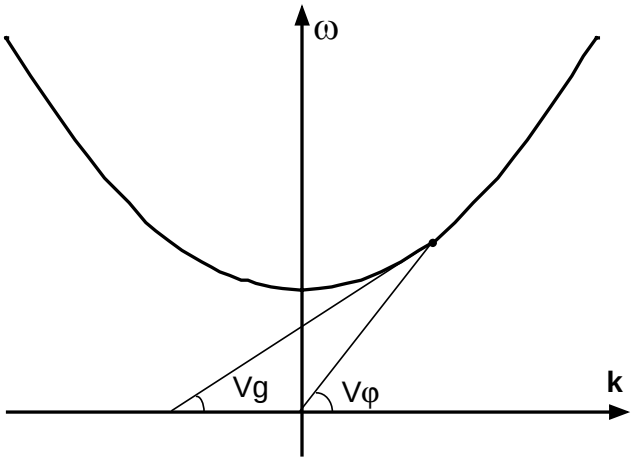

Figure 1. Dispersion relation in the ω-κ coordinates, with: $v_g = \frac{d\omega}{d\kappa} = \frac{3v_{th}^2}{2v_\varphi}$ *and* $v_\varphi = \frac{\omega}{\kappa}$.

For the large κ, $v_g \cong v_\varphi$ and therefore the group velocity is essentially at the thermal velocity.

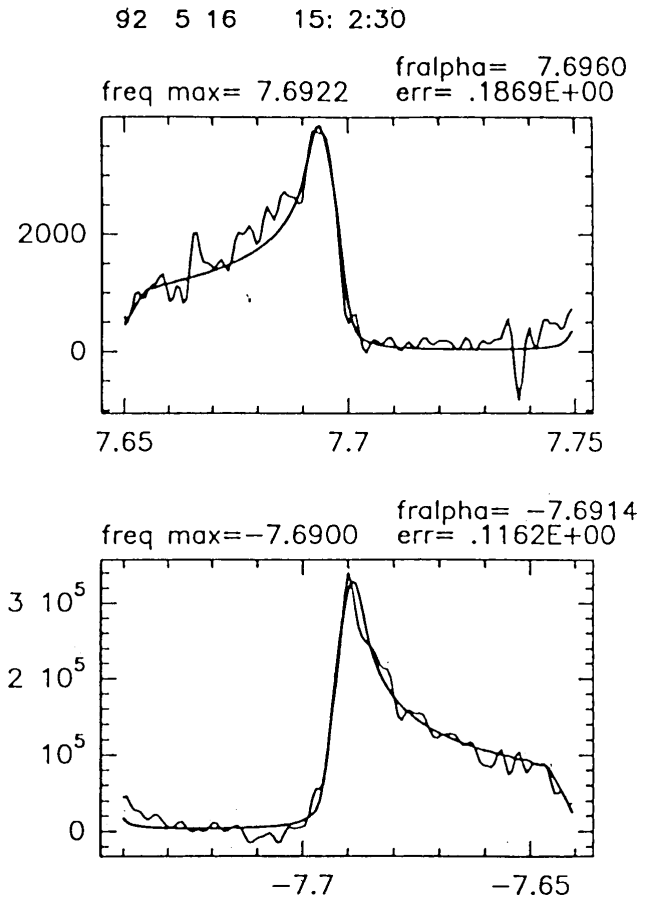

Figure 2. Examples of measured upshifted and downshifted plasma lines, with 10-s integration time and their fit to the model.

The analysis made previously neglected the magnetic field. In the case of the presence of the magnetic field, which is the case of the ionosphere, equation 8 slightly changes. The term depending on the gyrofrequency and on the angle between the κ vector and the magnetic field [$\omega_c^2 \sin^2\theta$] is added to the right side of the equation. In this chapter, we analysed the one dimensional motion. In the plasma, the electrostatic plasma waves propagate in all possible directions with the dispersion relation given previously.

The incoherent scatter technique gives the possibility to observe the plasma waves. In Figure 2, one shows the measurements of the plasma lines [*Kofman et al., 1995*] obtained by EISCAT radar. One can see two lines close to ±7.6 MHz, upshifted and downshifted, respectively due to plasma waves going towards and away from the radar.

The wide spectrum observed [$\approx$ *50 kHz*] is due to the technique used in these measurements. For the homogeneous ionosphere, the plasma line is very narrow with a width of few kHz due to the collisions between electrons and ions, electrons and neutrals and Landau damping [*see § 2.2.1*]. In these measurements, one used the long-pulse modulation. This implies that the covered ionosphere is not homogeneous and that the resonance frequency changes inside the radar bandwidth. The strong peak seen in the figure corresponds to the frequency peak of the F-region. In the ionosphere, there is no higher frequency than this one and this is why there is a sharp cut-off on the right [*left*] side of the upshifted [*downshifted*] line.

2.1.2. Ion acoustic waves.

In the neutral gas, acoustic waves are excited through the normal binary collisions.

In the absence of ordinary collisions, acoustic waves can occur through the intermediary of an electric field. Ions are massive compared with electrons; their velocity is much lower than the one of electrons and therefore acoustic waves are low-frequency oscillations.

Electrons move much faster than ions, because they are light [$\approx$ *1832 times for protons*] and therefore they can fast respond to the charge separation electric field. When the ions are perturbed, the electrons fast neutralise the perturbation and this makes the wave propagate.

One can see the acoustic waves in the plasma, like the waves in the neutral gas, where the neutral particles are the ions screened by the electrons. Therefore, in the fluid calculations, one can assume the quasi neutrality $n_e \approx n_i = n$, which means that the ions and the electrons fluctuate in the same way.

The momentum and the electric field are given by :

$$m_i n_i \left[\frac{\partial \mathbf{v}_i}{\partial t} + (\mathbf{v}_i \nabla)\, \mathbf{v}_i \right] = -e\, n_0 \nabla\varphi - c_i\, k\, T_i \nabla n_i \qquad (11)$$

$$\mathbf{E} = -\nabla\varphi$$

The fluid is accelerated under the combined electrostatic and pressure gradient forces. The electrons move but they cannot leave a region en masse because they will leave the ions. The electrostatic force, due to the charge separation, and pressure gradient force must be closely in balance. This condition leads to the Boltzmann relation :

$$n = n_0 \exp\left(\frac{e\,\varphi}{k\,T_e}\right) = n_0 \left(1 + \frac{e\,\varphi_1}{k\,T_e} + \ldots\right) = n_0 + n_1 \qquad (12)$$

with $n_1 = \dfrac{e\,\varphi_1}{k\,T_e}\, n_0$, $\varphi = \varphi_0 + \varphi_1$ and $\varphi_0 = 0$ because $\mathbf{E}_0 = 0$.

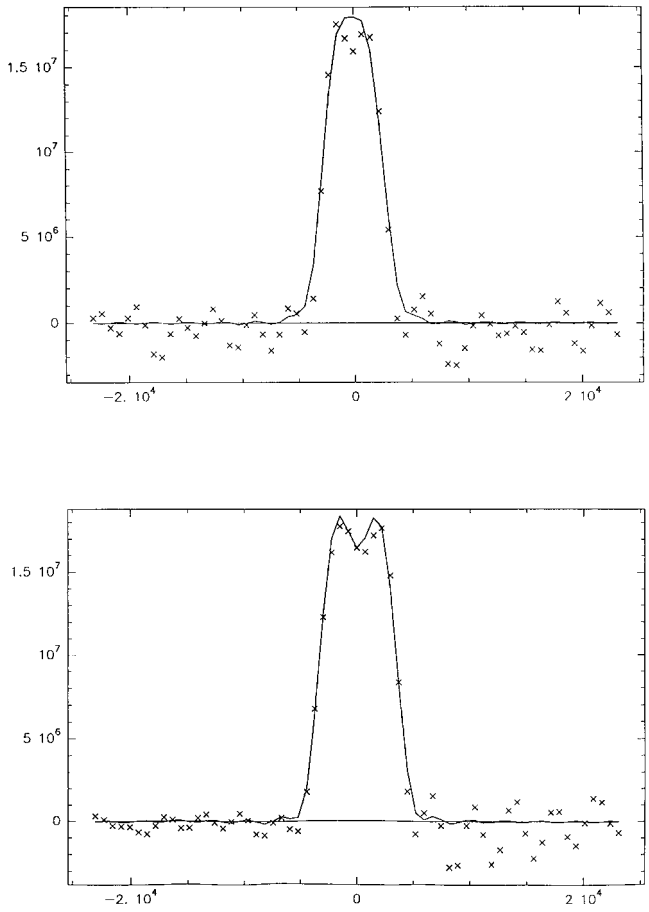

Figure 3. Ion waves spectra measured by incoherent scatter radar.

Therefore, the linearised ion equations using the Fourier/Laplace transformation are :

$$\begin{aligned} -j\,\omega\, m_i\, n_0\, v_{i1} &= -j\, e\, n_0\, \kappa\, \varphi_1 - j\, c_i\, k\, T_i\, \kappa\, n_1 \\ -j\,\omega\, n_1 &= -j\, n_0\, \kappa\, v_{i1} \end{aligned} \qquad (13)$$

Using equations 12 and 13, one obtains the dispersion relation for ion-acoustic waves.

$$\omega^2 = \kappa^2 \left(\frac{k\, T_e}{m_i} + \frac{c_i k\, T_i}{m_i} \right) \text{ or:}$$

$$\left(\frac{\omega}{\kappa} \right)^2 = \frac{k\, T_e + c_i\, k\, T_i}{m_i} = c_s^2$$

c_s as defined here is the sound speed.

It is a one dimensional case and therefore $c_i = 3$; for electrons, $c_e = 1$ because they are isothermal due to their fast movements relatively to the waves. Basically, ion waves have a constant velocity and $v_\varphi = v_g$.

The validity of our solution depends on the assumed quasi-neutrality and this imposes the conditions $(\kappa \lambda_d)^2 << 1$ where λ_d is the Debye length, which means that this approximation is only valid for long wavelengths. For short wavelengths, the ion acoustic wave turns into a ion plasma wave.

In Figure 3, we show the typical ion spectra [*see previous §*] measured by incoherent scatter radar at altitudes of 99 and 105 km. The crosses show the measurements and the continuous line the fit by the theoretical function. Those spectra are generated by the ion-acoustic fluctuations in ionospheric plasma. One can see the typical shoulders which are due to ion acoustic waves.

These spectra are typical when the ion temperature is close to the electron one. When the electron temperature is larger than the ion temperature, for instance $T_e / T_i \approx 2$ is a very frequent case in the F-region, the shoulders are much more pronounced. The ratio of the value at the maximum of the spectrum to the value at zero frequency determines the temperature ratio. The width of the spectrum determines the ion temperature. This dependence is a first order approximation, the ionospheric parameters are usually obtained by the fit of the measurements by the theoretical function on all the various plasma parameters [*see chapter by Schlegel, this volume*].

2.2. Kinetic derivation of dispersion relations

The alternative approach to study the waves in plasmas, which is probably richer especially in the description of instabilities, is the kinetic one. In order to describe the plasma gas, one introduces the single particles distribution function $f_j(\mathbf{r}, \mathbf{v}, t)$. From this function, one derives all moments : density, mean velocity, temperature [*energy*], pressure, etc.. To study the waves in plasmas, one usually applies the Vlasov equation which is derived from the Boltzmann equation including only electromagnetic interactions. Other types of collisions are neglected.

The Vlasov equation is:

$$\left(\frac{\partial}{\partial t} + \mathbf{v} \cdot \frac{\partial}{\partial \mathbf{r}} + \frac{q_j}{m_j}(\mathbf{E} + \mathbf{v} \times \mathbf{B})\frac{\partial}{\partial \mathbf{v}}\right) f_j(\mathbf{r}, \mathbf{v}, t) = 0 \qquad (15)$$

The fields **E** and **B** are the sum of those applied from outside sources and those included from collective motion of plasma particles. For the longitudinal waves, **E** can be determined using only the Poisson equation :

$$\varepsilon_0 \nabla \cdot \mathbf{E} = \rho_{ext} + \Sigma_j \int q_j n_j f_j \, d\mathbf{r} \qquad (16)$$

To obtain the dispersion relation, one needs to substitute the perturbation in the Vlasov equation :

$$\begin{aligned} \frac{f}{n} &= f_0 + \Delta f \exp(j(\kappa \cdot \mathbf{r} - \omega t)) \\ \mathbf{E} &= \mathbf{E}_0 + \Delta \mathbf{E} \exp(j(\kappa \cdot \mathbf{r} - \omega t)) \\ \mathbf{B} &= \mathbf{B}_0 + \Delta \mathbf{B} \exp(j(\kappa \cdot \mathbf{r} - \omega t)) \end{aligned} \qquad (17)$$

where f_0 is the equilibrium distribution function, Δf, $\Delta\mathbf{E}$ and $\Delta\mathbf{B}$ are perturbations [*assumed to be sinusoidal in order to apply a Fourier/Laplace analysis*] and n is the density.

2.2.1. Electrostatic waves

From the Vlasov and Poisson equations, one obtains the set of equations for the electrostatic waves.

$$\begin{aligned} \Delta f &= \frac{\frac{-q\partial f}{m\partial \mathbf{v}} \Delta \mathbf{E}}{j(\mathbf{v} \cdot \kappa - \omega)} \\ \nabla \mathbf{E} &= \frac{\rho}{\varepsilon_0} \Rightarrow \mathbf{E}(\kappa) = -j \frac{\kappa}{\kappa^2} \frac{\rho(\kappa)}{\varepsilon_0} \\ \Delta \mathbf{E} &= \frac{q^2 n}{\varepsilon_0 m \kappa^2} \int \frac{\kappa \frac{\partial f}{\partial \mathbf{v}}}{\mathbf{v} \cdot \kappa - \omega} d\mathbf{v} \cdot \Delta \mathbf{E} \end{aligned} \qquad (18)$$

The first equation is obtained after the linearisation of the Vlasov equation. The second is the Poisson equation. To obtain the third equation, the fluctuation of the charge density was obtained by the integration of the Δf over the velocity space and by the introduction into the Poisson equation. Thus:

$$1 = \frac{\omega_p^2}{\kappa^2} \int \frac{\kappa \frac{\partial f}{\partial \mathbf{v}}}{\mathbf{v}.\kappa - \omega} d\mathbf{v}, \quad \text{with:} \tag{19}$$

$$\omega_p^2 = \frac{q^2 n}{\varepsilon_0 m}$$

One names the dielectric function for longitudinal fluctuations the following quantity :

$$\varepsilon(\kappa, \omega) = 1 - \sum_j \frac{\omega_j^2}{\kappa^2} \int \frac{\kappa \frac{\partial f_j}{\partial \mathbf{v}}}{\mathbf{v}.\kappa - \omega} d\,\mathbf{v} \tag{20}$$

This form of dielectric function is only valid in the absence of magnetic field or in the direction parallel to the magnetic field, κ // $\mathbf{B}_0$.

This equation is difficult to evaluate in a simple way because of the existence of a singularity at $\omega = \mathbf{v}.\kappa$. The proper treatment of this problem was done by Landau in 1946 and this lead to the concept of the Landau damping of the waves which is a non-collisional damping. This problem is discussed in many text books and this is why we will here only summarise the results for studied waves.

In the case of the Maxwellian distribution of the particles, the dielectric function takes a special form.

$$\varepsilon(\kappa, \omega) = 1 + \sum_j \frac{\kappa_j^2}{\kappa^2} W\left(\frac{\omega}{\kappa\sqrt{T_j/m_j}}\right) \tag{21}$$

with $\kappa_j^2 = \frac{n q^2}{\varepsilon_0 T_j}$ [*where T_j is the temperature expressed in energy units*], and

$W(z) = \frac{1}{2\pi} \int_c \frac{x}{x-z} \exp(-\frac{x^2}{2})\, dx))$ is the Fried-Comte function.

The plasma modes correspond to the solutions for $\omega(\kappa)$ of the equation $\varepsilon(\kappa, \omega) = 0$.

2.2.2. Collective Modes

The simplest type of collective modes in the plasma is the electrostatic plasma wave. If one supposes that the plasma is only composed of electrons, the dispersion relation is given by Eq. [22].

$$1 + \frac{\kappa_e^2}{\kappa^2} W\left(\frac{\omega}{\kappa\sqrt{T_e/m_e}} \right) = 0 \qquad (22)$$

For high frequencies for which the condition $\frac{\omega}{\kappa\sqrt{T_e/m_e}} >> 1$ is fulfilled, one can use the asymptotic development of W. The formula $\omega_\kappa^2 \cong \omega_p^2 + 3\frac{T}{m}\kappa^2$ gives the solution of the real part of Eq. [22]. This describes the same mode as the one found in the fluid approximation.

The dispersion relation was solved supposing κ real and ω complex. Each ω mode has an imaginary part and this means that the fluctuations are damped or can grow. In this case, the imaginary part given by :

$$\gamma_\kappa = -\left(\frac{\pi}{8}\right)^{1/2} \omega_p \frac{\kappa_e^3}{\kappa^3} \exp\left(-\frac{\omega_\kappa^2}{2\,\kappa^2\,(T/m)} \right) \qquad (23)$$

describes the Landau damping of the waves. Figure 4 shows the customary physical picture of the Landau damping. The particles which move faster than the wave give energy to the wave and the particles which move slower damp the wave. This means that if there is locally a positive slope in the particle distribution function, near the phase velocity of the wave, the amplitude of the wave can grow. In this case, the number of particles moving faster than the wave is larger than those moving slower. The value of the damping depends on the derivative of the distribution function at the phase velocity.

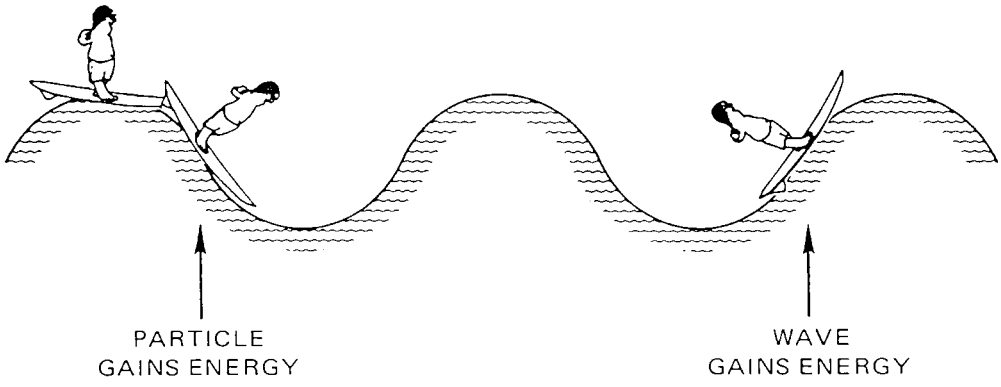

Figure 4. Customary physical picture of Landau damping.

2.2.3. Ion-Acoustic Waves

This mode is obtained for the plasma composed of ions and electrons. The dispersion relation Eq. [21] developed in the frequency range $\kappa\left(\frac{T_e}{m_e}\right)^{1/2} >> \omega >> \kappa\left(\frac{T_i}{m_i}\right)^{1/2}$ gives the resonance frequency and the growing rate given by Eq. [24]. This is a normal ion-acoustic mode which is strongly damped when T_e is close to T_i. The normal incoherent scatter spectrum corresponds to strongly damped waves.

$$\omega_\kappa = \left(\frac{T_e}{m_i} + \frac{3T_i}{m_i}\right)^{1/2}\kappa$$
$$\gamma_\kappa = -\left(\frac{\pi}{8}\right)^{1/2}\left[\left(\frac{m_e}{m_i}\right)^{1/2} + \left(\frac{T_e}{T_i}\right)^{3/2}\exp\left(-\frac{T_e}{2\,T_i} - \frac{3}{2}\right)\right] \qquad (24)$$

3. Instabilities

These are normal modes of a plasma that grow in space and/or in time and that have the following properties :

[1] relations between κ and ω are well defined, which means relatively weak fluctuations

[2] macro instabilities depend on the space properties of plasma

[3] micro instabilities are driven by the departure from the equilibrium of the plasma distribution

The border between these two categories is not clearly cut.

Due to the previous remarks and the Fourier/Laplace approach used in this analysis of the weak instabilities, the normal modes are usually described as plane waves: $n \propto n_1 \exp[\, j\,(\,\kappa.\mathbf{r} - \omega_\kappa t\,)\,]$. The usual Maxwellian distribution, due to the fact that its derivative is always negative, leads to non-growing modes. In order to yield instabilities, the modification of the distribution function from the one at equilibrium should occur and this needs a "*free energy*". This "*free energy*" comes from different sources like anisotropy of particles, relative drift in the ionosphere or the inhomogeneity of the plasma.

For instance, the instability can be caused by the plasma density gradient and this is a large-scale phenomenon.

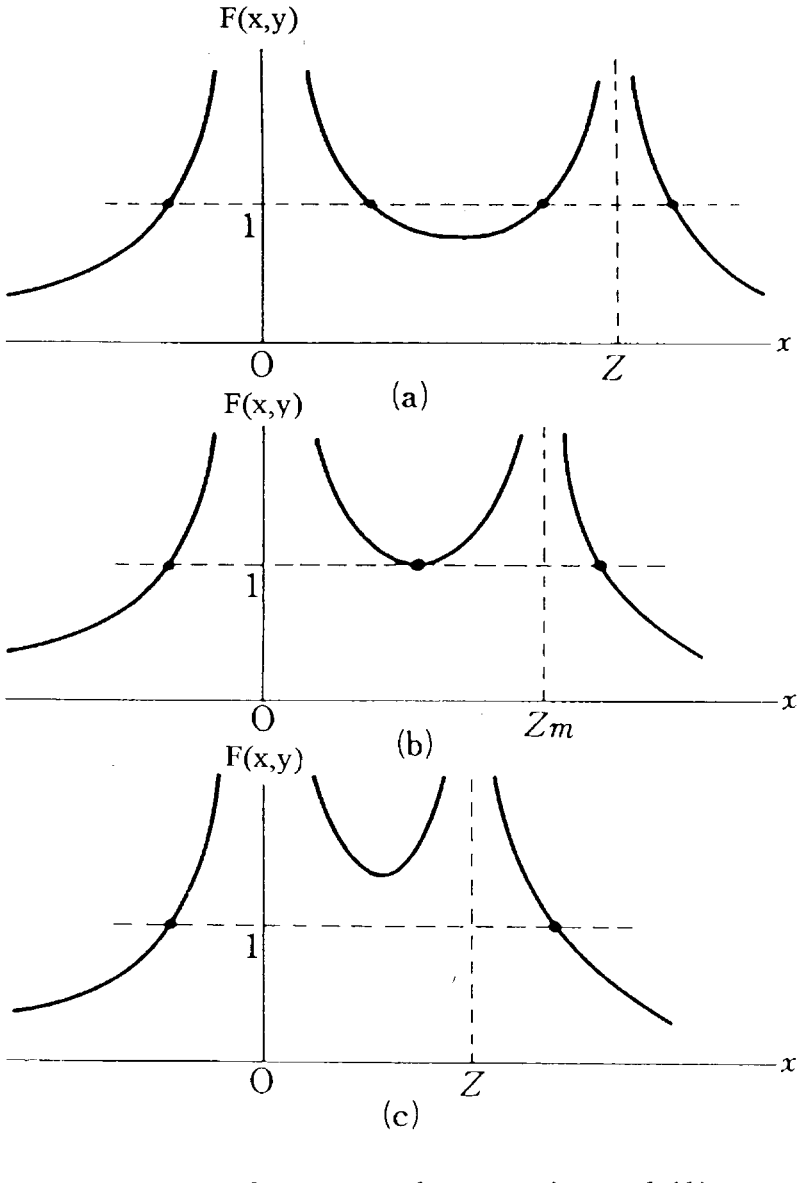

Figure 5. Beam-plasma instability

3.1. Beam-Plasma Instability

To study the beam-plasma instability, one assumes, for a simplified analysis, the plasma to be cold and uniform. This means that the temperatures fulfil $T_i \approx T_e \approx 0$. Therefore, fluid and kinetic descriptions give the same answer. The electrons are assumed drifting through ions with the velocity v_D. These two assumptions lead to the Dirac distribution function.

$$f(\mathbf{v}) = n_i \, \delta_i (v) + n_e \, \delta_e (v - v_D) \tag{25}$$

The dielectric function is obtained from the previous general formula in a simple way using the properties of the delta function.

$$\varepsilon(\kappa, \omega) = 1 - \frac{\omega_i^2}{\omega^2} - \frac{\omega_e^2}{(\omega - \kappa v_D)^2}$$

$$\omega^2_J = \frac{n e^2}{\varepsilon_0 m_j} \quad [\textit{where j stands for ions and electrons}]$$

$$x = \frac{\omega}{\omega_e} \text{ and } y = \frac{\kappa v_D}{\omega_e} \tag{26}$$

$$1 = \left[\frac{m_e}{m_i} \cdot \frac{1}{x^2} + \frac{1}{(x - y)^2}\right] = F(x,y)$$

The last equation can be solved to find the ion plasma modes. As shown in figure 5, there are two possible situations. The solution consists of four real roots which correspond to the stable plasma [*Fig. 5a,b*] or of two real and two complex roots which are the case of the unstable plasma [*Fig. 5c*], due to the imaginary part of the roots. These two complex roots are conjugated and this gives one damped and one growing mode. The maximum growth rate is given by the following formula :

$$\gamma \cong \omega_e \left(\frac{m_e}{m_i}\right)^{1/3} \tag{27}$$

From Figure 5, one can see that for sufficiently small *y*, which means for long-wavelength waves, the plasma is unstable.

This cold plasma approximation does not take into account the Landau damping and is good for the situations in the presence of fast streaming electrons.

3.2. Ion-Acoustic Instability

The conditions for the ion acoustic instability taking into account the Maxwellian plasma can also be easily derived in the direction parallel to the magnetic field. The "*free energy*" is the electron drift v_D relative to ions as previously. One-dimensional distribution functions are introduced into the equation for the dielectric function.

$$f_e(v) = \frac{1}{\sqrt{2\pi\, T_e/m_e}} \exp\left(-\frac{(v-v_D)^2}{2\, T_e/m_e}\right)$$

$$f_i(v) = \frac{1}{\sqrt{2\pi\, T_i/m_i}} \exp\left(-\frac{v^2}{2\, T_i/m_i}\right) \tag{28}$$

$$\varepsilon(\kappa,\omega) = 1 + \frac{\kappa_e^2}{\kappa^2} W\left(\frac{\omega - \kappa v_D}{\kappa\sqrt{T_e/m_e}}\right) + \frac{\kappa_i^2}{\kappa^2} W\left(\frac{\omega}{\kappa\sqrt{T_i/m_i}}\right)$$

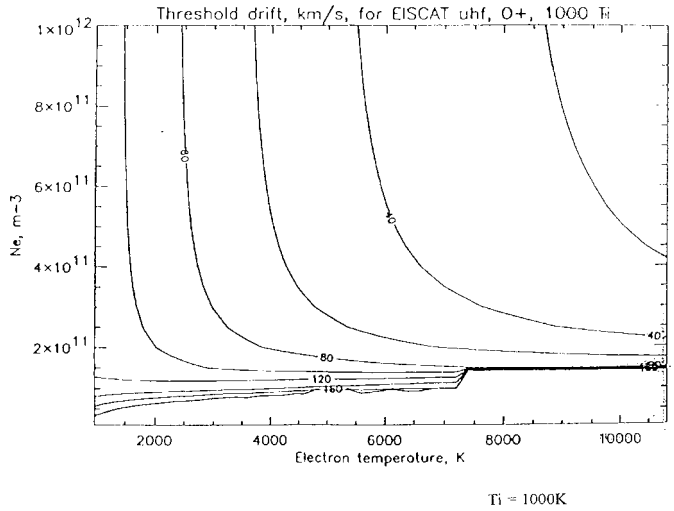

Figure 6. The threshold drift as a function of electron temperature and electron density. Ion temperature was fixed at 1000°K. For instance, for n_e=6 10^{11} m^{-3} and $T_e \approx$ 6000°K, the threshold drift is 40 km.s^{-1}.

For ion acoustic waves, one has searched for the solution with the wave speed fulfilling the following condition :

$$\sqrt{T_i / m_i} << \frac{\omega}{\kappa} << \sqrt{T_e / m_e} + v_D \tag{29}$$

The solution of the dispersion equation is :

$$\omega_\kappa = \pm \frac{\omega_i \, \kappa}{\sqrt{\kappa^2 + \kappa_e^2}}$$

$$\omega_i{}^2 = \frac{n\, e^2}{\varepsilon_0 \, m_i} \tag{30}$$

$$\gamma_\kappa \cong - \left(\frac{\pi}{8} \right)^{1/2} \left(\frac{m_e}{m_i} \right)^{1/2} \kappa \left\{ (c_s - v_D) + c_s \left(\frac{m_i}{m_e} \frac{T_e{}^3}{T_i{}^3} \exp(- \frac{T_i}{2T_e}) \right) \right\}$$

The physical description of the process is the following : the drift motion of electrons relative to ions interacts with one acoustic mode which lifetime increases. The other mode on the contrary is strongly damped. When the velocity increases, one mode can become unstable.

The acoustic waves are unstable when $v_D > c_s$ and strongly depend on the temperature ratio T_e / T_i. In figure 6 we show how the threshold drift, corresponding to $\gamma_\kappa = 0$, for the unstable acoustic waves depends on the temperature ratio and on the electron density for a κ vector of the EISCAT UHF radar. These are the exact calculations for the threshold. One can see that the drift velocity necessary to destabilise the plasma diminishes with the electron temperature. One

needs a very large drift velocity of electrons for the EISCAT κ vector to destabilise the plasma.

When the drift velocity is larger than the thermal velocity [$v_D > v_{th}$], the cold plasma regime and the fluid description work well and this instability is often called two-stream instability.

3.3. Two-stream Instability

This instability is strongly aspect angle dependent [see *Farley*, 1963, *Fejer and Kelley*, 1980]. The resonance frequency and the growing rate are given by the following formula in the fluid approximation :

$$\omega_\kappa = \frac{\kappa\,(\,\mathbf{v}_{De} + \psi\,\mathbf{v}_{Di})}{1 + \psi}$$

$$\gamma = \frac{1}{1+\psi} \left\{ \frac{\psi}{\nu_i} [\,(\omega_r - \kappa.\mathbf{v}_{Di}) - \kappa^2 c_s] + \frac{1}{L_N \kappa^2} \left[(\omega - \kappa.\mathbf{v}_{Di}) \left(\frac{\nu_i}{\Omega_i}.\kappa \right) \right] \right\} - 2\,\alpha N_0 \qquad (31)$$

with:

$$\psi = \frac{\nu_e \nu_i}{\Omega_e \Omega_i} \left(\frac{\kappa_\perp^2}{\kappa^2} + \frac{\Omega_e^2}{\nu_e^2} \frac{\kappa_{/\!/}^2}{\kappa^2} \right)$$

$$L_N = n_e \left(\frac{\partial n_e}{\partial z} \right)^{-1} \qquad (32)$$

$$c_s = \left(\frac{T_e + T_i}{m_i} \right)^{1/2}$$

where v_{De} is the electron drift velocity, v_{Di} the ion drift velocity and L_N the horizontal [*North-South*] gradient of the electron density.

Farley and Buneman [1963] have shown that waves are unstable in a cone of angle φ for which $v_{De} \cos \varphi > c_s$.

For smaller drift velocities, the plasma can still be unstable provided there is a plasma density gradient. The two-stream instability is more important at short wavelengths, while the gradient drift and recombination instabilities are more important for long wavelengths.

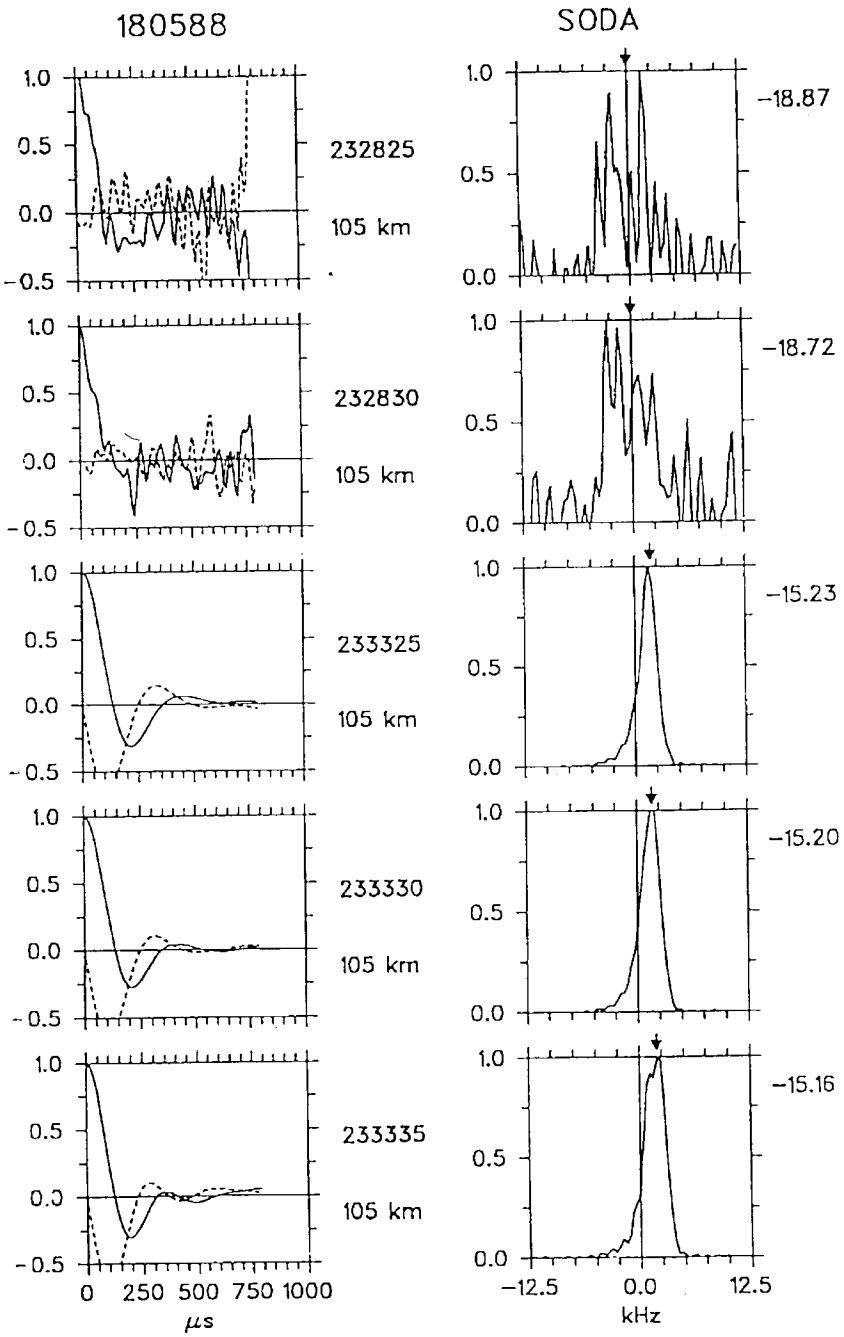

Figure 7. Example of five complex autocorrelation functions and the corresponding spectra for incoherent and coherent scatter echoes measured at 105 km altitude from Sodankylä. The arrow above the spectra shows the mean Doppler shift, the number on the right-hand side of the spectra indicates the logarithm of the volume backscatter cross section in m^{-1}.

4. Radar Measurements

4.1. Two-stream Instability

The classical incoherent scatter radar theory was studied by Hagfors, [*this volume*]. During the observations of plasma irregularities, the much stronger scattering occurs due to enhanced non-thermal plasma density fluctuations. Radars

only detect one particular Fourier component corresponding to the wave vector equal to the difference between the wave vector of the transmitter and the wave vector of the receiver. The density irregularities are strongly field aligned which requires measurements with a wave vector perpendicular to the magnetic field. Usually these non-thermal fluctuations are observed with radars using much lower frequencies [*ten to few tens of MHz*] than incoherent scatter radars. One calls this type of radars "*coherent radar*". EISCAT observations of two-stream instabilities are rare and were made for the first time by *Schlegel and Moorcroft* [1993]. Figure 7 shows some of these measurements. The spectral form of the narrow coherent echoes can be clearly seen in this figure. The authors have compared the cross sections of the different types of scattering: entirely coherent to almost totally incoherent [*figure 8*]. The cross section varies of more than two orders of magnitude. The echoes due to the scattering on the two-stream instability are much stronger. As it is shown in the theory, the cross section depends on the aspect angle and this dependency was studied by the authors.

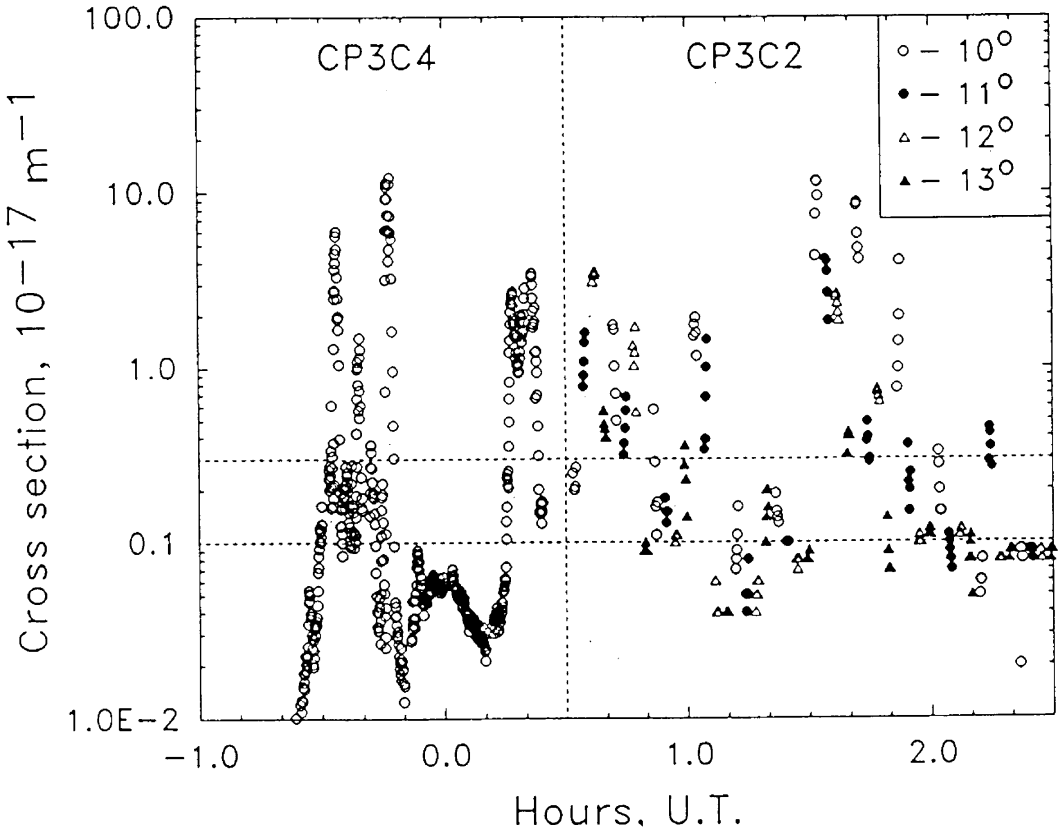

Figure 8. Scattering cross sections obtained from the Tromsö 360-μs pulse data during the coherent scatter experiment on May 18-19, 1988. Observations were made at four different elevation angles of the Tromsö antenna, as indicated by the different symbols. The two horizontal dashed lines separate regions where the scattering is almost entirely coherent (above the upper line) and where the scattering is almost totally incoherent (below the lower line).

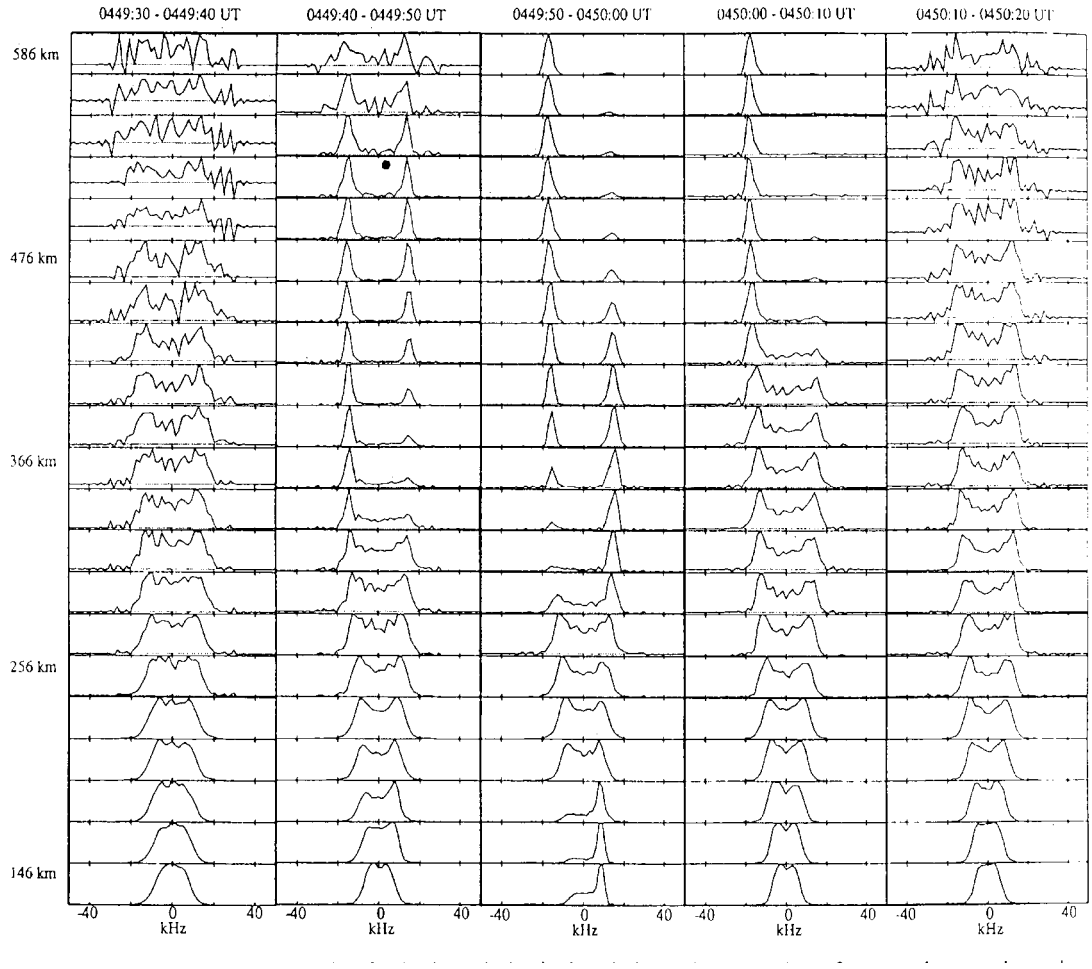

Figure 9. A sequence of 5 successive 10-s data intervals showing how the long-pulse spectra change from normal to anomalous and back again.

4.2. Anomalous spectra

Powerful spectra with strongly asymmetric features [*Figures 9 and 10*] have now been unambiguously observed with incoherent scatter radars both at UHF and VHF frequencies [*Foster et al.*, 1988; *Rietveld et al.*, 1991; *Collis et al.*, 1991; *Wahlund et al.*, 1993; *Forme et al.*, 1993; *Cabrit et al.*, 1995]. In all the cases cited here, all these "*coherent spectra*" feature one strong ion-acoustic peak. These echoes were observed along the magnetic field lines for altitudes ranging from the topside ionosphere all the way down to 140 km. Even though this was quite a unique event, the fact that the observations were made down to 140 km -an altitude where the collision frequency is very large- indicates that these echoes are produced by the electrons streaming up or down the magnetic field lines, at least at times. There is also some evidence [*Collis et al.*, 1991, *Cabrit et al.*, 1995] that the echoes can clearly come from the boundaries of arcs as opposed to the centres of the arc, at least at times [*Fig. 10*].

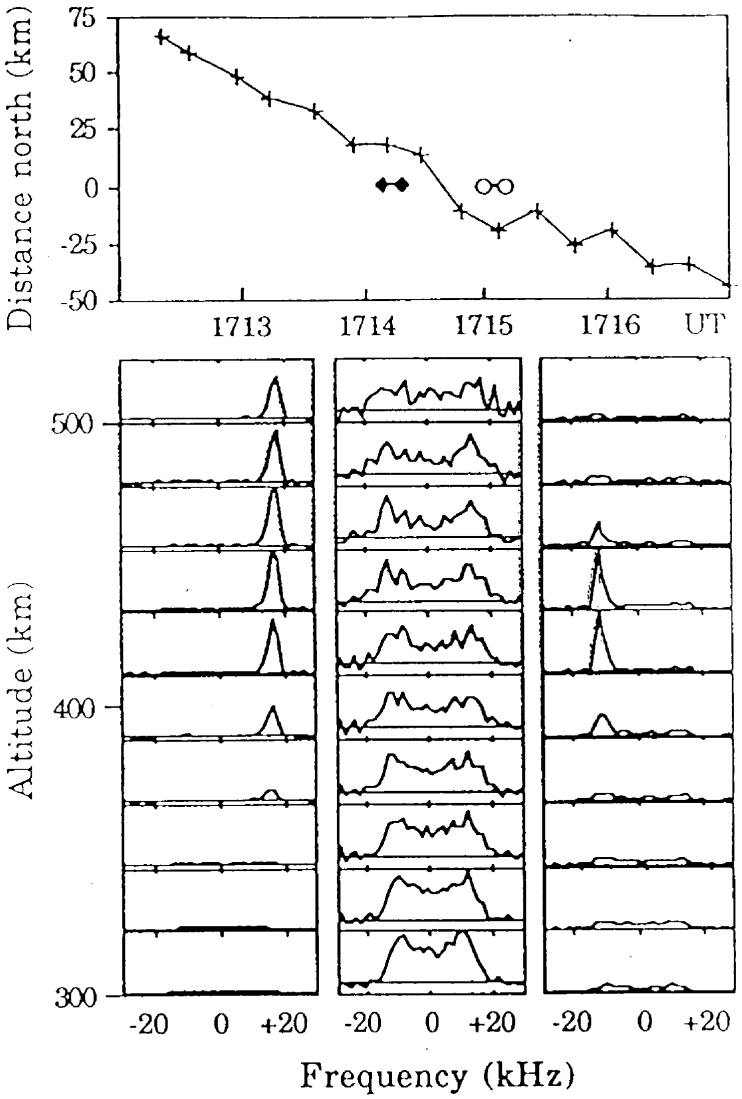

Figure 10. Upper panel : Field-line location (km north of radar) of maximum 630 nm intensity from the scanning photometer (+) in relation to upshifted (♦) and downshifted (o) spectral enhancements detected by EISCAT on 11 January 1989. Lower panels : Radar spectra showing upshifted (1714:10 to 1714:20 UT, left) and downshifted (1715:00 to 1715:10 UT, right) enhancements, contrasted with normal spectra (1714:20 to 1714:30 UT, centre). Amplitudes are normalised to the maximum in each stack, in the ratio 5:1:4, left to right.

The main characteristics of the observations can be summarised as follows :

[1] one of the ion-acoustic shoulders of the incoherent spectra is strongly enhanced. At some altitudes, both sides of the spectrum can be simultaneously enhanced during the time taken by the radar to integrate its signal;

[2] the power of the observed spectra is usually strongly enhanced. This means that the radar cross section can be clearly larger than the classical one associated with quiescent plasmas [*Figure 11*];

[3] the observations are recorded in directions that are close to parallel to the magnetic field line. There are however observations made in the direction at 27° to the magnetic field [*Cabrit et al.*, 1995];

[4] some of the observations show a reversal in the sign of the enhanced shoulder occurring at some altitudes [*approximately around 200 km*];

[5] the statistics seem to indicate that the upper shoulder [*ion-acoustic waves going down*] is more frequently enhanced than the lower shoulder at altitudes below 300 km. Conversely the lower shoulder is enhanced more frequently at altitudes exceeding 450 km [*Rietveld et al.*, 1991]. Finally, at least for the subset of events studied by *Rietveld et al.* [1991] between 300 and 450 km, neither shoulders dominated the statistics.

A theoretical explanation for the generation of these echoes is still a matter of debate. Two main classes of physical processes have been advanced so far. The first such class relies on relative drifts between the thermal species in the plasma to excite the unstable waves, following a mechanism first proposed by *Kindel and Kinnel* [1971] for the destabilisation of ion acoustic waves along the magnetic field. In that original paper, the destabilisation was done by electrons drifting through a stationary background of ions. *Rietveld et al.* [1991] and *St.-Maurice et*

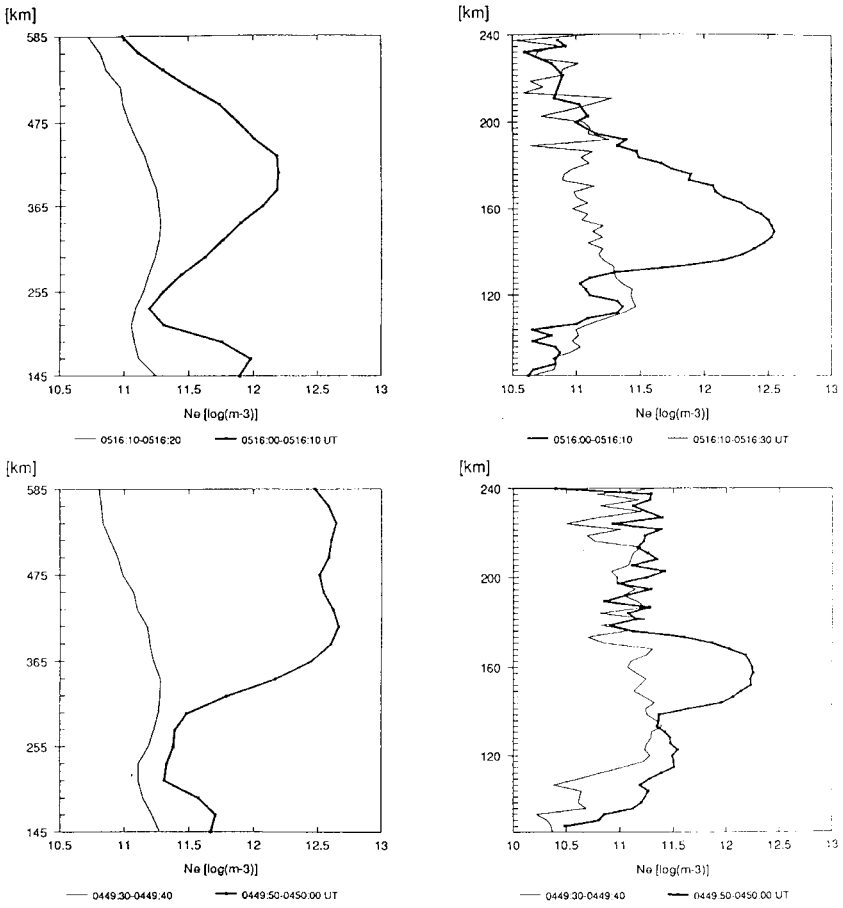

Figure 11. Power profiles obtained from 10-s intervals. The thin lines in the two left-hand panels show equivalent electron density variation (uncorrected for temperature), while the thick lines show the enhanced echoes from the long-pulse spectra. The two right-hand panels are the corresponding data for the low altitude, high resolution multipulse channel. Note the enhancements which reach a factor of 50 in the lower left panel.

al. [1996] used this mechanism by producing ionospheric currents in response to the magnetospheric generator. In one case, the generator was provided directly through an intense precipitation of soft to medium energy electrons from the magnetosphere. As these electrons were stopped by the neutral atmosphere, the divergence in the currents carried by the precipitating electrons was given to charged carriers from the thermal part of the plasma which then provided current closure. It has been assumed by *Rietveld et al.* [1991] as well as by *St.-Maurice et al.* [1996] that in the regions where these currents flow along the magnetic field, they would be carried by thermal electrons. *St.-Maurice et al.* [1996] have also proposed that intense conductivity gradients in the presence of strong ambient electric fields could also drive intense thermal currents along segments of the magnetic field, although a preconditioning of the plasma through some wave-induced enhancement in perpendicular conductivities [*perhaps due to cyclotron turbulence*] would be required for this mechanism to have a realistic chance to succeed. On the other hand, this mechanism would nicely explain the occurrence at times of echoes organised according to their position with respect to the gradient of arcs.

The main problem with the thermal current mechanism is that it requires very large parallel electric fields and, consequently, intense parallel current densities in order for the plasma to be destabilised under the conditions that exist near the regions of observations. Specifically, the required current densities would have to be of the order of 1 $mA.m^{-2}$, which has never been reported with direct observations. In fact, the modification of the ion velocity distribution in the presence of the strong ambient electric field, can lead to smaller than 1 $mA.m^{-2}$ value of required current density [*Cabrit et al.*, 1995]. More recent observations from satellites have so far pointed to the existence of current densities of the order of 100 $\mu A.m^{-2}$, which is still an order of magnitude less than required with the thermal current theory. However, another order of magnitude in parallel current densities cannot be ruled out, as long as the structures that carry these currents are narrow enough. One could think, for example, of small structures 100 meters in width, aligned in the north-south direction [*these have been observed with different instruments*] with short-living bursts existing on a time scale of the order of 1 ms to 1 s.

A completely different approach has also been proposed by *Forme* [1994]. In this case, the ion-acoustic waves would be produced by the non-linear cascade of electron plasma waves, using an analogy from the artificial ionospheric heating by electromagnetic waves. According to this scenario, low energy precipitating electrons would first excite electron plasma waves, which by cascade would then produce secondary plasma and ion-acoustic waves. This mechanism would be very successful at reducing the parallel current thresholds, but it has some difficulties in explaining how one can observe an upshifted ion-acoustic shoulder en-

hancement in the spectrum at times, and a strongly down-shifted structure at other times. Some experimental confirmation of the reality of this process in natural ionospheric situations should be feasible, through the observation of the behaviour of plasma lines during disturbed events, using the same incoherent scatter technique that is used to get the ion line [i.e. *the part of the spectrum that we have discussed so far*].

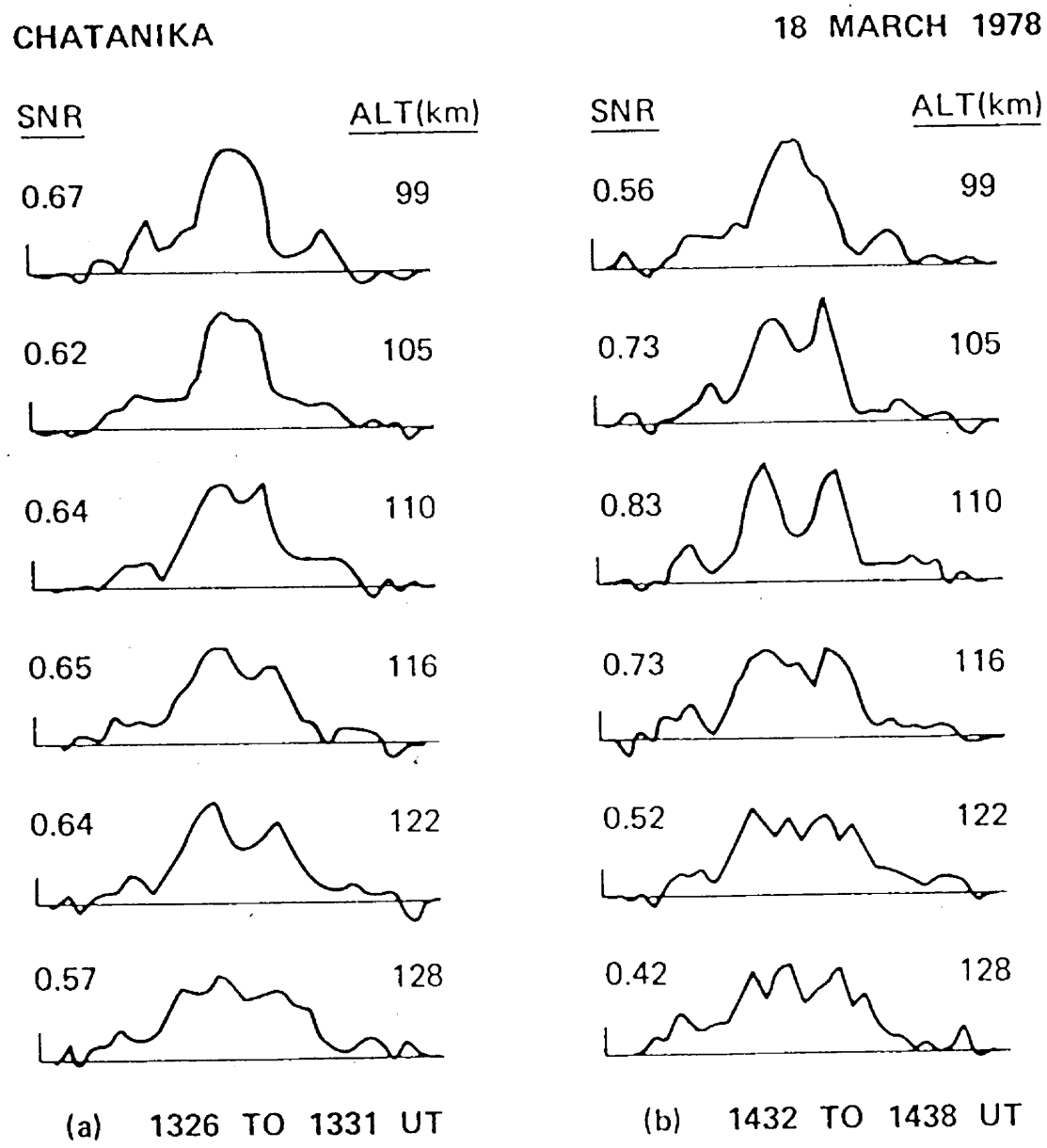

Figure 12. E region spectra from March 18, 1978, obtained with the multipulse autocorrelator using a 60-μs unipulse followed one interpulse period later by a burst of three 60-μs pulses that started at 0, 100 and 340 μs. The spectral window is 50 kHz wide. The two time periods were selected, in part, because of similar signal-to-noise ratios. (a) Typical spectra measured between 1326 and 1331 UT. (b) Unusual spectra measured between 1432 and 1438 UT. In particular, they are unusual at 105 and 110 km, though at 116 km the spectrum is still considerably wider than that in the earlier time period.

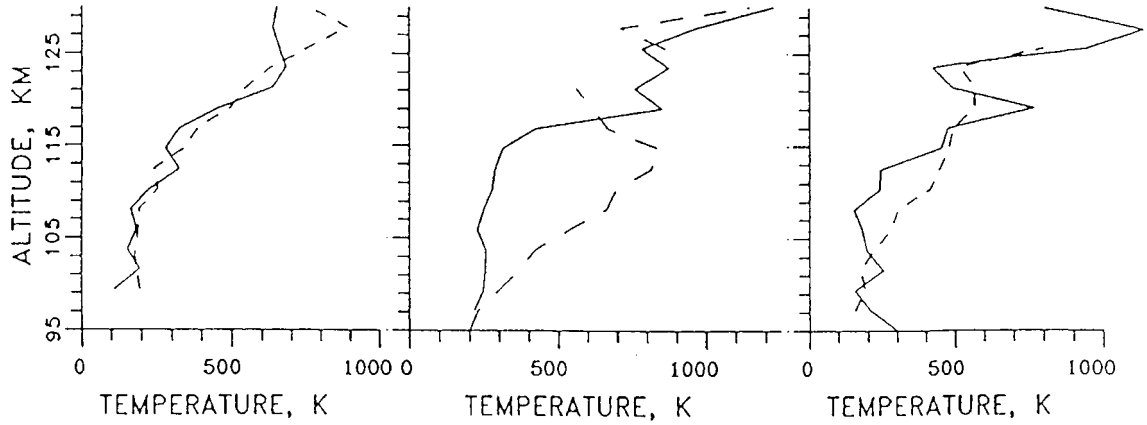

Figure 13. Ion (full lines) and electron (dashed lines) temperature profiles for selected times. There is no anomalous heating at 19.18 UT (left panel), very strong anomalous heating at 01.43 UT (centre panel), and low anomalous heating at 02.58 UT (right panel).

4.3. Electron heating by plasma waves.

The first observations of very large electron temperatures in the auroral E-region were made by *Schlegel and St.-Maurice* [1981] and *Wickwar et al.* [1981]. These phenomena have since been observed repeatedly. We note that while the data base is now relatively large as a result of years of observations, details about the theoretical explanation are still undergoing some discussions. In Figure 12, one can see the spectra measured in the E region for two periods. The spectra at 105 and 110 km [*first panel*] are typical of quiet conditions while the others [*second panel*] have a very unusual shape for the E-region [*Wickwar et al.*, 1981] since it has to be clearly associated with very large T_e, as indicated by the high "*shoulders*" in the spectrum.

In Figure 13, we show profiles of T_e and T_i for three different periods obtained on the same day. During the anomalous heating event shown in the figure, T_e reached 900 K at 114 km and 500 K at 105 km. This can be compared with 400 K and 200 K, respectively, for the quiet period at the same altitudes. A complete set of measurements [*obtained during the November 15-16 1984 EISCAT campaign*] is presented as a scatter plot of the electron temperature versus altitudes in Figure 14 [*St.-Maurice et al.*, 1990]. As we move from left to right, the full lines correspond to the envelopes within which we can find 1%, 5%, and 95% of the measurements. In Figure 15, the same electron temperature data is presented for altitudes between 110 to 115 km as function of the electron density and of the electron **E x B** drift, where **E** is the electric field, and **B** is the magnetic field [*St.-Maurice et al.*, 1990].

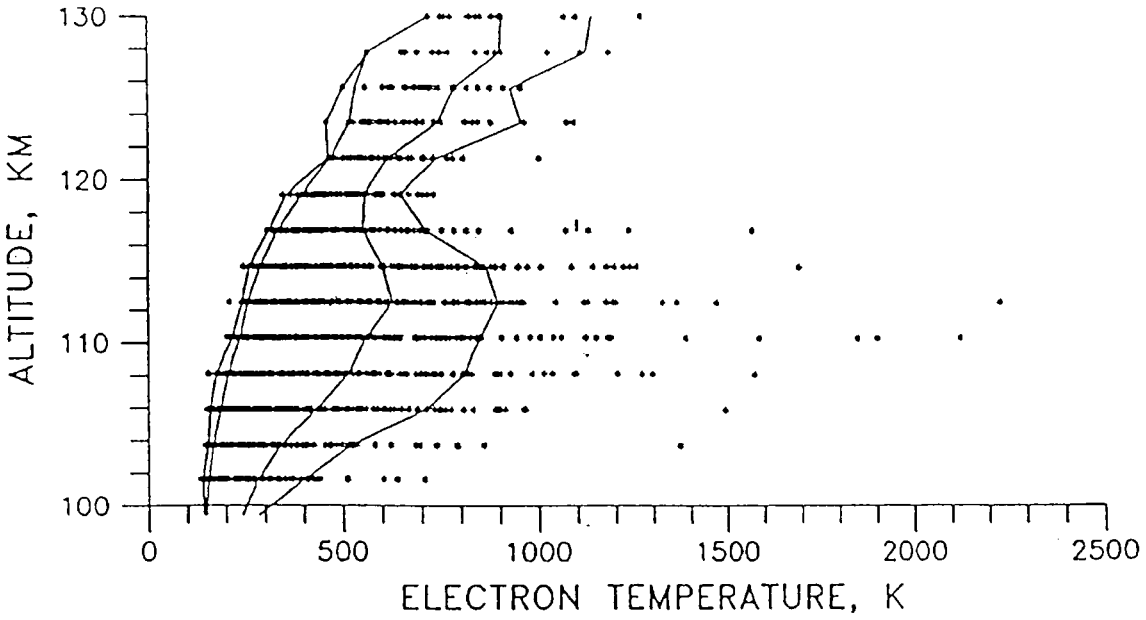

Figure 14. Scatter plot of electron temperatures measured at various altitudes on the night of November 15-16, 1984 with the EISCAT radar. The data cover 12 hours of measurements using 1 min integration time. The curves of electron temperature versus latitude correspond to the envelopes within which 1%, 5% and 95% of the measurements fall in moving from left to right respectively.

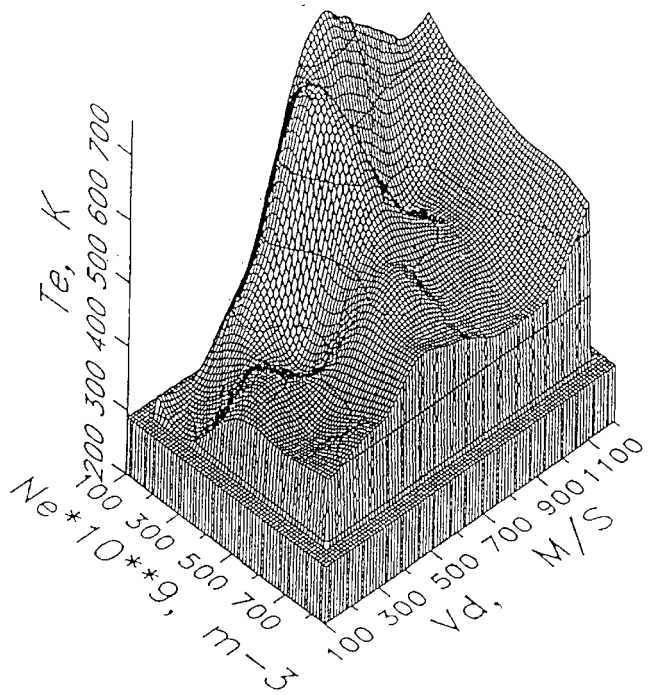

Figure 15. Electron temperature as a function of both the electron density and the magnitude of the E x B drift for data obtained in the 110 to 115 km altitude gates. This figure only shows the average behaviour of the electron temperature, and not the individual data points.

From the observational point of view, the anomalous heating can be characterised by the following features [*St.-Maurice et al.*, 1990] :

[1] T_e increases below 120 km when the electric field E increases. For E close to 75 mV.m^{-1} T_e is close to 1000 K at 112 km.

[2] T_e peaks around 112 km.

[3] T_e can be as large as 2000 K to 3000 K. This can happen about 5% of the time during very active conditions.

[4] the larger T_e becomes, the more short-lived a heating event appears to be.

[5] T_e is probably anti-correlated to the ambient electron density but is still quite variable even after allowing for this density effect.

This experimental description seems to be exhaustive but there now remains the question : what is the heating mechanism? The studies made by *Schlegel and St.-Maurice* [1981], *Wickwar et al.* [1981], and *Robinson* [1986] showed that one can eliminate all classical processes such as electron precipitation, heat conduction or classical frictional heating.

Precipitation can be eliminated because:

a) the electron temperature increases are not related to increases in the electron density and

b) the heating rates would have to be orders of magnitude greater than calculated [*Schlegel and St.-Maurice*, 1981].

Heat conduction is also out of the question simply because a strong peak is observed in the electron temperature around 112 km, which indicates a local heat source rather than conduction of heat from another region [*Schlegel and St.-Maurice*, 1981]. The classical frictional heating mechanism looks more promising since the electron temperatures are strongly correlated with the ambient electric field. However, this mechanism suffers from a kind of deficiency which is similar to that which is found with the other explanations : not only is the heating rate from this source an order of magnitude too small, but it is very difficult to use this mechanism to explain how the electron temperature would reach a peak at any particular altitude since both the heating and cooling rates are proportional to the neutral density in the region [*St.-Maurice*, 1987, reply to *D'Angelo and Merlino*, 1987). Note that *D'Angelo and Merlino* [1987] have nevertheless proposed frictional heating as a possibility by playing with the cooling rates of various species as a function of the altitude.

The above arguments have led people to conclude that the electrons are heated by plasma turbulence through large amplitude plasma waves generated by the

Farley-Buneman and/or gradient-drift instabilities. This readily explains why the electrons are hottest at 112 km altitude and also why no elevated electron temperatures are ever found in the E region when the electric field is less than 20 $mV.m^{-1}$ [*the latter being the threshold value for the Farley-Buneman instability*]. The basic theory simply uses the fact that the perturbed low frequency currents generated by the large amplitude electrostatic waves give rise to additional Joule heating. Beyond that point, two schools of thought have emerged over the years. These differences of opinion can be traced back to two different publications. First, *Robinson* [1986] suggested that the heating could be due to an anomalous increase in the electron Pedersen conductivity. The physical interpretation associated with this mechanism is that as they moved in response to the applied electric field, electrons would be scattered off the perpendicular to **B** by the perpendicular electric fields of large amplitude wave packets. The resulting increase in the diffusion coefficient would not only increase the particle heating rates, but also lead to a stabilisation of the instability, using a very similar value for the collision frequency at the wave, or perturbed, level.

While *Robinson's* [1986] idea is elegant because it simultaneously explains the electron heating rates and the fact that the large amplitude waves move at the phase velocity associated with threshold conditions, it has not gone without challenge. In particular, *St.-Maurice and Laher* [1985] concluded that a more straightforward way to heat the electrons was to have the waves evolve electric fields with a component parallel to the magnetic field. Such fields are observed, and the wave amplitudes inferred from this process seemed to be reasonable when compared to observations [*see also the review by St.-Maurice, 1990*]. Physically, for this alternate mechanism, electrons were seen to be much more mobile along the magnetic field than perpendicular to it. The electrons can therefore suffer large accelerations with rather small parallel fields and be heated in the process. The remaining question of the phase velocity was left behind with the original *St.-Maurice and Laher* [1985] explanation. *Hamza and St.-Maurice* [*July 1993, first paper*] are now proposing that in a situation for which the driving force is weakly affected by the instability, one should expect the non-linear phase velocities of the largest amplitude waves to correspond to zero growth rates simply because waves reach their largest amplitudes just before their "*instantaneous growth rate*" turns negative [*the instantaneous growth rate has to be distinguished from the statistical one, which has to be zero in steady state turbulence*].

While the debate about the physical mechanism is still going on and is certainly relevant, it seems important to emphasise that there now exists a general consensus about the fact that the electrons are heated by the intense plasma turbulence that takes place at E-region heights when the ambient electric fields are strong. The final resolution of the debate is now pointing to increasingly complex studies

of the plasma turbulence. It would therefore appear that a final resolution of the wave heating debate will indeed involve fully turbulent, strongly non-linear, conditions. Examples of the evolution in thinking that has been taking place recently can be found in recent papers by *Robinson* [1994] and *Hamza and St.-Maurice* [*the 2 July 1993 papers*].

5. Conclusion

The purpose of this short lecture is to show the different types of waves and instabilities existing in the ionospheric plasma and observable by the incoherent scatter technique. We describe the fluid and kinetic approach of waves in the plasma. The simplicity of the fluid approach and its possibility to give a nice physical insight of the waves guided us in using this description. Only the kinetic approach gives the possibility to introduce the Landau damping concept. There are many text books studying wave phenomena in plasma and this is why we are relatively concise in our lecture. The discussion of the observations is more developed. The physical and geophysical mechanisms responsible for the observations are indicated and analysed.

For people interested in the subject, we indicate here below an exhaustive bibliography.

6. References :

Barakat A. R. and **D. Hubert**, Comparison of Monte Carlo simulations and polynomial expansions of auroral non-Maxwellian distributions. Part 2 : The 1-D representation, *Annales Geophysicae*, **8**, 697-704, 1990.

Barakat A. R, R. W. Schunk and **J. P. St.-Maurice**, Monte Carlo calculations of the O^+ velocity distribution in the auroral ionosphere, *J. Geophys. Res.*, **88**, 3237-3241, 1983.

Cabrit B., H. Opgenoorth and **W. Kofman**, Comparison between EISCAT UHF and VHF back-scattering cross-section submitted to *J. Geophys. Res.*, **101**, 2369-2376, 1996.

Chen F., Introduction to Plasma Physics and Controlled Fusion, *Volume 1: Plasma Physics*, Plenum Press, second edition, 1984.

Collis, P. N., I. Haggström, K. Kaila and **M. T. Rietveld**, EISCAT radar observations of enhanced incoherent scatter spectra; Their relation to red aurora and field-aligned currents. *Geophys. Res. Lett.*, **18,** 1031-1034, 1991.

D'Angelo and **R. L. Merlino**, Are observed broadband plasma wave amplitudes large enough to explain the enhanced electron temperatures of high latitude E-region by St.-Maurice and Laher. *J. Geophys. Res.* , **92**, 321-323, 1987.

Dougherty J. P. and **D. T. Farley**, A theory of collision dominated electron density fluctuations in a plasma with applications to incoherent scattering. *J. Geophys. Res.*, **68**,5437-5486, 1963.

Evans J. V., Theory and Practice of Ionosphere Study by Thomson Scatter Radar, Proceedings of the IEEE, vol. **57**,No 4, 1969.

Forme. F. R. E., A new interpretation on the origine of enhanced ion acoustic fluctuations. *Geophys. Res. Lett.*, **21,** 1994.

Forme. F. R. E., J-E. Whalund, H. Opgenoorth, M. A. L. Persson and **E. V. Mishin**, Effects of current driven instabilities on the ion and electron temperatures in the topside ionosphere. *J. Atmos. Terr. Phys.*, **55**, 647-666, 1993.

Foster. J. C., C. del Pozo and **K. Groves**, Radar observations of the onset of current instabilities in the topside ionosphere. *Geophys. Res. Lett.*, **15,** 160 -163, 1988.

Gaimard P., C. Lathuillere and **D. Hubert**, Non-Maxwellian studies in the auroral F region : a new analysis of incoherent scatter spectra, *J. Atmos. Terr. Phys,* **58**, 415-433, 1996.

Hagfors T., Density fluctuations in a plasma in a magnetic field, with applications to the ionosphere *J. Geophys. Res..*, **66**, 1699-1712, 1961.

Hamza A. M. and **J. P. St.-Maurice**, A turbulent theoretical framework for the study of current-driven E Region irregularities at high latitudes: basic derivation and application to gradient-free situations *J. Geophys. Res.* **55**, 11587-11600, 1993.

Hamza A. M. and **J. P. St.-Maurice**, A self-consistent fully turbulent theory of Auroral E region irregularities. *J. Geophys. Res.* **55**, 11601-11614, 1993.

Hubert D., Auroral ion velocity distribution function : generalized polynomial solution of Boltzmannn's equation, *Planet. Space Sci.*, **31**, 119-127, 1983.

Hubert D., Non-Maxwellian velocity distribution functions and incoherent scattering of radar waves in the auroral ionosphere, *J. Atmos. Terr. Phys.*, **46**, 601-611, 1984.

Hubert D. and **A. R. Barakat**, Comparison of Monte Carlo simulations and polynomial expansions of auroral non-Maxwellian distributions. Part 1 : The 3-D representation, *Annales Geophysicae*, **8**, 687-696, 1990.

Hubert D. and **C. Lathuillere**, Incoherent scattering of radar waves in the auroral ionosphere in the presence of the high electric fields and measurements problems with the EISCAT facility. *J. Geophys. Res.* ., **84**, 3653-3662, 1989.

Ishimaru S., Basic Principles of Plasma Physics - A statistical approach, A lecture note and reprint series, 1973.

Igarashi and **K. Schlegel**, Electron temperature enhancements in the polar E-region measured with Eiscat, *J. Atmos. Terr. Phys.*, **49**, 273-280, 1987.

Kikuchi K., J. P. St.-Maurice and **A. Barakat**, Monte Carlo computations of F-region incoherent radar spectra at high latitudes and the use of a simple method for non-Maxwellian spectral calculations., *Annales Geophysicae*, **7**, 183-194, 1989

Kindel J. M and **C. F. Kennel**, Topside current instabilities, *J. Geophys. Res..*, **76**, 3051, 1971.

Kofman W., The F and E region studies by incoherent scatter radar *Adv. Space. Res.* **9**,5, 7-17, 1989.

Kofman W, C. Lathuillere and **B. Pibaret**, Neutral atmosphere studies in the altitude range 90 110 km using Eiscat, *J. Atmos. Terr. Phys.*, **48**, 837-847, 1986.

Lathuillere C. and **D. Hubert**, Ion composition and ion temperature anisotropy in periods of high electric fields from incoherent scatter observations, *Annales Geophysicae*, **7**, 285-296, 1989.

Lathuillere C., D. Hubert, C. La Hoz and **W. Kofman**, Evidence of anisotropic temperatures of molecular ions in the auroral ionosphere, *Geophys. Res. Lett.*, **18,** 163-166, 1991.

Lockwood M., B. J. I. Bromage and **R. B. Morne**, Non Maxwellian ion velocity distributions observed using Eiscat, *Geophys. Res. Lett.*, **14**, 111-114, 1986.

Loranc M. and **J. P. St.-Maurice**, A time-dependent gyro-kinetic model of thermal ion upflows in the high-latitude F region, *J. Geophys. Res..*,**99**, 17429-17452, 1994.

Moorcroft D. R. and **K. Schlegel**, Evidence for non-Maxwellian ion velocity distributions in the F-region, *J. Atmos. Terr. Phys.*, **50**, 455-465, 1988.

Perault. S, N. Bjornä, A. Brekke, M. Baron, W. Kofman, C. Lathuillere and **G. Lejeune**, Experimental evidence of non-isotropic temperature distributions of ions observed by EISCAT in the auroral F-region. *Geophys. Res. Lett.*, **11,** 519-522, 1984.

Raman R. S. V., J. P. St.-Maurice and **R. S. B. Ong**, Incoherent scattering of radar waves in the auroral ionosphere, *J. Geophys. Res.* **86**, 4751-4762, 1981.

Rietveld M. T., P. N. Collis and **J. P. St.-Maurice**, Naturally enhanced ion acoustic waves in the auroral ionosphere observed with the EISCAT 933-MHz radar. *J. Geophys. Res.* **96**, 19291-19305, 1991.

Robinson T. R., Towards a self-consistent non-linear theory radar auroral back-scatter, *J. Atmos. Terr. Phys.*, **48**, 417-422, 1986.

Robinson T. R., The role of natural E-region plasma turbulence in the enhanced absorption of HF radio waves in the auroral ionosphere : implications for RF heating of the auroral electrojet. *Annales Geophysicae,* **12**, 316-332, 1994.

Salpeter E. E., Plasma density fluctuations in a Magnetic field, *The Physical Rev.*, **122**, 6, 1663-1674, 1961.

Schlegel K., and **J. P. St.-Maurice**, Anomalous heating of the polar E-region by unstable plasma waves. *J. Geophys. Res.*, **86**, 1447-1452, 1981.

St.-Maurice J. P., Reply *J. Geophys. Res.* , **92**, 323-327, 1987.

St.-Maurice J. P., Electron heating by plasma waves in the high latitude E region and related effects : Theory, *Adv. Space. Res.* **10**,6,239-249, 1990.

St.-Maurice. J. P. and **R. Laher**, Are observed broadband plasma wave amplitudes large enough to explain the enhanced electron temperatures of the high latitude E-region? *J. Geophys. Res.* , **90,** 2843-2850, 1985.

St.-Maurice J. P. and **R. W. Schunk**, Auroral ion velocity distributions for a polarization collision model, *Planet. Space Sci.*, **25**, 243-260, 1977.

St.-Maurice J. P. and **R. W. Schunk**, Ion velocity distributions in the high latitude ionosphere. *Rev. Geophys. Space Phys.*, **17**, 99-134, 1979.

St.-Maurice J. P. and **R. W. Schunk**, Ion neutral momentum coupling near discret high-latitude ionospheric features, *J. Geophys. Res..*, **86**, 13, 11299-11321, 1981.

St.-Maurice J. P.,W. B. Hanson and **J. C. G. Walker**, Retarding potential analyser measurements of the effect of ion-neutral collisions on the ion velocity distribution in the auroral ionosphere, *J. Geophys. Res.* ., **81**, 5436-5446, 1976.

St.-Maurice J. P., W. Kofman and **E. Kluzek**, Electron heating by plasma waves in the high latitude E region and related effects : Observations, *Adv. Space. Res.* **10**, 6, 225-237, 1990.

St.-Maurice J. P., W. Kofman and D. James, In situ generation of intense parallel electric fields in the lower ionosphere, *J. Geophys. Res.*, **101**, 335-356, 1996.

Suvanto K., M. Lockwood, K. J. Winser, A. Farmer and **B. J. I. Bromage**, Analysis of incoherent scatter radar data from non-thermal F-region plasma, *J. Atmos. Terr. Phys.*, **51**, 483-495, 1989.

Whalund J-E., F.R.E. Forme, H.J. Opgenoorth, M.A.L. Persson, E.V. Mishin and **A.S. Volkitin**, Scattering of electromagnetic waves from a plasma: enhanced ion acoustic fluctuations due to ion-ion two stream instabilities. *Geophys. Res. Lett.*, **19,** 1919-1922, 1992.

Whalund J-E., H.J. Opgenoorth, F.R.E. Forme, M.A.L. Persson, I. Häggstrom and **J. Lilensten**, Electron energization in the topside auroral ionosphere : on the importance of ion-acoustic turbulence, *J. Atmos. Terr. Phys.* , **55**, 623-646, 1993.

Wickwar. V.B, C. Lathuillere, W. Kofman and **G. Lejeune**, Elevated electron temperatures in the auroral E layer measured with the Chatanika radar. *J. Geophys. Res.* , **86**, 4721-4730, 1981.

Wilson G.R., Kinetic modelling of O+ upflows resulting from ExB convection heating in the high latitude F-region ionosphere *J. Geophys. Res.*, **99**, 17453-17466, 1994.

Winkler E., J. P. St.-Maurice and **A.R. Barakat**, Results from Improved Monte Carlo : Calculations of Auroral Ion Velocity Distributions, *J. Geophys. Res.* , **97**, 8399-8423, 1992.

Winser K.J., M. Lockwood and **G.O.L. Jones**, Non-thermal plasma observations using EISCAT : aspect angle dependence, *Geophys. Res. Lett.*, **14**, 957-960, 1987.

Winser K.J., M. Lockwood, G.O.L. Jones and **K. Suvanto**, Observation of non-thermal plasma at different aspect angles, *Geophys. Res. Lett.*, **94**, 1439-1449, 1989.

MODULATION OF RADIOWAVES FOR SOUNDING THE IONOSPHERE: THEORY AND APPLICATIONS

Asko Huuskonen - Markku Lehtinen

1. Introduction

Modern incoherent scatter measurements rely on most complicated coding schemes to bring statistical accuracy to the measurements.Various methods to make use of longer transmission modulations than the required final resolutions have been developed in order to facilitate full use of radar duty cycle and thus make the results accurate enough for analysis. These methods include phase coding, multipulses, phase coded multipulses, alternating codes and many other methods and combinations of different methods [*Farley*, 1969, 1972*; Turunen and Silén*, 1984; *Turunen*, 1986; *Lehtinen and Häggström*, 1987; *Sulzer*, 1986, 1993; *Nygrén et al*., 1996; *Huuskonen et al*., 1996; *Markkanen and Nygrén*, 1996].

The data gathered by these methods never represent point values of the plasma properties in the ionosphere, but rather some averages of the plasma effective autocorrelation function in both the lag variable and the range variable. The functions specifying the form of the averages are called weighting or ambiguity functions. The idea behind all coding methods is to cause the ambiguity functions have a narrow form by choosing the phases of the transmission in a way so that responses from elsewhere than the peak itself completely or approximatively cancel out. In most general form, the ambiguity functions depend on both the range and the lagvariables.

The theory of ambiguity functions for pulse coding and phase coding methods was pioneered by *Woodman and Hagfors* [1969], *Farley* [1969,1972] and *Gray and Farley* [1973], where the reduced ambiguity functions for the lag variable are shown. The study has been developed by *Rino et al.* [1974] and *Huuskonen et al.* [1988] to include the reduced ambiguity functions for range. A fully general derivation of two-dimensional ambiguity functions appears in *Woodman* [1991]. That study is not restricted to the case of incoherent scatter. It covers e.g. also the case where plasma fluctuations may correlate over large distances. A recent treatment is given by *Lehtinen and Huuskonen* [1996] which is based on *Lehtinen* [1986].

In this paper, we will present the most important ambiguity function formulas, based on the formalism by *Lehtinen and Huuskonen* [1996]. We will visualize the functions by using the range-time diagrams and by showing in detail how the ambiguity functions are created graphically. The aim is to give sufficient

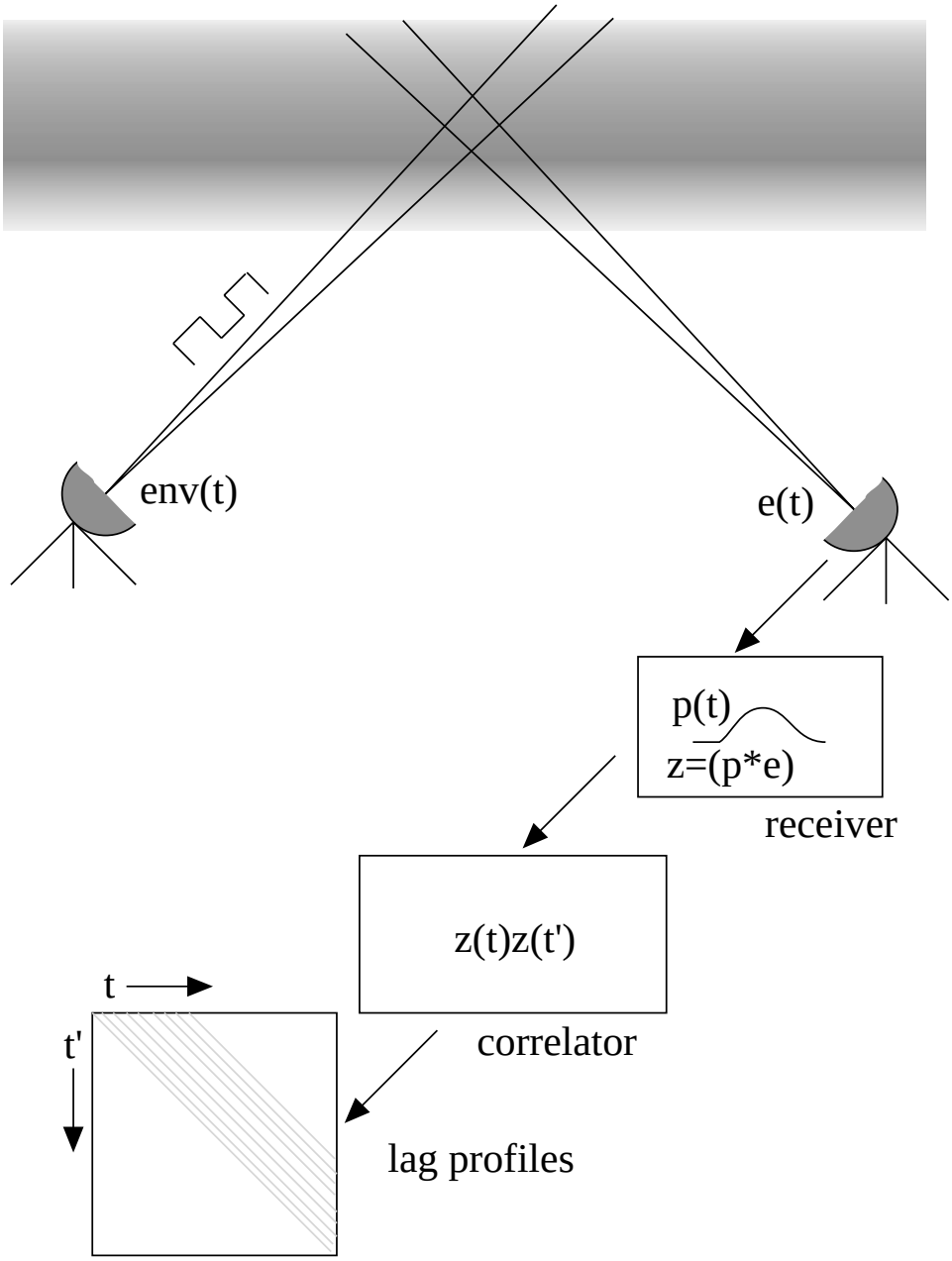

Figure 1. A schematic description of an incoherent scatter experiment

knowledge of the ambiguity functions so that the reader is able to understand how the most common incoherent scatter modulations, single pulses, pulse codes and alternating codes, work.

2. Ambiguity functions in practice

Figure 1 shows the equipment and processes relevant to our discussion. The transmitter antenna transmits a radiowave, modulated by env*(t)* to the ionosphere. Incoherent scattering occurs in the ionosphere, and a tiny part of the transmitted

power scatters towards the receiving antenna. In the bistatic configuration, shown in the figure, the scattering volume is formed by the geometrical intersection of the antenna beams. We will be mostly work with the monostatic configuration, where the receiver and transmitter antennas are in the same location. In the monostatic case a spatially narrow scattering volume is obtained by a suitable choice of the modulation and signal processing.

The receiver antenna detects, after the signal has been transferred to zero frequency by multiple analog [*or partly digital*] mixer stages, a complex voltage *e(t)*. The voltage is filtered by the received impulse response *p(t)* and sampled. The samples form a sample vector, from which a set of crossed products *z(t)z(t')* are calculated by the correlator device and stored.

Figure 2 introduces the standard tool, the range-time diagram, to display modulations and sampling. On the x-axis, the transmitter envelope is shown starting at time instant 0. The present envelope consists of three pulses, positioned at times 0, 2 and 6 in our normalized units. The modulation is called as a 3-pulse code. The oblique lines starting from the pulses show the locations of the pulses at later time instant.

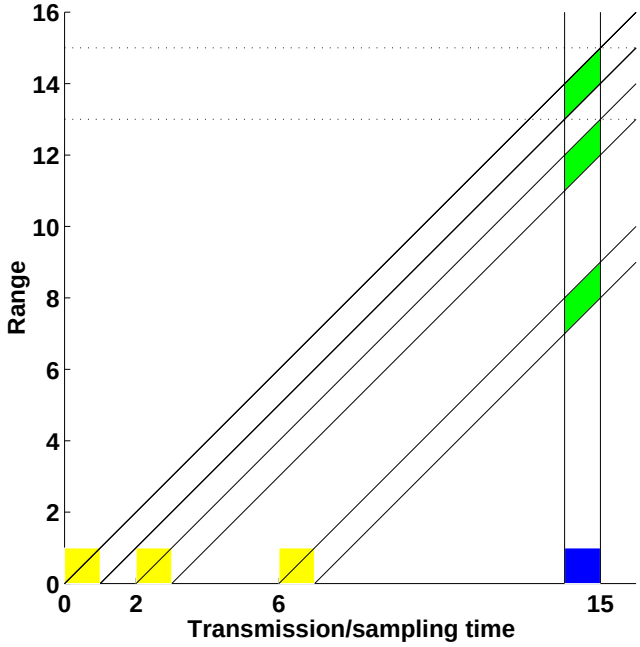

Figure 2. Range-time diagram for a three-pulse experiment. The transmitter envelope is denoted by the dotted blocks and the receiver impulse response by the solid block in the horizontal axis.

At time instant 15, another box of unit length is found. This box, from which a vertical line originates, shows the form and duration of the receiver impulse response [*p in the formulae*]. In our example, the impulse response is a box-car

of unit length, which means that the scattered signal returning from the ionosphere is averaged over that time interval before being sampled.

A note on the units is needed. In figure 2, both the time and range is measured by same units. The reception time corresponds to the total travel time from the receiver through the scattering volume to receiver. Therefore, if we think of monostatic case where the transmitter and receiver are located at the same place, the true range to the scattering volume is obtained by multiplying half of the total travel time by the velocity of light or the total travel time by half of the velocity of light.

The rhombic regions show the support of *the amplitude ambiguity function* of the sampled signal,

$$W_t^A(u;S) = p(t-u)\ \mathrm{env}(u-S) \qquad (1)\ [13]$$

where S is the range variable, u is the time variable and t is the sampling time. The numbers in brackets refer to *Lehtinen and Huuskonen* [1996]. Graphically the support is formed as the intersection of the oblique regions showing the pulse locations and the vertical columns denoting the sampling intervals. As both the impulse response and the envelope are of constant value, the amplitude ambiguity function is also constant within the support [*and zero elsewhere*].

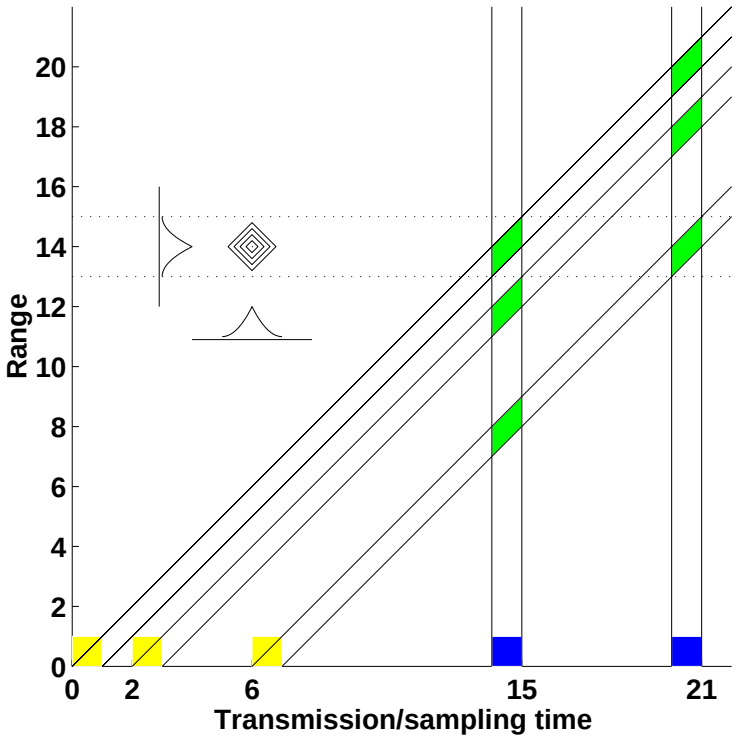

Figure 3. Amplitude ambiguity functions for sampling times 15 and 21 and ambiguity functions for the crossed product

The support of the amplitude ambiguity function is formed of three separate regions, which correspond to the three transmitted pulses. In the time dimension they span a unit time interval determined by the length of the impulse response. In the range direction on the other hand, the total range span is two units, because the transmitted pulses travel upwards during the finite time interval given by the filtering. The sampled signal is composed by all the elementary signals originating within the support of the amplitude ambiguity signal. Mathematically it is a weighted average of the elementary signals $e(u;d^3\boldsymbol{x})$ scattered from elementary volumes at $\boldsymbol{x}$ and received at times u:

$$z(t) = \int_{-\infty}^{\infty} du \int_{\boldsymbol{x}} e(u;d^3x)\, W_t^A(u;S(\boldsymbol{x})) \qquad (2)\ [12]$$

where $S(\boldsymbol{x})$ shows explicitely that the range is measured by the total travel time from transmitter to receiver via the elementary scattering volumes $\boldsymbol{x}$.

The final measurements are crossed products of two samples. Figure 3 illustrates the case for samples taken at time instants 15 and 21. The amplitude ambiguity functions of the samples both consist of three regions. When the ambiguity function for the product is caluclated, the important point to note is that only elementary scatters from the same altitude region correlate in the statistical sense. The part of the signal, whose region of origin does not have its counterpart in the other sample, averages to zero statistically. It is only seen as an increase of noise in the measurement. In our example it is noted that the first pulse of the first sample and the third pulse of the seconde sample give scatter from the same altitudes. Mathematically it is stated by the formula:

$$W_{t,t'}(\tau;S) = \int_{-\infty}^{\infty} du\, W_t^A(u;S)\, \overline{W_{t'}^A(u-\tau;S)} \qquad (3)\ [15]$$

which tells that *the two-dimensional ambiguity function* for the lagged product is a convolution of the amplitude ambiguity functions. At any range where that function of either measurement vanishes, the two-dimensional ambiguity function vanishes as well. In terms of $W_{t,t'}(\tau;S)$ the lagged product is expressed as:

$$\langle z(t)\,\overline{z(t')}\,\rangle / R = \int_{x} d^3x \int_{-\infty}^{\infty} d\tau\, P_0(x)\, W_{t,t'}(\tau;S(\mathbf{x}))\, \sigma_{eff}(\tau;\mathbf{x}) \qquad (4)\ [16]$$

which tells that the lagged product is a weighted average of the plasma scattering cross section $\sigma_{eff}(\tau;\mathbf{x})$. The single electron scattering power is given by $P_0(x)$.

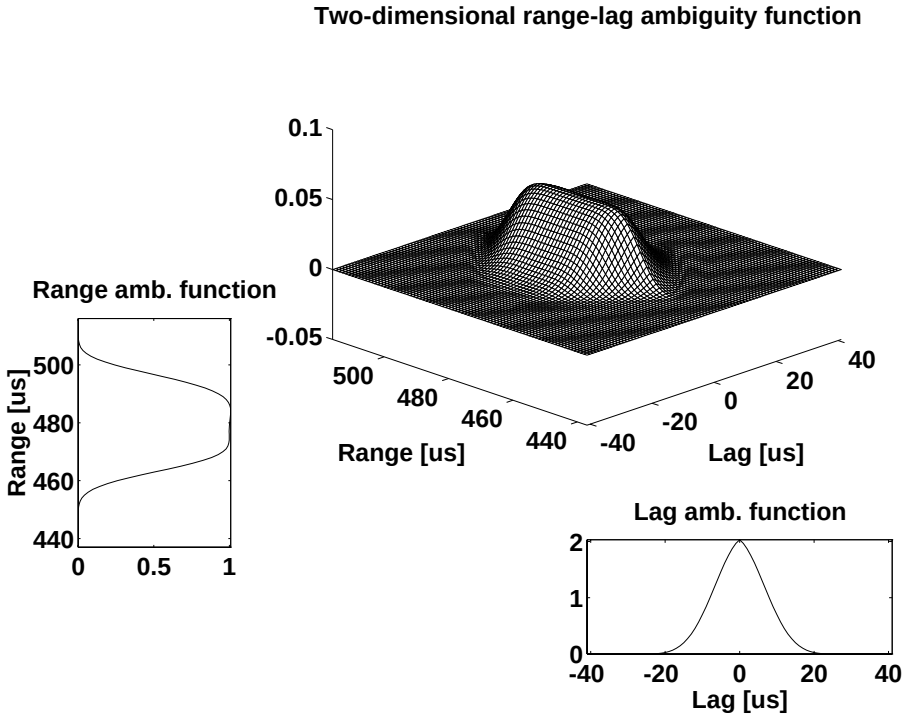

Figure 4. Two-dimensional and reduced ambiguity functions for the 40 μs pulse of EISCAT CP1K-experiment

From the convolution formula it is easy to see that the two-dimensional ambiguity function for our lagged product example is a pyramid, centered at range 14 and time delay 6, which corresponds to the difference of the sample times. The function if shown in Figure 3. The functions to the left and below show the reduced ambiguity functions for range and lag, obtained by integrating the two-dimensional function in the other variable. The *lag ambiguity function*, and its Fourier transform, the *spectral ambiguity function*, are central to the data analysis. However, we will not study them further here. The *range ambiguity function*, on the other hand, appears often in the following, because it is useful in showing how the modulations work. As a function of the basic functions, *env* and *p*, it is given by:

$$W_{t,t'}(S) = (p * \mathrm{env})(t-S)\ \overline{(p * env)(t'- S)} \qquad (5)\ [20]$$

Figure 4 shows the two-dimensional range-lag ambiguity function and the reduced ambiguity functions for range and lag for the 40 µs power profile pulse in the *EISCAT CP1K*-experiment. The filter used is a 25 kHz linear phase filter. The filtering effects are seen as smoothing in the range direction.

3. The lag profile principle

If in Figure 2 we step the reception time by one unit, the amplitude ambiguity function will step by one unit in time and range, retaining its shape. If we then sample the signal at constant intervals, we will get a sample vector $z(t_i)$, $i=1 \ldots N$, where all the elements have ambiguity functions of the same shape, but which are located at equidistant ranges.

Similarly, if the in Figure 3 we step both reception times by one unit, or increase the index i in the lagged product $z(t_i)z(t_{i+k})$ by one, we will obtain similar ambiguity functions, which will be located one unit higher in range, but at the same lag value. From a set of samples $z(t_i)$, $i=1 \ldots N$, we may calculate crossed products $z(t_{i+k})$, $i=1 \ldots N - k$. This is *the lag profile principle* which is central in understanding IS measurements. The principle tells that the form of the ambiguity functions for a given measurement depends only on the difference of the sampling times, whereas the range of the measurement changes by one step, if the sampling times are stepped accordingly. One way to think is that a lag profile consists of identical measurements made at a set of equidistant ranges.

4. Requirements for an experiment

The basic problems and requirements in the incoherent scatter modulation design have been summarized by *Lehtinen* [1986] as follows:

> "The main problem in conducting incoherent scatter measurements is the fact that, as the Thomson cross section is small and the electron densities are not very high, the signal received is weak. It is often smaller than the background noise from the sky and the receivers. Moreover, if the signal is received with the same antenna as is used for transmission, it is necessary to use small pulses instead of a continuous wave transmission, so that the responses from different altitudes would not be mixed with each other. This makes the situation still worse.
>
> There are four resolution requirements that have to be taken into account in a design of a measurement. The first one is *spatial resolution*. This resolution determines the basic pulse widths used. The second one is the *lag resolution*, by which we mean the time in which the phase and amplitude of the scattered signal itself does not change significantly. Thus, it is the typical

scale of the autocorrelation functions. The third one is the *time resolution*, by which we mean the time scale for the changes of the plasma parameters themselves. During this length of time it is possible to reduce measurement errors by repeating the experiment as many times as the radar duty cycles and other relevant factors allow. This is called integration, and consequently, the time resolution is often called integration time. The last one is then the required *accuracy* of the autocorrelation function estimates calculated.

In addition there are two basic extent requirements. The first one is that the experiment produces data from a long enough altitude interval to be useful. This poses a limit to the repetition frequency of the experiment. The second one is that the experiment must provide data over a broad enough lag interval. These intervals are called *range extent* and *lag extent*, respectively.

The requirements of having all of the resolutions accurate are contradictory with each other when the design of the experiment is restricted with technical factors, such as radar peak power, radar duty cycle etc. As it is often impossible to meet all the requirements with straightforward techniques, a number of different methods of coding the transmission, perhaps using a series of coded groups with different frequencies, are being employed to use the radar equipment as effectively as possible. These methods have in common the property that they produce data with specified resolutions, but with better accuracy than a simple pulse or a pair of pulses would do."

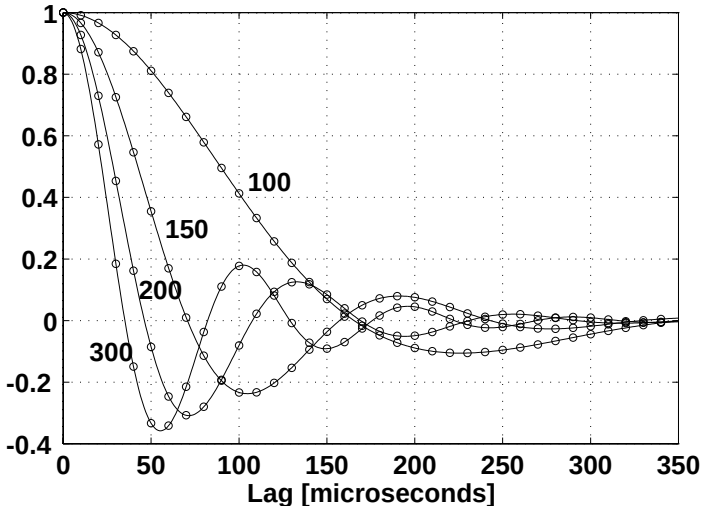

Figure 5. Plasma autocorrelation function for 931.5 Mhz. at altitudes given in the figure

Of the above requirements, the *range resolution*, *lag resolution* and *lag extents* are central for the modulation design. The plasma ACF at 100, 150, 200 and 300 km altitudes [*for frequency 931 MHz*] are shown in Figure 5, from

which it is possible to obtain rough estimates for the last two. The lag resolution should be better than the width of the ACF, as determined by the value of the first zero crossing. The crossing occurs at 160 μs at 100 km, at 70 μs at 150 km and below 50 μs higher up. The *lag resolution* used in practice varies from 20 and 40 μs in the E-region measurements and is generally below 15 μs in the F-region measurements. The required *lag extent* puts a constraint on the modulation design, because the total modulation length must exceed the lag extent. In practice, the longest lag measured varies from 300-350 μs in the E-region to 250 μs in the F-region, but may be shorter than that higher up. Precise numerical estimates for the sufficient lag resolution and extent are obtained by following the procedure presented by *Vallinkoski* [1988]. The range resolution required is about 3 km in the lower E-region and increases with increasing height. In the F-region, a range resolution of some tens of kilometers is sufficient.

The above is correct for E- and F-regions only. In the topside ionosphere, where hydrogen is important, the plasma ACF is much narrower and therefore a better lag resolution is needed. The ion velocities can only be high there, which still increases the required lag resolution. In the D-region, on the other hand, the plasma ACF is much wider and the lag resolution is of the order of milliseconds.

The operating frequency also affects lag resolution and extent. At 500 Mhz, which is the operating frequency of the *EISCAT Svalbard Radar*, the plasma ACF is roughly twice as wide as at the *EISCAT UHF*-frequency, which must be taken into account in the modulation design.

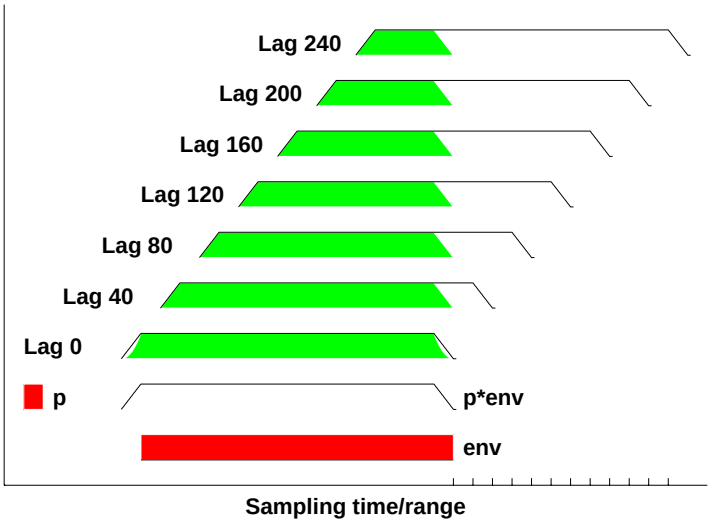

Figure 6. An illustration to show how the range ambiguity functions can be formed graphically. The pulse is 320 μs long and the receiver impulse response 20 μs long. The transmitter envelope env *is shown at the bottom, filter impulse response* p *and* p * env *next and the range ambiguity functions at multiples of 40 μs above.*

5. Single pulse modulation

The simplest modulation of all is an uninterrrupted pulse of sufficient length. The length of the pulse is chosen to exceed the lag extent, in order that the full length of the plasma autocorrelation function is measured. This kind modulations is called single pulse or long pulse modulation.

Figure 6 illustrates how the range ambiguity functions for a single pulse experiment can be formed graphically. We assume a transmitter envelope of 320 µs long, shown at the bottom of the figure, and a receiver impulse response, which is a box of 20 µs long. According to Eq. 5 the starting point is the convolution of the impulse response and the transmitter envelope, which is shown in the figure (*p* * env). The sampling interval is 20 µs and the sampling times are shown by small tics in the time axis. We will denote the sampling times by t_i, $i = 1 \ldots N$. In the *EISCAT CP1K* experiment the sampling time is 10 µs instead of 20 µs.

We can see in the figure how the range ambiguity functions for even multiples of 20 µs are created [*odd multiples have been excluded to keep the figure simple*]. First *p* * env is shifted by the value of the lag in question. Then the shifted *p* * env is multiplied by the unshifted one. The products are shown as shaded regions, which show the range ambiguity functions of the crossed products : $z(t_1)^* \overline{z(t_{1+k})}$, $k=0, 2, 4 \ldots 12$.

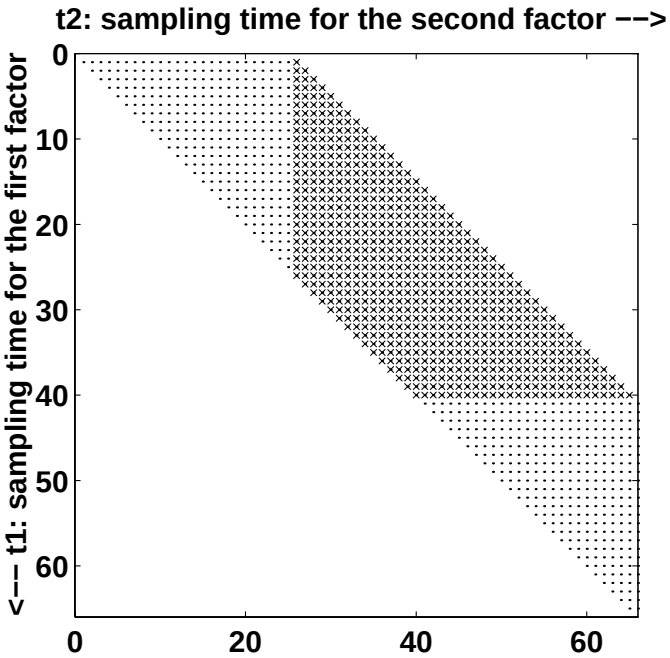

Figure 7. A lag profile matrix and crossed products belonging to a single gated long pulse measurement

It is seen that the range ambiguity function for the zero lag is as long as *p* * env, but that the ambiguity functions for the longer lag values are shorter. This means that the scattering volumes are of different size. This fact had twofold consequences. The shorter lags given an average over a larger altitude range which is a disadvantage is the plasma is not sufficiently homogeneous. On the other hand they collet a bigger signal than the longer lags, which increases the accuracy for low SNR.

The data from the present day long pulse experiments are processed so that a larger number of estimates of the longer lags are included in the final estimate. The selection procedure is illustrated in Figure 7, which shows a lag profile matrix. A lag profile matrix is formed by calculating all crossed products from the measured sample vector and by arranging the results so that y-axis is formed by the sample time of the first factor in the product and the x-axis by the sample time of the second factor. The products shown in Figure 6 are located on the first horizontal line. Points on any diagonal have the same difference of the sample times, i.e. the same lag value. The main diagonal contain points, where the sample times are equal. If both sampling times are advanced by one sampling unit, the next point on a lag profile is obtained.

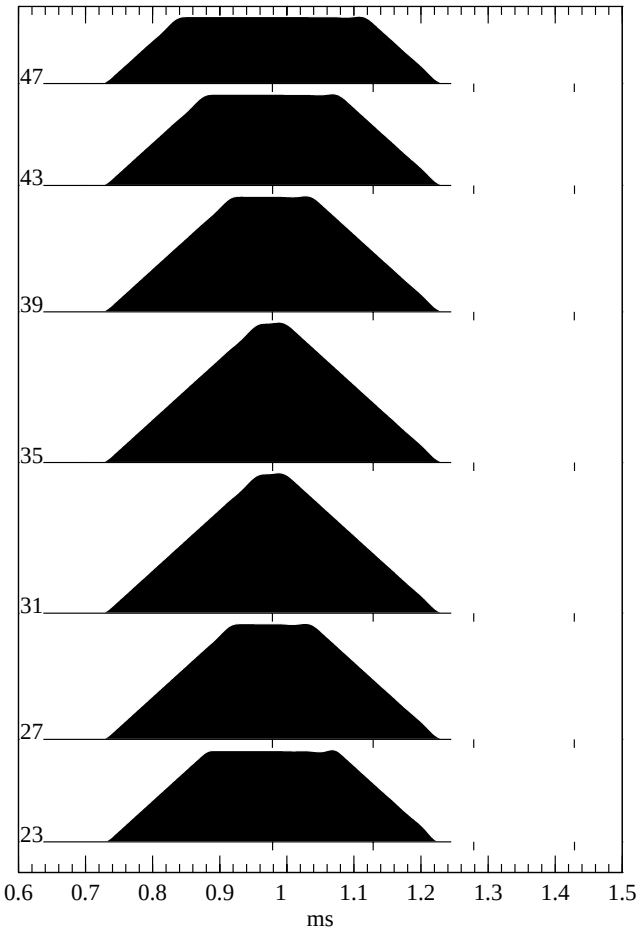

Figure 8. Range ambiguity functions for a gated long pulse experiment

When looking at the matrix elements selected for a gated long pulse measurement, we first notice that certain number of elements have been left unused from the lag profiles with small lag values. This has been done because the first elements in the lag profiles have center points at closer ranges than the longer lag values do. Another point to note is that more elements are included in the averaging for longer lag values. This compensates for the smaller scattering volumes which the individual measurements have. One should note that, if the next gate is formed by using the next 15 elements from the zero lag profile, certain elements in the non-zero lag profiles will be used by two consecutive gated measurements, i.e. the measurements will not be independent.The gating is done in order to reduce the number of result memory locations neededand also to ease the task of analysis programs.

The range ambiguity functions for the long pulse modulation of the *EISCAT CP1K*-experiment are shown in Figure 8. Here the pulse length is 350 μs, filtering is done by a 50 kHz Butterworth filter, and sampling is done at 10 µs intervals. Lag estimates are calculated at 10 µs intervals up to 250 µs and 15 estimates are added together for final gated zero lag estimate. It is seen that the functions have the same peak-to-peak coverages although they differ in details.

Figure 8 shows that the scattering volume for a long pulse measurement is long. It is easy to understand that the volume must necessarily be longer than the pulse itself, e.g. $350\ \mu s \approx 52$ km, and that a gated measurement has a even longer volume. This restricts the use of long pulses the the F-region, where the plasma properties do not change too much over such distances. Another fact is that a long pulse is the most efficient measurement in the region where it can be used.

In the above example, as well as in the practical examples, the pulse is is longer than the lag extent would require. A longer pulse is used because the scattered signal is stronger, which is advantageous at the long ranges and low electron densities. For very long ranges pulses as long as 2000 µs may be used.

6. Pulse codes

The single pulse modulation is unsuitable for E-region work, because the scattering volume is much longer than the scale height of the plasma parameters in the E-region. The first modulation method to give adequate range resolution in the E-region work was the pulse code [*multiple-pulse, multi-pulse*] method, pioneered by *Farley* [1972] and *Rino et al.* [1974]. The technique was developed into its full power when the interlaced multi-pulse codes [*Turunen and Silén*, 1984, *Turunen*, 1986] came into use with the *EISCAT UHF*-radar. The interlaced codes are based on the ability of the *EISCAT* transmitters to change frequency rapidly so that gaps are not left in the transmission and the full radar duty cycle can be used efficiently.

A classical pulse code modulation fullfils the following conditions:

[1] Code consists of N pulses of equal duration.

[2] The distance of any pair of pulses is an integer multiple of the smallest interpulse distance and all distances are different. The smallest distance gives the *lag resolution* of the code.

[3] The sum of the pulse length and receiver impulse response is less than the smallest distance of pulses.

Fullfilment of these conditions quarantees that all non-zero lags will have ambiguity functions of same size and shape and that the scattering volume is uniform, i.e. not formed by two or more separate volumes. This is illustrated by Figure 9, which shows how the range ambiguity functions for a 4-pulse code are formed. As in Figure 6, the calculation proceeds so that first *p* * env is calculated, assuming that *p* is in form similar to any of the pulses of the code, and then *p* * env is shifted by the lag value in question and the two functions are multiplied. The key point is the fact that only signals from the same altitude correlate with each other. At any non-zero lag, only one triangle in the *p* * env of the first sample coincide with the *p* * env of the second sample. Therefore only one altitude range produces a statistically meaningful average, the signal products from the other ranges only show up as noise which averages to zero. The exception is the zeroth lag, which gets contribution from four separate ranges.

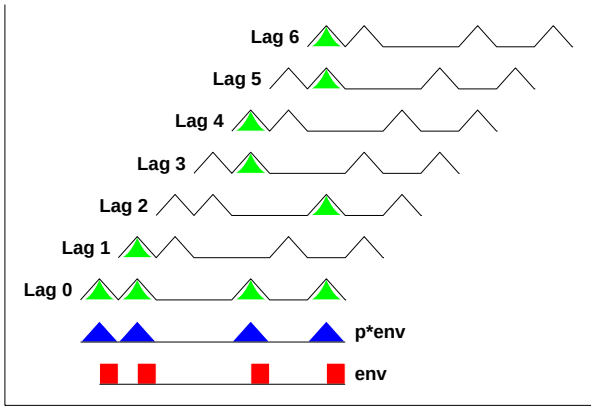

Figure 9. A 4-pulse code and how the range ambiguity functions are formed. The impulse response function is box-car shaped.

The six lag values in Figure 9 correspond to the time differences of the leading edges of the transmitted pulses. A 4-pulse code gives well behaving estimates at six different lag values, which correspond to the six different pulse pairs obtained from the code. In this sense we can thing a four pulse code as formed by four virtual two pulse codes, each giving measurements at one lag value. A multipulse code is more efficient that multiple two pulse codes would be. Four pulses are

sufficient to produce estimates at six different lag values, whereas six separate two- pulse measurements would require 12 pulses altogether for the same effect.

The range ambiguity function in Figure 9 are also similar to those of a single pulse of the length of the individual pulses in the pulse code. Such pulses are used to measure the zeroth lag estimates for the multipulse autocorrelation functions. The optimal use of the multipulse data requires that the zeroth lag of the multipulse is also used. Although any measurement is a sum of contributions from multiple altitudes, it is possible to use the data [*Lehtinen and Huuskonen*, 1986].

Any other lag value than those corresponding to pulse separations will lead to ambiguity functions which are of different shape and, in most cases, include several separate regions. An example is shown in Figure~5 of *Lehtinen and Huuskonen* [1996].

The design principles of the pulse codes put restrictions on the number possible pulse codes. The smallest pulse separation must be twice the basic pulse length to allow space for the receiver impulse response. Therefore the lag resolution will be at least twice the basic pulse length.In the case of the *EISCAT UHF* radar the following combinations have turned out to be the most practical ones:

Number of pulses	pulse length	smallest distance lag resolution	code sequence	lag values
4	20	40	[1 3 2]	1 ... 6
5	14	30	[2 5 1 3]	1 ... 9, 11

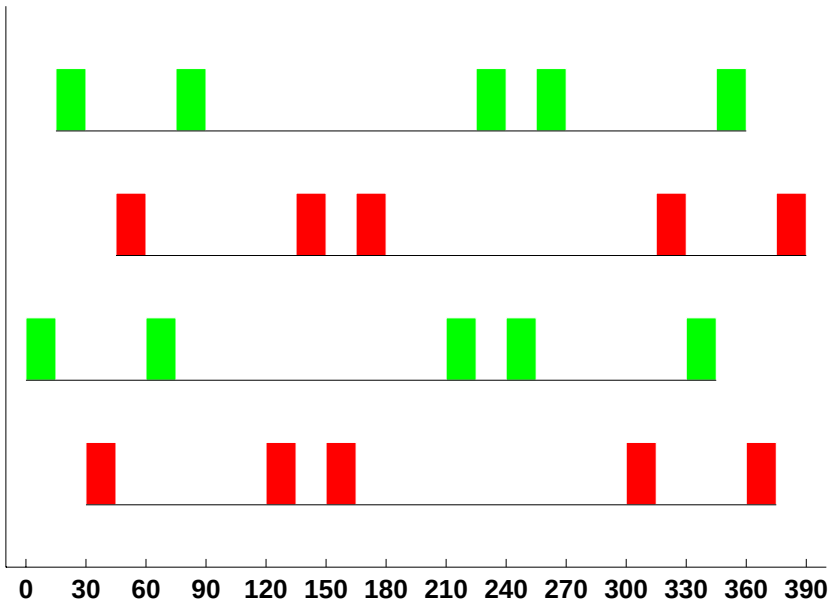

Figure 10. An interlaced 5-pulse code set used in EISCAT CP1H experiment.

The code sequence gives the pulse locations in units of the smallest distance [*lag resolution*]. The choice of the pulse lengths is constrained very much by the conditions required from pulse code. For instance,

[1]- The longest lag obtained from the 4-pulse code is only 240 µs long, which is not sufficient for all E-region conditions. Longer lags could be obtained by changing the lag resolution from 40 µs to 50 *µs*, but this would limit the use of the code to the lower E-region only, where the plasma ACF is wide.

[2]- The 14 µs pulse used in the 5-pulse code gives lower power than the 20 µs pulse use in the 4-pulse code. A longer pulse length would be optimal, but is not possible, as the total duration of the modulation would exceed the allowed limits.

The unavoidable gaps in the pulse codes lead to loss of radar duty cycle. The *EISCAT* radars are able to interlace many codes at different frequencies into the same transmission, and then only 1 µs is lost at every frequency change. An example is shown in Figure 10. Interlacing increases the number of independent lag estimates obtained. The 5-pulse codes in the figure use altogether 26 (x 15 µs) units of transmission time. Each code uses 5 units and gives 10 independent lag estimates [*we neglect the zero lag, which is ambiguous*], so that the 4 codes give 40 estimates. It is usual to include some power profile pulses in the transmission as well. The power values are then used as zero lags in the plasma autocorrelation function. The multipulse zero lags are mostly discarded as they represent sums of powers from many altitudes.

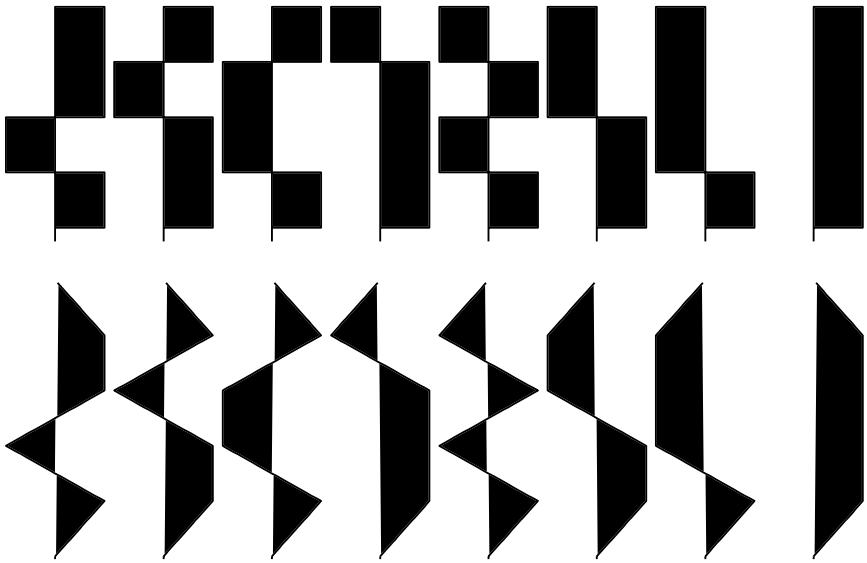

Figure 11. A 4-bit alternating code set (above) and p * *env for the codes (below)*

7. Alternating codes

Alternating codes [*Lehtinen and Häggström*, 1987] are the state-of-the-art modulation method for the E-region and lower F-region measurements and they have replace multipulse codes in most applications. An alternating code is an uninterrupted transmitter pulse, which consists of N parts, called bits or bauds, each having either positive or negative phase [*All pulses in a multipulse have same phase*]. If a sufficient number of these pulses, all different, are used together, it is possible to get measurement with a height resolution corresponding to the bit length, and not to the total pulse length. It is somewhat difficult to find these code sets, but once the set is available, it is fortunately much easier to understand how the code set works. In general, a N-code set consists of $2N$ codes, if N is a power of two. For other values we have to take twice the power of two which is larger than N. *Lehtinen and Häggström* [1987] gave codes up to lengths of 32 bits but recently an efficient method to find much longer codes have been developed [*Markkanen and Nygrén*, 1996].

To understand how alternating codes work we study 4-bit code set consisting of 8 codes in the upper panel of Figure 11. The bottom panel shows how p * env looks like for the codes, if the filter impulse response is as long as one bit in the code. Figure 12 shows how the range ambiguity functions for a lag [*equal to bit separation*] look like for each of the 8 individual codes. It is found that they all cover a altitude region which is four bits long, i.e. one bit less than the altitude span of p * env On the right one can see three decoded measurements whose peak-to-peak coverage is only 2 bits long, i.e. the range ambiguity functions are identical to those from a power profile pulse measurement with pulse length of one bit.

The decoding coefficient are obtained from the signs of the bauds which for the 8 codes in question are:

Bit	1	2	3	4	5	6	7	8	Code
1	+	+	+	-	-	-	-	+	
2	+	-	-	+	+	-	-	+	
3	-	+	-	+	-	+	-	+	
4	+	+	+	+	+	+	+	+	

Comparison of the signs and Figure 11 shows that the signs tell whether a altitude region gives a positive or negative contribution to the signal. The decoding signs for a lag estimate are obtained if delay the signs by one step and multiply them with the original. A comparison with Figure 12 shows indeed that the signs in the following table:

Prod	1	2	3	4	5	6	7	8	Code
(1,2)	+	-	-	-	-	+	+	+	
(2,3)	-	-	+	+	-	-	+	+	
(3,4)	-	+	-	+	-	+	-	+	

agree with the positively and negatively contributing regions in the individual range ambiguity functions. When each range ambiguity function is multiplied by the corresponding sign in the first row, the contibution from the upmost range will always be positive, but there will be equally many positive and negative contributions from ranges 2 and 3, which will cancel out precisely. This would not happen for a randomly chosen sign set, but is a result of the fact that the codes form an alternating code set. A similar cancellation of unwanted contributions happens for the second or third range, if the signs in the corresponding row are used. For the second lag one gets two estimates, for the two upmost ranges. Finally it is possible to one estimate for the third lag.

Figure 12 shows that we can treat an alternating code as a set of co-existing two-pulse experiments. The upmost decoded range ambiguity function would be obtained from an experiment containing the first two bits of the modulation only. The second ambiguity function would come the two next bit etc. In general, a *N*-bit alternating code corresponds to *N * (N-1) / 2* simultaneous two-pulse experiments.

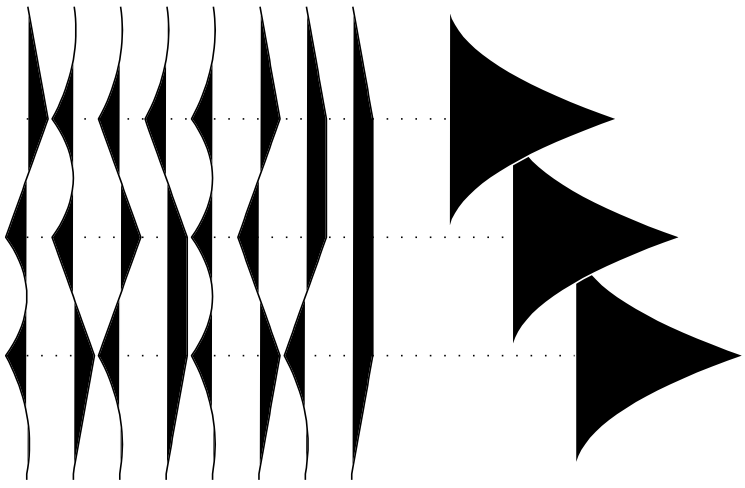

Figure 12. Range ambiguity functions for individual codes and for the decoded measurement

The great advantage of alternating codes is that the transmitter modulation time is used efficiently. This is seen by calculating the number of independent estimates obtained. Figure 10 shows that it is possible to fill in the transmission time by interlaces multipulses and power profile pulses. If the gaps in the transmission are filled by power profile pulses, altogether 46 independent

estimates are obtained. When all the transmission is on a single frequency, we will get altogether *26 * 25 / 2 = 325* pulse pairs, all giving one estimate, which is about 7 times that from the multipulse experiment.

If the signal-to-noise ratio is high, the situation is more complex, and a pulse code experiment may be more efficient in certain cases. Then, however, both modulations are able to measure the plasma autocorrelation function efficiently. It is fair to say that alternating codes produce a balanced performance, where superior accuracy at low signal levels is accompanied by a good accuracy at high signal levels. A thorough comparison is presented by *Huuskonen and Lehtinen* [1996].

Another advantage is that the bit length and the total pulse length are not related as in the case of multipulses, where only a couple of practical solutions exist. Let us assume that we wish to measure the autocorrelation function up to lag 320 µs, and that we wish to have a range ambiguity function similar to that of a 20 µs pulse. This means that the range resolution wanted is 16 times better than the total pulse length we have to use. This is possible by taking a 16-bit [*or 16-baud*] alternating code set into use. The lag and range resolutions will be equal. Alternating codes as well as multipulses are useful in the region where the range resolution needed is much better than the lag extent [*longer lag to measure*]. This is true in the E-region and lower part of F-region.

Note that the zero lag is not obtained from the alternating code with the good altitude resolution. In the zero lag estimate all range give a positive contribution and it is not possible to make the contributions from all but one range to cancel out. This is identical to what happened to the multipulse zero lag.

The present standard *EISCAT* experiment use alternating codes. The *CP-1-K* experiment [*Wannberg*, 1993] uses 16-baud codes with a 21 µs baud length. The future alternating code experiments, e.g. those planned for the *EISCAT Svalbard Radar*, will use oversampling and fractional lag production to improve the accuracy and speed of the experiments still [*Huuskonen et al.*., 1996].

8. Other coding techniques

Multipulses, alternating codes and long pulses cover most of the applications in incoherent scatter measurements. There are some special cases for which other types of codes, or combinations of the above, are needed.

If the required range resolution is very fine, e.g. 300 m in the E-region in the case of thin metal ion layers, the individual pulses in a pulse code or an alternating code are coded with a 13-bit Barker-code [*Gray and Farley*, 1973]. Examples of using Barker-codes pulse codes are found in *Turunen et al.* [1988]

and *Huuskonen* [1989]. *Wannberg* [1993] introduced the first Barker-coded alternating code experiment. These experiments combine a very fine altitude resolution with the typical E-region lag resolution. Any Barker-coded modulation, and especially those based on pulse codes, produce tiny ambiguities to the scattering volume. The main contribution comes from a sharply defined small altitude region, but there are minor unwanted contributions originating from elsewhere.

Also random codes [*Sulzer*, 1986] are a way of obtaining a very good range resolution. Random codes are coded long pulses, very much like alternating codes, which do not have the property of exact cancellation of the ambiguous contributions. The cancellation happens in a statistical sense after a sufficient number of different codes have been transmitted and processed. A high range resolution is also obtained by coding individual pulses in a pulse code by alternating codes [*Nygrén et al.*, 1996]. Now that a method of finding very long alternating codes is found, most efficient ambiguity free experiments are also available for high range resolutions [*Markkanen and Nygrén*, 1996].

Pulse-to-pulse experiments are used when the scattering volume is so close that the round trip time to the volume is shorter than the lag extent required. In the D-region case, the lag extent is of the order of 10 milliseconds, and the round trip time about 500 μs. Therefore the experiment is done so that reception happens after each pulse, about 100 µs in duration, and crossed products are calculated with the samples obtained from the subsequent pulses. The individual pulses are normally Barker-coded. The pulse-to-pulse *EISCAT CP-6* experiment is explained by *Turunen* [1986] and the data analysis problems by *Pollari et al.* [1989].

9. References

Farley D.T., Incoherent scatter correlation function measurements, *Radio Sci.*, ***4***, 935-953, 1969.

Farley D.T., Multiple-pulse incoherent-scatter correlation function measurements, *Radio Sci.*, ***7***, 661-666, 1972.

Gray R.W. and **D.T. Farley**, Theory of incoherent-scatter measurements using compressed pulses, *Radio Sci.*, ***8***, 123-131, 1973.

Huuskonen A., High resolution observations of the collision frequency and temperatures with the EISCAT UHF radar, *Planet. Space Sci.*, ***37***, 211-221, 1989.

Huuskonen A. and **M.S. Lehtinen**, The accuracy of incoherent scatter experiments: Error estimates valid for high signal levels, *J. Atmos. Terr. Phys.*, ***58***, 453-463, 1996.

Huuskonen A., **M.S. Lehtinen** and **J. Pirttilä**, Fractional lags in alternating codes: improving incoherent scatter measurements by using lag estimates at non-integer multiples of baud length, *Radio Sci.*, in press, 1996

Huuskonen A., **P. Pollari**, **T. Nygrén** and **M. Lehtinen**, Range ambiguity effects in Barker-coded multipulse experiments with incoherent scatter radars, *J. Atmos. Terr. Phys.*, ***50***, 265-276, 1988.

Lehtinen M., Statistical theory of incoherent scatter radar measurements, Ph.D. thesis, 97 pp, Univ. of Helsinki, Helsinki, Finland, *EISCAT Technical Note, 86/45*, EISCAT Scientific Association, Kiruna, Sweden, 1986.

Lehtinen M., On optimization of incoherent scatter measurements, *Adv. Space Res.*, ***9***(5), 133-(5), 1989.

Lehtinen M.S. and **I. Häggström**, A new modulation principle for incoherent scatter measurements, *Radio Sci.*, ***22***, 625-634, 1987.

Lehtinen M.S. and **A. Huuskonen**, The use of multipulse zero lag data to improve incoherent scatter radar power profile accuracy, *J. Atmos. Terr. Phys.*, ***48***, 787-793, 1986.

Lehtinen M.S. and **A. Huuskonen**, General incoherent scatter analysis and GUISDAP, *J. Atmos. Terr. Phys.*, ***58***, 435-452, 1996.

Lehtinen M.S., **L. Päivärinta** and **E. Somersalo**, Linear inverse problems for generalized random variables, *Inverse Problems*, ***5***, 599-612, 1989.

Markkanen M. and **T. Nygrén**, A 64-bit strong alternating code discovered, *Radio Sci.*, in press, 1996.

Nygrén T., **A. Huuskonen** and **P. Pollari**, Alternating-coded multipulse codes for incoherent scatter experiments, *J. Atmos. Terr. Phys.*, in press, 1996.

Pollari P., **A. Huuskonen**, **E. Turunen** and **T.Turunen**, Range ambiguity effects in a phase coded *D*-region incoherent scatter radar experiment, *J. Atmos. Terr. Phys.*, ***51***, 937-945, 1989.

Rino C.L., **M.J. Baron**, **G.H. Burch** and **O. de la Beaujardière**, A multipulse correlator design for Incoherent scatter radar, *Radio Sci.*, ***9***, 1117-1127, 1974.

Sulzer M.P., A radar technique for high range resolution incoherent scatter autocorrelation function measurements utilizing the full power of klystron radars, *Radio Sci.*, ***21***, 1033-1040, 1986.

Sulzer M.P., A new type of alternating code for incoherent scatter measurements, *Radio Sci.*, ***28***, 995-1001, 1993.

Turunen T., GEN-SYSTEM - a new experimental philosophy for EISCAT radar, *J. Atmos. Terr. Phys.*, ***48***, 777-785, 1986.

Turunen T. and **J. Silen**, Modulation patterns for the EISCAT incoherent scatter radar, *J. Atmos. Terr. Phys.*, ***46***, 593-599, 1984.

Turunen T., **T. Nygrén**, **A. Huuskonen** and **L. Jalonen**, Incoherent scatter studies of sporadic E using 300m resolution, *J. Atmos. Terr. Phys.*, ***50***, 277-287, 1988.

Vallinkoski M., Statistics of incoherent scatter multiparameter fits, *J. Atmos. Terr. Phys.*, ***50***, 839-851, 1988.

Vallinkoski M., Error Analysis of incoherent scatter measurements, Ph.D. thesis, 84+26 pp, Univ. of Helsinki, Helsinki, Finland, *EISCAT Technical Note*, *89/49*, EISCAT Scientific Association, Kiruna, Sweden, 1989.

Wannberg G., The G2-system and general purpose alternating code experiments for EISCAT, *J. Atmos. Terr. Phys.*, ***55***, 543-557, 1993.

Woodman R.F., A general statistical instrument theory of atmospheric and ionospheric radars, *J. Geophys. Res.*, **96**, 7911-7928, 1991.

Woodman R.F. and **T. Hagfors**, Methods for the measurement of vertical ionospheric motions near the magnetic equator by incoherent scattering, *J. Geophys. Res.*, ***74***, 1205-1212, 1969.

THE USE OF INCOHERENT SCATTER DATA IN IONOSPHERIC AND PLASMA RESEARCH

Kristian Schlegel

1. Introduction

The incoherent scatter [*IS*] technique provides simultaneously several parameters of the ionospheric plasma in a height range from about 90 to more than 1000 km and a time resolution of the order of minutes. Four of these parameters, the electron density n_e, the electron and ion temperatures T_e and T_i, and the ion drift [*line-of-sight*] *V* can generally be derived routinely. They will be called "*basic*" parameters in the following. Besides, the ion-neutral collision frequency can be obtained in case of sufficiently good signal-to-noise ratio [*SNR*] for altitudes below about 110 km [e.g. *Kirkwood*, 1986]. The relative abundance of ions with mass 16 AMU [O^+] and mass 30 AMU [NO^+, $O2^+$] can be estimated in the 150-250 km height range with sophisticated techniques [e.g. *Lathuillere et al.*, 1986] and also the abundance of H^+ ions above 500 km [e.g. *Wu and Taieb*, 1993].

In the following chapters several techniques are described how the basic parameters can be used to study various phenomena of the ionosphere and thermosphere. The paper should not be regarded as a thorough review article. The aim was to give basic informations about various techniques, to present typical examples, and to provide some useful references for further studies. Emphasize was placed on *EISCAT* related papers for the latter. The chosen subjects reflect some personal preference and do certainly not constitute a complete set. In addition they are restricted to E- and F-region heights, since D-region and mesospheric *IS* applications will be covered in a separate paper.

It is assumed that the reader has some knowledge about the principles and operation of an *IS*-system in general and about the basics of ionospheric and thermospheric physics [e.g. *Kelley*, 1989, *Hargreaves*, 1992].

2. Electric Fields

In order to derive an electric field vector from *IS*-data one needs in general three or more independent line-of-sight velocity estimates. These can be obtained by looking in the same scattering volume with three different receiving antennas [*Figure 1, upper left*] Such a radar, like *EISCAT*, is called a tri-static radar. If only one receiving antenna is available, as in the case of a mono-static radar, the independent velocity components can be obtained by looking subsequently into three different scattering volumes which are not too much separated in distance [*Figure 1, upper right*]. It is usually accomplished by tilting the antenna beam by

about ±10° with respect to the original direction. In this case one has to assume that the velocity vector is spatially constant over the distance of the respective scattering volumes and that it is temporally constant during the measuring interval consisting of three separate measurements. This may not always be true during strongly disturbed conditions.

In both cases the three measured velocity components will then be combined in order to obtain the velocity vector:

$$\mathbf{V} = \underline{\underline{\mathbf{T}}} \begin{pmatrix} V_1 \\ V_2 \\ V_3 \end{pmatrix} \tag{1}$$

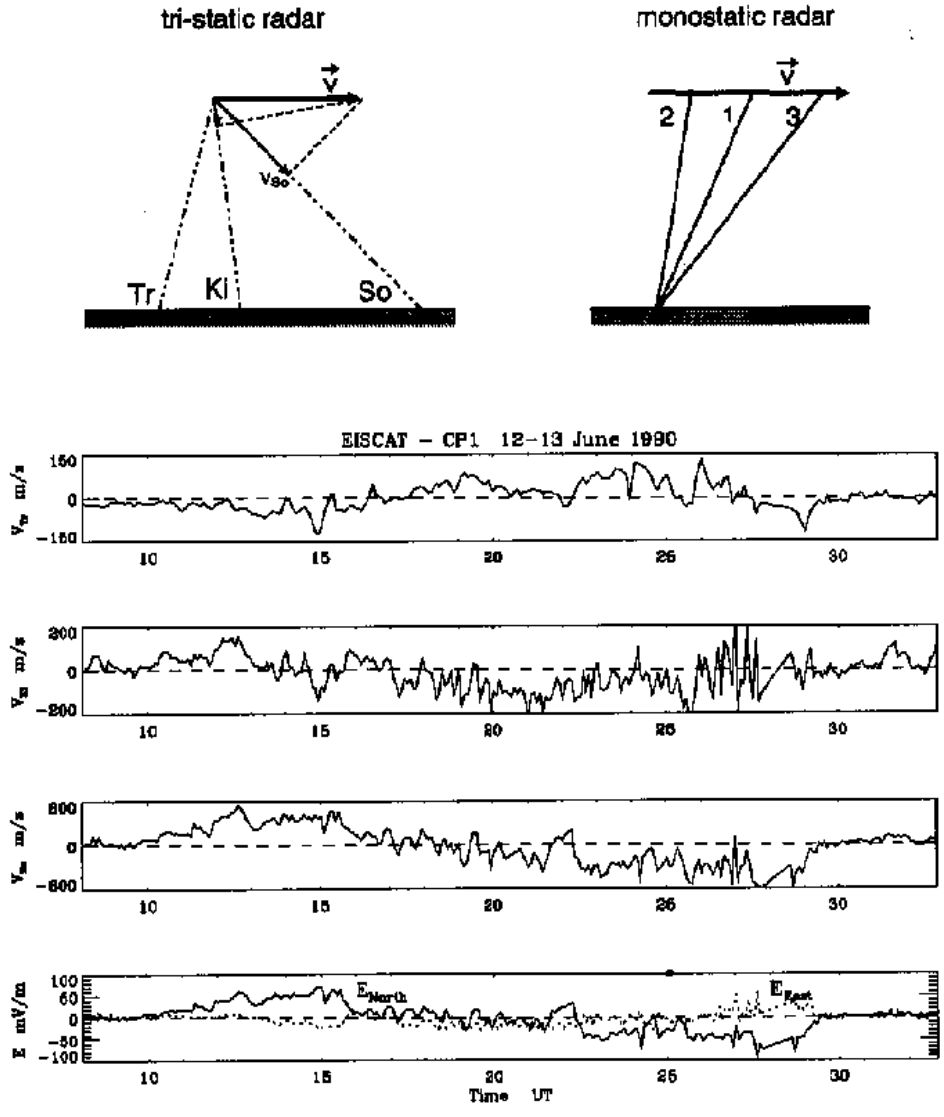

Figure 1. Measurements of the ion drift velocity vector with a tri-static(upper left) and a monostatic radar (upper right). Line-of-sight ion drift from Tromsoe, Kiruna and Sodankylae and the derived electric field for a one day EISCAT experiment.

$\underline{\mathbf{T}}$ is a transformation matrix the elements of which depend on the measuring geometry. For further use it is convenient to express the vector **V** in a plane perpendicular to the geomagnetic field **B**. In this case the transformation matrix also contains the magnetic field orientation [*Murdin*, 1979].

The electric field can finally be obtained from a simplified ion momentum equation [e.g. *Schunk*, 1975]

$$\frac{\nu_{in}}{\Omega_i} (\mathbf{V} - \mathbf{U}) = \mathbf{E} + \mathbf{V} \times \mathbf{B} \qquad (2)$$

In the F-region the ions are decoupled from the neutrals [$\nu_{in} \ll \Omega_i$] and therefore Eq. 2 reduces to

$$\mathbf{E} = - \mathbf{V} \times \mathbf{B} \qquad (3)$$

If **V** is expressed in a plane perpendicular to **B** then Eq. 2 decomposes into:

$$E_x = V_y B , \qquad E_y = - V_x B \qquad (4)$$

where B has to be taken from a magnetic field model [e.g. *IGRF 90*]. Here and in the following a coordinate system is used where the x-axis points to the east, the y-axis to the north and the z-axis upward, i.e. antiparallel to the magnetic field **B**. In case of *EISCAT* the tri-static point is usually taken at an altitude of 285 km.

In the lower panel of Figure 1 the line-of-sight velocities measured during a 24 hour experiment are displayed together with the derived electric field components perpendicular to **B** [E_{north} = *solid line*, E_{east} = *dotted line*]. It was a disturbed period [k_p *up to* 8^+] and therefore the electric fields reach quite high values. The maxima of the field in the afternoon and in the early morning and the turning of the field around 19-20 UT are quite typical for disturbed conditions. This behavior can be explained from the general pattern of the magnetospheric convection [e.g. *Senior et al.*, 1990, *Fontaine et al.*, 1986].

3. E-region electrodynamics

Due to the influence of the geomagnetic field the ionospheric conductivity is a tensor. It can be written as [*Bostrøm*, 1973]

$$\underline{\sigma} = \begin{pmatrix} \sigma_P & \sigma_H & 0 \\ -\sigma_H & \sigma_P & 0 \\ 0 & 0 & \sigma_\parallel \end{pmatrix} \qquad (5)$$

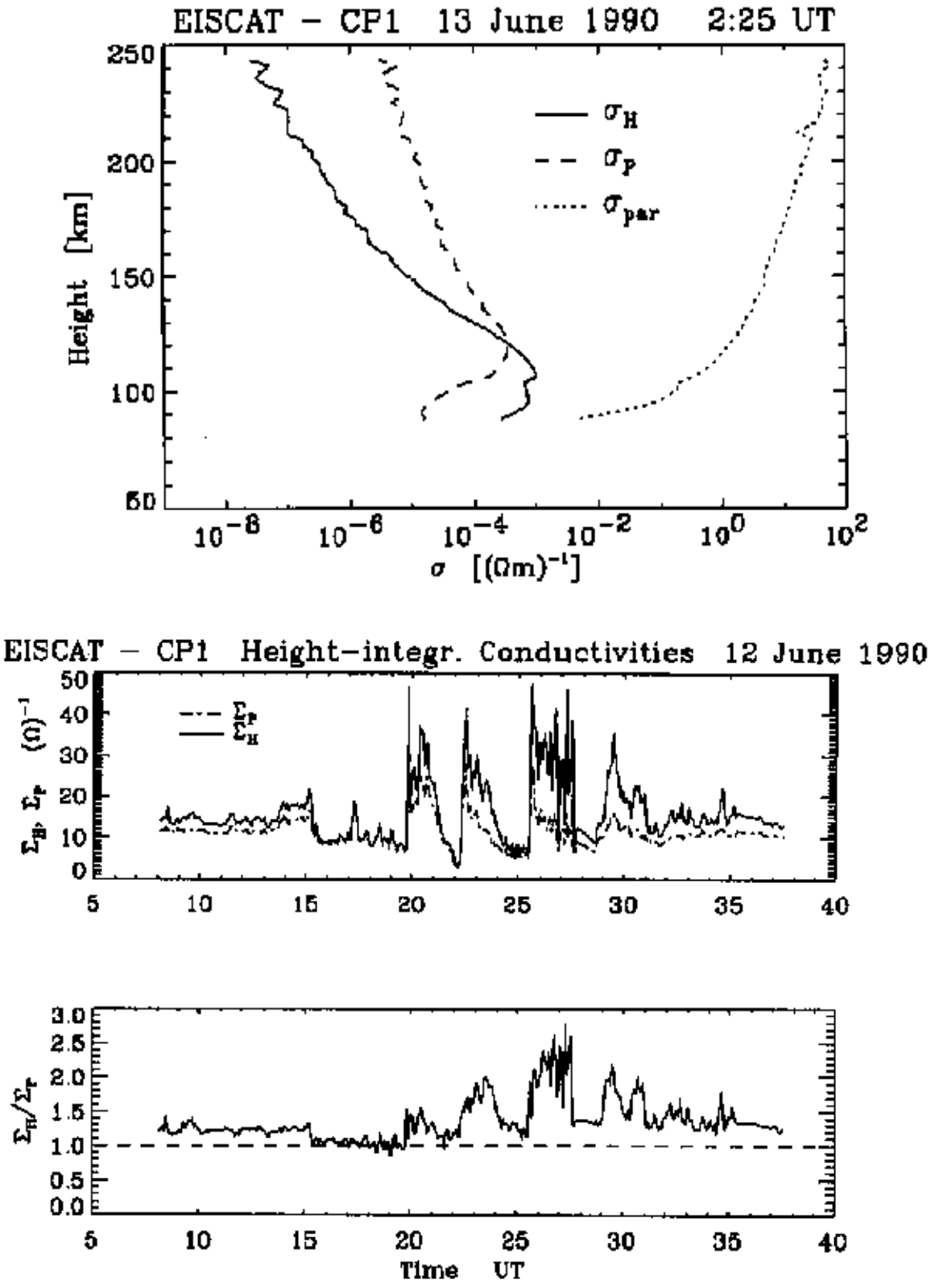

Figure 2. Upper panel: Height profiles of the components of the conductivity tensor in the ionosphere. Lower panels: Height-integrated Hall (Σ_H) and Pedersen (Σ_P) conductivities and conductivity ratio versus time.

Its components are the Pedersen conductivity

$$\sigma_P = \left\{ \frac{\nu_{en}\,\Omega_e}{\nu^2_{en} + \Omega_e} + \frac{\nu_{in}\,\Omega_i}{\nu^2_{in} + \Omega_i} \right\} \frac{e}{B}\, n_e \qquad (6)$$

the Hall conductivity

$$\sigma_H = \left\{ \frac{\Omega^2_e}{\nu^2_{en} + \Omega_e} - \frac{\Omega^2_i}{\nu^2_{in} + \Omega_i} \right\} \frac{e}{B}\, n_e \qquad (7)$$

and the conductivity parallel to the geomagnetic field

$$\sigma_{/\!/} = \left\{ \frac{1}{m_e\ \nu_{en}} + \frac{1}{m_i\ \nu_{in}} \right\}\ e^2\, n_e \qquad (8)$$

Here νe, νin are the electron- and ion-neutral collision frequencies, Ωe and Ωi the respective gyro frequencies and e is the electron charge.

The collision frequencies depend on the neutral density [e.g. *Kelley*, 1989], which has to be taken from a model [e.g. *MSIS 86*], the gyro frequencies can be computed from the local magnetic field induction *B*. Thus from the incoherent scatter parameters just the electron density n_e is needed to calculate the conductivities. It should be stressed however, that for these calculations density profiles of high range resolution [$\Delta h \approx$ *a few km*] are necessary which are usually provided by coded pulses.

Figure 2 [*upper panel*] shows an example. Since both the electron density and the collision frequencies are strongly height-dependent, the conductivities vary considerably with altitude. The maximum of the Hall conductivity is usually between 90 and 110 km, the maximum of the Pedersen conductivity between 120 and 130 km. The latter is also important at greater heights [*F-region*], whereas the Hall conductivity decreases strongly with altitude and is negligible above 200 km. The parallel conductivity is generally many orders of magnitude larger than the other two components because of the high mobility of the electrons parallel to **B**. The field lines can therefore be regarded as equipotential lines in the ionosphere.

Particularly for studies of ionosphere-magnetosphere coupling the height-integrated conductivities or conductances are important quantities. They are defined as:

$$\Sigma_H = \int_{h_o}^{h_1} \sigma_H\,(h)\,\mathrm{d}h \qquad \Sigma_P = \int_{h_o}^{h_1} \sigma_P\,(h)\,\mathrm{d}h \qquad (9)$$

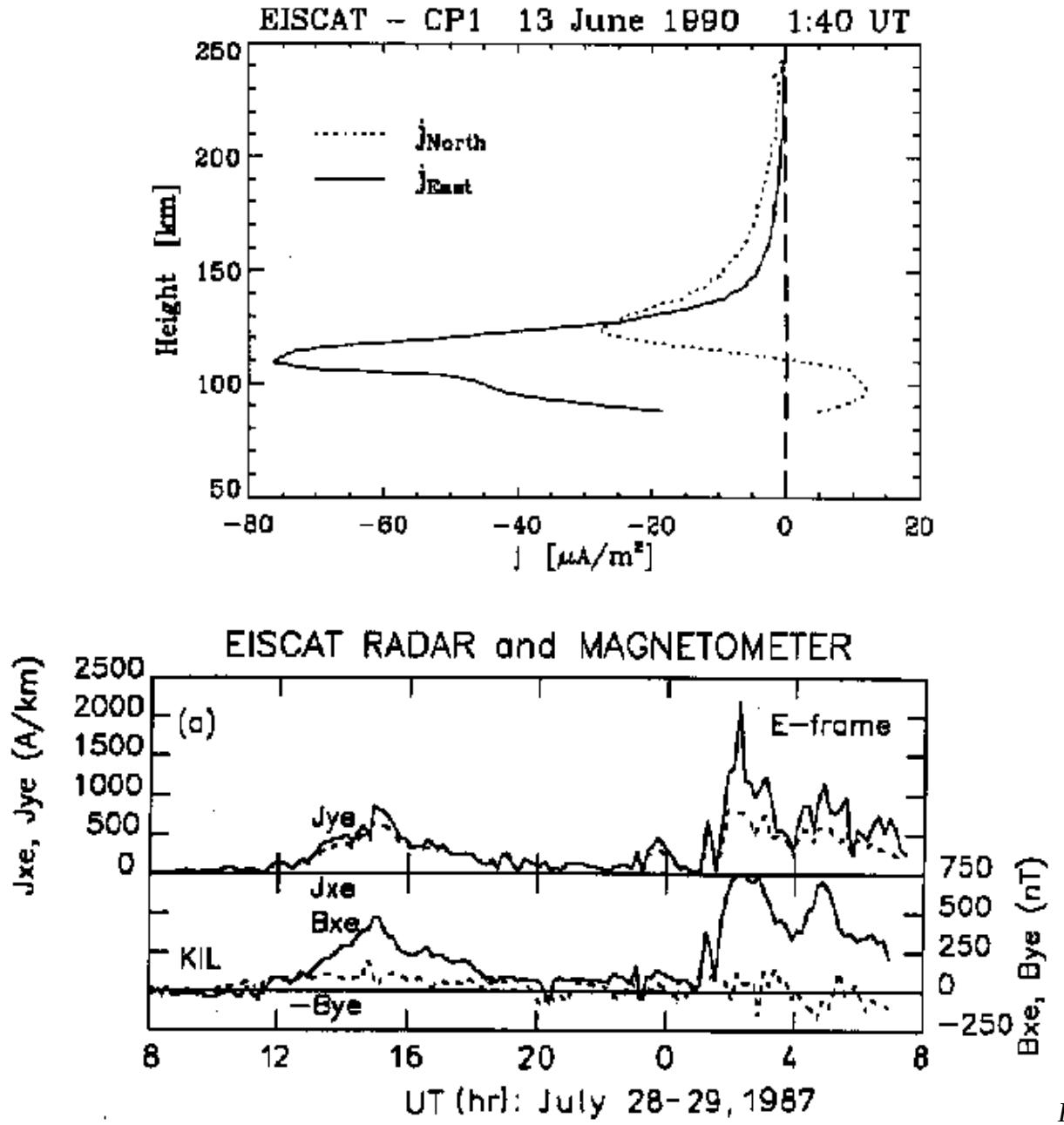

Figure 3. Upper panel: Height profiles of the northward and eastward components of the current density. Lower panels:Height-integrated currents and simultaneously measured magnetic field variations on the ground.

For the lower value of the height integral h_o usually a value between 80 and 90 km is taken, h_1 should be above 200 km.

Figure 2 [*middle panel*] shows Σ_H and Σ_P over a 30 hour interval. The bursts of enhanced conductance are caused by periodic particle precipitation which cause abrupt electron density enhancement in the E-region. An important quantity is the ratio of the conductances Σ_H/Σ_P [*Figure 2 lower panel*]. It is around unity during day-time and precipitation-free conditions and increases during precipitation events. Its value is regarded as a rough indicator of the energy of the pre-

cipitating particles. A recent review on high latitude conductances has been published by *Brekke and Moen* [1993].

As a next step in quantitative estimates of E-region electrodynamics, the current density can be computed from the equation [*Ohm's law*]

$$\mathbf{J} = \underline{\underline{\sigma}}\,\mathbf{E} \tag{10}$$

using the electric fields obtained as described in section 2.

If the coordinate system described in section 2 is used then this equation decomposes into the components:

$$\begin{pmatrix} \mathbf{j_P} = \sigma_P\,\mathbf{E}_\perp & \text{Pedersen current } (\perp \mathbf{B},\ /\!/\ \mathbf{E}) \\ \mathbf{j}_H = \sigma_H \dfrac{\mathbf{B} \times \mathbf{E}_\perp}{|\mathrm{B}|} & \text{Hall current } (\perp \mathbf{B},\ \perp \mathbf{E}) \\ \mathbf{j}_{/\!/} = \sigma_{/\!/}\,\mathbf{E}_{/\!/} & \text{parallel current} \end{pmatrix} \tag{11}$$

It should be noted that the parallel current cannot be directly calculated from *IS*-data since $\mathbf{E}_{/\!/}$ is generally too small to be measured. An estimate of $\mathbf{j}_{/\!/}$ may be obtained from:

$$\mathrm{div}\,(\,\mathbf{j}\,) = 0 \tag{12}$$

stating that the total current in the ionosphere is source free. This however needs a multi point measurement in order to derive the gradients of $\mathbf{j}_\perp$.

For the sake of completeness it should be noted that the electric field in eqs. 10, 11 in the general case is the effective electric field

$$\mathbf{E}_\perp{}^{eff} = \mathbf{E}_\perp + \mathbf{U} \times \mathbf{B} \tag{13}$$

which accounts for a neutral wind **U** [*see section 5*].

Figure 3 [*upper panel*] shows an example of the current density as a function of altitude computed from Eq. 10. The large westward current is a consequence of the strong eastward flow typical for the disturbed morning hours. The smaller northward current changes its sign due to the fact that the Hall and the Pedersen conductivity maximize at different height. Note that the westward current is not a pure Hall current but has a small Pedersen contribution because the electric field is not a purely northward field but has also a small westward component at that time [*see Figure 1*].

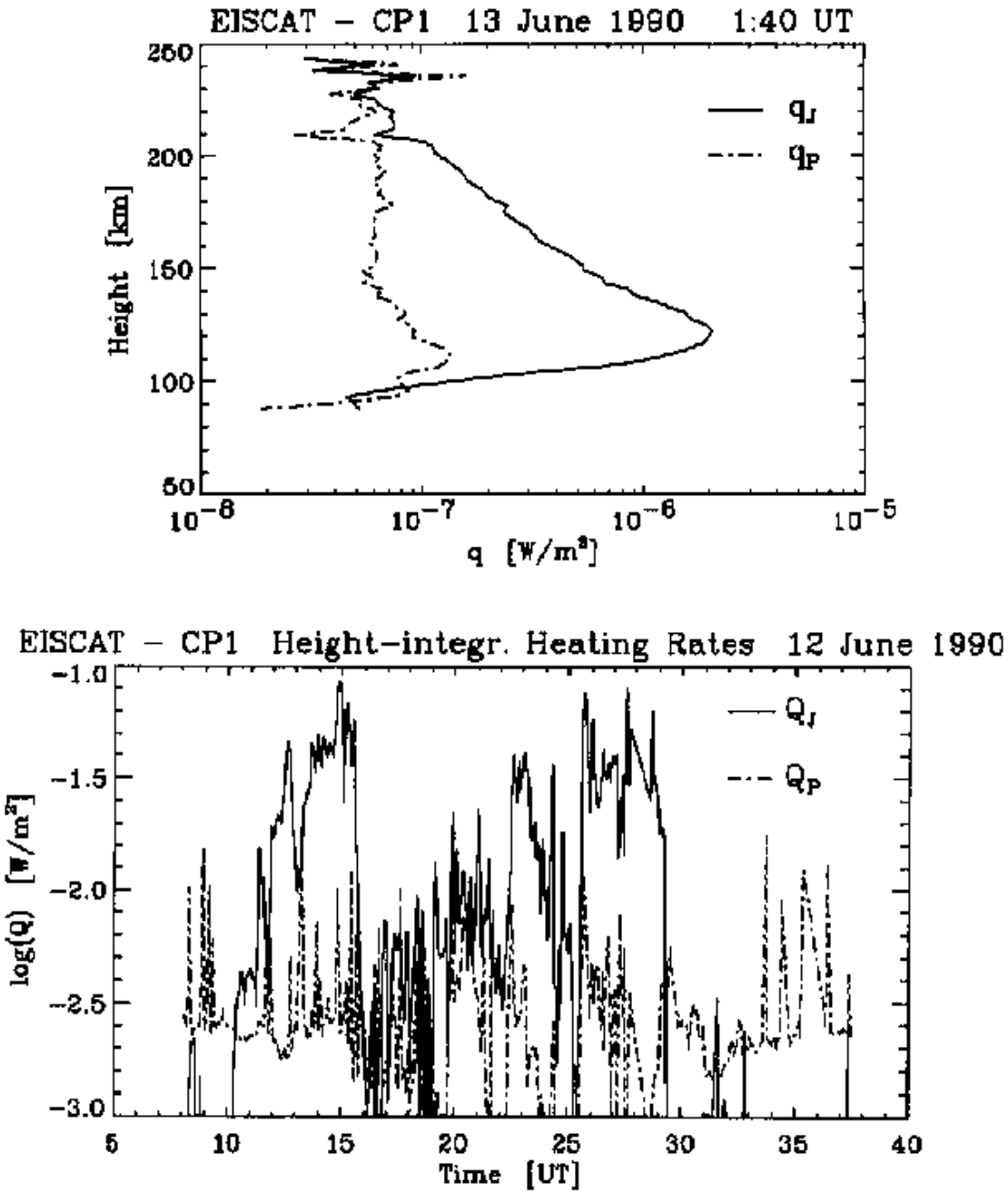

Figure 4. Upper panel:Height profiles of the Joule heating rate (q_J) and the heating rate of precipitating particles (q_P).Lower panel: Height-integrated Joule and particle heating rates versus time.

For time series of the current variation one again uses height-integrated values computed analogous to Eq. 9. Figure 3 [*lower panel*] shows an example for a 24-hour experiment [*Araki et al.*, 1989]. In this figure the response of a ground-based magnetometer to this current is also plotted. It is obvious that both curves are very well correlated. For a quantitative comparison, however, it has to be taken into account that the ionospheric current is not a line current and that a ground-based magnetometer picks up contributions from a large spatial volume. Suitable assumptions have therefore to be made for the latitudinal distribution of the current [*Lühr et al.*, 1994].

4. Heat sources and precipitation

There are several sources of energy input into the ionosphere, particularly acting at high latitudes. The ohmic losses of the E-region current produce an ion and electron heating [*energy density*] given by:

$$q_J = \sigma_P \; |\mathbf{E}_\perp|^2 \qquad (14)$$

Since this heating arises from the friction between the ions [*electrons*] and the neutrals it is also called frictional or Joule heating.

Both parameters in Eq. 14 can be derived from *IS*-data and therefore the computation of q_J is straightforward; Figure 4 [*upper panel*] shows an example.

Since σ_P is not negligible at F-region heights as already mentioned, Joule heating is also very important above the E-layer current region [e.g. *Baron and Wand*, 1983].

Another heat source provide the energetic electrons which precipitate into the E-region. The production of each electron-ion pair needs an energy of η = 35 eV. The energy density deposited in the precipitation region is therefore to a first order approximation [*Wickwar et al.*, 1975]:

$$q_P = \frac{1}{2}\,\eta\;\alpha_{eff}\;n_e^2 \qquad (15)$$

where α_{eff} is the effective electron-neutral recombination rate [e.g. *Schlegel*, 1985]. A profile of this particle heating during a strong precipitation event is also displayed in Figure 4 [*upper panel*]. This heat source is practically unimportant if no precipitation is present, e.g. during quiet conditions. This can be inferred from the lower panel of Figure 4 where both heating rates are plotted in a height-integrated form [*analogous to Eq. 9*] over an interval of 24 hours. Comparing Figure 4 with Figs. 1 and Figure 2 shows that the height integrated Joule heating maximizes during times when the electric field is elevated [*13:00-15:00 UT*] and the particle heating during precipitation events when n_e is increased. Particle heating is, however, generally smaller than Joule heating. A survey of high latitude heating rates has been presented by *Duboin* [1986].

The energy of both sources finally ends up in the neutral gas. During disturbed conditions the thermosphere is considerably heated at high latitudes. As intermediate step the Joule heating also raises the ion temperature above 120 km, whereas the soft precipitation leads to an increased electron temperature in the F-region.

The latter provides the main energy flow into the upper ionosphere. Since the energy of electrons with E < 10 eV is thermalized, i.e. distributed to the ambient electron gas, the heat flow can be estimated from the measured electron temperature. For this purpose the equation of the thermal heat conduction of the electrons:

$$c_e = - \alpha T_e^{5/2} \frac{\partial T_e}{\partial h} \qquad (16)$$

[α *is the heat conduction coefficient*] can be used which is divergent free:

$$\nabla c_e = 0 \qquad (17)$$

Since Eq. 16 contains only the electron temperature which is one of the basic parameters, the heat flow can be computed from the gradient of the T_e-profile. Figure 5 shows heat flows for a one day experiment with the *EISCAT-VHF*-radar [*Blelly and Alcaydé*, 1994]. The enhanced flow events are caused by soft particle precipitation whereas the almost constant "*background*" of about 20 $\mu W.m^{-2}$ correspond to solar EUV-heating [*the ionosphere is sunlit for 24 hours during May*].

The actual electron density profile in the E- and D-region during precipitation events depends strongly on the energy spectrum of the precipitating particles [*for energies E > 100 eV*]. Therefore algorithms have been constructed to invert the measured electron density profile into an energy spectrum [*Vondrak and Baron*, 1977]. These algorithms have been considerably refined in recent years

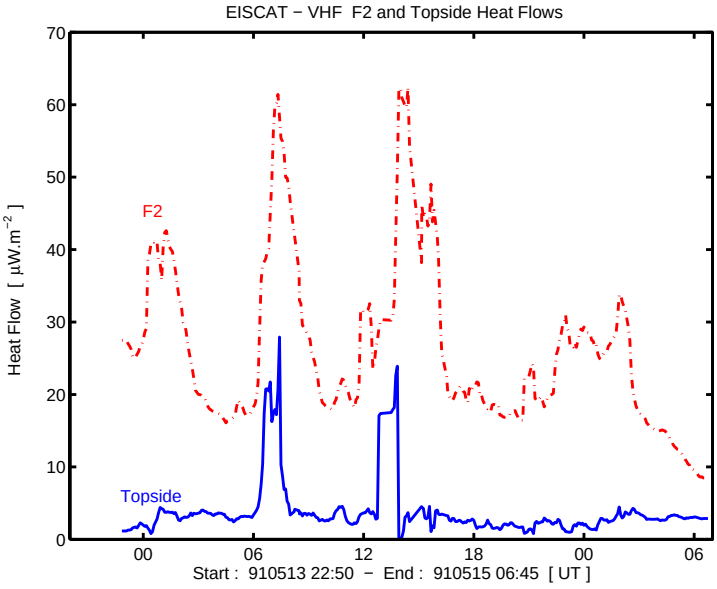

Figure 5. Heat flow into the topside ionosphere (1500 km) and into the F_2-region (300 km) as a function of time derived from EISCAT VHF measurements.

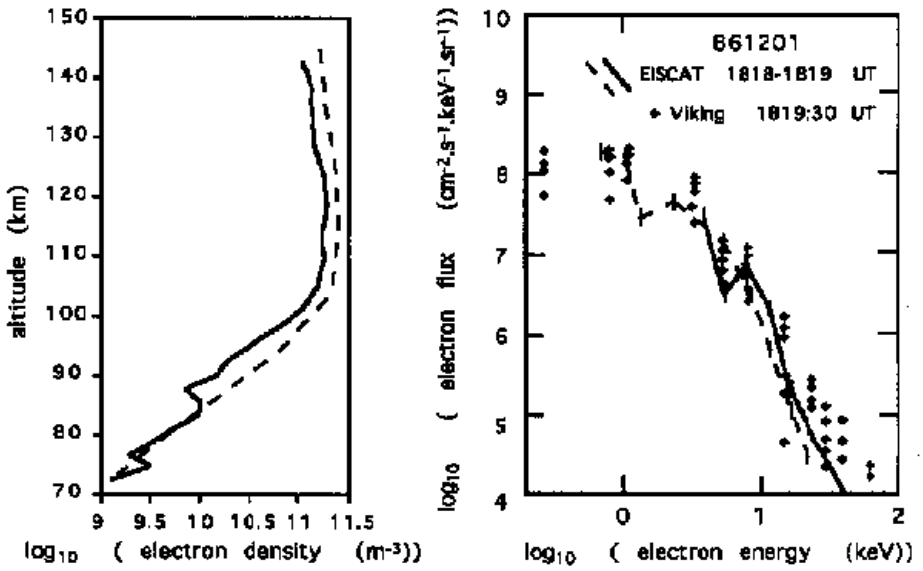

Figure 6. Electron density profile measured with EISCAT (left panel) and energy spectrum of precipitating electrons derived from it (right panel).The latter is compared to simulatneously measuerd electron energy spectra from the VIKING satellite.

and can now take not only precipitating electrons but also protons into account which mainly ionize in the D-region.

The inversion algorithm works in the following way: First a height profile of the electron production rate is computed from measured electron density profiles $n_e(h)$ with the help of a simplified continuity equation:

$$p(h) = \frac{\mathrm{d}\, n_e\,(h)}{\mathrm{d}\, t} + \alpha_{eff}\; n_e{}^2\,(h) - p^{EUV} \qquad (18)$$

For time series of the current variation one again uses height-integrated values computed analogous to Eq. 9. Figure 3 [*lower panel*] shows an example for a 24-modeled [*Kirkwood*, 1993]. The production is on the other hand caused by precipitating particles with energy fluxes $f(E)$ and can therefore be written for electrons [e] and protons [p]:

$$p = s_p\, f_p\,(E) + s_e\, f_e\,(E) \qquad (19)$$

where $s_{p,e}$ are the rate constants of various ionization reactions which are important in the height range under consideration.

The ionization rates of Eq. 19 are then fitted to the experimentally determined [*Eq. 18*] in a least-square sense by varying the fluxes at a number of fixed particle energies E [*e.g. assuming monoenergetic particles beams*]. A typical result is shown in Figure 6 [*Kirkwood and Osepian*, 1995]. In the right panel the deduced energy spectrum is displayed in comparison with flux data measured in-situ from the Viking satellite, in the right panel the electron density which was used to calculate the ionization rate [*Eq. 18*].

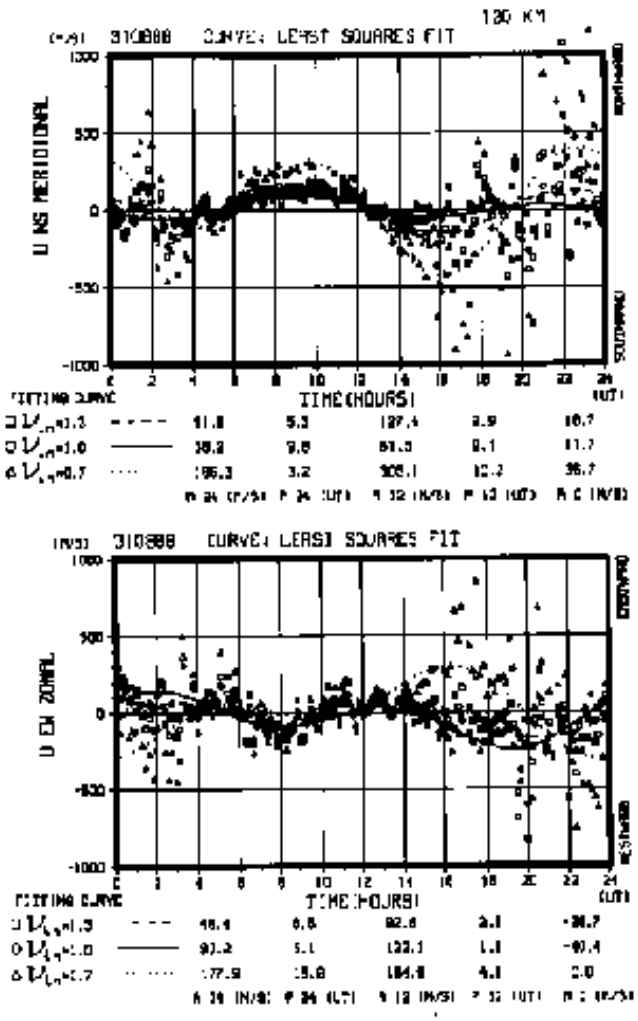

Figure 7. Neutral wind at 120 km altitude calculated for one day using different values for the ion-neutral collision frequncy. The respective curves are a fits of the measured velocities to a wind model assuming a diurnal and a semi-diurnal tide on top of a constant prevailing wind: U = $A_{24}\cos(2\pi/24(t-P_{24}))+A_{12}\cos(2\pi/12(t-P_{12}))+A_{0}$.

5. Neutral atmospheric properties

Since the *IS*-technique yields only plasma quantities, the estimate of parameters of the neutral atmosphere involves some calculations and assumptions.

Relatively straight forward is the calculation of the neutral wind at E-region heights. In a plane perpendicular to the magnetic field it follows from the ion momentum [*Eq. 2*] for the zonal [U_z] and the meridional [U_m] neutral wind components:

$$\left(\begin{array}{l} U_z = V_x - \dfrac{\Omega_i}{\nu_{in}} (\mathbf{E}_\perp + \mathbf{V} \times \mathbf{B})_z \\ \\ U_m = V_y - \dfrac{\Omega_i}{\nu_{in}} (\mathbf{E}_\perp + \mathbf{V} \times \mathbf{B})_m \end{array} \right) \qquad (20)$$

Here $\mathbf{E}_\perp$ is the electric field computed from Eq. 3 in the F-region, and **V** the vector of the ion drift obtained from tristatic measurements at E-region heights. The factor Ω_i/ν_{in} becomes considerably greater than unity above about 120 km. Thus errors in the determination of $\mathbf{E}_\perp$ and **V** are strongly magnified for greater heights. In practice, the neutral wind can therefore be estimated with Eq. 20 only between about 95 and 120 km, where the lower limit is usually determined by the poor signal-to-noise ratio of the data.

As an example for neutral wind estimates Figure 7 shows the meridional [*upper panel*] and zonal [*lower panel*] neutral wind component at 120 km altitude for a full day. It can clearly be seen that at night, when the SNR ratio is smaller than during daytime and consequently the accuracy of the measurements decreases, the scatter in the derived wind values considerably increases. The various curves in the figure correspond to a fit of the wind pattern to a diurnal and a semidiurnal tide [*see also section 6*]. Since the value of ν_{in} is crucial for the computed magnitude of **U**, values departing by ± 30% from the model value [*after MSIS 86*] have also been included in this figure [*Kunitake and Schlegel*, 1991].

At altitudes above the E-region a different technique has to be applied for a neutral wind estimate. A very simplified form of the momentum equation for the neutrals and ions parallel to the geomagnetic field can be written [Wickwar et al., 1984]:

$$V_{//} = U_{//} + V_d \qquad (21)$$

where:

$$V_d = - \frac{\sin I}{\nu_{in}} \left\{ g + \frac{k}{m_i n_e} \frac{\partial}{\partial h} [n_e (T_e + T_i)] \right\}$$

is the ambipolar diffusion velocity along the direction of B [I is the inclination of B, g is the acceleration of gravity and k is the Boltzman constant]. The meridional component of the neutral wind can then be expressed as:

$$U_m = U_v \sec I \; - \; (V_{//} - V_d) \tan I \qquad (22)$$

Equation 21 contains apart from νin and mi only parameters that can be obtained with the IS-technique. The vertical neutral wind Uv is generally small and can thus be neglected. Again νin is critical for these wind estimates [e.g. Burnside et al., 1987]. In the F-region it consists of three different collision processes:

$$\nu_{in} = \nu_{O^+-O} + \nu_{O^+-N_2} + \nu_{O^+-O_2} \qquad (23)$$

since O^+ is the principal ion and N_2, O_2 and O are the most important neutral constituents there.

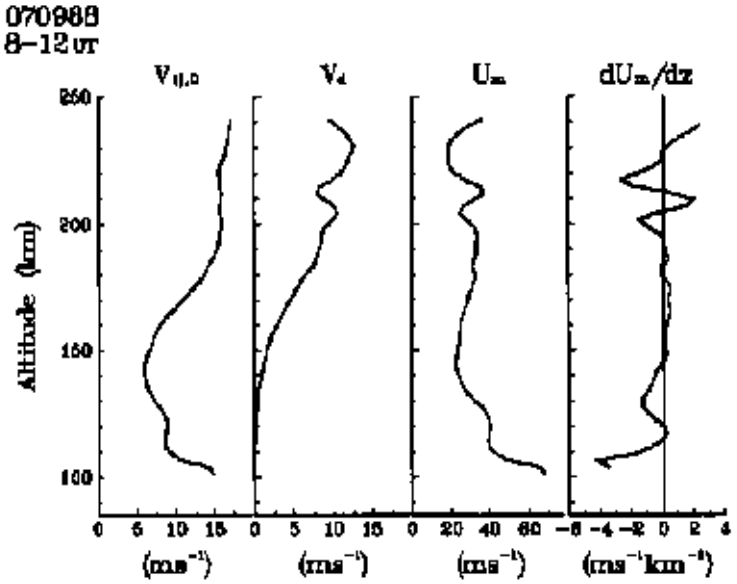

Figure 8. Height profiles of measured ion drift parallel to B ($V_{i//}$), the ambipolar diffusion velocity (V_d), the calculated meridional neutral wind (U_m) and its vertical gradient.

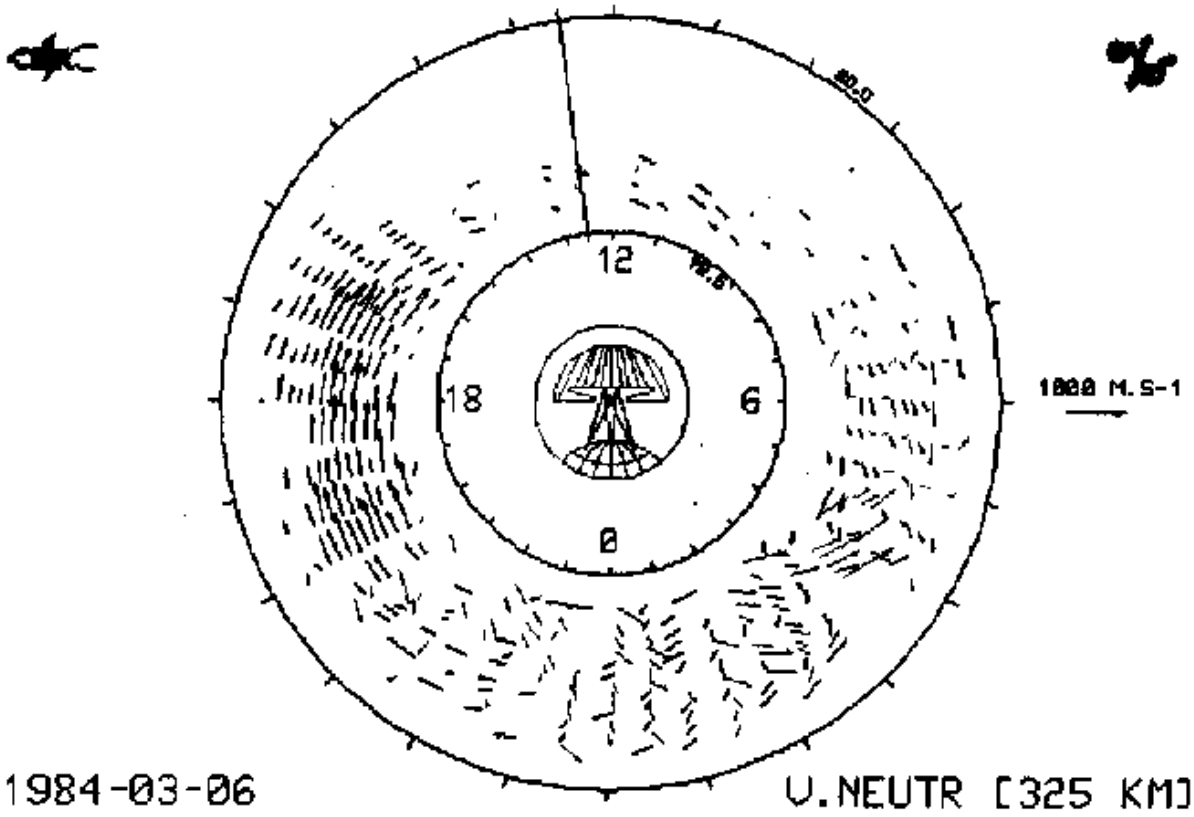

Figure 9. Neutral wind in the thermosphere derived for a whole day from EISCAT CP-3 data spanning a latitudinal range from 67° to 72°.

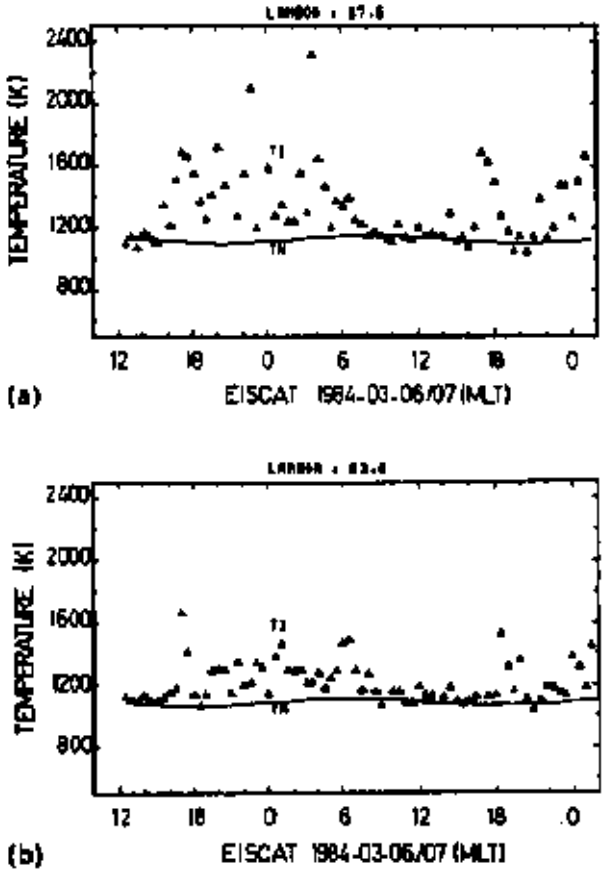

Figure 10. Neutral temperatures in the thermosphere derived simultaneously with the wind vectors shown in Figure 9. The measured ion temperatures are also included.

Figure 8 shows an example of an U_m-profile obtained in this way, together with the measured $V_{//}$ and the computed V_d [*Shibata and Schlegel*, 1993].

An estimate of the zonal component of the neutral wind u_z, is more complicated. A simplified form of the ion energy balance can to be used [*St. Maurice and Hanson*, 1982]:

$$(V_y - U_m)^2 + (V_x - U_z)^2 = \frac{3\,k}{m_n}\left\{(T_i - T_n) - \frac{m_i + m_n}{m_i}\frac{\nu_{ie}}{\nu_{in}}(T_e - T_i)\right\} \qquad (24)$$

with m_n being the mass of the neutral particles, and ν_{ie} the electron-ion collision frequency [e.g. *Banks and Kockarts*, 1973]. For the neutral gas temperature one can either insert model values or $T_i \approx T_n$ can be used as a first approximation.

If a longer series of good quality data points are available, Eq. 24 can be used to fit both the zonal wind and the neutral gas temperature [*Alcaydé and Fontanari*, 1986]. Figure 9 shows a clock-dial plot of neutral wind vectors for a whole 24-hour period derived in this way from *EISCAT-CP3* data spanning over a latitudinal range between 60° and 72.5°. Figure 10 contains the simultaneously obtained neutral temperatures together with the measured ion temperature.

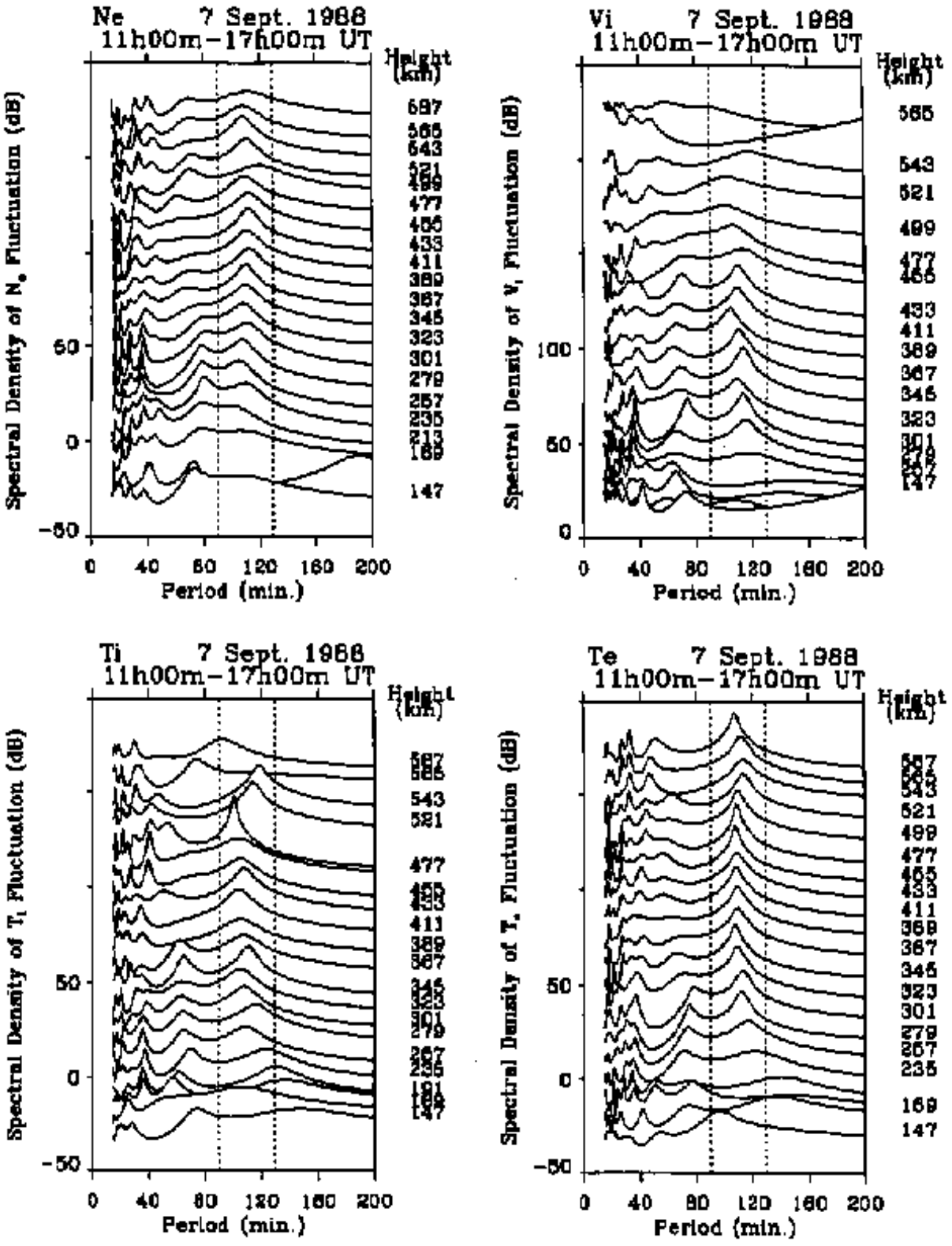

Figure 11. MEM spectra of TIDs present in the electron density (N_e), in the line-of-sight ion drift (V_i), in the ion temperature (T_i) and in the electron temperature (T_e) for several heights. The dashed lines indicate the bandwidth of the filters which have been used in the subsequent analysys.

If either neutral wind or neutral temperature data are provided by a different technique the missing quantity can also be calculated with the help of Eq. 22 and 24 [e.g. *Thuillier et al.*, 1990].

Neutral gas temperatures in the E-region can well be estimated from the assumption of $T_e \approx T_i \approx T_n$ which is valid during geomagnetic quiet conditions [e.g. *Kirkwood*, 1986]. Temperature differences between the three species are quickly equalized due to frequent collisions.

6. TIDs and Gravity Waves

Traveling ionospheric disturbances [*TIDs*] can most often be interpreted as the ionospheric signatures of gravity waves in the neutral atmosphere [*Hocke and Schlegel*, 1996]. They appear as wave-like fluctuations in all basic ionospheric parameters. A first step in the investigation of these wave phenomena is the determination of their wave frequency. This can be performed either by using a Fourier transformation [*FFT*] or the maximum entropy method [*MEM*] [e.g. *Ulrych and Bishop*, 1975]. The latter is usually preferred because it yields reliable results for shorter time series than the *FFT* which in principle assumes an infinite time sequence. Figure 11 shows such *MEM*-spectra of fluctuations in the basic parameters for 21 height steps between 147 and 587 km.

In order to make the *TIDs* more clearly visible in the data, digital filtering [*with Butterworth filters*] is applied [e.g. *Hocke*, 1994]. The width of the corresponding filter has to be adjusted in a way that the peak of the fluctuation frequency fits into its range.

Figure 12 shows filtered data of the ion velocity and the electron density. The corresponding filter width is indicated in Figure 11 as two dashed lines around the main frequency peak. The forward tilting of the wave fronts indicate a gravity waves as cause for the observed *TID*.

In a further treatment of the filtered data, amplitude profiles can be computed and profiles of phase relationship between the waves in the different parameters can be established. Figure 13 shows an example [*Hocke et al.*, 1995]. These phase relationships provide insight into the interaction processes between the neutral gas and the plasma and in turn clues for the determination of the cause of the *TID*. A gravity wave as the cause can for instance be uniquely identified [*Kirchengast et al.*, 1995].

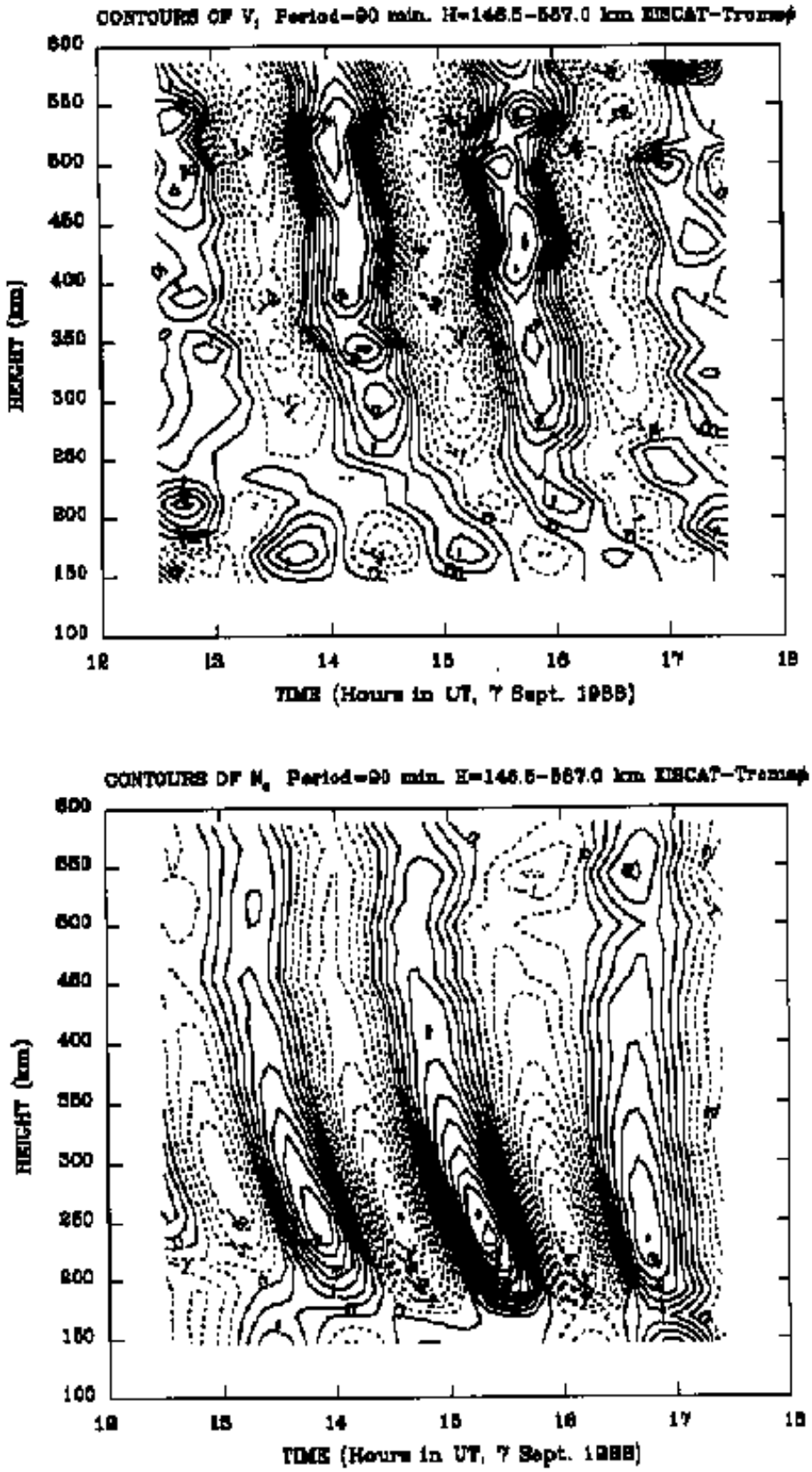

Figure 12. Waves in the line-of-sight ion drift velocity (upper panel) and in the electron density (lower panel) made visible by digital filtering of the respective time series. The bandwidth of the filter is indicated by dashed lines in Figure 11.

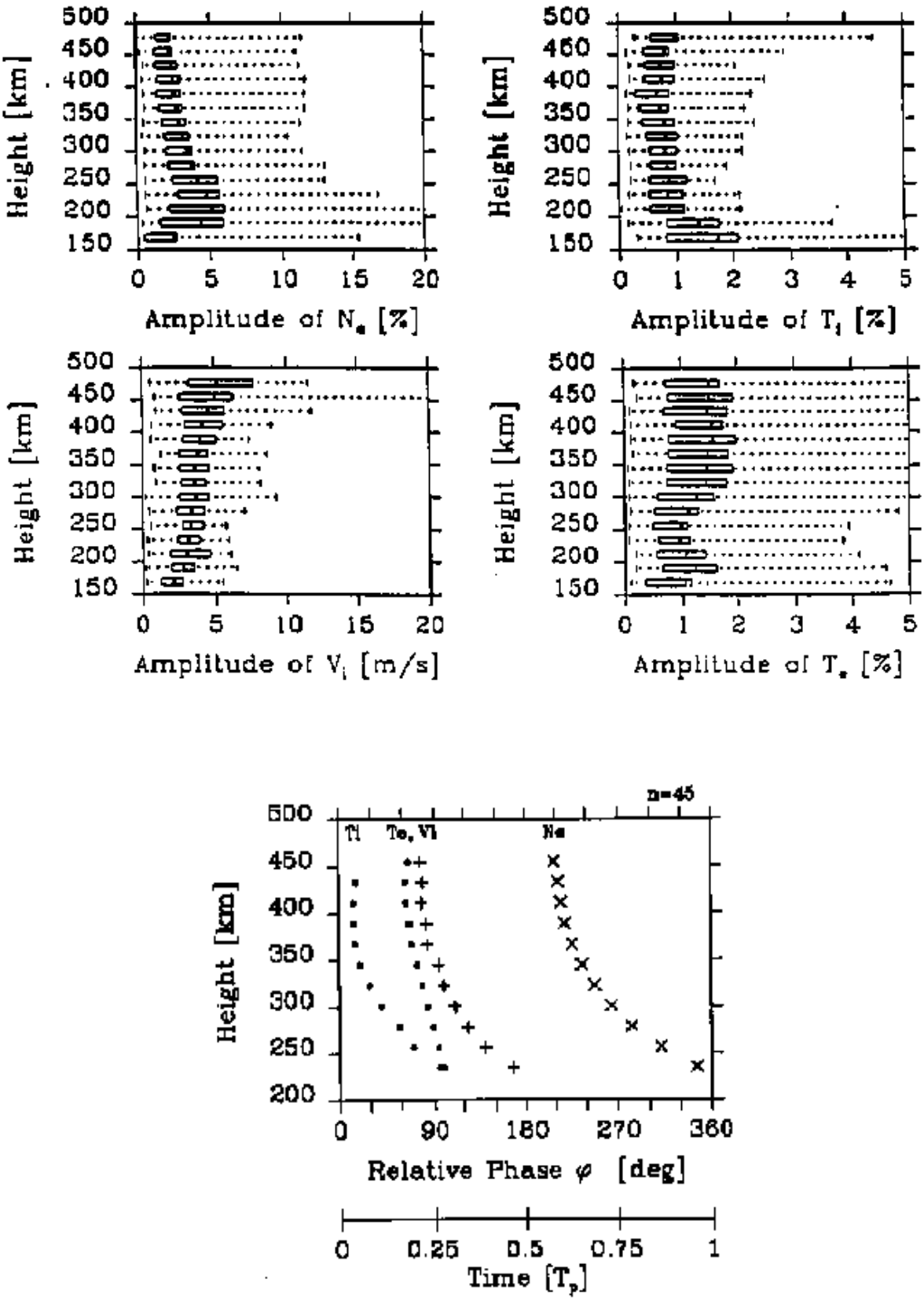

Figure 13. Upper panel:Average amplitude profiles of 45 TIDs in the four basic parameters. The boxes indicate the middle quartile of the data, the full dot the arithmetic mean. Lower panel: Average phase relationships between the TIDs in the four basic parameters.

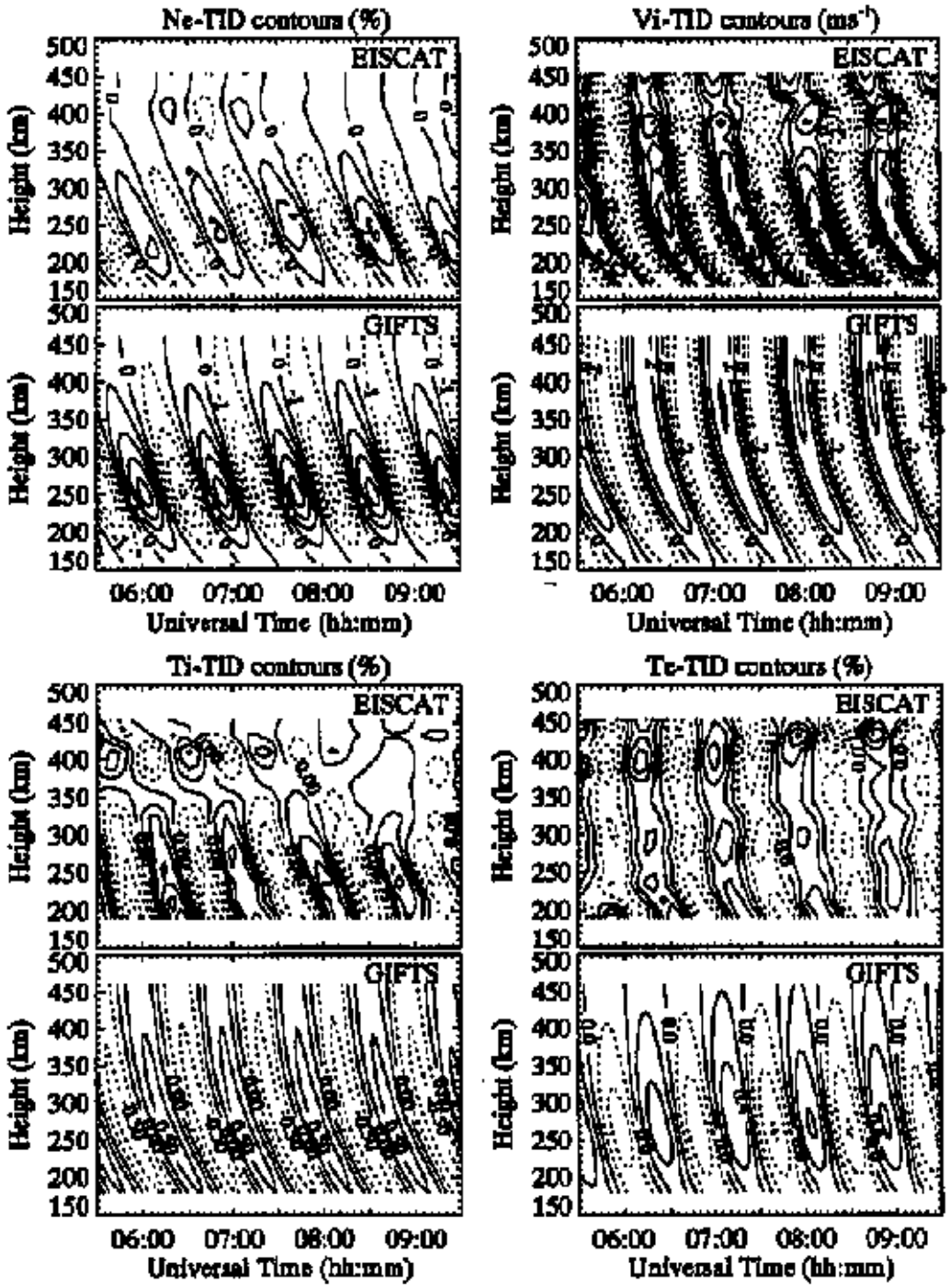

Figure 14. Comparison of measured (EISCAT) and modeled (GIFTS-Model) TIDs in the four basic parameters.

With some caution the wave frequency of the *TID*-fluctuations can be regarded as the wave frequency of the causing gravity wave. It has to be kept in mind, however, that a Doppler shift due to a neutral wind may be present which can be expressed as:

$$\omega_D = \mathbf{k} \,.\, \mathbf{U} \qquad (25)$$

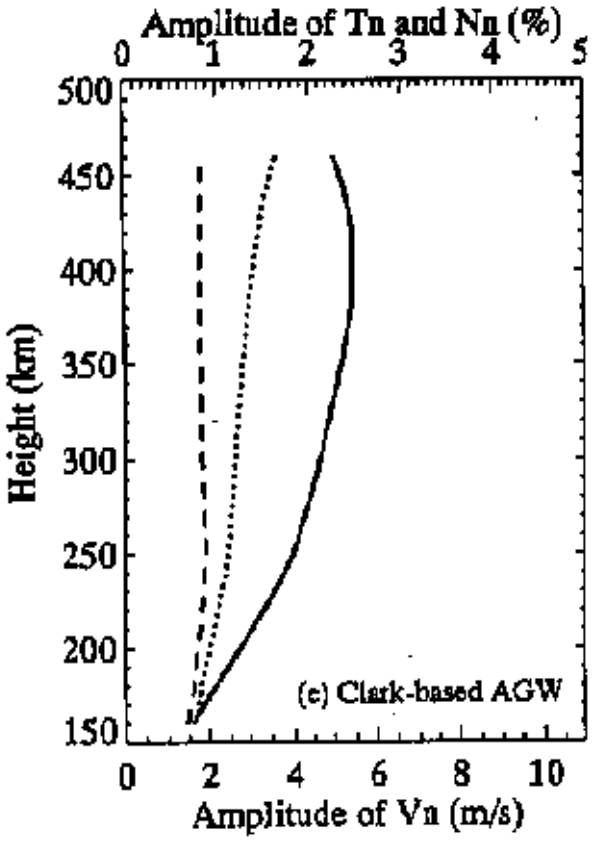

Figure 15. Amplitudes in the neutral temperature and in the neutral wind of the gravity wave which caused the TIDs displayed in Figure 14. These are results of the modeling process described in the text.

The fact that the frequency peak in Figure 13 is not at the same location at all height steps is most probably due to such Doppler shifts and indicate wind shears.

The direct calculation of other parameters of the *TID*-causing gravity wave is generally not possible from *IS*-data. The interactions between the neutral gas and the plasma are very complex so that no unique relationships exist between the gravity wave parameters [*vertical and horizontal wave numbers, neutral gas fluctuations*] and the plasma quantities. Instead, a modeling approach has turned out to be promising [*Kirchengast et al.*, 1995]. With a realistic ionospheric model [*Kirchengast*, 1992] the response of the plasma to a neutral atmospheric wave is calculated and the results are compared to measured *TIDs*. By varying the gravity wave parameters a best agreement between the measured and the model data can thus be achieved. Figure 14 shows as an example measured and calculated *TIDs* in a representation similar as Figure 12. The wave parameters of the neutral gas obtained in this way are displayed in Figure 15. This method yields very reliable results for gravity wave parameters but is rather time consuming. For a quick look purpose a reasonably realistic but very easy to handle algorithm has been developed for such a modeling approach [*Wuttke*, 1994].

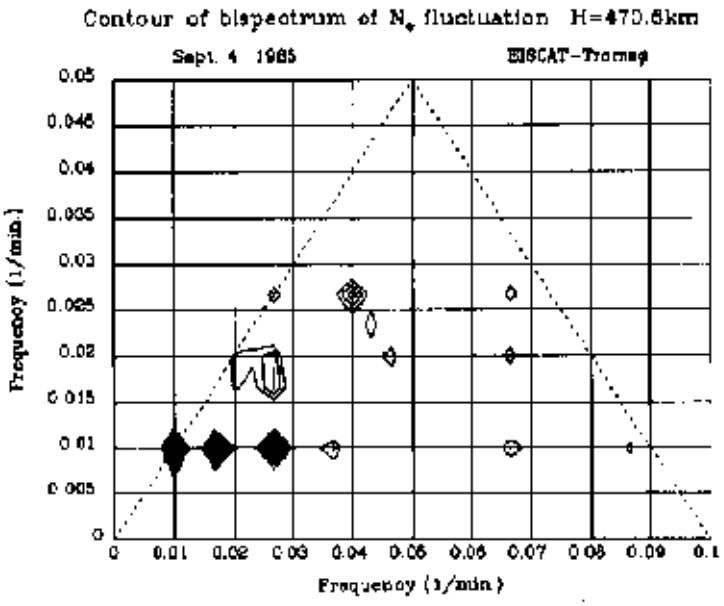

Figure 16. Example of a bi-spectrum to establish non-linear interaction of atmospheric waves. The contours indicate that (among others) the following frequency relationships exist: 0.01 + 0.017 = 0.027 0.01 + 0.027 = 0.037 0.027 + 0.04 = 0.067 (all in min^{-1})

TIDs and gravity waves in a wavelength range between about 15 minutes [*Brunt-Väisälä period*] and a few hours can be studied with the method described above. It has also been successfully applied to atmospheric tides which constitute waves with the period of one day and higher harmonics, e.g. 12 h, 8 h, 6 h etc. [*Hocke*, 1995; *Virdi and Williams*, 1993].

For studies of the propagation of *TIDs* and gravity waves other techniques have to be used in addition to the *IS* measurements [e.g. *Williams et al.*, 1993].

Waves in the thermosphere are frequently subject to non-linear interactions. A method for a quantitative examination of such an interaction which was originally derived for sea-wave coupling has been successfully applied to atmospheric waves [e.g. *Rüster*, 1992; *Ma and Schlegel*, 1991]. This technique uses the fact that the bi-spectrum defined by Eq. 26:

$$B(\omega_1,\omega_2) = \int\int R(\tau_1,\tau_2)\exp\{-i(\omega_1\tau_1 + \omega_2\tau_2)\}\, d\tau_1\, d\tau_2 \qquad (26)$$

[*where*: $R(\tau_1,\tau_2) = X(t)\,X(t+\tau_1)\,X(t+\tau_2)$ *is the third order moment of the time series X(t)*],

is different from zero only if a phase relationship exists between three different waves with frequencies ω_1, ω_2, ω_3 and the conditions:

$$\omega_1 \pm \omega_2 \pm \omega_3 = 0$$
$$\mathbf{k}_1 \pm \mathbf{k}_2 \pm \mathbf{k}_3 = 0 \qquad (27)$$

hold. Whereas the determination of the wave vector **k** is not possible from *IS*-data, different values of ω can usually be determined in a measured time series, as outlined above. Figure 16 shows an example of the bi-spectrum of three waves with various wave periods [*Ma and Schlegel*, 1993].

7. Ion temperature anisotropy

High electric fields which drive the ions through the neutral gas creating large differences in the velocity between both species, also cause a non Maxwellian velocity distribution of the ions and in turn ion temperature anisotropies.

It was shown theoretically that in such a case the ion temperatures measured parallel and perpendicular to the geomagnetic field **B** are different [*St-Maurice and Schunk*, 1977]. Both temperatures can be expressed as:

$$T_{//} = T_n (1 + \beta_{//} D'^2)$$
$$T_{\perp} = T_n (1 + \beta_{\perp} D'^2) \qquad (28)$$

where

$$D' = | \mathbf{V} - \mathbf{U} | / \sqrt{\frac{2\,k\,T_n}{m_n}}$$

is the normalized differential velocity and T_n is the neutral temperature. $\beta_{//}$ and $\beta_{\perp}$ are to a first approximation constants depending on the collision model and the mass ratio of ions and neutrals.

$T_{i//}$ can be directly measured with the *EISCAT-Tromsø* radar looking parallel to **B** [*CP-1 mode*]. A direct measurement perpendicular to **B** is not possible, but fortunately experiments from Kiruna and Sodankylä provide two independent temperature "*components*". The radar wave vector from both sites intersects with the geomagnetic field at different angles φ. Using a general relationship derived by *Raman et al.* [1981]:

$$T_{i\varphi} = T_{i\perp} \sin^2\varphi + T_{i//} \cos^2\varphi \qquad (29)$$

the temperatures measured from both sites can be expressed as functions of $T_{i//}$ and $T_{i\perp}$. Therefore from a tri-static *EISCAT* experiment three independent estimates $T_{i\varphi}$ of the ion temperature can be obtained. With Eq. 28 and 29 the three

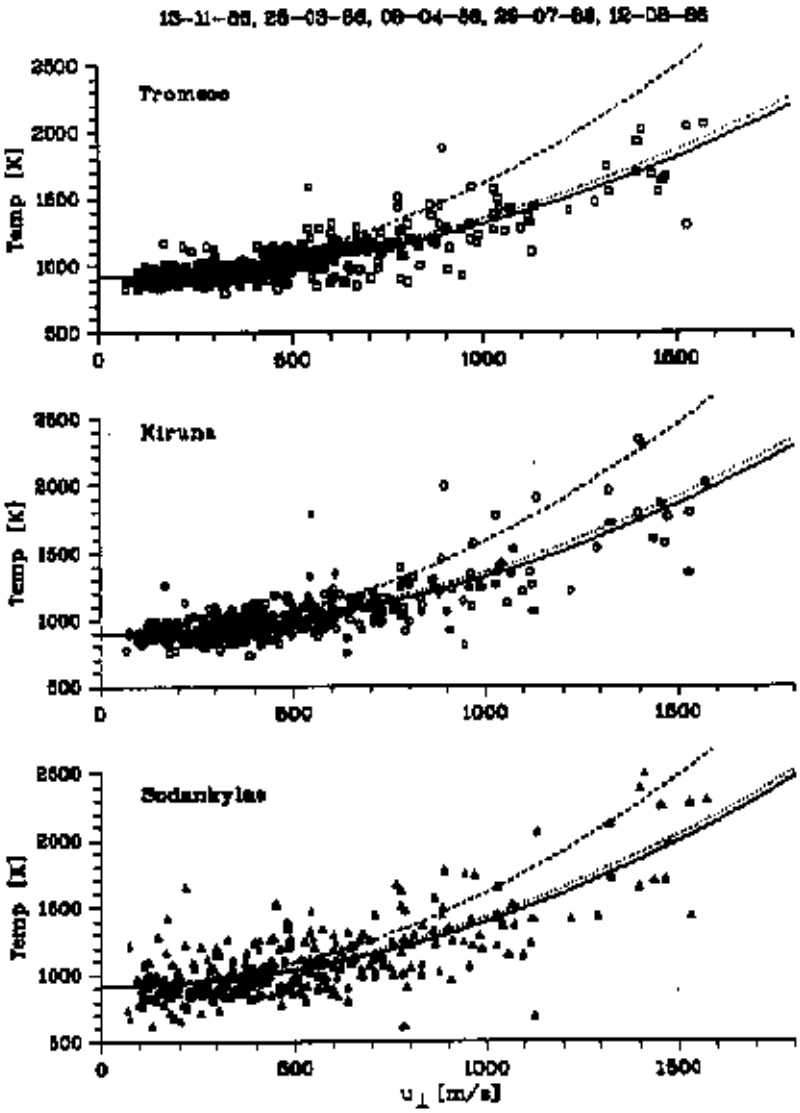

Figure 17. Ion temperatures measured from Tromsoe, Kiruna and Sodankylae plotted as a function of prevailing ion drift perpendicular to the geomagnetic field vector. The dashed curves indicate expected temperatures if a Maxwellian ion velocity distribution is assumed, the dotted and the solid curves are for two different bi-Maxwellian velocity distributions.

unknowns T_n , $\beta_{||}$ and $\beta_{\perp}$ can then be calculated. By comparing the derived values of the parameters $\beta_{||}$ and $\beta_{\perp}$ with those predicted by the kinetic theory, information about the ion-neutral interaction can be gained [e.g. *Hubert*, 1984]. Figure 17 shows as an example ion temperatures measured from the three *EISCAT* sites in comparison with computed results from different assumptions about the ion velocity distribution [*Glatthor and Hernandez*, 1990]. It is obvious from this figure that non-Maxwellian effects become important only for **E** x **B** drifts well above 500 m/s.

8. Coherent Structures

Plasma instabilities excited in the ionosphere create localized electron density structures with different scales in space and time. Such structures are usually investigated with *VHF*-radars providing a coherent integration. Since *IS*-facilities are in fact very powerful and sensitive coherent radars, it is easily possible to use them for such studies. A problem in these investigations is that many of the unstable plasma waves constituting the density structures propagate almost perpendicular to the geomagnetic field direction. The radar wave vector has thus to be directed almost perpendicular to **B** which cannot be easily achieved from geometrical considerations. *EISCAT* for instance was deliberately placed in a valley with relatively high mountains to the north in order to prevent contamination of the orders of magnitudes weaker incoherent scatter from strong coherent scatter. Thus with the *EISCAT* system only angles of about 85° with respect to **B** can be realized. Although the backscatter from coherent structures decreases considerably with the deviation angle from 90°, it can easily be received with an *IS*-facility because of the large transmitter power and the high antenna gains [*compared to a usual coherent radar*].Another fact which has to kept in mind is that the radar frequency of an *IS* facility is usually considerably higher than those of a coherent *VHF* radar. Thus the irregularities are probed at scale lengths:

$$l = \frac{\lambda_{radar}}{2} \tag{30}$$

which are usually smaller than 1 m.

The great advantage of *IS* facilities besides the higher sensitivity, is the much better spatial resolution of the measurements compared to those of a usual coherent radar, because of the large antenna aperture. Figure 18 shows as an example backscatter contours as a function of range [*height*] and time in the E-region which prove this ability [*Schlegel et al.*, 1990]. It also enables accurate measurements of the aspect angle sensitivity [*Moorcroft and Schlegel*, 1990].

Similar as in the *IS* case, the spectral shape of the signal scattered from coherent structures can be measured as well as its Doppler shift. Unfortunately there exists no theory so far to explain this spectrum quantitatively. Whereas the Doppler shift can be interpreted straight forward as the phase velocity of the unstable plasma waves, the width of the spectrum provides only some indirect information about the lifetime of the irregularities. Figure 19 shows an example of such measured Doppler spectra [*Mc Crea et al.*, 1991].

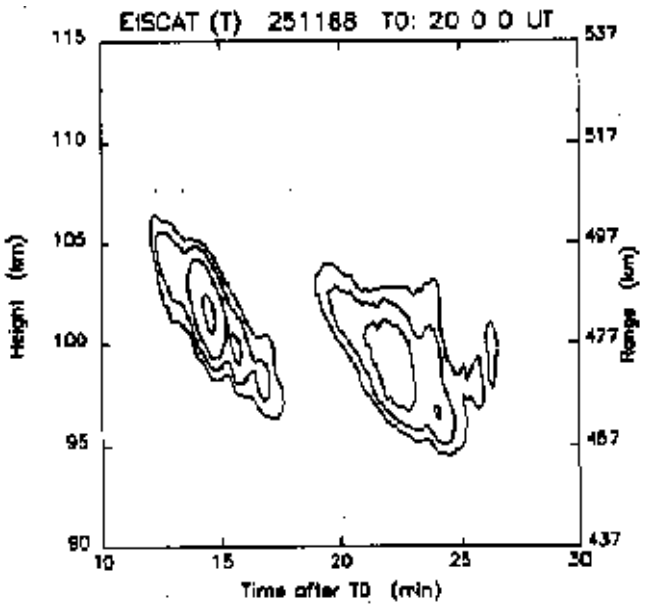

Figure 18. Contours of backscattered power from coherent structures in the ionospheric E-region which are caused by the modified two stream plasma instability.

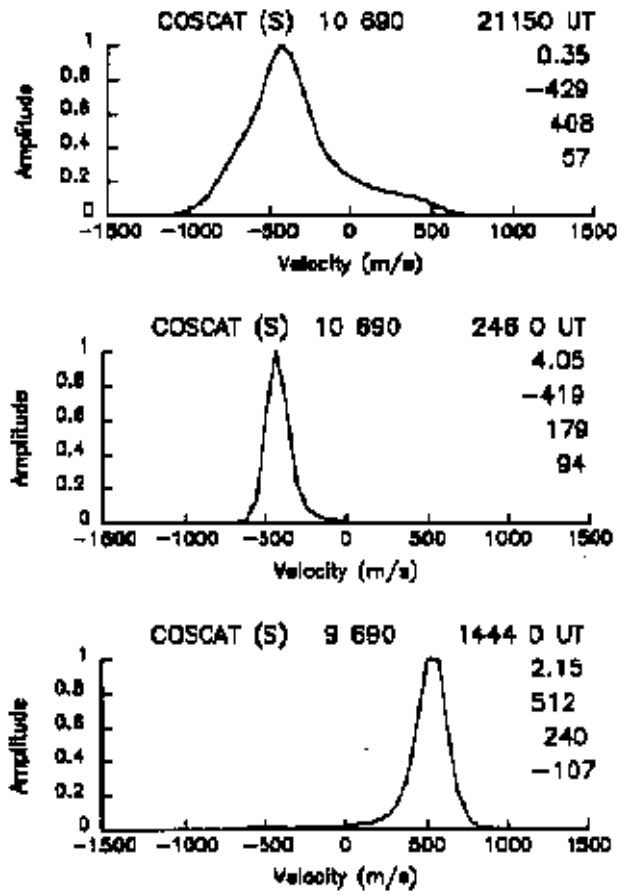

Figure 19. Three different Doppler spectra from coherent structures which are caused by unstable plasma waves, excited by the modified two stream plasma instability. The numbers on the right of each spectrum indicate the backscattered power, the Dopller shift, the width and the skewness.

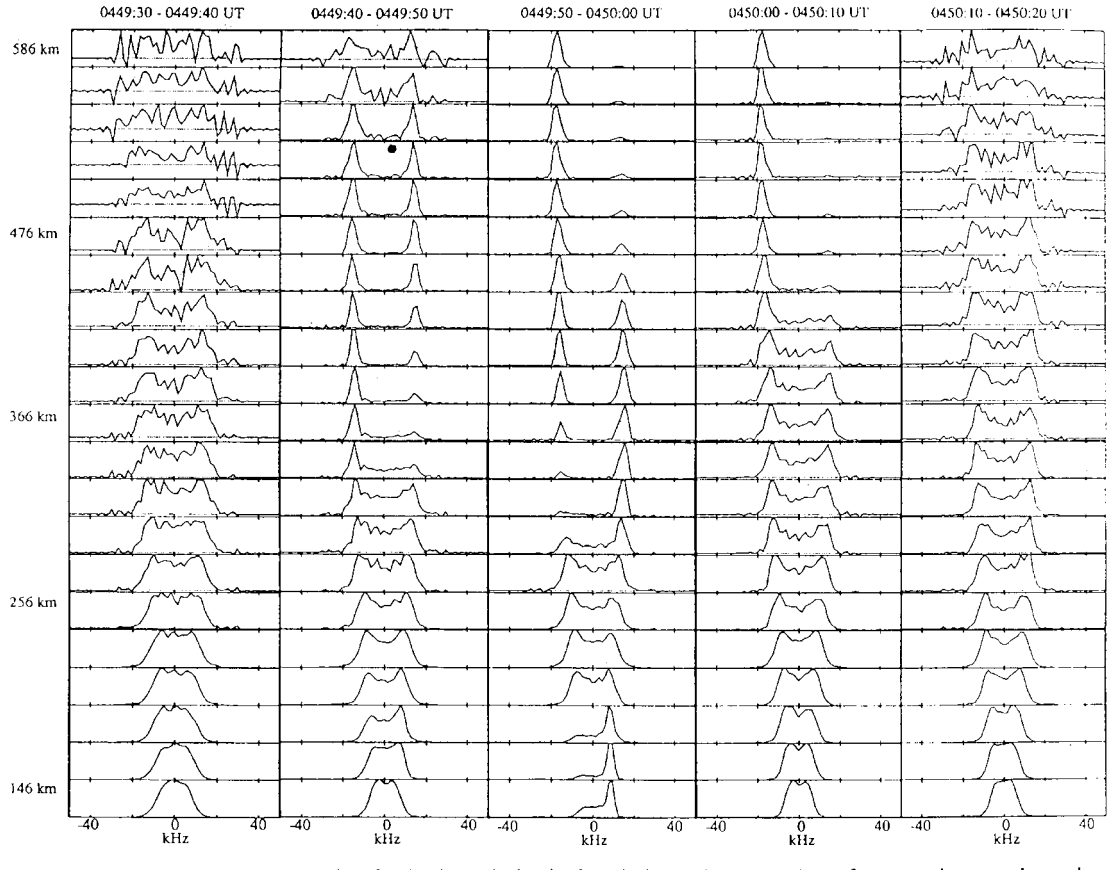

Figure 20. Profiles of IS spectra (10 sec integration) measured along the geomagntic field showing enhanced shoulders caused by coherent scatter.

Coherent echoes created by plasma instabilities are not only observed at E-region heights but also in the F-region [e.g. *Lockwood et al.*, 1988]. Some of them are assumed to be caused by the ion-acoustic instability. The corresponding unstable plasma waves propagate parallel **B** an can therefore be easily detected with an *IS* facility. In fact they can contaminate the usual *IS* spectrum by raising one of its shoulder. Figure 20 shows such an example [*Rietveld et al.*, 1991]. Such asymmetric echoes have also been observed in the top-side ionosphere [*Wahlund et al.*, 1993].

Another class of coherent echoes which have been very successfully studied with incoherent scatter facilities are the polar mesospheric summer echoes [*PMSE*]. They arise most probably from processes within the "*dusty*" plasma around 80-90 km [*Röttger et al.*, 1990].

9. References

Alcaydé D. and J. Fontanari, Neutral temperature and winds from EISCAT CP-3 observations, *J. Atmos. Terr. Phys.*, ***48***, 931-947, 1986.

Araki T., K. Schlegel, and H. Lühr, Geomagnetic effects of the Hall and Pedersen current flowing in the auroral ionosphere, *J. Geophys. Res.*, ***94***, 17185-17199, 1989.

Banks P.M. and G. Kockarts, Aeronomy, Academic Press, New York and London, 1973.

Baron M.J. and R.H.Wand, F-region ion temperature enhancements resulting from Joule heating, *J. Geophys. Res*., ***88***, 4114-4118, 1983.

Blelly P.-L. and D. Alcaydé, Electron heat flow in the auroral ionosphere inferred from EISCAT-VHF observations, *J. Geophys. Res.*, ***99***, 13181-13188, 1994.

Bostrøm R., Electrodynamics of the ionosphere, in *Cosmical Geophysics*, Ed. A. Egeland, O. Holter, A. Omholt, Universitetsforlaget, Oslo, Bergen, Tromsø, 1973.

Brekke A. and J. Moen, Observations of high latitude ionospheric conductances-a review, *J. Atmos. Terr. Phys.*, ***55***, 1493-1512, 1993.

Burnside R.G., C.A. Tepley and V.B. Wickwar, The O^+-O collision cross section: Can it be inferred from aeronomical measurements, *Ann. Geophys.*, ***5***, 343-349, 1987.

Cierpka K. and K. Schlegel, Parametric model simulations of gravity wave attenuation in the ionospheric F_2-layer, submitted to *J. Atmos. Terr. Phys.*, 1995.

Duboin M.L., Heating rates measured by EISCAT: latitudinal variations, *J. Atmos. Terr. Phys.*,***48***, 921-930, 1986.

Fontaine D., S. Perraut, D. Alcaydé, G. Caudal and B. Higel, Large scale structures of the convection inferred from coordinated measurements by EISCAT and GEOS 2, *J. Atmos. Terr. Phys.*, ***48***, 973-986, 1986.

Glatthor N. and R. Hernández, Temperature anisotropy of drifting ions in the auroral F-region, observed by EISCAT, *J. Atmos. Terr. Phys.*, ***52***, 545-560, 1990.

Hargreaves J.K., The solar-terrestrial environment, Cambridge Univ. Press, Cambridge, 1992.

Hocke K., Untersuchung des Phasen- und Amplitudenverhaltens von "travelling ionospheric disturbances" mit Hilfe von EISCAT-Daten, *Thesis*, MPAE-W-05-94-12, Katlenburg-Lindau, 1994.

Hocke K., K. Schlegel and G. Kirchengast, Phases and amplitudes of TIDs in the high-latitude F-region observed by EISCAT, *J. Atmos. Terr. Phys.*, ***57***, in press, 1995.

Hocke K., Tidal variations in the high latitude E- and F-region observed by EISCAT, *Ann. Geophys.*, in press, 1995.

Hubert D., Non-Maxwellian velocity distribution functions and incoherent scattering of radar waves in the auroral ionosphere, *J. Atmos. Terr. Phys.*, ***46***, 601-611, 1984.

Kelley M.C., *The earth's ionosphere*, Academic Press, San Diego, 1989.

Kirchengast G., R. Leitinger, and K. Schlegel, A high-resolution model for the ionospheric F-Region at mid- and high-latitude sites, *Ann. Geophys.*, ***10***, 577-596, 1992.

Kirchengast G., K. Hocke and K. Schlegel, The gravity wave-TID relationship: Insight via theoretical model-EISCAT data comparison, *J. Atmos. Terr. Phys.*, ***57***, in press, 1995.

Kirkwood S., Seasonal and tidal variations of neutral temperatures and densities in the high latitude lower thermosphere measured by EISCAT, *J. Atmos. Terr. Phys.*, ***48***, 817-826, 1986.

Kirkwood S., Modeling the undisturbed high-latitude E-region, *Adv. Space Res.*, ***13***(3), 102-104, 1993.

Kirkwood S. and A. Osepian, Quantitative studies of energetic particle precipitation using incoherent scatter radar. *J. Geomagn. Geoelectr.*, ***47***, 783-799, 1995.

Kunitake M. and K. Schlegel, Neutral winds in the lower thermosphere at high latitudes from five years of EISCAT data, *Ann. Geophys.*, ***9***, 143-155, 1991.

Lathuillere C. W. Kofman and B. Pibaret, Incoherent scatter measurements in the F1-region, *J. Atmos. Terr. Phys. ,**48***, 857-866, 1986.

Lockwood M., K. Suvanto, J.-P. St.-Maurice, K. Kikuchi, B.J.I. Bromage, D.M. Willis, S.R. Crothers, H. Todd and S.W.H. Cowley, Scattered power from non-thermal, F-region plasma observed by EISCAT – evidence for coherent echoes? *J. Atmos. Terr. Phys.*, ***50***, 467-485, 1988.

Lühr H., H. Geisler and K. Schlegel, Current density models of the eastward electrojet derived from ground-based magnetic field and radar measurements, *J. Atmos. Terr. Phys.*, ***56***, 81-91, 1993.

Ma S.Y. and K. Schlegel, Nonlinear wave-wave interaction related to gravity wave reflection in the auroral upper F-region with the EISCAT radar, *J. Atmos. Terr. Phys.*, ***55***, 719-738, 1993.

McCrea I. W., K. Schlegel, T. Nygren, and T. B. Jones, COSCAT, a new auroral radar facility on 930 MHz - System description and first results, *Ann. Geophys.*, ***9***, 461-469, 1991.

Moorcroft D. R. and K. Schlegel, Height and aspect sensitivity of large aspect angle coherent backscatter at 933 MHz, *J. Geophys. Res.*, ***95***, 19011-19021, 1990.

Murdin J., EISCAT UHF Geometry, *KGI-Report*, No 79:2, Kiruna, 1979.

Raman R.S.V., J.-P. St-Maurice, and R.S.B. Ong, Incoherent scattering of radio waves in the auroral ionosphere, *J. Geophys. Res.*, ***86***, 4751-4762, 1981.

Rietveld M.T., P.N. Collis and J.-P. St-Maurice, Naturally enhanced ion acoustic waves in the auroral ionosphere observed with the EISCAT 933-MHz radar, *J. Geophys. Res.*, ***96***, 19291-19305, 1991.

Röttger J., M. T. Rietveld, C. La Hoz, T. Hall, M. C. Kelley, and W. E. Swartz, Polar mesosphere summer echoes observed with the EISCAT 933-MHz radar and the CUPRI 46.9-MHz radar, their similarity to 224-MHz radar echoes, and their relation to turbulence and electron density profiles, *Radio Sci.*, ***25***, 671-687, 1990.

Rüster R., VHF radar observations in the summer polar mesosphere indicating non-linear interaction, *Adv. Space Res.*, ***12(***10), 85-88, 1992.

Schlegel K., Reduced effective recombination coefficient in the disturbed polar E-region, *J. Atmos. Terr. Phys.*, ***44***, 183-185, 1982.

Schlegel K., T. Turunen, and D. R. Moorcroft, Auroral radar measurements at 16-cm wavelength with high range and time resolution, *J. Geophys. Res.*, **95**, 19001-19009, 1990.

Schunk R.W., Transport equations for aeronomy, *Planet. Space Sci.*, ***23***, 437-485, 1975.

Schunk R.W. and A.F. Nagy, Electron temperatures in the F-region of the ionosphere: Theory and observations, *Rev. Geophys. Space Phys.*, ***16***, 355-399, 1978.

Senior C., D. Fontaine, G. Caudal, D. Alcaydé, and J. Fontanari, Convection electric fields and electrostatic potential over 61 < l < 72 invariant latitude observed with the EISCAT facility. 2. Statistical Results, *Ann. Geophys.*, ***8***, 257-272, 1990.

Shibata T. and K. Schlegel, Vertical structure of AGW associated ionospheric fluctuations in the E- and lower F-region observed with EISCAT – a case study, *J. Atmos. Terr. Phys.*, ***55***, 739-749, 1993.

St-Maurice J.-P. and R.W. Schunk, Auroral ion velocity distributions for a polarization collision model, Planet. *Space Sci.*, ***25***, 243-260, 1977.

St-Maurice J.-P. and W.B. Hanson, Ion frictional heating at high latitudes and its possible use for an in-situ determination of neutral thermospheric winds and temperatures, *J. Geophys. Res.*, ***87***, 7580-7602, 1982.

Thuillier G., C. Lathuiliere, M. Herse, C. Senior, W. Kofman, M. L. Duboin, D. Alcaydé, F. Barlier, and J. Fontanari, Coordinated EISCAT-MICADO interferometer measurements of neutral wind and temperature in E- and F-regions, *J. Atmos. Terr. Phys.*, ***52***, 625-636, 1990.

Ullrych T. J. and T. N. Bishop, Maximum entropy spectral analysis and autoregressive decomposition, *Rev. Geophys. Space Phys.*, ***11***, 183-200, 1975.

Virdi T.S. and P.J.S.Williams, Altitude variations in the amplitude and phase of tidal oscillations at high latitude, *J. Atmos. Terr. Phys.*, ***55***, 697-717, 1993.

Vondrak R.R. and M. Baron, A method of obtaining the energy distribution of auroral electrons from incoherent scatter radar measurements, In: *Radar Probing of the Auroral Plasma*, Ed. A. Brekke, Universitetsforlaget, Oslo, 1977.

Wahlund J.-E., H.J. Opgenoorth, F.R.E. Forme, M.A.L. Persson, I. Häggström and J. Lilensten, Electron energization in the topside auroral ionosphere: on the importance of ion-acoustic turbulence, *J. Atmos. Terr. Phys.*, ***55***, 623-696, 1993.

Wickwar V.B., J.M. Baron and R.D. Sears, Auroral energy input from energetic electrons and Joule heating at Chatanika, *J. Geophys. Res.*, ***80***, 4364-4367, 1975.

Williams P.J.S., T.S. Virdi, R.V. Lewis, M. Lester, A.S. Rodger, I.W. McCrea and K.S.C. Freeman, Worldwide Atmospheric gravity-wave study in the European sector 1985-1990, *J. Atmos. Terr. Phys.*, ***55***, 683-696, 1993.

Wu J. and C. Taieb, Observations of the structure of the thermospheric relative composition n(H)/n(O) with the EISCAT-VHF radar, *Ann. Geophys.*, ***11***, 485-493, 1993.

SOLAR WIND - MAGNETOSPHERE COUPLING

Mike Lockwood

1. Introduction

The solar wind brings energy, mass and momentum from the sun to the Earth. The geomagnetic field deflects the flow of plasma to generate the low density cavity that is the magnetosphere. The efficiency of the mechanisms by which the magnetosphere extracts some of the mass, energy and momentum of the passing solar wind are critically dependent on the orientation of the interplanetary magnetic field [*IMF*]. This is a weak field of solar origin which is embedded in the solar wind plasma. This review begins with a brief survey of the properties of the interplanetary medium, in which the Earth's magnetosphere is immersed [*section 2*]. The uses of the approximate, but self-consistent, formalism of magnetohydrodynamics [*MHD*] are then discussed in section 3, in particular the application of the "frozen-in flux" concept to the large-scale, high-conductivity magnetoplasmas in interplanetary space, the magnetosphere and the upper ionosphere. Were it to apply everywhere, frozen-in would allow very little transfer from the solar wind to the magnetosphere and much of the fascination of the coupled magnetosphere-ionosphere-thermosphere system would be lost. Fortunately, that is not the case, largely because of the phenomenon of magnetic reconnection, a localised breakdown of the frozen-in theorem. Reconnection is not just a curiosity of solar-terrestrial physics, it is a process which has considerable implications in other disciplines in science, for example astrophysicists believe it removes magnetic flux from proto-stars which would otherwise prevent them from condensing. On Earth, reconnection is both a nuisance and a help for researchers developing plasma fusion reactors, causing loss of confining field in tokomaks but allowing the development of large fields in devices called spheromaks. Solar-terrestrial physics [*STP*] is the discipline which developed the concept of reconnection and remains vital in its continued study, partly because it can be probed using a combination of remote sensing techniques [*such as radars, magnetometers and optical imagers*] and in-situ observations [*such as spacecraft particle detectors*]. Section 4 reviews the nature of the boundary separating the magnetosphere and interplanetary space, called the magnetopause. This is the interaction region where the extraction of mass energy and momentum takes place. Particular emphasis is placed on the experimental evidence for magnetopause reconnection, which is the dominant process which facilitates this extraction. In section 5 we will look at the subsequent transfer from the magnetopause to the ionosphere, including the key role of field-aligned currents in the energy and momentum transfer. The resulting effects in the ionosphere in the cusp region, the magnetic projection of the magnetopause are discussed in section 6, including the velocity

filter effect of the precipitating particles. In all these discussions, there will be a tendency to describe the steady-state cases because they are simplest. We do not, as yet, know of any long-term trends in the coupled magnetosphere-ionosphere-thermosphere system, and so if we average over sufficiently long periods [*the time scale involved depending on the phenomenon in question*], then we effectively produce a steady-state description. However, in recent years, there has been much interest in phenomena which take place on time scales that are too short for the system to be considered an equilibrium one, i.e. when steady state does not apply. Two key examples are the substorm cycle and the effects of transient bursts of magnetopause reconnection. Section 7 discusses how the steady-state concepts can be generalised to allow for this.

2. The characteristics of interplanetary space at the Earth's orbit

The hot solar corona ejects the supersonic solar wind. This process is continuous but still highly structured in time a space. Regions which appear dark in *X*-ray images of the sun are called coronal holes, and these regions of relatively thin coronal atmosphere are sources of enhanced solar wind in both speed and density. In addition, there are large coronal mass ejection events, these are seen every 2 days on average, and typically contain 10^{13} kg of plasma, move at about 500 km s^{-1} and carry 5×10^{18} W of power. On average, the solar wind power density is about 3×10^{-4} W m^{-2}, impinging on the Earth's magnetosphere which presents a cross sectional area of about $\pi(15\ R_E)^2 \approx 3 \times 10^{16}$ m^2 , giving a total incident power of about 10^{13} W, of which only a few percent is extracted by the magnetosphere. [Note, *distances in the magnetosphere are usually quoted in units of an Earth radius, $1R_E$ = 6370 km*]. To put these powers into some kind of perspective, mankind currently uses of order 10^{13} W from all sources while there is of order 2 x 10^{17} W incident on the Earth in the form of solar electromagnetic radiations, of which roughly 1/3 is reflected back into space.

	largest	smallest	mode
solar wind density, N_{sw} (m^{-3})	8.3×10^7	~ 0	6×10^6
solar wind velocity, V_{sw} (km s^{-1})	950	250	370
IMF field strength, B_{IMF} (nT)	85	~ 0	6
IMF Bz (GSM) (nT)	27	-31	0

Table 1. Characteristics of the interplanetary medium at the orbit of the Earth (at an Astronomical Unit , 1AU, from sun)

In a survey of over 10^5 hourly averages of measurements of interplanetary space at the Earth's orbit, taken over two solar cycles, *Hapgood et al*. [1991] give the distributions of key solar wind and *IMF* parameters. Table 1 summarises these distributions by giving the largest and smallest recorded values and the most common value [i.e. *the mode of the distribution*].

In all cases the interplanetary medium shows great variability. The *Bz* component of the *IMF* is the northward component in the *GSM* [*Geocentric Solar Magnetospheric*] coordinate system. It will later be explained how this component is a key factor controlling the transfer of solar wind energy, mass and momentum across the magnetopause. In the *GSM* coordinate system, the *X* component points from the Earth to the sun; *Z* is northward along the projection of the Earth's dipole axis onto the *YZ* plane [*normal to X*] and *Y* makes up the right hand set and points roughly towards dusk. The distribution of *Bz* [*GSM*] is symmetric about zero and so half the time the *IMF* points northward and half the time it is southward.

3. Magnetohydrodynamics

In a plasma, free electrically-charged particles can move relative to each other, such that a current flows. This current alters the magnetic field at all points in the cosmos, but the effect is strongest close to where the current flows. However, the interaction is a coupled one, because the magnetic field influences the motion of the charged particles, via the Lorentz force. Magnetohydrodynamics [*MHD*] is a set of equations, given here in their simplest form, which provides a self-consistent description of the behaviour of this coupled magnetoplasma. As its name implies, it is a fluid description and does not deal with individual particles, as would a kinetic approach. The advantages and limitations of *MHD* will be discussed in 3-5.

Before discussing *MHD*, it is worth remembering some central tenants of electromagnetism. Equations for the electric and magnetic fields [$\boldsymbol{E}$ *and* $\boldsymbol{B}$, *respectively*] can be derived from the relativistic Lorentz frame transformations for force and distance applied to the electrostatic force between two charged particles [e.g. *Lorrain and Corson*, 1970; *Jackson*, 1975]. In the non-relativistic limit, **E** and **B** can then be shown to transform from reference frame 1 to frame 2, where frame 2 moves at velocity **U** in frame 1, according to:

$$\mathbf{B}_2 = \mathbf{B}_1 \tag{1}$$

$$\mathbf{E}_2 = \mathbf{E}_1 + \mathbf{U} \times \mathbf{B} \tag{2}$$

This shows that the magnetic field is the same in any reference frame. It has been argued that this means that it also makes no sense to consider moving field

lines. To some extent, this may be true, but then it makes even less sense to argue that they must therefore be still, as that is simply the zero speed limit of the moving case! A better interpretation is that Eq. 1 allows us, at the non-relativistic speeds involved in most STP phenomena, to consider field lines as moving at any speed, including zero, as we wish. If we correctly describe the motions of charged particles, then that is all that field theory is intended to do. Note that if **B** is independent of frame so, by Ampère's law, must the current density **J** be also. This is reasonable, as current is the difference in fluxes of oppositely charged particles and this difference will be frame independent. The electric field, on the other hand varies with reference frame. Therefore we should always make it clear which frame any electric field estimate is measured in. Notice also that Eq. 2 shows that it is always possible to define a frame velocity **U** such that **E** is zero.

3.1. Ohm's Law for a plasma

If we take the momentum balance equation for the gas of any one species k [*density* N_k*, Pressure* P_k*, bulk flow velocity* $\mathbf{v}_k$*, mass* m_k *and charge* q_k] in a plasma:

$$N_k m_k \frac{\partial \mathbf{v}_k}{\partial t} = \nabla P_k + N_k m_k \boldsymbol{g} + N_k q_k [\mathbf{E} + \boldsymbol{v}_k \times \mathbf{B}] - \Sigma_{j \neq k} \boldsymbol{F}_{kj} \qquad (3)$$

the left hand side [*LHS*] is the inertial term, and the terms on the right hand side [*RHS*] are, in order, due to the pressure gradient, gravity, the Lorentz force and the frictional force due to collisions with all other species, j [$\boldsymbol{g}$ *is the acceleration due to gravity, and e the electronic charge*]. The force on the electrons due to the ions, $\mathbf{F}_{ei}$ is given by:

$$\mathbf{F}_{ei} = \vartheta_{ei} m_e (\mathbf{v}_e - \mathbf{v}_i) = - \mathbf{F}_{ie} \qquad (4)$$

where ϑ_{ei} is the electron-ion collision frequency. The current density, **J**, is given by:

$$\mathbf{J} = N_e e (\mathbf{v}_i - \mathbf{v}_e) = - \frac{N_e e \mathbf{F}_{ei}}{\vartheta_{ei} m_e} \quad . \qquad (5)$$

We define the plasma velocity as the weighted [*by mass*] mean of the electron and ion bulk flow velocities:

$$\mathbf{V} = \frac{m_e \mathbf{v}_e + m_i \mathbf{v}_i}{m_e + m_i} \qquad (6)$$

We here take the simplest case of a plasma with only one ion species, negligible collisions with neutrals and no pressure gradients [*all of which can be generalised at the expense of complexity; see Alfvén and Fälthammar, 1963*]. Taking Eq. 3 for an electron gas [$\times$-m_e] and for an ion gas [$\times$ m_i], adding the two expressions together and then substituting from Eq. 4, 5 and 6 we get the commonly used form of Ohm's law:

$$\mathbf{J} = \frac{N_e\, e^2}{(\,\vartheta_{ei} m_e)}\ [\mathbf{E} + \mathbf{V} \times \mathbf{B}] = \sigma\,[\mathbf{E} + \mathbf{V} \times \mathbf{B}] \qquad (7)$$

where σ is called the electrical conductivity. From Eq. 2 the term in square brackets in Eq. 7 is the electric field in the rest frame of the plasma [*in which* **V** *is zero*]. It should be remembered that this form is only approximate and has neglected pressure gradients and collisions with neutrals. As a result of the latter assumption, it is invalid in the lower ionosphere where there are considerable Hall and Pedersen conductivities introduced by collisions with neutrals. We here use it in the upper "*F-region"* ionosphere, the magnetosphere and in interplanetary space.

3.2. The induction equation and frozen-in flux

If, in addition to Ohm's law [Eq. 7], we use three of Maxwell's equations, namely the non- existence of magnetic monopoles, Ampère's law [*for a good conductor such that the displacement current can be neglected*] and Faraday's law in differential form:

$$\nabla \mathbf{B} = 0 \qquad (8)$$

$$\nabla \times \mathbf{B} = \mu_o\, \mathbf{J} \qquad (9)$$

$$\frac{\partial\, \mathbf{B}}{\partial\, \mathrm{t}} = -\,(\nabla \times \mathbf{E}) \qquad (10)$$

where μ_o is the permeability of free space. If we substitute using Eq. 9 and 10 into Eq. 7 and use Eq. 8 and the vector expression $\nabla\times(\nabla\times\mathbf{B})=\nabla(\nabla.\mathbf{B})-\nabla^2\mathbf{B}$, we can derive the induction equation:

$$\frac{\partial\, \mathbf{B}}{\partial\, \mathrm{t}} = \nabla \times (\mathbf{V} \times \mathbf{B}\,) + \frac{\nabla^2\, \mathbf{B}}{\mu_o\, \sigma}\ . \qquad (11)$$

The first term on the *RHS* is called the convective term and the second is the diffusive term. The ratio of the convective term divided by the diffusive term is called the magnetic Reynolds number R_m which, from dimensional analysis, is given by the order of magnitude expression

$$R_m = \nabla \times (\mathbf{V} \times \mathbf{B}) \frac{\mu_o \sigma}{\nabla^2 \mathbf{B}} \sim \mu_o \sigma V_c L_c \qquad (12)$$

where V_c is the characteristic scale speed of the plasma and L_c is its characteristic scale length.

How a magnetoplasma behaves depends critically on the magnitude of R_m. If R_m is very small [« 1], the convective term can be neglected and the induction equation [*Eq. 11*] reduces to a diffusion equation in which the field diffuses from high to low values. On the other hand, in the limit where R_m » 1, the diffusive term can be neglected. To understand the behaviour in this limit, consider any closed loop in the plasma *C*, which bounds an area *S*. Using Eq. 11 in the R_m » 1 limit, and then Stoke's theorem, the rate of change of flux threading that loop is

$$\frac{\partial F}{\partial t} = \int_S \frac{\partial \mathbf{B}}{\partial t} \mathbf{.ds} = \int_S \nabla \times (\mathbf{V} \times \mathbf{B}) \mathbf{.ds} = \oint_C (\mathbf{V} \times \mathbf{B}) \mathbf{.dl} \qquad (13)$$

If we think of field lines moving with the plasma velocity, **V**, the RHS of Eq. 13 would be the rate at which flux was convected across the line *C* which would thus equal to the rate of change of flux threading the loop. Given that this is the RHS , this means that Eq. 13 shows us that in this very high R_m limit, the magnetic field does move with the plasma velocity **V**. This is Alfvén's famous "*frozen-in flux*" theorem, so called because the field and the plasma are frozen together and move together.

Region	σ (mhos m^{-1})	V_c (m s^{-1})	L_c (m)	R_m
Base of corona	10^3	10^5	10^6	10^8
Solar Wind at 1 AU	10^4	10^5	10^9	10^{12}
Magnetosphere	10^8	10^5	10^8	10^{15}
Ionospheric F-region	10^2	10^3	10^5	10^4

Table 2. Typical order of magnitude estimates of the conductivity, σ, characteristic plasma velocity V_c, scale length L_c , and magnetic Reynolds number, R_m

Table 2 shows typical order-of-magnitude values for various regions in the solar-terrestrial system of all the terms in the approximate expression for R_m [*Eq. 12*]. It can be seen that in all cases the Reynolds number is extremely large

and thus we should expect frozen-in to be a valid approximation in all these regions.

In order to understand the basic behaviour of the magnetoplasmas in these various regions it is instructive to look at the relative densities of energy stored in the magnetic field, the thermal motions of particles and the bulk flow of the plasma, these are given by, respectively, $W_B = \mathbf{B}^2/2\mu_o$ [*see section 5.1*], $W_{th} = N\,k\,T$, and $W_V = m\,\mathbf{V}^2/2$, where k is Boltzmann's constant and T is the plasma temperature. Typical values are given in Table 3, for the same regions as in Table 2, except that the magnetosphere has been broadly sub-divided into the high density co-rotating inner torus called the plasmasphere and the low-density convecting outer region called the plasma trough.

Region	Ions	B nT	V ms^{-1}	N m^{-3}	T K	W_{th} Jm^{-3}	W_V Jm^{-3}	W_B Jm^{-3}
Base of Corona	H^+	10^5	10^4	10^{15}	10^6	10^{-2}	10^{-4}	10^{-2}
1 AU	H^+	5	5.10^5	5.10^6	5.10^4	10^{-12}	$\underline{10^{-9}}$	10^{-11}
M.sphere trough	H^+	50	10^5	10^4	10^7	10^{-12}	10^{-13}	$\underline{10^{-9}}$
Plasmasphere	H^+	5.10^3	10^4	10^9	10^4	10^{-10}	10^{-10}	$\underline{10^{-5}}$
F-region	O^+	5.10^4	10^3	10^{11}	10^3	10^{-9}	10^{-9}	$\underline{10^{-3}}$

Table 3. Typical order of magnitude estimates of energy densities in various regions of the solar-terrestrial system.

Where one energy density is clearly dominant, it has been underlined. In the interplanetary medium, the dominant energy density is in the bulk flow of the plasma and, as a result, frozen-in means that the *IMF* is dragged along with the solar wind flow. On the other hand, in the magnetosphere and F-region ionosphere the dominant energy density is that of the magnetic field and thus frozen-in results in the field constraining the plasma.

The dominance of the field energy density is greatest in the ionosphere. Indeed, the ionospheric and magnetospheric particles have very little effect on the field at low altitudes, that field being almost completely due to currents in the Earth's interior. As a result, the largest currents which flow as a part of STP phenomena cause magnetic perturbations of order 1000 nT, which is only 2% of the ionospheric field caused by the interior currents [*which is roughly constant at about* $B_i = 5 \times 10^{-5}\ T$]. In the sense that the magnetic field is roughly constant, we say that the ionosphere is incompressible. This is a very useful fact because the magnetic flux threading a certain region of the magnetosphere can change

with time. Because the field is constant at low altitudes, the ionospheric signature of such a flux variation will be a change in the area of the corresponding region in the ionosphere.

3.3. E x B drift and motional electric fields

From the induction equation [*Eq. 11*] in the R_m » 1 limit and Faraday's law [*Eq. 10*]:

$$\frac{\partial \mathbf{B}}{\partial t} = \nabla \times (\mathbf{V} \times \mathbf{B}) = - \nabla \times \mathbf{E}$$

$$\mathbf{E} = - (\mathbf{V} \times \mathbf{B}) \qquad (14)$$

$$\mathbf{V} = \frac{\mathbf{E} \times \mathbf{B}}{B^2} \qquad (15)$$

Thus for a magnetoplasma for which frozen-in applies, an electric field corresponds to a plasma motion perpendicular to both the applied electric and magnetic fields at speed *E* / *B*, often referred to as the "*E-cross-B drift*". **E** is perpendicular to **B**, ie. there is no field-parallel electric field, $E_{||}$, if frozen-in applies strictly.

Note that Eq. 14 and 15 can be derived from Ohm's law for a plasma [*Eq. 7*] if we take the conductivity σ to be infinite, as then Eq. 14 must be true to avoid an infinite current density. Hence the frozen-in approximation is sometimes referred to as the "*infinite conductivity limit*". However, as we saw in the last section, the applicability of frozen-in to solar-terrestrial plasmas is really caused by the large scale lengths [L_c] as much as by their high conductivities. From Table 2, we would expect the frozen-in approximation [*and thus Eq. 14*] to be least applicable in the F-region ionosphere. A recent paper by *Hanson et al.* [1994] demonstrates how good an approximation this is, even in the F-region. They took satellite observations of **E** in the topside ionosphere from measurements of the potential difference between two probes on long booms and of known separation. They compared these with estimates of - ($\mathbf{V} \times \mathbf{B}$) from magnetometer and ion drift meter observations. The results showed an extraordinary level of agreement and any [*small*] differences that were found were shown to be caused by experimental uncertainties.

Table 2 shows that frozen-in applies also in the interplanetary medium, where the solar wind flows with a plasma velocity $\mathbf{V}_{sw}$ in the Earth's frame of reference. From Eq. 14 there is no electric field in the rest frame of the solar wind flow [*in which V is zero*], but by Eq. 2 there will be an electric field of - ($\mathbf{V}_{sw} \times \mathbf{B}_{IMF}$) in

the Earth's frame. Because it corresponds to a bulk flow of a frozen-in plasma, this is often referred to as the motional electric field of the interplanetary medium. The direction of the solar wind flow is always close to antiparallel to the *X* axis, so for southward *IMF* [*Bz* < 0], this electric field points from dawn to dusk [*in the +Y direction*].

It is here worth noting a point about the term "*flux transfer*", often used in magnetospheric physics [e.g. *Holzer and Slavin*, 1979; *Russell and Elphic*, 1978]. Faraday's law [*Eq. 10*] in integral form is

$$\oint_C \mathbf{E} \cdot \mathbf{dl} = \frac{\partial F}{\partial t} = \frac{\partial}{\partial t}\left(\int_S \mathbf{B} \cdot \mathbf{ds} \right) \qquad (16)$$

where *F* is the flux threading the area *S* bound by the circuit *C*. [Note: *in the ionosphere, incompressibility means that the RHS reduces to B (∂A/∂t) because B is constant and the area A must change if the flux F changes*]. If we consider two loops *C* and C_1, which share a common segment across which there is a voltage Φ but the tangential electric field along either loop is everywhere else equal to zero, then from Eq. 10:

$$\Phi = \oint_C \mathbf{E} \cdot \mathbf{dl} = - \oint_{C_1} \mathbf{E} \cdot \mathbf{dl} = \frac{\partial F_C}{\partial t} = - \frac{\partial F_{C_1}}{\partial t}$$

where both line integrations are done in the same rotational sense. Thus the flux threading C_1 decreases at the same rate Φ as the flux threading the adjoining loop *C* increases. The voltage along the common segment is therefore identically synonymous with a flux transfer rate from *C* to C_1 [*dimensionally, the unit volts is the same as Wb* s^{-1}]. This is purely a consequence of Faraday's law. If we are also dealing with a frozen-in plasma, the plasma will also be transferred at the same velocity as the magnetic field lines from within C_1 to in *C*. We will later deal with events called "*flux transfer events*" or FTEs, a name which sometime causes disquiet: however from the above, it is identical in meaning to "*voltage bursts*".

3.4. The J x B and curvature forces and magnetic pressure

If we take the momentum equation [Eq. 3] for ions and add it to that for electrons, using the definition of plasma velocity **V** [Eq. 6], the plasma density $\rho = N_e (m_e + m_i)$, the plasma pressure $P = P_e + P_i$, the current density **J** given by

Eq. 5 and charge neutrality [$N_e = N_i$], we get the force balance equation for the plasma:

$$\rho \frac{\partial \mathbf{V}}{\partial t} - \nabla P - \rho \mathbf{g} = [N_e e \mathbf{V}_e - N_i e \mathbf{V}_i] \times \mathbf{B} = \mathbf{J} \times \mathbf{B} \qquad (17)$$

The term on the right is called the $\mathbf{J} \times \mathbf{B}$ force. If we substitute using Ampère's law Eq. 9 and use the vector relation [$(\nabla \times \mathbf{B}) \times \mathbf{B} = \nabla^2 \mathbf{B} / 2 + (\mathbf{B} . \nabla) \mathbf{B}$] we find that the $\mathbf{J} \times \mathbf{B}$ force can be combined with the plasma pressure term thus:

$$\nabla P + \mathbf{J} \times \mathbf{B} = - \nabla (P + \frac{B^2}{2\mu_o}) + (\mathbf{B} . \nabla) \frac{\mathbf{B}}{\mu_o} \qquad (18)$$

from this we see that a magnetic pressure [$B^2/2\mu_o$] is added to the plasma pressure P [*first term of RHS of Eq. 18*], and there is a second force which acts normal to **B** if the field lines have any curvature [*from the second term of the RHS of Eq. 18*]. This force vector lies in the plane of the curvature and acts so as to try to straighten the curved field lines. For this reason, it is often referred to as the "*tension force*". I prefer the term "*curvature force"* because a tension, as in stretched elastic band, will remain when the band becomes straight, whereas the force described by Eq. 18 will vanish when the field lines are straight. The second term on the *RHS* also provides a term which exactly cancels the field parallel component of the first term. Thus the magnetic pressure acts only perpendicular to **B**.

3.5. Uses, advantages and limitations

Magnetohydrodynamics has the huge advantage of being a self-consistent formalism. Application of a few simple rules is extraordinarily powerful, for example, as in predicting the motion of field lines and frozen-in plasma as kinked field lines straighten under the curvature force. It does lead to a lot of what is sometimes disparagingly referred to as "cartoon physics" because it empowers us to draw diagrams of field lines and from them deduce how they will behave. As with field theory, this has wide-ranging predictive power, as long as one obeys the rules. Other formulations are far more likely to be in error because they do not have the in-built consistency of *MHD* [see, for example, *Owen and Cowley*, 1991]. One also hears the complaint that what is really out there in space are moving, charged particles. This is a true statement, but rejection of *MHD* on these grounds is also a rejection of field theory and electromagnetism!

The major disadvantage of *MHD* is that it is a fluid approach and, as such, tells us nothing about the behaviour of the individual electron and ion species. Therefore we have to graft on kinetic or semi-kinetic treatments to predict particle distribution functions. An example of this type of hybrid theory is discussed here in section 4.5. A second, entirely separate, question involves the

validity of the frozen-in approximation or "*ideal MHD"*. This is an approximate formalism and does break down. Indeed, nearly all the fascination and beauty of the magnetosphere-ionosphere-thermosphere system stems from the fact that it does break down. With fully frozen-in plasmas there would be little energy, mass and momentum transfer from the solar wind, no aurora, no ring current etc. However, in the same way that the existence of relativistic effects does not stop Newtonian mechanics from describing a myriad of phenomena and systems, so the frozen-in approximation is valid for many regions and events of the solar-terrestrial system. The approach adopted here is one of using ideal *MHD*, with proper regard to where and how it can break down. It is an approach which has gained almost universal acceptance for no other reason than its success in describing the main features of the transfer from the solar wind to the ionosphere. Most importantly, it has enabled a large number of predictions to be made in advance of observations - much more significant in science than the use of a theory to explain observations after they have been made. Examples of this are legion, and include the basic prediction that the momentum and energy transfer from the solar wind into the ionosphere is enhanced during southward *IMF* [*section 5.5*]. We will here also discuss some more detailed predictions which have been later proved correct, predictions concerning the distribution functions of ion populations near the magnetopause [*section 4.5*] and cusp ion steps [*section 7.3*].

4. The magnetopause

Figure 1 is a noon-midnight cross-section of the magnetosphere at a time when the *IMF* points southward [after *Cowley*, 1991]. We view from the dusk side so that the sun is to the left and the GSM axes *X*, *Y* and *Z* are as shown. The solar wind [*SW*] flow is supersonic and super-Alfvénic and so the bow shock [*BS*] forms upstream of the obstacle presented by the Earth's magnetic field. The boundary of the magnetosphere, the magnetopause MP is compressed on the dayside by the dynamic pressure of the solar wind flow and, for reasons discussed later, the Earth's field is extended into a long tail on the nightside, very much as originally envisaged in *Chapman and Ferraro*'s seminal [1931] paper. The shocked interplanetary medium between *BS* and *MP* is called the magnetosheath *MS*. Currents flow in the magnetopause, called the Chapman-Ferraro currents, corresponding to the magnetic shear between the magnetosheath and the magnetosphere fields, $\mathbf{B}_{sh}$ and $\mathbf{B}_{sp}$. The Chapman-Ferraro currents flow in the $+Y$ direction in the subsolar region, but in the $-Y$ direction on the high-latitude tail magnetopause [*the high-latitude boundary layer or HLBL*]. In three-dimensions, these currents circulate around the topology in the geomagnetic field we call the magnetic cusp.

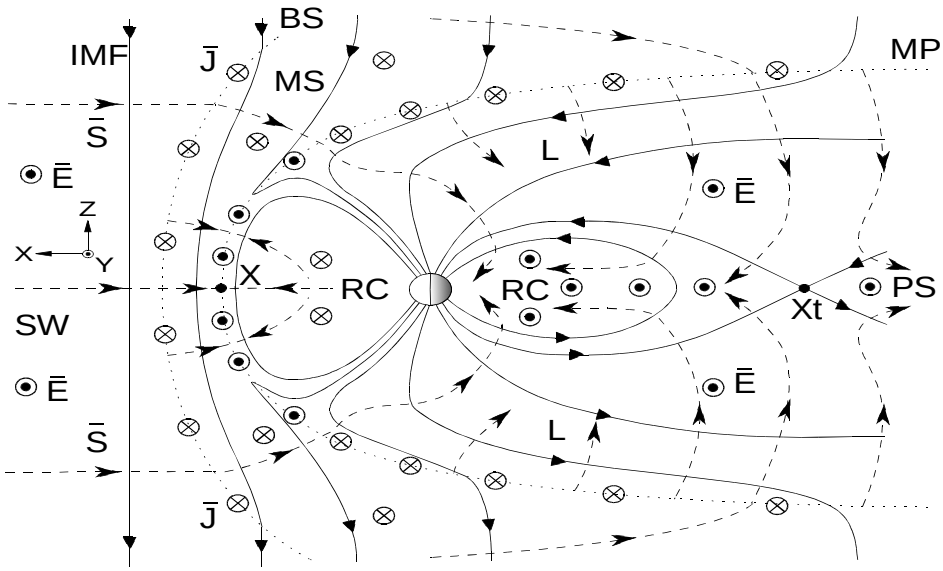

Figure 1. A noon-midnight cross-section of the magnetosphere, viewed from dusk with the sun to the left. When the IMF is southward ($B_z < 0$), field lines (solid lines) are opened at the magnetopause reconnection site, X, and convect antisunward under the action of the solar wind electric field, E, which exists in the Earth's frame of reference and everywhere points out of the plane of the diagram in the +Y direction. The flow of electromagnetic energy , or Poynting flux, **S** = **E x B**, *is shown by the dashed lines. Unless otherwise marked, vectors into and out of the plane of the diagram are currents. The open field lines are closed again by reconnection at the tail X-line, X_t. Labelled regions and boundaries are: solar wind SW; interplanetary magnetic field IMF; bow shock BS; magnetopause MP; magnetosheath MS; tail lobe L; the plasma sheet PS and its inner edge, the ring current RC. The dayside magnetopause (Chapman-Ferraro) currents are in the +Y direction, making* **J . E** *> 0, i.e. there is a sink of* **S**. *At latitudes above the magnetic cusp, the currents are into the diagram, making* **J . E** *< 0, i.e. a source of* **S**. *In steady-state the energy extracted from the solar wind at the lobe magnetopause is deposited in the plasma sheet, ring current and the ionosphere. During substorm growth phases, the extracted energy is also stored in the tail as the lobe field and energy density increase because open magnetic flux accumulates there. [After* Cowley, *1991]*

4.1. The magnetosheath

Because the field in the magnetosheath is usually weak, it is often ignored and the fluid flow of the plasma described in "gas-dynamic" models of the sheath [*Spreiter et al*., 1966]. These show that the flow stagnates at the nose of the magnetosphere [*where MP cuts the X axis*] and here the plasma density N is roughly 4 times the value in the undisturbed solar wind, N_{sw} and the temperature T is about 20 T_{sw}. Because there is no field, the sheath is symmetric about the X axis in these models and the flow speed just outside the magnetopause increases with distance from the nose. Where the boundary intersects the ZY plane [X=0], $V \approx 0.7V_{sw}$ with $N \approx 1.5N_{sw}$ and $T \approx 12T_{sw}$: at X= -10R_E , $V \approx 0.85V_{sw}$ with $N \approx 0.8N_{sw}$ and $T \approx 7T_{sw}$. Because V is lower near the nose of the magnetosphere, the frozen in field lines in the real magnetosheath become draped over the nose of the magnetosphere, as in figure 1 [*Crooker et al.*, 1985]. The sheath field at the

magnetopause, B_{sh}, thus becomes larger than in the *IMF* and is usually comparable to the interior field of the magnetosphere at the dayside boundary, B_{sp}. Both are typically 20 nT, but whereas $\mathbf{B}_{sp}$ will always point northward, $\mathbf{B}_{sh}$ can have any direction parallel to the boundary, depending on the *IMF* orientation. In an equilibrium situation, the enhanced dayside $\mathbf{B}_{sh}$ would cause an enhanced magnetic pressure, as shown by Eq. 18, and a corresponding decrease in the [*anisotropic*] particle pressure and density would be expected. This is called a plasma depletion layer [*PDL*] and is indeed observed, but only during northward *IMF* [*Phan et al.*, 1994]. This is the first indication that the system is not in equilibrium, at least during southward *IMF*. The *PDL* is missing because $\mathbf{B}_{sh}$, and the dayside magnetosphere, are eroded by a process called magnetic reconnection [*discussed here in section 4.3*] at a faster rate than that at which $\mathbf{B}_{sh}$ can be increased by the draping effect of the solar wind flow.

4.2. Boundary motions

The location of the dayside magnetopause is known to be closer to Earth if the solar wind dynamic pressure is high and/or if the *IMF* has a southward component [$Bz<0$] [*Maezawa*, 1974; *Roelof and Sibeck*, 1993; *Petrinec and Russell*, 1993]. The solar wind pressure acts to compress the dayside magnetosphere [*and increase the Chapman-Ferraro currents*], whilst increasingly southward *IMF* increases the rate of magnetic reconnection [*see next section*] and this erodes the dayside magnetopause [*Aubry et al.*, 1970], similar to the erosion of the *PDL*. The variability of the solar wind dynamic pressure and of the reconnection process, on a wide range of time scales, means that the magnetopause is virtually always in motion. This was first clearly demonstrated by the two-satellite *ISEE* mission, and boundary speeds of typically 50 km s^{-1} were found by timing the observed magnetopause crossings at the two satellites [*Russell and Elphic*, 1978]. The magnetopause motions are often oscillatory such that the boundary may cross the satellite many times during any one pass. Typically, satellites move at about 2 km s^{-1} normal to the boundary and so any one crossing is likely to be due to the boundary motion and not the satellite motion [*Hapgood and Lockwood*, 1995].

This dynamic nature of the boundary makes observations of many of its characteristics difficult. In addition, the boundary distorts, making accurate determination of the orientation of the boundary very difficult.

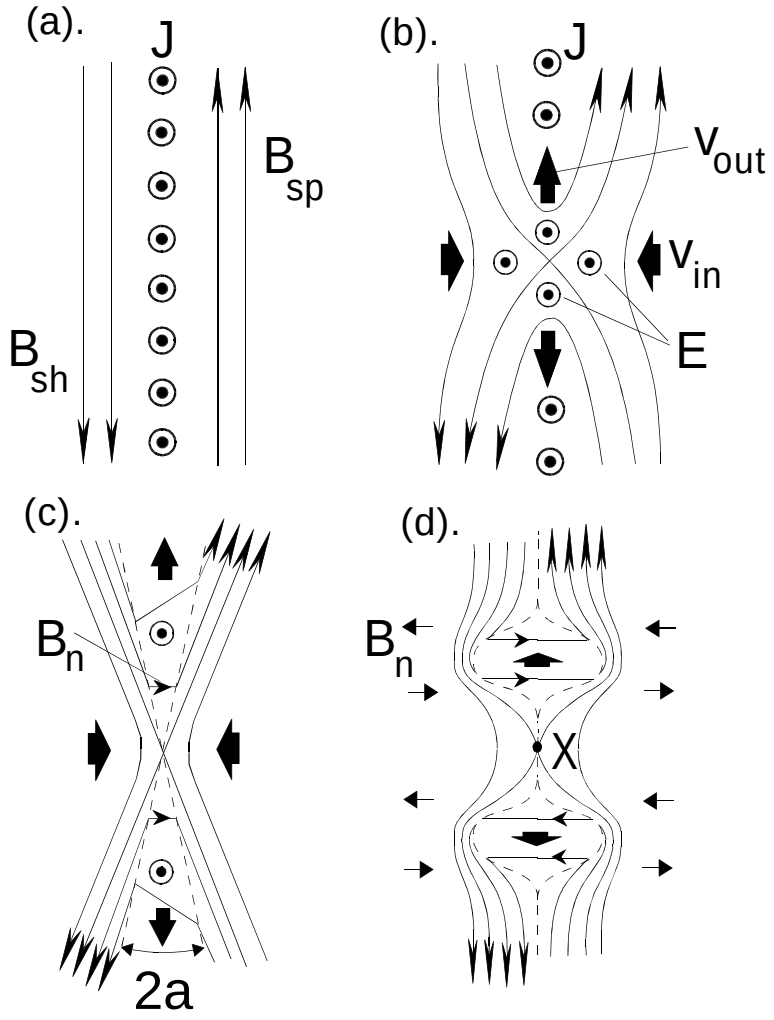

Figure 2. Magnetic reconnection between a southward-pointing magnetosheath field, B_{sh}, and the northward- pointing magnetospheric field, B_{sp}, at the low-latitude magnetopause. In (a) frozen-in applies everywhere and there is no magnetic flux threading the sheet of magnetopause current, J (i.e. there is tangential discontinuity in the field). In (b) diffusion in a localised disruption of the current sheet allows field lines to reconfigure such that they thread the magnetopause, giving a boundary-normal field component B_n and a rotational discontinuity (RD). Outside of the diffusion region, frozen-in applies and field lines **E x B** *drift into and away from the reconnection site at V_{in} and V_{out}, under the influence of a boundary-tangential electric field, E, called the "reconnection rate". In Petschek reconnection E is considerably increased by shocks (shown as dashed lines in c) which stand in the inflow. The angle of the outflow wedges, a, increases with E. A pulse of Petschek reconnection yields a pair of bulges in the outflow layer which propagate away from the reconnection site (as shown in d), yielding bipolar signatures in the boundary-normal field which have opposite polarity on opposite sides of the X-line.*

4.3. Magnetic reconnection

Figure 2 considers the magnetopause at low latitudes on the dayside, near the subsolar point in figure 1. If frozen-in applied strictly, $\mathbf{B}_{sh}$ and $\mathbf{B}_{sp}$ would be kept apart by the Chapman-Ferraro currents, as shown in 2_a. However, this current

sheet would be squeezed between the thermal and magnetic pressure of the sheath [*caused by the dynamic pressure of the solar wind*] and the magnetic pressure of the magnetosphere. This would cause the current layer to thin, until the characteristic scale length, L_c would become small enough for the magnetic Reynolds number to fall to near unity [*Eq. 12*]. From the induction Eq. 11, this means that the frozen-in approximation starts to break down and the field diffusion term becomes important. The fields diffuse from high values to the low values at the centre of the current sheet. The process of magnetic reconnection allows them to reconfigure at a singularity at the centre of the current sheet, as shown in figure 2_b, such that they thread the current sheet. These "*open*" field lines connect the interplanetary space and the magnetosphere: they are highly kinked and are accelerated away from the reconnection site by the curvature force. Away from the diffusion region, frozen-in applies and the motion of the $\mathbf{B}_{sh}$ and $\mathbf{B}_{sp}$ field lines towards the reconnection site [*at speed* $\boldsymbol{V}_{in}$] and of the open field lines away from it [*at speed* $\boldsymbol{V}_{out}$] both correspond to an electric field out of the plane of the diagram, called the reconnection rate, **E**. This process is often also referred to as "*merging*": this is possibly a more accurate name in that it is very unlikely that the field lines are cut and then joined back together [*reconnection implies a prior disconnection*] as this would involve the existence of a magnetic monopole, however briefly. However, I here use the term "*magnetic reconnection*" because that is what it is called in all other branches of plasma physics and also because that is the name given by *Dungey* [1953; 1961] who was the first to describe this process in this way and to understand its implications for the terrestrial plasma environment. It can be shown that the reconnection rate is much faster if a pair of shocks form and stand in the inflow region, as shown by the dashed lines in 2_c, this is called Petschek reconnection [see review by *Petschek*, 1995]. The outflow region between the shocks is sometimes called the reconnection layer, and sometimes the open low-latitude boundary layer [*open LLBL*]. The plasma speed in this open *LLBL* along the magnetopause, $\mathbf{V}_{out}$, is given by Eq. 15 to be E/B_n where B_n is the boundary-normal field in the current sheet. The diffusion region is often called the *X*-line and extends out of the plane of the diagram.

If we consider the simplest, symmetric case of steady-state with the Alfvén speed the same in the inflow regions on the two sides of the boundary [V_{Ain}], by conservation energy the inflow energy, dominated by the Poynting flux inflow towards the current sheet from both the magnetosphere and magnetosheath, equals the outflow, dominated by the kinetic energy of the outflow plasma in the open LLBL. In addition, the rate of mass inflow must equal the rate of mass outflow, from these relations it is easy to show that:

$$V_{out} = \frac{E}{B_n} \approx 2^{0.5}\, V_{Ain} = 2^{0.5}\, \frac{B_{in}}{(\mu_o \rho)^{0.5}} \qquad (19)$$

Thus the outflow velocity V_{out} is independent of the reconnection rate, E. Figure 2_c shows that increasing B_n would increase with the angle of the outflow wedges, a. An increase in reconnection rate would proportionally increase the boundary-normal field, B_n [*such that* V_{out} *is constant*] and thus increase the angle, a. If we have a reconnection pulse, therefore, we would expect the outflow wedge to increase in width and decrease again in response to the changes in a. This produces the pair of bulges in the open *LLBL*, one on each side if the reconnection site, containing the enhanced boundary normal field produced by the pulse, as shown in 2_d. This concept was discussed by *Southwood et al.* [1988] and has here been outlined by treating the system as quasi-steady. In fact figure 2_d shows the results from a proper analytic theory of time-dependent Petschek reconnection, developed by *Biernat et al.* [1987] and *Semenov et al.* [1992], similar features have been reproduced in 2-dimensional *MHD* simulations by *Scholer* [1988]. In figure 2_d there is no reconnection before and after the pulse so the open *LLBL* reduces to zero width before and after the pulse: in general there could be a reduced but non-zero rate between the pulses, in which case the open *LLBL* is continuous but varies in thickness. Notice that both the sheath and magnetosphere fields are draped over the bumps in the open *LLBL*. As the bulges evolve away from the reconnection site they may pass over a satellite. This would cause the field to tip away from, and then towards the Earth in the northern hemisphere. The same bipolar signature in B_n [*defined as the field component along the outward normal to the boundary*] would also be seen on either side of the magnetopause. In the southern hemisphere the signatures on either side of the boundary would have the reverse polarity with negative B_n followed by positive, as shown in 2_d. Such signatures are indeed observed and are discussed here in section 4.6.

Figures 2_c and 2_d show two limits of the general behaviour, steady and fully pulsed reconnection. There are a number of features produced by the reconnection in both these limits and by general cases between them. Firstly there is a boundary-tangential electric field, E_t and the boundary-normal magnetic field, B_n. These exist wherever the open field lines convect to from the *X*-line, but usually cannot be observed directly because of the problems associated with the boundary motions and orientation. However, this certainly does not mean that there is no evidence for reconnection in magnetopause observations. Also produced by the reconnection are open field lines which thread the magnetopause via a rotational discontinuity [*RD*] in the field and which convect away from the reconnection site. Usually the Alfvén speed [*defined in Eq. 19*] is greater on the

magnetospheric side of the boundary because the field is greater and the plasma density ρ is smaller. This means that the field rotation at the shock on the magnetospheric edge of the open *LLBL* propagates away from the reconnection *X*-line faster than does the corresponding kink at the shock which is on the sheath edge. This can be seen to be developing for the field lines further from the *X*-line in the outflow region in figure 2_c. Thus well away from the *X*-line, the field rotation becomes a single *RD* at the shock on the sheath edge of the *LLBL* in this case [*Vasyliunas, 1995*]. Magnetosheath plasma is found in the *LLBL* on the inside of the field reversal, which is often used as the best indicator of the magnetopause. Notice that this assumes a reconnection site which is near the nose of the magnetosphere where the sheath flow is small: away from this region, on the flanks of the magnetosphere, the increased sheath flow can convect the outer field kink faster than the inner one, in such cases an open *LLBL* may be seen on the outside, not inside, of the magnetic field *RD* [*Lin and Lee*, 1994]. In the next section we will look at the evidence for RDs in field lines convecting away from the reconnection site.

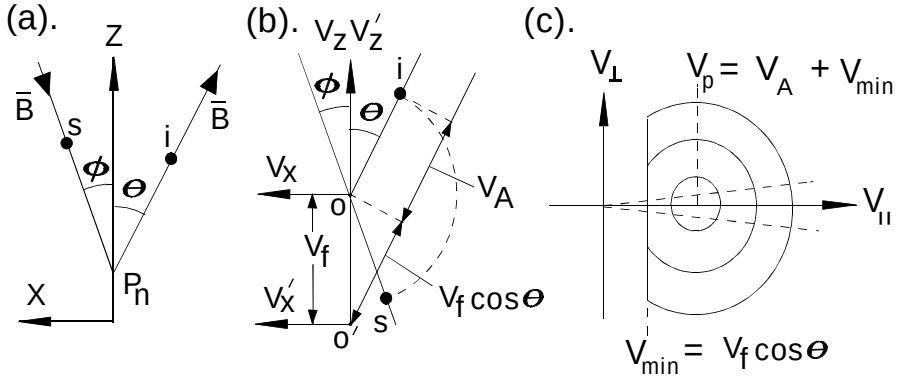

Figure 3. (a) The rotational discontinuity (RD) formed by a newly opened field line, threading the magnetopause at P_n and which evolves along the magnetopause in the Z direction at speed V_f in the Earth's frame of reference. The X direction is here the outward normal to the boundary. (b) A velocity space plot showing field-aligned bulk flow at the Alfvén speed, V_A, in the de Hoffmann-Teller frame (V_x,V_z with origin at O) both into the RD in the magnetosheath (at s) and away from the RD in the magnetosphere (at i). This geometric construction allows the calculation of the minimum (V_{min}) and bulk flow (V_p) field-aligned speed of injected particles in the Earth's frame (V_x,V_z) with origin at O'. (c) The truncated, drifting Maxwellian ion distribution function ("Cowley-D") injected at P_n shown in the Earth's frame as a function of the field parallel and field perpendicular ion velocities ($V_{//}$ and $V_{\perp}$). Between the dashed lines is the part of the distribution for which ions will reach the ionosphere without mirroring in the converging magnetic field lines. [Adapted from Cowley*, 1982].*

4.4. Stress-balance test and accelerated flows

Figure 3_a shows the *RD* formed by an opened field line, convecting away from the *X*-line in the z direction, with the x axis here used to denote the outward normal to the boundary. This figure is in the de-Hoffman-Teller [*dHT*] frame of reference in which the electric field is zero [*de Hoffman and Teller*, 1950]. If we think of the field lines moving with the plasma with velocity $\mathbf{E} \times \mathbf{B}/B^2$ [*i.e. frozen-in applies*] this means that they are at rest in the dHT frame. We can apply (a) Ampère's law [*in integral form*] to a box in the xz plane which encompasses the current sheet, along with (b) the balance of forces tangential to the boundary in the z direction, (c) conservation of mass and (d) the condition that the tangential electric field E_t must be continuous across the boundary. It is then possible to show that the plasma drifts into and out of the RD along the field lines at the local Alfvén speed [*taken here to be the same on the two sides of the boundary, for simplicity*] in the *dHT* frame. This is a general result for an ideal-*MHD*, time-stationary, *RD*. If we transform this result into the Earth's frame of reference, in which the field lines [*and the dHT frame*] are moving at speed $V_f = E_t/B_n$, we obtain:

$$\mathbf{V} = \mathbf{V}_f \pm \frac{\mathbf{B}}{(\mu_o \rho)^{0.5}}. \qquad (20)$$

This is called the Whalén relation and can easily be generalised to allow for an anisotropic plasma pressure [*a factor not included here for the sake of simplicity*] [*Fuselier et al.*, 1992]. The plus or minus refers to direction of the boundary-normal field B_n and thus is different on the two sides of the *X*-line.

Equation 20 is a vector equation and thus applies to any one component [*in any direction j*]. Tests of this relationship are called the stress-balance test, as Eq. 20 is based on the balance of boundary-tangential forces. When B_j is plotted against V_j in magnetopause data, a straight line is obtained, as predicted by Eq. 20] [*Paschmann et al.*, 1979; 1986; *Sonnerup et al.*, 1981; 1986; *Johnstone et al.*, 1986]. The inferred V_f are typically 150-300 km s^{-1} and the polarity of B_n reverses near the magnetic equator, such that field lines enter the magnetosphere in the northern hemisphere and leave in the southern, consistent with a low-latitude reconnection site *X*, as shown in figure 1 [*Paschmann*, 1984]. These results show that the magnetopause is an ideal-*MHD RD* [i.e. *the field lines thread the magnetopause and are frozen-in to the plasma*] - the only exception being in the small reconnection diffusion region. The open field lines are also seen to convect over the magnetopause, away from the reconnection site, at several hundred km s^{-1}. The one problematic result is that by *Fuselier et al.* [1993] who essentially found that ionospheric O^+ ions, invoked by Paschmann et al. to be in the *LLBL* from their stress-balance test results, were largely absent.

There are a number of possible explanations for this. When applying the stress test, it is important to ensure all relevant, and only relevant, particles are included: this may not have been possible with the limited temporal resolution of the data used by Fuselier et al. It is also possible that the problem is related to the observations of ion temperature rises in accelerated flow regions, which would not be expected for an ideal-*MHD RD* magnetopause [*Paschmann*, 1984].

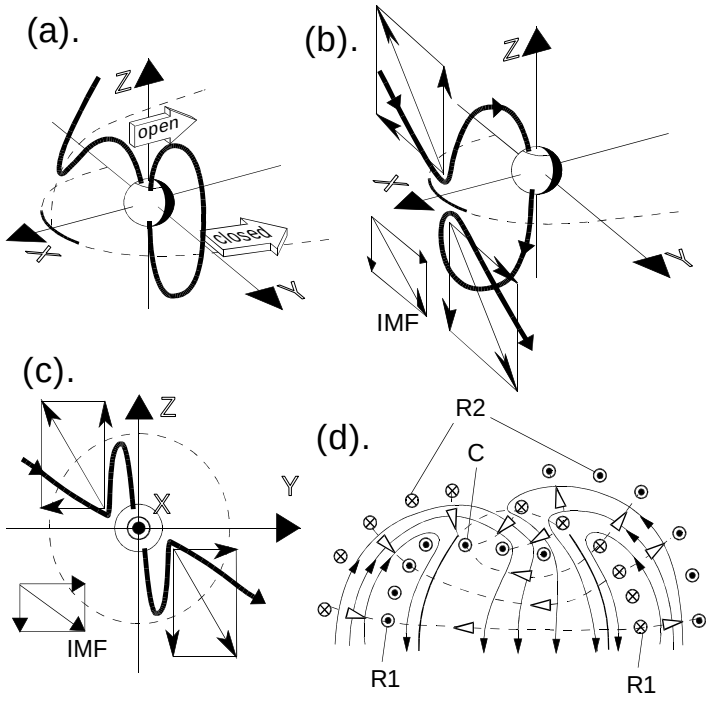

Figure 4. (a). The antisunward transfer of open flux produced by reconnection and of closed flux, due to non-reconnection or "viscous-like" interactions on closed field lines on the flanks of the magnetopause. (b) and (c). The origins of asymetric dayside flows and currents in the dayside magnetosphere-ionosphere system (the Svalgaard-Mansurov effect). Open field lines are shown shortly after they were formed by reconnection with an IMF that points southward ($B_z < 0$) and towards dusk ($B_y > 0$). The vectors show the "tension" forces resulting from the curvature of these newly-opened flux tubes. In both hemispheres, this force has a poleward component: in the northern hemisphere it also has a dawnward component (i.e. in the negative Y direction), whereas there is a duskward component in the southern hemisphere. (d) shows the resulting flow streamlines (solid lines and arrows), Pedersen currents (dashed lines and open arrows) and field aligned currents (into and out of plane of diagram) in the ionosphere: noon is to the top, dusk to the left and dawn to the right. The field-aligned currents are divided into Region 1 (R1), Region 2 (R2) and Cusp (C). The sense of dawn-dusk forces in (b) and (c), of the consequent dawn-dusk asymmetries in flows and Pedersen currents near noon in (d) and of the polarity of the cusp field-aligned currents are all reversed when IMF $B_y < 0$.

Consider the magnetosheath plasma flowing into the magnetosphere. In figure 3 the sheath ions incident on the magnetopause are marked s and those injected across the magnetopause into the open *LLBL* are marked *i*. Figure 3_b is a

velocity space diagram, with O being the origin of the *dHT* frame and O′ the origin in the Earth's frame. The incident sheath ions in 3_a are moving in the -z and -x directions, i.e. $V_x < 0$ and $V_z < 0$ in the *dHT* frame. The bulk flow speed is the local Alfvén speed V_A in this frame and this flow is at the point *s* in both 3_a and 3_b. After crossing the *RD*, the injected ions (i) are moving with $V_x < 0$ and $V_z > 0$. As the bulk flow ion speed is still V_A in the *dHT* frame, *i* must lie on the dashed circle radius V_A , centred on *O*, as shown in 3_b. In the Earth's frame, the crossing of the magnetopause [i.e. *from s to i*] corresponds to a large acceleration [*of almost* $2V_A$ *on the dayside where* θ *and* ϕ *are sufficiently close to zero that* $\cos\theta \approx \cos\phi \approx 1$].

Accelerated flows are indeed seen at the dayside magnetopause [e.g. *Smith and Rodgers*, 1992; *Scurry et al.*, 1994]. Their speed satisfies the stress balance test described above. In addition their direction is as predicted by the reconnection model. This is explained by figure 4_b which is a view of the dayside magnetosphere from mid-latitudes and mid-afternoon. The same situation is viewed from the sun in figure 4_c.

The diagrams show newly-opened field lines produced by reconnection at a subsolar magnetopause for a southward *IMF* which points toward dusk [*By* > 0]. The vectors show the curvature force on the kink in the newly opened field lines with components in the poleward and dawn-dusk directions. For this case, the zonal force [*and resulting field line and frozen-in plasma velocity*] is in the *-Y* direction in the northern hemisphere and in the *+Y* direction in the southern. These zonal directions are reversed when *IMF By* < 0. The observations by *Gosling et al.* [1990a] show that the direction of the accelerated flows depends on *By* as expected from figure 3.

An important point is that once field lines are open, plasma streams across the boundary along the open field line at all stages in its evolution, until it is re-closed by reconnection in the tail [*at* X_t *in figure 1*]. This has been confirmed by the stress balance test, not only on the dayside magnetopause, as described above, but also at the near-Earth tail boundary [*Sanchez et al.*, 1990; *Sanchez and Siscoe*, 1990] and recently by observations by the Geotail satellite in the far tail [*Siscoe et al.*, 1994]. However, the characteristics of the injected plasma change as the field line evolves. Figure 3 shows the *RD* for a newly-opened field line threading the dayside magnetopause, with the angles θ and ϕ being small. This acute-angle *RD* in the field corresponds to Chapman-Ferraro currents out of the plane of the diagram, as can be seen in figure 1. Note that for this dayside magnetopause **J** and **E** point in the same direction, i.e. **J** . **E** > 0. However, as the field line evolves, the angles θ and ϕ both increase and $(\theta+\phi)$ exceeds π. For this obtuse-angle *RD*, the equivalent construction to figure 3_b shows the ions are

decelerated, not accelerated, on crossing the boundary. The corresponding Chapman-Ferraro current is here into the plane of the diagram, i.e. $\mathbf{J} \cdot \mathbf{E} < 0$ [*see figure 1*] [*Hill*, 1979]. Note that in the tail lobe boundary, the field line velocity, V_f, is away from the Earth, whereas it is toward it on the dayside. Because the flow is super-thermal, very little of the ion distribution injected across the tail lobe magnetopause [*the high-latitude boundary layer, HLBL*] will have a velocity toward the Earth and will precipitate to the ionosphere. Those that do [*the hot tail of the population in the dHT frame*] will form a low-energy [*in the Earth's frame*], low-density precipitation in the polar cap. This contrasts with ions in the open *LLBL* on the dayside which are accelerated toward the Earth and precipitate in the "*cusp*" region. Electrons precipitate with roughly equal fluxes to the ions, in such a way as to maintain quasi-neutrality of the plasma [*Burch*, 1985].

During northward *IMF*, accelerated flows are still observed, but in such cases they are streaming away from a reconnection site at high latitudes on the dayside edge of the tail lobe *HLBL* [*Gosling et al.*, 1991; *Paschmann et al.*, 1990]. A survey of accelerated flow directions by *Scurry et al.* [1994] has confirmed that they emanate from a low-latitude reconnection site during southward *IMF*, but from a tail lobe site during northward *IMF*.

4.5. Particle populations

The previous section described how the bulk flow of the plasma into and away from the ideal *MHD RD* that is the magnetopause [*away from the X-line*]. About this bulk flow velocity there will be a thermal spread of speeds. One hot tail of the distribution of incoming sheath ions will have field-aligned flow speeds, $V_{||}$ which are away from the boundary. They will thus fail to cross the boundary. Ions with $V_{||} = 0$ will just manage to cross the boundary and in the Earth's frame will be accelerated to [$V_f \cos \theta$]. Hence this will be the minimum field-parallel velocity V_{min} of the injected sheath population; *Cowley* [1992] used such arguments to predict the D-shaped distribution function of the injected sheath population, as shown in figure 3_c. To make his predictions, he noted that there were three populations incident on the magnetopause, the sheath population from the outside and the ionospheric and ring current populations from the inside. Each of these populations will be scattered at the current sheet and some will be reflected by the boundary and some will be transmitted through it. Cowley assumed that in either case the pitch angle of the ion was conserved on interaction with the boundary. This is clearly not a good assumption when dealing with individual particles, but when dealing with a statistical ensemble the scattering does not alter the form of the distribution functions. The injected population in figure 3_c is a truncated drifting Maxwellian, often referred to as a "*Cowley - D*" distribution.

Almost ten years after these predictions were made, they were verified in observations of accelerated flows at the dayside magnetopause [*Gosling et al*., 1990b; *Smith and Rodgers*, 1991; *Fuselier et al*., 1991]. In addition to showing the D-shaped distribution functions of the accelerated injected ion flows in the open *LLBL*, Smith and Rodgers applied the stress-balance test and showed that the cut-off was at the velocity $V_{min} \approx V_f$ [*for close to the X-line* $\theta \approx 0$], as predicted by the theory. In addition, Fuselier et al. studied He^+ and He^{++} ions because these are known to be of magnetospheric and magnetosheath origin, respectively. They found not only the injected sheath ions, but all populations [*incident, transmitted and reflected*] were as predicted by Cowley, on both sides of the boundary. The distributions have also been reproduced in simulations by *Lin and Lee* [1993].

In figure 3_c there are two dashed lines at fixed pitch angle. Ions between these two lines are the only ones with a sufficiently field-aligned velocity vector to precipitate into the ionosphere without first mirroring in the converging magnetic field lines. This precipitation is discussed further in section 6.3. Lastly, we note that electrons do undergo a corresponding *dHT* acceleration on crossing the magnetopause, but the increase in speed is negligible compared to the speed with which they approach the magnetopause. [*For example, an electron with the same energy as an ion will have a greater speed by a factor of* $(m_i / m_e)^{½} \sim 40$].

4.6. Flux Transfer Events

As discussed in section 4.3, a pulse of enhanced reconnection rate is expected to cause a pair of bipolar signatures in the boundary-normal field, B_n, which move away from the reconnection site at the field line velocity, V_f. Such signatures have been known for over a decade and are termed flux transfer events [*FTEs*], first reported by *Russell and Elphic* [1978] and *Haerendel et al.* [1978]. The name originates from the interpretation because, as discussed earlier, a burst of enhanced reconnection rate, when integrated along the *X*-line, is a voltage burst which is synonymous with the term "flux transfer event". *By* definition, the flux is transferred from the closed to the open region by the reconnection, but it is seen some time later as it is transferred into the tail lobe under the action of the magnetic curvature force and the magnetosheath flow. This interpretation of *FTEs* predicts that their polarity reverses sense across the *X*-line, a feature which is found in experimental data if we infer the *X*-line to be at low latitudes on the dayside magnetopause [*Berchem and Russell*, 1984; *Rijnbeek et al*., 1984]. These statistical surveys also show that the events are almost exclusively a southward *IMF* phenomenon and repeat every 7 minutes on average. It should be stressed that this is an average value of what *Lockwood and Wild* [1993] find to be a highly skewed distribution, with a mode repeat time of 2-3 min. The dependence of the occurrence of *FTEs* on *IMF Bz* strongly implicates the reconnection

process, as do particle observations of the plasma in the centre of an *FTE* which reveal a mixture of sheath and magnetosphere plasma [*Thomsen et al.*, 1987], as expected for newly-opened flux along which plasma from both sides can flow across the boundary and mix, as described in the previous section. The *FTE* model presented in figure 2_d is slightly different from that presented by Russell and Elphic, although very similar in basic concept. The main difference is that Russell and Elphic used a circular newly-opened flux tube whereas figure 2_d is 2-dimensional and events are not defined in their extent out of the plane of the diagram. Not all scientists have agreed with this interpretation of magnetopause *FTE* signatures as resulting from reconnection bursts. In particular, *Sibeck* [1992] has used a conceptual argument that they are caused by magnetopause surface waves driven by solar wind dynamic pressure pulses. However, there are a number of problems with this interpretation, for example: the postulated pressure changes are not found in the sheath [*Elphic et al.*, 1994]; the boundary thickens rather than thins in an event [*Hapgood and Lockwood*, 1995]; the occurrence statistics with *IMF Bz* is not well reproduced; and there has been much debate as to if the pressure-pulse mechanism would really produce *FTE*-like signatures [*Lockwood*, 1991; *Song et al.*, 1994]. It seems that the original concept of *FTEs* is valid, however, Sibeck's work has highlighted the need for careful identification of *FTEs* as they are not the only cause of fluctuations in B_n.

5. Transfer of energy, mass and momentum from the magnetopause to the ionosphere

5.1. Poynting's theorem

If we compress a magnetic field by $d\tau$ in volume, we do work against the magnetic pressure which, by Eq. 18 is $\partial W_B = (B^2/2\mu_o)d\tau$. Thus the rate at which energy is stored in the field in a volume τ is:

$$\frac{\partial W_B}{\partial t} = \frac{\partial}{\partial t}\left(\int_\tau \frac{B^2}{2\mu_o} d\tau \right) = \frac{1}{\mu_o} \int_\tau (\mathbf{B} \,.\, \partial\mathbf{B}/\partial t)\, d\tau$$

If we substitute from Faraday's law Eq. 10, use the vector relation $\nabla \,.\, (\mathbf{E} \times \mathbf{B}) = \mathbf{B} \,.\, (\nabla \times \mathbf{E}) - \mathbf{E} \,.\, (\nabla \times \mathbf{B})$, Ampère's law Eq. 9, the divergence theorem and the definition of Poynting flux $\mathbf{S} = (\mathbf{E} \times \mathbf{B})/\mu_o$, we get Poynting's theorem:

$$\partial W_B/\partial t = - \int_A \mathbf{S} \cdot \mathbf{ds} - \int_\tau \mathbf{E} \cdot \mathbf{J}\, d\tau \qquad (21)$$

where the surface S surrounds the volume τ. The first term on the right is the divergence of the Poynting flux and the second is the ohmic heating term. If we use Ohm's law Eq. 7, we can show that the heating term has two parts:

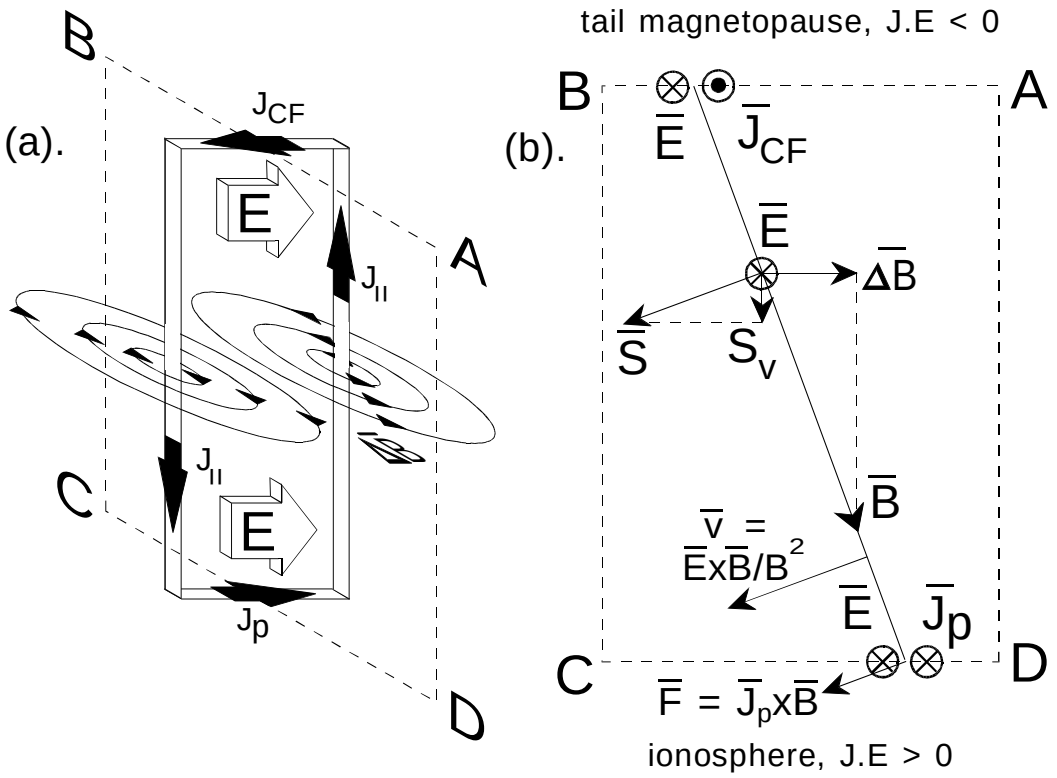

*Figure 5. The role of field-aligned currents $J_{//}$ in the transfer of energy and momentum from the magnetopause to the ionosphere.(a) shows an ideal matched pair of filamentary field-aligned currents which form a circuit with the Chapman-Ferraro currents (J_{CF}) in the tail magnetopause and the Pedersen currents (J_p) in the ionosphere. The field-aligned currents cause a field perturbation, $\Delta\boldsymbol{B}$, which tilts the field lines with respect to their orientation in the absence of the currents, as shown in (b). The electric field **E** applied by the solar wind flow is oppositely directed to the Chapman-Ferraro currents, making* $\mathbf{J} \cdot \mathbf{E} < 0$ *so that this portion of the magnetopause is a source of Poynting flux,* $\mathbf{S}=\mathbf{E} \times \mathbf{B}$ *(see figure 1). Conversely, the Pedersen currents are in the same direction as* **E**, *i.e.* $\mathbf{J} \cdot \mathbf{E} > 0$ *and the ionosphere is a sink of Poynting flux. Thus energy is extracted from the magnetosheath flow at the tail magnetopause and is deposited in the ionosphere. The tilting of the field lines produces a downward component of the Poynting flux, S_v, which transfers the energy from the magnetopause to the ionosphere. The motion of the ionospheric plasma at the velocity* $\mathbf{v} = (\mathbf{E} \times \mathbf{B})/B^2$ *is opposed by the frictional drag caused by the neutral atmosphere and is maintained by the* $\mathbf{J} \times \mathbf{B}$ *force associated with the Pedersen currents. These concepts are sometimes referred to as "line-tying".*

$$\int_{\tau} \mathbf{E} \cdot \mathbf{J}\, d\tau = \int_{\tau} \frac{J^2}{\sigma} d\tau - \int_{\tau} \mathbf{V} \cdot (\mathbf{J} \times \mathbf{B})\, d\tau \qquad (22)$$

where the first term on the *RHS* is the resistive energy dissipation and the second is the mechanical work done against the $\mathbf{J} \times \mathbf{B}$ force.

If we consider steady state, $\partial W/\partial t$ is zero and a region where $\mathbf{J} \cdot \mathbf{E} > 0$ is a sink of Poynting flux, i.e. energy goes from the electromagnetic field into the particles. Conversely regions of $\mathbf{J} \cdot \mathbf{E} < 0$ are sinks of Poynting flux, i.e. energy goes from the particles into the electromagnetic field. The dashed lines in figure 1 show the Poynting flux and how the dayside magnetopause is a sink of *S*, whereas the tail lobe boundary is a source. This means that energy is extracted from the solar wind flow at the tail lobe boundary [*HLBL*], but put into the accelerated ions on the dayside *LLBL*.

If we have no Ohmic heating [$\mathbf{J} \cdot \mathbf{E} = 0$] with non-steady state, a region of increasing magnetic field will be a sink of Poynting flux and conversely a region of decreasing field will be a source. An example of the former is the tail lobes during the growth phase of a substorm: energy is then stored in the lobe and it is a sink of the Poynting flux generated at the *HLBL* magnetopause [*as can be seen in figure 1*]. In the later phases of substorms, the lobe field decreases again, so the lobe becomes a source of Poynting flux which takes the stored energy and deposits in the tail plasma sheet, the ring current and the ionosphere. Thus the lobe acts as a store for the extracted energy which is later released in substorms.

5.2. The role of field-aligned currents

Figure 5 shows how field aligned currents can transfer the solar wind momentum and energy into the ionosphere [see *Southwood*, 1987]. The figure shows an idealised pair of straight field-aligned filamentary currents which close through an element of Chapman-Ferraro current at the magnetopause and a linear Pedersen current in the ionosphere. [*In reality, the Pedersen current will spread out over an extended region around the field-aligned current filaments, corresponding to the "return" flows required outside the filaments because the ionosphere is incompressible*]. These field-aligned currents [$\mathbf{J}_{||}$] cause a perturbation to the magnetic field $\Delta\mathbf{B}$, as shown. We show a segment of the tail magnetopause where $\mathbf{J}_{CF} \cdot \mathbf{E} < 0$, which is a source of *S* [*figure 1*] and, by definition $\mathbf{J}_{P} \cdot \mathbf{E} > 0$ which is a sink of *S*. Figure 5_b shows the plane *ABCD* between the filamentary field-aligned currents [*see* 5_a]. The perturbation $\Delta\mathbf{B}$ causes a tip in the field lines. In the ionosphere, the field line moves horizontally because of the $\mathbf{J}_P \times \mathbf{B}$ force which is opposed by the frictional drag on the

ionospheric plasma caused by collisions with the neutral gas. In steady-state these forces are balanced and the field lines move with constant speed corresponding to the $\mathbf{E} \times \mathbf{B}/B^2$. If we consider the magnetic flux F threading the current loop shown in 5_a, by Faraday's law Eq. 16, the rate of change of F is the integral of **E** . **dl** around the loop. If we assume frozen-in applies [*to a good approximation*] $E_{||}$ is zero and so we have

$$\oint \mathbf{E} \cdot \mathbf{dl} = E_t \, dl_m - E_i \, dl_i = \frac{\partial F}{\partial t} \qquad (23)$$

where E_t and E_i are the magnetopause and ionosphere electric fields and a length dl_m maps to a length dl_i in the ionosphere. The *RHS* of Eq. 23 is zero in steady state and thus, $E_i = E_t \, (dl_m / dl_i)$, we speak of the electric field mapping down field lines or, equivalently, the magnetopause voltage being equal to the voltage across the ionospheric footprint. [*In the simplified picture given in figure 5, $dl_m = dl_i$ and so the electric field is everywhere the same in this steady state limit*]. Figure 5_b also shows the Poynting flux, **S**, which because of the tilt of the field lines has a downward component, S_v, which connects the source at the magnetopause with the sink in the ionosphere.

Figure 5 therefore demonstrates how field-aligned currents transfer both electromagnetic energy and momentum from the magnetopause to the ionosphere. The concepts embodied in this figure are often referred to as "*line-tying*". It should be noted that the frictional drag in the ionosphere makes it difficult to move, but that current systems in the magnetosphere may change more rapidly, allowing field lines to bend, altering ΔB at any one location and its integral over the loop, F. From Eq. 23, the electric fields will then no-longer map from the magnetopause to the ionosphere. In terms of an electrical circuit analogy, the ionosphere is a resistor and the magnetosphere acts as an inductance. Thus in time-varying situations, the ionosphere will be slow to respond to a change in the tangential magnetopause electric field and the field-aligned currents will change on the inductive time constant of that response. For a single, step-function change in the magnetopause electric field, the ionospheric flows and the corresponding field aligned currents will rise asymptotically towards the steady-state value, with the inductive time constant. If the magnetopause electric field fluctuates then the ionospheric flows and the field aligned currents will, in general, show these fluctuations, but they will be inductively smoothed to a degree which depends on the ratio of the fluctuation period to the inductive smoothing time constant. From a variety of studies, we find the inductive time constant for the dayside to be of order 10-20 min. This has been estimated from electrical circuit analogies [*Holzer*

and Reid, 1975; *Sanchez et al.*, 1991], from line-tying arguments [*Coroniti and Kennel*, 1973] and measured directly from the response of dayside ionospheric flows and currents to southward and northward turnings of the *IMF* [*Nishida*, 1968; *Etemadi et al.*, 1988; *Todd et al.*, 1988; *Hairston and Heelis*, 1995].

Time-dependent situations will be discussed further in section 7.

5.3. Directly-driven ionospheric convection

Figure 4_a illustrates the two ways in which magnetospheric convection can be driven. The diagram shows a newly-opened field line convecting away from a subsolar reconnection site. Initially this motion is due to the curvature ["*tension*"] force, but as it straightens the magnetosheath flow becomes more important. The other flux tube shown remains closed and is convected into the tail by some form of momentum transfer across a tangential discontinuity [*TD*] magnetopause. Because this applies to all mechanisms, other than reconnection, they are grouped together under the term "*viscous-like interaction*". The nature of that interaction will not be discussed here, other than to mention that possible, valid and viable mechanisms include the Kelvin-Helmholtz instability, wave-driven diffusion, and field-aligned current generation by compressive magnetopause motions produced by solar wind buffeting. For either an open or a closed field line, the antisunward motion will, in steady-state, be communicated to the ionosphere by field-aligned currents, as discussed in relation to figure 5. The results are shown in figure 4_d which is a view of the northern hemisphere polar cap, with noon at the top and dawn to the right. [*Note there is a deliberate dawn-dusk asymmetry in this plot which will be discussed in the next section*]. The solid lines with arrows are flow streamlines in the F-region and topside ionosphere, which do not cross or touch because the ionosphere is incompressible. The dashed lines with open arrows show the E-region Pedersen currents. As these are parallel to the applied electric field they are everywhere normal to the F-region flow which is a frozen-in $(\mathbf{E} \times \mathbf{B})/B^2$ drift. The Pedersen currents are closed by field-aligned currents, shown as symbols into and out of the plane of the diagram. The dashed line across noon is the ionospheric projection of the reconnection *X*-line shown in 4_a, other [*non-reconnecting*] parts of the open-closed boundary are shown as solid lines [*nearer dawn and dusk*]. These non-reconnecting segments are called "*adiaroic*" [*from the Greek and meaning "not flowing across*"] [*Siscoe and Huang*, 1895]. Magnetopause reconnection, by definition, is the transfer of flux from closed to open. In this steady-state case, the open-closed boundary [*dashed line*] is still and flow streamlines crossing this boundary are driven by reconnection at that local time [*note that this is not necessarily the case in the time-varying situations discussed in section 7*]. The viscous-like momentum transfer is seen on the flow streamlines on the flanks of the open field line region where the sunward flow turns antisunward. The flows change direction at a convection reversal boundary

[*CRB*] which lies equatorward of the open-closed boundary [*OCB*]. The field-aligned currents at the *CRB* are down near at dawn and up near dusk and are called the region 1 [*R1*] currents, a name commendably free of the theory of their origin [*Iijima and Potemra*, 1976]. These must close in the Chapman-Ferraro currents, but first have to traverse the closed *LLBL*, between them and the open-closed boundary [*Siscoe et al.*, 1991] [N.B. *this cross-closed LLBL current is thought to give the* $\boldsymbol{J}\times\boldsymbol{B}$ *force which balances the weak viscous forcing on the closed LLBL field lines, Lotko et al.*, 1987]]. The antisunward flow poleward of the *CRB* must be matched by sunward flux transport equatorward of it, because the ionosphere is incompressible. This sunward transfer is confined to a relatively narrow band at auroral and sub-auroral latitudes by a second set of field-aligned currents, called the region 2 [*R2*], which close in the ring current, which have the opposite sense to the region 1 currents at the same local time. The double-annulus of field-aligned currents was discovered by *Iijima and Potemra* [1976].

The rate of flux transfer [i.e. *voltage*] between the dawn and dusk *CRBs* can be measured by satellites which fly across the polar cap at low altitudes, by integrating the observed electric field [*often taken from the ion drift using Eq. 14*] along the satellite orbit. This is often referred to as the "cross-cap potential" but is actually a potential difference [i.e. *a voltage*] and so I prefer the name transpolar voltage, Φ_{pc}. The observations show that Φ_{pc} increases with increasingly southward *IMF* [*Reiff et al.*, 1981; *Cowley*, 1984] up to values of over 100 kV. This is in accordance with expectations for the reconnection momentum transfer, as the reconnection process requires the antiparallel fields, and the maximum magnetic shear is when the *IMF* points due south. Curiously, this is well reproduced by global *MHD* models, which assume the frozen-in condition applies at all locations! [e.g. *Fedder et al.*, 1991]. This arises because the models make errors in tracing field lines and accidentally connect geomagnetic field lines with interplanetary ones to produce open field lines. The rate at which this happens is not dependent on the model grid size and mimics the reconnection behaviour in the real magnetosphere because the equations for the propagation of this numerical error are very like the diffusion term in the induction Eq. 11.

When the IMF is northward, the only expected antisunward flux transfer is that due to viscous interaction and the physically-meaningful mechanisms for viscous-like interaction predict no dependence on the orientation of the *IMF*. Thus the low values of Φ_{pc} under $Bz > 0$ conditions [< 30 *kV*] put a limit to the importance of viscous-like interactions. In fact Φ_{pc} gradually decreases to even lower values with increasing time since the *IMF* turned northward, implying that much of the residual voltage is in fact driven by continuing reconnection in the tail [*Xt in figure 1*] [*Wygant et al.*, 1983]. *Fox et al.* [1994] have shown how the ionospheric flow pattern can mimic viscous interaction processes as the polar cap contracts. They also found that the apparently-viscous voltage is enhanced when

the polar cap is contracting more rapidly, showing it is actually associated with the reconnection at X_t which caused the contraction. Thus the true level of viscous interaction voltage is the 5-10 kV observed several hours after a northward turning, when both the dayside and the tail *X*-lines [*X and* X_t *in figure 1*] are inactive. Note that viscously-driven voltages should be the same in both hemispheres, and the voltage on either flank should be matched in the two hemispheres.

The transpolar voltage □pc can often take on quite large negative values [sunward flux transfer] when the IMF is northward [Freeman et al., 1993]. This shows sunward or "reverse" convection and is primarily a phenomenon of the summer hemisphere polar cap [Crooker and Rich, 1993]. This is caused by reconnection at high latitudes between the magnetosheath field and the already-open flux of the tail lobe, and will discussed in section 5.5.

A second indication of the relative roles of reconnection and viscous-like processes is obtained by noting that the open field lines are transported antisunward out of the equatorial [XY] plane, whereas the antisunward transport of closed field lines will be seen in the equatorial plane as well as in the ionosphere. Observations of the voltage associated with anti-sunward flux transfer in the flanks of the magnetopause show it is small, typically <10 kV [Mozer, 1984]. These observations are, however, very difficult to make because the boundary motions will alter the amount of time that the satellite spends in the LLBL and the electric field is measured in the satellite 's frame and will be different in the moving frame of the boundary. However, this effect should cause both overestimation and underestimation of the voltage. Furthermore, boundary motions can be measured and accounted for with multiple craft and the voltage has been shown to be small in such cases [< 5 kV] similar to values deduced from □pc when the IMF has been northward for extended periods [Hapgood and Lockwood, 1995].

These observations show that reconnection is the dominant mechanism for the direct driving of magnetosphere-ionosphere convection, and the associated field-aligned currents.

5.4. The Svalgaard-Mansurov effect

As discussed in relation to figure 4b, low-latitude reconnection of the geomagnetic field with an IMF which has a large By leads to a motion of flux tubes in the ±Y direction, under the influence of the magnetic curvature force.

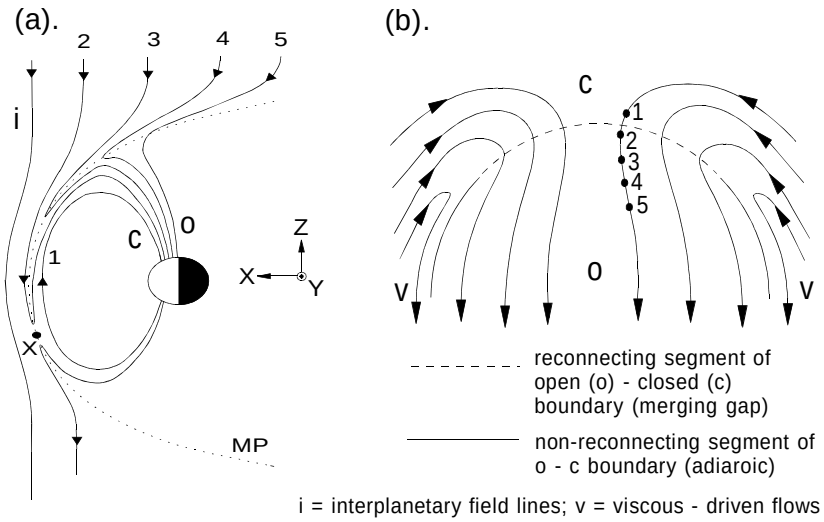

Figure 6. Schematic of the motion of newly-opened field lines away from a low-latitude reconnection site, X, when the IMF points southward. (a). Shows an noon-midnight section through the dayside magnetosphere, viewed from dusk and with the magnetopause as the dotted line MP. The field line 1 is closed (c), prior to being opened at X by reconnection with the draped interplanetary field line in the magnetosheath, i. Field lines 2-5 are open (o) field lines at different points in their subsequent evolution into the tail lobe. (b) shows the corresponding ionospheric flow streamlines in both hemispheres for steady-state conditions, the numbered dots being the locations of the field lines shown in (a): noon is at the top of the figure, dusk to the left and dawn to the right. The boundary between open and closed field lines is shown as a dashed line where it maps to the X-line (the "merging gap"), but as a solid line where it maps to a non-reconnecting segment of the magnetopause. The flows marked v are driven by viscous-like interactions between the magnetosheath flow and closed field lines.

This motion is communicated to the ionosphere [*by field aligned currents*] and this gives east or west flow, depending on the sense of By and the hemisphere in question. This effect was graphically illustrated by Greenwald et al. [1990] using conjugate radars to view the cusp regions in both hemispheres simultaneously. The effect was first noted in the E-region currents which correspond to these flows and is termed the Svalgaard-Mansurov effect after the scientists involved [see review by Cowley, 1981a]. In addition to the antisunward and sunward convection [and associated R1 and R2 field-aligned currents] discussed in the last section, figure 4d also shows the northern hemisphere flows [and associated R1/C field-aligned currents] corresponding to the By > 0 case presented in figures 4b and 4c [after Cowley et al., 1991b]. Westward flow is found on the straightening newly-opened field lines, immediately poleward of the open/closed boundary [OCB, shown as a dashed line] around noon. The momentum is transferred to the ionosphere by the field-aligned currents on the poleward and equatorward boundaries [C and noon R1, respectively] of this region [cf. figure 5]. The equatorward part of this pair lies near the open-closed boundary and so is generally taken to be part of the region 1 ring. The poleward part lies on open

field lines and is called the cusp or mantle currents. The origin of these currents at the magnetopause, in terms of the unbending of the kinked newly-opened field lines was discussed by *Saunders* [1989] and *Mei et al.* [1995].

5.5. Convection for southward and northward IMF

Figure 6_a shows a view from dusk of a newly-opened field line evolving away from a dayside reconnection site, *X*, during southward *IMF*. The positions of the field line are shown at times 1-5 [*in steady state this is also a snapshot showing the simultaneous positions of 5 different field lines*]. In position 1 the field line is closed [*c*] but in 2-5 it is open [*o*]. The reconnection site has deliberately been placed away from the geomagnetic equator to stress the precise location at which the field line is opened does not matter - other than the X-line must be between the two magnetic cusps to open closed flux *[this is what is here meant by a "low-latitude" X-line*]. Figure 6b is a simplified version of figure 4_d for *IMF By* ~ 0, which shows the corresponding locations of that field line in the F-region ionosphere. The flow is steady state and streamlines only cross the open-closed boundary at the ionospheric projection of X [*the dashed line*]. The viscously-driven cells are labelled *v*.

Figure 7_a shows one of the possible corresponding situations during northward *IMF*. In this case, the reconnection site *X* is at the front edge of one tail *lobe [here the northern hemisphere lobe*] and the reconnection takes place between already open field lines in the lobe and the draped sheath field lines. Figure 7_b shows the northern hemisphere ionosphere. The open-closed boundary is everywhere adiaroic as no low-latitude reconnection is taking place. The projection of *X* [*the dashed line*] is poleward of this boundary. The numbers show the evolution of an open field line, which remains open after reconnection at *X*, but such that it threads the boundary near the Earth, instead of at a large distance down the tail. This field line is then moved around the [*in this case*] dawn flank, under the competing influences of magnetic tension and sheath flow, and eventually would return to be reconfigured again at *X* [*if the reconnection remains active for longer than the circulation time*]. Thus this produces a circulation flow cell in the lobe. Figure 7_b is for *IMF By* ~ 0 and shows two symmetrical lobe cells [*L*] with reconfigured field lines passing to both the dawn and dusk sides. The other [*southern*] hemisphere lobe is not subject to this effect and would be stagnant other than for the viscous flow cells. This situation has recently been reported in observations for extended periods of time when the *IMF* is northward [*Freeman et al*., 1993].

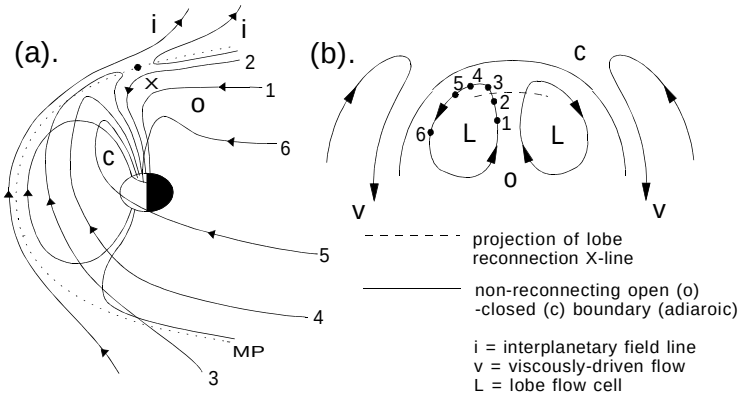

Figure 7. The same as figure 6, but for a steady-state case with reconnection at a northern-hemisphere lobe site, X, during northward IMF. In (a), the field lines 1 and 2 were opened during a prior period of southward IMF and have remained open: they are seen convecting towards X, where they are reconfigured (such that the point where they thread the magneto-pause is moved from the far tail to immediately sunward of X). Field lines 3-6 show the evo-lution of these reconfigured open field lines around the dusk flank of the Earth (in this case) forming a circulation in the polar cap. For the case of small B_y component of the IMF, there is a corresponding circulation on the dawn flank, and two symmetrical flow cells in the io-nospheric polar cap ("lobe cells", L) as shown in (b). These sit poleward of any viscously-driven cells, forming a four-cell pattern. In cases of large $|B_y|$ (not shown) one of the lobe flow cells will dominate, giving a three-cell pattern with a single circulation cell in the polar cap in the sense determined by the polarity of B_y.

Figure 7 therefore is consistent with the observations of large negative Φpc discussed in section 5.3, that voltage being between the centres of the two lobe cells. These are surrounded by the viscous cells giving a four-cell form of the overall convection. Figure 7 is also consistent with the observations of accelerated flows away from a lobe reconnection site by *Gosling et al.* [1991], and with the observations of accelerated flows towards the equator at low latitudes by *Paschmann et al.* [1990]. The latter are on field lines like 3 in figure 7 which are now often referred to as an "*overdraped lobe*" [*Crooker*, 1992].

Figure 8 considers a second situation which can occur during northward *IMF*. In this case, the overdraped lobe field lines [*ol*] are reconnected at a second *X*-line *X1* that is in the opposite hemisphere to *X*. This second reconnection re-closes the overdraped-lobe field lines, like 2 and 3, producing the closed field line 4. A four-cell flow pattern again results [*figure 8b*], but unlike the case in figure 7, the open/closed boundary is not all adiaroic, there is a merging gap [*dashed line*], with the opposite polarity voltage to that seen in the southward *IMF* case [i.e. *a dusk-to-dawn electric field*]. In this case, the southern hemisphere would also show a four-cell pattern with sunward flow in the central polar cap as the

open field lines are reconnected at *X1*. The principle difference from figure 8_b is that in the southern hemisphere there would be no projection of *X*.

A special case of figure 8 is when the same field line is simultaneously reconnected at X and X1, i.e. the two X-lines have the same footprint in both hemispheres. This is the original topology envisaged by Dungey [1963] when he first considered the northward IMF case. However, it requires a considerable coincidence for this to happen and the general case shown in figure 8 is much more likely [Russell, 1972] [note, however, X and X1 could swap hemispheres].

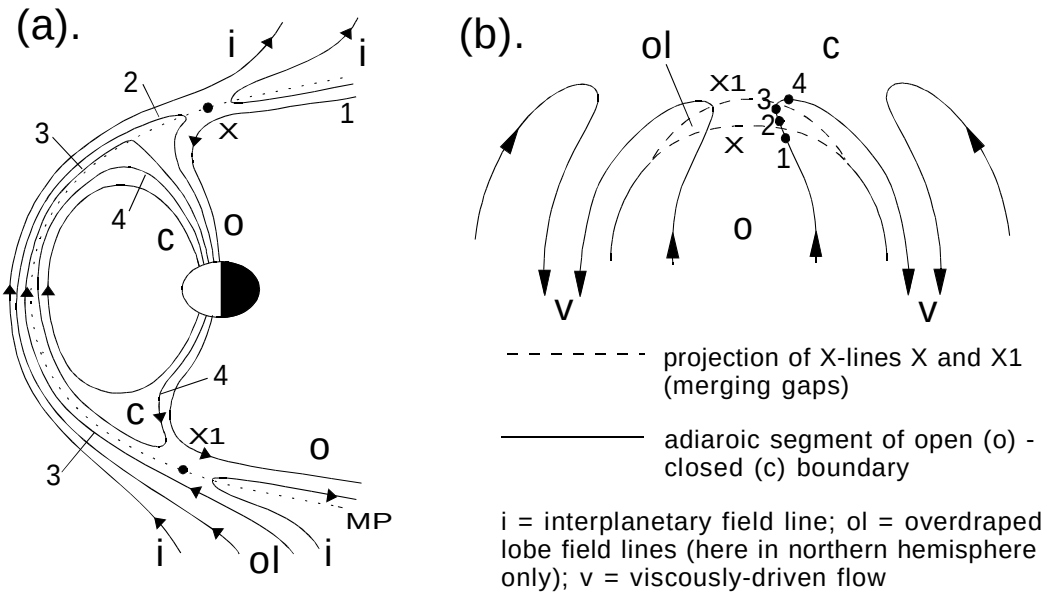

Figure 8. Same as figure 7 for a case when lobe reconnection occurs in both hemispheres (at X and X1). The reconnection site X produces "overdraped lobe" (ol) field lines (2 and 3), which are subsequently closed at X1 to give (4).

The topologies shown in figures 7 and 8 are not mutually exclusive. It is possible that *X* may be more extensive than X_1 and some overdraped field lines will be re-closed in the other hemisphere [*as in figure 8*] while others circulate around the dawn or dusk flank without further reconnection, as in figure 7. In addition, figures 7 and 8 are far from the only topologies possible for northward *IMF*, and the reader is referred to *Cowley* [1981b] and *Crooker* [1992] for further discussion. If the *IMF* |*By*| is large, one lobe cell dominates and the flow pattern becomes three-celled [*as in figure* 12_b] [*Heelis*, 1984].

6. The cusp

The previous sections have dealt with the momentum and electromagnetic energy transfer from the solar wind to the magnetosphere and dayside ionosphere. In this section we look at the mass transfer, which is also associated with some energy transfer in the form of the kinetic energy of the precipitating particles. This has been left until this section because the convection described in the previous section is a crucial factor in the precipitation characteristics, because of the velocity filter effect.

6.1. The velocity filter effect

In order to illustrate this effect and study its implications, it is valuable to again make magnetospheric field line straight and parallel [*as in figure 5*] [*Onsager*, 1994]. Generalisation for the real magnetospheric magnetic field is straightforward if we formulate the description of precipitation to ionospheric heights in terms of speeds and distances in the ionosphere and the time-elapsed since reconnection. This also has the great advantage of making it easy to generalise for non-steady-state situations [*Lockwood and Smith*, 1994; *Lockwood*, 1995a] [*section 7*]. This idealised magnetosphere is presented in figure 9, in both parts of which the magnetopause is on the left and the ionosphere on the right. The magnetospheric field lines are all horizontal and the field-aligned distance from the magnetopause to the ionosphere is d at all times. A uniform convection electric field is applied everywhere out of the diagram, so that flux tubes convect toward the top of the page at speed V_C. We will here be concerned mainly with precipitation into the ionosphere and, because the real magnetospheric field converges with decreasing altitude, there is a mirror force which acts on particles with a gyratory motion [i.e. *with a pitch angles greater than zero*] and reflects them back into the magnetosphere. The only particles which reach the ionosphere start with pitch angles close to zero, i.e. their motion is field aligned. We therefore here consider only zero pitch angle particles, which have a velocity V_i which is field parallel and an energy $e_i = (m_i v_i^2)/2$. Once injected across the magnetopause [*and in the case of ions significantly accelerated*] the particles are assumed to undergo adiabatic and scatter-free motion, which means that e_i and V_i remain constant. The distribution function *f(ei)* also remains constant under these circumstances, by what is known as Liouville's theorem. Thus the time-of-flight from the magnetopause to the ionosphere is $\tau_i = d/v_i$. If we consider a magnetopause source point P as shown in figure 9_a, the field line onto which the particles are frozen will have moved a distance dc from P by the time the particles arrive at the ionosphere, where

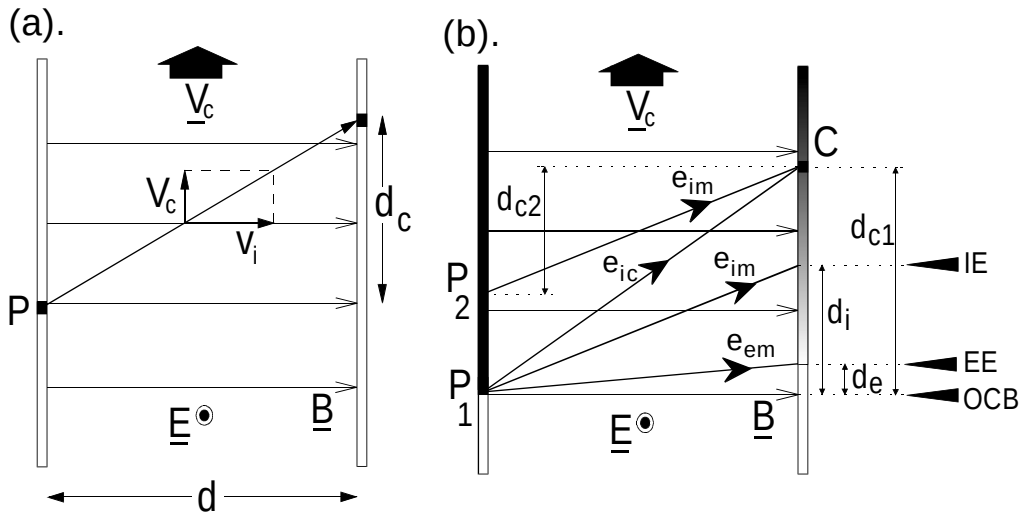

Figure 9. *Schematic explanation of the velocity filter effect. Magnetospheric field lines are considered straight, over the distance d between the magnetopause on the left and the ionosphere on the right. A uniform convection electric field is applied out of the plane of the diagrams, causing the field lines and the frozen-in plasma to drift up the page at speed V_c. (a) shows the distance d_c that an ion of field-aligned velocity V_i is convected during its time-of flight along the distance d. (b) shows such trajectories for the maximum energy electrons and ions (e_{em} and e_{im}) from P_1, forming the electron and ion edges (EE and IE, respectively). The shaded part of the magnetopause is an extended source region, as generated by opening field lines by reconnection at P_1 (i.e. the field line through P_1 is the open-closed boundary, OCB). At C a range of ion energies is seen between e_{ic} and e_{im}, corresponding to the range of source locations between P_1 and P_2*

$$d_c = \tau_i V_c = d \frac{V_c}{v_i} = d V_c \left(\frac{m_i}{2e_i} \right)^{1/2} \tag{24}$$

Thus the position where a particle from *P* participates into the ionosphere depends on its energy e_i. If we inject a full spectrum of energies e_i at one point *P* they are spread out according to Eq. 24 and we will only see ions [*of one species*] with one energy at any one point in the ionosphere [i.e. *the ionospheric spectrum for a point source is a delta function, irrespective of the spectrum injected at P*]. Different species are seen with energies in proportion to their masses. The energy detected in the ionosphere falls with increasing d_c and this dispersion is what we call the velocity filter effect. In the cusp we see both the convection velocity V_c and the energy-position dispersion showing the velocity filter effect [*Rosenbauer et al*., 1975; *Shelley et al*., 1976; *Reiff et al*., 1977]. However, we also see a range of ion energies at any one point and that shows that the source is not a point. Reconnection provides the ideal way of producing this extended source region because once a field line is opened the plasma streams continuously across

the boundary. A complication, however, is that the injected particle population changes with position and **J . E** , as discussed in section 4.5. Figure 9_b illustrates the extended source generated by reconnection, shaded black. The leading edge of the source region, P_1 , is the reconnection site and the field line through this point is the magnetic separatrix or open-closed field line boundary [*OCB*]. The point P_2 is downstream of the *X*-line such that each newly-opened field line produced at P_1 threads the boundary at P_2 at a certain time-elapsed since reconnection. The maximum energy of injected ions with detectable fluxes is e_{im}. The point *C* in the cusp ionosphere is a distance d_{c1} downstream from the ionospheric footprint of P_1 and a distance d_{c2} from that of P_2 . Ions of energy e_{im} from P_2 reach the point *C*, where Eq. *24* shows $e_{im} = (m/2)(d\ V_c/d_{c2})^2$. Ions of energy $e_{ic} = (m/2)(d\ V_c/d_{c1})^2$ reach *C* from P_1. Because $d_{c1} > d_{c2}$, $e_{ic} < e_{im}$ and because P_1 is the edge of the source region, d_{c1} is a maximum and thus e_{ic} is a minimum. Hence a range of ion energies between the maximum, e_{im} , and the lower cut-off, e_{ic} , would be seen at *C*, corresponding to the range of source locations between P_1 and P_2. Putting in typical values, *Lockwood and Smith* [1993] show that the source region for the cusp particles must be at least 10 R_E in extent along the magnetopause.

Figure 9_b also shows the trajectories of the ions and electrons from P_1 having the maximum energies with detectable fluxes, e_{im} and e_{em} . From Eq. 24, the peak-energy electrons reach the ionosphere at a distance d_e downstream from the *OCB* and form what is called the electron edge [*EE*] because no electrons can be detected upstream of this. The ions have a corresponding edge [*IE*] at di from the *OCB*, where $d_i » d_e$ because $m_i » m_e$ and $e_i \sim e_m$ [Eq. 24]. *Gosling et al.* [1990c] have reported a satellite pass near the magnetopause which showed exactly this predicted structure of electron and ion edges near the magnetopause. The observations also showed the corresponding evolution of the various magnetospheric particles as they began to escape along the opened field lines into the magnetosheath. However, it can also be noticed that although injected electrons were detected between the electron and ion edges, they were of low flux, and the electron flux increased considerably as the satellite crossed the ion edge, into the accelerated flow region where D-shaped injected ion distributions were observed. This phenomenon is not predicted for a simple velocity filter effect on the electrons, and is even more marked in the ionosphere [see *Onsager et al.*, 1993]. The answer is almost certainly associated with the fact that the cusp appears to remain quasi-neutral, i.e. the density of injected electrons remains almost equal to that of the ions [*Burch*, 1985], thus between the ion and electron edges few electrons precipitate because there has not yet been time for the ions to reach the ionosphere.

6.2. The magnetic cusp

The name "*cusp*" is derived from the dayside magnetic topology of field lines which extend to the dayside magnetopause. The concept of the cusp is as old as that of the magnetosphere itself, as both first appeared in the paper by *Chapman and Ferraro* [1931] [*who called the magnetic cusps* "*horns*"]. In figure 1, the magnetic cusp is the point about which the Chapman-Ferraro currents circulate. In a fully-closed magnetosphere, like that initially considered by Chapman and Ferraro, the cusp field line maps to a neutral point on the magnetopause.

In an open magnetosphere, a boundary-normal field B_n is added to those parts of the magnetopause where the newly-opened field lines evolve away from the reconnection site, which is very likely to include the magnetic cusp region. Typically field lines evolve along the magnetopause at $V_f \sim 250$ km s^{-1}, whereas the ionospheric convection speed is ~ 1 km s^{-1}. From Eq. 14 this corresponds to an ionospheric electric field of ~ 50 mV m^{-1}, given that the ionospheric field is $B_i = 5 \times 10^{-5}$ T . The boundary tangential electric field at the magnetopause can then be estimated for steady-state cases using Eq. 23 to be $E_t \sim 1$ mV m^{-1} [*this employs a circular flux tube with a typical magnetosphere field just inside the boundary of* $B_{sp} = 20$ *nT so that* $dl_m/dl_i = (B_i/B_{sp})^{½} = 50$]. Because $V_f = E_t/B_n$ we therefore find that the boundary normal field is typically $B_n \sim 4$ nT. Thus the boundary normal field is small compared to B_m and does not fundamentally alter the basic cusp topology.

There is, however, a significant effect of boundary-normal field on how field lines map from the magnetopause to the ionosphere. If we consider a fully-closed model of the magnetosphere, the entire magnetopause maps to a point cusp [*as, for example, in the empirical Tsyganenko models in which the boundary-normal field is zero almost everywhere because of the way the models are constructed*]. However, if low-latitude reconnection commences with constant voltage of 100 kV, the area of the cusp in the ionosphere grows at $10^5/(5\times10^{-5}) = 2 \times 10^9$ $m^2 s^{-1}$ and this growth continues for about 12 min., until the precipitation on the first-opened field lines is no longer called cusp [*Lockwood and Davis,* 1995]. *By* this time, the area of the ionospheric cusp has grown from 0 to its maximum of 1.44×10^6 km^2 . Given that the peak cusp width is observed to be roughly 5° of latitude [*about 600 km*], this means the longitudinal extent has grown to about 2000 km. This "*opening*" of the cusp has been modelled by [*Crooker et al.,* 1991]. Figure 1 is for equinox conditions whereas at the sol-stices the summer magnetic cusp is tipped toward the sun, while the winter cusp is tipped away. These dipole tilt effects will also have a diurnal variation.

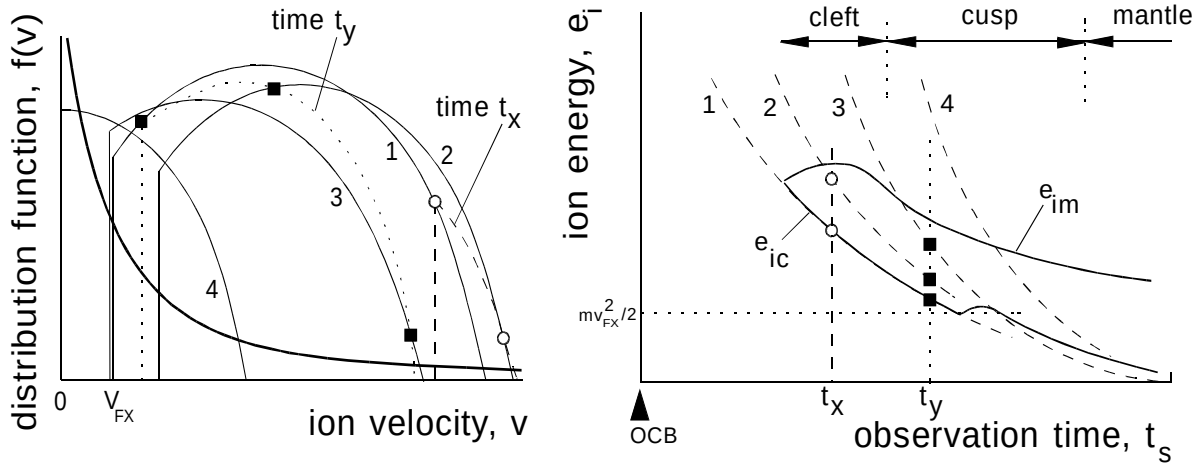

Figure 10. Injected magnetosheath ions at the magnetopause and in the ionosphere, and their evolution with time elapsed since reconnection. (a) shows the field-parallel sections 1-4 of the Cowley-D distribution functions in the (open) LLBL, injected across the magnetopause when the field line is at the X-line (1) and in positions 2-4 shown in figure 5. Because of time-of-flight effects, these are dispersed along the corresponding dashed lines in (b), which is an energy-time spectrogram for the steady-state case, also showing the minimum (e_{ic}) and maximum (e_{im}) energies of detectable ion fluxes. The latter is set by the one-count level of the instrument which typically varies with ion velocity as shown by the thicker solid line in (a). The distribution function seen at time t_x (in the cusp) and at t_y (in the cleft) are shown in part (a) by dotted and dashed lines, respectively. The solid squares and open circles show the correspondence of points in (a) to those in (b). [After Lockwood, *1995]*

6.3. The particle cusp

The discovery of magnetosheath-like plasma precipitating inside the magnetosphere [*Heikkila and Winningham*, 1971; *Frank*, 1971] was initially interpreted in terms of particle entry at the null points of the magnetic cusp; hence the particles were given the name "*cusp*". However, transfer of plasma into a null point is not an adequate explanation because a breakdown of frozen-in is still required to give transfer onto magnetospheric field lines. In addition, as shown in section 6.1, the dispersed cusp ion precipitation, with a range of energies seen at any one point in the ionosphere, rules out any point-like source like a magnetic null [*Lockwood and Smith*, 1993; *Onsager et al.*, 1993]. It was soon realised that magnetosheath plasma precipitated over a broad local time sector on the dayside, and so the additional concept of the "*cleft*", mapping to a closed *LLBL* field line torus containing sheath plasma, was introduced by *Heikkila* [1972]. Mechanisms for populating a closed *LLBL* with sheath plasma have been controversial, one possibility being the re-closure of open flux during northward *IMF* which is

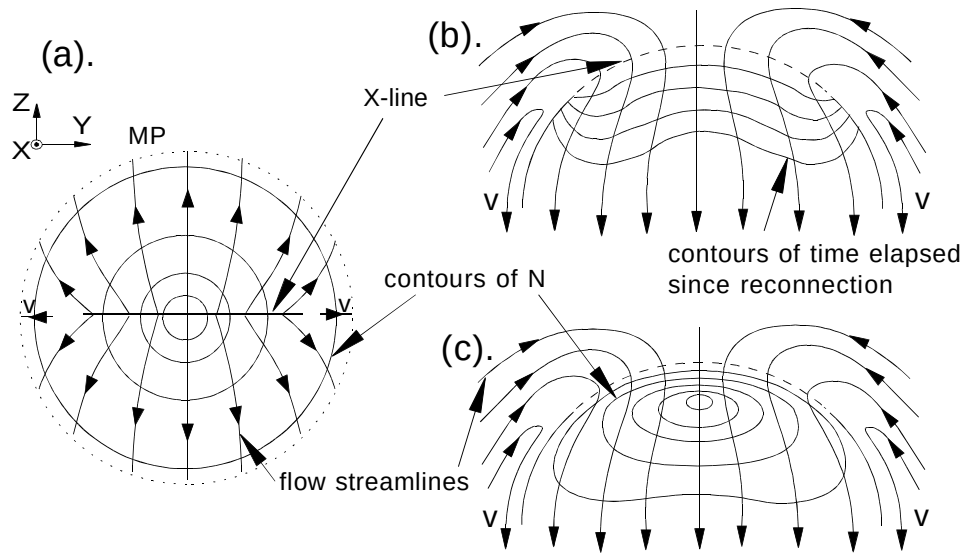

Figure 11. Flows and magnetosheath plasma densities for the situation described in figure 5. (a) is the view of the dayside magnetopause from the sun with the concentric circles being contours of the magnetosheath plasma density (just outside the magnetopause) and the arrows showing the magnetospheric flow streamlines (just inside magnetopause) along which the newly-opened field lines evolve (see figure 5_a). Viscously-driven flows are shown on the flanks of the magnetosphere. (b) and (c) show the corresponding steady-state ionospheric flows in both hemispheres (figure 5_b) along with contours of time-elapsed since reconnection in (b) and precipitating magnetosheath plasma density in (c).

illustrated in figure 8 [*Song and Russell*, 1992] which has been simulated using a global *MHD* model by *Richard et al*. [1994]. Alternatively smaller-scale patchy reconnection may do the same job [*Nishida*, 1989]. However, there is an argument that says there is no need to invoke a closed *LLBL* to explain cleft precipitation, as will be discussed below.

Hill and Reiff [1977] showed that the cusp ions precipitation did include ion energies consistent with the accelerated ions seen at the dayside magnetopause and recently *Lockwood et al.* [1994] have deconvolved the time-of-flight effects to show the precipitating ions to be consistent with the truncated, drifting Maxwellian at the dayside magnetopause, as predicted by *Cowley* [1982]. Thus the cusp is the ionospheric signature of the accelerated flows seen on the dayside magnetopause.

If we consider a field line in position 5 in figure 6 [*for southward IMF*], a satellite observing it in the ionosphere will see no ions from the point where it presently threads the magnetopause because they have not had time to reach the ionosphere. It will, however, be able to see ions from where the field line used to thread the magnetopause, when it was in positions 2-4. The highest energy ions would come from when the field line was in position 4 , whereas the lower cut-off

energy ions would have the longest time of flight and would have come from the *X*-line [*hereafter called position 1*], as illustrated in section (6.1). From the theory of the ion injection and acceleration discussed in section (4.5), along with the *Cowley and Owen* [1989] model of how a field line accelerates under magnetic tension and the sheath flow [i.e. *how V_f varies with position*], we can derive the sequence of injected ion spectra shown in figure 10_a for the field line positions shown in figure 6 [*Lockwood*, 1995a; b; *Lockwood and Smith*, 1994]. Notice how the minimum ion velocity V_{min} rises between positions 1 and 2 as V_f increases, but subsequently falls to zero as θ increases to greater than $\pi/2$. These truncated, drifting Maxwellian spectra are the field-parallel part of the Cowley-D distributions which reach the ionosphere without mirroring [*see figure 3_c*]. The ion spectra injected at any one point on the magnetopause are then dispersed in position according to Eq. 24, such that a satellite intersects different energies at different times. The dashed lines in figure 10_b show where the spectra in 10_a are dispersed . The plot is in the energy-time spectrogram format, showing the ion energy e_i as a function of observing time, t_s. This case is for a satellite which is moving poleward when the *IMF Bz* < 0 so that it is moving away from the open-closed boundary. The dashed lines are given by Eq. 24 with a satellite velocity $V_s = d_c/t_s$. Figure 10_b also shows the minimum [e_{ic}] and maximum [e_{im}] detected ion energies as solid lines. The minimum is set by the time-of-flight cut-off but the maximum is where the distribution function falls below the minimum detectable value, the "*one-count level*" shows as a solid line in 10_a.

At time $t_s = 0$ the satellite crosses the *OCB*. At t_x, it sees ions which were injected when the field line was in a range of positions, including 1 and 3, and the spectrum is as shown by the dashed line in figure 10_a: the open circles in both 10_a and 10_b show the part injected when the field line was in positions 2 and 3 [*remember both e_i and $f(e_i)$ are conserved for adiabatic scatter-free motion*]. At a later t_s [= t_y], when the satellite is further poleward, it sees the spectrum given by the dotted line [*the solid squares showing those ions injected when the field line was in positions 1, 2 and 3*]. In both cases, a clear cut-off energy [e_{ic} *in* 10_b] is seen. All ions at the cut-off come from near the reconnection site [*Lockwood et al.*, 1994]. The spectrum seen at t_y is very like that in the magnetosheath and would be classified as "*cusp*", whereas that at t_x has higher average energy and lower density, and would almost certainly be classified as "*cleft*". Figure 10_b shows that, in this case, they do not differ in the injection and transport processes and if one thinks of cleft as the projection of the *LLBL* it is here on open, not closed, field lines. As the time elapsed since reconnection increases the precipitation evolves from cleft to cusp to other classifications called "*mantle*" and "*polar cap*" [*Cowley et al.*, 1991a]. This is a key feature of the plasma entry

facilitated by reconnection. All the characteristics of the precipitating ions [*including the cut-off energy, e_{ic}, the density, N, and the temperature, T*] evolve as a function of time elapsed since reconnection as the field line migrates from the reconnection site into the tail lobe. From the above discussion, we see that this evolution has three causes: the changing characteristics of the sheath at the point where the field line threads the boundary; the changing ion acceleration on injection across the boundary; and the time-of-flight dispersion effects.

However, figures 6 and 10 are two dimensional and apply to the noon-midnight meridian only. This is investigated in figure 11. Figure 11_a is a view from the sun, with an *X*-line lying in the equatorial plane. The streamlines, along which the newly-opened field lines evolve away from the *X* line over the magnetopause, are shown along with the circular contours of magnetosheath density at the boundary. Parts (b) and (c) show the corresponding ionospheric flow streamlines, as in figure 6_b. Figure 11_b also shows the contours of time-elapsed since reconnection and 11_c shows the precipitation density, *N*. Along each streamline, the number density firstly rises with elapsed time since reconnection [*as lower-energy ions have time to arrive*] but then it maximises and falls because the particles begin to flow superthermally away from the Earth instead of precipitating. This can be seen in figure 11_c. However, there is another factor highlighted by 11_a, namely that the field lines reconnected near the *X* axis [$Y \approx 0$] will experience higher density inflow than those reconnected at larger $|Y|$, where sheath densities are lower. This is manifest as a local time variation in densities, which peak near noon in 11_c. In addition, the field line velocity V_f will be larger away from the stagnation region and so the ion acceleration will be greater [*giving larger ion energy, e*] at greater $|Y|$ where *N* is lower.

It is thus possible that the lower *N*/higher *e* precipitation away from noon is not a closed *LLBL* [*cleft*] precipitation, but also arises from the same processes as the higher density and lower energy cusp precipitation, as must be the case for the cleft near noon. This is consistent with the statistical patterns of the various classifications of magnetosheath precipitations presented by *Newell and Meng* [1992]. If we separate the precipitation into classifications of cleft, cusp, and mantle using the densities, figure 11_c looks very much like the Newell and Meng patterns. These statistical patterns show cleft and mantle precipitations covering the same broad *MLT* extent of the dayside, which is consistent with the idea that they share the same injection and transport processes: given that the mantle is on open field lines this implies the cleft is also. Figure 11_c shows why the higher-density cusp has a somewhat smaller *MLT* extent. The origin of the small step in the characteristics used by *Newell and Meng* [1988] to distinguish cleft from cusp is unclear in this interpretation.

6.4. The cusp aurora

The magnetosheath electrons and ions which precipitate into the cusp/cleft ionosphere generate a characteristic aurora. The relatively low energies of these particles means that the aurora is dominated by 630 and 636.4 nm [*red line*] emissions of atomic oxygen, with much lower intensities of the 557.7 nm [*green line*]. This is because the $^1D_2$ electron state is readily excited [*1.96 eV above ground state, the ^3P doublet*] whereas very few atoms are excited to the $^1S_0$ [*4.17 eV above the ^3P*]. The excitation is largely caused by the elevation of the ionospheric electron temperature such that the electrons on the hot tail of the ionospheric gas are very efficient in exciting the $^1D_2$ state [*Rees and Roble*, 1986; *Mantas and Walker*, 1976; *Wickwar and Kofman*, 1984].

A complication in interpreting images of the cusp/cleft emissions is that the $^1D_2$ state de-excites [*with the emission of a red line photon*] after a radiative lifetime which, if unquenched, has a value of 110 s [*compared with 0.74 s for the green line*]. During this time the excited atomic oxygen moves with the thermospheric wind [*typically 0.5 km s^{-1}*] and so emission occurs at an average distance of $\sim 110 \times 0.5 = 55$ km downwind from the point of excitation. However, there is a spread of lifetimes, and hence distances, if quenching by collisions is present, and the image will be smeared. In addition, the altitude of the excitation is not well known and a lower altitude gives more quenching and the lifetime is reduced.

A region of dominant red-line emission was first reported by *Sandford* [1964]. This was shown to poleward of the more energetic dayside auroral precipitation by *Eather and Mende* [1971]. The association with the newly-discovered cusp precipitation was made by *Heikkila* [1972]. Recent observations have shown that this red-line aurora either contains, or is made up of, a series of poleward-moving events when the *IMF* is southward [e.g. *Sandholt et al.*, 1985; 1992; *Fasel*, 1995].

6.5. The cusp ionosphere

The electron heating in the cusp region which was invoked above as a major cause of the cusp/cleft aurora was inferred in a statistical survey of the topside ionosphere by *Titheridge* [1976] and has been directly observed by satellite [*Brace et al.*, 1982; *Curtis et al.*, 1982] and incoherent scatter radar observations [*Wickwar and Kofman*, 1984; *Watermann et al.*, 1994]. With very high time resolution [*10s*] measurements, *Lockwood et al.* [1993] have recently reported that the electron temperature enhancements can sometimes only consist of a series of poleward-moving events, very similar to the behaviour of the red-line auroral transients mentioned in the previous section.

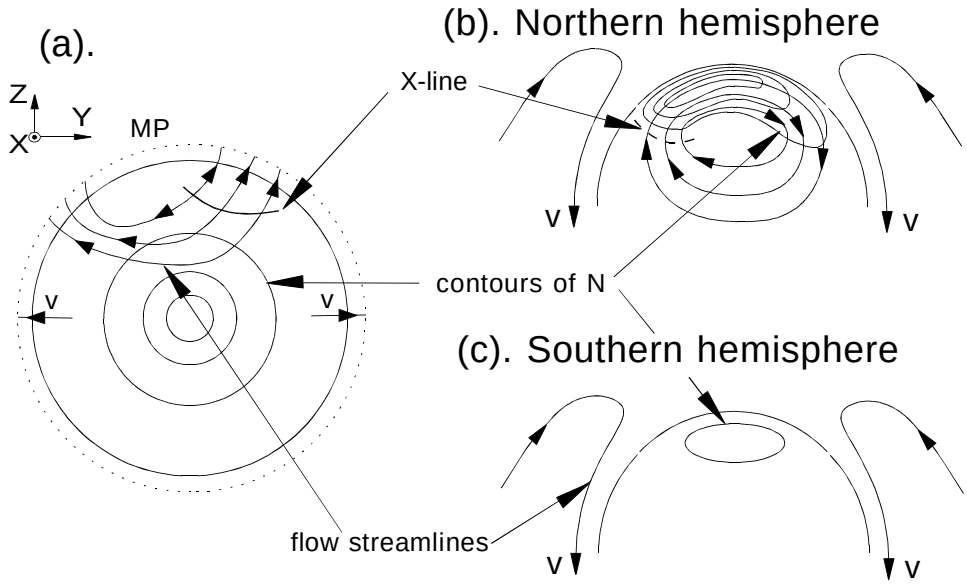

Figure 12. (a) is equivalent to figure 11, for the case with IMF $B_z > 0$, IMF $B_y > 0$ and reconnection in the northern hemisphere lobe only. (b) and (c) are equivalent to figure 11(c), for the northern and southern hemisphere ionospheres, respectively.

The behaviour of the plasma densities in the cusp/cleft region is complex. The precipitating particles enhance the densities as well as the electron temperatures. However, unlike the temperature which reaches peak values almost instantly after the precipitation commences, the density grows while the precipitation persists[*Whitteker*, 1977; *Watermann*, 1994]. Note that this residence time of a field line in the cusp precipitation region does not depend on the ionospheric convection speed, but on how quickly the field line evolves over the magnetopause to the region where the flow is superthermally tailward thereby cutting off access to the ionosphere. We can estimate the residence time from the behaviour of the low-energy cut-off ions observed in the cusp: e_{ic} in the cusp region falls from about 5 keV to 100 eV which, for a distance of 16 R_E from the *X*-line to the ionosphere, correspond to flight times of about 104 s and 737 s, respectively. During the difference in time-elapsed since reconnection of 10.5 min., the cusp is seen. This is sufficient for a considerable enhancement of the F-region [*a factor of about 2-4 over typical winter values*]. However, the cusp region is also where the tension force on newly-opened field lines can generate fast convection in the east-west direction if |*By*| is large [*section 5.4*]. These fast flows act to deplete the plasma and reduce the enhancement caused by the cusp precipitation [*Rodger*, 1994]. The fast flows will also cause strong ion heating, a molecular rich iono-

sphere, anisotropic and non-Maxwellian ion velocity distributions and are very likely to be involved in generating the plasma upflows into the magnetosphere that are called the cleft ion fountain [*Lockwood et al.*, 1985a; 1985b].

6.6. The cusp currents

Sections 6.1-6.5 show that the term cusp is applied to many different phenomena. Another example of this are the *By*-dependent field-aligned currents which bring the east-west flows associated with the Svalgaard-Mansurov effect to the ionosphere [*McDairmid et al.*, 1978; *Taguchi et al.*, 1993]. These are often referred to as the cusp currents. Some authors have preferred the title 'mantle' currents because they are sometimes found in the precipitation region termed mantle, rather than in the cusp precipitation region. This debate is best understood in terms of the evolution of the newly-opened field lines: the precipitation evolves from cusp to mantle classifications roughly 12 min after reconnection [*see the previous section*]. This is also roughly the time scale for a field line to straighten. As the field-aligned currents on newly-opened field lines are associated with this unbending, we should expect them to be close to the cusp/mantle boundary, but they can be in either region in any one case. The pattern of field-aligned currents for non-zero *IMF By* shown in figure 4_d was proposed by *Cowley et al.* [1991b] from considerations about how newly-opened field lines will evolve. Thus they were able to make predictions of where the particle precipitations of various classifications will be seen relative to the field-aligned currents. Initial studies by *de la Beaujardiere et a*l. [1993] are consistent with these predictions.

6.7. The northward IMF cusp

I have concentrated on the cusp during southward *IMF*. This is because relatively little is known, and even less understood, about the northward *IMF* cusp. Figure 12_a corresponds to figure 11_a for the case with a lobe reconnection site in the northern hemisphere and *IMF By* > 0. Figure 12_b shows the circulation in the open field line region which results, as discussed in section (5.5). The reconnection reconfigures open field lines which thread the magnetopause far down the tail and along which there is little or no cusp precipitation. After reconfiguration the field line thread the dayside magnetopause and cusp precipitation results with reverse dispersion seen where the convection is sunward [*figure* 12_b].*Woch and Lundin* [1992] have demonstrated that the accelerated ions are found on the poleward edge of such reverse dispersion signatures for sunward convection during northward *IMF*, as opposed to the equatorward edge for antisunward convection during southward *IMF*. In the other hemisphere [*figure* 12_c], there is no lobe circulation and field lines only thread the tail magnetopause. Thus there will be little magnetosheath-like precipitation, and any there is will continue to decay in energy and density as the field lines are

further extended down the tail. Following a turning of the *IMF* from southward to northward, the precipitation may persist for longer than the time constant with which the flow in the polar cap decays and then we may be able to observe a stagnant cusp precipitation, albeit briefly [e.g. *Potemra et al*., 1992]. However, the time constant for flow decay appears to be 10-20 min. [*see sections 5.2 and 7.2*] which is comparable with, or longer than, the time of about 12 min. in which the precipitation classed as cusp evolves into the precipitation classed as mantle. Thus observations of a broad, stagnant cusp precipitation during northward *IMF* could imply that the satellite is moving roughly perpendicular to the flow streamlines and along lines of constant elapsed time since reconnection [e.g. *a meridional pass at noon in figure* 12_b].

Another possibility is that field lines have been reconnected away from the nose of the magnetosphere, such that the tension force is closely matched to and almost balances the sheath flow. In such cases, it may be possible for the field line to be held for an extended period such that it threads the dayside magnetopause, thereby generating a stagnant, undispersed yet dense cusp precipitation. Note that the small V_f would mean that there would not be any accelerated ions in such cases.

7. Non-steady state

In section 6, brief mention was made of recent observations of transient events in the dayside cusp region. It is not a coincidence that these have all been detected using ground-based instruments. Satellite data suffer from what is known as spatial/temporal ambiguity. For example, a low-altitude satellite has an orbital period of about 90 min. *By* comparing data from successive orbits we can study fluctuations which are of period 90 min. or greater. Similarly, if we are not concerned with spatial structure of scale less than, say, 10 km [*which the satellite covers in about 1 s*], we can study fluctuations of 1 s or faster using the satellite. However, there can be no information on the range of periods between about 1s and 90 min from such an ionospheric satellite. Ground-based remote-sensing instruments, on the other hand, can observe the same region of space for several hours and can achieve time resolutions of 1s or less. Thus they are ideal for observing the periods which satellites cannot.

One of the key variations which has been studied in the ionosphere is the substorm cycle [*period usually 1 - 3 hours*]. On the dayside, there has also been much interest in fluctuations in the cusp region on time scales of several minutes. Both are beyond the Nyqvist sampling limit of ionospheric satellites.

7.1. Substorm growth phase

Careful inspection of figure 1 shows that some of the Poynting flux flow lines [*dashed lines*] which emanate from the *HLBL* end in the tail lobe rather than at the tail neutral sheet. The lobe is a sink of Poynting flux if there is a positive $\partial \Phi_T / \partial t$ [*Eq. 21*] and energy is stored as magnetic energy because the tail lobe flux increases. This storage can be because either the lobe field increases or the tail cross section area increases [*tail flaring*], or both. In either case, the total tail lobe flux increase is caused by the rate at which field lines are opened at X exceeding the rate at which they are closed at X_t. Such an imbalance is expected following a southward turning of the *IMF*, when the dayside reconnection responds very rapidly to the appearance of increased magnetic shear across the low-latitude magnetopause. However, there is no way that this information can be transmitted to a distant *X*-line in the tail, where the reconnection remains unaffected for a period of 30 min. or more [*Cowley and Lockwood*, 1992]. *By* Faraday's law, the difference between the dayside and nightside reconnection voltages is the rate of increase of the open flux [$\partial \Phi / \partial t > 0$]. This corresponds to an increase in the energy stored and, because the ionosphere is incompressible, will be signalled by an increase in the area of the open field line region in the ionosphere [*Akasofu et al.*, 1992]. From Eq. 23, this rate of change of the lobe flux causes the steady-state electric field mapping to break down, such that the dawn-dusk electric field in the ionosphere is less than it would be in steady state. Thus the electric field in the *HLBL* during the growth phase has two effects: it causes deposition of energy in the tail and causes some flow/electric field in the ionosphere. The latter is called the directly-driven system. When averaged over several substorm cycles, there is no nett change in F and so there must be other periods in the substorm cycle [*in the expansion/recovery phases*] in which there is destruction of lobe flux. The flows/currents associated with release of the stored energy/flux in the tail lobe is called the storage system. Thus on average, steady-state mapping of electric fields from the magnetopause to the ionosphere will apply, but it does not apply at any one instant. This was deduced from observations of the response of ionospheric convection to changes in the *IMF* by *Lockwood et al.* [1990]. These observations indicate the 10-20 min inductive smoothing time constant [*for both rising and falling flows*] discussed insection 5.2.

These concepts have been vital in understanding non-steady state situations following changes in *IMF* orientation [*Lockwood et al.*, 1990]. The variability of the polarity and strength of *IMF Bz* [*Lockwood*, 1991; *Lockwood and Wild*, 1993] is such that it fluctuates much more rapidly than the time constant for the magnetosphere-ionosphere system to approach steady state, and we should therefore expect non-steady behaviour to be normal rather than exceptional and the ionosphere-magnetosphere system to usually be in non-equilibrium states of transition. Indeed, it is possible that the rare steady convection events [*also called*

convection bays, Sergeev et al., 1994] are caused by a coincidental *IMF* fluctuation which happens to cause the dayside reconnection voltage rate to remain close to that in the nightside tail for an extended period.

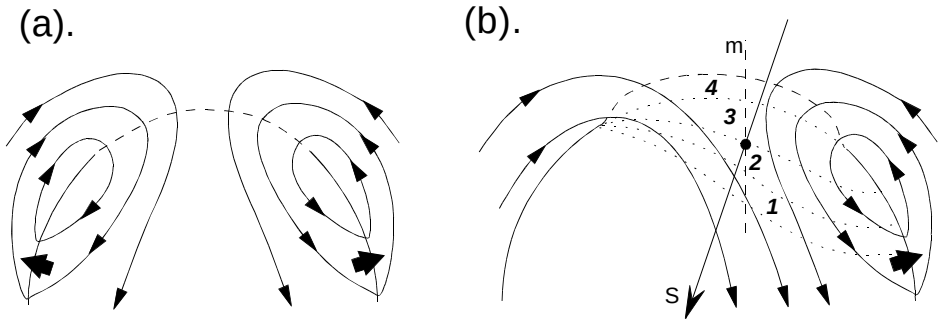

Figure 13. Ionospheric flow for the non-steady state magnetosphere-ionosphere system when the dayside reconnection voltage exceeds the tail reconnection voltage, as during substorm growth phases. This causes expansion of the polar cap region of open flux, as shown by the solid arrows. The merging gap is shown as a dashed line and adiaroic segments of the open-closed boundary are solid lines. Note flow streamlines cross the moving adiaroic boundaries (in the Earth's frame) although the plasma and frozen-in flux do not: no reconnection is taking place at the corresponding segment of the magnetopause and the boundary and plasma move together in the boundary-normal direction. (a) flow for IMF $B_z < 0$, $B_y = 0$. (b). flow in the northern hemisphere for pulsed reconnection for IMF $B_z < 0$, $B_y > 0$. The regions of newly-opened flux 1-4 are produced by successive reconnection bursts. S shows a typical path of a low-altitude polar-orbiting satellite and m the meridian scanned by a dayside auroral photometer.

7.2. The behaviour of the open-closed boundary

Siscoe and Huang [1985] introduced the important concept of non-reconnecting parts of the magnetopause which map to "*adiaroic*" [*meaning "not flowing across"*] segments of the open-closed boundary in the ionosphere. In the boundary rest frame, the flow speed must be zero [*there is no flux transport from closed to open field lines, i.e. no reconnection*]. However, if the adiaroic boundary moves in the Earth's frame, this means that there will be plasma/field line flow in the Earth's frame also. As a result, flow streamlines will cross moving adiaroic segments of the open-closed boundary, although the plasma and frozen-in flux tubes do not cross the boundary. This cannot happen in steady state, for which there are no boundary motions and hence flow streamlines only cross the open closed boundary at the merging gaps.

The fact that electric fields do not map from the magnetopause to the ionosphere is also important to our understanding of how the open-closed boundary will behave. Until recently most data was of poor time resolution or so highly averaged that scientists became very familiar with the steady-state concepts of mapping electric fields. However, consideration of one of a number of non-steady situations soon leads to an appreciation that this concept cannot be applied on shorter time scales. For example, following a northward turning of the *IMF*, the noon open-closed boundary [*and the last-to-have-been-opened field lines immediately poleward of it*] initially relax poleward. However, the subsequent behaviour if the *IMF* persists in its northward orientation reveals that magnetopause electric fields do not map to the ionosphere. Were the magnetopause electric field to map to the ionosphere in this case, the last-opened field lines [*still in the solar wind and thus still subject to the dawn-to-dusk motional electric field*] and the open-closed boundary would continue to migrate poleward and into the nightside. This does not happen. The cusp/cleft aurora ceases moving poleward roughly 10-20 min after a northward turning and satellite particle observations do not reveal such nightside locations of the sunward edge of the polar cap boundary. Because there is no low-latitude reconnection, the dayside polar cap boundary will be adiaroic following a northward turning. Thus there will initially be poleward flow at the same speed as the boundary motion, but both this flow and the boundary motion will decay over the 10-20 min inductive smoothing time.

Siscoe and Huang [1985] demonstrated how a two-cell flow pattern can arise for a simple circular and expanding polar cap, with dayside but no nightside reconnection [i.e. *in the growth phase of a substorm*]. This situation is depicted in figure 13_a. The dashed line maps to an active dayside reconnection *X*-line. The flow into the polar cap causes it to expand. The solid segments of the open closed boundary are adiaroic and these expand outward, as shown by the thick arrows near dawn and dusk. The plasma and frozen-in flux tubes move with the adiaroic boundaries and the flow streamlines cross the boundary, although there is no closure of the open flux there.

7.3. Effects of reconnection rate pulses

Section 4.6 discussed how reconnection rate pulses are thought to generate characteristic signatures at the magnetopause called flux transfer events. In recent years there has been much interest in understanding what the ionospheric signatures of such events would look like and hence determining their size and contribution to the total flux transfer rate from the dayside to the nightside [i.e. *to the transpolar voltage* Φ_{pc}].

Given that the ionospheric flows have a 10-20 min. rise time following a reconnection pulse, a short pulse will initially cause the open-closed boundary to migrate equatorward, rather than exciting poleward flow. This effect is seen in the equatorward edge of cusp precipitation [*Burch*, 1973], in radar observations of the cusp [*Foster et al.*, 1980] and in optical observations of the cusp/cleft aurora [*Sandholt et al.*, 1985; *Pudovkin et al.*, 1992]. *Cowley and Lockwood* [1992] have provided an explanation of the subsequent flows as the magnetosphere-ionosphere system attempts to return equilibrium with the new amount of open flux, with reduced magnetic flux in the dayside magnetosphere and more in the tail lobe. A key prediction of this model is that each region of newly-opened flux produced by a reconnection burst is appended directly sunward of that produced by a prior reconnection burst and these regions are abutted up against each other. This situation is shown in figure 13_b. In this sketch, the reconnecting segment of the open-closed boundary [*dashed line*] has just produced the patch 4 by migrating equatorward in response to a fourth reconnection pulse. The previous three pulses produced patches 1-3, which are abutted and separated by dotted lines. The flows and evolution of the patches are shown for *IMF By* weakly positive in the northern hemisphere. If the reconnection pulses repeat on a period shorter than the inductive smoothing time, the poleward flow will be relatively constant and the patches produced by successive reconnection pulse drift poleward together. This gives an explanation of the poleward-moving events of enhanced electron temperature [*Lockwood et al.*, 1993] and of the red-line auroral transients in the cusp region [*Sandholt et al.*, 1992].

A reconnection pulse must give growth in area of a patch of newly-opened flux in the ionosphere and we would expect magnetosheath electron precipitation on these newly-opened field lines. The patch of 630 nm-dominant aurora thus formed should then migrate with the newly-opened field lines and fade as the they become appended to the tail lobe [*10-20 min later*]. The direction of the motion would initially be controlled by the polarity of the *IMF By* component, by the Svalgaard-Mansurov effect. Later in their lifetime, when the magnetic curvature force is reduced, events would move more poleward under the influence of sheath flow. All these features are indeed observed in transient cusp events seen in 630 nm emissions [*Sandholt et al.*, 1992; *Lockwood et al.*, 1995]. Furthermore, simultaneous radar data show that there are plasma flow bursts within each optical event when |*By*| is large, and the plasma moves with the same velocity as the event as a whole, as expected if the patch is made up of newly-opened field lines produced by a reconnection burst [*Lockwood et al.*, 1989]. *Pinnock et al*. [1993] have shown that one of a string of such flow bursts was an elongated channel coincident with the cusp precipitation. The occurrence of these events is very similar to that of *FTEs*, in that they occur almost exclusively during southward *IMF* when they repeat with a skewed distribution of periods about a

mean of 7 min [*Fasel*, 1995], strikingly similar to that for *FTEs* [*Lockwood and Wild*, 1993]. The evidence that they are caused by reconnection pulses and thus related to magnetopause *FTEs* is therefore very strong indeed. However, on only one occasion have simultaneous observations of the two phenomena been possible [*Elphic et al*., 1990].

Figure 13_b also provides an explanation of the phenomenon of cusp ion steps. Because each patch is produced by a discrete reconnection burst, the elapsed time since reconnection changes discontinuously across the boundaries which separate the events. Section (6.3) showed how the cusp precipitation characteristics are a function of the time elapsed since reconnection [*including the lower cut-off energy, e_{ic} , and the density, N*]: thus we expect discontinuous changes in the precipitation at each step, as seen for example by the satellite *S* at *p* in figure 13_b. Cusp ion steps were predicted from the flow excitation theory of *Cowley and Lockwood* [1992] by *Cowley et al*., [1991] and were independently reported in observations by *Newell and Meng* [1991]. *Lockwood and Smith* [1992] have inverted the theory to allow the reconnection rate to be computed from the dispersion characteristics. *Lockwood and Smith* [1994] have extended the theory to allow for cases when the satellite is moving toward/away from the open-closed boundary more slowly than the convection speed [i.e. *longitudinal passes by an ionospheric satellite or for a mid-altitude satellite*]. In these cases the steps can take on a variety of different forms. The observations by *Lockwood et al* [1993] of cusp ion steps on the boundaries between poleward-moving events are important support for the theory of the effects of pulsed reconnection as they show that the two predicted features are indeed related.

7.4. Travelling convection vortices

There are other transient events in the cusp ionosphere which have not received much attention in this tutorial. Chief amongst these are travelling convection vortices [*TCVs*] which are seen throughout the dayside, usually using chains and networks of magnetometer stations [*Friis-Christensen et al*., 1988; *Glaßmeier et al*., 1989]. These events appear to travel away from noon around the polar cap boundary in both the afternoon and morning sector, unlike the *By*-dependent motion of the poleward-moving auroral and radar events discussed in the previous section. They have the form of a matched pair of filamentary field aligned currents, like figure 5, but whereas an *FTE* event would move in the direction from C to D, such that the convection velocity in the event centre was equal to the phase velocity of the event, *TCVs* travel perpendicular to that direction and at a faster phase speed [*of order 5 km s^{-1}*]. There are flow vortices associated with these events [*speeds of about 1 km s^{-1}*] [*Lühr et al*., 1995] and as an event passes east/west over a meridian, a tripolar poleward flow signature is seen for a twin vortex event. This is very different from the reconnection pulse events [*for which the inductive smoothing yields a steady poleward flow with a*

small modulating ripple at the frequency of the reconnection pulses, along with periodic longitudinal flow bursts if the IMF |By| is large]. TCVs have in the past been confused with *FTE* flow burst events, for example, it is now clear that the flow burst event described by *Todd et al*. [1986] was in fact a *TCV* [*Lühr et al.*, 1993]. Similarly, what are now called *TCVs* have also been interpreted as rapid motions of the cusp [*Potemra et al*., 1992] and so-called plasma transfer events [*Heikkila et al*., 1989].

TCV's have been linked with buffeting of the magnetosphere by solar wind dynamic pressure changes, and this is an integral part of the theory of *Kivelson and Southwood* [1991]. The resulting propagating deformation of the magnetopause causes a flow vorticity and drives the filamentary field-aligned currents. The phase motion of the events then corresponds to the motion of the deformation around the magnetopause. However, one major mystery is the appearance of magnetosheath-like precipitation in these events, particularly in the upward field-aligned current filament [*Potemra et al*., 1992], causing an auroral transient which appears to be on closed field lines as it moves longitudinally equatorward of the cusp/cleft aurora [*Lühr et al.*, 1995; *Heikkila et al.*, 1989]. *TCVs* do often occur in a series of events, and this may offer an explanation of the multiple injection events, seemingly onto closed field lines, reported by *Woch and Lundin* [1991]. One valid and viable mechanism, which may fit with the dynamic pressure pulse model of *TCVs*, is of enhanced magnetosheath density patches which indent the magnetopause to the extent that reconnection takes place behind the embedding filament, as simulated by *Ma et al.* [1991]. However, these ideas remain mere speculation in relation to *TCVs* at the present time. *Lockwood* [1995b] has shown that some of the multiple injection events may be fitted into a single *X*-line reconnection model if fluctuations in the sheath density cause changes the magnetopause Alfvén speed.

7.5. Poleward-propagating longitudinal flow changes

Section 5.4 showed how longitudinal flows in the dayside cusp/cleft ionosphere were driven when the *IMF* $B_z < 0$ and $|B_y|$ is large, by the magnetic curvature force on the newly-opened field lines. Thus if the *IMF* B_y shows periodic oscillations during southward *IMF*, we would expect the longitudinal flow in the ionosphere to oscillate in polarity [*provided the period is not too short compared to the response time*]. These changes would migrate poleward with the reconnection-driven antisunward flux transfer. Such events have recently been reported by *Stauning et al*. [1994] and fit very well with the expectations of the magnetic curvature force effect. Several authors have suggested that these poleward-moving disturbances are the same as the poleward-moving transient events discussed in section 7.3 and thus the latter are simply the effects of *IMF* B_y changes with steady reconnection rate [e.g. *Newell and Sibeck*, 1993]. However,

this would produce a patch of red-line aurora of roughly constant area which would be swept back and forth in the east-west direction by the flow changes: in fact the poleward-moving auroral events show consistent and repetitive motion to the east or west [*depending on the sense of the IMF By*] [*Lockwood et al*., 1995]. In addition, the flow bursts are still seen when the *IMF By* is large but steady. Hence these two phenomena are quite distinct.

8. Summary

This tutorial has given the basic concepts which allow us to gain a considerable understanding of how energy, mass and momentum are transferred from the solar wind into the ionosphere. The basic of paradigm of ideal *MHD* applying everywhere, except at a few localised breakdowns where reconnection takes place, as originally conceived by *Dungey* [1961], is remarkably successful. One might have expected progress in recent years to have revealed more cases in which this paradigm is inadequate. However, the opposite has proven to be true and our improved understanding has allowed more phenomena to be understood in these terms. In addition, the publication record shows that this model is the only one which has had genuinely predictive power in the area of solar-wind magnetosphere coupling. Numerical simulation results increasingly are able to reproduce simpler conceptual explanations. However, this is not to say that all is understood. Some key areas where our understanding is lacking include: the maintenance of cusp quasi-neutrality; the origin of structured cusp electron precipitation [*and hence of the gaps between the 630 nm transients*]; the electron acceleration to give 557.7 nm transients; the origin of magnetosheath-like precipitation in *TCVs*; origins of multiple injection events; effects of magnetosheath Alfvén speed changes; the causes of viscous-like interactions; the variations of the inductive smoothing time constant and its effects; the spectrum and causes of reconnection rate variations in both time and space. With new facilities like the *Cluster*, *Interball* and *Geotail* satellite missions, the *EISCAT Svalbard Radar*, the *CUTLASS SuperDARN* radars and many others, we have a genuine opportunity to answer some of these puzzles.

Acknowledgements:

The author gives particular thanks to Prof. S.W.H. Cowley for his remarkably clear help, tuition and insight.

9. References

Akasofu S.-I., C.-I. Meng, and **K. Makita**, Changes of the size of the open field line region during substorms, *Planet. Space Sci., **40**,* 1513-1524, 1992.

Alfvén H., and **C.-G. Fälthammar**, Cosmical electrodynamics, Clarendon Press, Oxford, 1963.

Aubry M. P., C. T. Russell and **M. G. Kivelson**, Inward motion of the magnetopause before a substorm, *J. Geophys. Res., **75***, 7018, 1970.

Berchem J., and **C. T. Russell**, Flux transfer events on the magnetopause: Spatial distribution and controlling factors, *J. Geophys. Res., **89***, 6689-6703, 1984.

Biernat H.K., M.F. Heyn, and **V.S. Semenov**, Unsteady Petschek reconnection, *J. Geophys. Res., **92***, 3392-3396, 1987.

Brace L.H., R.F. Theis, and **W.R. Hoegy**, A global view of the F-region electron density and temperature at solar maximum, *Geophys. Res. Lett., **9**,* 989-992, 1982.

Burch J.L., Rate of erosion of dayside magnetic flux based on a quantitative study of polar cusp latitude on the interplanetary magnetic field, *Radio Sci., **8***, 955-961, 1973.

Burch J. L., Quasi-neutrality in the polar cusp, *Geophys. Res. Lett., **12**,* 469-472, 1985.

Chapman S. and **V.C.A. Ferraro**, A new theory of magnetic storms. Part I. The initial phase, *Terr. Mag. Atmos. Elect., **36**,* 77, 1931.

Coroniti F.V. and **C.F. Kennel**, Can the ionosphere regulate magnetospheric convection?, *J. Geophys. Res., **78***, 2837-2851, 1973.

Cowley S.W.H., Magnetospheric asymmetries associated with the Y-component of the *IMF*. *Planet Space Sci., **29**,* 79, 1981a.

Cowley S.W.H., Magnetospheric and ionospheric flow and the interplanetary magnetic field, in *Physical basis of the Ionosphere in the Solar-Terrestrial System*, AGARD CP-295, pp. 4/1-4/14, 1981b.

Cowley S.W.H., The causes of convection in the Earth's magnetosphere: A review of developments during IMS, *Rev. Geophys., **20***, 531-565, 1982.

Cowley S.W.H., Solar wind control of magnetospheric convection, in *Achievements of the international magnetospheric study, IMS*, pp483-494, ESA SP-217, ESTEC, Noordwijk, The Netherlands, 1984.

Cowley S.W.H., Acceleration and heating of space plasmas: basic concepts, *Annales Geophys.*, ***9***, 176, 1991.

Cowley S. W. H and **M. Lockwood**, Excitation and decay of Solar wind-driven flows in the magnetosphere - ionosphere system, *Annales Geophys.*, ***10***, 103-115, 1992.

Cowley S.W.H and **C.J. Owen**, A simple illustrative model of open flux tube motion over the dayside magnetopause, *Planet. Space Sci.*, ***37***, 1461, 1989.

Cowley S.W.H., M.P. **Freeman**, **M. Lockwood**, and **M.F. Smith**, The ionospheric signature of flux transfer events, in *"CLUSTER - dayside polar cusp", ESA SP-330*, editor C.I Barron. European Space Agency Publications, Nordvijk, The Netherlands, pp 105-112, 1991a.

Cowley S.W.H., J.P. Morelli and **M. Lockwood**, Dependence of convective flows and particle precipitation in the high-latitude dayside ionosphere on the X and Y components of the interplanetary magnetic field, *J. Geophys. Res.*, ***96***, 5557-5564, 1991b.

Crooker N.U., Reverse convection, *J. Geophys. Res.*, ***97***, 19363-19372, 1992.

Crooker N.U. and **F.J. Rich**, Lobe-cell convection as a summer phenomenon, *J. Geophys. Res.*, ***98,*** 13,403-13,407, 1993.

Crooker N.U., J.G. Luhmann, C.T. Russell, E.J. Smith, J.R. Spreiter and **S.S. Stahara**, Magnetic field draping against the dayside magnetopause, *J. Geophys. Res.*, ***90***, 3505-3510, 1985.

Crooker N.U., F.R. Toffoletto, and **M.S. Gussenhoven**, Opening the cusp, *J. Geophys. Res.*, ***96***, 3497-3503, 1991b.

Curtis S.A. *et al.*, DE-2 cusp observations: role of plasma instabilities in topside ionospheric heating and density fluctuations, *Geophys. Res. Lett.*, *9*, 997-1000, 1982.

de la Beaujardiere O., P. Newell, and **R. Rich**, Relationship between Birkeland current regions, particle participation, and electric fields, *J. Geophys. Res.*, ***98***, 7711-7720, 1993.

de Hoffmann F. and **E. Teller**, Magneto-hydrodynamic shocks, *Phys. Rev.*, *80*, 692, 1950.

Dungey J. W., Conditions for the occurrence of electrical discharges in astrophysical systems, *Phil. Mag.*, ***44***, 725, 1953.

Dungey J. W., Interplanetary magnetic field and the auroral zones, *Phys. Rev. Lett.*, ***6***, 47, 1961.

Eather R.H. and **S.B. Mende**, Airbourne observations of auroral precipitation patterns, *J. Geophys. Res.*, ***76***, 1746, 1971.

Elphic R.C., W. Baumjohann, C.A. Cattell, H. Lühr and **M.F. Smith**, A search for upstream pressure pulses associated with flux transfer events: An AMPTE/ISEE case study, *J. Geophys. Res*., ***99***, 13,521-13,527, 1994.

Elphic R. C., M. Lockwood, S. W. H. Cowley and **P. E. Sandholt**, Signatures of flux transfer events at the dayside magnetopause and in the ionosphere: combined ISEE, EISCAT and optical observations, *Geophys. Res. Lett.*, *17*, 2241-2244, 1990.

Elphinstone R.D., J.S. Murphree, D.J. Hearn, L.L. Cogger., P.T. Newell, and **H. Vo**, Viking observations of the UV dayside aurora and their relation to DMSP particle boundary definitions, *Ann. Geophys.*, ***10***, 815-826, 1992.

Etemadi A., S. W. H. Cowley, M. Lockwood, B. J. I. Bromage, D. M. Willis and **H. Lûhr**, The dependence of high-latitude dayside ionospheric flows on the north-south component of the *IMF*, a high time resolution correlation analysis using EISCAT "POLAR" and AMPTE UKS and IRM data, *Planet. Space Sci.*, ***36***, 471, 1988.

Fasel G.J., Poleward-Moving auroral forms: a statistical study, *J. Geophys. Res.*, ***100***, 11891-11905, 1995.

Fedder J.A., C.M. Mobarry and **J.G. Lyon**, Reconnection voltage as a function of *IMF* clock angle, *Geophys. Res. Lett.*, ***18***, 1047-1050, 1991.

Foster J.C., G.S. Stiles, and **J.R. Doupnik**, Radar observations of cleft dynamics, *J. Geophys. Res.*, ***85***, 3453-3460, 1980.

Fox N.J., M. Lockwood, S.W.H. Cowley, M.P. Freeman, E. Friis-Christensen, D.K. Milling, M. Pinnock and **G.D. Reeves**, EISCAT observations of unusual flows in the morning sector associated with weak substorm activity, *Annales Geophys.* ***12***, 541-553, 1994.

Frank L.A., Plasmas in the Earth's polar magnetosphere, *J. Geophys. Res.*, ***76***, 5202, 1971.

Freeman M.P. and **D.J. Southwood**, The effects of magnetospheric erosion on mid- and high-latitude ionospheric flows, *Planet. Space Sci.*, ***36***, 509, 1988.

Freeman M.P., C.J. Farrugia, L.F. Burlaga, M.R. Hairston, M.E. Greenspan, J.M. Ruohoniemi and **R.P. Lepping**, The interaction of a magnetic cloud with the earth: ionospheric convection in the northern and southern hemispheres for a wide range of quasi-steady interplanetary magnetic field conditions, *J. Geophys. Res.*, ***98***, 7633-7655, 1993.

Friis-Christensen E., M.A. McHenry, C.R. Clauer and **S. Vennerstrom**, Ionospheric traveling convection vortices observed near the polar cleft: A triggered response to sudden changes in the solar wind, *Geophys. Res. Lett.*, ***15***, 253-256, 1988.

Fuselier S.A., D.M. Klumpar and **E.G. Shelley**, Ion reflection and transmission during reconnection at the Earth's subsolar magnetopause, *Geophys. Res. Lett.*, ***18***, 139-142, 1991

Fuselier S.A., E.G. Shelley and **D.M. Klumpar,** Mass density and pressure changes across the dayside magnetopause, *J. Geophys. Res.*, ***98***, 3935-3942, 1993.

Glaßmeier K.-H., M. Hoenisch and **J. Untied**, Ground-based and satellite observations of traveling magnetospheric convection twin vortices, *J. Geophys. Res.*, ***94***, 2520-2528, 1989.

Gosling J.T., M.F. Thomsen, S.J. Bame, R.C. Elphic and C.T. Russell, Plasma flow reversals at the dayside magnetopause and the origin of asymmetric polar cap convection, *J. Geophys. Res.*, ***95***, 8073-8084. 1990a.

Gosling J.T., M.F. Thomsen, S.J. Bame, R.C. Elphic and **C.T. Russell**, Cold ion beams in the low-latitude boundary layer during accelerated flow events, *Geophys. Res. Lett.*, ***17***, 2245-2248, 1990b.

Gosling J.T., M.F. Thomsen, S.J. Bame, T.G. Onsanger and **C.T. Russell**, The electron edge of the low-latitude boundary layer during accelerated flow events, *Geophys. Res. Lett.*, ***17***, 1833-1836, 1990c.

Gosling J. T, M. F. Thomsen, S. J. Bame, R. C. Elphic and **C. T. Russell**, Observations of reconnection of interplanetary and lobe magnetic field lines at the latitude magnetopause., *J. Geophys. Res.*, ***96***, 14097-14106, 1991.

Greenwald R.A., K.. Baker, J.M. Ruohoniemi, J.R. Dudeney, M. Pinnock, N. Mattinand and **J.M. Leonard**, Simultaneous conjugate observations of dynamic variations in high-latitude dayside convection due to changes in *IMF* B_y, *J. Geophys. Res.*, ***95***, 8057, 1990.

Haerendel G., G. Paschmann, N. Sckopke, H. Rosenbauer and **P. C. Hedgecock**, The frontside boundary layer of the magnetopause and the problem of reconnection, *J. Geophys. Res.*, ***83***, 3195-3216, 1978.

Hairston M.R. and **R.A. Heelis**, Response time of the polar ionospheric convection pattern to changes in the north-south direction of the *IMF*, *Geophys. Res. Lett.*, ***22***, 631-634, 1995.

Hanson W.B., W.R. Coley, R. A. Heelis, N.C. Maynard and **T.L. Aggson**, A comparison of in situ measurements of E and -V x B from Dynamics Explorer 2, *J. Geophys. Res.*, ***98***, 21,501-21,516, 1994.

Hapgood M.A. and **M. Lockwood,** Rapid changes in *LLBL* thickness, *Geophys. Res. Lett.*, ***22***, 77-80, 1995.

Hapgood M. A., Y. Tulunay, M. Lockwood, G. Bowe and **D. M. Willis**, Variability of the interplanetary medium at 1 AU over 24 years: 1963-1986, *Planet. Space Sci.*, ***39***, 411-423, 1991.

Heelis R. A., The effects of interplanetary magnetic field orientation on dayside high-latitude convection, *J. Geophys. Res.*, ***89***, 2873, 1984.

Heikkila W.I., The morphology of auroral particle precipitation, *Space Res.*, ***12***, 1343, 1972.

Heikkila W. J. and **J. D. Winningham**, Penetration of magnetosheath plasma to low altitudes through the dayside magnetospheric cusps, *J. Geophys. Res.*, ***76***, 883, 1971.

Heikkila W.J., T.S. Jorgensen, L.J. Lanzerotti and **C.J. Maclennan**, A transient auroral event on the dayside, *J. Geophys. Res., 94*, 15,291-15,305, 1989

Hill T.W., Rates of mass, momentum, and energy transfer at the magnetopause, in *Proceedings of the Magnetospheric Boundary Layers Conference, Alpbach*, pp. 325-333, ESA SP-148, ESA, Paris, 1979

Hill T.W. and **P.H. Reiff**, Evidence of magnetospheric cusp proton acceleration by magnetic merging at the dayside magnetopause, *J. Geophys. Res.*, ***82***, 3623-3628, 1977.

Holzer T.E. and **G.C. Reid**, The response of the dayside magnetosphere-ionosphere system to time-varying field-line reconnection, *J. Geophys. Res.*, ***80***, 2041-2049, 1975.

Holzer R. E. and **J. A. Slavin**, A correlative study of magnetic flux transfer in the magnetosphere. *J. Geophys. Res.*, ***84***, 2573, 1979.

Iijima T. and **T. A. Potemra**, Large-scale characteristics of field-aligned currents associated with substorms, *J. Geophys. Res.*, ***85***, 599, 1976.

Jackson J.D., Classical electrodynamics, Wiley, 1975.

Johnstone A.D., D.J. Rodgers, A.J. Coates, M.F. Smith and **D.J. Southwood**, Ion acceleration during steady-state reconnection at the dayside magnetopause, in *Ion acceleration in the magnetosphere and ionosphere*, ed. T. Chang, AGU Monograph 38, 136-145, 1986.

Kivelson M.G. and **D.J. Southwood**, Ionospheric travelling vortex generation by solar wind buffeting of the magnetosphere, *J. Geophys. Res.*, ***96***, 1661-1667, 1991.

Lin Y. and **L.C. Lee**, Structure of the dayside reconnection layer in resistive *MHD* and hybrid models, *J. Geophys. Res.*, ***98***, 3919-3934, 1993.

Lin Y. and **L.C. Lee**, Reconnection layer at the flank magnetopause in the presence of shear flow, *Geophys. Res. Lett*. ***21***, 855-858, 1994.

Lorrain P. and **D. Corson**, Electromagnetic fields and waves, p 261, W.H. Freeman, 1970.

Lockwood M., Flux Transfer Events at the dayside magnetopause: Transient reconnection or magnetosheath pressure pulses?, *J. Geophys. Res.*, ***96***, 5497-5509, 1991.

Lockwood M., The location and characteristics of the reconnection X-line deduced from low-altitude satellite and ground-based observations: 1. Theory, *J. Geophys. Res.*, in press, 1995a.

Lockwood M., Overlapping cusp ion injections: An explanation invoking magnetopause reconnection, *Geophys. Res. Lett*. ***22***, 1141-1144, 1995b.

Lockwood M. and **C.J. Davis**, The occurrence probability, width and terracing of cusp precipitation in the topside ionosphere for fully-pulsed reconnection at the dayside magnetopause, *J. geophys. Res.*, ***100***, 7627-7640,

Lockwood M. and **M.F. Smith**, The variation of reconnection rate at the dayside magnetopause and cusp ion precipitation, *J. Geophys. Res.*, ***97***, 14,841-14,847, 1992.

Lockwood M. and **M.F. Smith**, Comment on "Mapping the dayside ionosphere to the magnetosphere according to particle precipitation characteristics" by Newell and Meng, *Geophys. Res. Lett.*, ***20,*** 1739-1740, 1993

Lockwood M. and **M.F. Smith**, Low- and mid-altitude cusp particle signatures for general magnetopause reconnection rate variations: I - Theory, *J. Geophys. Res.*, ***99***, 8531-8555, 1994.

Lockwood M. and **M.N. Wild**, On the quasi-periodic nature of magnetopause flux transfer events, *J. Geophys. Res.*, ***98***, 5935-5940, 1993.

Lockwood M., T.E. Moore, J.H. Waite, Jr., C.R. Chappell, J.L. Horwitz and **R.A. Heelis**, The geomagnetic mass spectrometer - mass and energy dispersions of ionospheric ion flows into the magnetosphere, *Nature*, ***316***, 612-613, 1985a.

Lockwood M., M.O. Chandler, J.L Horwitz, J.H. Waite, Jr., T.E. Moore and **C.R. Chappell**, The cleft ion fountain, *J. Geophys. Res.*, ***90***, 9736-9748, 1985b.

Lockwood M., P.E. Sandholt, S.W.H. Cowley and **T. Oguti**, Interplanetary magnetic field control of dayside auroral activity and the transfer of momentum across the dayside magnetopause, *Planet. Space Sci.*, ***37***, 1347, 1989

Lockwood M., S.W.H. Cowley and **M.P. Freeman**, The excitation of plasma convection in the high latitude ionosphere, *J. Geophys. Res.*, ***95***, 7961-7971, 1990.

Lockwood M, W.F. Denig, A.D. Farmer, V.N. Davda, S.W.H. Cowley and **H. Lühr**, Ionospheric signatures of pulsed magnetic reconnection at the Earth's magnetopause, *Nature, **361** (6411)*, 424-428, 1993.

Lockwood M, T.G. Onsager, C.J. Davis, M.F. Smith and **W.F. Denig**, The characteristics of the magnetopause reconnection X-line deduced from low-altitude satellite observations of cusp ions, *Geophys. Res. Lett.* **21**, 2757-2760, 1994.

Lockwood M., S.W.H. Cowley, P.E. Sandholt and **U.P. Lovhaug**, Causes of plasma flow bursts and dayside auroral transients; An evaluation of two models invoking reconnection pulses and changes in the Y component of the magnetosheath field, *J. Geophys. Res.*, ***100***, 7613-7626, 1995.

Lotko W., B.U.O. Sonnerup and **R.L. Lysak**, Non-steady boundary layer flow including ionospheric drag and parallel electric fields, *J. Geophys. Res.*, ***92***, 8635-8648, 1987.

Lühr H., W. Blawert and **H. Todd**, The ionospheric plasma flow and current patterns of travelling convection vortices: a case study, *J. Atmos. Terr. Phys.*, ***55,***, 1717-1727, 1993.

Lühr H., M. Lockwood, P.A. Sandholt, T.L. Hansen and **T. Moretto**, Multi-instrument ground-based observations of a Travelling Convection Vortex event, *Annales Geophys.*, ***14***, 162-181, 1995.

Ma Z.A., J.G. Hawkins and **L.C. Lee**, A simulation study of impulsive penetration of solar wind irregularities into the magnetosphere at the dayside magnetopause, *J. Geophys. Res.*, ***96,*** 15,751-15,765, 1991.

Maezawa K., Dependence of the magnetopause position on the southward interplanetary magnetic field, *Planet. Space Sci.*, ***22***, 1443, 1974.

Mantas G.P. and **J.C.G. Walker**, The penetration of soft electrons into the ionosphere, *Planet. Space Sci.*, ***24***, 409-423, 1976.

McDairmid I.B., J.R. Burrows and **M.D. Wilson**, Magnetic field perturbations in the dayside cleft and their relationship to the *IMF, J. Geophys. Res.*, ***83***, 5357, 1978.

Mei Y., N.U. Crooker and **G.L. Siscoe**, Cusp currents from ionospheric vorticity generated by gasdynamic and merging flow fields at the magnetopause, *J. Geophys. Res*., ***100***, 7641-7647, 1995.

Mozer F.S., Electric field evidence for viscous interaction at the magnetopause, *Geophys. Res. Lett.*, ***11***, 981, 1984.

Newell P. T. and **C. I. Meng,** Ion acceleration at the equatorward edge of the cusp: low altitude observations of patchy merging, *Geophys. Res. Lett*, ***18***, 1829-1832, 1991.

Newell P. T. and **C. I. Meng**, The cusp and the cleft/*LLBL*: Low altitude identification and statistical local time variation, *J. Geophys. Res.*, ***93***, 14,549, 1988.

Newell P.T. and **C.-I. Meng**, Mapping the dayside ionosphere to the magnetosphere according to particle precipitation characteristics, *Geophys. Res. Lett.*, ***19***, 609-612, 1992.

Newell P.T. and **D.G. Sibeck**, B_y fluctuations in the magnetosheath and azimuthal flow velocity transients in the dayside ionosphere, *Geophys. Res. Lett*. ***20***, 1719- 1722, 1993.

Nishida A., Coherence of geomagnetic DP2 fluctuations with interplanetary magnetic field variations, *J. Geophys. Res.*, ***73***, 5549, 1968.

Nishida A., Can random reconnection on the magnetopause produce the low-latitude boundary layer?, *Geophys. Res. Lett.*, ***16***, 227-230, 1989.

Onsager T.G., A quantitative model of magnetosheath plasma in the low latitude boundary layer, cusp and mantle, J.A. Holtet and A. Egeland (eds), *Physical Signatures of Magnetospheric Boundary Layer Processes*, 385-400, 1994.

Onsager T.G., C.A. Kletzing, J.B. Austin and **H. MacKiernan**, Model of magnetosheath plasma in the magnetosphere: cusp and mantle precipitations at low altitudes, *Geophys. Res. Lett.*, ***20***, 479-482, 1993.

Owen C.J. and **S.W.H. Cowley**, Heikkila's mechanism for impulsive plasma transport through the magnetopause: A reexamination, *J. Geophys. Res.*, ***96,*** 5565-5574, 1991.

Paschmann G., Plasma and Particle observations at the magnetopause: implications for reconnection, in *Magnetic Reconnection in Space and Laboratory Plasmas, ed. E.W. Hones, Jr., AGU Monograph 30*, pp114-123, 1984.

Paschmann G., B.U.Ö. Sonnerup, I. Papamastorakis, N. Sckopke, G. Haerendel, S.J. Bame, J.R. Asbridge, J.T. Gosling, C.T. Russell and **R.C. Elphic**, Plasma acceleration at the Earth's magnetopause: Evidence for reconnection, *Nature*, ***282***, 243-246, 1979.

Paschmann G., I. Papamastorakis, W. Baumjohann, N. Sckopke, C.W. Carlson, B.U.Ö. Sonnerup and **H, Lühr**, The magnetopause for large magnetic shear: AMPTE/IRM observations, *J. Geophys. Res.*, ***91***, 11099-11115, 1986.

Paschmann G., B.U.Ö. Sonnerup, I. Papamastorakis, W. Baumjohann, N. Sckopke and **H, Lühr**, The magnetopause and boundary layer for small magnetic shear: convection electric fields and reconnection, *Geophys. Res. Lett.*, ***17***, 1829-1832, 1990.

Petrinec S.M. and **C.T. Russell**, An empirical model of the size and shape of the near-earth magnetotail, *Geophys. Res. Lett*. ***20***, 2695-2698, 1993.

Phan T.-D., G. Paschmann, W. Baumjohann and **N. Sckopke**, The magnetosheath region adjacent to the dayside magnetopause: AMPTE/IRM observations, *J. Geophys. Res.*, ***99***, 121-141, 1994.

Petschek H.E., The concept of rapid magnetic field reconnection: a retrospective view, in *Physics of the Magnetopause*, ed. P. Song, B.U.Ö. Sonnerup and M.F. Thomsen, Geophysical Monograpph 90, pp 21-28, American Geophysical Union, 1995.

Pinnock M., A.S. Rodger, J.R. Dudeney, K.B. Baker, P.T. Newell, R.A. Greenwald and **M.E. Greenspan**, Observations of an enhanced convection channel in the cusp ionosphere, *J. Geophys. Res.*, ***98,*** 3767-3776, 1993

Potemra T.A., R.E. Erlandson, L.J. Zanetti, R.L. Arnold, J. Woch and **E. Friis-Christensen**, The dynamic cusp, *J. Geophys. Res.*, ***97,*** 2835-2844, 1992.

Pudovkin M.I., S.A. Zaitseva, P.E. Sandholt and **A. Egeland**, Dynamics of aurorae in the cusp region and characteristics of magnetic reconnection at the magnetopause, *Planet. Space Sci.*, ***40,*** 879-887, 1992.

Rees M.H. and **R.G. Roble**, Excitation of the $O(^1D)$ atoms in aurora and emission of the [OI] 6300Å line, *Can. J. Phys.*, ***64***, 1608-1613, 1986.

Reiff P. H., T. W. Hill and **J. L. Burch**, Solar wind plasma injection at the dayside magnetospheric cusp, *J. Geophys. Res.*, ~~*82*~~, 479-491, 1977.

Reiff P. H., R. W. Spiro and **T. W. Hill**, Dependence of polar cap potential drop on interplanetary parameters, *J. Geophys. Res.*, ***86***, 7639, 1981.

Richard R.L., R.J. Walker and **M. Ashour-Abdalla**, The population of the magnetosphere by solar wind ions when the interplanetary magnetic field is northward, *Geophys. Res. Lett.* ***21***, 2455-2458, 1994.

Rijnbeek R. P., S. W. H. Cowley, D. J. Southwood and **C. T. Russell**, A survey of dayside flux transfer events observed by the ISEE 1 and 2 magnetometers, *J. Geophys. Res.*, ***89***, 786-800, 1984.

Rodger A.S., M. Pinnock, J.R. Dudeney, K.B. Baker and **R.A. Greenwald**, A new mechanism for polar patch formation, *J. Geophys. Res.*, **99**, 6425-6436, 1994.

Roelof E.C. and **D.G. Sibeck**, Magnetopause shape as a Bivariate function of interplanetary magnetic field B_z and solar wind dynamic pressure, *J. Geophys. Res.*, ***98***, 21,421-21,450, 1993.

Rosenbauer H., H. Greenwaldt, M.D. Montgomery, G. Paschmann and **N. Skopke**, HEOS-2 plasma observations in the distant polar magnetosphere: the plasma mantle, *J. Geophys. Res.*, ***80***, 2723-2737, 1975.

Russell C.T., The configuration of the magnetosphere, in *Critical Problems of Magnetospheric Physics*, edited by E.R. Dyer, p.1, Nat. Acad. Sciences, Washington, 1972.

Russell C. T. and **R. C. Elphic**, Initial ISEE magnetometer results: Magnetopause observations, *Space Sci. Rev.*, ***22***, 681-715, 1978.

Sanchez E.R. and **G.L. Siscoe**, IMP 8 magnetotail boundary crossings: a test of the *MHD* models for an open magnetosphere, *J. Geophys. Res.*, ***95***, 20771-20779, 1990.

Sanchez E.R., G.L. Siscoe, J.T. Gosling, E.W. Hones, Jr. and **R.P. Lepping**, Observations of rotational discontinuity-slow mode expansion fan structure of the magnetotail boundary, *J. Geophys. Res.*, ***95***, 61-73, 1990.

Sanchez E.R., G.L. Siscoe and **C.-I. Meng**, Inductive attenuation of the trans-polar voltage, *Geophys. Res. Lett.*, ***18,*** 1173-1176, 1991.

Sandford B.P., Aurora and airglow intensity variations with time and magnetic activity at southern high latitudes, *J. atmos. terr. Phys.*, ***26***, 749, 1964.

Sandholt P.E., A. Egeland, J.A. Holtet, B. Lybekk, K.Svenes and **S. Asheim, S.**, Large- and small-scale dynamics of the polar cusp, *J. Geophys. Res.*, ***90***, 4407-4414, 1985.

Sandholt P.E., M. Lockwood, W.F. Denig, R.C. Elphic and **S. Leontjev**, Dynamical auroral structure in the vicinity of the polar cusp: multipoint observations during southward and northward *IMF*, *Annales Geophys.*, ***10,*** 483-497, 1992.

Saunders M.A., The origin of cusp Birkeland currents, *Geophys. Res. Lett.*, ***16***, 151-154 ,1989.

Scholer M., Magnetic flux transfer at the magnetopause based on single X-line bursty reconnection, *Geophys. Res. Lett.*, ***15***, 291-294, 1988.

Scurry L., C.T. Russell and **J.T. Gosling**, A statistical study of accelerated flow events at the dayside magnetopause, *J. Geophys. Res.*, ***99***, 14,815-14,829, 1994.

Semenov V.S., I.V. Kubyshkin, V.V. Lebedeva, M.V. Sidneva, H.K. Biernat, M.F. Heyn, B.P. Besser and **R.P. Rijnbeek**, Time-dependent localised reconnection of skewed magnetic fields, *J. Geophys. Res.*, ***97***, 4251-4263, 1992.

Sergeev V.A., T.I. Pulkkinen, R.J. Pelinen and **N.A. Tsyganenko**, Hybrid state of the tail magnetic configuration during steady convection events, *J. Geophys. Res.*, ***99***, 23,571-23,582, 1994.

Shelley E. G., R. D. Sharp and **R. G. Johnson**, He++ and H+ flux measurements in the dayside magnetospheric cusp, *J. Geophys. Res.*, ***81***, 2363, 1976.

Sibeck D.G., Transient events in the outer magnetosphere: boundary waves or flux transfer events?, *J. Geophys. Res.*, ***97,*** 4009-4026, 1992.

Siscoe G.L. and **T.S. Huang**, Polar cap inflation and deflation, *J. Geophys. Res.*, ***90***, 543, 1985.

Siscoe G.L., W. Lotko and **B.U.Ö. Sonnerup**, A high-latitude, low-latitude boundary layer model of the convection current system, *J. Geophys. Res.*, ***96,*** 3487-3495, 1991.

Siscoe G.L., L.A. Frank, K.L. Ackerson and **W.R. Paterson**, Properties of the mantle-like magnetotail boundary layer: GEOTAIL data compared with a mantle model, *Geophys. Res. Lett*., ***21***, 2975-2978, 1994.

Smith M.F. and **Rodgers D.J.**, Ion distributions at the dayside magnetopause, *J. Geophys. Res.*, ***95***, 11617-11624, 1991.

Song P. and **C.T. Russell**, Model of the formation of the low-latitude boundary layer for strongly northward interplanetary magnetic field, *J. Geophys. Res.*, ***97,*** 1411-1420, 1992.

Song P., G. Le and **C.T. Russell**, Observational differences between flux transfer events and surface waves at the magnetopause, *J. Geophys. Res.*, ***99***, 2309-2320, 1994.

Sonnerup B.U.O., G. Paschmann, I. Papamastorakis, N. Sckopke, G. Haerendel, S.J. Bame, J.R. Ashbridge, J.T. Gosling and **C.T. Russell**, Evidence for magnetic field reconnection at the Earth's magnetopause, *J. Geophys. Res.*, ***86***, 10049-10067, 1981.

Sonnerup B.U.Ö., I. Papamastorakis, G. Paschmann and **H, Lühr**, The magnetopause for large magnetic shear: analysis of convection electric fields from AMPTE/IRM, *J. Geophys. Res.*, ***95,*** 10541-10557, 1986.

Southwood D. J., C. J. Farrugia and **M. A. Saunders**, What are flux transfer events?, *Planet. Space Sci.*, ***36***, 503-508, 1988.

Southwood D. J., The ionospheric signature of flux transfer events, *J. Geophys. Res.*, ***92***, 3207-3213, 1987

Spreiter J.R. A.L. Summers and **A.Y. Alksne**, Hydromagnetic flow around the magnetosphere, *Planet. Space Sci.*, ***14***, 223-253, 1966.

Stauning P., E. Friis-Christensen, O. Rasmussen and S. Vennerstrøm, Progressing polar convection disturbances: Signature of an open magnetosphere, *J. Geophys. Res.*, ***99***, 11,303-11,317, 1994.

Taguchi S., M. Sugiura, J.D. Winningham and **J.A. Slavin**, Characterization of the *IMF* B_y dependent field-aligned currents in the cleft region based on DE 2 observations, *J. Geophys. Res.*, ***98,*** 1393-1407, 1993.

Titheridge J.E., Ionospheric heating beneath the magnetosphereic cleft, *J. Geophys. Res.*, ***81***, 3221-3226, 1976.

Thomsen M. F., J. A. Stansberry, S. J. Bame, S. A. Fuselier and **J. T. Gosling**, Ion and electron velocity distributions within flux transfer events, *J. Geophys. Res., 92*, 12,127-12,136, 1987.

Todd H., B. J. I. Bromage, S. W. H. Cowley, M. Lockwood, A. P. van Eyken and **D. M. Willis**, EISCAT observations of bursts of rapid flow in the high latitude dayside ionosphere, *Geophys. Res. Lett., **13**,* 909- 913, 1986.

Todd H., S.W.H. Cowley, A. Etemadi, B.J.I. Bromage, M. Lockwood, D.M. Willis and **H. Lühr**, Flow in the high-latitude ionosphere: measurements at 15-second resolution made using the EISCAT "POLAR" experiment, *J. Atmos. Terr. Phys., **50**,* 423-446, 1988.

Vasyliunas V.M., Multiple-branch model of the open magnetopause, *Geophys. Res. Lett., **22**,* 1145-1147, 1995.

Watermann J., O. de la Beujardiére, D. Lummerzheim, J. Woch, P.T. Newell, T.A. Potemra, F.J. Rich and **M. Shapshak**, The dynamic cusp at low altitudes: a case study utilizing Viking, DMSP-D7 and Sondrestrom incoherent scatter radar observations, *Ann. Geophysicae*, **12**, 1114-1157, 1994.

Whalen J.A., J. Buchau and **R.A. Wagner**, Airbourne ionospheric and optical observations of noon-time aurora, *J. atmos. terr. Phys., **33***, 661, 1971.

Whitteker. J.H., The transient response of the topside ionosphere to precipitation, *Planet. Space Sci., **25**,* 773-768, 1977.

Wickwar V.B. and **W. Kofman**, Dayside auroras at very high latitudes: the importance of thermal excitation, *Geophys. Res. Lett., **11**,* 923-926, 1984.

Woch J. and **R. Lundin**, Temporal magnetosheath plasma injection observed with Viking: a case study, *Ann. Geophysicae, **9,*** 133-142, 1991.

Woch J. and **R. Lundin**,Magnetosheath plasma precipitation in the polar cusp and its control by the interplanetary magnetic field, *J. Geophys. Res., **97,*** 1421-1430, 1992.

Wygant J. R., R. B. Torbert and **F. S. Mozer**, Comparison of S3-2 polar cap potential drops with the interplanetary magnetic field and models of magnetopause reconnection, *J. Geophys. Res., **88**,* 5727, 1983.

10. Glossary of acronyms

AU	astronomical unit (= distance from the sun to Earth)
CRB	convection reversal boundary
dHT	de Hoffman-Teller (velocity/frame)
FTE	flux transfer event
GSM	geocentric solar magnetospheric (coordinates)
HLBL	high-latitude boundary layer
IMF	interplanetary magnetic field
LHS	left hand side
LLBL	low-latitude boundary layer
MHD	magnetohydrodynamics
OCB	open-closed (field line) boundary
PDL	plasma depletion layer
RD	rotational discontinuity
RE	Earth radius
RHS	right hand side
STP	solar terrestrial physics
TCV	travelling convection vortex
TD	tangential discontinuity

11. Symbols

a	angle of reconnection outflow wedges
ds	element of area
dl	element of length
dl_m	length in the magnetopause
dl_i	length in the ionosphere
d	field-aligned distance from X-line to ionosphere
d_c	distance along flow streamline
e	the charge on the electron
e_i	ion energy
f	distribution function
g	acceleration due to gravity
k	Boltzmann's constant
m	mass
q	electronic charge
t	time
v	velocity
x	axis normal to the magnetopause
z	axis in the magnetopause plane in direction of $\mathbf{V}_f$
A	area
B	magnetic field (or induction or flux density)
$\mathbf{B}_{sh}$	magnetosheath field near the magnetopause
$\mathbf{B}_{sp}$	magnetospheric field near the magnetopause
B_z	northward component of **B** (usually of the *IMF*)
B_n	outward normal field component to the magnetopause
B_i	magnetic field in the ionospheric F-region
E	electric field
E_t	tangential electric field component at the magnetopause
E_i	ionospheric electric field
F	magnetic flux
$\mathbf{F}_{jk}$	force on gas *j* due to collisions with gas *k*
J	current density
$\mathbf{J}_{CF}$	magnetopause (Chapman-Ferraro) current density
$\mathbf{J}_P$	ionospheric Pedersen current density
L_c	characteristic plasma scale length
N	number density
P	plasma pressure
R_m	magnetic Reynold's number
S	Poynting flux
S_v	vertical component of **S**
T	plasma temperature
U	relative velocity of two reference frames
V	plasma velocity
V_A	Alfvén speed
Vc	characteristic plasma scale speed
$\mathbf{V}_f$	field line velocity (dHT frame velocity)
V_{min}	minimum velocity of injected ion population
V_p	velocity of peak of distribution function (i.e. f(V_p) is a maximum)
W_B	energy density in magnetic field
W_{th}	energy density in thermal particle motions
W_V	energy density in bulk flow of particles
X	GSM axis
Y	GSM axis
Z	GSM axis
υ_{jk}	the collision frequency for momentum transfer between gas j and gas k
σ	electrical conductivity
ρ	plasma mass density
μ_o	the permeability of free space
t_i	ion time of flight
Φ	voltage
Φ_{pc}	transpolar voltage
θ	angle that magnetospheric field makes with magnetopause
ϕ	angle that magnetosheath field makes with magnetopause

AURORA/SUBSTORM STUDIES WITH INCOHERENT-SCATTER RADARS

Y. Kamide

1. Introduction

The ultimate energy source of substorms and plasma convection in the magnetosphere is the solar wind. The ionosphere, particularly the polar ionosphere, where dynamic auroras occur and intense currents flow, couples electrically with the magnetosphere through magnetic field lines. It can be said that the solar wind tells the magnetosphere what to do [see *Lockwood,* 1996], although it does not give detailed instructions as to how to do it. In other words, the solar wind provides the magnetosphere with the boundary and initial conditions, and, given these conditions, magnetospheric and ionospheric processes such as substorms and plasma convection take place internally in the system.

The earth's magnetic field connects the ionosphere at high latitudes and the magnetosphere, causing an exchange of energy and momentum between the two regions. Thus, the ionosphere and the magnetosphere are coupled in so many different ways that the subject of the magnetosphere-ionosphere system is notoriously difficult to subdivide practically: all magnetospheric processes are controlled by electrodynamics in the ionosphere in some way, and all ionospheric processes bear on the multi-faceted state of the magnetosphere. Moreover, the magnetosphere-ionosphere system is intrinsically nonlinear and unsteady, and is affected directly and indirectly by changes in the solar wind. The boundaries between any adjacent plasma regions of earth's electromagnetic environment are not simple, stationary, topological borders, but represent the dynamic areas where unique physical processes operate. The coupling in the magnetosphere and the polar ionosphere implies active interactions between hot but low-density plasmas in the magnetosphere and cold but high-density plasmas in the ionosphere [*Baumjohann and Treumann*, 1996].

Under this interaction mechanism, many exciting large-scale and small-scale phenomena, such as acceleration of charged particles, auroral displays, burst in electric fields and currents, are occurring. Electric fields in the high-latitude ionosphere and the associated magnetospheric plasma convection, which is induced by the solar wind, change the morphology and composition of the ionosphere [see *Schlegel*, 1996]. These changes in the ionosphere thus produce variations in the thermospheric structure and the neutral wind system [see *Richmond*, 1996]. It is these variations in the ionosphere-thermosphere system that, in turn, modify magnetospheric processes. The entire dynamic coupling chain takes place through

fields, currents, heat flow and frictional interactions with their own characteristic time scales.

The purpose of this paper is to examine the degree to which spatial and temporal variations in large-scale electromagnetic phenomena, such as auroras and electric fields and currents during magnetospheric substorms, play a principal role in the physical linkage involved in solar wind-magnetosphere-ionosphere interactions. It is demonstrated that the construction of incoherent-scatter radars and their subsequent upgrading in operational techniques during the last two decades have made it possible to unveil some of the basic characteristics of ionospheric parameters at the different phases of substorms. Radar data offer a unique opportunity to understanding quantitatively the convection/substorm relationship if examined properly as well as effectively along with other ground-based and satellite measurements of major ionospheric parameters.

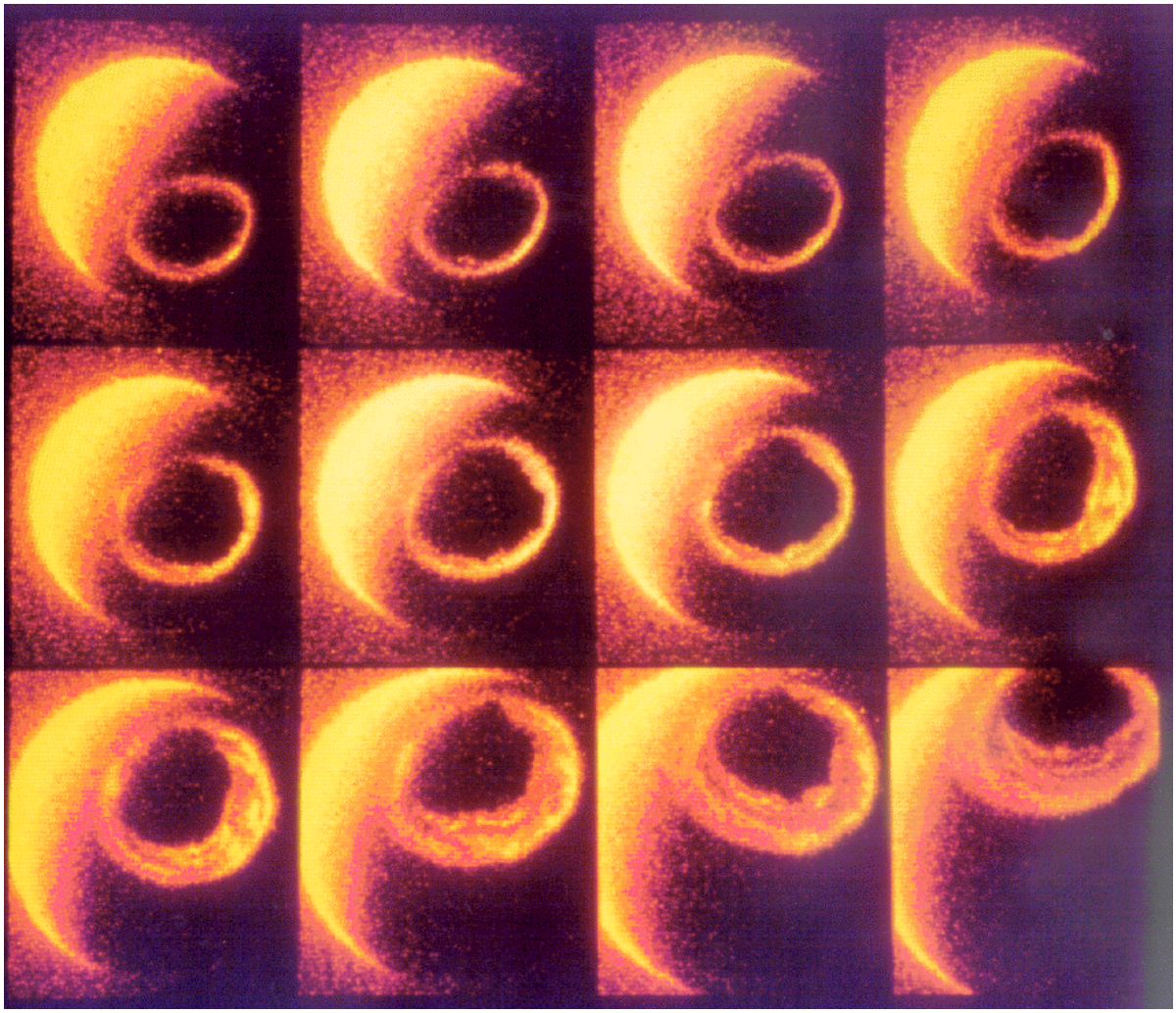

Figure 1. A sequence of 12 consecutive auroral images taken from the DE 1 spacecraft, displaying global auroral activity at ultraviolet wavelengths. [Courtesy of L. A. Frank]

2. Auroras

2.1. Auroras from space

The aurora, one of the dominant manifestations of the magnetospheric substorm, is perhaps the most fascinating and captivating majestic natural phenomenon to be seen on the earth's surface, although unfortunately this impressive multi-color display can be observed regularly only by a limited number of people living near the polar regions. Anyone who has ever witnessed the display of infinite shapes and movements of the aurora in the entire sky knows that the whole drama can never be described with adequate vocabulary invented by human being. The aurora appears as a tremendous spectacle in the dark sky, with structured displays moving rapidly but erratically in all directions, changing the combination of color.

The aurora has continuously been a subject of curiosity for space physicists as well as for the natives living at high latitudes. Not until recently was it well documented that the aurora on a global scale behaves in a well-defined, systematic manner, with characteristic features that recur under similar conditions in terms of the degree to which the solar wind interacts with the magnetosphere [*Akasofu*, 1964, 1977]. It has become possible, with the imaging capability of several polar-orbiting spacecraft, to monitor nearly the entire auroral displays from above the northern and southern poles, so that we are beginning to use extensively spacecraft images to construct a relatively complete picture of auroral physics [e.g., *Anger et al.*, 1973; *Frank et al.*, 1988; *Craven and Frank*, 1991]. Figure 1 shows a sequence of 12 consecutive auroral images taken from the Dynamics Explorer 1 satellite, from over the northern polar region. It is noticed that a brightening of auroras occurred in the midnight sector [*at the fourth image at upper right*] and proceeded eastward and westward, as well as poleward, with the maximum epoch by the sixth and seventh frames.

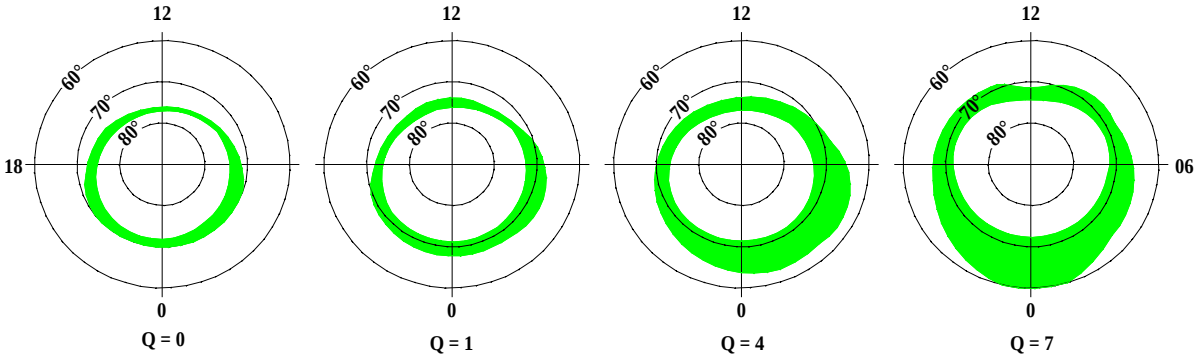

Figure 2. Auroral oval determined by Feldstein and Starkov [1967] in geomagnetic coordinates. To show the relative location of the auroral belts, the geomagnetic Q index is referred to.

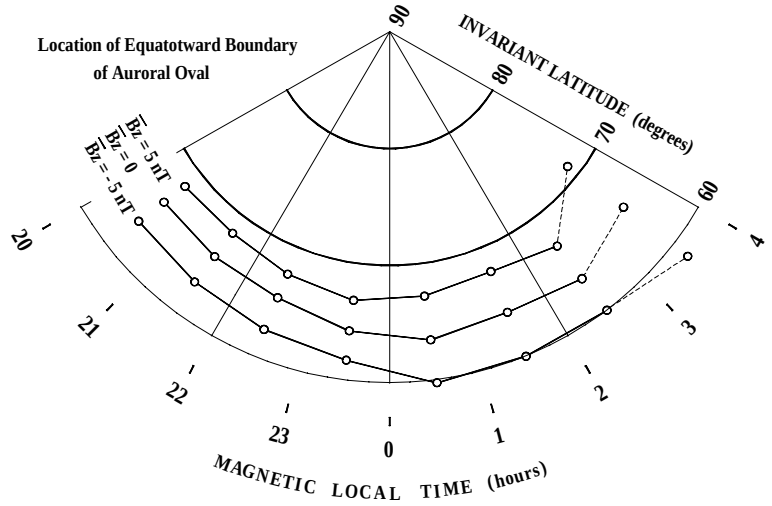

Figure 3. Location of the equatorward boundary of the diffuse electron precipitation at different local times [in MLT] in the dark sector for three B_z values of the IMF. After Kamide and Winningham [1977].

2.2. The auroral oval

If one looks at our planet, the earth, from space, it has two annular rings-shaped glows, one surrounding the north and the other surrounding the south polar regions. These annular belts of auroral luminosities are often called the auroral ovals. The auroral oval delineates approximately the area called the polar cap, where geomagnetic field lines are "open," being connected to the interplanetary magnetic field [*IMF*].

The size of the auroral oval changes considerably with geomagnetic activity: see Figure 2. The "classical" auroral oval [*or belt*], which is defined statistically as the locus of high frequency [≥ 75%] of auroral appearance [*Feldstein*, 1966], has been used extensively to order geophysical phenomena. The size of the auroral oval is not fixed in space but varies with magnetic activity. During active periods the classical auroral oval expands equatorward, reaching the latitude of the auroral zone, while it contracts poleward during periods of low geomagnetic activity [*Feldstein and Starkov*, 1967]. *Meng et al*. [1977] showed that the global auroral distributions indeed are close to the shape of an off-centered circle, instead of the oval shape, during extremely quiet periods.

A southward *IMF* results in a net magnetic flux transfer from the dayside to the nightside, causing the equatorward shift of the auroral oval [*Cowley*, 1982]. An extensive study of auroral motions indicated that the north-south component of the *IMF* controls the size of the auroral oval, although there is a difficulty in examining whether its location depends solely on the *IMF* or on both the *IMF* and geomagnetic activity because of the existence of the close statistical relationship between the southward *IMF* and geomagnetic disturbances.

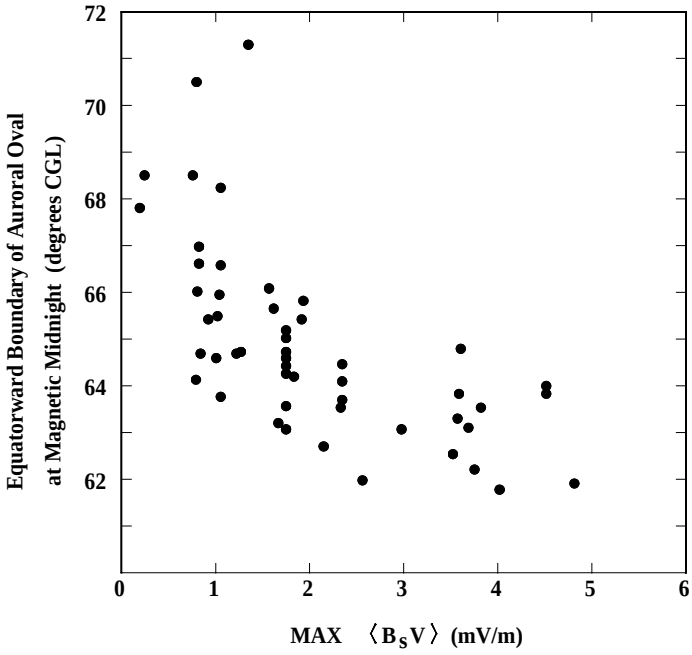

Figure 4. Location of the equatorward boundary of the auroral oval plotted agaist the maximum 30-min average B_z V value during six hours preceding the time of each auroral observation. After Nakai and Kamide [1983].

In addition to visual auroras, we may be able to use several other measurable parameters to quantify the size of the auroral oval. One of them is electron precipitation observed by polar orbiting satellites. Figure 3 shows the average location of the equatorward boundary of the "diffuse" precipitation for three different *IMF* B_z values. It is clearly seen that the *IMF* dependence of the oval location in the morning sector is stronger than that in the evening sector. When the B_z value decreases from 5 nT to –5 nT, the boundary tends to move equatorward by 8 degrees in the morning sector while only 5 degrees in the evening sector [*Kamide et al.*, 1977]. Assuming that the diffuse electrons in the auroral oval originate in the inner boundary of the plasma sheet, this local time dependence of the auroral oval may be accounted for by the low-energy plasma motion in the magnetotail in which a large-scale uniform electric field is superposed on the corotation electric field.

The importance of the delineation of the auroral oval boundaries lies not only in auroral morphology at the ionospheric level but also in dynamic processes in the magnetosphere. It is generally accepted that the B_z component of the *IMF* is the important factor that does control the size of the average oval, but correlation coefficients of the nightside auroral oval with 1-hr average B_z are rather low, falling between 0.4 and 0.7, indicating that the auroral oval does not always follow the *IMF* B_z variations in a linear form. *Nakai and Kamide* [1983] tried to determine the most probable time scale of the auroral oval response to *IMF* variations. Aurora imagery data with high time resolution were used in such a way that

the maximum value of 30-min average B_z V during several hours preceding each of the satellite pass is calculated. It was found that this simple parameter correlates well with the oval location and the correlation tends to be improved gradually as the time scale becomes larger. Figure 4 shows the latitude of the oval boundary against the maximum B_z V during six hours preceding each satellite pass time. It is noticeable, however, that the relationship between the oval size and the maximum B_z V is well represented by a curved line, indicating that the rate of the oval expansion at larger B_z values becomes lower.

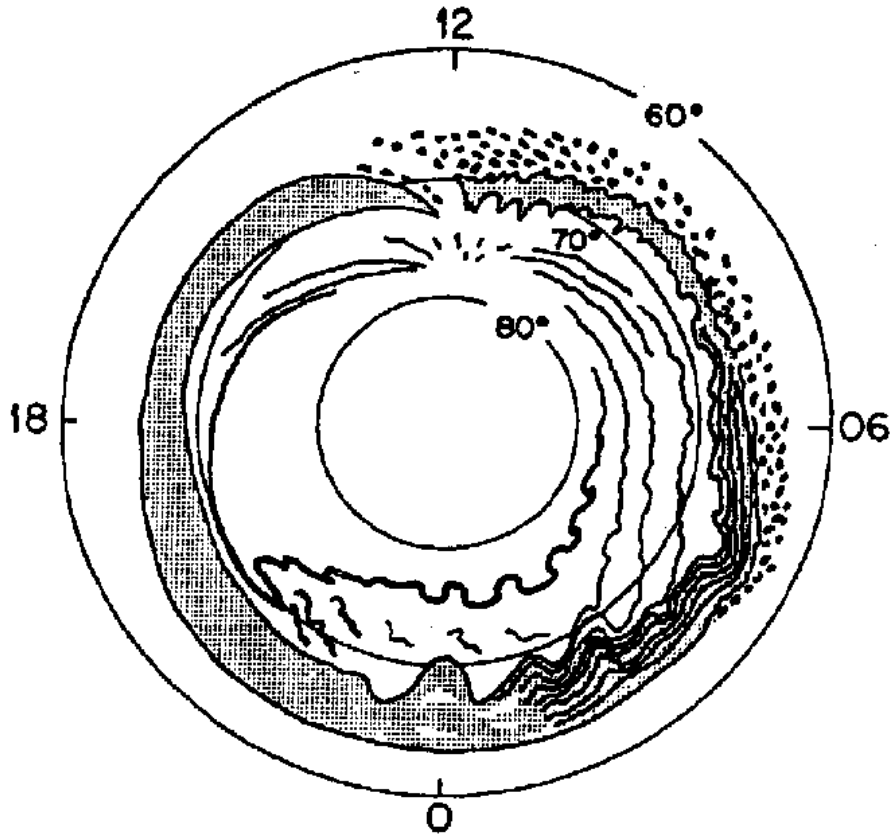

Figure 5. Schematic diagram showing the main characteristics of auroras for the average disturbed condition. Discrete auroral arcs are indicated by solid lines and the diffuse auroral regions are shaded. After Akasofu [1976].

2.3. The auroral substorm as a manifestation of magnetosphere-ionosphere coupling

What is an auroral substorm? An auroral substorm occurs primarily in the auroral oval. The term substorm originally entered the vocabulary of the space physicist through a study of the dynamics of discrete auroral forms [*Akasofu*, 1964]. It was found that the development of highly dynamic auroral forms follows a repeatable pattern, serving a framework in which a variety of observations of particles and fields in the high-latitude ionosphere are properly ordered. The auroral substorm involves a brightening of auroral arc forms in the midnight sector with

the subsequent poleward motion which is accompanied by a specific type of auroral display called the westward traveling surge. The earth's magnetic field undergoes a considerable perturbation, particularly at high latitudes, during the auroral substorm. This is called the polar magnetic substorm.

Figure 5 shows the main characteristics of auroras during auroral substorms, in which there are essentially two auroral belts, diffuse and discrete auroras [*Akasofu*, 1976]. The diffuse aurora can be defined as a broad band of structureless auroral luminosity with a latitudinal width of, at least, several tens of kilometers which is separated from the discrete aurora. The diffuse aurora often covers a significant part of the field of view of an all-sky camera, making it difficult to recognize its presence from a single ground station. Thus, the auroral oval defined by *Feldstein and Starkov* [1967] using all-sky camera data does not necessarily represent accurately the distribution of the diffuse aurora. This character of the diffuse aurora contrasts in many ways with that of the discrete aurora. The discrete aurora is a curtain-like structure and considerably variable in its morphological features and energy spectra of its precipitating energetic electrons.

3. The Solar Wind and Substorms

3.1. Solar wind-magnetosphere dynamo

The solar wind is an ionized gas, flowing continuously from the solar corona and filling up the interplanetary space. As the solar wind, which carries the solar magnetic field, interacts with the earth's magnetosphere, as much as several 10^6 MW of power is generated through a dynamo process. The efficiency of the dynamo action depends on the relative orientation of the solar wind's magnetic field, i.e., the *IMF*, and the earth's magnetic field. This process is basically the same as that of an *MHD* generator.

The generated energy through the natural power plant is partially discharged and eventually dissipated in the polar ionosphere through such a non-linear plasma processes as substorms. The discharge process produces a great variety of phenomena in the magnetosphere and the ionosphere: see *Kamide and Baumjohann* [1993] for details. The aurora substorm is one of the manifestations.

If the ionosphere does not exist at all, we would not expect much: see Section 5 for the characteristics of the ionosphere. A number of exciting phenomena, such as auroral displays, occur because the energy from the solar wind-magnetosphere dynamo is transmitted mainly to the nightside ionosphere through the magnetotail. It is also important to note that the ionosphere is not merely a passive load, but it does constitute a complex feedback system with the magnetosphere. The amount of energy released in the high-latitude ionosphere during a single substorm is in fact negligibly small, compared to the free energy available in the magnetosphere

which is powered from the solar wind-magnetosphere dynamo. It is therefore possible to assume that substorms are a random process that occurs any time regardless of the amount of the energy that the magnetosphere-ionosphere system gains from the solar wind.

Studies have shown, however, that substorms do not occur at random but the magnetosphere is a rather efficient system in both extracting the solar wind energy and converting the extracted energy into the substorm energy on such a rather short timescale as a few hours. The magnitude and the location of substorms, as well as the probability of substorm occurrence are all correlated well with the degree to which the magnetosphere couples with the solar wind.

3.2. Substorm intensity

The magnitude of substorms, in terms of the total current of the auroral electrojets, has been shown to be correlated with the southward component of the *IMF*. The total electrojet, thus the energy of substorms dissipated in the polar ionosphere, is more intense when the *IMF* is more southward directed. The magnetosphere reaches the "ground" state only during a prolonged period of a large positive B_z value, and under such a condition the auroral oval contracts to its minimum size. The midday and midnight portions of the auroral oval contract to invariant latitudes of 81-82º and 72-73º, respectively. The total area of the minimum size of the polar cap which is surrounded by the auroral oval is approximately 7.5 10^6 km^2.

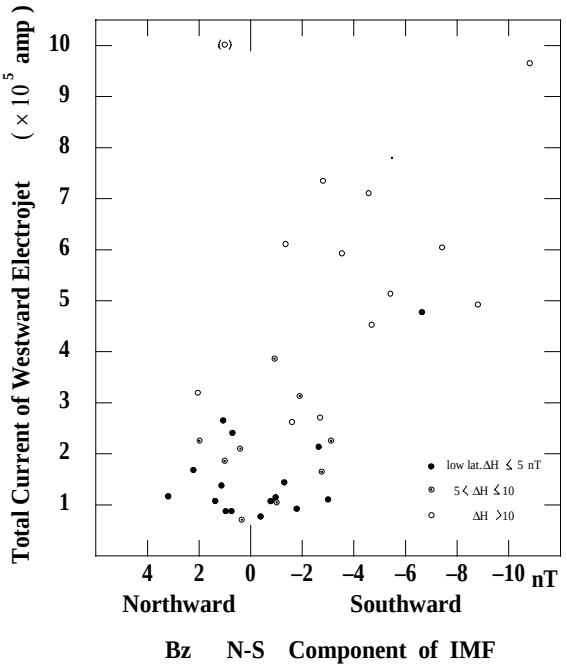

Figure 6. Dependence of the intensity of the total westward auroral electrojet on the north-south component of the interplanetary magnetic field for different values of mid-latitude positive H perturbations [indicated by different symbols]. After Kamide and Akasofu [1974].

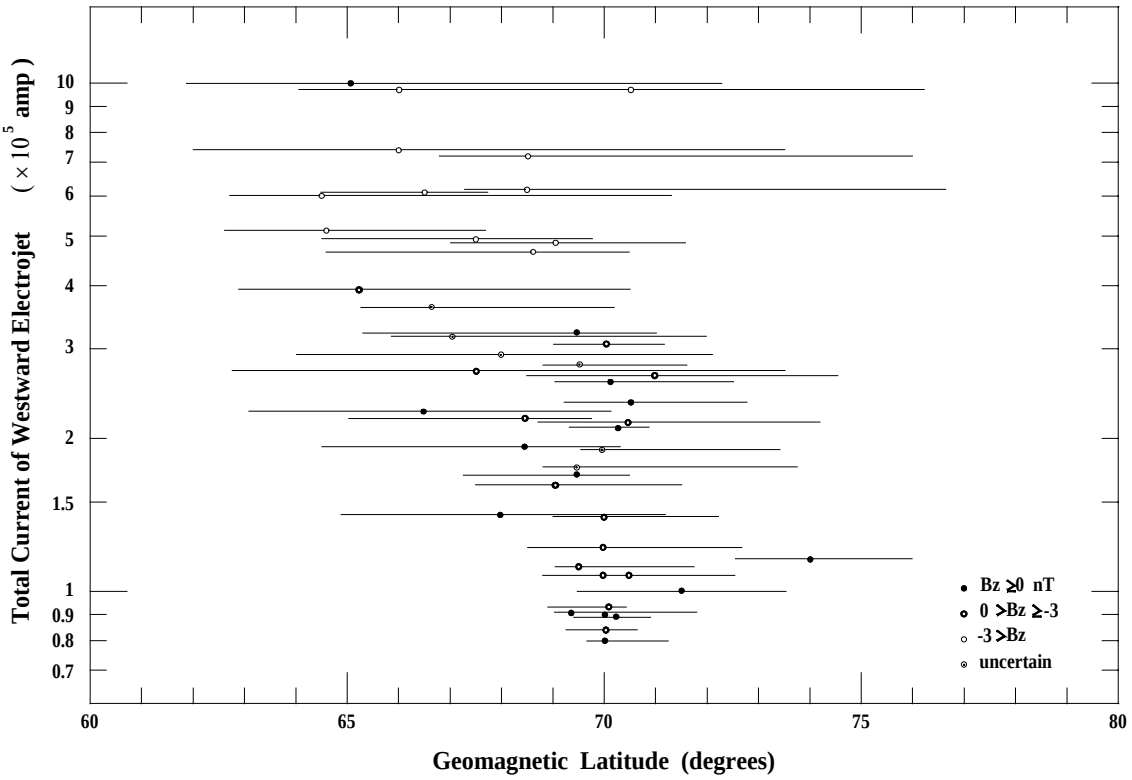

Figure 7. Location and the total current intensity of the auroral electrojet during the maximum phase of substorms for different values of the IMF B_z component [indicated by different symbols]. After Kamide and Akasofu [1974].

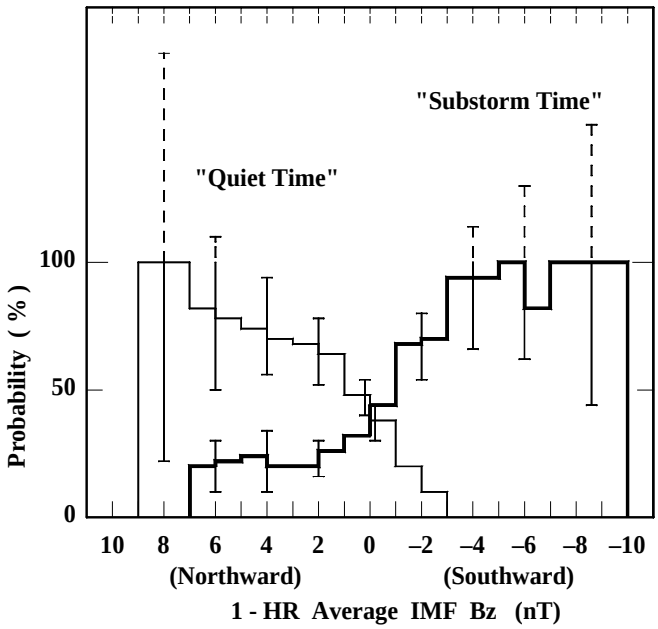

Figure 8. Probability of substorm time [represented by the heavy line] and quiet time [by the light line] as a function of the Bz value of the IMF. After Kamide et al. [1977].

On the basis of a detailed examination of the latitudinal dependence of electrojet intensity, *Kamide and Akasofu* [1974] discussed the magnitude of substorms in terms of the total current of the westward auroral electrojet. The corresponding north-south polarity of the *IMF* and mid-latitude geomagnetic perturbations were also examined. Figure 6 shows the statistical relationship between the total current of the westward electrojet and the B_z value of the *IMF*. Average B_z values during the hour preceding the maximum phase of substorms were used. It can be seen that for substorms associated with a northward *IMF* and a southward *IMF* of small magnitudes [*less than approximately 3 nT*], the intensity of the total westward electrojet is small [*at most 4. 10^5 A*]. The only exception [*the bracketed circle*] in Figure 6 occurred during a magnetic storm.

3.3. Location of substorm occurrence

The location of the substorm expansion onset is also controlled by the polarity of the *IMF*: substorms occur at higher latitudes when the *IMF* is less southward-directed. Figure 7 shows the latitude of the electrojet center during the maximum phase of substorms as a function of the total current intensity; the half widths [*which are different on the equatorward and poleward sides of the center*] of the electrojet are also shown by a horizontal line. It is clear that the region of the electrojet shifts systematically equatorward as the total current intensity increases; an increase in substorm intensity from 10^5 to 10^6 A in the total current intensity is associated with an equatorward shift from 70º to 65º. There is also a tendency for the latitudinal width of the electrojet to increase for greater values of the current intensity.

One interesting feature is that weak substorms, regardless of whether they are associated with a positive B_z or a weak negative B_z of the *IMF*, tend to occur along the contracted auroral oval at higher latitudes. Such small, yet important, substorms cannot be detected without, at least, several meridian chains of stations. In terms of the total electrojet current intensity, the intensity of substorms ranges from less than 10^5 A to more than 10^6 A. Since Joule heating of the auroral electrojet is a significant part of substorm energy dissipated in the polar ionosphere, it is important to note that there is a difference of more than 10^2 in the amount of dissipated energy between weak and intense substorms [*Baumjohann and Kamide*, 1984; *Lu et al*., 1995]. This means that the parameters that control the total energy of substorms must have a similar dynamic range. It is conceivable that the magnetic field intensity B or energy $B^2/8\pi$ at the location of the substorm origin in the magnetotail is an important factor in determining the substorm intensity, since weaker substorms tend to occur at higher latitudes and thus at greater geocentric distances than stronger substorms.

3.4. Probability of substorm occurrence

There is one important problem which is crucial in seeking substorm generation mechanisms [see, for example, *McPherron*, 1970; *Lui*, 1991; *Lyons*, 1995]. Does substorm occurrence probability depend on the B_z component of the *IMF* [*or equivalently on the size of the auroral oval*]? If the occurrence frequency has a strong dependence on the *IMF* direction, it is reasonable to state that the occurrence frequency of substorms is closely related to the amount of energy stored in the magnetotail, since there is a definite relationship between the *IMF* B_z and the magnetic energy stored in the magnetotail [e.g., *Fairfeild and Lepping*, 1981]. If, on the contrary, the occurrence probability has no such dependence, substorms may be regarded as a random process. This dependence was difficult to examine critically because of the lack of continuous observational data on the entire polar region.

Lui et al. [1975] have shown that the substorm "seeing" probability decreases as the auroral oval size decreases. It was then suggested that although the seeing probability is not the same as the occurrence probability, there is the possibility that the latter decreases as the auroral oval contracts poleward.

Figure 8 shows the frequency [*probability*] of observing substorms as well as quiet times as a function of the *IMF* B_z [*Kamide et al.*, 1977]. The probability P [*in percent*] was computed as $P = S / T \times 100$, where S is the number of substorm events in every 1 nT interval of B_z and T is the total number of the samples in the same B_z interval. The substorm probability presented in Figure 8 is the probability of a substorm observation with electron spectra by polar-orbiting satellites, ISIS 1 and 2. It is seen that the substorm probability increases as B_z decreases; however, this increase does not occur in a simple way. In the range $B_z \geq 2$ nT the probability is almost constant at the 20-30% level. It then increase monotonically for greater southward *IMF*, and if the magnitude of the southward B_z is larger than 5 nT, the substorm probability becomes essentially 100%.

This statistical result somewhat restricts our options in seeking generation mechanisms for magnetospheric substorms. Figure 8 clearly shows that substorms do not occur with an equal probability for different values of the *IMF* B_z component for different sizes of the auroral oval. Since the magnetospheric substorm can be considered a process by which the magnetosphere tends to remove sporadically the excess energy in the magnetotail, the substorm occurrence probability is closely related to the amount of energy stored in the magnetotail. This implies that the triggering mechanism has something to do with an increase in the stored energy. In what way? We do not have, at present, a satisfactory answer to this simple question.

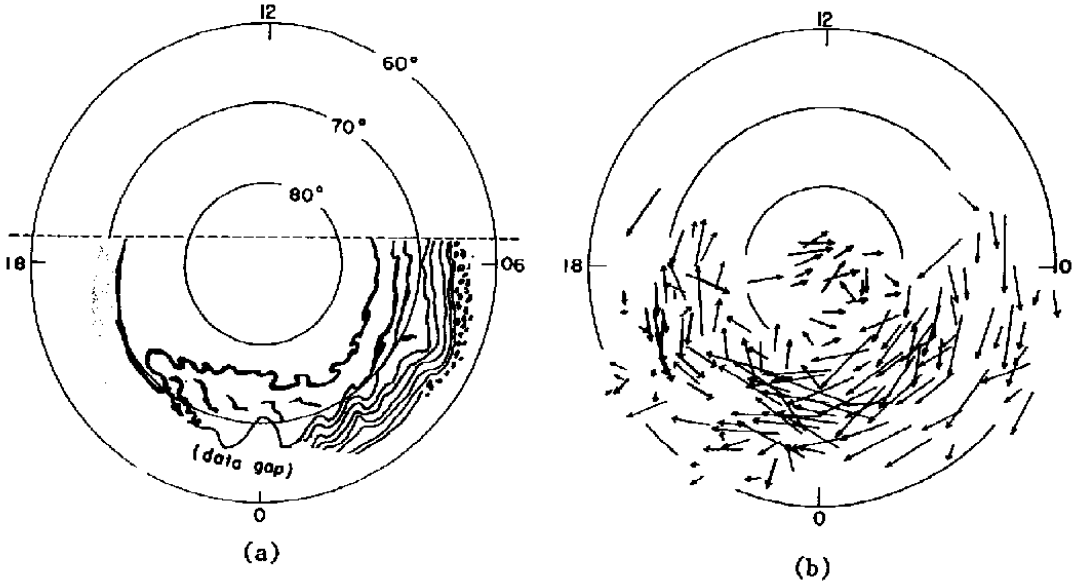

Figure 9. [a] Schematic diagram of auroral features during a typical auroral substorm. [b] Distribution of equivalent current vectors with reference to the auroral features shown in [a]. The magnitude of each current vector is normalized for the maximum magnitude of the magnetic perturbation of 500 nT. After Kamide and Akasofu [1975].

4. The Auroral Electrojets

Figure 9 shows a nightside half of Figure 5, which is a schematic diagram of auroral characteristic features. In order to identify global auroral behavior with high-latitude ionospheric currents, the distribution of equivalent current vectors [see *Kroehl and Richmond*, 1977 for details on the practical procedure of calculating the equivalent current function] is plotted for the maximum phase of substorms. It is clear that the current flow at high latitudes is concentrated in the auroral oval, forming the auroral electrojets. The auroral electrojets are the most prominent current flow at high latitudes.

The term "auroral electrojet" was used originally to describe a specific class of current configuration in which spatially concentrated currents flow at auroral latitude. How and how much concentrated is not defined quantitatively, but there is no doubt that the concentration of the current flow has a close connection with auroral displays, particularly with the discrete aurora. In fact, in the past, it has been tacitly assumed that the auroral electrojets are most intense in the region of bright auroral luminosity. Is this really the case?

It is legitimate to assume that precipitating auroral electrons are responsible for active auroral displays and, at the same time, for enhancing the rate of ionization of the upper atmosphere and the ionospheric conductivity, thus increasing the ionospheric currents. There is no a priori guarantee, however, that the corres-

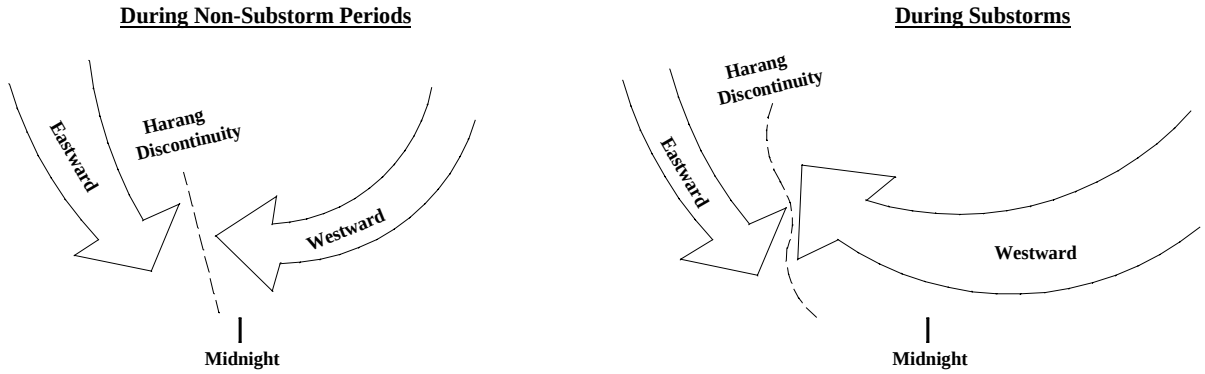

Figure 10. Sketch of the auroral electrojets during substorms [right] and during non-substorm times [left].

ponding electric field is unchanged in the auroral region when intense auroral precipitation occurs during substorms.

Figure 10 shows schematic illustrations of the auroral electrojets, eastward and westward, for relatively quiet periods and for disturbed times. The so-called Harang discontinuity region is defined by the boundary region between the two electrojets, or the boundary between the regions of northward and southward electric fields. One of the differences between substorm and non-substorm times lies in the local time of the Harang discontinuity. During substorms, the westward electrojet penetrates deep into the evening sector through the midnight sector. Typical values of ionospheric electric fields and conductivities for the two conditions are listed in Table 1, where high degree of variability in these parameters is noted, depending upon the intensity of substorms and even on the substorm phases during a single substorm.

During Nonsubstorm Times

	Eastward Electrojet	*Westward Electrojet*
Center of Electrojet	Near 1800 MLT	Near 0600 MLT
Electric Field [E]	20-50 $mV.m^{-1}$ [Northward]	0-20 $mV.m^{-1}$ [Southward]
Pedersen Conductivity [Σ_P]	2-5 S	2-5 S
Hall Conductivity [Σ_H]	2-5 S	2-10 S

During Substorms

	Eastward Electrojet	*Westward Electrojet*
Center of Electrojet	Near 1800 MLT	Anywhere in the dark sector
Electric Field [E]	20-50 $mV.m^{-1}$ [Northward]	0-100 $mV.m^{-1}$ [Southward]
Pedersen Conductivity [Σ_P]	5-10 S	10-20 S
Hall Conductivity [Σ_H]	5-10 S	20-50 S

Table 1. Typical values of ionospheric conductivities and electric fields during substorms and nonsubstorm times

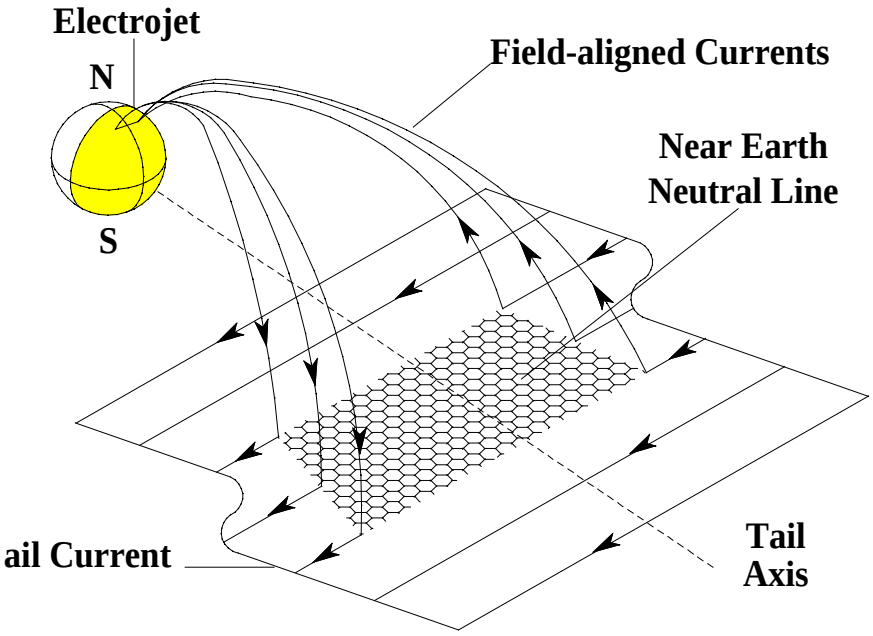

Figure 11. The diversion or disruption of the tail current through the ionosphere during the substorm expansion phase. After McPherron [1991].

During substorms, the ionospheric current flow is affected essentially in two ways to accommodate the enhanced energy input from the solar wind via increased dissipation: see *Baumjohann and Treumann* [1996]. On one hand, the current flow in the "convection" auroral electrojets increases directly relating to the energy input from the solar wind along with the directly-driven process in solar wind-magnetosphere interactions [see *Akasofu*, 1981; *Baker et al*., 1985; *Rostoker et al*., 1983; *Pellinen*, 1993]. On the other hand, the solar wind energy which is not directly dissipated via enhanced convection in the auroral electrojets is stored once in the magnetotail, mainly in the form of magnetic energy by enhancing the neutral sheet current. This is accomplished by a significant distortion of the nightside magnetospheric field lines into a tail-like configuration even at small radial distances where the field is basically dipolar. After some 30-min. long phase of energy storage, the magnetic tension is suddenly released at expansion phase onset. This is equivalent to the partial disruption of the tail current, generating short-circuiting the neutral sheet current in an azimuthally limited region of the tail and diverting its current along magnetic field lines and through the auroral ionosphere in the midnight sector [*McPherron et al*., 1973]. Sudden release of energy which has previously been stored in the magnetotail leads to the formation of the so-called substorm current wedge with enhanced westward current flow in the midnight ionosphere: see Figure 11 [*McPherron*, 1991].

What leads to the short-circuiting of the neutral sheet current and the formation of the substorm current wedge is to be unveiled in future studies. The substorm current wedge expands both poleward and westward during the course of the ex

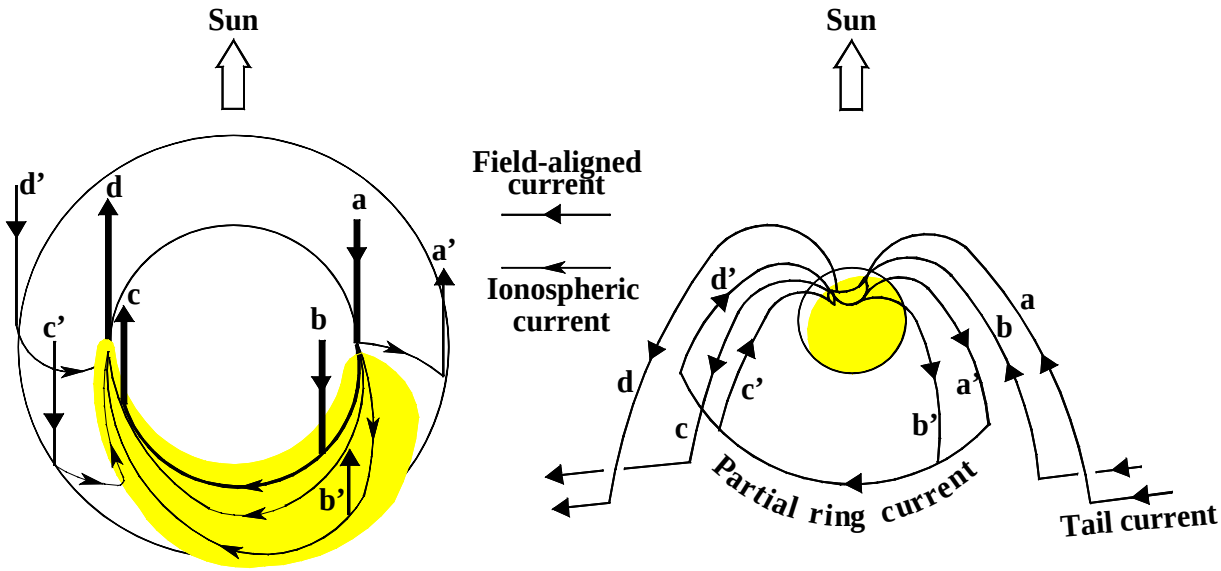

Figure 12. [a] Model current system for polar substorms. The dotted area represents the region of the westward electrojet. [b] Schematic illustration of the three-dimensional current system for magnetospheric substorms. After Kamide et al. [1976].

pansion phase. Its western edge is always collocated with the head of the westward traveling surge, a unique auroral form typically associated with the substorm expansion phase [*Meng et al.*, 1978; *Baumjohann et al.*, 1981]. The detailed structure of ionospheric electric fields, conductances, and ionospheric and field-aligned currents in the substorm-disturbed region, especially near the head of the surge, can be unfolded by incoherernt-scatter radars [see, for example, *Banks and Doupnik*, 1975; *de la Beaujardiere et al.*, 1977].

A diversion of a fraction of the cross-tail current occurs along field lines to the ionosphere, within which the current flow is westward; see Figure 11. How is the current distributed in the auroral ionosphere? Figure 12 summarizes the vast amount of Chatanika radar observations [*Brekke et al.*, 1974], showing an empirical model of the three-dimensional current system for substorms [*Kamide et al.*, 1976]. The westward electrojet, which is one of the dominant manifestations of substorms, is fed by the field-aligned currents in a manner suggested by the wedge current model, but a significant part of the downward field-aligned currents in the morning sector flows southward, and then flows out of the ionosphere as the upward currents.

It is evident that the current pattern is much more complicated in the evening sector than in the morning sector. There are downward field-aligned currents in the area of the eastward electrojet. The intense upward currents are connected with the westward electrojet in the premidnight sector and also with the northward ionosphere current, which is eventually connected to the inward field-aligned currents through the eastward electrojet. Thus, the integrated intensity of the upward field-aligned currents is much more intense than that of the downward

currents, showing the existence of a net field-aligned current [e.g., *Iijima and Potemra,* 1976]. This is consistent with the observations made by polar-orbiting satellites and with the inference from ground magnetic perturbations at mid-latitudes. This current configuration is also in good agreement with radar observations which show that the northward ionospheric current prevails in the evening sector [*Horwitz et al.,* 1978]. It is indicated that the eastward electrojet flows northeastward as it approaches the midnight sector and eventually connects to the westward electrojet in the Harang discontinuity region.

Without early observations by the Chatanika radar, it would have not been possible to reach such a realistic three-dimensional current system. Multi-radar studies from the *EISCAT KST* (Kiruna-Sodankilä-Tromsö) and *ESR* (EISCAT-Svarbard) radars are capable of making clear the changes of this system at different substorm phases. It should be noted that the global current patterns change quite dramatically in association with substorm times, or with the substorm phases [*Kamide and Kroehl,* 1994; *Kamide et al.,* 1996]. Thus, to understand the energy flow from the solar wind through the magnetosphere to the ionosphere on an individual bases, it is essential to describe details of temporal variations of the substorm current system before and during the substorms. This problem relates closely to the major question of the magnetospheric substorm and in particular to the evaluation of the relative importance of two energy dissipation mechanisms: the "directly driven" and "unloading" processes [*Akasofu,* 1981], both of which have been proposed as playing an essential role in magnetospheric substorms.

5. Ionospheric Electrodynamics During Substorms: Radar Measurements

The ionosphere is produced primarily by the ionizing action of ultraviolet radiation from the sun and auroral energetic particles that strike the upper atmosphere. Electric currents flow throughout the ionosphere and are strongly influenced by the presence of the earth's magnetic field. The motions of the ionospheric particles are affected by collisional interaction with upper-atmospheric particles, as well as by electric fields extended into the magnetosphere. In other words, the ionosphere is the physical link between the magnetosphere and the neutral atmosphere [*Killeen et al.,* 1985]. In particular, the polar ionosphere is a dynamic region, playing a key role in our understanding of the most fundamental plasma process, the substorm, occurring in the magnetosphere-ionosphere coupling system [e.g., *Foster et al.,* 1986]. It is the region where beams of auroral precipitation collide with atoms and molecules, ionizing and exciting them. Auroras result, intense electrojet currents flow, and a significant amount of heating is generated: see Section 2.

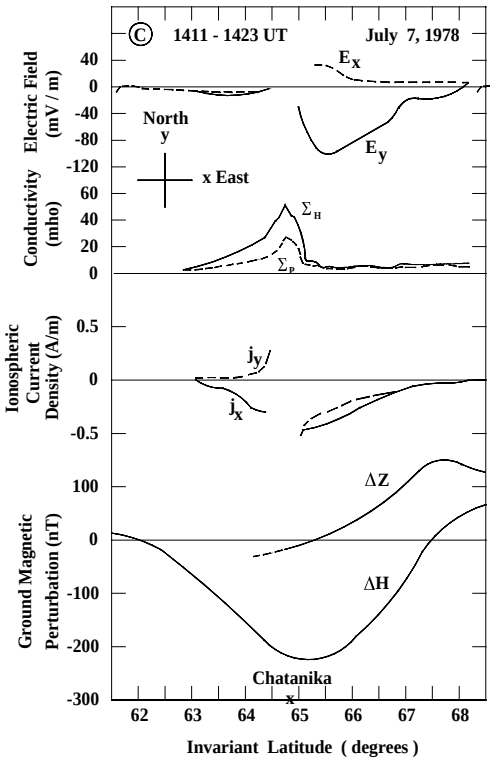

Figure 13. Latitudinal profiles of the electric field, height-integrated conductivity, and ionospheric current, and the corresponding magnetic perturbations for the morning sector. After Kamide and Vickrey [1983].

There has been a growing realization that the polar ionosphere plays a principal role in large-scale magnetospheric processes; however, spatial/temporal variations in electric fields and currents have proved to be extremely complicated. Toward understanding of such complicated observations under various substorm conditions in terms of the basic assumptions that lead to reproducing the main features of observed phenomena, incoherent scatter radars are capable of examining many different parameters in the ionosphere [see *Schlegel*, 1996; *Richmond*, 1996]. These parameters obtained by the radars during the different phases of substorms can then be compared with satellite measurements of electric fields and currents as well as with simulation studies in which the corresponding parameters can be changed to a realistic degree to demonstrate how the basic equations/assumptions are able to reproduce the key character of radar observations.

To address the question of whether it is the changes in the conductivity or in the electric field that are most important in producing enhanced currents, i.e., the auroral electrojets, in different regions of the polar ionosphere, it is then essential to be able to measure more than one ionospheric parameter simultaneously at more than one site. One of the merits of the operation of coherent scatter radars is that in certain modes of operation, the radar beam can probe the altitude/latitude distribution of electron density and line of sight plasma drifts from which the electric fields, conductivities, and currents in the ionosphere can be determined [see *Robinson et al.*, 1985].

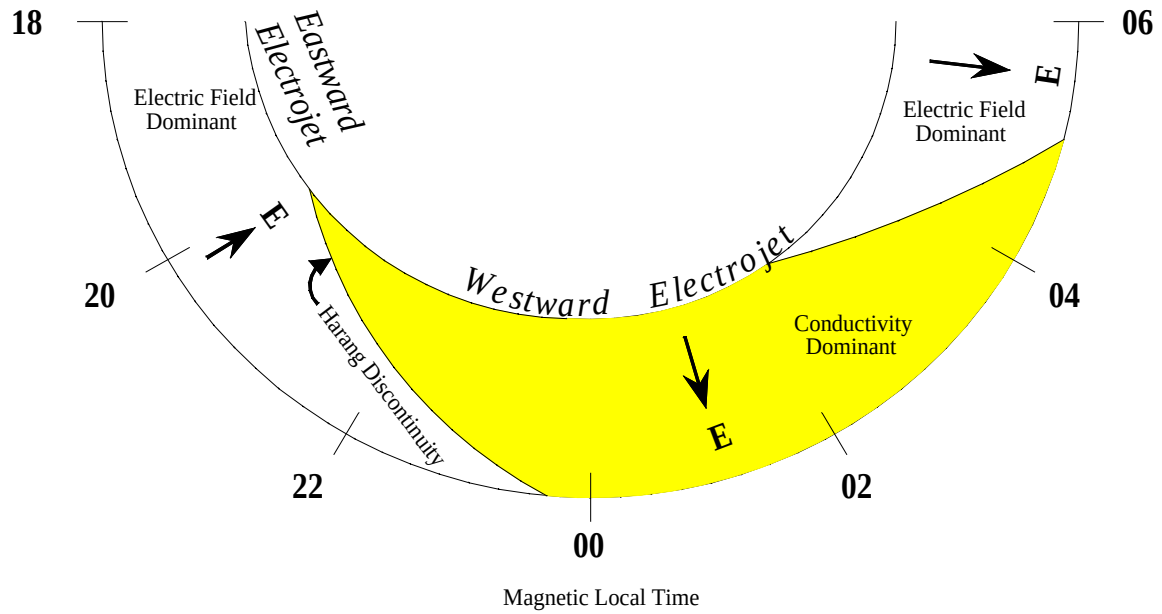

Figure 14. Schematic diagram of the auroral electrojets showing different roles of electric fields and conductivities in the eastward and westward electrojets at different latitudes and local times.

In order to clarify the different roles of the conductivity and electric field in the different electrojet regions, data from the Chatanika radar were used, examining how they change over latitude during substorms [*Kamide and Vickrey*, 1983]. The latitude profile of the ionospheric current in the morning sector indicates, as shown in Figure 13, that the westward electrojet was flowing in the region between 63° and 68°, having a northward [*southward*] component in the equatorward [*poleward*] half of the electrojet. An interesting feature of this latitudinal profile is that in the equatorward half of the westward electrojet, the conductivity was high while the electric field was small. The situation tended to be reversed in the poleward half, where the southward electric field was very intense but the conductivities dropped drastically. This characteristic implies that bright auroras and the corresponding energetic electron precipitation were present only in the equatorward half of the morning westward electrojet. The center of the electrojet seemed to be located in the region sandwiched by two peaks in the southward electric field and the conductivity.

The ratio between the Hall conductivity and the electric field has also been examined as a function of magnetic local time. If we use commonly adopted units, S and mV/m, respectively, their average ratio for the eastward electrojet is found to be less than 0.5, whereas that for the midnight sector westward electrojet before 03:00 MLT is close to 4. The Hall conductivity of the midnight sector westward electrojet is sometimes 15 times greater than that in the eastward electrojet.

In the region of the eastward electrojet in the evening sector, the northward electric field is the main contributor to the magnitude of electrojet current, in the sense that the field magnitude is greater, compared to the southward field magni-

tude in the westward electrojet. Another point of interest is that there are essentially two modes to the westward electrojet: one in which the contributions to the electrojet magnitude are "conductivity dominant" and the other "electric field dominant." The exact classification into these two modes of the westward electrojet using observed data is difficult, if not impossible, because the corresponding currents are contiguous everywhere. The substorm westward electrojet near midnight is characterized mainly by the relatively high Hall conductivity, whereas the westward electrojet in the morning sector is dominated by the large southward electric field.

Figure 14 summarizes these characteristics quite nicely. The boundary between the conductivity dominant and electric field dominant westward electrojets is not as clear in reality as is indicated in Figure 14. However, an important point is that, although it has been a common practice to assume that the westward electrojet is associated during substorms with a conductivity enhancement, a part of the westward electrojet in the later morning sector can be intensified without having high conductivity values. In particular, the latitudinal profile of the westward electrojet in the early morning sector [01:00-03:00 MLT] would indicate that its poleward portion has a relatively strong southward electric field while its equatorward portion has a relatively high Hall conductivity.

It is of great importance to investigate further whether the eastward electrojet in the evening sector and the westward electrojet in the late morning sector in Figure 14 may be driven by a voltage source in the magnetosphere, while the substorm westward electrojet in the midnight sector is supplied from a current source by, for example, the disruption of portions of the magnetotail currents. It has already been shown that there are basically two types of current systems: *DP 1* and *DP 2* [*Nishida and Kokubun*, 1971; *Baumjohann*, 1983]. *Clauer and Kamide* [1985] indicated that these two modes can coexist at all times during disturbed periods and the relative strength of these currents varies from time to time, making individual current patterns very complex. Furthermore, the pattern of "*enhanced*" *DP 2* has been shown to appear throughout substorm activity: see, for example, *Shue and Weimer* [1994]. Note that Figure14 supports the idea that the conventional *DP 2* currents are governed by electric field enhancements while the substorm *DP 1* currents are mainly caused by strong conductivity increases, accompanying the breakup auroras.

It is important to realize that on days with nearly persistent energy input from the solar wind, both processes are typically operating at the same time. It is conceivable that this is the reason why substorm signatures, such as the distribution of magnetic perturbations vectors and electric fields and its time changes, are quite complicated. Although it has long been argued that certain substorm-

associated phenomena are consistent or inconsistent with either the directly-driven process or the loading-unloading process, one could resolve such confusion by realizing that the magnetospheric substorm involves the two processes simultaneously. As demonstrated in *Kamide and Kokubun* [1996], coordinated radar observations with spacecraft will increase the potential of understanding the relative importance of the two processes during the different phases of substorms.

6. Modeling of Electric Fields and Currents in the Polar Ionosphere

6.1. Basic Equations

The active role of the polar ionosphere is to link the magnetospheric plasma and the neutrals in the thermosphere. The self-consistent chain for the entire magnetosphere-ionosphere coupling system represents a closed loop consisting of a number of individual links [see Figure 15, *Vasyliunas*, 1970]. Studies of theoretical models, which are intended to examine the entire loop, and those intended to aid in the understanding of "local" chains, or individual links, must be complementary to each other. It is in the local regions where remarkable energy conversion processes such as substorms are taking place. It is important to realize that although incoherent-scatter radars are a powerful tool with which to sense the electrodynamic state of the ionosphere, they also provide us with essentially

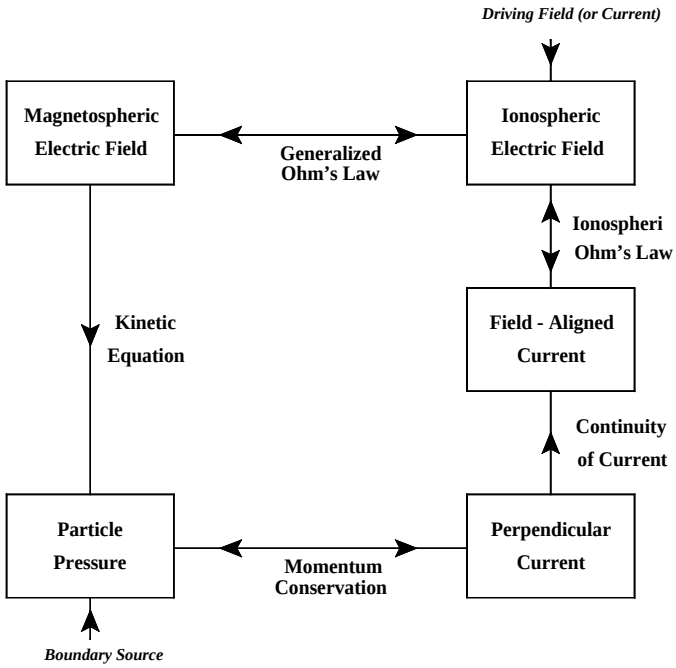

Figure 15. Logic diagram for a self-consistent calculation of magnetosphere-ionosphere coupling associated with magnetospheric convection. Each line joining two adjacent boxes is labeled with the physical principle or equation that links the two physical quantities. After Vasyliunas [1970].

"point" measurements. The radar measurements need to be complemented/normalized by numerical simulations of the entire chain of processes. This section presents the basic equations for simple models with special emphasis placed on ionospheric electrodynamic processes. It attempts to obtain a set of numerical solutions to the equations governing the magnetosphere-ionosphere system in such a way as to include far less idealization or simplification by referring to more essential observational characteristics than would be required for pure theories. In this way, it is possible to demonstrate how the basic assumptions lead to the main signatures in the high-latitude ionosphere, as observed by incoherent-scatter radars.

In order to simplify conditions, a number of assumptions are made throughout the entire calculation process. The most important and crucial assumptions we employ are as follows:

[1] The ionosphere is regarded as a two-dimensional spherical current sheet with a height-integrated layer conductivity.

[2] The earth's magnetic field lines are taken to be equipotentials, neglecting parallel electric fields.

[3] Only steady-state solutions are considered.

The continuity equation for electric currents under these simplifying conditions is expressed as

$$\text{div } \mathbf{J} = j_{||} \sin \chi \tag{1}$$

where $\mathbf{J}$ is the height-integrated ionospheric current density, $j_{||}$ is the density of the field-aligned current [*positive for a downward current*], and χ is the inclination angle of a geomagnetic field line with respect to the horizontal ionosphere. Ohm's law for the ionospheric current is written as

$$\mathbf{J} = \underline{\underline{\Sigma}}\, \mathbf{E} = - \underline{\underline{\Sigma}}\, \nabla \Phi \tag{2}$$

where $\mathbf{E}$ and Φ are the electric field and the corresponding electrostatic potential, respectively, in the frame rotating with the earth, and $\underline{\underline{\Sigma}}$ is the dyadic of the height-integrated ionospheric conductivity. The combination of Eqs. (1) and (2) yields

$$\nabla \cdot [\, \underline{\underline{\Sigma}}\, \nabla \Phi \,] = - j_{||} \sin \chi \tag{3}$$

which is to be solved for Φ under suitable boundary conditions. The boundary conditions we employ can be:

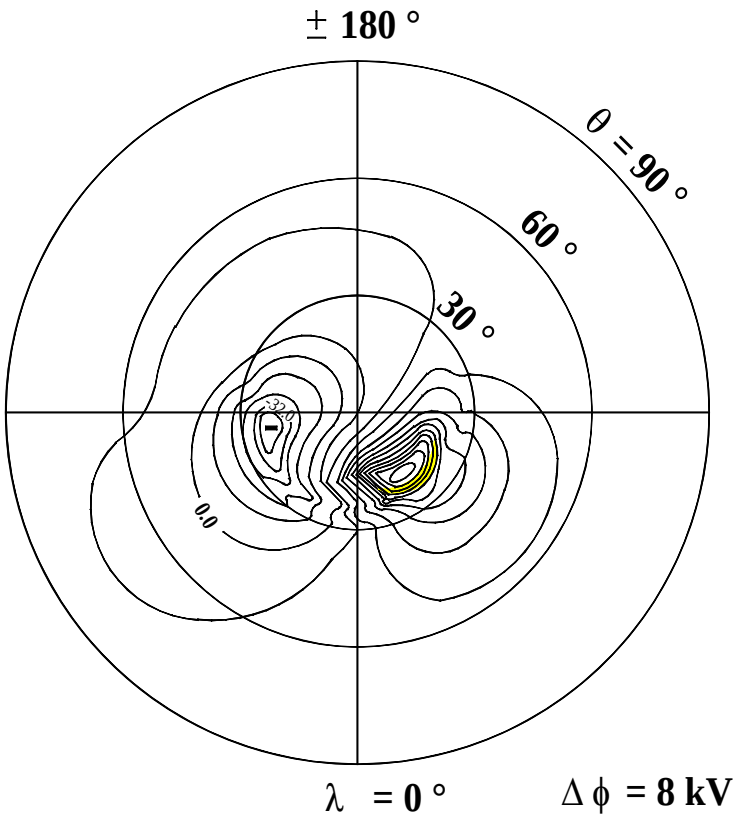

Figure 16. Electric potential distribution [8-kV contour interval] over the northern hemisphere for a typical medium-size substorm. After Kamide and Matsushita [1979].

$$\begin{aligned} \Phi &= 0 \qquad \text{(at the poles)} \\ \frac{\partial \Phi}{\partial \theta} &= 0 \qquad \text{(at the equator)} \end{aligned} \tag{4}$$

where θ is the colatitude. As long as we concentrate on the high-latitude ionosphere [*say*, $\theta \leq 30^{o}$] , the boundary conditions are not very important. In solstitial seasons, however, an asymmetry in the ionospheric conductivity between the northern and southern hemispheres is present, and hence the resultant electric currents are also expected to be asymmetric. In such cases, actual calculations are made for both the northern and southern hemisphere, depending on the season.

Given a specific conductivity model and an assumption about the field-aligned current distribution, one can solve Eq. (3) to find the electric potential Φ in the high-latitude ionosphere. The differential equation corresponding to Eq. (3) is solved numerically to obtain the most probable potential value at each of the grid points in the scheme. By using the [θ, λ] coordinate system, in which θ is colatitude and λ is longitude, measured eastward from midnight, Eq. (3) can be reduced to the form

$$A\frac{\partial^2 \Phi}{\partial \theta^2} + B\frac{\partial \Phi}{\partial \theta} + C\frac{\partial^2 \Phi}{\partial \lambda^2} + D\frac{\partial \Phi}{\partial \lambda} = F \tag{5}$$

where

$$A = \sin^2\theta\,\Sigma_{\theta\theta}, \qquad D = \sin\theta\frac{\partial \Sigma_{\theta\lambda}}{\partial \theta} + \frac{\partial \Sigma_{\lambda\lambda}}{\partial \lambda},$$

$$B = \sin\theta\left[\frac{\partial \sin(\theta\,\Sigma_{\theta\theta})}{\partial \theta} - \frac{\partial \Sigma_{\theta\lambda}}{\partial \lambda}\right], \qquad F = -a^2 j_{||} \sin^2\theta \sin\chi,$$

$$C = \Sigma_{\lambda\lambda}, \qquad \sin\chi = \frac{2\cos\theta}{(1 + 3\cos^2\theta)^{1/2}},$$

and a is the radius of the current sheet. Note that if all the conductivity gradients are neglected Eq. (5) is reduced to the Poisson equation. Further, in the region where $j_{||} = 0$, the Laplace equation is obtained.

The component of the height-integrated ionospheric current **J** is given by

$$\begin{bmatrix} J_\theta \\ J_\lambda \end{bmatrix} = \begin{bmatrix} \Sigma_{\theta\theta} & \Sigma_{\theta\lambda} \\ -\Sigma_{\theta\lambda} & \Sigma_{\lambda\lambda} \end{bmatrix} \begin{bmatrix} E_\theta \\ E_\lambda \end{bmatrix} \tag{6}$$

where the electric field component is expressed as:

$$E_\theta = -\frac{\partial \Phi}{a\,\partial \theta}, \qquad E_\lambda = -\frac{\partial \Phi}{a \sin\theta\,\partial \lambda} \tag{7}$$

6.2. Typical substorm

A model calculation for a “typical” substorm is presented. Note that actual substorms exhibit highly variable processes in the magnetosphere-ionosphere system. Based on models of the average distribution of the ionospheric conductivities and of field-aligned currents derived from radar and satellite observations, the electric potential is solved [see *Kamide and Matsushita*, 1979]. Figure 16 shows the result. If the potential at the pole is assumed to be zero as one of the boundary conditions, the highest and lowest potential values are 88 and -40 kV, respectively. The large difference between the magnitudes of these values indicates how strongly the conductivity gradients *[both in the background day-night gradient and in the auroral oval*] influence the overall potential distribution. There is also a considerable distortion of the equipotential contours within the nightside conductivity inhomogeneity, which produces an accumulation of the space charges. A comparison of this potential pattern for the typical substorm model with the pattern for quiet periods [*not shown here*] shows how intense auroral enhancements can change the pattern of equipotential contours. For example, the potential centers undergo a significant shift from quiet periods to sub-

storms; the high potential contours move toward midnight, while the low contours move away from midnight.

The distribution of the ionospheric current vectors *[not shown here*] indicates the following important features:

[1] The eastward electrojet flows in the equatorward half of the evening auroral belt, while the westward electrojet flows in wider regions in the evening and morning sectors.

[2] The main part of these electrojets is supplied by the assumed field-aligned currents, because the ionospheric current in the polar cap and mid-latitudes is very small.

[3] The westward electrojet appears to have two peaks, one at premidnight and one in the early morning hours. The maximum current density of the westward electrojet in the premidnight sector is produced primarily by the assumed high conductivity associated with a bright aurora. On the other hand, the westward electrojet in the morning sector occurs mainly as a result of the large electric field there, although the contribution from the enhanced conductivity is not negligible. The morning electrojet has a considerable southward component, which connects the downward field-aligned current [*to the north*] and the upward current [*to the south*] via the Pedersen current.

[4] The eastward electrojet is about one-third less intense than the westward electrojet.

[5] The eastward electrojet has a northward component, which becomes more intense with the progress of local time; even a totally northward current is seen in the premidnight sector. This means that a significant fraction of the eastward electrojet turns northward and eventually joins the westward electrojet.

Kamide and Matsushita [1979] simulated the variability of the ionospheric electric fields and currents in relation to the distribution of the field-aligned currents, which varies considerably during magnetospheric substorms. Changes in several parameters to a realist degree of the typical substorm model have been assumed. These changes are the result of intensity variations and locations shifts for field-aligned currents; effects of electric conductivity variations and seasonal changes; and effects of additional field-aligned currents and an expanded auroral oval.

7. The Role of Ground Magnetic Observations in Aurora/Substorm Studies

7.1. The concept of magnetogram-inversion techniques

Historically, ground-based magnetic records have been widely used to examine physical processes occurring in the magnetosphere and the ionosphere, since the magnetic data obtained at the earth's surface include valuable information about a variety of source currents flowing in the near-earth environment, including the ionosphere and magnetosphere, the magnetopause, and the earth's interior [see *Nishida*, 1978]. However, for that very reason, namely, that the data contain too much information, it has been a serious problem to evaluate the relative importance of these currents in generating the particular patterns of global or local magnetic perturbations that we are attempting to study [see *Akasofu et al.*, 1980].

It is well known that in reality, ionospheric currents, such as the intense auroral electrojets, are connected to field-aligned currents in a very complicated fashion, reflecting the variability of the degree of the magnetosphere-ionosphere coupling and causing a variety of different types and patterns of auroras and ground magnetic perturbations. As pointed out by *Potemra* [1987], however, the debate between Chapman and Birkeland concerning the existence of the field-aligned currents continued until the mid-1960s [*Zmuda et al.*, 1966], primarily because it is not possible to determine uniquely the separate effects of ionospheric and field-aligned currents only from ground magnetometer observations, on which the past studies have heavily relied.

Several computational techniques called the magnetogram-inversion methods have been proposed; see reviews, for example, by *Rees* [1982], *Kamide* [1982], *Feldstein and Levitin* [1986], *Glassmeier* [1987], and *Mishin* [1990]. These numerical schemes are designed to compute not only the global distribution of both ionospheric and field-aligned currents, but also ionospheric electric fields and the Joule heating rate. Once we understand properly the origins of ground magnetic perturbations in terms of various source currents, ground-based observations have an advantage over "more direct" measurements by radar and satellite, since variations in the geomagnetic field are being monitored continuously at a relatively large number of fixed points on the earth's surface. This contrasts with the intrinsic ambiguity in determining the global three-dimensional current system on an individual basis from single satellite passes, which have difficulties separating temporal and spatial changes.

This section describes the essence of the magnetogram-inversion scheme, along with its assumptions and limitations. Although several magnetogram-inversion techniques start with the same set of basic equations, the practical procedures as well as the points of emphasis vary considerably, depending on different

algorithms. The major algorithms [e.g., *Fayermark*, 1977; *Mishin et al.*, 1979; *Kamide et al.*, 1981] for obtaining the three-dimensional current system and ionospheric electric fields require, first of all, that an ionospheric equivalent current system can be adequately derived from an array of ground-based magnetic field measurements.

The equivalent current system is a toroidal horizontal sheet current $\mathbf{J}_T$ assumed to be flowing in a shell at a 110-km altitude, whose associated magnetic field matches the external portion of the observed magnetic variation field **b**. The toroidal current can be expressed in terms of an equivalent current function ψ. In the lower atmosphere, the magnetic variation can be expressed in terms of magnetic potential V as

$$\mathbf{b} = -\nabla V. \tag{8}$$

With a given equivalent current function ψ and given conductivities, one is able to derive the ionospheric electric field, horizontal current, and field-aligned current under the following simplifying assumptions:

[1] the electric field is electrostatic;

[2] geomagnetic field lines are effective equipotentials, i.e., there is no "parallel" electric field;

[3] the dynamo effects of ionospheric winds can be neglected;

[4] the magnetic contributions of magnetospheric ring currents, magnetopause currents, and magnetotail currents to the equivalent current function can be neglected; and

[5] geomagnetic field lines are effectively radial.

The height-integrated horizontal ionospheric current **J** can be expressed as the sum of the toroidal [*equivalent*] current $\mathbf{J}_P$ and a "potential" current $\mathbf{J}_T$ as

$$\mathbf{J} = \mathbf{J}_T + \mathbf{J}_P \tag{9}$$

where the second component can be written in terms of a current potential τ. This is a special case of the well-known Helmholtz theorem for vector analysis. The potential component can be considered as a closing current for field-aligned currents. The requirement that the three-dimensional current be divergence-free means that the field-aligned current density $j_{||}$ [*positive downward*] satisfies the relation

$$j_{||} = \nabla \cdot \mathbf{J} = \nabla \cdot \mathbf{J_P} \tag{10}$$

since $\mathbf{J}_T$ is by definition divergence-free. The current system represented by $j_{||}$ and $\mathbf{J}_P$ together produces no ground magnetic variation under the assumption that the toroidal component of **J** is just the equivalent current system.

Since the horizontal ionospheric current is related to the electric field **E** by

$$\mathbf{J} = \underline{\underline{\Sigma}}\, \mathrm{E} = \Sigma_P \mathbf{E} + \Sigma_H \mathbf{E} \times \mathbf{n}_r \tag{11}$$

where Σ_P and Σ_H are the height-integrated Pedersen and Hall conductivities, respectively, Eq. (9) is then rewritten as

$$\underline{\underline{\Sigma}} \,.\, \nabla \Phi = - \nabla \tau - \nabla \psi \times \mathbf{n}_r \tag{12}$$

where $\mathbf{J}_P = - \nabla \tau$. A partial differential equation for the electrostatic potential Φ in terms of ψ can be obtained by taking the curl of Eq. (12) as

$$\nabla \times [\nabla \psi \times \mathbf{n}_r] = \nabla \times (\underline{\underline{\Sigma}} \,.\, \nabla \Phi). \tag{13}$$

The magnetogram-inversion technique requires knowledge of the height-integrated Pedersen and Hall conductivities. Note in particular that the *KRM* numerical scheme [*Kamide et al.,* 1981] accepts essentially any anisotropic distribution of the conductivities. In spherical coordinates θ [*colatitude*] and λ [*east longitude*], one obtains

$$A \frac{\partial^2 \Phi}{\partial \theta^2} + B \frac{\partial \Phi}{\partial \theta} + C \frac{\partial^2 \Phi}{\partial \lambda^2} + D \frac{\partial \Phi}{\partial \lambda} = F \tag{14}$$

where the coefficients of this second-order differential equation are given by

$$A = \sin \theta \, \Sigma_H, \qquad D = \frac{\partial \Sigma_P}{\partial \theta} + \frac{\partial \Sigma_H}{\sin \theta \, \partial \lambda},$$

$$B = \frac{\partial \sin (\theta \Sigma_H)}{\partial \theta} + \frac{\partial \Sigma_P}{\partial \lambda},$$

$$C = \frac{\Sigma_H}{\sin \theta}, \qquad F = \frac{\partial}{\partial \theta}\left(\sin \theta \frac{\partial \psi}{\partial \theta}\right) + \frac{1}{\sin \theta} \frac{\partial^2 \psi}{\partial \lambda^2}$$

With a given current function ψ [*or its function, F*] and given conductivities and their gradients [*in A, B, C, and D*], the electric potential Φ can be solved for certain boundary conditions. Once the electric potential is obtained by solving Eq. (14) numerically, the components of the height-integrated ionospheric current can be readily calculated by Eq. (9). By inserting the ionospheric currents into Eq. (10), it is possible to derive the distribution of the field-aligned current density, obtaining the three-dimensional current system.

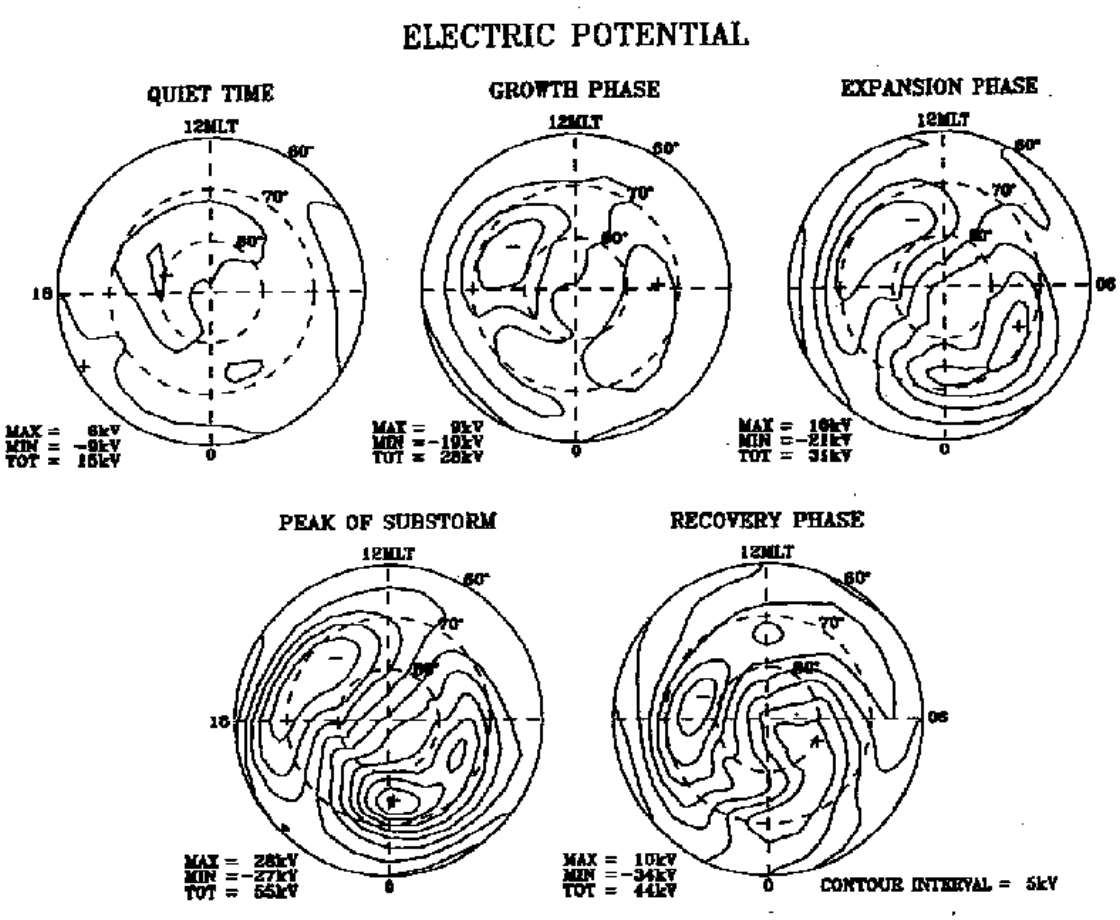

Figure 17. Average distribution of the ionospheric electric potential for the five phases of substorms. The maximum and minimum potential values, as well as the total potential difference are shown for each diagram. Contour interval: 5 kV. After Kamide et al. [1996].

Many recent studies have proven that the magnetogram-inversion technique is a powerful tool for evaluating quantitatively the three-dimensional current systems responsible for magnetic disturbances that occur at high latitudes associated with auroral displays. These “remote-sensing” schemes have also been shown to be quite useful in discussing magnetosphere-ionosphere coupling and in providing basic information, such as the electrostatic potential at the polar cap boundary, numerical modeling of magnetospheric plasma processes [*Wolf and Kamide*, 1983] and thermospheric wind patterns through the Joule heat dissipation from the ionospheric current. Unlike satellite measurements, the determination of electrodynamic parameters in the high-latitude ionosphere, using the magnetogram-inversion scheme, is not based on in situ data, but rather primarily on indirect magnetic measurements on the earth’s surface. However, with the magnetogram-inversion scheme it is possible to estimate the ionospheric quantities on a global scale [*instead of only along satellite orbits*] with a time resolution of about 5 min or even less over extended periods of time.

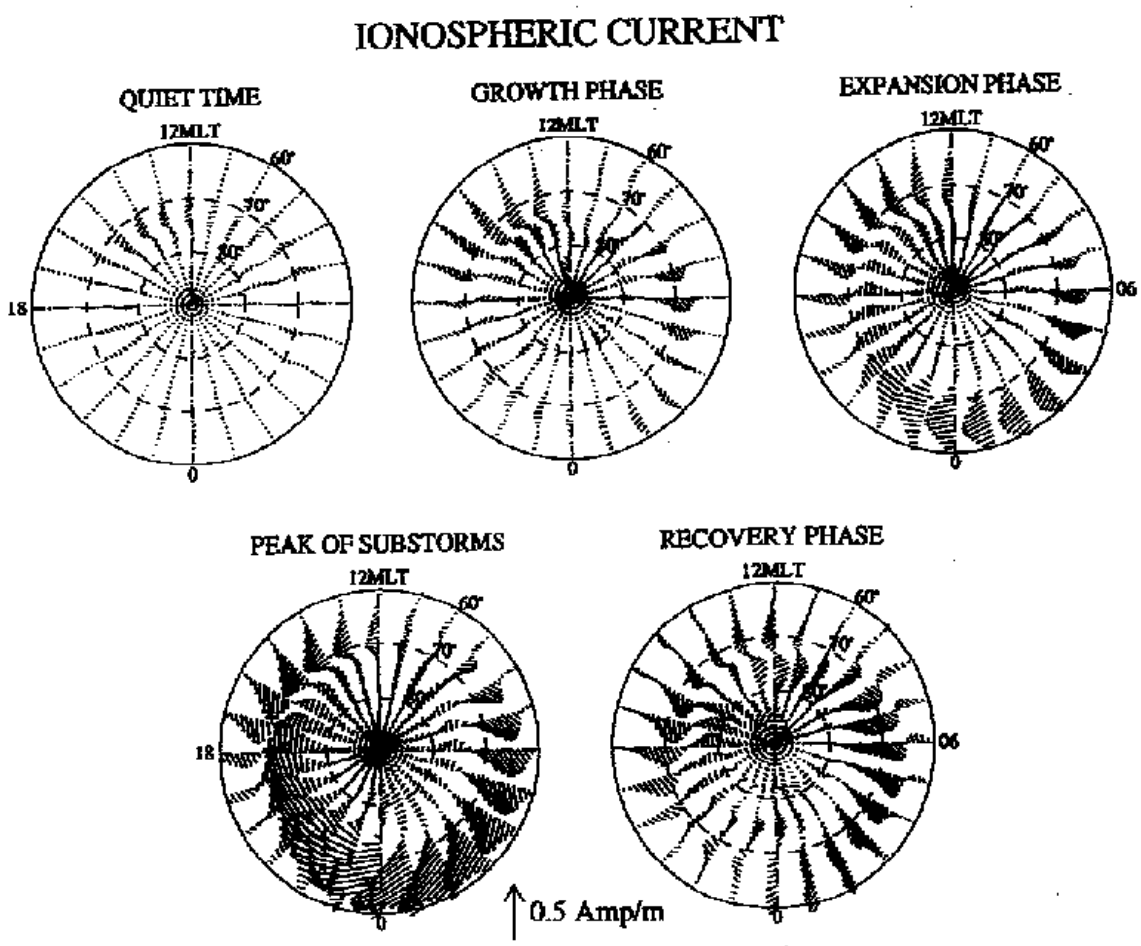

Figure 18. Average distribution of ionospheric current vectors for the five phases of substorms. The scale length of vector arrows is shown at the bottom. After Kamide et al. [1996].

The development of this particular method in the field benefited from considerable progress in other areas, such as in situ or more direct observations of electric fields by satellites and incoherent scatter radars. It would be useful to modify the numerical algorithm in such a way that simultaneous measurements of electric fields, conductivities, and field-aligned currents by satellite and radar could be incorporated into the scheme.

7.2. Applications to substorms

The *KRM* algorithm has been applied to a number of different sets of ground-based magnometer data for both quiet and disturbed periods. In this section we demonstrate one such recent study in which the *KRM* algorithm was extensively used to obtain the average patterns of ionospheric parameters for the different substorm phases. Five-minute resolution magnetometer data from the *IMS* meridian chains of observatories constitute the basic data set to estimate the distribution of ionospheric electric fields and currents as well as of field-aligned currents. From this data set, *Kamide et al*. [1996] have identified quiet times and four substorm phases: the growth phase, the expansion phase, the peak time, and the recovery phase.

Figures 17 and 18 show the global distribution of the ionospheric electric potential, and ionospheric current vectors, respectively, for the five different epochs. To obtain these average patterns, each of the KRM output plots has been normalized to the specific value: quiet time, –20 nT in the *AL* index, the growth phase, –100 nT; the expansion phase, –250 nT; the maximum epoch, –500 nT, and the recovery phase, –250 nT.

In Figure 17, the typical twin-vortex pattern in terms of the electrostatic potential can be identified, except for the quiet time. It can be seen that the dynamic range in the total potential difference is much smaller than that of the current density, indicating that the electric field is relatively important during quiet times. The difference in the total potential drop across the polar cap between the growth phase and the expansion phases is only 2 kV. Similarly, the decrease in total potential from the peak to the recovery phase of substorms is only less than 10%, when the corresponding current decreases considerably from 500 nT to 250 nT. These results clearly demonstrate that a large-scale electric field is dominant not only during the growth phase but also during the recovery phase of substorms. The overall pattern becomes most complicated during the recovery phase of substorms, as the relative size of the high/low potential vortices varies with respect to the substorm phases. The location of the peak potential is different at different substorm phases as well. With an increase in the electrojet current from the growth phase to the expansion phase, the peak of the high potential vortex approaches the midnight sector while the peak location of the low potential vortex seems to remain at approximately 15:00-16:00 *MLT*.

Figure 18 shows the distribution of ionospheric current vectors corresponding to the five substorm phases. During the growth phase of substorms, the eastward electrojet expands both latitudinally and longitudinally, and its intensity is almost doubled. The westward electrojet begins to grow during the growth phase and is centered at 06:00 MLT. During the growth phase, the intensities of the eastward and westward electrojets are nearly equal. At the expansion onset, however, the midnight portion of the westward electrojet is intensified dramatically, from less than 0.1 Am^{-1} before the expansion onset to nearly 0.4 Am^{-1} after the onset; however, its morning portion remains almost the same. At the maximum epoch of substorms, the westward electrojet extends over a wide *MLT* range including the evening sector where it intrudes into the region poleward from the eastward electrojet.

The substorm westward electrojet peaks in the midnight sector. It is significant that most of the changes in the current system occur as an addition of an intense westward current in the dark sector. During the recovery phase, the ionospheric current pattern strongly parallels that of the growth phase.

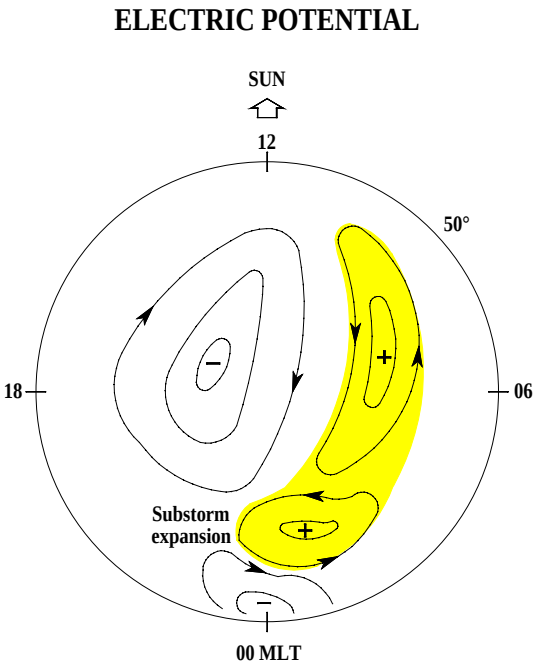

Figure 19. Schematic diagram showing two pairs of the electric potential cells, representing the effects of enhanced plasma convection and of the substorm expansion. The high potential area combining the two effects is hatched.

8. Future Direction

8.1. Two-component auroral electrojet

Interest in electrodynamic phenomena in the earth's high-latitude ionosphere has recently increased to a significant degree. This is primarily because of the availability of new experimental techniques for measuring a number of physical quantities in the polar ionosphere, but also due to the growing realization that the high-latitude region play a key role in large-scale coupling between the magnetosphere and the ionosphere.

How can the existence of the two electrojet components shown in Figure 14 be seen in the global potential patterns? Figure 19 is a schematic illustration of a pair of potential cells of enhanced convection and another pair of substorm expansion cells, coexisting during the expansion phase through the early recovery phase of a substorm. The convection pair represents large-scale magnetospheric plasma convection, which is controlled primarily by solar wind-magnetosphere interactions, such as "merging" and "viscous-like" processes, whereas the substorm-expansion pair results from substorm activity centered in the midnight sector. It is these substorm cells that are distorted strongly by enhanced ionospheric conductivities and associated with intense auroral displays in the midnight sector.

Figures 17 and 18 show that the global patterns of electric fields and currents in the ionosphere change systematically with the substorm phases. The changes can

be described in terms of two different components. Each one of the two components has its own characteristic distribution and timescale within the auroral electrojets. The auroral electrojet does not grow and decay as a whole; rather, only the portion in the midnight sector is enhanced at the time of auroral breakup. The other portion is controlled primarily by the electric field, which does not necessarily reflect auroral activity. It is known that the substorm expansion develops in a longitudinally localized region near midnight and then expands both eastward and westward, creating a conductivity-rich electrojet. The range of the conductivity-rich electrojet is limited in local time, depending perhaps on the strength of the substorm expansion.

These two components can be identified as the signatures for the directly driven and the unloading processes, respectively. The auroral electrojets associated with direct energy input from the solar wind into the magnetosphere flow primarily in the dusk and dawn sectors and increase in association with enhanced convection. This is a typical signature for the substorm growth phase which precedes the expansion phase onset.

Unloading of energy stored in the tail during the growth phase leads to the formation of the intense westward electrojet in the midnight sector during the expansion phase of a substorm. The enhancement in the conductivities results from an enhanced ionization caused by accelerated electrons, reflecting the unloading of energy from the magnetotail. It is important to emphasize that the directly driven component is present throughout the entire lifetime of a substorm, indicating that the solar wind energy is continuously fed to the magnetosphere, though with varying degrees. This component becomes, therefore, relatively dominant again during the late recovery phase as the unloading component wanes. Because of the existence of these two physically-different ingredients in the auroral electrojet, it is very important to locate a particular phenomenon observed by an incoherent-scatter radar with respect to the substorm-disturbed region. Caution must be exercised also to map accurtately the radar location to the auroral electrojet, which is quite dynamic during the expansive phase of substorms.

Some generally accepted interpretations have been found in a variety of observations, leading to a first-approximation model for auroras and substorms and their associated current configuration, but there are many problems that are either not satisfactorily settled in terms of basic physical concepts or are still subject to considerable controversy. One of the difficulties lies in the fact that, like all other natural phenomena, the magnetosphere-ionosphere system is influenced by many unknown conditions and that it is impossible to repeat the same experiment in the system under constant conditions. Thus, one may often fail to find the crucial parameters that fundamentally control the whole system of the magnetosphere and the polar ionosphere.

Many recent studies have dealt with the characteristic features of substorms presented by using a number of individual "snapshots" of the large-scale distribution of high-latitude electric fields and currents at key substorms times. In particular, a combination of ground-based and spacecraft data and modeling techniques, such as the AMIE technique [*Richmond and Kamide*, 1988] and the RCM [*Rice Convection Model*] algorithm, have been shown to be quite powerful in mapping the global patterns of the electric potential and their substorm changes. It is also important to reveal that the thermospheric neutral winds accelerated by energy dissipation processes associated with substorms do significantly influence the ionospheric and magnetospheric electrodynamics [e.g., *Forbes and Harel*, 1989; *Lu et al.*, 1995].

During the long history of the study of polar magnetic disturbances, magnetic field vectors observed on the "two-dimensional" earth's surface were the only tools from which the representative "three-dimensional" current system could be inferred. It is only during the last two decades that several new powerful techniques, including radars, have become available for studying the three-dimensional current system and, as a result, our knowledge of the large-scale current distribution in the ionosphere and magnetosphere as well as the driving electric field has evolved considerably. Polar-orbiting satellites establish that field-aligned currents that supply the major portions of the auroral electrojets are a permanent feature of the magnetosphere, but satellite data are not capable of determining how they close in the ionosphere. Measurements of the ionospheric electric field data from radars have revealed how convection electric fields at high latitudes relate to the substorm auroral electrojets. Without the systematic data set from incoherent scatter radars, it would not have been possible to shed light on so many outstanding issues in substorm research, resulting in perhaps ionospheric currents being merely inferred from ground magnetic records. It is very important to realize that once enhancements in the ionospheric currents are separated into those in the electric field and in the conductivity, a number of important but unsolved questions regarding substorm dynamics can be discussed quantitatively.

8.2. Future direction

In order to compare properly, as well as most effectively, magnetosphere-ionosphere-ground signatures for substorms and convection, it is necessary to identify what a radar is measuring with respect to such a "natural" frame of reference as the convection/substorm frame, not in man-made coordinate systems such as latitude, MLT, etc. This is particularly the case when substorm-disturbed regions need to be mapped from radar altitudes to the ground. It is also important to note that statistical potential patterns do not always exist in individual cases, and moreover, substorms themselves do not "know" where magnetic midnight is located, although substorm expansion onsets have been reported to occur most likely near midnight in a statistical sense [*Craven and Frank*, 1991]. The follow-

ing is a list of some of the research subjects which will rely strongly on the improved measurements of the auroral ionosphere by incoherent scatter radars in the future:

[1] ***Longitudinal changes in ionospheric parameters***: Substorms undergo many local, small-scale changes in the structure of the electric field and current in the polar ionosphere, particularly in the dark sector. Statistical potential patterns do not always conform to individual cases. It is important to identify local substorm signatures near midnight on the basis of a data set from the combined satellite and radar measurements of electric fields and worldwide ground-based magnetometers, where it can be shown that enhancements in the "normal" electric fields [*generated by solar wind-magnetosphere interactions*] and the substorm expansion-related electric fields can coexist during substorms. Toward this goal, it is desirable to observe not only the latitudinal profiles of ionospheric electrodynamics but also longitudinal changes of the parameters, particularly near the region of the head of the traveling surge.

[2] ***Role of the ionospheric conductivity***: The auroral ionosphere is not only a passive medium. The ionospheric electric field would be modified or changed completely by polarization charges deposited by ionospheric currents near strong gradients in the conductivity distribution. The modified electric field will then be mapped to the magnetosphere, the efficiency of which is of course regulated by the existence of the "parallel" electric field. No systematic study has so far been conducted to answer the question: What role does the polar ionosphere play in the expansion onset of substorms? Significant contributions from incoherent scatter radars with fine resolution measurements are therefore expected.

[3] ***Importance of neutral winds in substorms***: One very important but unsettled question is why the convection electrojet near dawn and dusk is still dominant at the late recovery phase, at which interval the interplanetary magnetic field is most often northward-directed. It is conceivable that the electric field caused by neutral winds in the thermosphere becomes relatively dominant during the recovery phase. In fact, according to *Killeen et al.* [1985], *DE 2* observations indicate that the thermosphere neutral wind is influenced by *E*- and *F*-region ion drifts with a few hours of time delay at high latitudes. The thermosphere does follow convecting plasmas in the ionosphere with [*unknown*] time lags, generating thermospheric winds [*Lyons et al.*, 1985]. It is this variation in the ionosphere-thermosphere system that, in turn, alters electric fields and plasma processes in the magnetosphere. Studies of this entire feedback system have not even begun ins spite of its importance in understanding the magnetosphere-ionosphere-thermosphere coupling via electric fields, field-aligned currents, and particle precipitation. Further observations of the height dependence of the neutral wind by means of incoherent-scatter radars will offer a unique opportunity to examine the role of the neutral wind in the large-scale electric field at the different phases of substorms.

Acknowledgements:

I would like to thank Denis Alcaydé for his constant and consistent encouragement throught the preparation of this manuscript. I also wish to thank Lou Frank for the use of his auroral image data.

9. References

Akasofu S. -I., The development of the auroral substorm, *Planet. Space Sci.*, **12**, 273, 1964.

Akasofu S.-I, Recent progress in studies of DMSP auroral photographs, *Space Sci. Rev.*, **19**, 169, 1976.

Akasofu S. -I., Physics of Magnetospheric Substorms, *D. Reidel Publ. Co.*, 1977.

Akasofu S. -I., Energy coupling between the solar wind and the magnetosphere, *Space Sci. Rev.*, **28**, 121, 1981.

Akasofu S.-I., J. L. Kisabeth, G. J. Romick, H. W. Kroehl, and B.-H. Ahn, Day-to-day and average magnetic variations along the IMS Alaska meridian chain of observatories and modeling of a three-dimensional current system, *J. Geophys. Res.*, **85**, 2065, 1980.

Anger C.D., T. Fancott, J. McNally, and H.S. Kerr, the Isis-2 scaning auroral photometer, *Appl. Opt.*, **12**, 1753, 1973.

Baker D. N., T. A. Fritz, R. L. McPherron, D. H. Fairfield, Y. Kamide, and W. Baumjohann, Magnetotail energy storage and release during the CDAW 6 substorm analysis intervals, *J. Geophys. Res.*, **90**, 1205, 1985.

Banks P. M., and J. R. Doupnik, A review of auroral zone electrodynamics deduced from incoherent scatter radar observations, *J. Atmos. Terr. Phys.*, **37**, 951, 1975.

Baumjohann W., Ionospheric and field-aligned current systems in the auroral zone: A concise review, *Adv. Space Res.*, **2**, 55, 1983.

Baumjohann W., and R. A. Treumann, Basic Space Plasma Physics, *Imperial College Press*, London, 1996.

Baumjohann W., R. J. Pellinen, H. J. Opgenoorth, and E. Nielsen, Joint two-dimensional observations of ground magnetic and ionospheric electric fields associated with auroral-zone currents: current systems associated with local auroral breakups, *Planet. Space Sci.*, **29**, 431, 1981.

Brekke A., J. R. Doupnik, and P. M. Banks, Incoherent scatter measurements of E region conductivities and currents in the auroral zone, *J. Geophys. Res.*, **79**, 3773, 1974.

Clauer C. R., and Y. Kamide, DP 1 and DP 2 current systems for the March 22, 1979, substorms, *J. Geophys. Res.*, **90**, 1343, 1985.

Cowley S. W. H., The causes of convection in the earth's magnetosphere: A review of developments during the IMS, *Rev. Geophys. Space Phys.*, **20**, 531, 1982.

Craven J. D., and L. A. Frank, Diagnosis of auroral dynamics using global auroral imaging with emphasis on large-scale evolutions, in *Auroral Physics, edited by C. -I. Meng, M. J. Rycroft, and L. A. Frank, 275, Cambridge University Press*, 1991.

de la Beaujardiere O., R. Vondrak, and M. Baron, Radar observations of electric fields and currents associated with auroral arcs, *J. Geophys. Res.*, **82**, 5051, 1977.

Fairfield D. H., and R. P. Lepping, Simultaneous measurements of magnetotail dynamics by IMP spacecraft, *J. Geophys. Res.*, **86**, 1396, 1981.

Fayermark D.S., Reconstruction of the three-dimensional current system of the high-latitude region from ground-based geomagnetic measurements, *Geomagn. Aeron., Engl. Transl.* **17**, 114, 1977.

Feldstein Y.I., Peculiarities in the auroral distribution and magnetic disturbance distribution in high latitudes caused by the asymmetrical form of the magnetosphere, *Planet. Space Sci.*, **14**, 121, 1966.

Feldstein Y.I. and G.V. Starkov, Dynamics of auroral belt and polar geomagnetic disturbances, *Planet. Space Sci.*, **15**, 209, 1967.

Feldstein Y.I. and A.E. Levitin, Solar wind control of electric fields and currents in the ionosphere, *J. Geomag. Geoelectr.*, **38**, 1143, 1986.

Forbes J. M., and M. Harel, Magnetosphere-thermosphere coupling: An experiment in interactive modeling, *J. Geophys. Res.*, **94**, 2631, 1989.

Foster J. C., J. M. Holt, R. G. Musgrove, and D. S. Evans, Ionospheric convection associated with discrete levels of particle precipitation, *Geophys. Res. Lett.*, **9**, 1001, 1986.

Frank L. A., and J. D. Craven, Imaging results from Dynamics Explorer 1, *Rev. Geophys.*, **26**, 249, 1988.

Glassmeier K.H., Ground-based observations of field-aligned currents in the auroral zone: Methods and results, *Ann. Geophys.*, **5**, 115, 1987. 1987.

Horwitz J. L., J. R. Doupnik, P. M. Banks, Y. Kamide, and S.-I. Akasofu, The latitudinal distributions of auroral zone electric fields and ground magnetic perturbations and their response to variations in the interplanetary magnetic field, *J. Geophys. Res.*, **83**, 2071, 1978.

Iijima T., and T. A. Potemra, The amplitude distribution of field-aligned currents at northern high latitudes observed by TRIAD, *J. Geophys. Res.*, **81**, 2165, 1976.

Kamide Y., The relationship between field-aligned currents and the auroral electrojets: A review, *Space Sci. Rev.*, **31**, 127, 1982.

Kamide Y., and S.-I. Akasofu, Latitudinal cross section of the auroral electrojet and its relation to the interplanetary magnetic field polarity, *J. geophys. Res.*, **99**, 3585, 1994.

Kamide Y., and S.-I. Akasofu, The auroral electrojet and global auroral features, *J. geophys. Res.*, **80**, 3585, 1975.

Kamide Y., and W. Baumjohann, Magnetosphere-Ionosphere Coupling, *Springer-Verlag*, New York, 1993.

Kamide Y., and S. Kokubun, Two component auroral electrojet: Importance for substorm studies, *J. Geophys. Res.*, **101**, in press, 1996.

Kamide Y., and S. Matsushita, Simulation studies of ionospheric electric fields and currents in relation to field-aligned currents, 2, Substorms, *J. Geophys. Res.*, **84**, 4099, 1979.

Kamide Y., and H. W. Kroehl, Auroral electrojet activity during isolated substorms at different local times: a statistical study, *Geophys. Res. Lett.*, **21**, 389, 1994.

Kamide Y., and Winningham, A statistical study of the 'instantaneous' nightside auroral oval: The equatorward boundary of electron precipitation as observed by the Isis 1 and 2 satellites, *J. geophys. Res.*, **82, 5573,** 1977**.**

Kamide Y., and J. F. Vickrey, Relative contribution of ionospheric conductivity and electric field to the auroral electrojets, *J. Geophys. Res.*, **88**, 7989, 1983.

Kamide Y., F. Yasuhara and S.-I. Akasofu, A model current system for the magnetospheric substorm, *Planet. Space. Sci.*, **24**, 215, 1976.

Kamide Y., A. D. Richmond, and S. Matsushita, Estimation of ionospheric electric field, ionospheric currents, and field-aligned currents from ground magnetic records, *J. Geophys. Res.*, 86, 801, 1981.

Kamide, Y., W. Sun, and S.-I. Akasofu, The average ionospheric electrodynamics for the different substorm phases, *J. Geophys. Res.*, **101**, 99, 1996.

Kamide Y., P.D. Perreault, S.-I. Akasofu, and J.D. Winningham, Dependence of substorm occurrence probability on the interplanetary magnetic field and on the size of the auroral oval, *J. Geophys. Res.*, **82**, 5521, 1977.

Killeen T. L., R. A. Heelis, P. B. Hays, N. W. Spencer, and W. B. Hanson, Neutral motions in the polar thermosphere for northward interplanetary magnetic field, *Geophys. Res. Lett.*, **12**, 159, 1985.

Kroehl H. W., and A. D. Richmond, Magnetic substorm characteristics described by magnetic potential maps for 26-28 March 1976, in Dynamics of the Magnetosphere, *edited by S.-I. Akasofu, pp. 269, Reidel, Hingham, MA,* 1979.

Lockwood M., Solar wind/magnetosphere coupling, *this volume*, 1996.

Lui A.T.Y., C.D. Anger, and S.-I. Akasofu, The equatorward boundary of the diffuse aurora and auroral substorms as seen by the Isis 2 auroral scanning photometer, *J. Geophys. Res.*, **80**, 3603, 1975.

Lui A. T. Y., A synthesis of magnetospheric substorm models, *J. Geophys. Res.*, **96**, 1849, 1991.

Lu G., A. D. Richmond, B. A. Emery, and R. G. Roble, Magnetosphere-ionosphere-thermosphere coupling: Effect of neural winds on energy transfer and field-aligned current, *J. Geophys. Res.*, **100**, 19643, 1995.

Lyons L. R., A new theory for magnetosphere substorms, *J. Geophys. Res.*, **100**, 19069, 1995.

Lyons L. R., T. L. Kelleen, and R. L. Waterscheid, The neutral wind "flyweel" as a source of quiet-time, polar cap currents, *Geophys. Res.*, Lett., **12**, 101, 1985.

McPherron R. L., Growth phase of magnetospheric substorms, *J. Geophys. Res.*, **75**, 5592, 1970.

McPherron R. L., Physical processes producing magnetospheric substorms and magnetic storms, *in Geomagnetism, edited by J. A. Jacobs, pp. 593-739, Academic Press*, 1991.

McPherron R. L., and R. H. Manka, Dynamics of the 1054 UT March 22, 1979, substorm event: CDAW 6, *J. Geophys. Res.*, **90**, 1175, 1985.

McPherron R. L., C. T. Russell, and M. P. Aubry, Satellite studies of magnetospheric substorms on August 15, 1968, 9. Phenomenological model of substorms, *J. Geophys. Res.*, **78**, 3131, 1973.

Meng C.-I., R. H. Holzworth, and S.-I. Akasofu, Auroral circle - delineating the polar boundary of the quiet auroral belt, *J. Geophys. Res.*, **82**, 164, 1977.

Meng C.-I, A.L. Snyder, and H.W. Kroehl, Observations of auroral westward traveling surges and electron precipitations, *J. Geophys. Res.*, **83**, 757, 1978.

Mishin V.M., The magnetogram inversion technique and some applications, *Space Sci. Rev.*, **53**, 83, 1990.

Mishin V.M., A.D. Bazarzhapov, and G.B. Shpynev, Electric fields and currents in the earth's magnetosphere, in *Dynamics of the Magnetosphere, ed. by S.-I. Akasofu, 249, Reidel, Hingham, MA*, 1979.

Nakai H. and Y. Kamide, Response of nightside auroral oval boundaries to the interplanetary magnetic field, *J. Geophys. Res.*, **88**, 4005, 1983.

Nishida A., Geomagnetic Diagnosis of the Magnetosphere, *Springer-Verlag, New York*, 1978.

Nishida A. and S. Kokubun, New polar magnetic disturbances, Sqp, SP, DPC, and DP 2, *Rev. Geophys. Space Phys.*, **9**, 417, 1971.

Pellinen R. J., How does magnetospheric convection relate to the expansion onset of substorms?, *J. Atmos. Terr. Phys.* Phys., **55**, 1089, 1993.

Potemra T.A., Birkeland currents: Recent contributions from satellite magnetic field measurements, *Phys. Scripta*, **18**, 152, 1987.

Rees M. H., Scientific results of the U.S. IMS ground-based program, *Rev. Geophys. Space Phys.*, G20, 654, 1982.

Richmond A.D., Ionosphere-thermosphere coupling with special emphasis on auroral/polar regions, *this volume*, 1996.

Richmond A. D., and Y. Kamide, Mapping electrodynamic features of the high-latitude ionosphere from localized observations: Technique, *J. Geophys. Res.*, **93**, 5741, 1988.

Robinson R.M., F. Rich, and R.R. Vondrak, Chatanika radar and S3-2 measurements of auroral zone electrodynamics in the midnight sector, *J. Geophys. Res.*, **90**, 8487, 1985.

Rostoker G., S. -I. Akasofu, W. Baumjohann, Y. Kamide, and R. L. McPherron, The roles of different input of energy from the solar wind and unloading of stored magnetotail energy in driving magnetospheric substorms, *Space Sci. Rev.*, **46**, 93, 1987.

Schlegel K., The use of incoherent scatter data in ionospheric and plasma research, *this volume*, 1996.

Shue J. -H., and D. R. Weimer, The relationship between ionospheric convection and magnetic activity, *J. Geophys. Res.*, **99**, 401, 1994.

Vasyliunas V.M., Mathematical models of magnetospheric convection and its coupling to the ionosphere, in *Particles and Fields in the Magnetosphere, ed. by B.M. McCormac, 60, Reidel, Hingham, MA*, 1970.

Wolf R.A., and Y. Kamide, Inferring electric fields and currents from ground magnetometer data--A test with theoretically derived input, *J. Geophys. Res.*, **88**, 8129, 1983.

Zmuda A.J., J.H. Martin, and F.T. Heuring, Transverse magnetic disturbances at 1100 kilometers in the auroral region, *J. Geophys. Res.*, **71**, 5033, 1966.

IONOSPHERE-THERMOSPHERE INTERACTIONS AT HIGH LATITUDES

A. D. Richmond

1. Thermosphere-Ionosphere Environment

The thermosphere is that tenuous part of the Earth's atmosphere lying between about 85 km and 500 km. Its base is at the cold mesopause, where temperatures can drop to 120 K. Its upper boundary with the overlying exosphere is indistinct, but is defined as that altitude where the mean free path of atoms and molecules is equal to the atmospheric scale height, that is, the distance over which pressure decreases by a factor of 1/*e*. Below that altitude collisions between atoms and molecules occur sufficiently frequently that the medium obeys the laws of fluid mechanics. The thermosphere's name derives from the high temperature of its upper portions, which measures at least 500 K but sometimes exceeds 2000 K during very disturbed conditions [*Figure 1*].

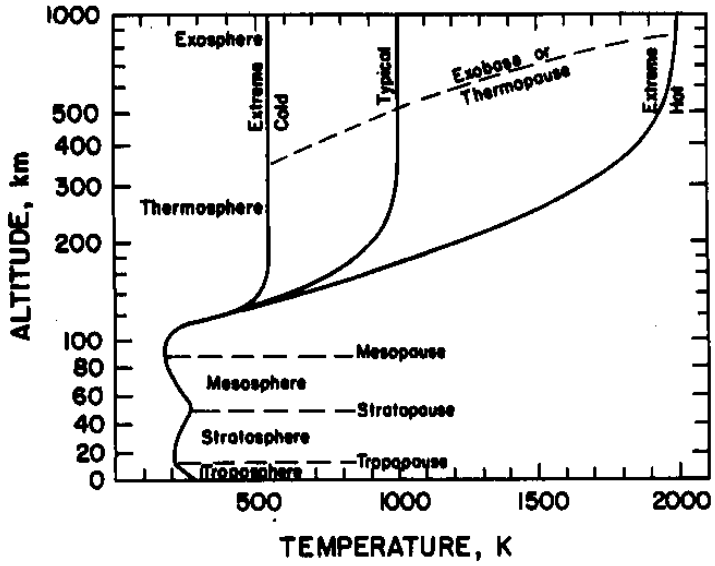

Figure 1. A typical atmospheric temperature profile and two extreme thermospheric temperature profiles. Also shown are the altitudes of the tropopause, stratopause, mesopause, and thermopause which mark the upper limits of the troposphere, stratosphere, mesosphere, and thermosphere respectively, as defined by extrema in the temperature profile or, in the case of the thermopause (exobase), by the altitude where the atomic mean free path equals one pressure scale height. The 'typical' profile is also listed in Table 1. Note that the altitude scale is linear below 100~km and logarithmic above 100~km. (From Richmond, 1991).

The high temperature results from strong heating by solar ultraviolet radiation and, sporadically, by electric currents and energetic particle precipitation at high latitudes. Cooling by infrared radiation is inefficient in the thermosphere, unlike lower atmospheric regions, so that the temperature tends to build up until down-

ward heat conduction suffices to offset the heating. Thus the lower thermosphere has a strong vertical temperature gradient that helps to conduct the heat sufficiently rapidly.

The thermosphere is heterogeneous. Atomic oxygen, O, is produced by dissociation of molecular oxygen, O_2, in the presence of solar ultraviolet radiation. Atomic oxygen can recombine by three-body collisions only in the lower thermosphere where collisions are frequent, and so its density in the upper thermosphere builds up to the point that it becomes the dominant species above about 200 km. Long mean-free-paths in the upper thermosphere facilitate rapid diffusion, allowing the density of each species to decrease with increasing altitude according to a scale height that is determined by its individual mass, rather than according to an average scale height as is the case in the well-mixed lower atmosphere. Figure~2 shows how the densities of heavier species like molecular nitrogen and oxygen decrease more rapidly with increasing height than the lighter atomic oxygen.

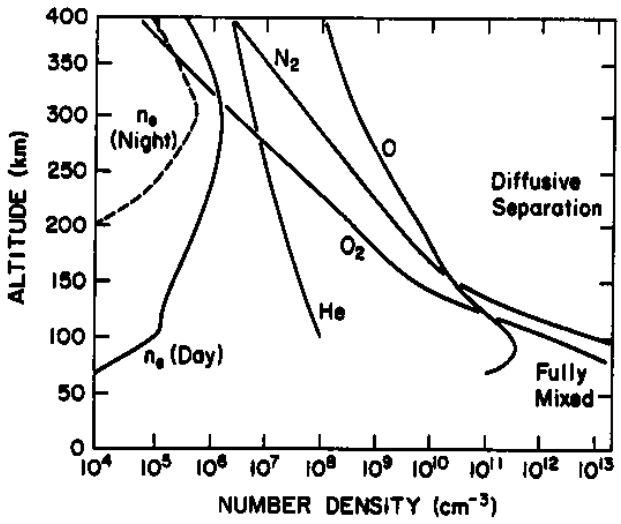

Figure 2. Typical number densities of major thermospheric neutral species, along with typical day and night electron densities. The major constituents N_2 and O_2 are fully mixed below 100 km, while rapid diffusive separation occurs above 120 km. (From Roble, 1977).

Note that the exponential rate of density decrease is less in the upper thermosphere [*above 150 km*] than below, largely owing to the high temperature that produces a large scale height. Typically, the atomic-oxygen scale height is on the order of 50 km in the upper thermosphere, as compared with a total-density scale height of only 5 km in the cold mesopause region.

The ionosphere is composed of the ions and free electrons embedded in the upper atmosphere, created by extreme-ultraviolet and X-ray radiation [*together sometimes called XUV radiation*] and by energetic particles precipitating from the magnetosphere. The F region of the ionosphere, lying at altitudes of 150 km to 1000 km, usually contains the largest electron- and ion-density concentrations.

The peak electron density generally lies at altitudes of around 200-400 km at middle and high latitudes. Figure~2 shows typical midlatitude daytime and nighttime electron-density distributions. Even at the peak, the number density of electrons is only on the order of 10^{-3} that of the neutrals. To a very good approximation the ionosphere is electrically neutral: there are equal numbers of electrons and singly charged positive ions at heights above 90 km. Minuscule departures from electric neutrality, however, result in non-negligible electric fields. The ions are influenced by a variety of photochemical, diffusive, dynamical, and electrodynamical processes that largely determine the distributions of the ion and electron densities.

The neutral and ionized components of the upper atmosphere interact strongly. Ions are created from neutrals by photoionization and auroral-particle impact, and the ions interact chemically with the neutrals. Ions and electrons react strongly to electric fields, both in terms of bulk transport and in terms of electric-current flow. Through collisions with the neutrals, the ions transfer momentum and exert a major influence on upper-atmospheric winds. The Joule heating produced by strong auroral electric fields and currents can affect the temperature, circulation, and composition of both the neutral and plasma constituents in important ways. The plasma density distribution is additionally affected by neutral winds that induce plasma transport along geomagnetic-field lines. Winds also modify the electric fields and currents through dynamo action. The mutual interactions among neutral dynamics, plasma dynamics, and electrodynamics create a variety of interesting phenomena that pose challenges for modeling and interpretation.

2. Gas Laws and Pressure Coordinates

The partial pressure p_j of the jth constituent of the upper atmosphere obeys the ideal gas equation:

$$p_j = n_j \, k \, T_j, \tag{1}$$

where n_j is the number density of the constituent, k is the Boltzmann constant [$1.381\ 10^{-23}\ J.K^{-1}$], and T_j is the temperature of the constituent. The temperature is assumed here to be isotropic. The neutral constituents normally have equal temperatures, but the electrons and ions can have higher temperatures than the neutrals. The total number density n and total mass density ρ are:

$$n = \sum_{j} n_j \tag{2}$$

1	2	3	4	5	6	7	8	9	10	11	12
z	T	m	H	ρ	n_e	D_E/H^2	$\mu_m/\rho H^2$	$\sigma_P B^2/\rho$	$\sigma_H B^2/\rho$	$2\pi/N$	C
(km)	*(K)*	*(amu)*	*(km)*	*(kg.m^{-3})*	*(m^{-3})*	*(10^{-4}s^{-1})*				*(s)*	(m.s^{-1})
0	288	29.0	8.4	1.23+00						594	178
10	223	29.0	6.6	4.14-01						525	157
20	217	29.0	6.4	8.89-02						293	273
30	227	29.0	6.7	1.84-02						293	287
40	250	29.0	7.4	4.00-03						287	325
50	271	29.0	8.0	1.03-03						339	298
60	247	29.0	7.4	3.10-04		.005				384	241
70	220	29.0	6.6	8.28-05	4.04+08	.012				364	227
80	199	29.0	6.0	1.85-05	9.85+08	.033	.000			329	228
90	189	28.9	5.7	3.12-06	2.11+10	.037	.001		.000	307	234
100	191	28.4	5.9	5.30-07	1.39+11	.032	.008	.000	.016	260	285
110	236	27.3	7.6	8.92-08	1.49+11	.006	.033	.015	.097	230	416
120	372	26.1	12.5	1.91-08	1.54+11	.000	.077	.231	.295	246	640
130	507	25.2	17.8	6.95-09	1.56+11		.131	.489	.217	308	724
140	613	24.5	22.2	3.38-09	1.58+11		.197	.551	.116	361	771
160	763	23.3	29.2	1.19-09	1.67+11		.376	.598	.044	447	820
180	856	22.2	34.5	5.39-10	1.84+11		.640	.722	.027	513	846
200	914	21.2	38.8	2.80-10	2.98+11		1.02	1.27	.027	564	866
250	981	19.2	46.8	7.40-11	1.10+12		2.79	5.52	.037	652	902
300	1002	17.8	52.4	2.45-11	1.32+12		6.81	7.54	.019	710	928
350	1009	16.8	56.7	9.21-12	1.16+12		15.6	7.01	.007	755	943
400	1011	16.1	60.2	3.74-12	8.21+11		34.0	5.15	.002	786	963
500	1012	14.6	68.2	7.10-13	3.23+11		140.	1.97	.000	814	1054
600	1012	12.2	84.5	1.55-13	1.46+11						
800	1012	6.0	182.	1.42-14	6.65+10						
1000	1012	4.0	289.	4.07-15	5.38+10						

Table 1: Typical daytime upper atmospheric parameters. Columns~2-5 are from the U.S. Standard Atmosphere (1976) at altitudes of 80 km and below, and from the MSIS-86 thermospheric model (Hedin, 1987) at 90 km and above (for March equinox, 30° north latitude, 11 local time, solar 10.7 cm flux = 120 10^{-22} W.m^{-2}.Hz^{-1}, A_p magnetic activity index = 10). Electron densities (column 6) are from the International Reference Ionosphere (for March equinox, 30° north, 200° east, 11 local time, sunspot number = 70). Eddy diffusion coefficients are from the U.S. Standard Atmosphere (1976) at 90 km and above, and are assumed to decrease at lower heights. A number like 4.04+08 means 4.04 10^8. The characteristic rates in columns 7-10, as discussed in Section 5, are given as multiples of the characteristic rate for coriolis effects, 10^{-4} s^{-1}.Adapted from Richmond (1991).

Z: altitude;
T: temperature;
m: mean molecular mass(1 amu=1.661 10^{-27} kg);
H: pressure scale height;
ρ: mass density;
n_e: electron number density;

D_E : the eddy diffusion coefficient;
μ_m: the molecular viscosity coefficient;
σ_P,σ_H: Pedersen and Hall conductivities;
B: geomagnetic field strength;
N: the angular Brunt-Väisälä frequency;
C: the limiting speed for simple gravity waves.

$$\rho = \sum_{j} n_j m_j \tag{3}$$

where m_j is the mass of the j constituent.

The mean molecular mass is:

$$m = \frac{\rho}{n} \tag{4}$$

The relation of the total pressure p to the density is obtained by summing Eq. 1 over all species:

$$p = \sum_{j} n_j \; k \, T_j = \frac{\rho}{m} \; k \, T \, , \tag{5}$$

where the mean temperature is defined as

$$T = \frac{p}{n \, k} \tag{6}$$

Since the neutrals dominate the total gas density, T is essentially the neutral temperature. The internal energy density of the gas per unit mass is $c_v \, T$, and the specific enthalpy is $c_p \, T$, where c_v and c_p are the specific heats at constant volume and pressure, respectively, which are related by:

$$c_p = c_v + \frac{k}{m} \tag{7}$$

For a pure monatomic gas like O, c_v would be 3/2 (k / m), while for a pure diatomic gas like N_2 or O_2, c_v would be 5/2 (k / m). Typical values of the total density, temperature, and mean molecular mass are listed in Table 1.

Under most circumstances the atmosphere is in "*hydrostatic equilibrium*", meaning that the vertical pressure gradient force balances gravity:

$$\frac{\partial \, p}{\partial \, z} = - \, \rho \, g = - \, \frac{p}{H} \tag{8}$$

$$H = \frac{k \, T}{m \, g} \tag{9}$$

where z is altitude, g is the acceleration of gravity, and H is the "p*ressure scale height*", the exponential scale by which pressure decreases with increasing altitude.

When hydrostatic equilibrium holds, pressure or its negative logarithm

$$Z = - \ln \left\{ \frac{p}{p_0} \right\} \tag{10}$$

where p_0 is an arbitrary reference pressure, can be used as a vertical coordinate in place of z.

Two advantages of using "*pressure coordinates* are that upper-atmospheric phenomena tend to be better organized with regard to pressure than altitude, and that the equations of large-scale dynamics assume a simpler form when Z rather than z is the independent variable.

The dependent variable that replaces p is the "*geopotential*" Φ:

$$\Phi (z) = \int_0^z g (z') \, d z' \tag{11}$$

which varies approximately linearly with altitude, except for variations associated with the relatively small decrease of g with increasing height.

The hydrostatic equation 8 becomes:

$$\frac{\partial \Phi}{\partial Z} = g H \tag{12}$$

A dimensionless vertical velocity W can be defined as:

$$W = - \frac{1}{p} \frac{d p}{d t} \tag{13}$$

where the derivative of p with respect to time t is taken following the motion of the fluid element.

When multiplied by H, W represents the vertical velocity relative to a constant-pressure surface, which itself may be moving with respect to the Earth.

3. Mass Continuity

Each constituent satisfies a continuity equation:

$$m_j \frac{\partial n_j}{\partial t} + \nabla \cdot (m_j m_j \mathbf{v}_j) = P_j \tag{14}$$

where $\mathbf{v}_j$ is the mean velocity of the particles and P_j is the net photochemical production rate, i.e., the difference between production and loss. If the mean velocity of the medium is defined as:

$$\mathbf{v} = \frac{1}{\rho} \sum_{j} m_j n_j \mathbf{v}_j \tag{15}$$

then the velocity $\mathbf{v}_j$ of the constituent can be expressed as:

$$\mathbf{v}_j = \mathbf{v} + \mathbf{v}_{dj} \tag{16}$$

where $\mathbf{v}_{dj}$ is the "*diffusion velocity*", i.e., the velocity of the *j* species with respect to the mean velocity of the medium.

The mean velocity **v** is essentially the neutral wind velocity, since neutrals by far outnumber ions. The total-gas continuity equation is obtained by summing Eq. 14 over all species. In this process, the diffusion fluxes sum to zero and the net production terms cancel because of mass conservation:

$$\frac{\partial \rho}{\partial t} + \nabla \cdot (\rho \mathbf{v}) = 0 \tag{17}$$

Under hydrostatic equilibrium, the mass contained between two constant-pressure surfaces is essentially constant, since the pressure difference between the two surfaces is equal to the weight per unit area of the air between them. The total-gas continuity equation can then be written as:

$$\frac{1}{p} \frac{\partial}{\partial Z} (p W) + \nabla_p \cdot \mathbf{v}_h = 0 \tag{18}$$

where $\mathbf{v}_h$ is the horizontal wind component and where the subscript p on ∇_p indicates that the horizontal partial derivatives associated with the ∇ operator are taken with p [*or* Z] held constant rather than z.

In the thermosphere, photochemical production and loss are relatively unimportant processes for molecular nitrogen and for the minor species argon, helium,

and atomic hydrogen. On the other hand, photochemical processes are important for the major thermospheric constituent O and for minor constituents like N and NO. Thermospheric atomic oxygen is created by photodissociation of molecular oxygen. It is lost by recombination into diatomic oxygen in three-body collisions that require a relatively dense atmosphere. Thus loss of O occurs primarily near the base of the thermosphere. The production and loss rates of O_2 are basically just one-half the O loss and production rates, respectively, since mass must be conserved. At 200 km, roughly 4 % of the O_2 molecules are photodissociated during 12 hours of sunlight. At 100 km, roughly 1 % of the O atoms recombine to O_2 during a 24-hour day. Because these fractions are relatively small, photochemical production and loss of O and O_2 can be ignored when dynamical changes happening in less than a day are being considered.

In contrast, the lifetimes of ions are relatively short. When sunlight or strong auroral particle precipitation is present, the lifetimes of the dominant ions between 90 km and 150 km are on the order of one minute; production and loss are often nearly in balance, and "*photochemical equilibrium*" prevails. At higher altitudes the loss rate slows down because of a change in composition from predominantly molecular ions, which recombine rapidly with electrons, to atomic

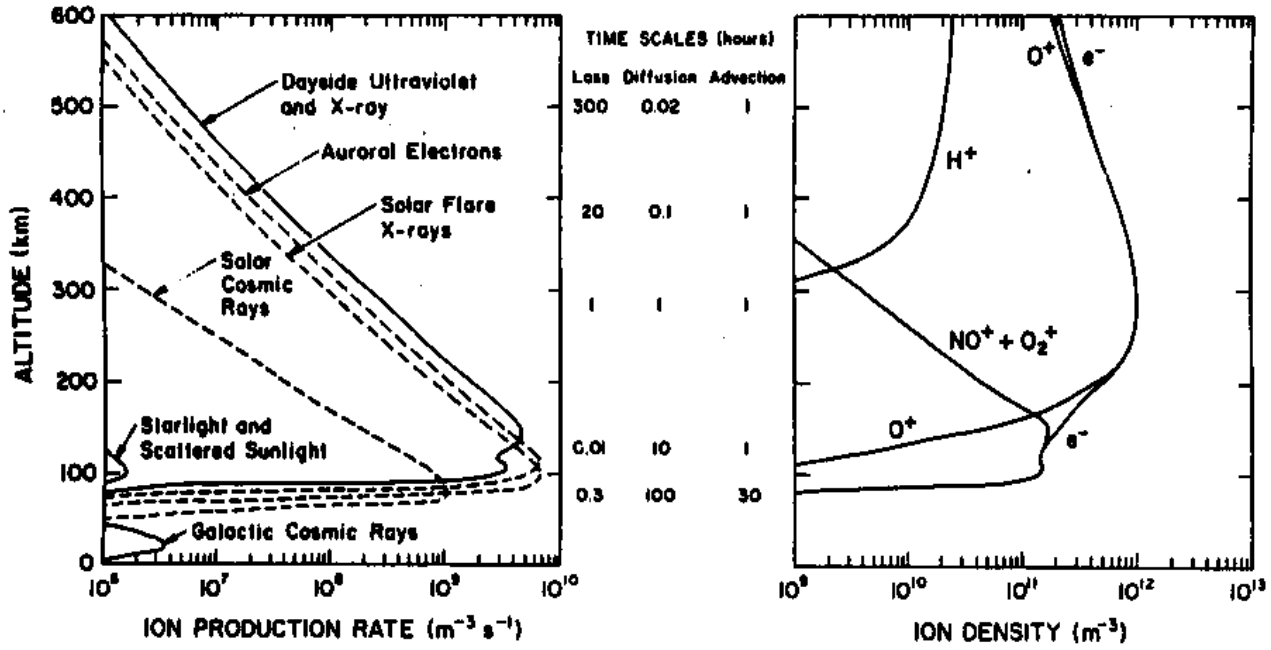

Figure 3. (Left) Typical ion production rates from various sources. Solid lines show regular sources. During the day, direct solar extreme ultraviolet (EUV) light is the main ionization source. At night, EUV scattered from the geocorona as well as that from stars helps maintain the E-region ionosphere. Other sources are highly variable in time, and are shown with dashed lines: solar-flare X rays and EUV (dayside only) and auroral electrons and solar cosmic rays (high latitudes only). (Middle) Representative time scales at various altitudes for different physical processes affecting the daytime ionosphere. (Right) Typical daytime ion and electron densities. (From Richmond, 1987).

oxygen ions, which are lost primarily by charge-exchange reactions with the relatively sparse diatomic nitrogen and oxygen molecules. Transport by mean motions as well as by diffusion parallel and perpendicular to the geomagnetic field then has time to have a significant impact on the plasma densities.

Figure 3 illustrates the height distributions of various ion production rates and daytime ion densities, along with characteristic time scales of chemical loss, of diffusion, and of advection.

The ionosphere is horizontally stratified on the large scale, meaning that vertical gradients of densities are normally much stronger than horizontal gradients. Consequently, the vertical component of ion transport by advection [$\mathbf{v}$] and by diffusion [$\mathbf{v}_{dj}$] usually has a greater impact on ion density than does the horizontal component of transport. [*Exceptions to this can occur in the polar region where rapid horizontal ion drift velocities convect plasma over significant distances, creating "tongues" and "troughs" of plasma density*]. In the F-region electric fields convect plasma perpendicular to the magnetic field at the velocity:

$$\mathbf{u}^e = \frac{\mathbf{E} \times \mathbf{B}}{B^2} \qquad (19)$$

where **E** and **B** are the electric and magnetic field vectors.

For a strong auroral electric field of 0.1 $V.m^{-1}$ and a typical magnetic-field strength of $5.\ 10^{-5}$ T, the magnitude of $\mathbf{u}^e$ is 2000 $m.s^{-1}$. Where **B** is tilted away from the vertical this drift can have a vertical component: a typical drift magnitude of 300 $m.s^{-1}$ in the magnetic meridional plane has about a 50 $m.s^{-1}$ vertical component when **B** has a dip angle $I = 80°$, i.e., when it is 10° off-vertical. Over the roughly 1-hour lifetime of F-region ions, that vertical drift alone would move the ionosphere about 200 km if other effects like diffusion along geomagnetic-field lines did not also intervene.

Neutral winds at F-region heights tend to impose their velocity component projected along **B** onto the ions, although again diffusion can intervene to modify the net ion velocity along **B**. The large-scale winds are predominantly horizontal. A wind **v** in the magnetic northward direction has a projection of $v \cos I$ along the magnetic field line **B**, which in turn projects along the upward direction with a value $- v \cos I \sin I$. A typical value of 120 $m.s^{-1}$ for **v** in the magnetic meridional plane thus tends to impose a vertical motion on the order of 20 $m.s^{-1}$ on the plasma for $I = 80°$, downward if the wind is poleward, and upward if the wind is equatorward. The neutral-wind effect generally increases in importance with decreasing magnetic latitude in the polar regions because of the factor $\cos I$. At low magnetic latitudes the factor $\sin I$ intervenes to make the neutral-wind effect on plasma motions again small.

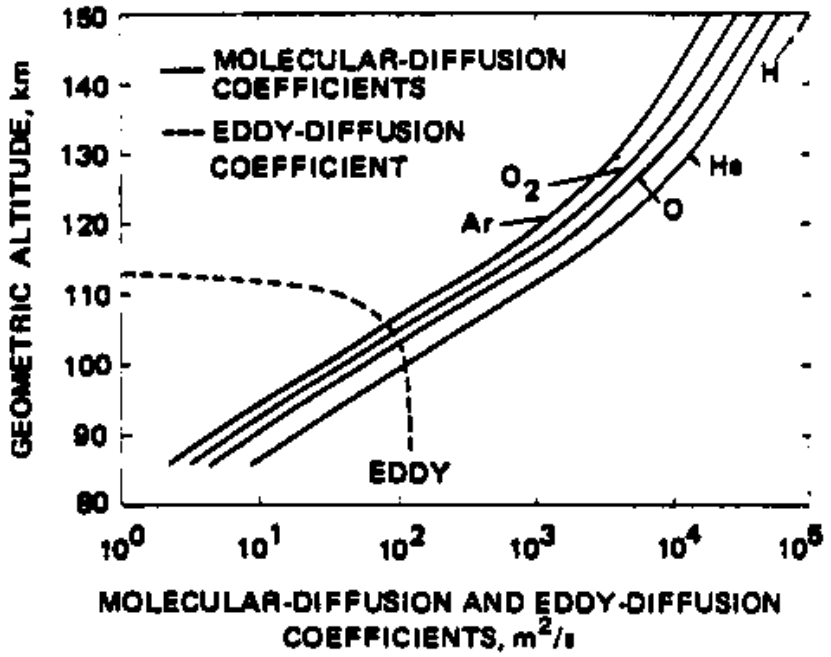

Figure 4. Molecular- and eddy-diffusion coefficients.(From U.S. Standard Atmosphere, 1976).

4. Diffusion Velocities and Electric Currents

For neutral species, the diffusion velocity can be calculated from:

$$\mathbf{v}_{dj} = D_j \left[- \frac{\nabla n_j}{n_j} - (1 + \alpha_j) \frac{\nabla T}{T} + \frac{m_j}{k T} \mathbf{g} \right] - D_E \nabla \ln \left(\frac{m_j n_j}{\rho} \right) \qquad (20)$$

where D_j is the molecular diffusion coefficient, α_j is the thermal diffusion coefficient, and D_E the eddy diffusion coefficient.

Thermal diffusion turns out to be important primarily for the light species H and He, for which the *U.S. Standard Atmosphere* [*1976*] uses values of $\alpha_j = 0.40$. Figure 4 shows estimated mean values of the diffusion coefficients in the height range 85-150 km.

Molecular diffusion is dominant above 110 km, while eddy diffusion dominates below 100 km. The crossover point, which can vary in space and time, is often called the *"turbopause"*.

In the upper thermosphere D_j is very large, and in order for moderate diffusion velocities to be maintained the multiplier of D_j in Eq. 20 must be small. In this situation, called "*diffusive equilibrium*", n_j varies with height z as:

$$n_j = n_{j0} \left(\frac{T_0}{T} \right)^{1+\alpha_j} \exp \left(- \int_{z_0}^{z} \frac{\mathrm{d}\, z'}{H_j (z')} \right) \tag{21}$$

$$H_j \equiv \frac{k\, T}{m_j\, g} \tag{22}$$

where n_{j0} and T_0 are the number density and temperature at the arbitrary reference height z_0 and H_j is the pressure scale height of the *j*th species.

The rate of exponential density decrease with altitude thus depends on the mass of the species, and lighter species decrease less rapidly in density with increasing altitude than heavier species, as apparent in Figure 2.

For charged species, the Lorentz force associated with electric and magnetic fields comes into play. Thermal diffusion is usually ignored. It is convenient to consider separately diffusion parallel and perpendicular to the geomagnetic field **B**. Parallel to **B** the diffusion velocity of the *j*th species is:

$$v_{dj//} = \frac{1}{\nu_j} \left(- \frac{1}{n_j\, m_j} \frac{\partial\, p_j}{\partial\, s} + \mathbf{g} \,.\, \mathbf{b} + \frac{q_j}{m_j} E_{//} \right) \tag{23}$$

where ν_J is the effective *"collision frequency"* for momentum transfer with other species, *s* is distance along **B**, **b** is a unit vector along **B**, q_j is the particle charge, and $E_{//}$ is the electric-field component parallel to **B**.

The ion collision frequency is dominated by collisions with neutrals, and decreases exponentially with increasing altitude. The electron collision frequency is dominated by collisions with neutrals below about 200 km, but at higher altitudes collisions with ions can dominate.

For electrons, the terms in parentheses in Eq. 23 are usually in approximate balance above 150 km, where ν_J is relatively small; if they were not, very large electron diffusion velocities would result. The small mass of electrons causes the gravitational term in Eq. 23 to be negligible in comparison with the pressure-gradient and electric-field terms. Under these conditions,

$$E_{//} \approx - \frac{1}{n_e |\, q_e |} \frac{\partial\, p_e}{\partial\, \mathrm{s}} \ , \tag{24}$$

where subscripts *e* refer to electrons, and where $|q_e|$ is the magnitude of the electron charge [$1.602\ 10^{-19}\ C$].

This parallel electric field has a downward component below the F-region peak, and an upward component in the topside ionosphere. Its magnitude is on the order of 10^{-6} V.m^{-1}, estimated from the quantity $k\ T_e\ /\ |q_e|\ L$, where T_e is the electron temperature [$\sim 10^3\ K$] and L is a characteristic scale length for electron-density gradients [$\sim 10^5\ m$].

Consider for simplicity that there is a single positive ion species [e.g., O^+]. When Eq. 24 is used in Eq. 23 for the ions, the latter equation becomes:

$$v_{di//} = \frac{1}{\nu_i}\left(- \frac{1}{n_i\, m_i} \frac{\partial\,(p_i + p_e)}{\partial\, s} + \mathbf{g}\ .\ \mathbf{b} \right) \qquad (25)$$

where subscript *i* refers to ions.

The ion and electron partial pressures are comparable, being in the ratio of the ion and electron temperatures. Thus the effective pressure that contributes to ion diffusion is considerably greater than the ion pressure alone. The strong electric coupling between ions and electrons tends to cause them to tend to diffuse together, a process called "*ambipolar diffusion*". In the high ionosphere, where $1/\nu_i$ is very large, the two terms in brackets in Eq. 25 must nearly balance, producing a state of *"diffusive equilibrium"*. In this situation, the plasma scale height is determined essentially by the ion mass and the sum of the ion and electron temperatures, and it is thus greater than the scale height of neutral atoms that have a mass and temperature equal to those of the ions.

A small deviation of $E_{//}$ from the value that balances the ion and electron velocities parallel to **B**, i.e. from the value approximately given by Eq. 24, will result in different ion and electron velocities, and therefore an electric current. Let us denote the deviation by $E'_{//}$. It is primarily the electron velocity that is affected, since electrons are much more mobile than the massive ions. The parallel current density is approximately:

$$J_{//} = \sum_{j} n_j\, q_j\, v_{dj//} = \sigma_{//}\ \ E'_{//} \approx n_e\, q_e\, v_{de//} \approx \frac{n_e\, q_e^2}{m_e\, \nu_e} E'_{//} \qquad (26)$$

where $\sigma_{//}$ is the *"parallel conductivity"*.

Typical daytime values of $\sigma_{//}$ are shown in Figure 5.

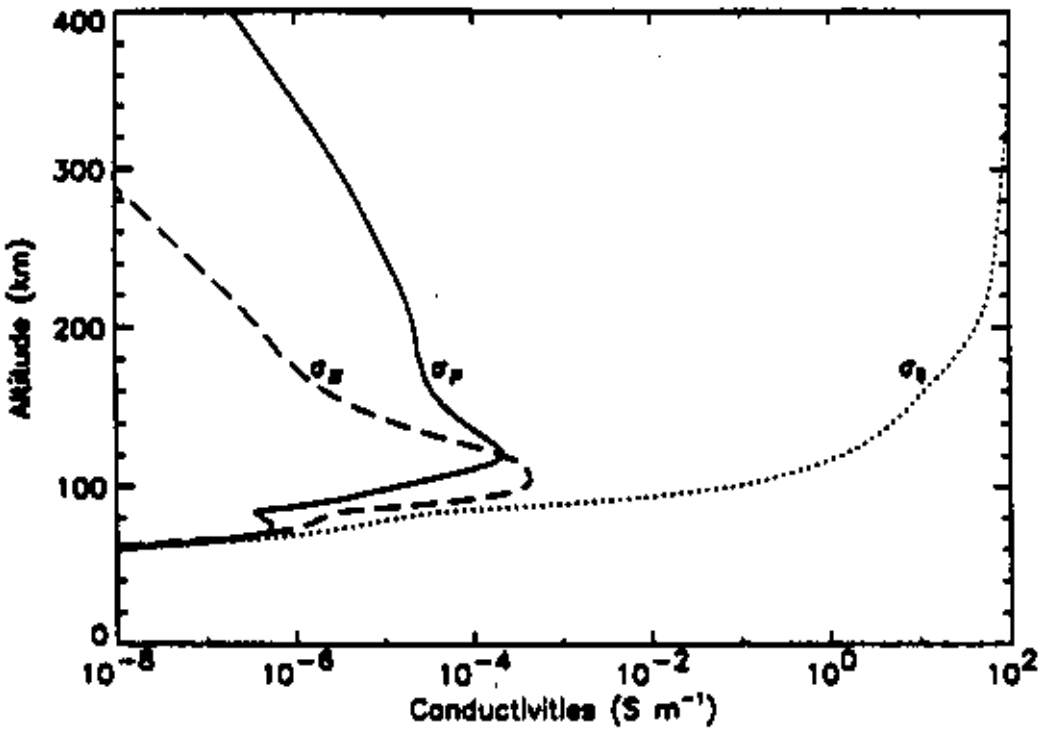

Figure 5. Noontime parallel ($\sigma_{//}$), Pedersen (σ_P), and Hall (σ_H) conductivities at 44.6°N, 2.2°E, for solar-minimum conditions on March 21. (From Richmond, 1995b).

In the upper ionosphere they are on the order of 10^2. Normally, $J_{//}$ is on the order of 10^{-5} A.m^{-2} or less, even in regions of strong auroral currents. Thus, $E'_{//}$ is usually less than 10^{-7} V.m^{-1} in the upper ionosphere, much less than the field associated with ambipolar diffusion.

Perpendicular to the geomagnetic field, the dominant forces on charged particles are the Lorentz force and the frictional force due to collisions with neutrals. Neglecting the gravitational and pressure-gradient forces, the force-balance condition is:

$$q_j \left[\mathbf{E}_\perp + (\mathbf{v} + \mathbf{v}_{dj\perp}) \cdot \mathbf{B} \right] - m_j \nu_j \mathbf{v}_{dj\perp} = 0 \qquad (27)$$

where subscripts $\perp$ denote the component perpendicular to **B**.

Equation 27 can be solved for $\mathbf{v}_{dj\perp}$ by vector algebra:

$$\mathbf{v}_{dj\perp} = \frac{\nu_j \Omega_j (\mathbf{E}_\perp + \mathbf{v} \times \mathbf{B}) - \Omega_j^2 \mathbf{b} \times (\mathbf{E}_\perp + \mathbf{v} \times \mathbf{B})}{B (\nu_j^2 + \Omega_j^2)} \qquad (28)$$

where Ω_j is the [*signed*] angular *"gyrofrequency"* of the *j*th species,

$$\Omega_j = \frac{q_j B}{m_j} \tag{29}$$

It is the electric field measured in the reference frame moving at velocity **v**, [$\mathbf{E}_\perp$ + **v** x **B**], that drives the perpendicular diffusion. The electric current perpendicular to **B** is:

$$J_\perp = \sum_j n_j q_j v_{dj\perp} = \sigma_P (\mathbf{E}_\perp + \mathbf{v} \times \mathbf{B}) + \sigma_H \mathbf{b} \times (\mathbf{E}_\perp + \mathbf{v} \times \mathbf{B}) \tag{30}$$

where the *"Pedersen* σ_P*"* and *"Hall* σ_H *"* conductivities are:

$$\sigma_P = \frac{n_e |q_e|}{B} \left(\frac{\nu_e |\Omega_e|}{\nu_e^2 + \Omega_e^2} + \frac{\nu_i \Omega_i}{\nu_i^2 + \Omega_i^2} \right) \tag{31}$$

$$\sigma_H = \frac{n_e |q_e|}{B} \left(\frac{\Omega_e^2}{\nu_e^2 + \Omega_e^2} - \frac{\Omega_i^2}{\nu_i^2 + \Omega_i^2} \right) \tag{32}$$

Equations 31 and 32 are derived under the approximation that the collision frequencies and gyrofrequencies of all ion species are represented by the mean values ν_i and Ω_i, respectively. Typical values of σ_P and σ_H in the sunlit ionosphere are shown in Figure 5.

Equations 26 and 30 are an expression of Ohm's Law, with the current density proportional to the effective electric field; however, the factors of proportionality represent a tensor rather than a scalar. That is, the current does not flow in the direction of the electric field. Because the parallel conductivity is so large, $E'_{//}$ must normally be very small in order for the electric current to remain moderate. Thus the electric field tends to be nearly perpendicular to the geomagnetic field, even though current readily flows both along and across the field. In the plane perpendicular to the geomagnetic field, the direction of the current can make an angle of up to 88° with respect to the electric field, which occurs at around 100 km altitude.

5. Neutral Dynamics

Unlike charged-particle motions, horizontal neutral motions are not in force balance, and inertia must be taken into account. If all the neutrals are treated as a single fluid, as is usually appropriate except when diffusive effects need to be considered, the following momentum equation applies:

$$\frac{d\,v}{d\,t} + 2\,\Omega \times \mathbf{v} + \frac{\nabla\,p}{\rho} + \frac{\nabla \cdot \underline{\underline{S}}}{\rho} = \mathbf{g} + \frac{\mathbf{J} \times \mathbf{B}}{\rho} \qquad (33)$$

where Ω is the angular rotation rate of the Earth, of magnitude $7.29\ 10^{-5}\ s^{-1}$, and $\underline{\underline{S}}$ is the viscous momentum flux tensor or viscous stress tensor.

This equation is expressed in the rotating reference frame of the Earth, which results in the appearance of the *"Coriolis acceleration"* - $2\,\Omega \times \mathbf{v}$ [see e.g. *Holton*, 1979]. The centrifugal acceleration associated with rotation has been absorbed into the total gravitational acceleration **g** in Eq. 33. The term $(\mathbf{J} \times \mathbf{B}) / \rho$ is the *"Ampère acceleration"*.

It is conceptually useful to write the Ampère acceleration in terms of the difference between the neutral velocity and the electrodynamic velocity $\mathbf{u}^e$ defined by Eq. 19. By making use of Ohm's Law Eq. 30, we can obtain:

$$\frac{\mathbf{J} \times \mathbf{B}}{\rho} = \frac{\sigma_P\,B^2}{\rho}\,(\mathbf{u}^e - \mathbf{v}_\perp) + \frac{\sigma_H\,B^2}{\rho}\,\mathbf{b} \times (\mathbf{u}^e - \mathbf{v}_\perp) \qquad (34)$$

where $\mathbf{v}_\perp$ is the component of **v** perpendicular to **B**, and where the quantities $\sigma_P\,B^2 / \rho$ and $\sigma_H\,B^2 / \rho$ are sometimes called the *"Pedersen-drag"* and *"Hall-drag"* coefficients.

The first term in Eq. 34 causes acceleration of the air, perpendicular to the magnetic field, in the direction of the electromagnetic drift and opposite to the direction of the wind. It tends to accelerate the wind towards the electrodynamic velocity. At altitudes where the ion angular gyrofrequency exceeds the ion-neutral collision frequency and where ions drift at nearly the electrodynamic velocity $\mathbf{u}^e$ [*above about 130 km*], the Pedersen-drag coefficient $\sigma_P\,B^2 / \rho$ is just the mean rate at which a neutral particle suffers a collision with an ion. This rate is proportional to the ion [*and electron*] density, which varies considerably with altitude, time of day, latitude, season and solar cycle. It is also often called the *"ion-drag"* coefficient. The second term in Eq. 34, proportional to $\sigma_H\,B^2 / \rho$, acts at a right angle to the first. When $\mathbf{v}_\perp$ is more important than $\mathbf{u}^e$ this component of acceleration tends to turn the wind in a manner similar to the Coriolis effect. Because the geomagnetic field is downward over most of the northern hemisphere and upward over most of the southern hemisphere, the horizontal component of this deflecting acceleration is opposite to the Coriolis acceleration.

The horizontal momentum equation, under the assumption that viscous stresses are predominately associated with vertical shears of horizontal winds, can be written:

$$\left(\begin{array}{l} \dfrac{\mathrm{d}\,\mathbf{v}_h}{\mathrm{d}\,t} + f\,\hat{\mathbf{z}} \times \mathbf{v}_h + \nabla_p\,\Phi - \dfrac{1}{\rho H}\dfrac{\partial}{\partial Z}\left[\dfrac{\mu_m + \mu_{turb}}{H}\dfrac{\partial\,\mathbf{v}_h}{\partial Z}\right] \\ \qquad + \dfrac{\sigma_P B^2}{\rho}\left(\mathbf{v}_e + \sin^2 I\,\mathbf{v}_n\right) - \dfrac{\sigma_H B^2}{\rho}\sin I\,\hat{\mathbf{z}} \times \mathbf{v}_h \\ \qquad = \dfrac{\sigma_P B^2}{\rho}\left(\mathbf{u}^e_e + \sin^2 I\,\mathbf{u}^e_n\right) - \dfrac{\sigma_H B^2}{\rho}\sin I\,\hat{\mathbf{z}} \times \mathbf{u}^e_h \end{array} \right) \tag{35}$$

$$f = 2\,\Omega\,\sin\lambda \tag{36}$$

where λ is geographic latitude; $\hat{\mathbf{z}}$ is a unit upward vector; μ_m and μ_{turb} are the molecular and turbulent coefficients of viscosity; subscripts *e* and *n* denote components in the magnetic eastward and northward directions, respectively; and *h* denotes a horizontal component.

The horizontal pressure-gradient acceleration is represented by $\nabla_p\,\Phi$ in pressure coordinates. The coefficient of molecular viscosity is approximately:

$$\mu_m = 1.87\ 10^{-5}\left(\frac{T}{273.15}\right)^{0.69}\ \mathrm{kg.m^{-1}.s^{-1}} \tag{37}$$

while the coefficient of turbulent viscosity is commonly related to the turbulent diffusion coefficient by:

$$\mu_{turb} = \rho\ D_E\,P_r \tag{38}$$

where P_r is the *"Prandtl number"*, whose value depends on the nature of the turbulence, but is generally greater than unity.

The relative importance of the terms in Eq. 35 for horizontal motions is variable. When certain terms are relatively small, their effects can often be neglected. A useful way to determine the most important terms is to evaluate characteristic time rates associated with each, where the appropriate rate for a term is a typical magnitude of that term divided by a typical value of the wind velocity. Those terms having the largest rates are most important. A diurnal variation of the wind, with an angular frequency of $2\,\pi$ / (1 day), has a characteristic rate equal to that frequency, or $0.7\ 10^{-4}\ \mathrm{s^{-1}}$. More rapid wind variations like those associated with gravity waves have correspondingly greater rates. The horizontal component of the Coriolis acceleration has a characteristic rate of *f*, which varies with latitude but is on the order of $10^{-4}\ \mathrm{s^{-1}}$ at midlatitudes.

To estimate a characteristic rate for molecular viscosity, we can use the pressure scale height *H* as a typical vertical scale length for large-scale motions, and replace derivatives with respect to altitude by 1/*H*, obtaining a characteristic time

rate of $\mu_m / \rho H^2$. That quantity is listed in Table 1. It increases rapidly with altitude, and is comparable with the inertial rates around 200 km. Because viscosity must be balanced by the other terms in Eq. 35, its characteristic rate cannot increase indefinitely with altitude, but tends to saturate by virtue of the fact that the vertical shear of the wind decreases, so that the characteristic vertical scale becomes greater than H. On the other hand, the vertical scale can be less than H for some types of motions, like gravity waves with short vertical wavelengths, and these motions may be strongly influenced by viscosity well below 200 km.

The characteristic rate for turbulent viscosity is $D_E \; P_r / H^2$. The values of D_E / H^2 listed in Table 1 give a lower estimate for this rate [i.e., *with* $P_r = 1$].

The Pedersen-drag term on the left-hand side of Eq. 35 has a characteristic rate of $\sigma_P B^2 \sin^2 I / \rho$ in the magnetic north-south direction and $\sigma_P B^2 / \rho$ in the magnetic east-west direction. The Hall-drag term has a characteristic rate of $\sigma_H B^2 \left| \sin^2 I \right| / \rho$. Typical daytime values of the Pedersen-drag and Hall-drag coefficients are listed in Table 1. The daytime Hall-drag rate can become comparable to the inertial rates around 125 km, but it falls off above that altitude. The daytime Pedersen-drag rate increases steadily with altitude up to the peak of the F region, where it can easily exceed 10^{-3} s^{-1}.

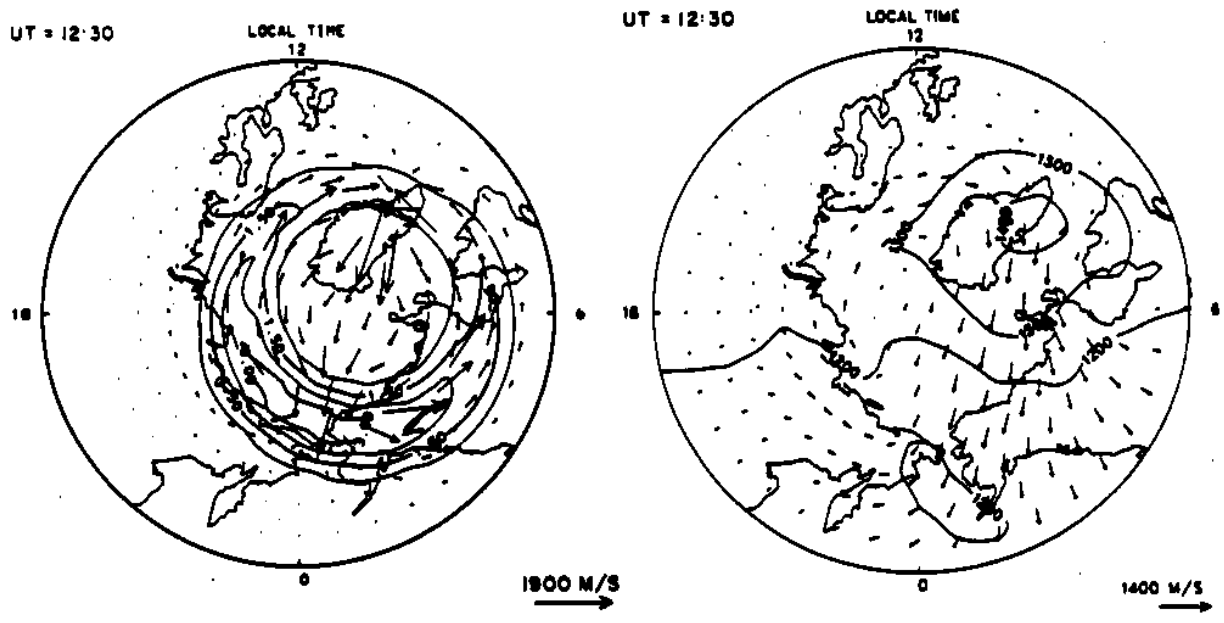

Figure 6. (Left) Horizontal component of parameterized electrodynamic drift velocities $\mathbf{u}^e$ *(arrows) and energy flux of precipitating electrons (contours with intervals of 0.75 mW.m*$^{-2}$ *at 12:30 UT on 22 March 1979. (Right) Simulated neutral winds (arrows) and temperatures (contours labeled in kelvins) at approximately 300 km, at 12:30 UT on 22 March 1979. (From Roble et al., 1987).*

At midlatitudes, the electrodynamic velocity $\mathbf{u}^e$ is often considerably smaller than the wind velocity **v**, and the main effects of the Ampère acceleration are just those of the Pedersen- and Hall-drag terms on the left-hand side of Eq. 35. At high magnetic latitudes, $\mathbf{u}^e$ often exceeds **v** in magnitude, so that the terms on the right-hand side of Eq. 35 can dominate, acting as forcing terms that accelerate the wind rapidly towards the ion convection velocity.

There is no simple characteristic rate associated with the horizontal pressure gradient. For long time scales the pressure sometimes tends to adjust through density and temperature changes of the air in such a way as to come into balance with the other forces. For example, in the lower thermosphere where ion drag and viscosity are often unimportant, it is possible to have part of the air motion in geostrophic balance, with the horizontal pressure-gradient force approximately balancing the Coriolis force. Such a situation is common in the lower atmosphere, where winds tend to flow along isobars. In the upper thermosphere, the pressure-gradient force will tend to be in approximate balance with the ion-drag and viscous forces. When $\mathbf{u}^e$ is small, all three forces in the upper thermosphere tend to be parallel to the wind direction: the wind is directed more nearly perpendicular to isobars than parallel to them. Since the upper-thermospheric pressure is larger on the day side than on the night side of the Earth, owing to daytime thermospheric expansion, the wind blows generally away from the day side toward the nightside in the upper thermosphere.

Figure 6 shows the distributions of ion and neutral velocities at 300 km between 47.5° geographic latitude and the North Pole, as simulated by the National Center for Atmospheric Research Thermosphere General Circulation Model [*NCAR TGCM*]. The simulation is for a geomagnetic storm. The imprint of the pattern of ion convection on the neutral velocity in the auroral zone and polar cap is evident. Ion drag tends to accelerate the neutrals towards the ion velocity, but inertia and competing forces prevent full coincidence between the ion and neutral velocities. The imprint of the evening cell of the polar ion-convection pattern appears clearly in the neutral velocity, but the imprint of the morning cell is less pronounced, in part because of lower electron density, and hence ion-drag, during the latter part of the night.

6. Energy Balance, Temperatures, and Vertical Winds

The temperature and pressure variations in the thermosphere respond to exchanges of energy. The equation for conservation of thermodynamic energy can be expressed in terms of the rate of change of pressure and of specific enthalpy as:

$$\frac{d}{dt}(c_p T) - \frac{1}{\rho}\frac{dp}{dt} + \frac{1}{\rho}\nabla \cdot \mathbf{q} = Q \qquad (39)$$

where **q** is heat flux and *Q* is the net heating associated with a variety of processes: absorption of solar ultraviolet radiation, heat deposition by energetic magnetospheric particles, chemical heating, infrared cooling, viscous heating, and Joule heating.

In terms of high-latitude thermosphere-ionosphere interactions, Joule heating is of particular importance. The heating rate per unit mass is given by:

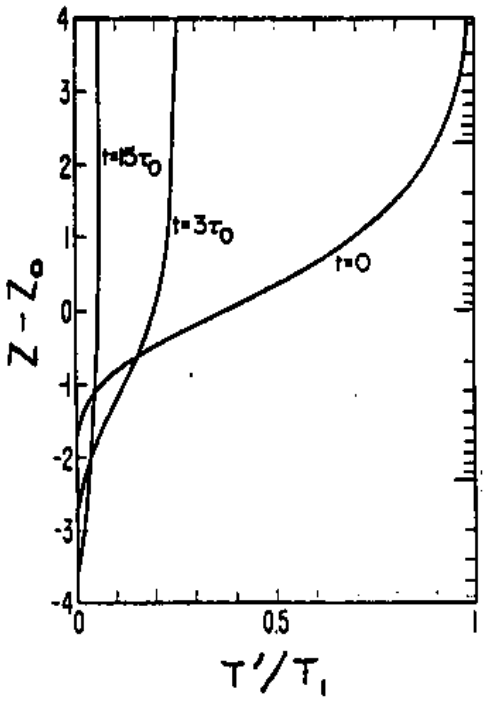

Figure 7. Decay of a temperature perturbation T by molecular heat conduction in an idealized atmosphere, with no other addition or loss of heat. T_1 is the asymptotic high-altitude temperature perturbation at t=0. Z is normalized altitude, measured in scale heights, and Z_0 is the normalized transition altitude of the perturbation profile at t=0. τ_0 is a time constant equal to the inverse heat-conduction rate coefficient at Z_0. See text for further explanation.

$$Q_J = \frac{\mathbf{J} \cdot (\mathbf{E} + \mathbf{v} \times \mathbf{B})}{\rho} = \frac{\sigma_P B^2}{\rho}(\mathbf{u}^e - \mathbf{v}_\perp)^2 \qquad (40)$$

The contribution of Joule heating to the heat budget of the thermosphere above 130 km can exceed that of sunlight during aurorally disturbed periods. During disturbed periods the height-integrated and globally averaged Joule heating usually exceeds that associated with precipitating energetic particles by a factor of

2-3. Joule heating tends to occur higher than particle heating, where it has a relatively stronger effect on the thermospheric temperature because of the lower mass density.

The heat flux is due to molecular heat conduction, transport of heat in association with species diffusion, and turbulent heat conduction. On large scales, the horizontal components of heat conduction can be neglected. The upward heat flux is:

$$q_z = - \kappa_m \frac{\partial T}{\partial z} + \sum_j (n_j m_j c_{pj} + \alpha_j n_j k T) \hat{\mathbf{z}} \cdot \mathbf{v}_{dj} - \kappa_{turb} \left(\frac{g}{c_p} + \frac{\partial T}{\partial z} \right) \qquad (41)$$

The molecular heat conduction coefficient κ_m is closely related to the molecular coefficient of viscosity and is adequately approximated throughout the thermosphere by:

$$\kappa_m = 1.5 \, c_p \, \mu_m \qquad (42)$$

The turbulent heat conduction coefficient κ_{turb} is approximately related to the eddy diffusion coefficient by:

$$\kappa_{turb} = \rho \; D_E \, c_p \qquad (43)$$

The molecular heat conduction coefficient κ_m is closely related to the molecular coefficient of viscosity and is adequately approximated throughout the thermosphere by:

$$\kappa_m = 1.5 \, c_p \, \mu_m \qquad (42)$$

The turbulent heat conduction coefficient κ_{turb} is approximately related to the eddy diffusion coefficient by:

In pressure coordinates, considering only the vertical component of heat flux, Eq. 39 becomes:

$$\left(\begin{array}{l} \frac{d}{dt} (c_p T) + W g H \\ \quad - \frac{1}{\rho H} \frac{\partial}{\partial Z} \left[\frac{\kappa_m}{H} \frac{\partial T}{\partial Z} + \frac{\kappa_{turb}}{c_p H} \left\{ g H + \frac{\partial}{\partial Z} (c_p T) \right\} \right] \\ \quad = Q \end{array} \right) \qquad (44)$$

Molecular heat conduction has a major effect on thermospheric energetics. At high altitudes rapid conduction is responsible for the nearly isothermal vertical temperature profile. As with viscosity, a characteristic time rate for heat conduction to be effective can be defined by considering the case where vertical gradients have a characteristic scale of H. The characteristic time-rate-of-change associated with molecular heat conduction in Eq. 44 is then seen to be:

$$\alpha_\kappa = \frac{\kappa_m}{c_p \rho H^2} \tag{45}$$

Because of Eq. 42, the characteristic rate for molecular heat conduction is simply 1.5 times that for molecular viscosity.

In order to understand the manner in which heat conduction affects the evolution of the thermospheric temperature in response to a perturbation, it is instructive to look at a simplified solution to a one-dimensional [*vertical*] version of Eq. 44, conceptually representative of a global average. Advection and turbulent conduction are ignored, and c_p and κ_m / H are assumed constant. Eq. 44 then yields

$$\frac{\partial T}{\partial t} - \alpha_\kappa \frac{\partial^2 T}{\partial Z^2} = \frac{Q'}{c_p} \tag{46}$$

where Q' is the perturbation heat input.

The characteristic rate α_κ for heat conduction is assumed to vary with Z as

$$\alpha_\kappa (Z) = \alpha_0 \ e^Z \tag{47}$$

because of its inverse dependence on air density, where α_0 is a constant.

Assume an initial temperature of the form:

$$T = T_0 + T' = T_0 + T_1 \ \exp\{ - e^{(Z_0 - Z)} \} \tag{48}$$

where T_0, T_1 and Z_0 are constants.

The initial profile of T' / T_1 [*at* $t = 0$] is plotted in Figure 7. T becomes asymptotically isothermal at low and high altitudes, where it approaches values of T_0 and $T_0 + T_1$, respectively. Z_0 represents a normalized transition altitude between these two asymptotic regimes. The solution to Eq. 46, assuming that $Q' = 0$ after $t = 0$, is:

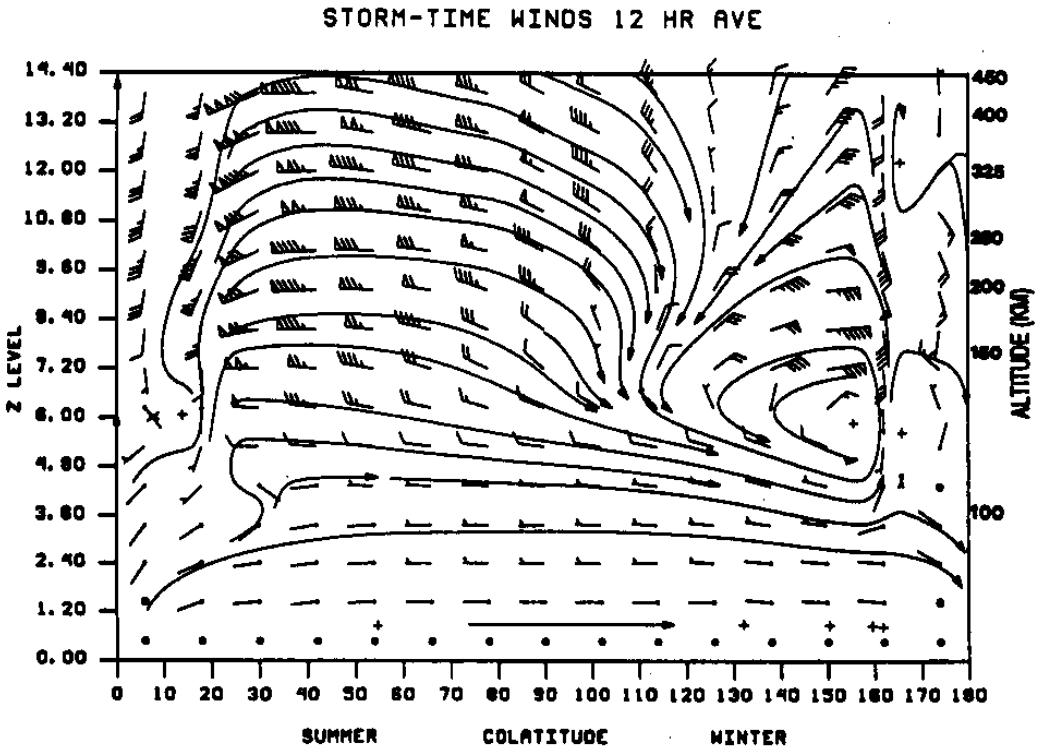

Figure 8. Meridional wind and streamlines between 80 km and 450 km averaged over 12 hours of a simulated storm at solstice using a two-dimensional model. The Z level is defined by a value of p_0 = 1.05 Pa in (10). The wind-barb notation is as follows: short barb (5 m.s^{-1}); long barb (10 m.s^{-1}); and flag (50 m.s^{-1}). The vertical components of the winds have been scaled so that the shafts of the wind arrows are parallel to streamlines. The normal summer- to winter flow is altered by Joule heating that is centered around 21° and 159° colatitude. The summertime equatorward flow is strengthened, while the normal wintertime poleward flow is reversed at middle latitudes. (From Brinkman et al., 1992).

$$T'(Z, t) = \frac{T_1 \tau_0}{t + \tau_0} \exp\left(\frac{-\tau_0 e^{(Z_0 - Z)}}{t + \tau_0} \right) \tag{49}$$

$$\tau_0 = \frac{1}{\alpha_\kappa(Z_0)} \tag{50}$$

This solution retains the same functional form as the initial temperature perturbation profile, but the maximum perturbation decreases as $1 / (t + \tau_0)$ and the normalized transition altitude lowers as $-\ln(1 + t / \tau_0)$ with increasing time, as seen in Figure 7. The characteristic rate for molecular heat conduction, α_κ, determines how rapidly the perturbation penetrates to lower heights, and how rapidly it decays in time.

The conductive response to variations in heating can dominate globally averaged temperature variations. Spatially localized heating, however, tends to pro-

duce advective motions that can dominate the local response. In particular, localized heating makes the air more buoyant that its surroundings, causing it to rise. The adiabatic cooling associated with the vertical advection tends to come into rough balance with the heating after some period of time, at least at lower altitudes where heat conduction is not too rapid. This cooling is represented by the first two terms on the left-hand side of Eq. 44 when the time derivative following fluid motion, $\mathrm{d}\,(\,c_p\,T\,)\,/\,\mathrm{d}\,t$, is dominated by the vertical advective derivative $W\,\partial\,(\,c_p\,T\,)\,/\,\mathrm{d}\,Z$. Balancing these two terms with the heating then gives:

$$W\,\frac{\partial\,(\,c_p\,T\,)}{\partial\,Z}+W\,g\,H\approx Q \tag{51}$$

This yields a [*dimensional*] vertical velocity of:

$$W\,H\;\approx\;\frac{\mathrm{Q}}{\mathrm{g}+[\,\partial\,(\,c_p\,T\,)\,/\,\partial\,Z\,]} \tag{52}$$

An intense heating rate of 1000 W.kg^{-1}, as would occur when the ion drag parameter is 10^{-3} s^{-1} and the velocity difference between the neutrals and ions is 1000 m.s^{-1}, produces an upward velocity of the order 100 m.s^{-1} according to this estimator. The upward motion in the region of net heating must be balanced by outward flow at high altitudes and downward motion outside the heating region. This downward motion produces compressive heating, and thus the original localized heat input tends to become distributed over a larger area. Figure 8 shows an example of the mean meridional circulation driven by a combination of solar and auroral heating for storm conditions. The summer-to-winter flow is driven by solar heating. Strong auroral Joule heating reverses that flow at upper midlatitudes in the winter hemisphere.

The vertical circulation associated with non-uniform thermospheric heating affects the composition: air rich in heavier molecular species is raised to higher altitudes in regions of net heating, while sinking motions elsewhere tend to deplete those species.

In addition, there can be horizontal transport of the altered air when the winds are strong, as illustrated in Figure 9. The high-latitude upwelling of molecular species increases the plasma loss rate, so that strong heating during magnetic storms can result in electron-density depletions that are a part of ionospheric storm phenomena.

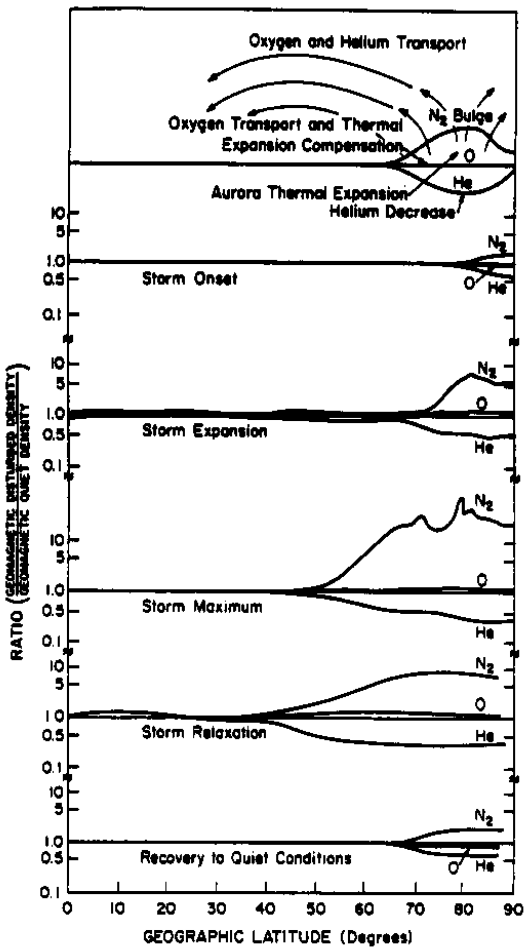

Figure 9. Schematic of the thermospheric compositional response to geomagnetic storms as a function of latitude at various times during the storm. The ratio is storm-time departure relative to geomagnetically quiet conditions. (From Roble, 1977).

7. Gravity Waves and Tides

Atmospheric observations reveal a wide variety of wave motions, from short-period and small-scale sound waves to long-period and global-scale planetary waves. The exponential decrease in atmospheric density with increasing height tends to be accompanied by growth in the amplitude of velocity and temperature perturbations associated with the waves, so that large wave amplitudes are commonplace in the thermosphere. The main thermospheric wave motions are {\it gravity waves} with periods from a fraction of an hour to several hours, and {\it atmospheric tides} with periods around 12 hours and 24 hours. Gravity waves are of interest because of information they provide about transient atmospheric processes that generate them, and because of their potential to transport momentum and energy between different atmospheric layers. Tides are the dominant form of wind in the lower thermosphere, and they impact the dynamics of the entire thermosphere and ionosphere.

Gravity waves with periods longer than about 1/2 hour are approximately in hydrostatic balance, and thus satisfy Eq. 12, 18, 35, and 44. To understand the basic properties of such waves, let us work with linearized versions of those equations by making replacements like:

$$H \rightarrow H_0 + H' \tag{53}$$

and dropping all quantities of quadratic or higher order involving the primed terms.

For simplicity, let us also neglect viscosity, heat conduction, diffusion, the Coriolis acceleration, mean winds [i.e., $\mathbf{v}_0$], and gradients of m, c_p, and g. The linearized equations are then:

$$\frac{\partial \Phi'}{\partial Z} - g H' = 0 \tag{54}$$

$$\frac{\partial W'}{\partial Z} - W' + \nabla_p \cdot \mathrm{v}_h' = 0 \tag{55}$$

$$\frac{\partial \mathbf{v}_h'}{\partial \mathrm{t}} + \nabla_p \Phi' = \frac{\mathbf{J} \times \mathbf{B}}{\rho} \tag{56}$$

$$g \frac{\partial H'}{\partial t} + H_0^2 N^2 W' = \frac{k}{m c_p} Q' \tag{57}$$

where the angular *"buoyancy frequency"*, N, also called the angular *Brunt-Väisälä frequency*, is defined by:

$$N^2 = \frac{g}{H_0} \left(\frac{k}{m c_p} + \frac{\partial H_0}{\partial z} . \right) \tag{58}$$

The dimensionless quantity $k / (m c_p)$ is 2 / 7 for an atmosphere that is predominantly N_2 and O_2, and 2 / 5 for an atmosphere that is predominantly O. N is the natural frequency at which air parcels undergoing vertical adiabatic motion tend to oscillate owing to buoyancy forces. Typical values of the buoyancy period $2 \pi / N$ are listed in Table 1.

The terms on the right-hand sides of Eq. 56 and 57 can be considered as source terms. In the thermosphere, the Amp\‘ere force and Joule heating caused by auroral electric currents can produce gravity waves that have been observed to travel a good fraction of the Earth’s circumference. However, most of the gravity waves observed in the thermosphere appear to originate from the lower atmos-

phere, where the source can be latent heat release, non-linear dynamical phenomena neglected in Eq. 54 - 57, or other processes.

Outside of source regions the right-hand sides of Eq. 56 and 57 vanish, and we can examine the solution for a monochromatic wave that varies in time and in the horizontal *x*-direction as:

$$\exp(\mathrm{i}\, \omega t - \mathrm{i}\, \kappa \mathrm{x}) \tag{59}$$

where i is $\sqrt{-1}$, κ is the horizontal wavenumber and ω is the angular frequency. The horizontal phase trace velocity of the wave is

$$v_{px} = \frac{\omega}{\kappa} \tag{60}$$

which is in the positive *x* direction when ω and κ have the same sign.

Equations 54 - 57 yield:

$$\frac{\partial \Phi'}{\partial \mathrm{Z}} - g H' = 0 \tag{61}$$

$$\frac{\partial W'}{\partial Z} - W' - \mathrm{i}\, \kappa v_x' = 0 \tag{62}$$

$$\mathrm{i}\, \omega v_x' - \mathrm{i}\, \kappa \Phi' = 0 \tag{63}$$

$$\mathrm{i}\, \omega g H' + H_0^2 N^2 W' = 0 \tag{64}$$

If H_0 is assumed to be constant with height, Eq. 61 - 64 have nontrivial solutions in which the primed variables vary with altitude as:

$$\exp\left[\frac{1}{2} \pm \mathrm{i}\, K \right] Z \tag{65}$$

where *K* is a dimensionless vertical wavenumber given by

$$K = \frac{1}{2}\left[\frac{\kappa^2 C^2}{\omega^2} - 1 \right]^{½} = \frac{1}{2}\left[\frac{C^2}{v_{px}^2} - 1 \right]^{½} \tag{66}$$

$$C \equiv 2 H_0 N \tag{67}$$

C has the units of velocity, and for an isothermal atmosphere is a little under the speed of sound.

When $v_{px} < C$, K is real, and the solutions have a propagating oscillatory structure in the vertical, with a wavelength of $2\pi H_0 / K$. Such waves are called *internal* gravity waves, and C is their limiting speed. If ω is positive, the solution with the plus sign in Eq. 65 has downward phase propagation, while that with the minus sign has upward phase propagation. When $v_{px} > C$, K is imaginary, and the solutions have an exponential structure in the vertical. Both the propagating and the exponential solutions have a factor proportional to exp(Z / 2) that causes the amplitude to grow with increasing altitude, unless such growth is overwhelmed by a large imaginary K. Thus upward propagating waves can attain large amplitudes in the thermosphere. Conversely, waves propagating downward have their amplitudes exponentially suppressed, so that waves generated in the upper atmosphere are difficult to detect at lower altitudes.

Typical values of C at different altitudes are listed in Table 1. Because C generally varies with height, K also varies with height, and Eq. 65 does not strictly represent the vertical structure of the waves. However, if K varies sufficiently slowly with height and does not approach zero, then approximate solutions to Eq. 61 - 64 can be found which have an exponential dependence as:

$$\exp\left[\int_{z_0}^{z}\left(\frac{1}{2} \pm i\,K(Z'')\right)dZ''\right] \tag{68}$$

These solutions are still wave-like with respect to height when K is real, but the wavelength varies with height. Regions where K approaches zero will tend to reflect propagating waves.

The vertical [*upward*] phase trace velocity of an internal wave is

$$v_{pz} = \pm\frac{\omega H_0}{K} \tag{69}$$

with the upper or lower sign corresponding to the upper or lower sign in Eq. 65 or 68.

The group velocity, which gives the velocity with which the energy in a wave packet would travel, is found by differentiating ω with respect to κ and K, using the dispersion relation Eq. 66. Solving Eq. 66 for ω^2 gives:

$$\omega^2 = \frac{\kappa^2 C^2}{4K^2 + 1} \tag{70}$$

The horizontal component of group velocity is:

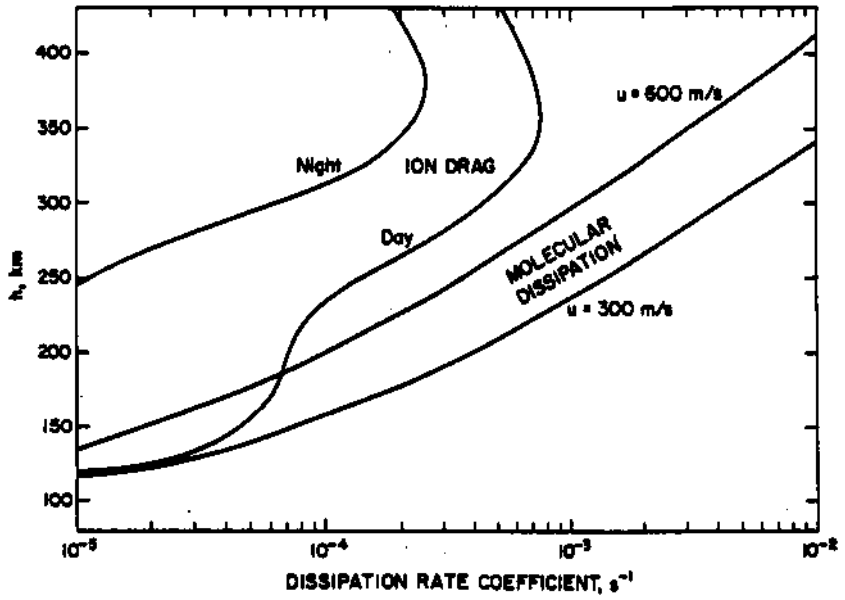

Figure 10. Contributions to the wave energy dissipation rate coefficient due to molecular dissipation and to ion drag. For molecular dissipation the coefficient is shown for two different horizontal wave phase velocities v_{px} (represented by u here): 300 m.s^{-1} and 600 m.s^{-1}. For ion drag the coefficient is shown for typical (not extremum) day and night conditions. (From Richmond, 1978).

$$v_{gx} = \frac{\partial \omega}{\partial \kappa} = \frac{\omega}{\kappa} = v_{px} \tag{71}$$

The vertical component of group velocity is:

$$v_{gz} = \mp H_0 \frac{\partial \omega}{\partial K} = \pm \frac{H_0 \omega}{K} \frac{4K^2}{4K^2 + 1} = \frac{-4K^2}{4K^2 + 1} v_{pz} \tag{72}$$

which has the opposite sign of the vertical phase trace velocity and is smaller in magnitude, although the magnitudes become similar when K is large in comparison with 1/2.

Gravity waves can be generated at all heights in the atmosphere, but the energy available for generation generally decreases with increasing altitude. At any given altitude in the upper atmosphere most of the wave energy usually comes from lower levels, and so most observable waves have upward group velocities. Since the vertical group and phase velocities have opposite signs, the phase propagation of these waves is usually downward.

Dissipation of gravity waves in the thermosphere arises from ion drag, viscosity, and heat conductivity. The characteristic rates for ion drag and viscosity listed in Table 1 are indicative of the importance of those effects; for viscosity, the rates are appropriate for waves with a vertical wavelength of $2\pi H$. The characteristic

dissipation rate due to molecular heat conduction is about 1.5 times that due to molecular viscosity. For both of these molecular processes, the characteristic rate is approximately proportional to the inverse square of the vertical wavelength. From the dispersion relation Eq. 66, it can readily be seen that waves with short vertical wavelengths are those with horizontal phase speeds that are slow in comparison with *C*. Thus slow-moving waves tend to be rapidly dissipated as they propagate into the upper thermosphere. Figure 10 shows representative gravity-wave dissipation rates due to ion drag and to molecular processes, the latter for two different horizontal phase trace speeds v_{px} [*labeled u in the figure*].

The primary way in which gravity waves imprint their signature on the ionosphere is through the vertical plasma motions they can induce. A gravity wave produces undulations in the ionosphere that propagate with the phase velocity of the wave. These are known as Traveling Ionospheric Disturbances [*TIDs*]. Figures 11 and 12 show examples of the manner in which the ionospheric undulations propagate horizontally and vertically.

Waves that propagate from the lower atmosphere into the thermosphere must have horizontal phase velocities less than the value of *C* in the mesosphere, which Table 1 shows to be around 230 m.s^{-1}. Higher-speed waves become evanescent, and so that value can be considered as a high-speed cutoff for wave penetration. [*Background winds and temperature variations can cause the value of the cutoff to vary by about ± 25 %*]. By contrast, waves that are generated by auroral electric currents and that propagate into the upper thermosphere can have much larger phase speeds, on the order of 800 m/s, since these waves are generated within a scale height or so of 130 km, where the value of *C* is large. Thus the observed phase speed of a TID gives a clue about its possible source: TIDs moving faster than 350 m/s are unlikely to originate in the lower atmosphere, while those moving slower than 200 m.s^{-1} may very well have a lower-atmospheric source.

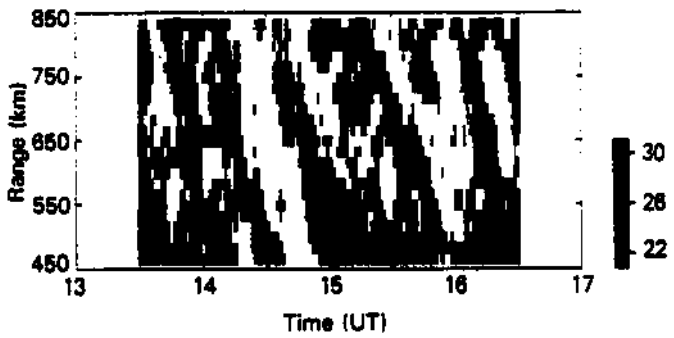

Figure 11. Backscattered power from a north-looking beam of the Goose Bay Radar on 1988 November 25. The streaks show the effects of equatorward-propagating traveling ionospheric disturbances. (From Samson et al., 1990).

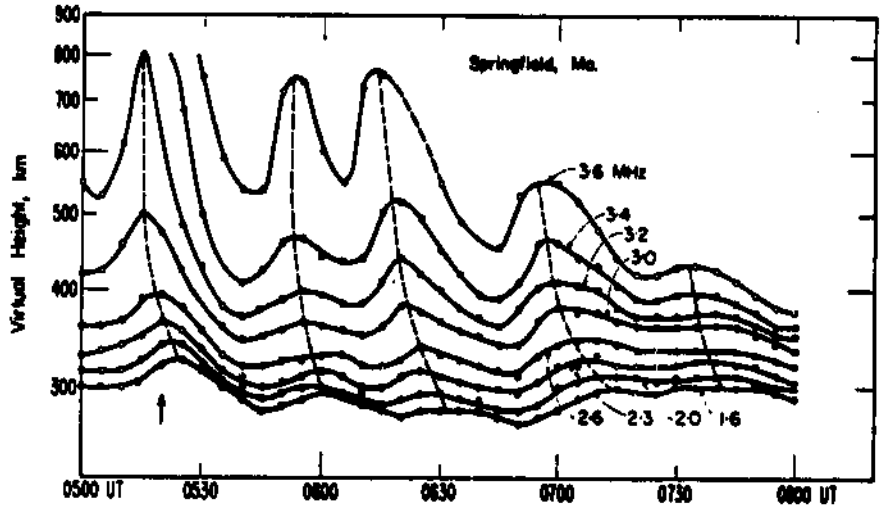

Figure 12. Variations of ionospheric virtual heights (radar pulse delay divided by twice the speed of light) at different radar frequencies (in Mhz). A wave feature with a mean period of around 35 min and downward-propagating phase features is apparent at all heights. (From Georges, 1968).

Atmospheric tides are global oscillations with periods of one solar or lunar day, or some integral fraction thereof. Solar tides are the dominant form of wind in the thermosphere. Tides have many of the characteristics of gravity waves, such as amplitude growth with altitude and downward phase propagation in the presence of upward energy propagation. In fact, tides can be described by the same equations as gravity waves, Eq. 54 - 57, with the addition of Coriolis acceleration to Eq. 56. However, the variation of the Coriolis parameter *f* with latitude means that plane-wave solutions of the form Eq. 59 are not possible. Rather, discrete modes appear as possible solutions, at least in a horizontally arises from the requirement that solutions be continuous around the Earth. Although the variation of a mode in longitude is simply sinusoidal, the variation in latitude is more complex. When realistic latitudinal variations of atmospheric temperature and mean zonal winds are taken into account, the latitudinal and vertical structures of the tidal modes become coupled. Nevertheless, wavelike features in the vertical structure remain. The main source of solar tides is the daily variation of solar radiation absorbed by oxygen in the thermosphere, by ozone in the stratosphere and mesosphere, and by water vapor in the troposphere. Lunar tides are driven by lunar gravitational forcing, and have amplitudes typically only a few percent those of solar tides. Upward-propagating tides are clearly visible in the lower thermosphere: at high latitudes, semidiurnal [*12-hour*] tides are usually strongest, while at low latitudes, both semidiurnal and diurnal [*24-hour*] tides are important. Figure 13 shows the daytime wind in the lower thermosphere on three days in August, 1974, above the Arecibo incoherent-scatter radar.

The slow downward progression of eastward and westward wind regimes are clearly evident, associated primarily with the tides.

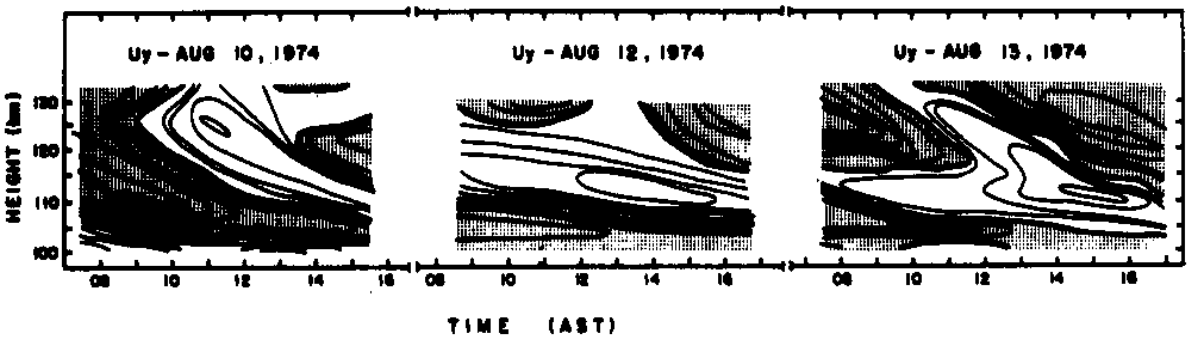

Figure 13. Eastward component of the neutral wind above Arecibo, Puerto Rico, for 10, 12, and 13 August 1974. Contour levels are 20 m.s^{-1}, and shaded contours show westward winds. (From Harper, 1977).

8. Dynamo Effects of Thermospheric Winds

Winds contribute to the electric current through the so-called "*dynamo electric field*" $\mathbf{v} \times \mathbf{B}$ in Eq. 30, which is the electric-field component associated with the transformation from the Earth-based reference frame to the reference frame moving with the wind. As in an electric dynamo, an electromotive force is created as the conducting medium is moved through the magnetic field. The electric field **E** in the Earth-based reference frame is influenced by dynamo effects, because divergent current driven by the dynamo electric field creates space charge that results in a polarization electric field. The current must be divergence-free in three dimensions, and the large-scale electric field is normally electrostatic, with negligible geomagnetic-field-aligned component:

$$\nabla \cdot \mathbf{J} = 0 \tag{73}$$

$$\mathbf{E} = -\nabla \Phi_e \tag{74}$$

$$E_{//} = 0 \tag{75}$$

where Φ_e is the electrostatic potential.

Equations 74 and 75 require that geomagnetic field lines be equipotentials. At high latitudes, Equation 73 effectively relates the geomagnetic-field-aligned current density at the top of the conducting ionosphere to the height-integrated horizontal ionospheric current density. That is, current must flow into or out of the top of the ionosphere from the magnetosphere in order to balance any divergence or convergence of the horizontal current.

When Ohm's Law Eq. 30 is used to replace $\mathbf{J}\perp$ in Eq. 73, it can be seen that the field-aligned current is related both to the electrostatic field **E** and to the

dynamo field **v** x **B**. It was noted in Section 5 that the wind in the high-latitude F-region tends to have a pattern with some similarity to the electrodynamic convection velocity $\mathbf{u}^e$ (= {**E** x **B**} / B^2) that is produced largely by magnetospheric processes. The similarity becomes less at lower altitudes, where the characteristic rate associated with ion drag is slower. As a result, **v** x **B** has some tendency to be directed opposite to **E**, but to have a weaker magnitude. Consequently, the field-aligned current associated with **v** x **B** tends to be opposite to, but weaker than, that associated with **E**. Figure 14 shows an example of the electric-field-driven and wind-driven field-aligned current distributions at the top of the ionosphere from a simulation with the NCAR TGCM. Note that the scales for the two components are different, since the wind-driven current is considerably weaker. The tendency for anticorrelation of the two current components is evident.

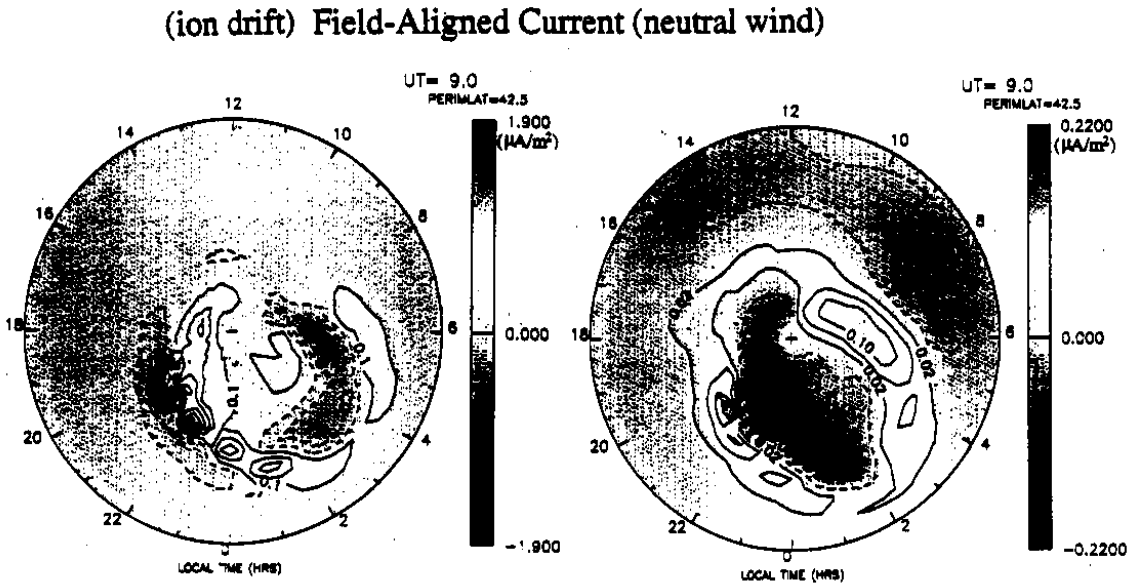

Figure 14. Components of the field-aligned current density for 1992 March 29, 09:00 UT, over northern latitudes above 42.5$° geographic, estimated with the Assimilative Mapping of Ionospheric Electrodynamics (AMIE) procedure and the NCAR Thermosphere-Ionosphere General Circulation Model (TIGCM). Local noon is at the top. (Left) Current driven by the electric field (contour interval 0.2 μA.m^{-2}. (Right) Current driven by the dynamo effect of thermospheric winds (contour interval 0.04 μA.m^{-2}). Solid contours are downward current; dashed contours are upward current. (From Lu et al., 1995).

There are indications that the magnitude and direction of the electric field on geomagnetic-field lines that are open to the solar wind, in the polar cap, are relatively insensitive to ionospheric conditions; i.e., the magnetosphere tends to act as a voltage generator. At those latitudes, it is appropriate to consider the thermospheric winds as tending to reduce the strength of the field-aligned currents, without affecting the electric field, as in the example above. However, at lower latitudes where geomagnetic-field lines are closed, it is not always possible

for the magnetosphere to absorb changes in the field-aligned current and still maintain current continuity. Instead, the electric field may change in a way that tends to preserve the field-aligned current density. In simplified terms, the magnetosphere can be considered to act as a current generator rather than a voltage generator. Figure 15 illustrates how the electric field can be modified by the winds.

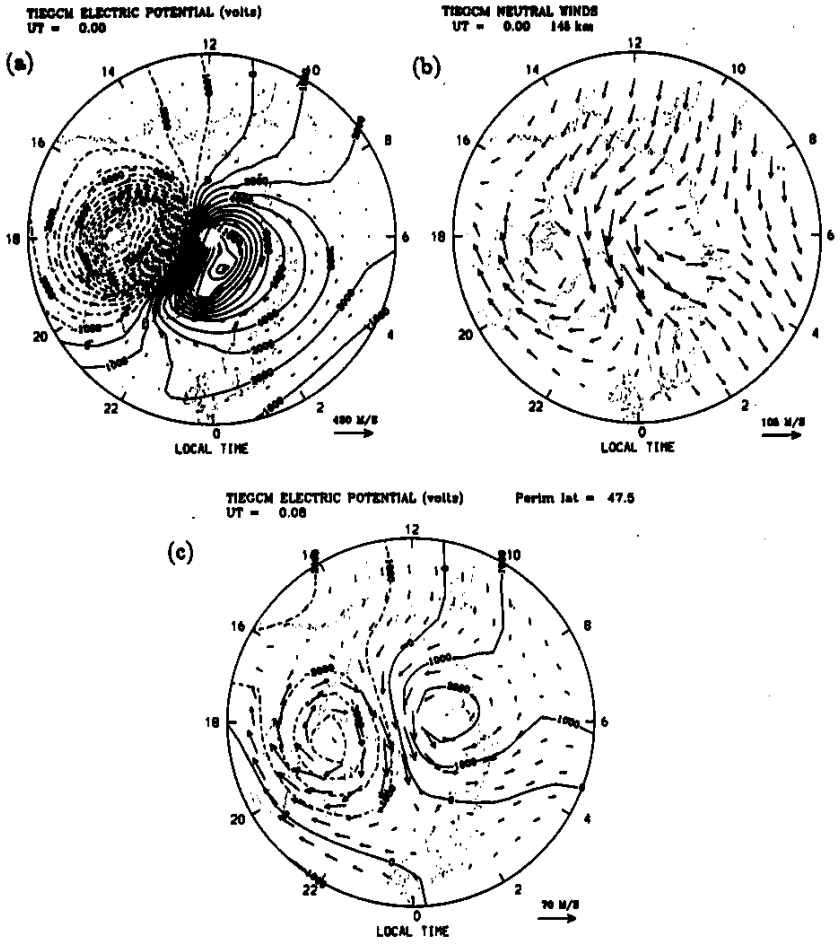

Figure 15. Results of a TIE-GCM simulation illustrating the "flywheel" effect for solar-minimum equinox conditions. Contour intervals are 1000 V; vector velocity scales vary, as shown at the lower right of each plot. (a) Electric-potential contours and ion-drift vectors in geographic coordinates between 47.5° and the North Pole, at 00:00 UT, for a diurnally reproducible simulation with an imposed cross-polar-cap potential of 30 kV. (b) Corresponding neutral wind vectors at 145 km altitude. (c) Electric potential contours and ion-drift vectors one time-step later, after field-aligned current between the ionosphere and the outer magnetosphere has been cut off. (From Richmond, 1995a).

This time, a modified version of the *NCAR TGCM* is used, the Thermosphere-Ionosphere-Electrodynamics General Circulation Model [*TIE-GCM*]. The *TIE-GCM* calculates the ionospheric-dynamo effects of thermospheric winds, and considers self-consistently the feedback of the dynamo electric fields and currents on the neutral dynamics. Figure 15_a shows the imposed electric potential and the

ion-drift velocities for a steady-state simulation, while Figure 15_b shows the wind at 145 km, an altitude that is representative of the height-averaged dynamo effects. Figure 15_c shows the electric potential and ion drifts one time step later, after the field-aligned currents to the outer magnetosphere have artificially been cut off. The pattern is somewhat similar to that in Figure 15_a, except for being weaker and rotated about two hours in local time. This electric-potential pattern can be considered to be that component produced by the ionospheric dynamo if the magnetospherically imposed currents are not allowed to change, contrary to the simulation of Figure 14. The tendency for the wind-produced ion convection to have the same pattern as magnetosphere-produced convection has been called the *"flywheel"* effect. That is, the inertia of the neutral winds can be considered to help maintain the ion convection imposed by the magnetosphere. The fact that the pattern is rotated in local time can be attributed to the inertia of the winds in the presence of the Earth's rotation.

Acknowledgments.

I thank Gang Lu for helpful comments on the manuscript. The National Center for Atmospheric Research is sponsored by the National Science Foundation. This work was partly supported by the NASA Space Physics Theory Program.

9. References

Brinkman D.G., R.L. Walterscheid, A.D. Richmond, and S.V. Venkateswaran, Wave-mean flow interaction in the storm-time thermosphere: a two-dimensional model simulation, *J. Atmos. Sci.*, **49**, 660-680, 1992.

Georges T.M., HF doppler studies of travelling ionospheric disturbances, *J. Atmos. Terr. Phys.*, **30**, 735-746, 1968.

Hargreaves J. K., *The solar-terrestrial environment*, Cambridge Univ. Press, Cambridge, 1992.

Harper R.M., Tidal winds in the 100-200 km region at Arecibo, *J. Geophys. Res.*, **82**, 3243-3250, 1977.

Hedin A.E., MSIS-86 thermospheric model, *J. Geophys. Res.*, **92**, 4649-4662, 1987.

Holton J.R., *An Introduction to Dynamic Meteorology*, Academic Press, New York, 1979.

Kelley M. C., *The Earth's Ionosphere: Plasma Physics and Electrodynamics*, Academic Press, San Diego, 1989.

Lu G., A.D. Richmond, B.A. Emery, and R.G. Roble, Magnetosphere-ionosphere-thermosphere coupling: effect of neutral wind on energy transfer and field-aligned current, *J. Geophys. Res.*, **100**, 19,643-19,659, 1995.

Rees M. H., *Physics and Chemistry of the Upper Atmosphere*, Cambridge Univ. Press, New York, 1989.

Richmond A.D., Gravity wave production, propagation, and dissipation in the thermosphere. *J. Geophys. Res.*, **83**, 4131-4145, 1978.

Richmond A.D., Thermospheric dynamics and electrodynamics, in *Solar-Terrestrial Physics, Principles and Theoretical Foundations*, (R.L. Carovillano and J.M. Forbes, eds.), D. Reidel Publishing Company, Dordrecht, Holland, 523-607, 1983.

Richmond A.D., The ionosphere, in *The Solar Wind and the Earth*, (S.-I. Akasofu and Y. Kamide, eds.), Terra Scientific Publishing Company, Tokyo, 123-140, 1987.

Richmond, A.D., The neutral upper atmosphere, in *Geomagnetism and Aeronomy*, (J.A. Jacobs, ed.), **4**, 403-479, 1991.

Richmond A.D., The ionospheric wind dynamo: effects of its coupling with different atmospheric regions, in *The Upper Mesosphere and Lower Thermosphere*, edited by R. M. Johnson and T. L. Killeen, pp. 49-65, Am. Geophys. Union, Washington, DC, 1995a.

Richmond A.D., Ionospheric electrodynamics, in *Handbook of Atmospheric Electrodynamics*, Vol. II, edited by H. Volland, pp. 249-290, CRC Press, Boca Raton, Florida, 1995b.

Roble R.G., The thermosphere, in *The Upper Atmosphere and the Magnetosphere*, pp. 57-71, NAS Press, Washington, D.C., 1977.

Roble R.G., The Earth's thermosphere, in *The Solar Wind and the Earth*, edited by S.-I. Akasofu and Y. Kamide, pp. 245-264, Terra Sci. Pub. Co., Tokyo, 1987.

Roble R.G., J.M. Forbes, and F.A. Marcos, Thermospheric dynamics during the March 22, 1979 magnetic storm, 1. Model simulations, *J. Geophys. Res.*, **92**, 6045-6068, 1987.

Samson J.C., R.A. Greenwald, J.M. Ruohoniemi, A. Frey, and K.B. Baker, Goose Bay Radar observations of Earth-reflected atmospheric gravity waves in the high-latitude ionosphere, *J. Geophys. Res.*, **95**, 7693-7709, 1990.

U.S. Standard Atmosphere, U.S. Gov. Printing Off., Washington, D.C., 1976.

Volland H., *Atmospheric Tidal and Planetary Waves*, Kluwer Academic Publishers, Dordrecht, Netherlands, 1988.

RADAR OBSERVATIONS OF THE MIDDLE AND LOWER ATMOSPHERE

Jürgen Röttger

1. Introduction

Scatter and reflection of electro-magnetic waves from irregularities in the refractive index of the Earth's atmosphere has been a very essential research subject in radio science. Total reflection of high frequency waves was the major mechanism to study the ionosphere with the traditional ionosondes. Forward and backscattering from atmospheric and ionospheric irregularities was found at higher frequencies and, after the invention of the radar technique, have become most effective means to study the atmosphere and ionosphere. The incoherent or Thomson scatter radars as well as the mesosphere-stratosphere-troposphere [*MST*] radars have proved very essential for the studies of the Earth's environment from a few kilometers to more than 1000 km altitude. Many review papers on the theory, the techniques and the achieved results exist [*Gage and Balsley*, 1980; *Mathews*, 1984; *Hocking*, 1985; *Collis and Röttger*, 1990; *Röttger and Larsen*, 1990; *Röttger and Vincent*, 1996]. These references deal essentially with coherent and incoherent scatter of the middle and lower atmosphere. Coherent scatter radars are used in addition to study irregularities in the ionospheric E- and F-region [e.g., *Crochet et al.*, 1979; *Greenwald*, 1996].

Mesosphere-stratosphere-troposphere [*MST*] radars, which are the main subject of this paper, are particularly used for studies of the dynamics of the middle and lower atmosphere. The scattering and reflection process from atmospheric and ionospheric irregularities in the refractive index, which lead to the radar echoes, is still not fully revealed, since the actual structure of the irregularities causing *MST* radar echoes is very difficult to measure. However, it is certain that particular atmospheric characteristics, such as relevant information on the structure and dynamics [e.g., *Gage*, 1990], can be uniquely determined by the *MST* radars, which make their applications invaluable for lower and middle atmosphere research. These applications as well as the studies of the scattering/reflection mechanisms and the originating inhomogeneities and irregularities, and the research of the structure and dynamics of this atmospheric region remain as challenging tasks.

After recapitulating some categories of radars used to study the ionosphere and the atmosphere, the incoherent scatter and *MST* radar scatter processes are briefly introduced in order to exhibit the transition between these two processes, which takes place in the mesosphere. Then the features of the transition from coherent to incoherent radar scatter are discussed. Thereafter we concentrate on

Radar Methods for Investigations of the Lower and Middle Atmosphere and the Thermosphere/Ionosphere

Typical operation parameters (approximate)

Radar Method	Frequency Range	Wavelength in m	Average Power in kW	Antenna Dimension in Wavelengths	Height Region
MF Radar	MF-HF	150-50	0.01-1	1-10	M,LT/Io
HF Radar*	HF	300-10	0.01-5	0.5-1	Th/Io
Coherent Radar^	HF-VHF	30-1	0.1-1	5-50	Th/Io
Meteor Radar	HF-VHF	10-6	0.1-10	2-10	M,LT
MST Radar	VHF	6-7	1-100	5-50	M,S,T
Incoherent Scatter Radar	VHF-UHF	6-0.25	100-300	100-300	M,LT/Io
ST Radar	VHF-SHF	6-0.1	1-500	10-500	S,T
BL Radar	UHF	0.3	0.01-0.1	10	T

MF = 0.3-3.0 MHz
HF = 3.0-30 MHz
VHF = 30-300 MHz
UHF = 300-3000 MHz
SHF = 3-30 GHz
* = Ionosonde

M = Mesosphere
S = Stratosphere
T = Troposphere
LT = Lower Thermosphere
Th/Io = Thermosphere/Ionosphere
^ = Irregularity Scatter

Table 1. Radar methods for investigations of the lower and middle atmosphere and the thermosphere/ionosphere and typical operation parameters.

the scattering and reflection mechanism of the *MST* radar echoes, and discuss a few common techniques applied with these radars. Some tropospheric observations with the EISCAT *UHF* radar are described. Examples of polar mesosphere echoes, recorded with the EISCAT *VHF* radar, are then briefly addressed, together with a short synopsis of potential mechanisms causing these echoes. Finally justifications for using the EISCAT Svalbard Radar in combination with a dedicated *MST* radar for studies of the middle and lower atmosphere in polar regions are outlined.

This article is a composition of several tutorials and reviews the author had presented during the recent years, which partially had been published at diversified places [see: *Röttger in list of references*]. It was attempted in this summary article to combine these presentations and adjust the chapters in a most logical way, although it is admitted that this may not have been successfully achieved everywhere. To cover such a broad context, it has been tried, though, to arrange the chapters that most of them can also be read as stand-alone discourses.

The literature in this field has become quite superfluous and cannot at all be reproduced in the list of references here. Only essential reviews and tutorials, puplished in the past 10-15 years, and source references of the initial work as well as of presented diagrams and tables are included in the attached list of references. Readers are also referred to several *Handbooks of MAP* [see: *certain references to these handbooks*], and special issues of *Radio Science* published in 1980, 1985, 1990, 1995 and 1997 following the *Workshops on Technical and Scientific Aspects of MST Radar*. Some papers on D-region studies with the EISCAT incoherent scatter radars can be found in the special issues of the *Journal of Atmospheric and Terrestrial Physics* of 1983, 1985, 1987, 1989, 1991, 1993 and *Annales Geophysicae* in 1996, which followed the *EISCAT Workshops*. The most recent review on advances in radar techniques for studies of the *MST* region is written by *Hocking* [1997], and *Cho and Röttger* [1997] summarised the status of observations and theory of Polar Mesosphere Summer Echoes and their relation to Noctilucent Clouds.

2. Ionospheric and Atmospheric Radars

Radars operating in the frequency ranges from *MF* [*medium frequency*] to *UHF* [*ultra-high frequency*] are used to investigate the structure and dynamics of the troposphere, stratosphere, mesosphere, the ionosphere and the thermosphere, as well as even the exosphere. In Table 1 the different kinds of such radars are summarised, together with typical operation parameters and the observable altitude regions.

The *HF* radars, either modern digital ionosondes [e.g., *Reinisch*, 1996] irregularity scatter radars [e.g., *Hanuise and Crochet*, 1977; *Greenwald*, 1996], are applied for E- and F-region studies, also *UHF* radars are occasionally used for this purpose. These coherent scatter radars are often just called coherent radars. The term coherent is used here in order to discriminate between the incoherent scatter and the coherent scatter processes, responsible for these observations. The digital ionosondes are useful complements to study the electron density profiles in the upper D-region and the E-region such as during sporadic-E events, to calibrate incoherent scatter radar electron density profiles and to measure drift velocities and incidence angles.

MF radars, making use of partial reflection from electron density inhomogeneities, are particularly applied to measure electron density profiles of the ionospheric D-region as well as the horizontal wind velocity in this altitude range, comprising the mesosphere. The partial reflection method is applied to measure electron densities as function of height in the ionospheric D-region and also allows to deduct the collision frequency between ions and neutrals. The experiment uses MF or *HF* radars in the frequency range of about 2-6 *MHz*. The ordinary and extra-ordinary components of the radar wave, which is partially reflected from D-region electron density irregularities, are attenuated differently. Comparing the amplitudes of these components, the electron density profile is deduced. This method, which is also called the differential absorption technique, was successfully applied for more than thirty years. A summary description and history of this development, which began decades ago, can be found in *Röttger and Vincent* [1996].

This principle partial reflection or scattering mechanism is also used by radars operating in the same frequency range of the *MF* or low *HF* bands to measure mesospheric and lower thermospheric turbulence and wave structures [*Hocking*, 1987]. It is also extensively applied to measure wind velocities by means of the spaced antenna correlation technique [*Briggs*, 1980, 1984]. This method is also called partial reflection drift technique using *MF* radars. More recently the name mesosphere-lower thermosphere [*MLT*] radars has been introduced [*Manson et al.*, 1990], since it has become one of the major tools to continuously observe winds, tides and gravity waves in this altitude region. Certain extensions of this technique have been introduced, such as the Imaging-Doppler-Interferometer [*IDI*] technique [*Adams et al.*, 1985], which is applied to measure winds as well as incidence angles and aspect sensitivity of partially reflected *MF* radar echoes from the mesosphere.

The meteor radar technique is one of the oldest to study upper mesosphere processes. Radar echoes scattered from ionised meteor trails, which drift under the action of the neutral wind, are analysed. By measuring the line-of-sight Doppler velocity, the range of the echo and its arrival angle the wind profile is computed [*Roper*, 1984]. The meteor radar observations agree well with simultaneous incoherent scatter radar and *MST* radar observations. Mean winds and tides between about 80 km and 100 km altitude have been deduced with this technique at many places on the globe. Since the optimum frequencies of the meteor radars are in the range of the *MST* radars around 30-70 *MHz*, some of these *MST* radars have been actively or passively used for meteor radar applications.

The mesosphere-stratosphere-troposphere [*MST*] radars, operating in the lower *VHF* band, usually near 50 *MHz*, detect echoes from turbulence-induced irregularities and gradients of the radio refractive index [*Woodman and Guillen*,

1974]. These radars are applied to investigate winds, waves, turbulence and stability in the indicated altitude regions. The turbulence can be in the clear or the cloudy air. The smaller versions of the *MST* radars, covering only the lower stratosphere and the troposphere altitudes, are called *ST* radars. These radars are also operated in the *UHF* and *SHF* bands [*Woodman*, 1980a,b; *Gage*, 1990]. Operational applications of *ST* radars have developed in the last decade, and such *ST* radars are then called wind profilers [*Gage*, 1990; *Röttger and Larsen*, 1990; *Czechowsky*, 1994].

Incoherent scatter [*also known as Thomson scatter*] radars, making use of scatter from free electrons in the ionospheric plasma, are applied to study the ionosphere, and thus the mesosphere and thermosphere as well as the exosphere [*Mathews*, 1984; *Hagfors, this issue*].

For studies of meteorological phenomena the weather radars, detecting echoes from precipitation [*rain, snow and hail*], are normally operated in the *SHF* bands above a few *GHz*. These latter radars will not be discussed here, and details can for instance be found in the books by *Battan* [1973], *Gossard and Strauch* [1983], *Doviak and Zrnic* [1984] and *Sauvageot* [1992]. Also echoes from lightning are not discussed here and reference is made to *Williams et al.* [1990], who reviewed the observations at *UHF* and *SHF*, and *Röttger et al.* [1995], who presented the first *VHF ST* radar observations of lightning echoes.

3. Scattering Properties of incoherent scatter and *MST* radars

A schematic view of the different mechanisms causing scattering and reflection of electro-magnetic waves in the troposphere, stratosphere, mesosphere and thermosphere/ionosphere are represented in Tables 2a and 2b [*Röttger and Vincent*, 1996]. In the ionised part of the atmosphere [*Table 2a*], namely the ionosphere, the reflection of radio waves is determined by the electron density, defining the plasma frequency f_N. For radio waves of frequency $f = f_N$ total reflection occurs. This allows the height profile of electron density to be determined, as it is traditionally done with ionosondes [*sometimes also called HF radars*]. For $f > f_N$, and if there is a vertical gradient or irregularities in electron density, partial reflection occurs, which is used with the *MF* radars.

When the operating frequency f is much higher than the plasma frequency, i.e. $f \gg f_N$, scattering of radio waves takes place. This scattering process in the ionosphere can primarily be due to two different contributions:

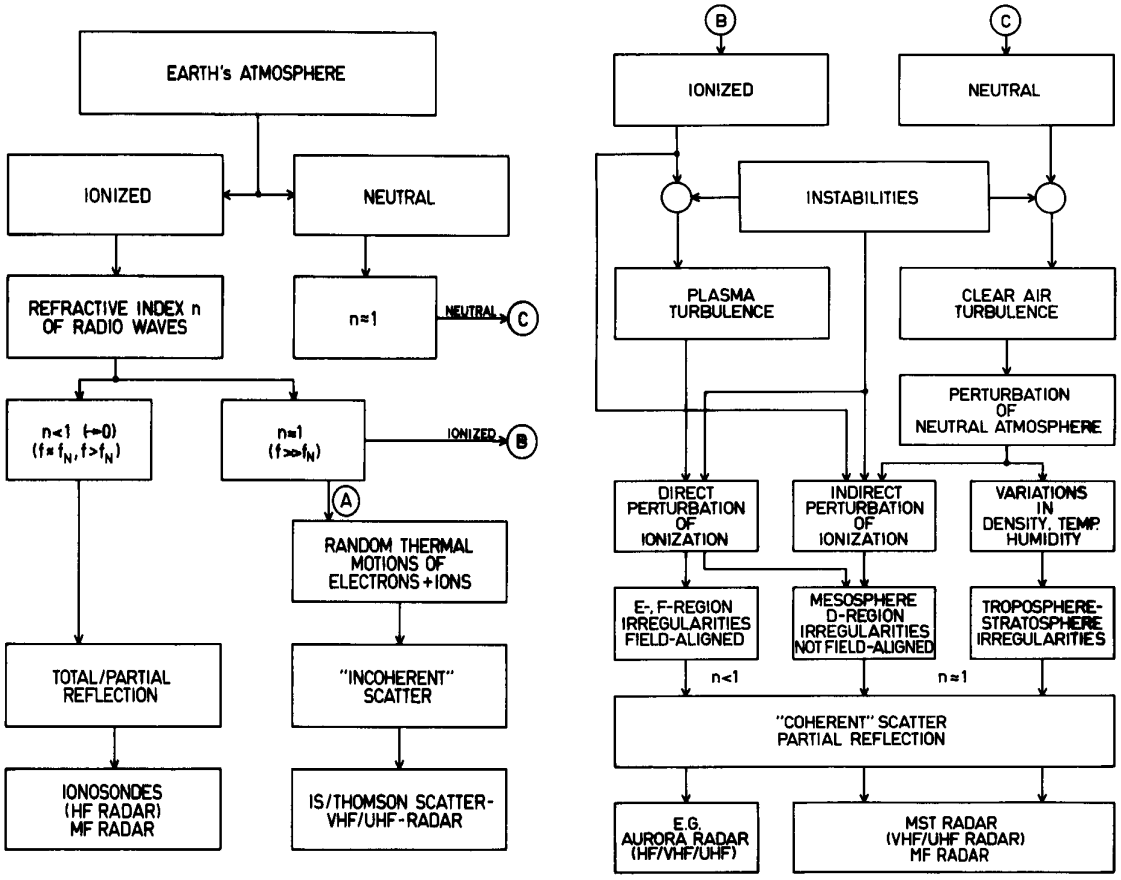

Table 2. (a: left) Scattering and reflection from refractive index variations of the atmosphere, resulting in total or partial reflection and incoherent (Thomson) scatter; (b: right) Scattering and reflection from irregularities of the refractive index due to plasma and neutral air turbulence or stable structures in the clear air.

a) random thermal motions of electrons and ions cause "*incoherent*" scatter [see: *Hagfors, this issue*], which is also called "*Thomson scatter*", since it results from the collective Thomson scattering of the free electrons in the radar volume,

b) different kinds of plasma instabilities, generated either by natural [*Fejer and Kelley*, 1980] or artificially [*by ionospheric heating*: *Rietveld et al.*, 1993] generated instabilities can cause plasma waves and plasma turbulence which result in a direct perturbation of the ionisation.

These perturbations are known as E- and F-region irregularities. They cause scattering and partial reflection of *MF*, *HF*, *VHF* and *UHF* signals. Well known instruments to study these irregularities and the corresponding ionospheric dynamics are the auroral or equatorial electrojet radars, for instance [e.g., *Fejer and Kelley*, 1980]. Also F-region irregularities are observed at high latitudes with obliquely beaming *HF* radars [*Greenwald*, 1996]. Usually, these backscatter processes are highly anisotropic with the maximum scatter cross section occurring perpendicular to the Earth's magnetic field direction. Artificial Periodic Inhomogeneities, created by standing wave pattern during ionospheric heating experiments also cause scattering and can be used for diagnostics of the

mesosphere [*Belikovich et al.*, 1986]. The EISCAT heating facility was used for this purpose [*Goncharov et al.*, 1993].

With respect to the neutral part of the atmosphere [*Table 2b*], it is established that the refractive index n is almost equal to one for radio waves in the *HF*, *VHF* and *UHF* bands. In the neutral atmosphere dynamic and convective instabilities cause clear air turbulence, which result in a perturbation of humidity, temperature and density. Mixing of different air masses and inversion layers also cause discontinuities of these parameters. The corresponding irregularities in the refractive index, which can randomly vary due turbulent velocity fluctuations or prevail as stably stratified layers, scatter or partially reflect radar signals, respectively.

Clear air turbulence in the mesosphere results in a perturbation of the ionisation [*D-region irregularities*]. It should be noted that these irregularities are not created by plasma instabilities, but are induced by neutral air turbulence due to the high collision frequency between molecules and ions. These D-region irregularities are therefore regarded in a first approach as replica of structures in the neutral atmosphere, and they are not aligned along the Earth's magnetic field. It is also accepted that chemical and hydration processes cause ionisation perturbations in the D-region. Considerable refractive index changes due to these mesosphere irregularities can occur for radar signals in the low *VHF* band, which is made use of by the *MST* radars.

3.1. Some Basics of Incoherent Scatter [IS] from the D-region

A very appropriate addition to these kinds of radars for studies of the lower ionosphere, the mesosphere and the regions above are the Thomson scatter radars, which are customarily called incoherent scatter radars. These *IS* [*incoherent scatter*] radars are used to observe backscatter from the ionosphere. The scatter cross section of incoherent scatter is usually much smaller than the one of "*turbulence*" scatter detected by *MST* radars.

Up to altitudes of the lower thermosphere and the upper mesosphere [*around 90-100 km*], the ionosphere is governed by collisions of the ions with neutral molecules. At these altitudes, in the collision dominated regime of incoherent scatter, the plasma temperature and ion-neutral collision frequency [*neutral density*] can be deduced from the spectra of the scattered signals in addition to the electron density and the ion [*neutral*] velocity. From the spectral width certain deductions of ion composition can be obtained, such as for instance the negative ion density and the ion mass. *Mathews* [1984] has reviewed the incoherent scattering from the collision dominated D-region and pointed out that this method

offers a unique advantage in inferring mesospheric parameters with very high precision, such as for example the ratio of the neutral number density and the neutral temperature. However, ion chemistry, i.e. negative and positive ions, have also to be carefully considered [*Turunen*, 1996].

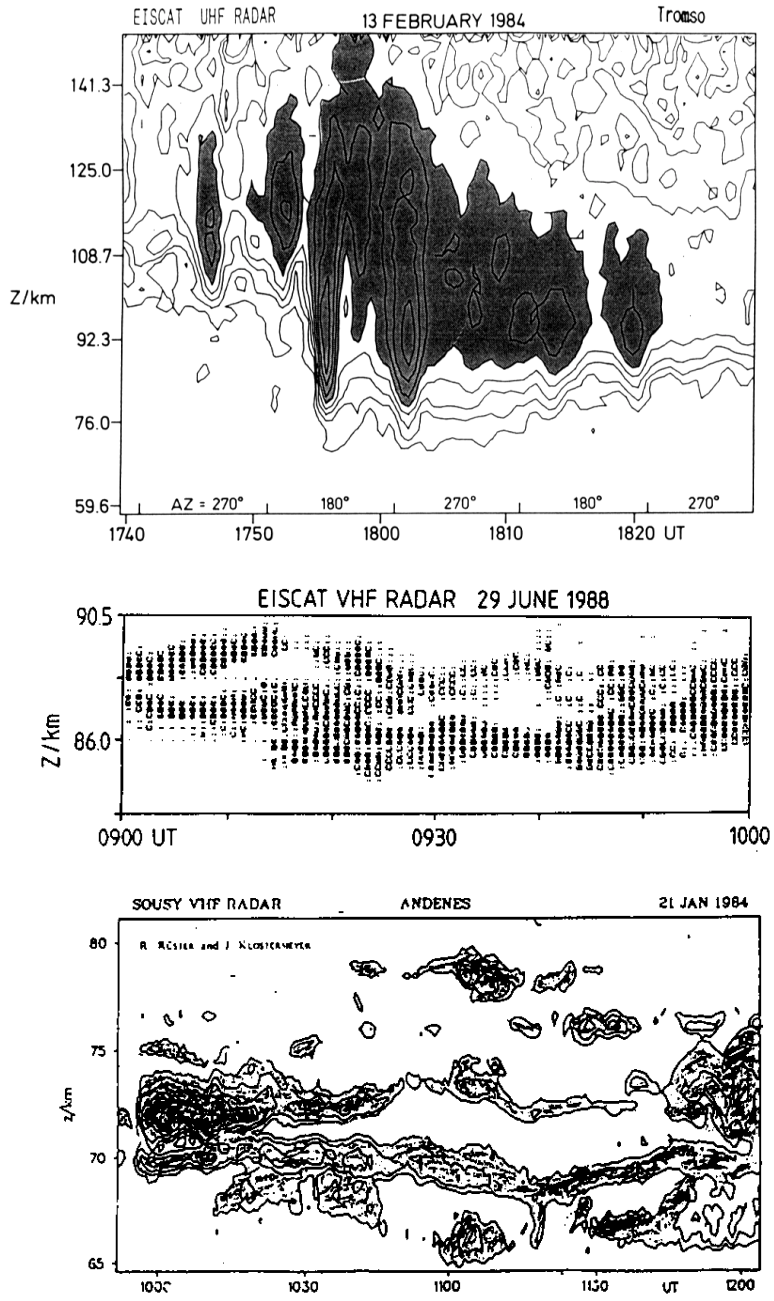

Figure 1. (a: top panel) Height-time contour plot of electron density measured with the EISCAT UHF (931 MHz) incoherent scatter radar during energetic particle precipitation. The maximum electron density was $8x10^{10}$ m^{-3}, the spacing between two contour levels corresponds to a factor of √2. (b: middle panel) Height-time-intensity plot of polar mesosphere summer echoes (PMSE), measured with the EISCAT VHF (224 MHz) radar. The peak level is 16 dB above the noise level; (c: bottom panel) Height-time contour plot of mesosphere echoes in winter measured with the SOUSY VHF (53.5 MHz) radar at polar latitudes (Rüster and Klostermeyer, 1987).

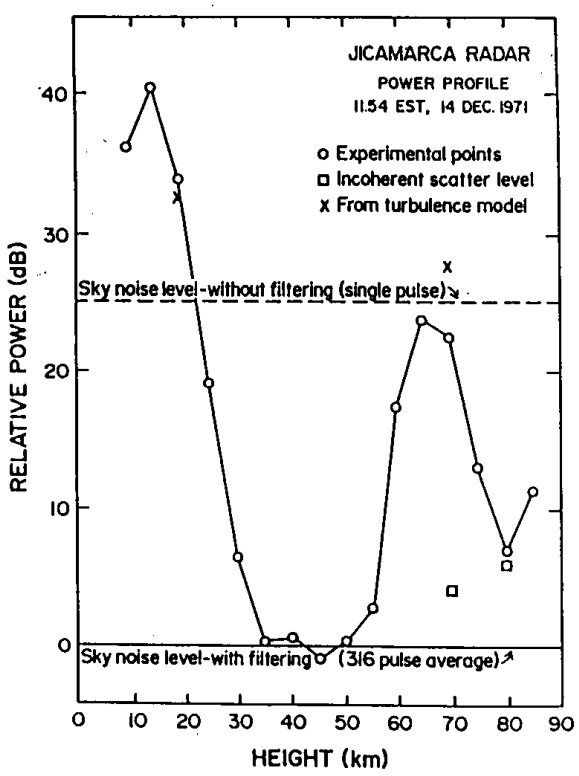

Figure 2. First backscatter power profile obtained from fluctuations of the refractive index in the mesosphere, stratosphere and troposphere, measured with the 50-MHz radar at Jicamarca, Peru (Woodman and Guillen, 1974).

The incoherent radars mostly operate in the *VHF* and *UHF* band at frequencies between 50 *MHz* and 1300 *MHz*. There exist only a few incoherent scatter radars, such as the Jicamarca radar in Peru, the Arecibo Observatory on Puerto Rico, the Millstone Hill radar near Boston, USA, the Sondrestromfjord radar in Greenland, the MU radar in Japan and the EISCAT radars in northern Scandinavia and on Svalbard [see *Röttger*, 1989; and *Hocking*, 1997; *for a detailed lists*]. More recently radars in Russia and the Ukraine were known to observe the ionosphere with the incoherent scatter technique. The Jicamarca radar and the MU radar are also used as *MST* radars due to their low operating frequency around 50 *MHz*. The IS radars in Arecibo and Millstone Hill [*430 MHz*], EISCAT [*930 MHz*] and Sondreström [*1.3 GHz*] are also used for troposphere and stratosphere observations.

The transmitter power of *IS* radars is usually higher than one megawatt and the antenna gains are substantially larger than those of the *MST* radars. Altitude resolutions are typically in the range of a few hundred meters to some kilometers or more and time resolutions can be as good as 10 seconds but have to be up to several 10 minutes depending on the signal-to-noise ratio and the temporal variation of the observed processes. The lowest altitude from which IS radars obtain echoes is around 55 - 60 km, depending on the radar power and antenna area, and of course the electron density.

Due to viscous subrange limitations in the mesosphere [*Hocking*, 1985], when neutral turbulence fluctuations are very strongly damped at the scales corresponding to the IS radar wavelengths of less than some meters, the *IS* radars are usually supposed to be insensitive to "*turbulence scatter*" from the mesosphere. However, turbulent fluctuations and the corresponding eddy diffusion starts to dominate molecular diffusion in the mesosphere. The interpretation of incoherent scatter spectra then becomes ambiguous depending on which type of diffusion dominates the scattering mechanisms.

An example of a height-time-intensity diagram of incoherent scatter echoes is shown in Figure 1a. These short-lived electron density enhancements are frequently detected with the EISCAT radars, operated on 931 *MHz* and 224 *MHz* in the auroral region [*Röttger*, 1991]. High energy particles from the magnetosphere penetrate down into the mesosphere, where they cause such enhancements of the electron density. In summer even stronger echoes are detected around the mesopause altitude, which are shown in Figure 1b [*Röttger* et al., 1990]. These polar mesosphere summer echoes [*PMSE*] result from irregularities, which are related to aerosols and ice particles in the low-temperature mesopause, which will be briefly discussed in a later chapter. In Figure 1c backscatter echoes observed on 53.5 *MHz* are shown, which are related to the background electron density in the mesosphere being perturbed by neutral turbulence as will be discussed now.

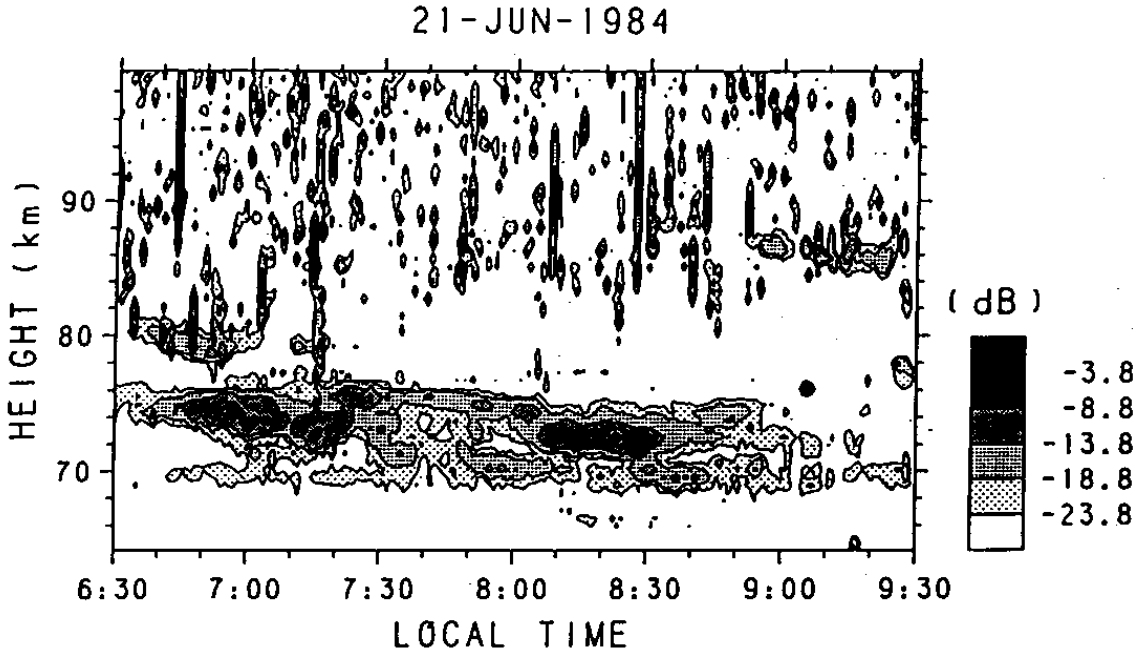

Figure 3. Height-time contour plot of mesosphere radar echoes measured with the MU (46.5 MHz) radar in mid-latitudes in Japan (Sato et al., 1985).

3.2. Some Basics of the Mesosphere-Stratosphere-Troposphere [MST] Radar

The technique of using sensitive clear-air radars to investigate the upper atmosphere at altitudes from the troposphere to the mesosphere owes much of its success to the early days of ionospheric incoherent backscatter observations. It was found that radars operating in the low *VHF* band [≈ 50 *MHz*] also produce echoes from the middle and lower atmosphere in addition to those from the ionosphere. *Woodman and Guillen* [1974] used the incoherent scatter radar at the Jicamarca Radio Observatory in Peru and were the first to analyse such echoes from the mesosphere and the stratosphere. The first power profile obtained by backscatter from fluctuations in the refractive index in the clear air of the mesosphere and the stratosphere is presented in Figure 2. *Woodman and Guillen* [1974] showed that these strong echoes are not due to incoherent scatter but caused by turbulence scatter. The measurements carried out by *Woodman and Guillen* in 1971 used the Jicamarca radar operating at 50 *MHz*, with 1 MW peak power, 5 km range resolution and the vertical pointing antenna with an aperture of 84000 m^2. Because of the altitude coverage, these kinds of radar were later named mesosphere-stratosphere-troposphere [*MST*] radars.

The main parameters measured directly with an *MST* radar are the intensity or power, the Doppler spectrum shift and the Doppler spectrum width of the radar echoes. Figure 3 shows a typical examples of a height-time contour plots of echoes from the mesosphere measured with the MU radar in Japan [*Sato et al.*, 1985]. Such observations at other *MST* radars show very similar features. The echo structures are observed in thin laminae [*at 70 km*] and short-lived blobs [*at 07:00 around 75 km*] as well as in thick layers [*long lasting structures around 70-75 km in Figure 2*]. Thin and persistent laminae are displayed in Figure 4 [*an example of VHF radar observations at low latitudes at the Arecibo Observatory on Puerto Rico*], are often characterised by a narrow spectrum width, i.e. small turbulent velocity fluctuations, whereas the thick and intense layers can have a wide spectrum resulting from large turbulent velocity fluctuations. The short and

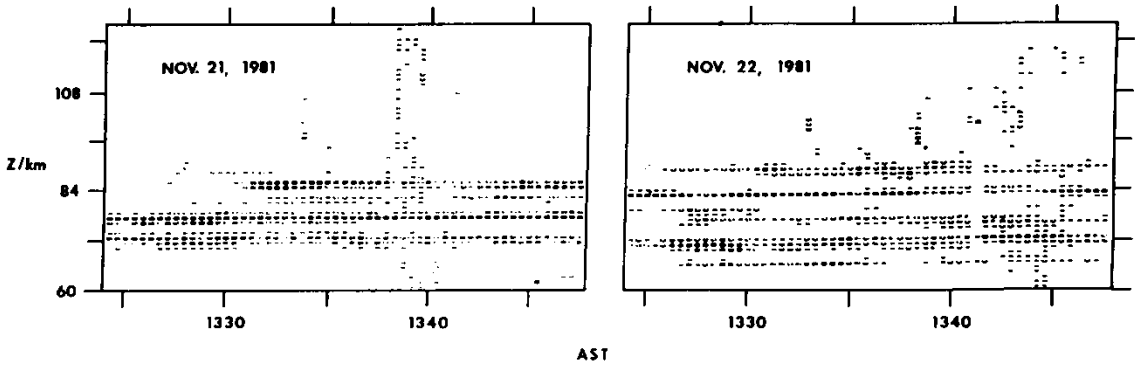

Figure 4. Height-time intensity plots of mesospheric radar echoes measured at 46.8 MHz at low latitudes at Arecibo, Puerto Rico.

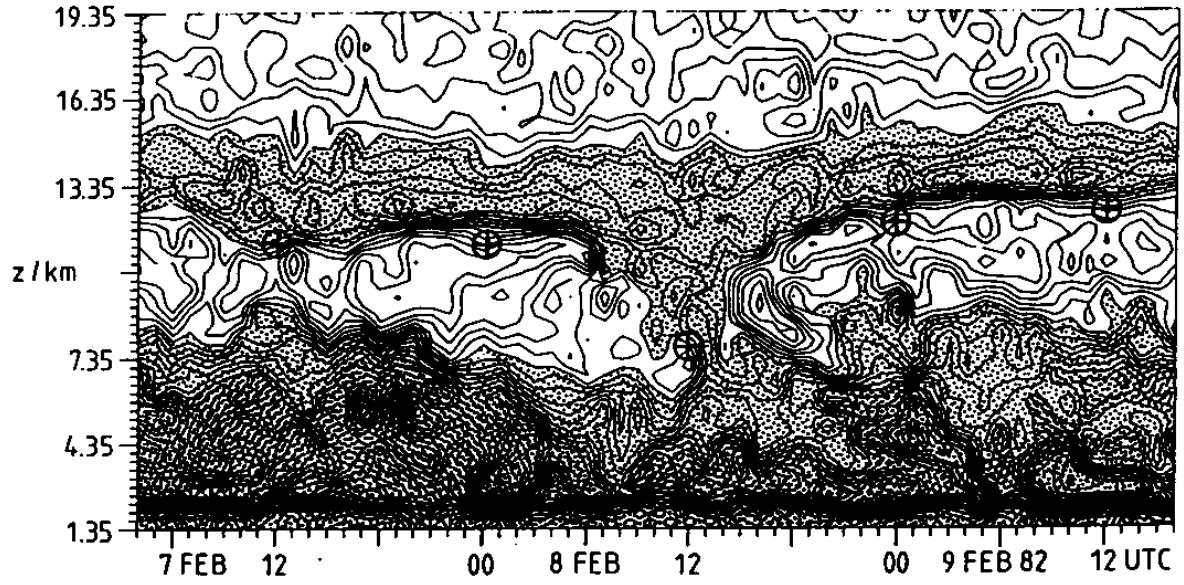

Figure 5. Radar echo power contours measured with the SOUSY-VHF-Radar (53.5 MHz) showing the tropopause and a tropopause break during a frontal passage (contour line difference is 2 dB). The shading shows regions of high echo power. The circled cross hairs show the tropopause, measured with radio sonde.

localised power bursts above 80 km in Figures 3 and 4 are not due to "*turbulence scatter*" but are due to meteor echoes. The mesosphere turbulence echoes occur only during daylight hours or strong particle precipitation in polar regions, when sufficient ionisation is existent in the mesosphere. Other extra-ordinary echoes are observed in the high latitude summer mesopause region, which are the polar mesosphere summer echoes [*section 7*].

Figure 5 shows a height-time contour plot of *VHF* radar echoes from the lower stratosphere and the troposphere, measured with the 53.5 *MHz* Sousy *VHF* radar in Germany [*Röttger and Larsen,* 1990]. These echoes are regularly observed with vertically pointing radar beam up to the lower or middle stratosphere, depending on radar sensitivity. Echoes from the lower troposphere are usually strongest, although the echoes at higher tropospheric altitudes or above the tropopause [*circles in Figure 5*] can also be enhanced due to increased turbulence or larger stability. The latter is frequently observed to occur above the tropopause. We note that these observations allow the detection of the tropopause and frontal passages [*Gage*, 1990; *Röttger and Larsen*, 1990].

For pure turbulence scattering, the echo intensity of the layers, laminae and blobs is a measure of the intensity of turbulence. For partial reflection, the echo intensity is a measure of the steepness and magnitude of the refractive index gradient. *Hocking* [1985, 1997] has reviewed the radar scatter mechanisms of these small scale structures in the mesosphere and lower thermosphere. Regardless of the irregularities causing these *MST* radar echoes, the Doppler shift of the echoes is in a first approach

proportional to the bulk radial velocity of the backscatter or reflection region. This feature is commonly used to deduce the three-dimensional velocity vector. The Doppler power spectrum width can, with certain precautions, be a fair estimate of the turbulent velocity fluctuations. The temporal variation of intensity is a measure of the persistency of turbulence or the stability of the gradient of refractive index. By means of measuring the intensity at different antenna beam directions, the anisotropy of turbulence and gradient structures is investigated. By combining measurements of velocity fluctuations at different beam directions, the covariance of horizontal and vertical velocities, namely the Reynold stress due to atmospheric waves, is determined [*Vincent and Reid*, 1983]. Using three or more horizontally spaced antennas, the horizontal velocity vector and the horizontal coherence are deduced. This spaced antenna technique is also used in the interferometer mode which allows to investigate the fine structure of turbulence and gradients [*Röttger and Ierkic*, 1985].

The outlined quantities are typically measurable with altitude resolutions of 150 m to about 1 km between about 60 km and 90 km in the mesosphere and up to about 30 km in the stratosphere, depending on radar sensitivity and atmospheric conditions. The time resolution is adapted to the physical phenomenon of interest and can be as good as a fraction of a second. Of particular interest is the turbulence occurrence and its intensity. These are linked to the turbulence energy dissipation rate. This in turn determines the structure constants of irregularities in the electron density, which in total constitute the turbulence refractive index structure constant C_n^2. This quantity can be deduced under certain conditions from radar echo power measurements, which then yield the turbulence energy dissipation rate. The dissipation rate can also be determined from the Doppler spectrum width, if instrumental effects are negligible or removed. All approaches need the knowledge of background profiles of temperature and electron density.

3.3. A Short View on the Transition from Turbulence Scatter [MST] to Incoherent Scatter [IS]

The main features of IS radar and *MST* radar scattering processes have been basically discussed in the previous chapters. In the mesosphere these processes are interlaced, and one has to attempt to separate these. Essential criteria, characterizing these two different processes, are the scattered power [*scatter cross section*] and the shape of the Doppler spectra of these radar echoes. For both cases the monostatic backscatter results from variations of the refractive index at scales of half the radar wavelength, called the "*Bragg wavelength*".

Scatter of electro-magnetic waves results from fluctuations in the refractive index in the scattering medium. The following discussions are based on the primary origin of these fluctuations in the neutral atmosphere caused by turbulence. These fluctuations are usually described by the *Kolmogoroff* spectrum, which is sketched in

Figure 6. The spectral density *E(k)* of these fluctuations is a function of the spatial wavenumber *k*. The spectral density is largest at small wavenumbers, i.e. at large spatial perturbation scales. It decreases with spatial wavenumber, i.e. the perturbations are getting weaker with shorter spatial scales. A detailed discussion of these universal spectral forms was given for *MST* radar techniques by *Hocking* [1985]. The *Kolmogorov* spectrum is basically partitioned into several subranges: the buoyancy subrange, the inertial-convective subrange and the viscous-diffusive subrange. These subdivisions had to be introduced when not only turbulent diffusion has to be considered but also diffusion of other additives, such as electrons and heavy ions in the mesosphere. These are discussed for the particular phenomena of polar mesosphere summer echoes by *Cho and Kelley* [1993], for instance, but will not be treated here. In the inertial-convective subrange the spectral density is $E(k) \propto \varepsilon^{2/3} k^{-5/3}$, where the large turbulence eddies decay into smaller eddies. This is followed by

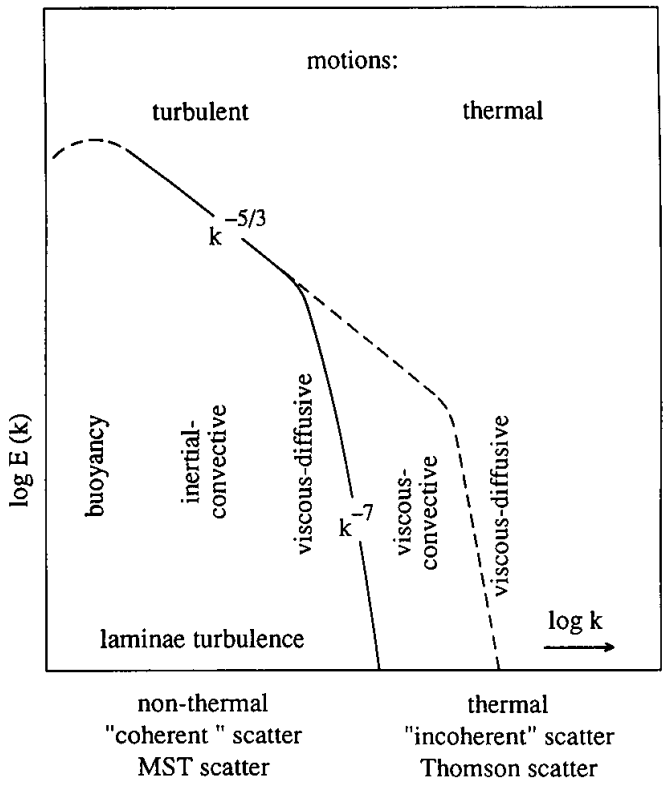

Figure 6. Simplified Kolmogoroff spectrum, showing the spectral density E(k) of atmospheric fluctuations as function of spatial wavenumber $k = 2\pi/\underline{x}$, with $\underline{x}$ spatial coordinate. Whereas the continuous line indicates the spectral density of neutral fluctuations, which are in a one-to-one correspondence with fluctuations of the ionized atmosphere (mesosphere, D-region), the dashed line shows the extension into a viscous-convective subrange in the electron gas resulting from fluctuations of electrons in the presence of heavy ions in the mesosphere (after Cho and Kelley, 1993).

the viscous-diffusive subrange, where turbulence is dissipated into heat. The fluctuation spectral density is $E(k) \propto (\varepsilon/\nu^2)^2 k^{-7}$, where ε is the turbulence energy dissipation rate and ν the kinematic viscosity. A steep fall-off of the fluctuations in the viscous-diffusive subrange is noticed. Finally, at sufficiently small spatial scales, the turbulence induced fluctuations will no more exist and only thermal motions of the molecules will remain. When part of these molecules, which are in thermal equilibrium, are ionised [i.e. *in the mesosphere*], the refractive index changes are due to the random thermal motions of the charged particles in the ionospheric plasma, namely the electrons in the presence of the ions. This Figure 6 also indicates the scales of turbulent and thermal motions at which "*coherent*" *MST* radar scatter and "*incoherent*" scatter dominates, respectively.

The original "*turbulence scatter*" theory of *MST* radars bases on scatter from isotropic turbulence at scales in the inertial-convective subrange of the *Kolmogoroff* spectrum. Beyond the viscous-diffusive subrange incoherent scatter from the free electrons occurs. There is consequently a transition from "*turbulence scatter*" in the inertial-convective subrange via the viscous-diffusive subrange to "*incoherent scatter*" at spatial wavenumbers beyond the high limit of the viscous-diffusive subrange, where the process is in thermal equilibrium. The former scatter is called "*coherent scatter*", or "*MST* scatter". The latter is commonly called "*incoherent scatter*", but also the terms Thomson scatter or thermal scatter are used. It has to be noted that this transition region depends on the radar wavelength, the height and turbulence intensity. For the radars in question, operating between 50 *MHz* and 500 *MHz*, this range is in the mesosphere.

The subranges of the *Kolmogorov* spectrum are limited at the outer and inner scales of turbulence, which in turn are dependent on the turbulence energy dissipation rate, the buoyancy frequency and the kinematic viscosity. These parameters change with function of altitude. *Hocking* [1985] has calculated these for reasonable atmospheric models. In Figure 7 these range limits are shown as function of height and spatial wavenumber.

The turbulent velocity fluctuations in the inertial subrange cause the backscattered radar signal to be widened. The width of the measured Doppler spectrum of a radar at wavelength λ is given by [*Hocking*, 1985]:

$$\omega_t = \left\{ \frac{32 < w^2 >}{\lambda^2} \right\}^{1/2} \qquad (1)$$

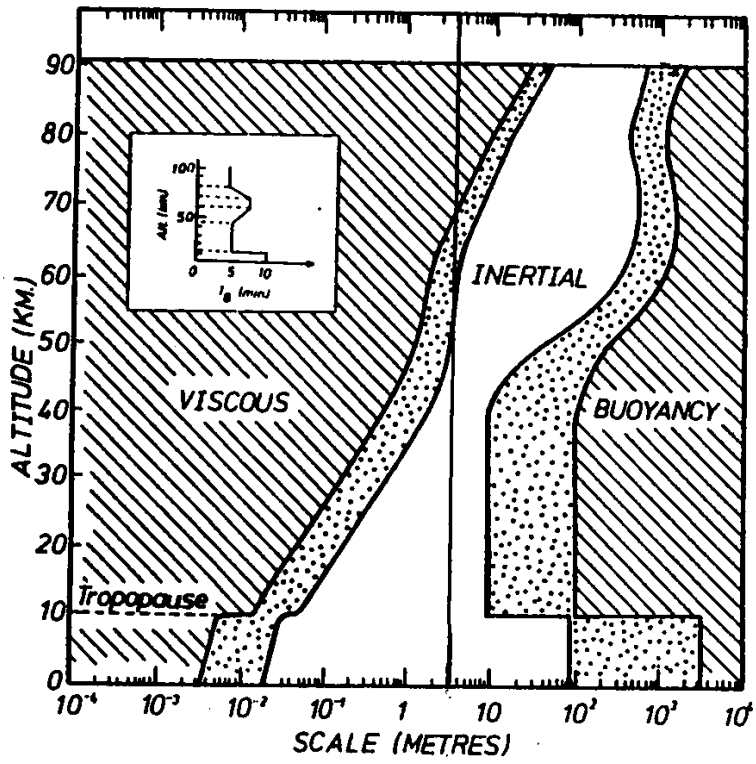

Figure 7. Viscous, inertial and buoyancy subranges as function of altitude and spatial scale. The vertical line at the scale of 3 m shows the Bragg wavelength for monostatic 50 MHz radars (Hocking, 1985).

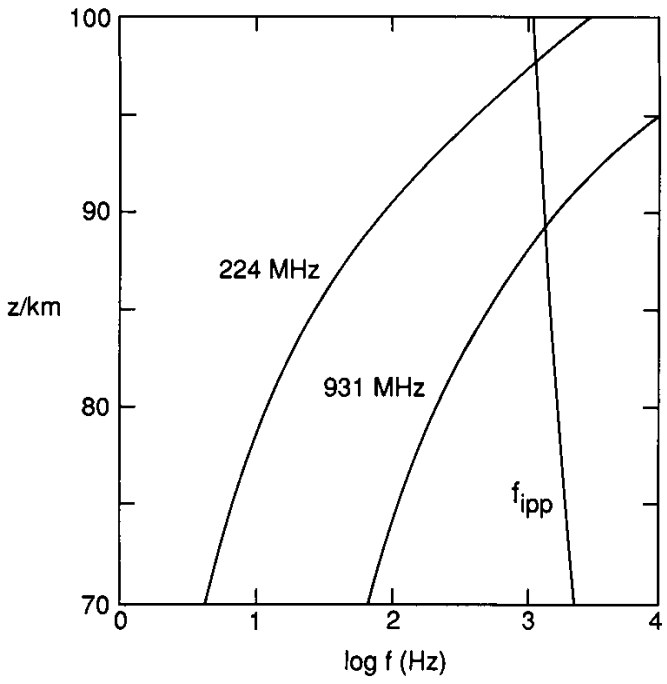

Figure 8. Half-power width (in logarithmic units) of power spectra of incoherent scatter echoes from the mesosphere and lower thermosphere for the frequencies 224 MHz and 931 MHz of the EISCAT radars. f is the Doppler frequency and z is the altitude. f_{ipp} = c/2z (c = speed of light) is the minimum pulse repetition frequency, which can be used in pulse-to-pulse modulation.

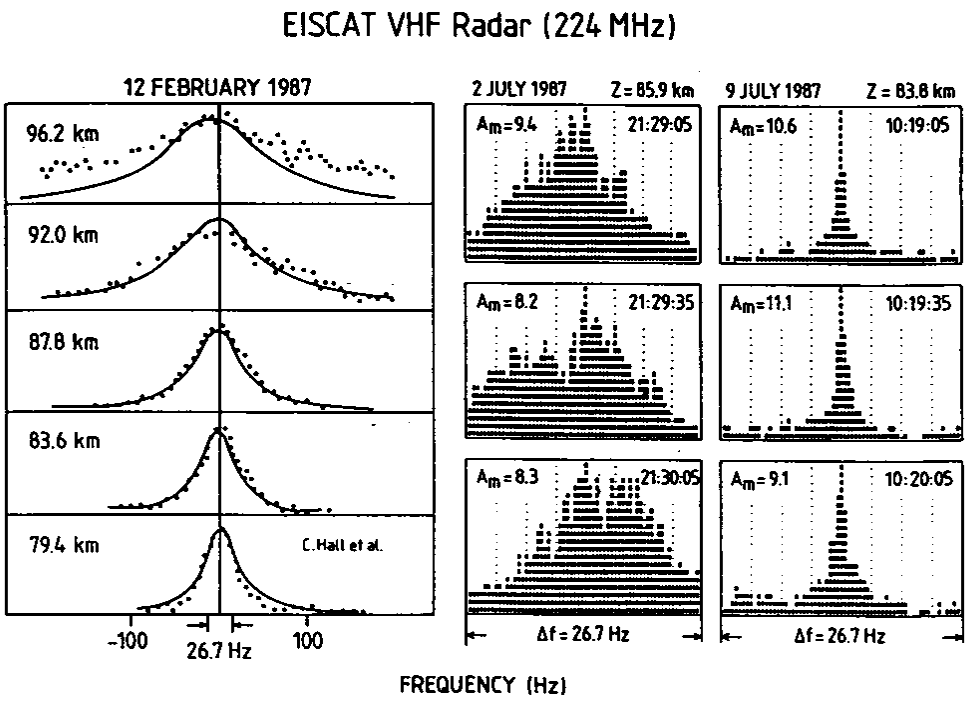

Figure 9. (a: left) Power spectra of incoherent scatter echoes from the mesosphere measured with the EISCAT VHF (224 MHz) radar and fitted theoretical spectra. (b: right) Amplitude spectra of polar mesosphere summer echoes measured with the EISCAT VHF (224 MHz) radar for turbulent (2 July 1987) and quiet (9 July 1987) conditions.

This assumes that all other effects, such as beam and shear broadening for instance, can be neglected or are eliminated from the measured data. The root mean squared turbulent velocity fluctuations $< w^2 >$ are in turn related to the turbulence energy dissipation rate ε.

Thermal fluctuation cause the Doppler spectrum of the *IS* radar signal to be widened. In the collision-dominated regime [*mesosphere*] of the Thomson scatter process, the variation of the spectrum width, of course naturally proportional to the square of the radar frequency, is primarily determined by ionospheric parameters [*Mathews*, 1985] and can be expressed in simplified form:

$$\omega_s \propto \frac{T_i}{\nu_{in}} \cdot \sqrt{\frac{m_i + m_n}{m_i \; m_n}} \cdot (1 + \Lambda^-) \qquad (2)$$

with T_i the temperature of the ions [*assumed equal to the temperature of the neutrals in the mesosphere*], ν_{in} the collision frequency of ions and neutrals, m_i the mean mass of the positive ions and m_n the mean mass of the neutral molecules. The term Λ^- is the ratio of the number density n_i^- of negative ions and the number density n_e of free electrons, which is usually called the electron density.

It is obvious from Eq. 2 that this spectrum of incoherent scatter echoes widens with increased Λ^- and gets narrowed with the collision frequency ν_{in}. The reason is that collisions damp the plasma waves which create refractive index variations. The latter, increasing exponentially with altitude, has the noticeable effect that the incoherent scatter spectra are getting narrower with decreasing altitude. Figure 8 shows calculated incoherent scatter spectral width for the EISCAT radar frequencies 220 *MHz* and 931 *MHz*, deduced after *Collis and Röttger* [1990]. Even for strong turbulence in the mesosphere, the spectral width resulting from turbulence induced electron density variations should usually be narrower than the spectral width of the incoherent scatter signal.

As long as the spectral width is smaller than the radar pulse repetition frequency f_{ipp}, the so-called pulse-to-pulse technique can be applied. In other words, the signal coherence time [*the inverse of the spectrum width*] in the pulse-to-pulse case is longer than the interpulse period, which is the inverse of the pulse repetition frequency. As Figure 8 shows, this condition holds for incoherent scattering from altitudes below about 85-90 km. Since the coherence time of turbulence scatter and reflection is much longer than the coherence time of incoherent scatter, the pulse-to-pulse technique is always applied in *MST* radar systems. This has the obvious advantage in the application of coherent integration and complementary coding, including truncated codes [*Ghebrebrhan and Crochet*, 1992]. In the incoherent scatter case the multi-pulse, *Barker* coding or long-pulse technique has to be applied above altitudes of 90 km. More detailed discussion of these techniques can be found in *Röttger* [1989]; the alternating code technique is now replacing the multi-pulse technique [*Wannberg*, 1993].

Examples of measured incoherent scatter spectra are shown in Figure 9a for mesospheric altitudes between 79 km and 96 km, which indicate the widening with increasing altitude [*compare with Figure 8*]. In Figure 9b examples of spectra from altitudes around 85 km are displayed, which are much narrower than the incoherent scatter spectra [note: *the indicated frequency span of 26.7 Hz in Figure 9b, as compared to the 200 Hz span in Figure 9a*]. These spectra in Figure 9b show signatures of polar mesosphere summer echoes [*PMSE, see section 7*], which are again different to incoherent or pure turbulence scatter. However, the width of these spectra of *PMSE* in Figure 9b is still determined essentially by turbulent fluctuations. These spectra can be as narrow as a few *Hertz*, which is an indication of very weak turbulence, and a different scattering process. *Röttger et al.* [1990] have described these spectra in more detail.

Spectra of *MST* radar echoes from the stratosphere and the troposphere are usually even narrower than the spectra shown in Figure 9b, since the turbulence intensity is usually weaker in these lower altitudes and the scatter could be replaced or affected by partial reflections.

As Figure 7 shows, that Bragg wavelengths of *VHF* radars operating at 50 *MHz* are in the viscous subrange above about 70 km altitude. This means that scatter from turbulence induced ionisation irregularities should be too weak to cause a detectable radar echo. Following this model, only below about 60 - 70 km such echoes should occur, provided that sufficient electron density exists in this lower part of the ionosphere.

The scatter cross section for incoherent scatter is in a first approximation given by the number of electrons in the radar scatter volume times the cross section of a single electron $4\pi r_e^2$ [r_e *is the classical electron radius*]. *Collis et al.* [1992] have calculated the expected ratio of turbulence induced and incoherent scatter power as function of altitude for the EISCAT 224 *MHz* radar [*Figure 10*]. Depending on turbulence intensity, these echoes could be equal in power in the altitude region up to about 70 km. *Collis et al.* [1992] have actually found events of turbulence induced scatter superimposed on incoherent scatter observed around 68 km altitude with the EISCAT 224 *MHz* radar. This proves the superposition of incoherent scatter and turbulence scatter at these mesospheric altitudes.

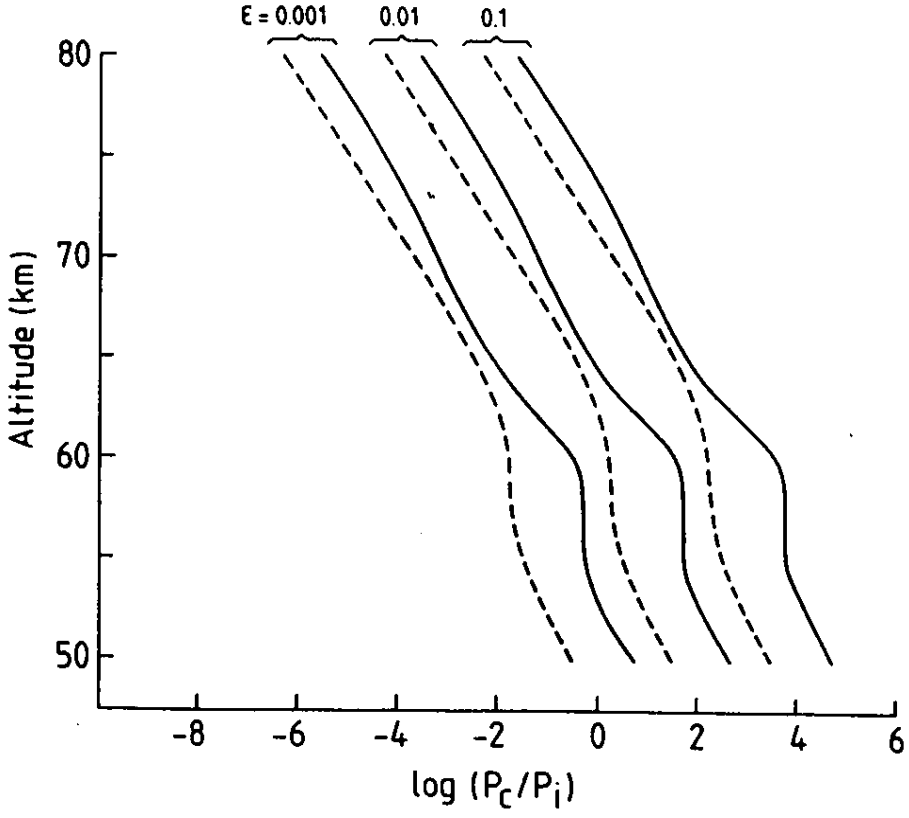

Figure 10. Ratio of echo power for scatter from pure turbulence (P_c) and incoherent scatter (P_i), calculated for the EISCAT VHF (224 MHz) radar for weak and strong turbulence energy dissipation rates ε (Collis et al., 1992).

4. The Scattering and Reflection of *MST* Radar Signals

Let us now discuss in a somewhat more quantitative way the influence of turbulence-induced irregularities in electron density, neutral air density and temperature as well as humidity on the scatter and reflection process governing the *MST* radar method. More details of these mechanisms are described by *Gage and Balsley* [1980], *Hocking* [1985], *Gage* [1990], *Röttger and Larsen* [1990].

The *MST* radar echoes are caused by scattering or reflection from irregularities of the atmospheric refractive index. As in all backscattering processes of electromagnetic waves, the backscatter arises from the component of the spatial spectrum of the variation of the refractive index n, whose spatial scale is half the radar wavelength for monostatic backscatter radars. This scatter is therefore also called Bragg scatter [*Gossard and Strauch*, 1983]. The refractive index variations in the atmosphere result from random irregularities generated by turbulence, or to steep gradients introduced by horizontal layering or structuring of the atmosphere. The refractive index variations are directly related to variations of the atmospheric parameters: humidity, temperature, pressure [*corresponding to air density*] and electron density. The refractive index for the troposphere, stratosphere and mesosphere [*ionospheric D-region*] at *VHF* and *UHF* is:

$$n = 1 + \left(77.6 \frac{p}{T} + 3.75 \cdot 10^5 \frac{e}{T^2} \right) \cdot 10^{-6} - 40.3 \frac{n_e}{f_o^2} \qquad (3)$$

where e is the partial pressure of water vapor [*humidity*] in *mb*, p the atmospheric pressure in *mb*, T the absolute temperature in *Kelvin*, n_e is the ionospheric electron density in m^{-3}, and f_o the radar operating frequency in *Hz*.

The wet term, proportional to humidity, is usually most important up to the middle troposphere, whereas, in the upper troposphere and stratosphere, the dry term, proportional to pressure and inversely proportional to the temperature. For radars operating in the lower *VHF* band, the ionisation of the D-region [*given by* n_e] determines the refractive index in the height region between about 60 km and 100 km. Polarization [*Faraday rotation*] and absorption effects are mostly neglected for *VHF* and *UHF* signals in the entire height range of the troposphere, stratosphere and mesosphere, although these are made use of by the *MF* radars detecting partial reflection echoes from the lower ionosphere, as mentioned earlier. During stong D-region ionisation in high latitudes the *Faraday* rotation can be quite pronounced at 50 *MHz* for antenna beam directions almost parallel to the Earth's magnetic field. At frequencies larger than several ten *MHz* [e.g., *at 50 MHz*], the turbulence-induced scatter term will get very weak in the upper mesosphere [*because of viscous subrange limitations*] and the incoherent scatter term will usually dominate the signal. For scales in the inertial subrange, clear-air turbulence in the mesosphere can yield perturbations in the ionisation [*D-region irregularities*] and correspondingly in the

radio refractive index n. In the presence of highly hydrated ions [*clusters*], however, the fluctuations in the electron gas can extend to much smaller scales than the neutral turbulence, which also could cause an enhancement of the refractive index perturbations [*Cho and Kelley*, 1993]. Note that these irregularities are not created by plasma instabilities, - they are either induced by turbulence in the neutral atmosphere because of the dominating collisions between ions and neutral molecules in this height region or are resulting from cluster ions which cause the electron diffusion and recombination to be changed and cause *PMSE* [see *Figure 1b*]. The D-region irregularities are in certain cases be replica of neutral air turbulence, when one can neglect these latter sources or creation mechanisms due to chemical, hydration and recombination effects etc. [*for more detailed discussions see Cho and Kelley*, 1993; *Röttger*, 1994a; *Cho and Röttger*, 1997; *or Klostermeyer*, 1997].

When atmospheric turbulence or other small scale perturbations in the electron gas in the mesosphere mixes the vertical profile of the refractive index and the associated gradients, fluctuations of n result, which in turn cause scattering and reflection of radar waves. It is useful to define a refractive index structure constant C_n^2 which is related to the mean square fluctuations $\langle dn^2 \rangle$ of the refractive index by

$$C_n^2 = a \langle dn^2 \rangle L_o^{-2/3} \qquad (4)$$

where a is a constant [$\cong 5$] and L_o is the outer scale of turbulence in the inertial subrange, which is proportional to the square root of turbulence energy dissipation rate ε and the -3/2 power of the buoyancy frequency ω_B of the atmosphere.

The turbulence refractive index structure constant can be expressed as:

$$C_n^2 = 0.7\ \varepsilon^{2/3}\ M^2\ \omega_B^{-2}\ F^{1/3} \qquad (5)$$

Here F is the filling factor, i.e. the relative portion of the scatter volume which is filled with turbulence irregularities, and M the generalised potential refractive index gradient.

For the unionised atmosphere it is found for the troposphere, where the humidity e is not negligible [*specific humidity* $q = e / 1.62\ p$]:

$$M_t = -79 \cdot 10^6 \frac{p}{T^2} \left(1 + 15.5 \cdot 10^3 \frac{q}{T}\right) \cdot \left(\frac{T\ \omega_B^2}{g} - \frac{7.8 \cdot 10^3}{(1 + 15.5 \cdot 10^3 \frac{q}{T})} \frac{dq}{dz} \right); \qquad (6)$$

for the stratosphere [*humidity e is neglected*]:

$$M_s = -79 \cdot 10^6 \frac{p}{T^2} \cdot \frac{\omega_B^2}{g}; \qquad (7)$$

and for the mesosphere [*dominated by electron density* n_e]:

$$M_m = \frac{r_e \lambda^2}{2\pi} \left(n_e \left(\frac{\omega_B^2}{g} - \frac{d\rho}{\rho\, dz} \right) - \frac{dn_e}{dz} \right) \qquad (8)$$

It needs to be noted that in these equations the vertical gradients of humidity *dq/dz*, temperature *dT/dz*, density $d\rho/dz$ and electron density dn_e/dz represent averages over the volume of turbulence, and that during turbulence development, these gradients will change. These derivations have been presented by *Hocking* [1985], who pointed out the said limitations. Observational evidence for these dependencies are given by the fact that the mesosphere *VHF* radar echoes in non-auroral latitudes only exist during daylight hours when there is sufficient ionisation. Noticeable evidence for this was presented by *Rastogi et al.* [1988] who described an increase in *MST VHF* radar scatter from the mesosphere during sudden electron density enhancement observed by 430 *MHz* incoherent scatter radar at Arecibo during a solar flare. *Czechowsky et al.* [1989] describe the relation of mesosphere winter echoes in auroral latitudes [see *Figure 1c*] on the D-region electron density deduced by riometer measurements. Also *Collis et al.* [1992] have detected on 224 *MHz* a turbulence echo in the mesosphere during enhanced electron density and turbulence intensity. In Figure 5 the *VHF* radar echo enhancements in the lower troposphere are noticed, which result essentially from humidity gradients in the lower troposphere and stable temperature gradients above the tropopause and in the tropopause break.

The radar reflectivity η at the wavelength λ for pure and volume scattering from isotropic turbulence in the inertial subrange is:

$$\eta = 0.4\, C_n^2\, \lambda^{-1/3} \qquad (9)$$

These relations hold only for radar wavelengths which are larger than the inner scale of the inertial subrange of turbulence fluctuations. As pointed out earlier, this inner scale depends on turbulence intensity and the kinematic viscosity. The latter increases as a function of altitude [see *Figure 7*], which places a lower limit to radar wavelengths which can be used to detect echoes from the middle atmosphere. For scatter from fluctuations in the viscous subrange, which result from fluctuations of neutral turbulence in the mesosphere an appropriate formalism to determine η is not available yet, since the dependency on background gradients of electron density is not quite solved so far.

The mean received radar echo power P_s for volume scatter is given by the radar equation:

$$P_s = \frac{\alpha^2 A_E P_t \delta r}{4 \pi r^2} \cdot \eta \qquad (10)$$

where P_t is the transmitter power, A_E the effective antenna area, r the distance to the centre of the scattering volume, δr is the range gate width [*corresponding to the radar pulse length*], and η the radar reflectivity.

Since it is assumed that partial reflections from steep vertical gradients of the refractive index are also observed by vertically beaming *VHF* radars, the radar equation has to be extended for this condition. Then the power received by reflection is:

$$P_r = \frac{\alpha^2 P_t A_E^2}{4 \lambda^2 r^2} \cdot |\rho^2| \qquad (11)$$

where $|\rho^2|$ is the amplitude reflection coefficient.

Model for Scatter/Reflection Mechanisms of MST Radar Signals

(*conceptual synopsis*)

Mechanism	Angular Spectrum	Coherence Time	Reflectivity Structure
BRAGG SCATTER (a) isotropic (b) anisotropic	constant wide	short short	random turbulence (a) isotropic (b) anisotropic
FRESNEL SCATTER (a) stratified (b) spread	narrow wide	intermediate intermediate	multiple laminae in stable environment (a) horizontally stratified (b) range, angle spread
FRESNEL (partial) REFLECTION (a) specular (b) diffuse	narrow very narrow	long very long	one dominating laminae in stable environment (a) very smooth (b) corrugated (rough)

Table 3. Conceptual synopsis of models for scatter and reflection mechanisms of MST radar signals and typical characteristics: angular spectrum (aspect sensitivity), coherence time and the generating reflectivity structures.

The conditions of pure isotropic, volume filling scatter from turbulence induced fluctuations is usually not realistic, and it is also generally not possible to discriminate between these different processes of scattering and partial reflection without investigating particular features of the *MST* radar echoes, such as their aspect sensitivity, temporal and spatial coherency and their spectral shape or their amplitude distribution functions. Now these different qualifications are discussed.

4.1. Composition of Scattering and Reflection from the Mesosphere, Stratosphere and Troposphere

There is no unified opinion noticeable yet which mechanism may be the most relevant to cause the echoes of *MST* radars from the mesosphere, stratosphere and the troposphere. One only could distinguish so far between the major process of scattering/reflection from refractive index irregularities due to temperature, humidity and electron density fluctuations on the one side and the other two processes, namely scatter from hydro-meteors [*rain drops*] in the troposphere as well as incoherent scatter from free electrons in the mesosphere, which cause the observed radar echoes. The major echoing process dominating the *MST* radar methods can be described by several mechanisms as is defined in Table 3.

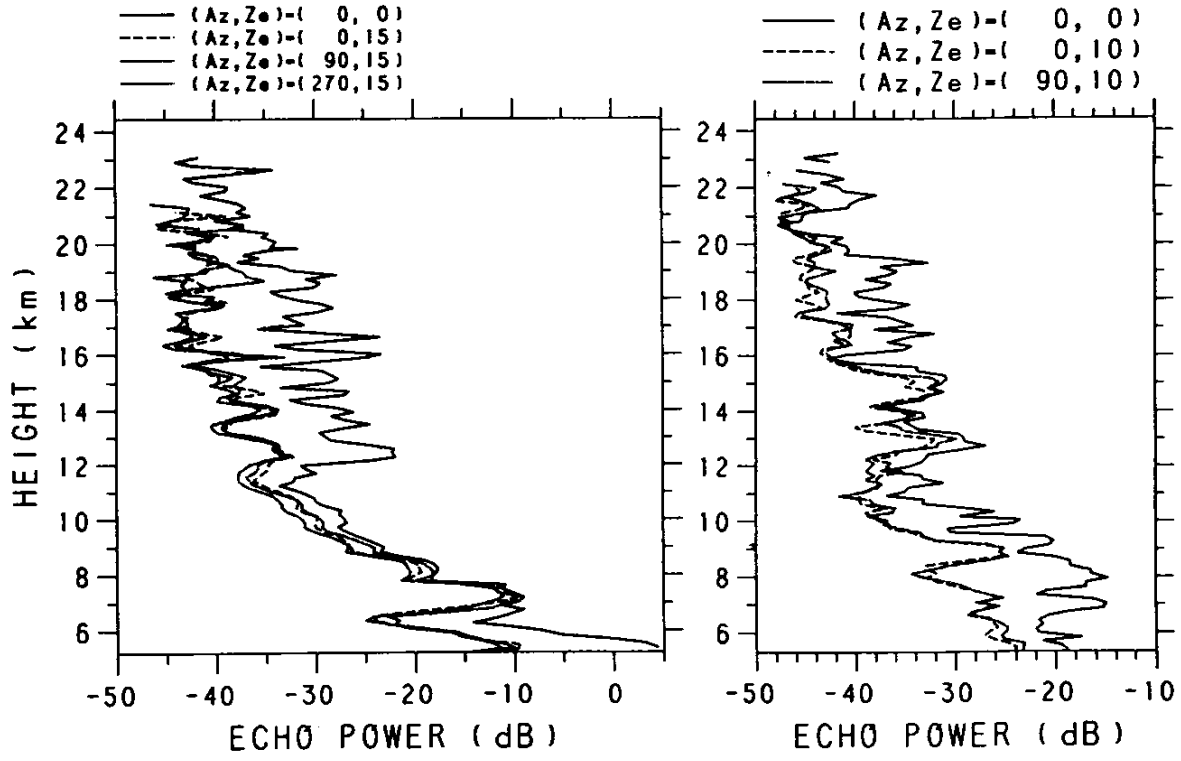

Figure 11. Height profiles of echo power observed with the 46.5 MHz MU radar at different zenith and azimuth angles. The echo power is highest in the zenith direction, proving the strong aspect sensitivity of the scattering/reflecting regions in the troposphere and lower stratosphere (Tsuda et al., 1986).

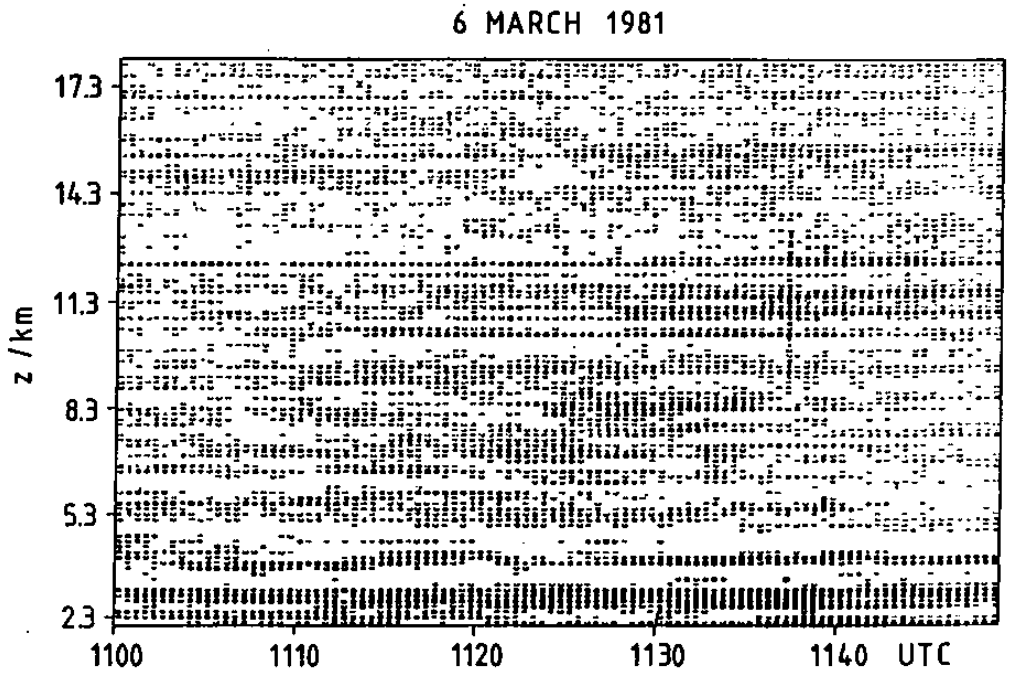

Figure 12. Height-time intensity plot of tropospheric and lower stratospheric fine structure observed with 150 m height resolution and vertical beam at 53.5 MHz. The mean background profile is subtracted to improve the display of the thin layers and persistent laminae (Hocking and Röttger, 1983).

In order to explain the relevant *MST* radar observations, the two different basic echoing mechanisms, scattering and reflection, have to be assumed. These, however, have to be adapted into quite diverse deviations from these two idealistic cases. For monostatic radars, backscatter and reflection arises from the component of the spatial spectrum of the variation of the refractive index n, whose spatial scale along the axis of the radar beam is half the radar wavelength, i.e. a few meters for low *VHF* and less than a meter at *UHF*. This process is frequently called turbulence scatter, if a radar volume is homogeneously filled with randomly distributed, and isotropic irregularities; whereas it is called [*partial*] reflection if inhomogeneities in form of stable discontinuities or steps of the refractive index exist. The latter case more likely applies to longer radar wavelengths. It is known that these two idealised cases rarely occur but have to be replaced by more realistic models.

Since it can be assumed from the aspect sensitivity [*Figure 11*] and persistency [*Figure 12*] of radar echoes that partial reflections from steep vertical gradients of the refractive index [*discontinuities*] are observed by vertically beaming radars operating around 50 *MHz*, the radar equation for this condition was introduced. The amplitude reflection coefficient, however, cannot be uniquely determined, since it strongly depends on the shape of the refractive index profile within a distance of less than one radar wavelength [*Röttger and Liu*, 1978; Woodman and Chu, 1989].

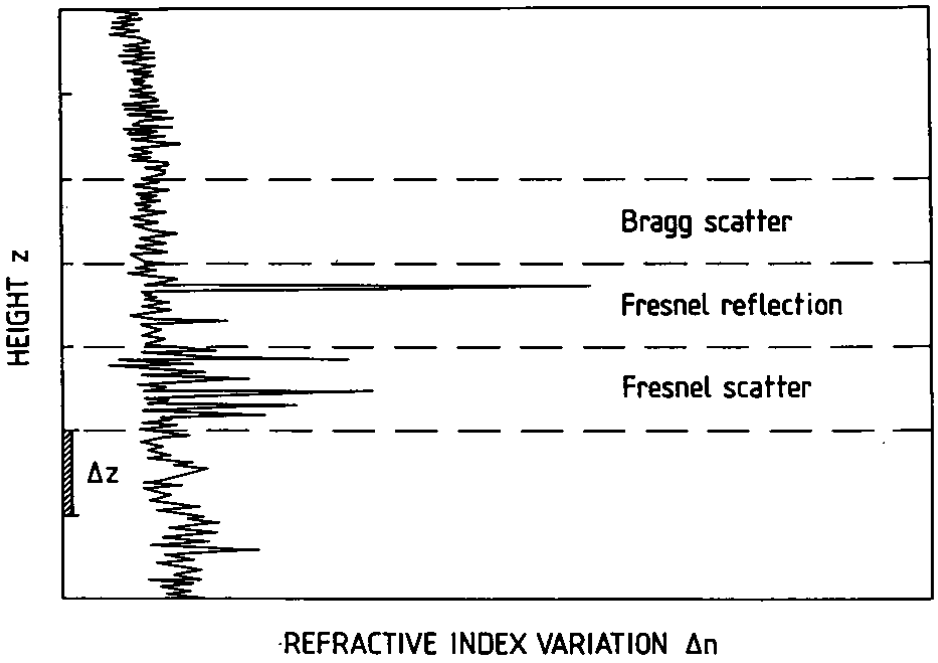

Figure 13. Schematics of small-scale vertical variations of the refractive index showing the three main processes Bragg scatter, Fresnel scatter and Fresnel reflection, accepted to be the cause of the MST radar echoes in the troposphere and stratosphere; _z is a typical range gate width.

It is also frequently observed that there is more than one partially reflecting refractive index structure in the radar volume. Recent high resolution in-situ temperature measurements [*Luce et al.*, 1995] support this assumption of partial reflection from thin sheets or laminae [*Figure 12*], at least for the stratosphere.

It is not readily possible to discriminate between the different basic processes of scattering and partial reflection, detected by *MST* radar, but in general it has become accustomed in the *MST* radar community to apply a nomenclature which is basing on the principal schematics of the different refractive index formations shown in Figure 13 [*Röttger and Larsen*, 1990], and summarised also in Table 3. There exist many papers dealing with the theory as well as experimental methods to investigate the scattering and reflection mechanisms and only the basic characteristics will be delineated.

As defined in Table 3, the principle scattering mechanism in *MST* radar applications is frequently also called "*Bragg scatter*" [*Gossard and Strauch*, 1983], rather than turbulence scatter. This term results from the physical mechanism of constructive interference of backscatter from spatial spectrum components at the Bragg wavenumber $k = 4\pi/\lambda$ of refractive index fluctuations in a turbulence layer, which is much wider than many radar wavelengths λ. The Bragg scatter can be isotropic, i.e. without causing a radar aspect sensitivity, if the turbulent irregularities of refractive index are homogeneously random and statistically similar in all directions. Bragg scatter can also be anisotropic, causing an aspect sensitivity if the statistical

properties of the irregularities, namely their correlation distances, are dependent on direction. Although the angular [*spatial*] dependence of the radar echoes, i.e. the aspect sensitivity, for these two processes - isotropic and anisotropic Bragg scatter - is different, the temporal variations of the radar echoes should be similar because of the randomly fluctuating irregularities. The *Doppler* spectrum should approximately reveal a Gaussian shape.

"*Fresnel scatter*" [*Gage et al.*, 1981; *Hocking and Röttger*, 1983] occurs if, instead of a random ensemble of irregularities, just a few refractive index discontinuities in vertical direction exist in the range gate. These discontinuities are still randomly distributed in the vertical, but have a large extent, i.e. a long correlation distance in the horizontal direction. The radar echo characteristics resemble a distinct aspect sensitivity, but because the discontinuities are statistically independent, the temporal echo characteristics should be similar to those of Bragg scatter. Because of the statistical distribution of the discontinuities, the average power profile should fairly smoothly vary with altitude. The term Fresnel scatter is used because the discontinuities should have a horizontal extent which is at least in the order of a Fresnel zone.

"*Fresnel reflection*" [*Röttger and Larsen*, 1990] is observed if a single, dominating discontinuity of the refractive index exists in vertical direction, which has a large horizontal extent, similar to the ensemble of discontinuities for the case of

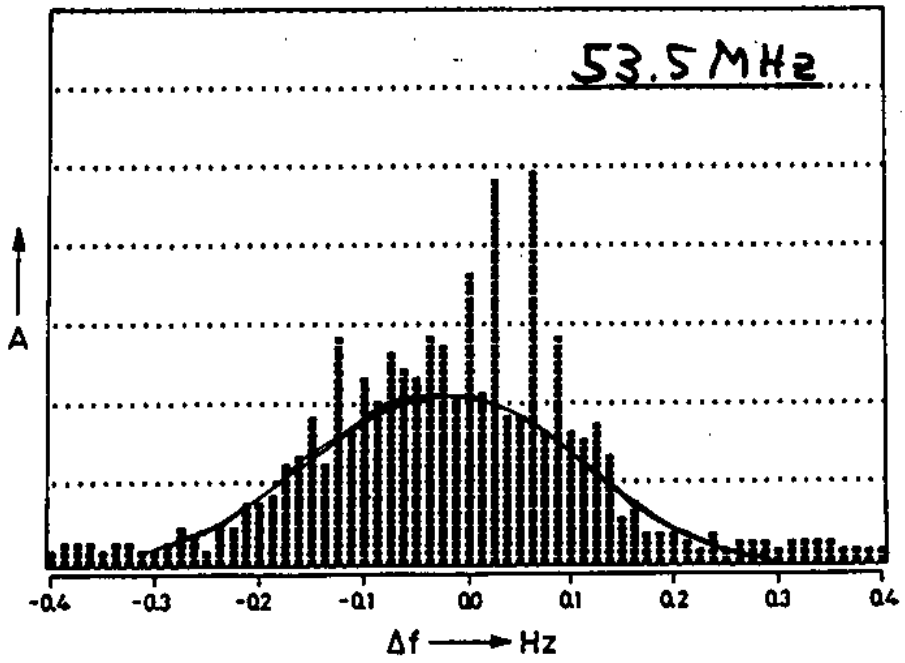

Figure 14. Amplitude spectrum of a 53.5 MHz radar echo from the troposphere measured with vertically pointing antenna and 150 m height resolution over eight minute post-integration time, showing spikes due to Fresnel scatter/reflection and a Gaussian-shaped background due to Bragg (turbulence) scatter.

Fresnel scattering. A very distinct aspect sensitivity should be observed. High resolution vertical power profiles or height-time intensity plots should reveal outstanding spikes, or thin and persistent structures, respectively. Also the temporal characteristics should indicate long coherence times. This kind of process is also called "partial reflection", because only a very small fraction of the incident power is reflected. Fresnel reflection is also called "*specular reflection*" by some authors if the horizontal surface of the discontinuity is assumed to be very smooth, and it is called "*diffuse reflection*" if the discontinuity is assumed to be corrugated or somewhat rough.

Fresnel scatter and reflection occur more likely on longer radar wavelengths, i.e. in the low *VHF* band. The terms Fresnel scatter and Fresnel reflection have been introduced due to the condition that the horizontal correlation distance of the discontinuities is in the order of the Fresnel zone $[r \cdot \lambda]^{1/2}$, where r is the distance between the radar and the scatter/reflection volume, and λ is the radar wavelength. For correlation distances smaller than a fraction of the Fresnel zone, anisotropic or isotropic Bragg scatter can dominate. The Fresnel zones of radars in the *UHF* and *VHF* band are usually smaller than the region in the troposphere and stratosphere, which is illuminated by the radar beam. Thus, the beam width limiting effect has not to be considered. It is perceived that the definition of Fresnel scatter and Fresnel reflection depends on the range gate width, i.e., it is more likely to observe Fresnel scatter with coarse height resolution, and to observe Fresnel reflection with good height resolution. The discontinuities must be in the order of a radar wavelength, or less in vertical direction, but widely extended in horizontal direction, which, because of diffusion reasons, is more likely to happen at larger vertical scales. The nomenclature of thin "*sheets*" or "*laminae*" to describe the 50 *MHz* observations [*Röttger*, 1980] was introduced and taken from oceanography where a similar fine structure is observed. The reason for the coexistence of refractive index turbulence and discrete discontinuities [*sheets or laminae*] in the atmosphere could be for instance due to the gradients developing at boundaries of turbulence layers, or some other yet unproved mechanisms. For instance, *Hocking et al.* [1991] have suggested that viscosity waves and thermal-conduction waves can be a cause for the reflections detected with *MST* radar. Simulations and computations, compared with distribution functions of radar echoes on 50 *MHz*, demonstrate that signals do occur from certain altitudes which are consistent with the model of reflection from a single, diffuse sheet, causing focussing and defocussing. The existence of sheets in the temperature microstructure, which would be needed for Fresnel reflection or Fresnel scattering, was proven by in-situ observations in the lower atmosphere reported by *Luce et al.* [1995].

Although a fine structure of radar echo power is also observed on 430 *MHz* [*Woodman*, 1980a] and on 2380 *MHz* [*Woodman*, 1980b], it is not obvious that the fine structure observed on 50 *MHz* with vertical beam, is of similar origin or nature.

It is likely that radars in the *UHF* band will only detect Bragg scatter from thin turbulence layers, whereas radars in the *VHF* band will usually detect a combination of the different processes, particularly when using a vertical beam [*Röttger and Liu*, 1978]. At 50 *MHz* there are usually weak Gaussian-shaped background spectra observed on which narrow spikes are superimposed [*Figure 14*]. The Gaussian parts of the spectra are supposed to be partly due to Bragg scatter from a background of turbulence, and partly due to scatter from off-vertical irregularities carried by the wind [*beam width broadening*]. The superimposed spikes in discrete frequency bins are either due to Fresnel scatter, or more likely due to Fresnel or diffuse reflection from a rough surface, i.e. several discrete regions of high reflection coefficient which move with different velocities. It is noted that the spectra of 50 *MHz* radars are not particularly governed by the spikes if the antenna is pointed far enough off-zenith [$>10^o$ - 15^o], such that the isotropic Bragg scatter component dominates. It is also noted from spectra, as well as from the aspect sensitivity, that Fresnel scatter and particularly Fresnel reflection yield generally a larger echo power than Bragg scatter from turbulence.

5. Spaced Antenna and Interferometer Techniques

The traditional method applied with *MST* radars to measure wind velocities is the so-called Doppler-Beam-Swing [*DBS*] technique. More frequently also the so-called spaced antenna mode [*Briggs*, 1984] has been adopted to deduce the wind velocity from the cross correlation analysis of signals received at separate antennas. This is the so-called spaced antenna [*SA*] technique. Both these methods of course allow the measurement of some additional parameters, such as the signal power, the coherence time, the angular dependence or the spatial coherence as well as the amplitude distribution functions. These are useful parameters to study the scattering/reflection mechanism. Neither the Doppler nor the original spaced antenna method [*which dates back several decades, see references in Briggs*, 1984] need the measurement of the spatial distribution of the signal phases on the ground. Several advantages exist when amplitude and phase [i.e., the complex amplitude] measurements with a spaced antenna set-up are done [*Röttger and Ierkic*, 1985]. The applicability of this radar interferometer method to deduce additional signal parameters, which the conventional Doppler and spaced antenna methods cannot supply, has been convincingly confirmed during the recent years [*van Baelen et al.*, 1990, 1991; *Palmer et al.*, 1991]. The application of the interferometer mode has gained improved insight into the spatial structure of the scattering/reflecting irregularities and can also replace electronic beam steering by digital off-line processing [*Röttger and Ierkic*, 1985; *Kudeki and Woodman*, 1990].

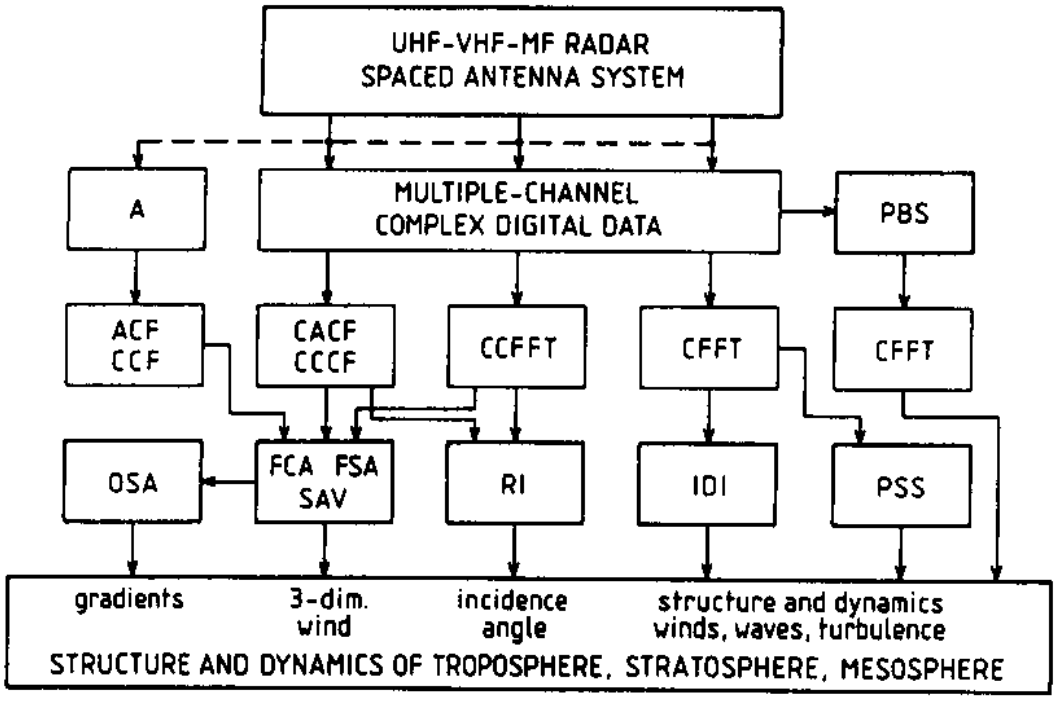

Table 4. Advanced methods to analyze MST radar signals detected with spaced antenna arrays of UHF, VHF and MF radar systems: A = modulus of complex amplitude, ACF = auto-correlation function, CCF = cross-correlation function, CACF, CCCF = complex auto/cross-correlation function, CCFFT = complex cross fast Fourier transform, CFFT = complex Fourier transform, OSA = oblique spaced antenna method, FCA = full correlation analysis, FSA = full spectrum analysis, SAV = spaced antenna velocity deduction, RI = radar interferometry, IDI = imaging Doppler interferometry, PBS = post-beam steering, PSS = post-statistics-beam steering. These methods are applied to investigate the structure and dynamics of the troposphere, stratosphere and mesosphere with MST radars.

In accordance to the term frequency domain interferometry, the method using several antennas is called the spatial domain interferometry or simply spatial interferometry. The spatial domain interferometry improves the resolution in the direction perpendicular to the beam direction [i.e., *mostly horizontal*], whereas the frequency domain interferometry [e.g., *Kudeki and Stitt,* 1987; *Palmer et al.*, 1990] allows to improve the resolution in the radial [i.e, *range*] direction. The former method allows for instance to measure the angular spectrum [i.e., *the aspect sensitivity*], the incidence angle, the corrected vertical and horizontal velocity as well as to determine horizontal phase velocities and the momentum deposition of atmospheric gravity waves and to track turbulence blobs. Post-beam-steering and the cross spectra analysis can be applied to study waves and turbulence in the stratosphere and the mesosphere, respectively. The original method of cross spectrum and coherence analysis was developed to study scattering from E-region irregularities with the 50-*MHz* Jicamarca *VHF* radar. This method was also applied to measure incidence angles with the Chung-Li *VHF* radar and to investigate polar mesosphere summer echoes with the 224-*MHz* EISCAT *VHF* radar. One envisages essentially

more details of the scattering/reflection mechanism by the application of the spatial and frequency domain interferometry.

In Table 4 the different methods have been summarised, which can be applied with *MST* radar in the spaced antenna mode to measure atmospheric parameters. This is particularly emphasised since it is often thought that the spaced antenna method is barely the spaced antenna drift technique to measure the drift speed of refractive index irregularities and deduce the horizontal wind. This technique is only a minor part of the total, indicated by the branch including the square-law detector in Table 4. All further applications make use of the phase information, such as the interferometer, the post-beam-steering and the post-statistics method used with the SOUSY-, the Chung-Li and the Jicamarca *VHF* radar, respectively.

Also the oblique spaced antenna method has been applied [*Liu et al.*, 1991], and radar imaging using a set-up of spaced antenna modules has been done for studying the irregularity structure [*Kudeki and Surucu*, 1991; *Huang et al.*, 1995].

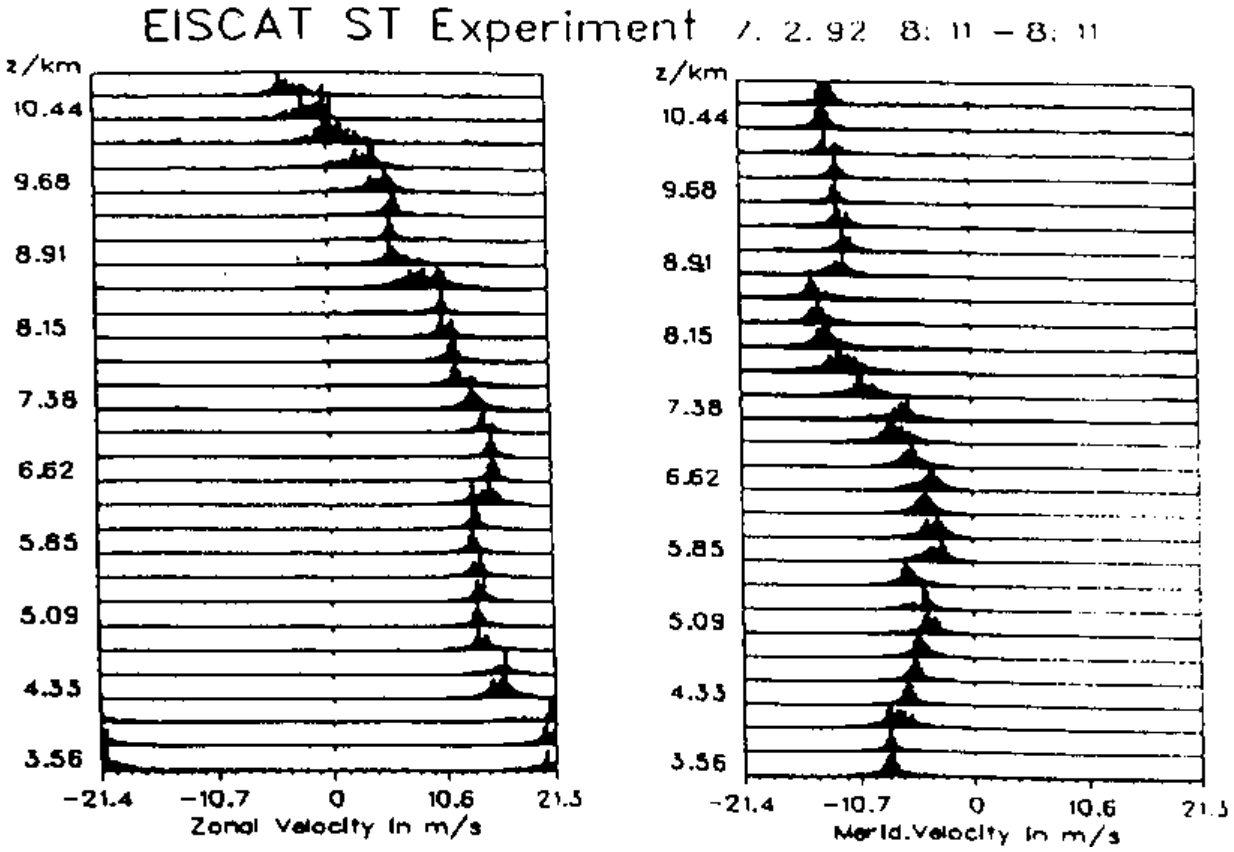

Figure 15. Profiles of spectra of echoes from the troposphere and lower stratosphere measured on 7 Feb. 1992, 08:11 UT, with the EISCAT UHF radar.

6. Example of Stratosphere-Troposphere Observations with EISCAT

MST radars are usually operated in the Doppler mode, where several antenna beam directions are used to deduce the three-dimensional wind velocities from the Doppler power spectrum. Figure 15 shows an example of tropospheric scatter measured with the EISCAT *UHF* radar [*Röttger*, 1994b]. Low elevation antenna beam directions had to be used in this stratosphere-troposphere mode due to transmit-receive recovery effects. A range resolution of 750 m was chosen, corresponding to a 250 m altitude extent of the scatter volume, when beaming at 20° elevation angle. The variation of the Doppler shift with height is a direct measure of the horizontal wind profile *[shown in Figure 15 are the zonal and meridional components*] and the width of the spectra is a coarse estimate of the turbulence strength. It is obvious that at these low elevation angle and high frequency, the echoes are exclusively caused by turbulence scatter.

The on-line pre-processing is done by computations of the auto-correlation function [*ACF*], which is the standard data preprocessing and compression method applied in EISCAT incoherent scatter experiments. The system hardware is optimised for instrumental *DC* suppression. However, the kind of pre-processing does not include *DC*-elimination as usually done in *MST* radar applications. A small amount of instrumental *DC* still remains and distorts weak atmospheric echoes at small Doppler shift. The *ACFs* are particularly contaminated by the *DC* component, which results from ground clutter from near-by high mountains. A special regression algorithm was developed to remove the *DC* contamination from the *ACF*. This needs to be performed before the transformation into the frequency domain, which usually is done for Doppler spectra analysis, since the truncation of the *ACF* would strongly widen the *DC* component in the Doppler spectrum and spoil the atmospheric echo.

This algorithm, described by *Röttger* [1994b], turned out to be very efficient. In *MST* radar applications the removal of instrumental and ground clutter *DC* is usually done by high pass filtering of the real and imaginary part of the coherently integrated raw data separately over a certain time interval which is long compared to variations of the scatter signal. This filtering is done before any further off-line treatment of the data. In the EISCAT system the complex autocorrelation function is first computed on-line. Depending on time scales to be investigated the auto-correlation functions are integrated over as much as several seconds or tens of seconds. This has the advantage of extreme data compression, which is necessary in ionospheric applications. This, however, seemed to have a disadvantage for stratosphere-troposphere applications in the presence of a strong *DC* component due to ground clutter.

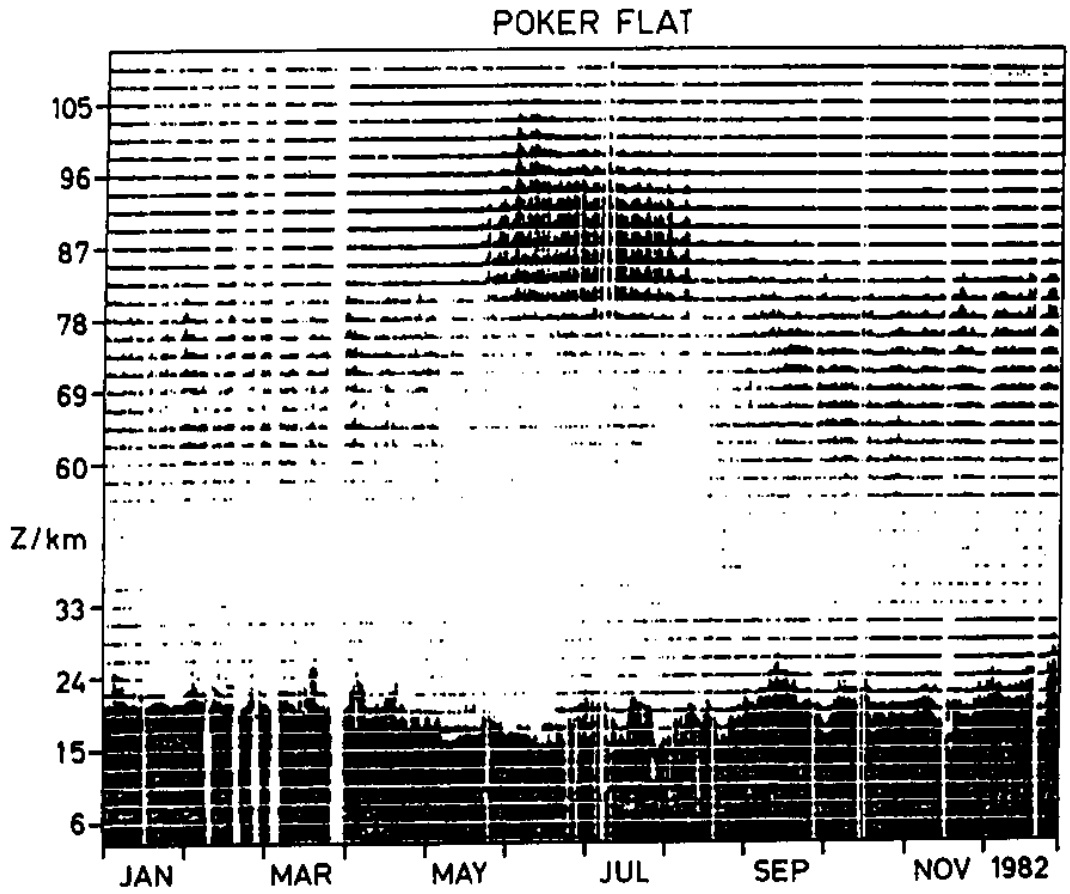

Figure 16. Seasonal variation of MST radar echoes measured with the 49.9 MHz Poker Flat radar in Alaska, showing the increase in mesospheric echo power and of the altitude of the echoes during the summer months June and July (Ecklund and Balsley, 1981). These summer echoes were later named Polar Mesosphere Summer Echoes - PMSE.

7. Particularities of Polar Mesosphere Summer Echoes

During the early operation of the Poker Flat *MST* radar in Alaska unusual mesospheric echoes were observed during the summer time [*Balsley et al.*, 1980], as shown in Figure 16. After a long period of scepticism, whether or not these echoes could be created by enhanced neutral turbulence, several more reasonable explanations were suggested, which base on fact that the polar mesopause is very cold in summer [*Cho and Kelley*, 1993].

These polar mesosphere summer echoes [*PMSE*] have now been observed over frequency ranges of about three orders of magnitude between 2.7 *MHz* and 1.3 *GHz*. Echoes of similar characteristics were also observed in mid latitudes [*Thomas et al.*, 1992] as early as the Poker Flat observations, and therefore the term mesosphere summer echoes is also used. A summary of the history of the *PMSE* observations is found in [*Röttger*, 1994a], of which the part dealing with the scattering properties of irregularities is repeated here.

The scattering mechanism is basically the same on all these frequencies, namely refractive index irregularities have to exist at spatial scales of half the radar wavelength, i.e., between about 50 m and 10 cm. It is regarded as very unlikely that the same properties of irregularities can cause the scattering over these wide ranges. The polar mesosphere summer echoes comprise a nice example of the transition from "*coherent*" to "*incoherent*" scatter, when applying radars in a wide frequency range covering the buoyancy subrange to the outer limits of the viscous-diffusive subrange [*Figure 6*]. An example proving the coexistence of incoherent scatter and the particular scatter causing the *PMSE* is shown in the results of EISCAT observations on 931 *MHz* [*Figure 17*]. The weak and noisy incoherent scatter spectra noticed in all the range gates are dominated by very strong echoes with narrower spectral width in the range gates 84.7 km [*Röttger et al.*, 1990], which are attributed to the *PMSE* scatter.

The EISCAT *VHF* [224 *MHz*] and *UHF* [931 *MHz*] radars have been used frequently in the recent years to investigate the polar mesosphere summer echoes. Almost all of the experiments were carried out in a single channel mode, i.e., only one antenna had been used for transmitting and for receiving. In those observations only the basic parameters, echo power, radial velocity and spectral width have been obtained. Attempts using two collinear antenna sections of the EISCAT *VHF* system in the interferometer mode were done by *La Hoz et al.* [1989]. As more and more novel features of *PMSE* have been reported and are still far from completely understood [*Cho and Kelley*, 1993; *Cho and Röttger*, 1997], it became obvious that more extended information on the irregular structure causing the *PMSE* is needed. *Klostermeyer* [1997] has developed a theory to explain *PMSE* scatter, which appears challenging. Higher spatial resolution would be required to resolve apparent fine structure of the irregularities. More progress has now been achieved by applying the radar interferometer technique as introduced to the *VHF* radars for studying the lower and middle atmosphere by *Röttger and Ierkic* [1985] and successfully applied with EISCAT by *Pan and Röttger* [1996].

The frequency domain intereferometer method had also been introduced successfully to study at *PMSE* with EISCAT [*Franke at al.*, 1992]. With the spatial interferometer method cross spectra of signals received at separated/spaced antennas pointing into the same direction, overlapping with the transmitting antenna had been determined. From these cross spectra, the coherence and the phase as function of Doppler frequency are deduced. The height-time-intensity [*HTI*] plot of *PMSE* is shown in the upper panel of Figure 18a, which is reproduced from *Pan and Röttger* [1996]. The intensity [*echo power*] is displayed, where 45 dB corresponds to the noise level. Thus, the signal-to-noise ratio was in the order of 20 dB. From this HTI plot a clearly layered structure is evident in the first 15 minutes of the observations. Two spectacular events occurred consecutively after the initial period of a persistent

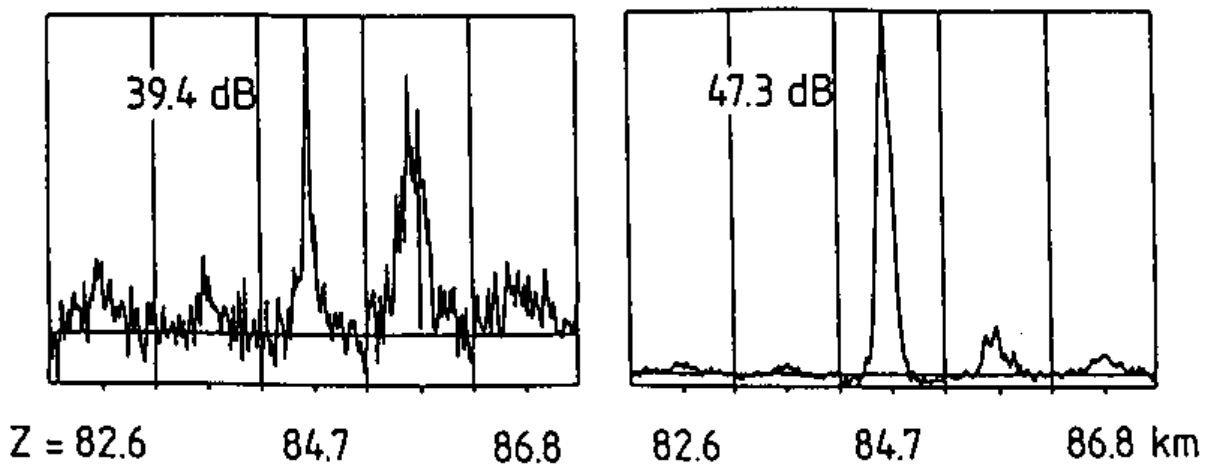

Figure 17. Power spectra of weak mesospheric incoherent scatter echoes and strong polar mesosphere summer echoes measured with the EISCAT UHF (931 MHz) radar at 00:33:00-00:33:40 UT and 00:37:00-00:17:40 UT on 2 July 1988. Each individual spectrum is an average over 10 sec and covers the frequency range ±205 Hz. The strong spike observed in the range gate 84.7 MHz is caused by PMSE.

and stratified structure of the layer. At about 09:38 UT the layer was lifted upward, followed by a downward motion and a billow structure then occurred soon thereafter. This event is appearing as a cat's eye structure that happened right after the originating up- and down-lift of the layer. The vertical displacement of the layer was about ±1.6 km. The disturbed layer became stratified again after about 09:55 UT. Such observations of cat's eye structures in mesospheric radar echoes were reported earlier [*La Hoz et al.*, 1989] and are also seen as wave breaking events in noctilucent clouds [*Thomas*, 1991]. These relate to intensity and velocity variations, which is expanded here into observations of spatial structure of the irregularities causing the *PMSE*.

For a detailed structural study of this *PMSE* event the dynamic auto- and cross-spectra can be examined. The latter result from the signals detected at the two spatially separated receiving antennas, from which the coherence spectra [*modulus of the normalised cross-spectra*] are deduced. These are shown in the center [b] and lower panels [c] of Figure 18, respectively. These spectra result from a 64-point FFT spectrum performed per record of two seconds, and ten of these spectra are coherently averaged to obtain the displayed auto- and coherence-spectra. The corresponding time step in this display is twenty seconds.

The high coherence values indicate that there exist deterministic individual scattering targets in the layer. It is assumed that these are patches of smaller irregularities which are frozen-in to deterministic spatial structures, which could result from the different mechanisms as those suggested for instance by *Havnes et al.* [1992].

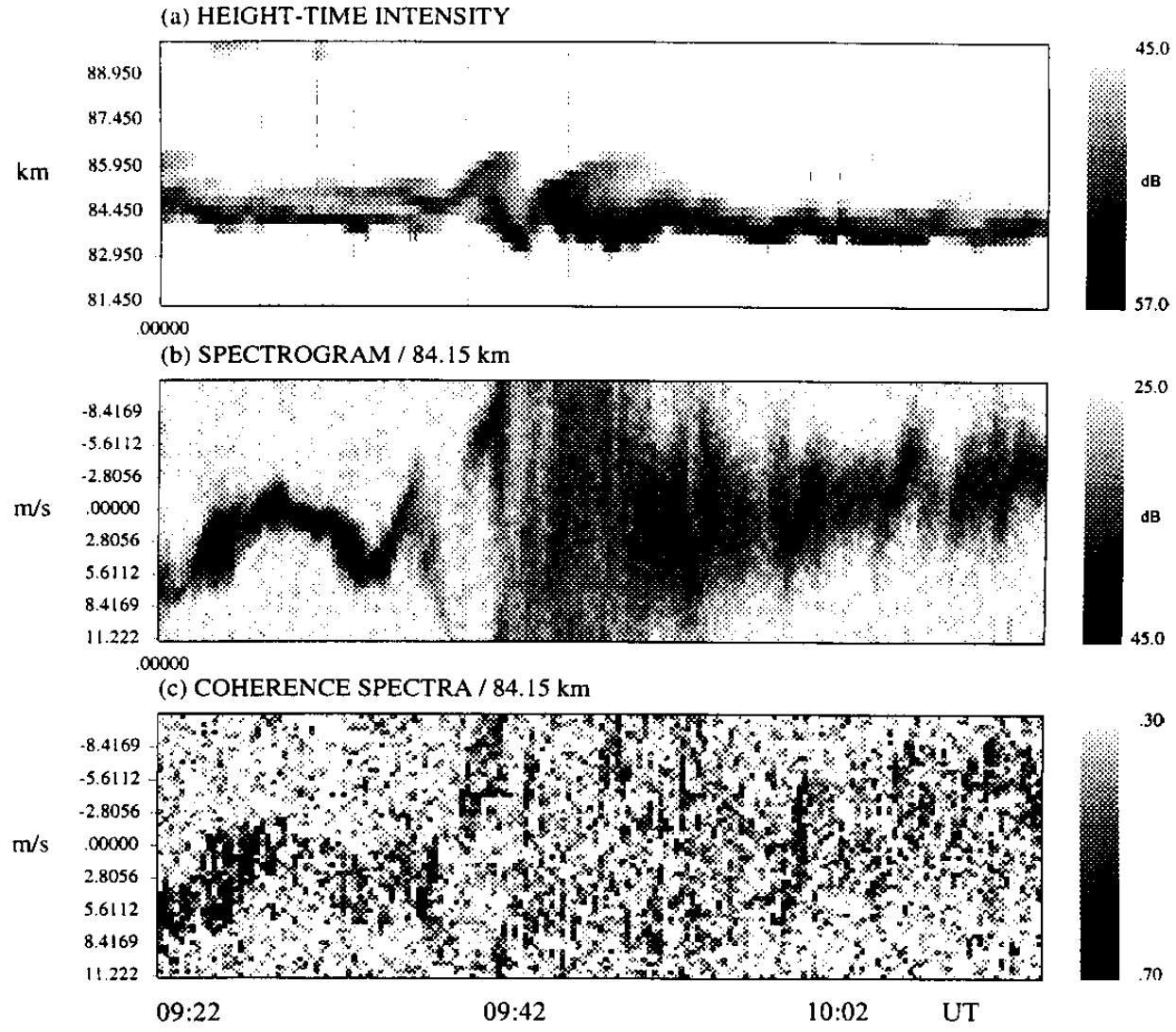

Figure 18. (a) Height-time-intensity plot of PMSE observed with the EISCAT VHF radar (224 MHz) on 16 June 1994. (b) Dynamic autospectra of the echoes in range gate 84.15 km. (c) Coherence spectra, deduced by the interferometer measurements of these echoes. The coherence limits are 0.3 to 0.7.

Due to the quite narrow spectral width, observed until the wave breaking, and the relatively high spatial coherence it occurs to us that the scattering structures are not governed by turbulence, rather than related to a stable environment. These pre-existing patches of irregularities, lined up in relatively narrow layer, are just affected by wave motion. It is also argued that these pre-existing patches of fairly stable irregularity structures are just torn apart and blurred up by the turbulence event.

The feature of some distributed peaks found in certain Doppler cells of the coherence spectra in Figure 18c can be explained by the radar beam being filled with several detached structures. It is suggested that the *PMSE* is well organised during the initial observation period, and the wave breaking process just serves as a mech-

anism of de-organising the *PMSE* irregularities. The observed effect, that an originally stable structure of scattering irregularities is only perturbed by neutral turbulence, was originally suggested by *Röttger* [1994a]. This can be supported by our observations of regions of high coherence, which are randomly distributed during the time after 09:42 UT when the violent turbulence was observed. It is argued that there is the same scattering mechanism responsible for the *PMSE* during all our observations. It is also likely that those in-situ observations by *Lübken et al.* [1993], reporting wide layers of *PMSE* with strong velocity fluctuations and thin layers with weak velocity fluctuations can be explained by these observations.

It has been shown that spatial interferometer measurements are essential to understand the intrinsic *PMSE* irregularity structure. It is not indisputable that different scattering mechanisms are involved in these observations of *PMSE*, which show calm as well as highly turbulent conditions. The appearance of layers and variations in spectral width/fluctuations just displays the effect of the neutral atmosphere on pre-existing irregularities. These irregularities are, thus, effective tracers of the neutral atmosphere dynamics in the narrow range of observation.

8. Interpretations of Scattering and Reflection Processes

The interpretation of radar returns from the clear air of the middle and lower atmosphere has been and still is in a long-lasting dispute. Is this just resulting from a semantic misunderstanding or preference of approaches to study the phenomenon or does it result from different physical phenomena? There are certainly different meteorological and aeronomical phenomena, which cause the different signal characteristics. In any case one can discriminate between the two extreme models of the echoing process itself:

[1] Scatter by random, non-deterministic fluctuations of the refractive index in space and time, which can be isotropic and anisotropic. These fluctuations result from neutral air turbulence of convective or dynamic origin. The anisotropic approach, however, is already at the limit of becoming deterministic in two coordinates.

[2] Reflection is from a refractive index discontinuity between horizontally stratified air masses of different refractive index, resulting from horizontal flow pattern, radiation, evaporation or electron density structures in the mesosphere.

There are also clear indications for the coexistence of the two major mechanisms, namely the thin and almost horizontally stratified laminae of refractive index, which appear to be corrugated by background turbulence, the pronounced aspect sensitivity and long persistency which transits into isotropy and random fluctuations at larger aspect angles and the non-Gaussian shape of the Doppler spectra and signal components.

It was suggested by *Röttger* [1994] that principally five different classes of mesospheric irregularities occur, causing the polar mesosphere summer echoes at different radar frequencies:

[1] Steep gradients of electron density,

[2] electron density irregularities caused by mixing in gradients by neutral turbulence,

[3] extension of fluctuations in the electron density to shorter scales than in the neutral density due to presence of heavy cluster ions [*extended subranges as shown Figure 6 due to enhanced Schmidt number; Cho and Kelley*, 1993],

[4] electrostatic waves due to of highly charged aerosols,

[5] charge accumulation in electron clouds dressing multiply charged aerosols and ice particles.

The processes causing *PMSE* are interlaced and range from partial reflection [*around several MHz*], turbulence scattering [*around a few 10 MHz*], scattering related to enhanced Schmidt numbers or electrostatic waves [*several 10 MHz to several 100 MHz*] to enhanced Thomson [*incoherent*] scatter [*around 1 GHz or higher*].

In Table 5 [*from Röttger*, 1994a], the different mesospheric phenomena are summarised, which had been assumed to cause scattering of radar and radio waves. All the scattering/reflection mechanism of the electro-magnetic waves causing the *PMSE* require that refractive index irregularities exist at spatial scales of half the radar wavelength [*for monostatic radar backscatter*]. In Table 5 the scale relates to the irregularity and the half radar wavelength scale. The assumed phenomena are ordered according to the scales at which they can occur and cause scattering. Examples of *PMSE* of all the referenced radars were described by *Röttger* [1994a], and references can be found therein. Detailed descriptions of the status of observations and theories were published by *Cho and Kelley* [1993] and *Cho and Röttger* [1997]. Further theories related to the generation mechanisms of polar mesosphere summer echoes have recently been published [see *review by Cho and Röttger* [1997], *and Klostermeyer* [1997]].

The summary of the present knowledge indicates that the essential requirements for *PMSE* are cold mesopause temperatures, modulated by long-period waves and tides, and the D-region ionisation. Also needed are some contaminating constituents, e.g. aerosols or dust or ice particles [*Cho and Kelley*, 1993; *Klostermeyer*, 1997]. Neutral turbulence is playing a certain, but likely not the dominant role in the creation of the *PMSE*. However, the *PMSE* characteristics are undoubtedly also affected by short-period waves and turbulence. The most proper conditions for these kind of mesosphere characteristics are found in the polar mesosphere in summer. It is not excluded, however, that similar conditions can occasionally also occur at lower latitudes, which is supported by observations of

strong mesosphere radar echoes in midlatitudes. *Balsley* et al. [1995] have reported less frequent *PMSE* in the Antarctic, which they explain by higher mesopause temperatures in the southern hemisphere polar atmosphere. It is recognised that *PMSE* studies give a wealth of information on the aeronomy of the mesosphere. Also a multitude of dynamical effects, such as gravity wave propagation [*Czechowsky et al.*, 1989], saturation and breaking into turbulence [*Fritts et al.*, 1988], steepening and the possible occurrence of solitary waves can be studied [*Röttger*, 1991]. It is to be assumed that these dynamical effects do not cause the *PMSE*, but the *PMSE* act as sensors, in a similar way as noctilucent clouds [*Thomas*, 1991; *Reid*, 1995], which are to be associated with the polar mesospheric clouds and likely *PMSE*, allow the study of mesospheric chemistry and dynamics.

Long-period waves can undergo non-linear steepening or tilting when their phase velocity approaches the wind velocity. Through the approach of superadiabatic lapse rate and velocity shear, Kelvin-Helmholtz instability [*KHI*] is activated and quasi two-dimensional turbulence is generated. Turbulence scatter or Fresnel reflection from the boundaries of the turbulence layers can occur. Also steep temperature inversions [*stable sheets or laminae*] could be caused by the steepened waves, which can be seen by Fresnel reflection.

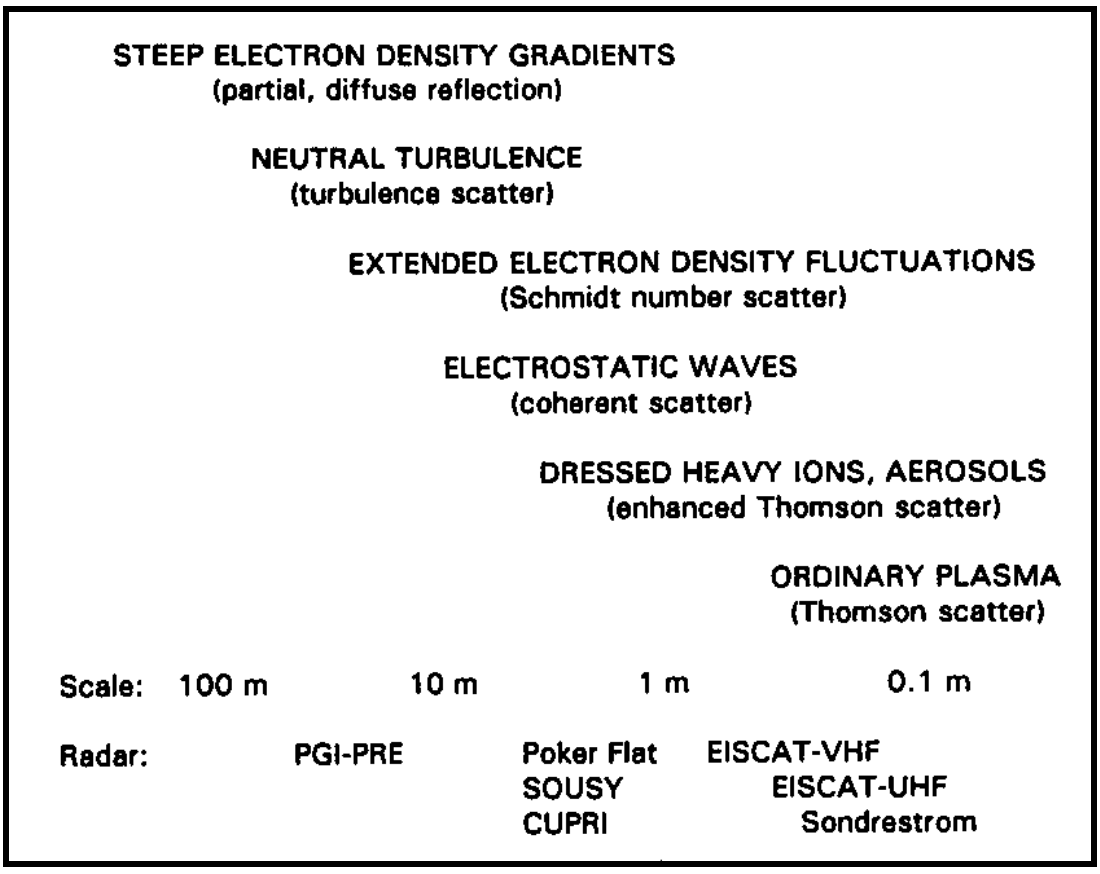

Table 5. Mesospheric phenomena recognized as possible causes for polar mesosphere summer echoes.

Short-period waves, propagating upwards from lower atmospheric sources or generated in-situ by *KHI* or by two-dimensional turbulence arising from long-period waves, undulate these layers of turbulence or the laminae of temperature inversions. Besides of transferring energy to long-period wave modes by wave-wave interaction these short-period waves can grow in amplitude by *KHI* [*local generation*] or due to energy conservation of upward propagating waves. Non-linear tilting, steepening and/or parametric instability can occur. The development of tilting can be observed by Fresnel reflection due to the concurrent distortion of isotherms during *KHI*.

Non-linear tilting of short period waves can cause overturning and breaking through the Rayleigh-Taylor instability [*RTI*]. Since this happens at certain phases of the wave, localised regions of small-scale turbulence occur. These are seen by *VHF* radars as blobs or bursts, which are propagating with the phase speed of the wave. Blobs can spread into wider spatial scales by multiple repetition of *KHI*/RTI and cause thick layers of strong turbulence. Through the turbulence layers corrugated temperature gradients are generated and the layers can dissolve into multiple sheets or laminae which can be regarded as remnants of active turbulence. Again waves, generated elsewhere, can undulate these turbulence layers and the laminae. Also viscosity waves and thermal-conduction waves have been suggested as a cause of partial reflection from the middle atmosphere [*Hocking et al.*, 1991]. The recent theory of *Klostermeyer* [1997] to explain the *PMSE* seems to offer a most attractive explanation.

There had been some interesting recent developments and approaches for improving our understanding of the radar returns and the atmospheric structure, these are: The measurement of the frequency dependence of the *MST* radar echoes, the analysis of the signal statistics, modelling of the structures and the resulting radar returns, interferometer applications in space and frequency, and wind field measurements for instance. Further understanding will be gained by the combination of radar measurements with other methods, such as in-situ measurements with balloons, rockets and aircrafts. Also the extension of radar systems by radio-acoustic-sounding systems [*RASS*] and LIDAR measurements is turning out to be very useful and should be followed up in further coordinated campaign operations.

9. Future High-latitude Mesosphere Observations with Radar

The mesosphere can be studied with the incoherent scatter, as well as with the *MST* [mesosphere-stratosphere-troposphere], radar technique. Incoherent scatter measurements of the lower thermosphere and mesosphere allow the derivation of electron density, ion-neutral collision frequency [*neutral density*] and temperature, ion [*neutral*] velocity, ion composition and the density of negative and positive ions, provided some assumptions can be applied. Occasionally coherent scatter from

ionisation irregularities can mask the incoherent scatter measurements, particularly in summer when Polar Mesosphere Summer Echoes occur.

EISCAT observations of the middle atmosphere and lower thermosphere had been summarised by *Röttger* [1994c]. At the frequencies used by EISCAT in Tromsø [*224 MHz and 931 MHz*], as well as at the EISCAT Svalbard Radar [*ESR*] operating frequency of 500 *MHz*, the turbulence scatter contribution to echoes from mesospheric altitudes is usually negligible. The reason is that the radar wavelength on 500 *MHz* is much smaller than the scales of turbulence which can exist in the mesosphere. To operate the 500 *MHz* as an *MST* radar to study mesospheric turbulence will therefore be impossible, unless a separate radar on a lower frequency such as 50 *MHz* would be set up. Simultaneous operation of a 50 *MHz* and a 500 *MHz* radar would be a useful combination for mesospheric studies, however, since the former would be sensitive to mesospheric clear air turbulence and the latter to ionospheric electron density. A 50 *MHz* radar would be also an optimum choice for studies of the troposphere and lower stratosphere, since it detects echoes from clear air turbulence and inversion layers.

An appropriate complement to the 500 *MHz* incoherent scatter radar would be an *MST* radar [*operated at frequencies in the 50 MHz band*], which uses ionisation irregularities, related to neutral air turbulence and the effects of heavy ions, as scatterers for studying the mesosphere. Compared to the incoherent scatter radar the *MST* radar has to be operated on relatively low frequencies, around 50 *MHz*, to obtain sufficient scatter cross sections. Usually the scatter cross section in *MST* scatter case is orders of magnitude larger than the scatter cross section in the incoherent scatter case. Consequently the transmitter power and antenna gain of an *MST* radar operated on 50 *MHz* can be much smaller than that of the incoherent scatter radar operated on 500 *MHz*. *MST* radars operate with beam directions close to the vertical and a mechanical antenna rotation to low elevation angles is therefore not needed for this application. The *MST* radar measurements allow the deduction of the three-dimensional velocity profiles as well as turbulence intensity in the mesosphere, stratosphere and the troposphere.

Now observations of the mesosphere, stratosphere and the troposphere will be briefly outlined, which can be made with an *MST*/ST radar operated in the polar or Arctic atmosphere. The mesosphere observations are to be done in the incoherent scatter mode and/or the *MST* mode.

9.1. Coupling Processes between the Lower Thermosphere and the Mesosphere

Particular phenomena in the polar atmosphere and the auroral ionosphere, namely particle precipitation, Joule heating, electric fields and Lorentz forcing as well as vertical transport of constituents and momentum, which result from magnetosphere-

ionosphere coupling, have an impact on the middle atmosphere. Furthermore dynamic processes, such as tides and gravity waves, which originate in the lower atmosphere [*troposphere*] and the middle atmosphere [*stratosphere and mesosphere*], propagate upwards into the thermosphere. These mutual coupling processes, which affect the structure, dynamics and aeronomy of the middle atmosphere and lower thermosphere, take place uniquely in the high latitude mesosphere, where the effects from the magnetosphere and ionosphere merge with the effects from the lower and middle atmosphere.

The EISCAT *UHF* and *VHF* radars have already demonstrated the ability to study coupling processes from above to below in the lower thermosphere of the auroral zone. Several mesosphere/D-region investigations have been done with EISCAT, such as for instance the impact of precipitating electrons and protons on the D-region electron density and composition. How these coupling processes between the magnetosphere and the ionosphere, the thermosphere and the middle atmosphere take place in the polar region is so far unknown, since appropriate radar instruments are not operated at these high latitudes near 80°. For instance, the influx of solar protons into the polar mesosphere and upper stratosphere evidently has an influence on the ozone budget and can be studied by the Svalbard Radar. It would also be useful to allow simultaneous radar experiments in the auroral zone [*EISCAT*] and in the Arctic [*Svalbard*] to study the meridional variation of these effects and how their extension to lower altitudes in the middle atmosphere takes place.

Specifically, the EISCAT Svalbard Radar in the *MST* mode should be applied to observe and study mesospheric temperature and winds, the possible auroral influences and the transport of nitric oxide as well as solar proton events [*SPE*] and the resulting polar cap absorption phenomena [*PCA*] and their impact on middle atmosphere ozone and dynamics. The extent of Polar Mesosphere Summer Echoes [*PMSE*] and their relation to Polar Mesosphere Clouds [*PMC*] and Noctilucent Clouds [*NLC*], Sudden Sodium and Sporadic-E layers needs to be studied in polar latitudes. The winter anomaly of absorption and its relation to stratospheric warming in the polar vortex is not known in the high latitudes of 80°. Most essential appears also the climatological study of winds, tides and long period waves and particularly the climatology of atmospheric gravity waves [*AGW*] in the polar mesosphere, the supposed acceleration of the mean wind by AGW momentum deposition and the effect on the mesopause temperature.

For these obvious reasons the EISCAT Svalbard Radar should will have the capability to make high standard observations of the D-region and the mesosphere, in addition to the planned studies of the ionosphere and thermosphere. An additional *MST* radar, operated in the low *VHF* band near 50 *MHz* will be an invaluable tool and complement to the EISCAT Svalbard Radar for studies of the middle and lower atmosphere at very high latitudes.

9.2. The Polar Stratosphere and Troposphere Investigated by ST Radar

There are certain phenomena in the polar middle and lower atmosphere which need to be studied by radar, in addition to the multitude of other experiments which are already applied for these studies in the Arctic and Antarctic, particularly those directed to the ozone problem. Only those phenomena will be discussed, which are assumed to be investigated with an *ST* radar [*stratosphere-troposphere radar*]. These are the structure and dynamics of the troposphere and the lower stratosphere in the polar region. The capabilities of *ST* radars for these studies are outlined in the referenced review articles.

With *ST* radar wind profilers it is possible to study dynamic processes in a wide scale range from planetary and synoptic scale disturbances to small-scale gravity waves and clear air turbulence. The wind field variations occurring in the polar vortex can be monitored continuously by *ST* radar wind profiler, although only at one location and up to about 20-30 kilometers height. In polar regions it seems of special interest to investigate with radar the exchange processes between the troposphere and the lower stratosphere, namely the variation of the tropopause height and the dynamics of tropopause foldings and fronts. The possibility to study vertical transport between the troposphere and the stratosphere, and the transport within the stratosphere by means of the mean vertical motion and by turbulent diffusion, is challenging. The transport and deposition of energy and momentum by gravity waves in the lower stratosphere, which can be measured with *ST* radar, is also believed to have an impact on the mean stratospheric circulation and the polar stratosphere temperature. Furthermore, Polar Stratospheric Clouds, which are assumed to be related to mountain waves, have control of the ozone depletion. The formation of mountain waves can be studied by *ST* radar and thus the dynamics in and around Polar Stratospheric Clouds can also be investigated by the EISCAT Svalbard Radar in the *ST* mode. Such an *ST* radar, if it would be operated continuously, would also yield invaluable input data for meteorological modelling and forecasting. In summary, *ST* radar observations can contribute considerably to the study of the structure and dynamics of the Arctic stratosphere, which is outlined in the sketch of Figure 19.

It is critical to understand the dynamics of the polar stratosphere before a complete picture of the ozone depletion phenomenon can be obtained. Expert scientists propose that further acquisition and examination of a broad range of chemical as well as dynamical observables will be necessary to address the challenging and important question of whether the processes leading to the Antarctic/Arctic ozone hole can also occur in other parts of the Earth's atmosphere.

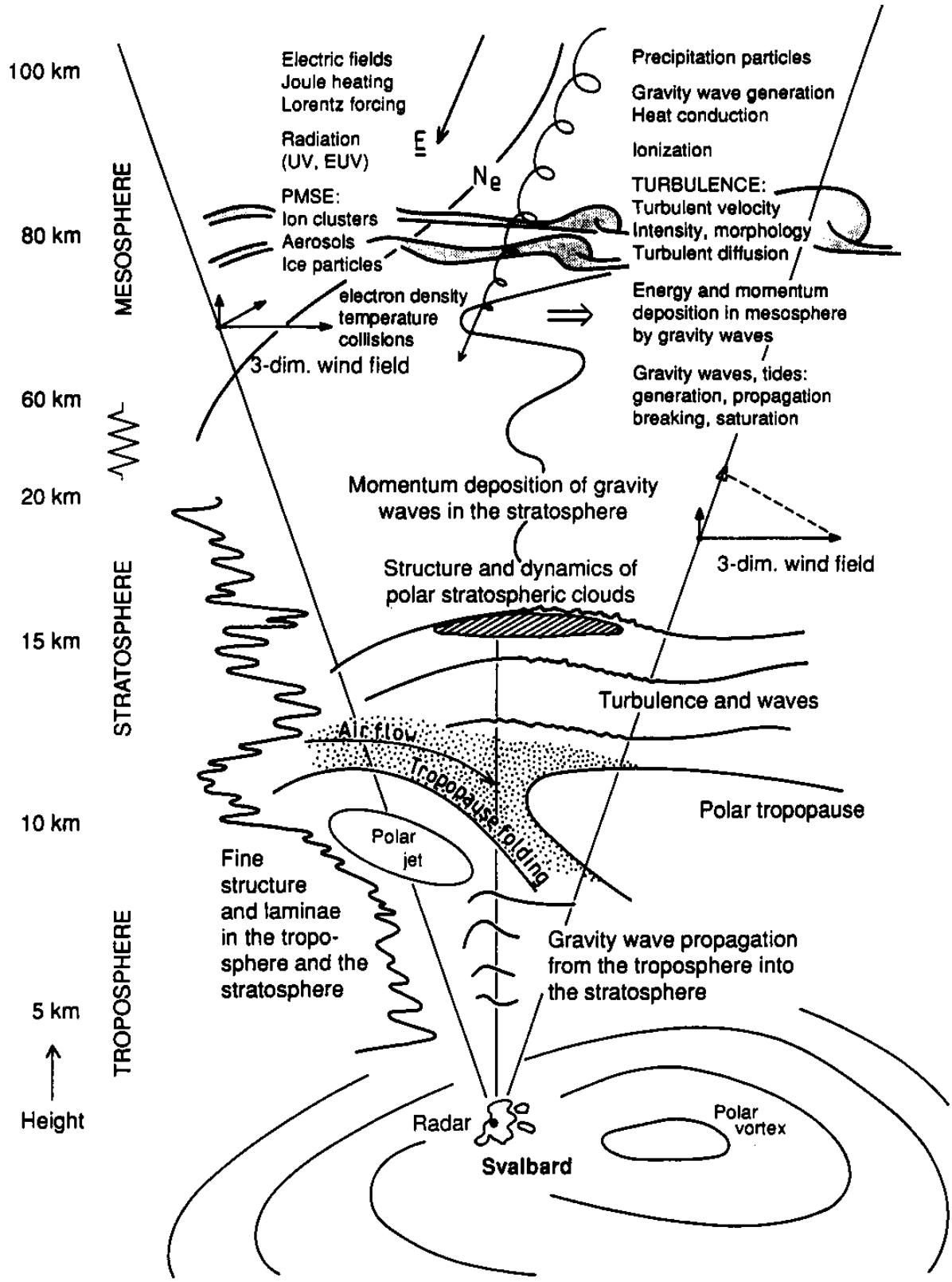

Figure 19. A sketch of the structure and dynamics of the troposphere, stratosphere and mesosphere, as well as aeronomic and electrodynamic phenomena in the lower ionosphere, which can be observed by MST radar and incoherent scatter radar.

10. Realization of an MST Radar on Svalbard

None of such *ST* radar observations outlined above have been done so far at the high latitudes of 80° of Svalbard. In northern Scandinavia and Svalbard several campaigns were performed so far using different kinds of instruments, but *ST* radar[*s*] were not employed on Svalbard. It is noted in several recent publications on the ozone campaigns that investigations of Polar Stratospheric Clouds are impossible without a rather significant initial investment in high-technology sensors such as satellites, mobile lidar systems and dedicated aircraft. The EISCAT Svalbard Radar, together with an appropriate *MST* radar, could become a most appropriate and cost-efficient instrument to support these studies effectively. It is also worth repeating here that more then just one parameter can be measured simultaneously by *ST* radar, including the three-dimensional wind velocity, its small-scale divergence and the covariance of the velocity field, as well as the turbulence intensity and morphology and fine-scale and meso-scale structure of the troposphere and the lower stratosphere.

The present EISCAT *UHF* and *VHF* radars in Tromsø cannot be used for the presented research tasks to study the troposphere and the stratosphere. Firstly because their location is not close to the polar cap, secondly that a frequency of 50 *MHz* would be preferred; thirdly because ground clutter heavily masks almost all the tropospheric and lower stratospheric ranges and the recovery and pulse repetition frequency are not sufficient; and finally because the EISCAT radars cannot be operated continuously, which is deemed essential for most of the outlined climatological studies. Rather than upgrading and modifying the EISCAT radar systems for this purpose, which might be quite expensive, one should aim to add *MST* capabilities to the EISCAT Svalbard Radar in an expansion phase and by adding a separate 50 *MHz* [*M*]*ST* radar system [*Röttger and Tsuda*, 1995].

11. Summary

This article, consisting of a combination of several tutorials and reviews, is supposed to be used as an introduction to radar research of the lower and middle atmosphere in high latitudes. Since there is an overlap or transition region of incoherent and coherent scatter in the mesosphere, which particularly the EISCAT radars can observe, it was tried to describe briefly the differences of these scattering processes. In general, this article is aimed to summarise basics of atmospheric research using the *MST* radars, and possibilities are pointed out how this can be achieved in the high latitudes by combining the new 500 *MHz* EISCAT Svalbard Radar with an *MST* radar to be established on Svalbard.

One regards combinations of radars operating at different frequencies as an essential tool to investigate these dynamical and aeronomical phenomena. The combination of radar observations with other instrumentation such as lidar and

rockets as well as remote sensing from the ground and space will be needed to fully understand the dynamics, structure and aeronomy of the mesosphere, and the dynamics and structure of the stratosphere and troposphere.

Acknowledgements.

The author thanks the editor, Denis Alcaydé, for his encouragement to prepare this article and for his patience to get it finished. He appreciates the numerous useful discussions with many colleagues on the complex phenomenon of scattering and reflection from the middle atmosphere and the techniques applied to study these processes.

12. References:

Adams, G.W., D.P. Edwards, and J.W. Brosnahan, The imaging Doppler interferometer: data analysis, *Radio Sci.*, **20**, 1481-1492, 1985.

Balsley, B.B., W.L. Ecklund, D.A. Carter and P.E. Johnston, The MST radar at Poker Flat, Alaska, *Radio Sci.*, **15**, 213-223, 1980.

Balsley, B.B., R.F. Woodman, M. Sarango, R. Rodriguez, J. Urbina, E. Ragaini, J. Carey, M. Huaman and A. Giraldez, On the lack of southern hemisphere polar mesosphere summer echoes, *J. Geophys. Res.*, **100**, 11685-11693, 1995.

Battan, L.J., Radar observations of the atmosphere, *The University of Chicago Press*, 1973.

Belikovich, V.V., E.A. Benediktov, and G.I. Terina, Diagnostics of the lower ionosphere by the method of resonance scattering of radio waves, *J. Atmos. Terr. Phys.*, **48**, 1247-1253, 1986.

Briggs, B.H., Radar observations of atmospheric winds and turbulence: a comparison of techniques, *J. Atmos. Terr. Phys.*, **42**, 823-833, 1980.

Briggs, B.H., The analysis of spaced sensor records by correlation techniques, *Handbook for MAP*, **13**, ed. R.A. Vincent, 166-186, 1984.

Cho, J.Y.N., and M.C. Kelley, Polar mesosphere summer radar echoes: observations and current theories, Rev. of Geophys., **31**, 243-265, 1993.

Cho, J.Y.N., and J. Röttger, An updated review of polar mesosphere summer echoes: Observation, theory, and their relation to noctilucent clouds and subvisible aerosols, *J. Geophys. Res.*, **102**, 2001-2020, 1997.

Collis P.N. and J. Röttger, Mesospheric studies using the EISCAT UHF and VHF radars: a review of principles and experimental results *J. Atmos. Terr. Phys.*, **52**, 569-584, 1990.

Collis, P.N., M.T. Rietveld, J. Röttger, and W.K. Hocking, Turbulence scattering layers in the middle mesosphere observed by the EISCAT 224 MHz radar, *Radio Sci.*, **27**, 97-107, 1992.

Crochet, M., C. Hanuise, and P. Broche, HF radar studies of two-stream instability during an equatorial counter-electrojet, *J. Geophys. Res.*, **84**, 5223-5233, 1979.

Czechowsky, P., I.M. Reid, R. Rüster and G. Schmidt, *J. Geophys. Res.*, **95**, 5199-5217, 1989.

Czechowsky, P., Principles of wind profilers, in Utilization of UHF/VHF radar wind profiler networks for improving weather forecasting in Europe, *COST*, 74, ed. C. Lafaysse, European Commission EUR 15450 EN, 21-43, 1994.

Doviak, R.J. and D. Zrnic, Doppler radar and weather observations, *Academic Press*, pp.458, 1984.

Ecklund, W.L., and B.B. Balsley, Long-term observations of the arctic mesosphere with the MST radar at Poker Flat, *J. Geophys. Res.*, **86**, 7775, 1981.

Fejer, B.G., and M.C. Kelley, Ionospheric irregularities, Rev. Geophys., **86**, 401-454, 1980.

Franke, S.J., J. Röttger, C. La Hoz, and C.H. Liu, Frequency domain interferometry of polar mesosphere summer echoes with the EISCAT VHF radar, *Radio Sci.*, **27**, 417-428, 1992.

Fritts, D.C., S.A. Smith, B.B. Balsley, and C.R. Philbrick, Evidence for gravity wave saturation and local turbulence production in the summer mesosphere and lower thermosphere during the STATE experiment, *J. Geophys. Res.*, **93**, 7015-7025, 1988.

Gage, K.S., Radar observations of the free atmosphere: Structure and dynamics, in Radar in Meteorology, ed. D. Atlas, Amer. Met. Soc., 534-565, 1990.

Gage, K.S. and B.B. Balsley, On the scattering and reflection mechanism contributing to clear air radar echoes from the troposphere, stratosphere and mesosphere, *Radio Sci.*, **15**, 243-257, 1980.

Gage, K.S., B.B. Balsley, and J.L. Green, Fresnel scattering model for the specular echoes observed by VHF radars, *Radio Sci.*, **16**, 1447-1453, 1981.

Ghebrebrhan, O., and M. Crochet, On full decoding of truncated ranges for ST/MST radar applications, IEEE Transact. Geosc. Remote Sens., **30**, 38-45, 1992.

Goncharov, N.P., M.T. Rietveld, and J. Röttger., Creation of artificial periodic inhomogeneities for studies of the middle atmosphere and lower thermosphere, in Proc. 6. Workshop Techn. Scient. Asp. MST Radar, SCOSTEP, 436-440, 1993.

Gossard, E.E. and R.G. Strauch, Radar observations of clear air and clouds, Elsevier Publ. Comp., 1983.

Greenwald, R.A., The role of coherent radars in ionospheric and magnetospheric research, in Modern Ionospheric Science, eds. H. Kohl, R. Rüster, K. Schlegel, EGS Katlenburg-Lindau, 391-414, 1996

Hagfors, T., Plasma fluctuations excited by charged particle motion and their detection by weak scattering of radio waves, this issue, 1997.

Hanuise, C., and M. Crochet, Multifrequency HF radar studies of plasma instabilities in Africa, *J. Atmos. Terr. Phys.*, **39**, 1097-1101, 1977.

Havnes, O., F. Melandsø, C. La Hoz, T. K. Aslaksen, and T. Hartquist, Charged dust in the Earth's mesopause; effects on radar backscatter, Phys. Scr., **45**, 535-544, 1992.

Hocking, W.K., Measurements of turbulent energy dissipation rates in the middle atmosphere by radar techniques: A review, *Radio Sci.*, **20**, 1403-1422, 1985.

Hocking, W.K., Radar studies of small scale structure in the upper middle atmosphere and lower ionosphere, Adv. Space Res., (1)327-(1)338, 1987.

Hocking, W.K., Recent advances in radar instrumentation and techniques for studies of the mesosphere, stratosphere and troposphere, *Radio Sci.*, in press, 1997.

Hocking, W.K and J. Röttger, Pulse length dependence of radar signal strength for Fresnel scatter, *Radio Sci.*, **18**, 1312-1324, 1983.

Hocking, W.K, S. Fukao, M. Yamamoto, T. Tsuda, and S. Kato, Viscosity waves and thermal conduction waves as a cause of 'specular' reflectors in radar studies of the atmosphere, *Radio Sci.*, **26**, 1281-1303, 1991.

Huang, C.H., E. Kudeki, S.J. Franke, C.H. Liu, and J. Röttger, Brightness distribution of mid-latitude E region echoes detected at the Chung-Li VHF radar, *J. Geophys. Res.*, **100**, 14703-14715, 1995.

Klostermeyer, J., A height- and time-dependent model of polar mesosphere summer echoes, *J. Geophys. Res.*, **102**, 6715-6727, 1997.

Kudeki, E. and G.R. Stitt, Frequency domain interferometry: A high resolution radar technique for studies of atmospheric turbulence, Geophys. Res. lett., **14**, 198-201, 1987.

Kudeki, E., and F. Surucu, Radar interferometric imaging of field-aligned plasma irregularities in the equatorial electrojet, *Geophys. Res. Lett.*, **18**, 41, 1991.

La Hoz, C., J. Röttger and S. J. Franke, Spatial interferometry measurements with the EISCAT VHF radar, *Handbook for MAP*, 28, SCOSTEP Sec., Urbana, IL, 185-191, 1989.

Luce, H., M. Crochet, F. Dalaudier, and C. Sidi, Interpretation of VHF ST radar vertical echoes from in-situ temperature sheet observations, *Radio Sci.*, **30**, 1002-1025, 1995.

Lübken, F.J., G. Lehmacher, T.A. Blix, U.P. Hoppe, E.V. Thrane, J.Y.N. Cho, and W.E. Swartz, First in-situ observations of neutral and plasma fluctuations within a PMSE layer, *Geophys. Res. Lett.*, **20**, 2311-2314, 1993.

Liu, C.H., J. Röttger, G. Dester, S.J. Franke, and C.J. Pan, The oblique spaced antenna method for measuring the atmospheric wind field, J. Atmos. and Oceanic Techn., 8, 247-258, 1991.

Manson, A.H., C.E. Meek, R. Schminder, D. Kürschner, R.R. Clark, H.G. Müller, R.A. Vincent, A. Philips, G.J. Fraser, W. Singer, and E. Kazimirovsky, Tidal winds from the MLT global network during the first LTCS campaign - September 1987, *J. Atmos. Terr. Phys.*, **52**, 175-183, 1989.

Mathews, J., The incoherent scatter as tool for studying the ionospheric D-region, *J. Atmos. Terr. Phys.*, **46**, 975-986, 1984.

Palmer, R.D., R.F. Woodman, S. Fukao, M.F. Larsen, M. Yamamoto, T. Tsuda, and S. Kato, Frequency domain interferometry observations of tropo/stratospheric scattering layers using the MU radar: Description and first results, Geophys. Res. lett., **17**, 2189-2192, 1990.

Palmer, R.D., M.F. Larsen, R.F. Woodman, S. Fukao, M. Yamamoto, T. Tsuda, and S. Kato, VHF radar interferometry measurements of vertical velocity and the effect of tilted refractivity surfaces on standard Doppler measurements, *Radio Sci.*, **26**, 417-427, 1991.

Pan, C.J. and J. Röttger, Structures of polar mesosphere summer echoes observed with the EISCAT VHF radar in the interferometer mode, STEP Handbook, in Proc. 7. Workshop Techn. Scient. Aspects MST radar, SCOSTEP, 252-255, 1996.

Rastogi, P.K., J.D. Mathews, W.P. Ying, and J. Röttger, Simultaneous VHF and UHF radar observations of the mesosphere at Arecibo during a solar flare: a check on the gradient mixing hypothesis, *Radio Sci.*, **23**, 97, 1988.

Reid, G.C., Charge balance at the summer polar mesopause: Ice particles, electrons, and PMSE, in The upper mesosphere and lower thermosphere, Geophys. Monogr. Ser., AGU, 201-207, 1995.

Reinisch, B., Ionosonde, in The Upper Atmosphere, eds. W. Dieminger, G.K. Hartmann, R. Leitinger, Springer Berlin II.3.2.2, 370-381, 1996.

Rietveld, M.T., H. Kohl, H. Kopka, and P. Stubbe, Introduction to ionospheric heating at Tromsø - Experimental overview, *J. Atmos. Terr. Phys.*, **55**, 577-599, 1993.

Röttger, J., Structure and dynamics of the stratosphere and mesosphere revealed by VHF radar observations, Pageoph, **118**, 494-527, 1980.

Röttger, J., The instrumental principles of MST radars and incoherent scatter radars and the configuration of radar system hardware, in *Handbook for MAP*, **30**, 54-113, 1989.

Röttger, J., MST Radar and Incoherent Scatter Radar Contributions to Studying the Middle Atmosphere, *J. Geomagn. Geoelectr.*, **43**, p.563-596, 1991.

Röttger, J., Polar Mesosphere Summer Echoes: Dynamics and Aeronomy of the Meso- sphere, *Adv. Space Res.*, **14**, 9, (9)123-(9)137, 1994a.

Röttger, J., EISCAT stratosphere-troposphere experiment performance, in Proc. 6. Workshop Techn. Scient. Aspects MST Radar, *SCOSTEP*, 340-345, 1994b.

Röttger, J., Middle Atmosphere and Lower Thermosphere Processes at High Latitudes studied with the EISCAT Radars, *J. Atmos. Terr. Phys.*, **56**, 1173-1195, 1994c.

Röttger, J. and C.H. Liu, Partial reflection and scattering of VHF radar signals from the clear atmosphere, *Geophys. Res. Lett.*, **5**, 357-360, 1978.

Röttger, J., and H.M. Ierkic, Postset beam steering and interferometer applications of VHF radars to study winds, waves and turbulence in the lower and middle atmosphere, *Radio Sci.*, **20**, 1461-1480, 1985.

Röttger, J., and M.F. Larsen, UHF/VHF radar techniques for atmospheric research and wind profiler applications, in Radar in Meteorology, *American Met. Soc*., 235-281, 1990.

Röttger, J., M.T. Rietveld, C. La Hoz, T. Hall, M.C. Kelley, and W.E. Swartz, Polar mesosphere summer echoes observed with the EISCAT 933-MHz radar and the CUPRI 46.9-MHz radar, their similarity to 224-MHz radar echoes, and their relation to turbulence and electron density profiles, *Radio Sci.*, **25**, 671-687, 1990.

Röttger, J., C.H. Liu, C.J. Pan, and S.Y. Su, Characteristics of lightning echoes observed with VHF radar, *Radio Sci.*, **30**, 1085-1097, 1995.

Röttger, J. and T. Tsuda, Studies of the polar middle and lower atmosphere by an MST radar on Svalbard, *J. geomag. geoelectr*., 929-942, 1995.

Röttger, J. and R.A. Vincent, Observations of the middle atmosphere and lower thermosphere by radars, in The Upper Atmosphere, eds. W. Dieminger, G.K. Hartmann, R. Leitinger, *Springer Berlin II.3.2.1*, 327-370, 1996.

Rüster, R., and J. Klostermeyer, Propagation of turbulence structures detected by VHF radar, *J. Atmos. Terr. Phys.*, **49**, 743, 1987.

Roper, R.G., MWR meteor wind radars, *Handbook for MAP*, 13, ed. R.A. Vincent, 124-134, 1984.

Sato, T., T. Tsuda, S. Kato, S. Morimoto, S. Fukao, and I. Kimura, High resolution MST observations of turbulence using MU radar, *Radio Sci.*, **20**, 1452, 1985.

Sauvageot, H., Radar Meteorology, *Artech House, Boston*, 1992.

Thomas, G.E., Mesospheric clouds and the physics of the mesopause region, *Rev. Geophys*., **29**, 553-575, 1991.

Thomas, L., I. Astin, and I.T. Prichard, The characteristics of VHF echoes from the summer mesopause at mid-latitudes, *J. Atmos. Terr. Phys.*, **54**, 969-977, 1992.

Turunen, E., Incoherent scatter radar contributions to high-latitude D-region aeronomy, *J. Atmos. Terr. Phys.*, **58**, 707-725, 1996.

van Baelen, J.S., T. Tsuda, A.D. Richmond, S.K. Avery, S. Kato, S. Fukao, and M. Yamamoto, Comparison of VHF Doppler beam swinging and spaced antenna observations with the MU radar: First results, *Radio Sci.*, **25**, 629-640, 1990.

van Baelen, J.S., Radar interferometry technique: Three-dimensional wind measurement theory, *Radio Sci.*, **26**, 1209-1218, 1991.

Vincent, R.A., and I.M. Reid, HF Doppler measurements of mesospheric gravity wave momentum flux, *J. Atmos. Sci*., **40**, 1321-1333, 1983.

Wannberg, G., The G2-system and general purpose alternating code experiments for EISCAT, *J. Atmos. Terr. Phys.*, **55**, 543-557, 1993.

Williams, E.R., V. Mazur, and S.G. Geotis, Lightning investigations with radar, in Radar in Meteorology, ed. D. Atlas, *Amer. Met. Soc*., 143-150, 1990.

Woodman, R.F., and A. Guillen, Radar observations of winds and turbulence in the stratosphere and mesosphere, *J. Atmos. Sci*., **31**, 493-505, 1974.

Woodman, R.F., High altitude resolution stratospheric measurements with the Arecibo 430-MHz radar, *Radio Sci.*, **15**, 417-422, 1980a.

Woodman, R.F., High altitude resolution stratospheric measurements with the Arecibo 2380-MHz radar, *Radio Sci.*, **15**, 423-430, 1980a.

Woodman, R.F., and Y.H. Chu, Aspect sensitivity measurements of VHF backscatter made with the Chung-Li radar: plausible mechanisms, *Radio Sci.*, **24**, 113-125, 1989.